UNIVERSITY OF SHEFFIELD
Department of Civil and Structural Engineering

SIMULATION OF STEEL/CONCRETE COMPOSITE STRUCTURES IN FIRE

By Paul Stuart Rose

29 November, 1999

A thesis submitted in partial fulfilment of the requirements for the Degree of Doctor of Philosophy.

FOR MY WIFE, HELEN

ABSTRACT

A finite element code has been developed at the University of Sheffield to simulate the structural response of steel and composite framed buildings subjected to fire. The steel skeleton is represented using two-noded line elements, the steel-to-steel connections using spring elements and the flooring system by isotropic flat shell elements. Structures are therefore considered as a complete entity, allowing a more realistic prediction of structural behaviour at elevated temperature.

A series of numerical simulations of fire tests carried out on the full-scale, eight-storey composite frame at the B.R.E. laboratory at Cardington in 1995 and 1996 have been conducted. These tests have been subject to a number of significant parametric studies including slab thickness and secondary beam connection strength and stiffness.

The concrete floor slab element has also been extended to a layered flat shell element allowing the inclusion of material non-linearities, thermal bowing, thermal degradation, anisotropic properties and a more advanced cracking model.

Using the new concrete floor slab element the Cardington fire tests have been simulated in detail, to further understanding of the structural reaction in fire. Another series of parametric studies have been conducted considering again the thickness of the floor slab, the effect of the slab temperature gradient, the compressive strength, tensile strength and load ratios. These have all been compared to results from the Cardington fire tests.

Current design methods based on isolated element design are considered by comparing the results of analyses in which the concrete floor is either included as a continuous slab in an extensive subframe, or is treated simply as forming the flanges of composite beams in a three-dimensional skeleton. These examples show clearly the effects of membrane and bridging actions of the continuous floor slab.

The implications for future design developments are discussed with particular reference to the parametric studies conducted.

TABLE OF CONTENTS

LIST OF FIGURES

CHAPTER 1

CHAPTER 2

CHAPTER 3

CHAPTER 4

CHAPTER 5

CHAPTER 6

CHAPTER 7

LIST OF TABLES

CHAPTER 2

CHAPTER 5

NOTATION

Only general notations used in this thesis are presented here. Symbols that have been only used once and are of a more specific nature have been explained when they arise in the text.

A	Arbitrary point.
B	Strain-displacement matrix.
C	Generalised stress-strain matrix.
C_s	Specific heat of steel.
E_{20}	Elastic modulus of the material at 20°C.
E_t	Tangent modulus of the material.
f	Shear force.
F	Vector of externally applied nodal force.
G	Shear modulus.
h	Shape functions
H_w	Matrix of shape functions.
I_{yy}, I_{xx}...etc	Second moment of area.
J	Jacobian operator.
K	Local stiffness.
[K]	Tangent stiffness matrix.
k_s	Thermal conductivity of steel.
l	Member length.
M_f	Applied moment at the fire limit state.
M_p	Plastic moment.
M_{cr}	Elastic critical stress.
m, n...etc	Stress resultants.
O	Arbitrary point on the centroidal axis
P	Elastic critical load.
P_y	Yield stress.
{Q}	External nodal forces (Local co-ordinates).
{q}	Nodal displacements (Local co-ordinates).
R	External nodal forces (Global co-ordinates).
R	Load ratio.

r_1, r_2...etc	Sampling points.
$\{\delta\}$	Vector of displacements at nodal positions.
$[I]$	Identity matrix.
X, Y, Z	Global co-ordinates.
x, y, z	Local co-ordinates.
W	Virtual work.
α	Weighting factor.
Δ	Prefixed to other term, denotes an increment.
δ	Prefixed to other term, denotes virtual variation.
∂	Denotes partial differentiation.
ε	Strain.
σ, τ	Stress.
σ_{20}	Stress at 20°C.
θ	Rotation.
γ	Shear strains.
λ	Slenderness ratio.
Π	Potential energy.
$\{\ \}$	Denotes a column vector.
$\langle\ \rangle$	Denotes a row vector.
$[\ ]$	Denotes a matrix.
$[\ ]^{-1}$	Denotes a matrix inverse.
$\|\ \|_2$	Denotes a norm vector.
Σ	Denotes a summation.
d	Denotes ordinary differentiation.
$'$	Denotes differentiation with respect to a single argument.
$''$	Denotes second derivative with respect to a single argument.

ACKNOWLEDGEMENT

The author wishes to express his thanks to Dr Ian Burgess and Professor Roger Plank for their supervision, advice and encouragement throughout this research project.

Support from the European Coal and Steel Community from October 1995 to September 1998 is gratefully acknowledged.

DECLARATION

Except where specific reference has been made to the work of others, this thesis is the result of my own work. No part of it has been submitted to any University for a degree, diploma, or any other qualification.

Paul Stuart Rose

1. INTRODUCTION

Fires happen on a daily basis, forcing the average person to run a risk of 1:1500 of being involved in a fatal building fire accident [1]. Of fatalities in building fires, 76% occur in domestic buildings such as hotels, offices and shops [1]. Fire safety in buildings is essential to ensure safety of life and to minimise material and financial losses to both the occupants and associated organisations such as insurance companies (it was estimated that the cost of fire to UK business in 1983 was over £900 million per year [2]). Smoke detection equipment and reduced travel distances to fire-protected stairs are classed as typical safety measures. To protect property, active measures using sprinkler systems, or passive measures such as structural protection and containment are commonly used. The Building Regulations [3] are used to control the fire resistance that a building must attain, on the basis that,

> *"The building shall be designed and constructed so that, in the event of fire, its stability will be maintained for a reasonable period."*

The Building Regulations [3] fire resistance criterion is based not just on the minimum evacuation time of the building, but concerns also for the safety of fire fighters, risk of structural collapse and fire spread. Time periods are classified as 0.5, 1 and 2 hours and are dependent on type of building, height, floor area and cubic capacity of the building or compartment.

Steel is a major construction material in the UK, being used in an estimated 57% of multi-storey buildings and between 90 and 95% of single-storey factory and warehouse structures during the 1991 to 1992 period [4]. Steel has become so popular of late, because of its fast erection sequences and lighter structures, allowing longer spans and smaller foundations. Steel does have a disadvantage compared to other structural materials in that it has high thermal conductivity, therefore rising in temperature and losing strength and stiffness rapidly in fire. The steel industry has recognised this deficiency and has invested much research into the use of protective materials and design methods with the aim of reducing protective material costs and the impact of protection on the construction programme.

1.1. THE GROWTH OF A FIRE

In order to gain an understanding of fire resistance of structural elements, it is essential to form some knowledge on the growth of fire. The growth and decay of fire is complex because it is dependent on fuel load and the surrounding environment. It may be simplified into the following phases, shown schematically in Figure 1-01.

1. *The Growth Period* ~ The reason for fire growth is the progressive ignition of materials, usually from a small local source. The feedback of generated heat results in further generation of flames. A sufficiently high temperature of the gases emitted from the fuel must be attained during the ignition phase at which point, provided a ready supply of oxygen is available, the fire becomes self-sustaining. This point at which the fire reaches ignition temperature is called the 'flash point' or 'ignition temperature'.

   After ignition has been established, the fire spreads from the ignition source. In the early stages, interaction with the compartment will be negligible due to their relative sizes, and the fire behaviour will be similar to a fire in the open. Once the fire becomes established at a local level, it will continue to grow provided fuel and oxygen are available. Hot gases begin to rise to the ceiling and to form a layer, causing both the ceiling and walls to heat up and to re-radiate the heat. The fire at this stage may be referred to as a compartment fire, as the geometry and physical properties of the compartment begin to influence the fire. Ventilation of the compartment is significant in controlling the supply of oxygen, and hence the rate of fire growth; therefore if a door is opened or the windows are broken the rate of growth may change dramatically. The temperature within the compartment is now increased through radiation from the walls and ceiling, with fuel remote from the ignition site increasing in temperature. The fire growth continues until the fuel vapour within the compartment reaches ignition temperature, at which point there is a sudden transition from a growing fire to a fully developed fire, which is known as 'flashover'.

2. *Steady State Combustion* ~ The fire severity from this point becomes totally dependent upon the ventilation of the compartment. It is usually openings

such as windows that control the rate of burning of the fire. Provided fuel is available, the fire will continue to burn at a steady rate until it begins to run out of fuel and the decay stage is entered.

3. *Decay* ~ As the fuel supply decreases, the fire reduces gradually in severity and will eventually die.

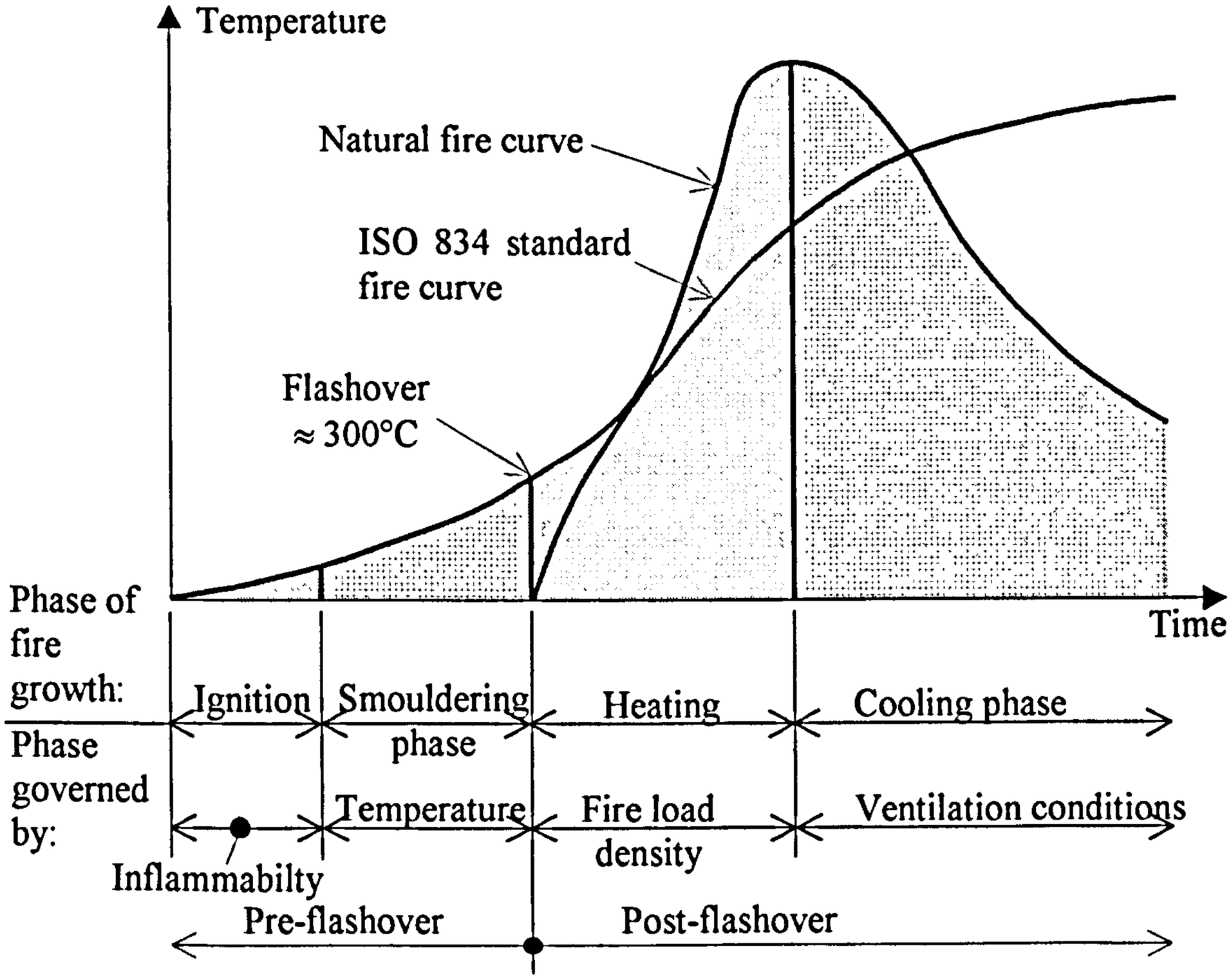

Figure 1-01. The development of an uncontrolled fire and ISO 834 standard fire curve

1.2. FIRE TESTING

To define the growth of a fire for experimental purposes is problematic, as no two fires are ever alike since the surrounding environment influences the growth and decay of the fire. For this reason, a standard rate of heating assumed to vary with time is given in BS 476: Part 20 [5] and the International Standard ISO 834 [6], which is given by

$$T = 20 + 345\log_{10}(8t + 1) \qquad 1\text{-}01$$

where

T is the furnace temperature (°C),

T_0 is the ambient temperature prior to testing,

t is the test time (minutes).

As Figure 1-01 shows, the standard fire curve does not follow the pattern of a natural fire as it neglects the growth phase prior to flashover and the decay phase. Other factors that affect the rate of growth of a fire include the size and nature of the fire load, the degree of ventilation and the size and shape of the compartment. However, the use of the standard curve allows comparison of results between different fire tests. Three criteria are required to be met during a fire test, being insulation, integrity and load-bearing capacity. Insulation and integrity are predominantly dealt with by non-structural fire protection materials and are therefore not considered here. For load-bearing beams the structure is considered to have failed when either the deflection rate reaches $L^2/9000d$ (where L is the beam span and d is the beam depth) for deflections that are greater than $L/30$, or when a maximum deflection of $L/20$ is reached. A column is considered to have failed when the applied load can no longer be supported. These definitions of failure are based on BS 476: Part 21 [7]. These procedures of testing raise a number of questions concerning the interpretation of results and the limitations of standard tests; for example

1. Member behaviour subjected to the standard fire curve may be different from other fire scenarios encountered.

2. It may not be justifiable to consider an isolated member if the test is to model a beam within a continuous structure subject to restraint from surrounding areas.

3. The cost of tests is extremely high, so that the effect of the member's cross-sectional size, span (which is controlled by the furnace size), restraint and structural configuration cannot economically be investigated in full.

Figures 1-02 and 1-03 show schematic column and beam testing facilities.

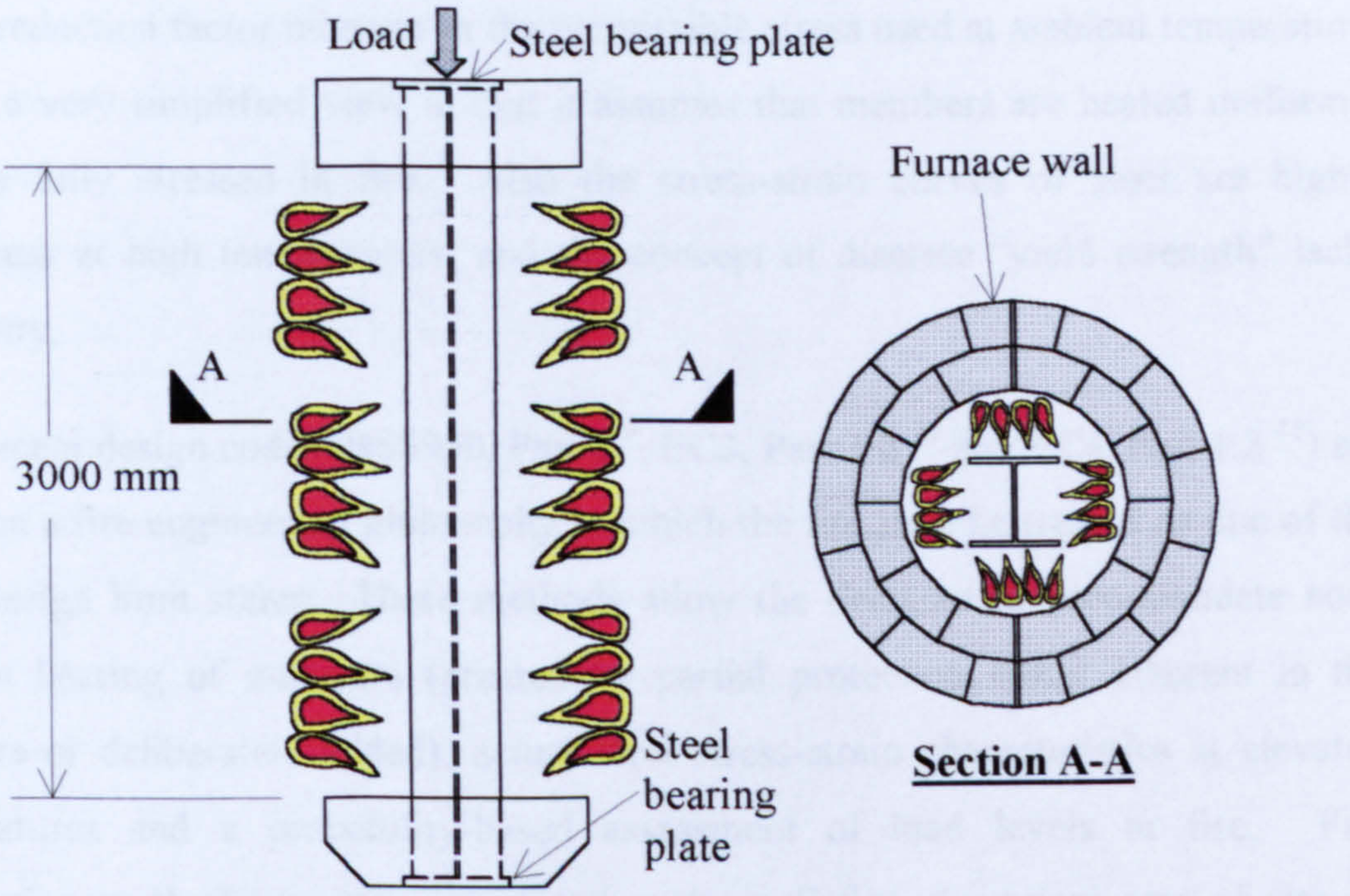

Figure 1-02. Typical test arrangement for simple columns

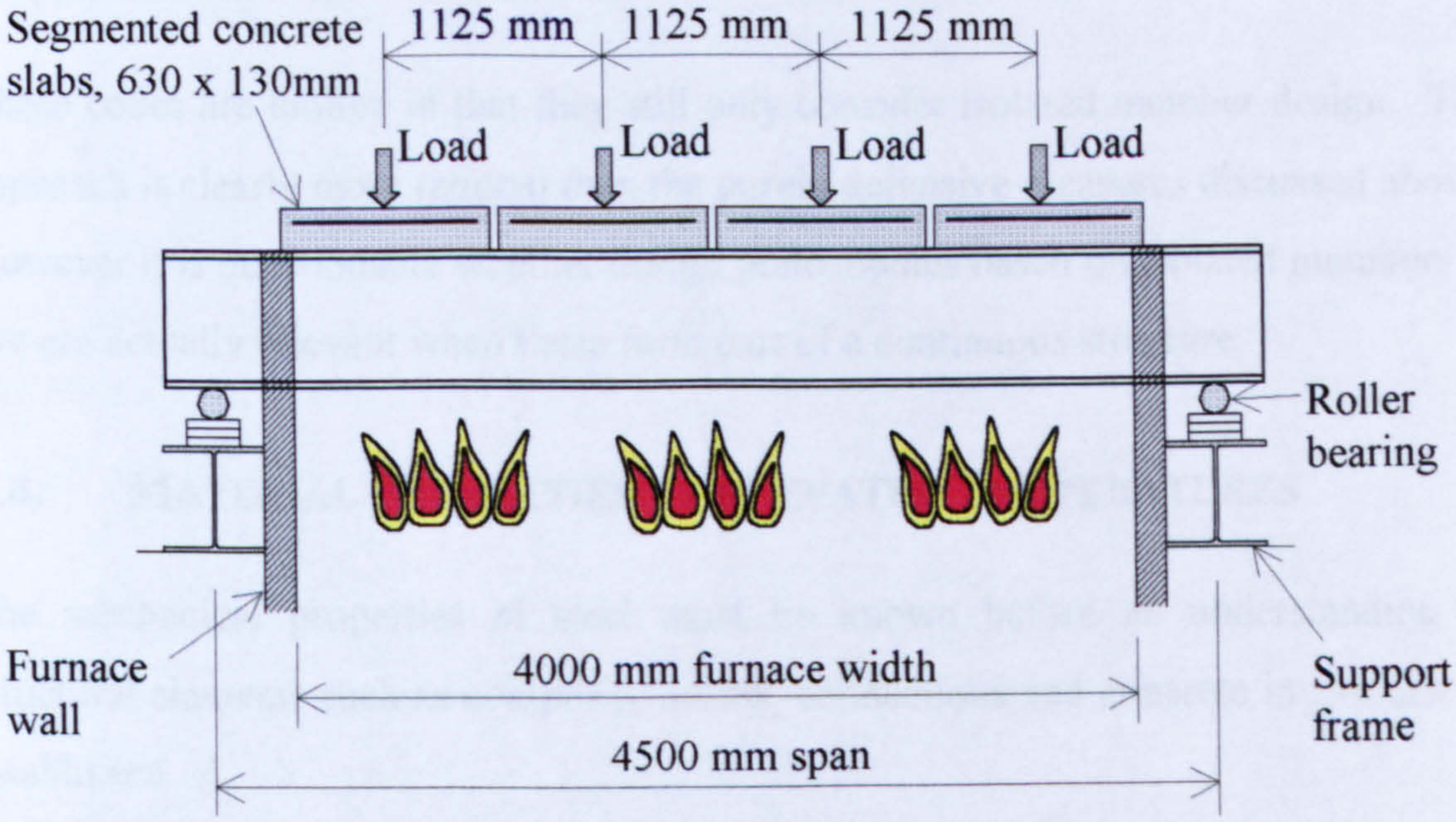

Figure 1-03. Typical test arrangement for simple beams

1.3. REVIEW OF CURRENT FIRE DESIGN PHILOSOPHIES

An early philosophy of fire engineering used in permissible-stress design codes was that passive protection (in the form of insulation) should be applied to limit the steel temperature to a maximum permitted value of approximately 550°C at the end of the required fire resistance period. This method fits well with permissible-stress design codes such as BS449 [8]. The passive method is based on the assumption that the yield strength of steel has been reduced at this temperature by a factor that is equal to the

design reduction factor inherent in the permissible stress used at ambient temperature. This is a very simplified view in that it assumes that members are heated uniformly and are fully stressed in fire. Also the stress-strain curves of steel are highly curvilinear at high temperatures, and the concept of discrete "yield strength" lacks credibility.

More recent design codes (BS5950, Part 8 [9], EC3, Part 1.2 [10] and EC4, Part 1.2 [11]) are based on a fire engineering philosophy in which the fire may be treated as one of the basic design limit states. These methods allow the designer to accommodate non-uniform heating of members (created by partial protection either inherent in the structure or deliberately added), actual steel stress-strain characteristics at elevated temperatures and a probability-based assessment of load levels in fire. Fire engineering methods are also concerned with predicting the actual rate of rise of temperature within the steel members.

These codes are limited in that they still only consider isolated member design. The approach is clearly more rational than the purely defensive measures discussed above. However it is questionable whether design philosophies based on isolated members in fire are actually relevant when these form part of a continuous structure.

1.4. MATERIAL PROPERTIES AT ELEVATED TEMPERATURES

The mechanical properties of steel must be known before an understanding of structural elements such as composite beams, connections and concrete in fire can be established.

1.4.1. THERMAL PROPERTIES OF STEEL

The most important mechanical properties of steel are strength (yield stress), stiffness (elastic modulus) and thermal expansion coefficient (α).

The stress-strain behaviour of steel at elevated temperatures is highly dependent on the rate of heating, due to the onset of creep at temperatures exceeding 450°C (creep being defined as a continuous time-dependent deformation under constant load and constant temperature). Making the assumption of a linear heating rate up to a limiting temperature of 600°C, and failure times of 30 to 120 minutes, practical heating rates

may be defined as 5°C/minute for well-insulated sections and 20°C/minute for exposed sections (Lawson and Newman) [12]. Therefore, if the heating rates of small-scale tests are kept between these limits the results obtained should be representative of the behaviour of steel in large-scale tests. The stress-strain characteristics of steel may be established using either of two methods:

- Isothermal (steady state) tests, in which a constant temperature is applied to the tensile test specimen. The specimen is then loaded to induce strain at a steady rate that will produce the stress-strain curve for a given temperature. Traditionally, isothermal tests have been used for mechanical engineering applications.

- Anisothermal (transient) tests, in which a constant load is applied to the tensile test specimen and then the temperature is increased. The resulting strains are measured, with the effect of thermal strains being deducted after obtaining results from unloaded specimens subjected to the same temperature conditions. Stress-strain curves at particular temperatures are obtained by interpolation from a family of curves at different stresses.

A review of both types of test has been conducted by Kirby and Preston [13], who conclude that anisothermal tests indicate lower strengths but that they can be claimed to be more realistic.

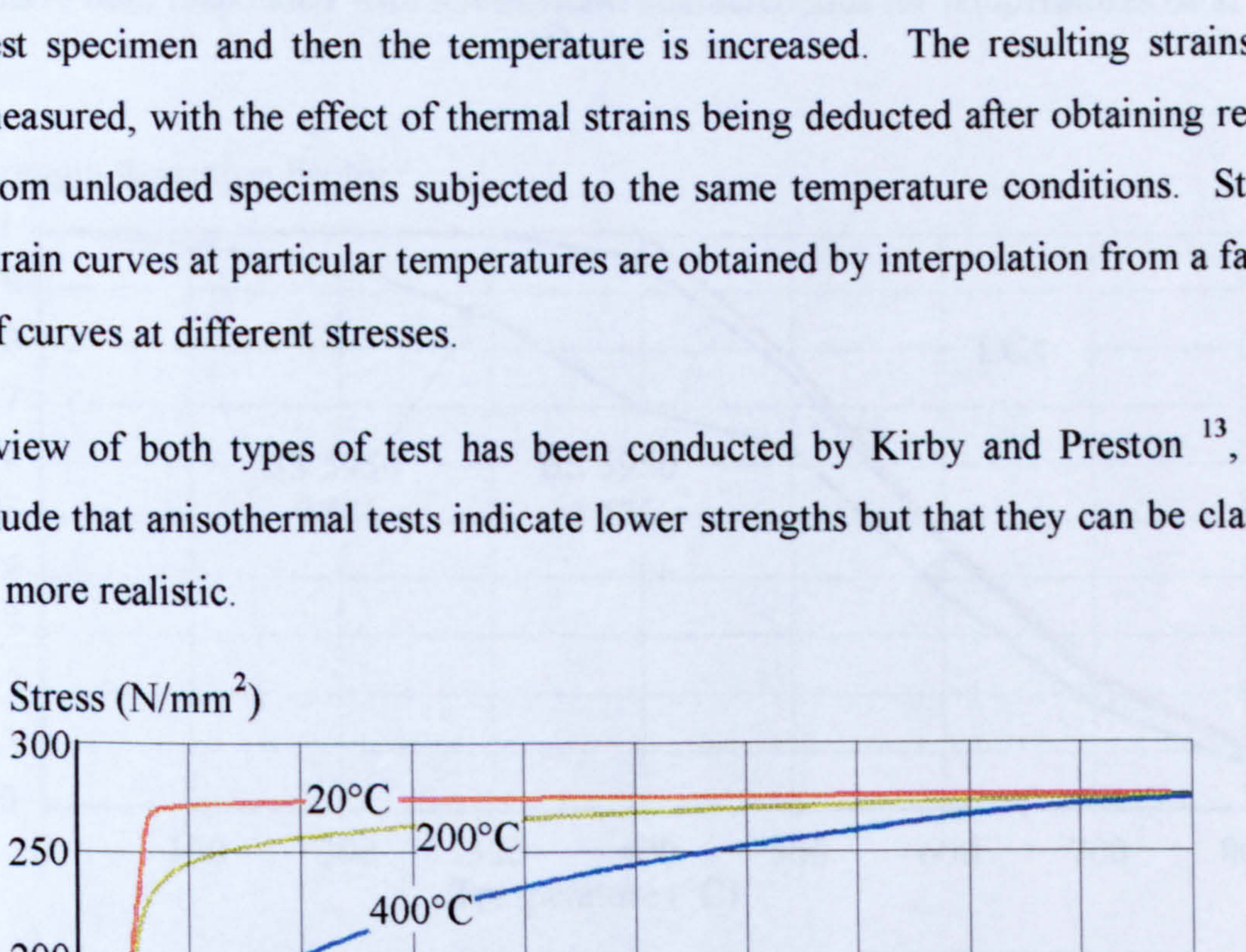

Figure 1-04. Ramberg-Osgood stress-strain diagram for grade 43 Steel with 275N/mm² yield stress

British Steel [12] conducted a series of anisothermal tests to obtain the family of stress-strain curves for Grade 43 steel which are embodied within BS5950, Part 8 [9]. These are shown in Figure 1-04. It may be assumed that the effect of creep is implicitly accounted for in the stress-strain characteristics.

Traditionally, assumptions have been made that critical conditions would normally be reached at a temperature lower than 600°C. Thus investigations of the mechanical properties of steel have normally been restricted to a maximum of 600°C. Recently, advances have been made in the understanding of structural response to fire, leading to the realisation that structures can survive steel temperatures beyond 600°C. This has called for the range of temperatures to be reconsidered, and BS5950, EC3 and EC4 have both responded with stress-strain characteristics for temperatures of at least 800°C.

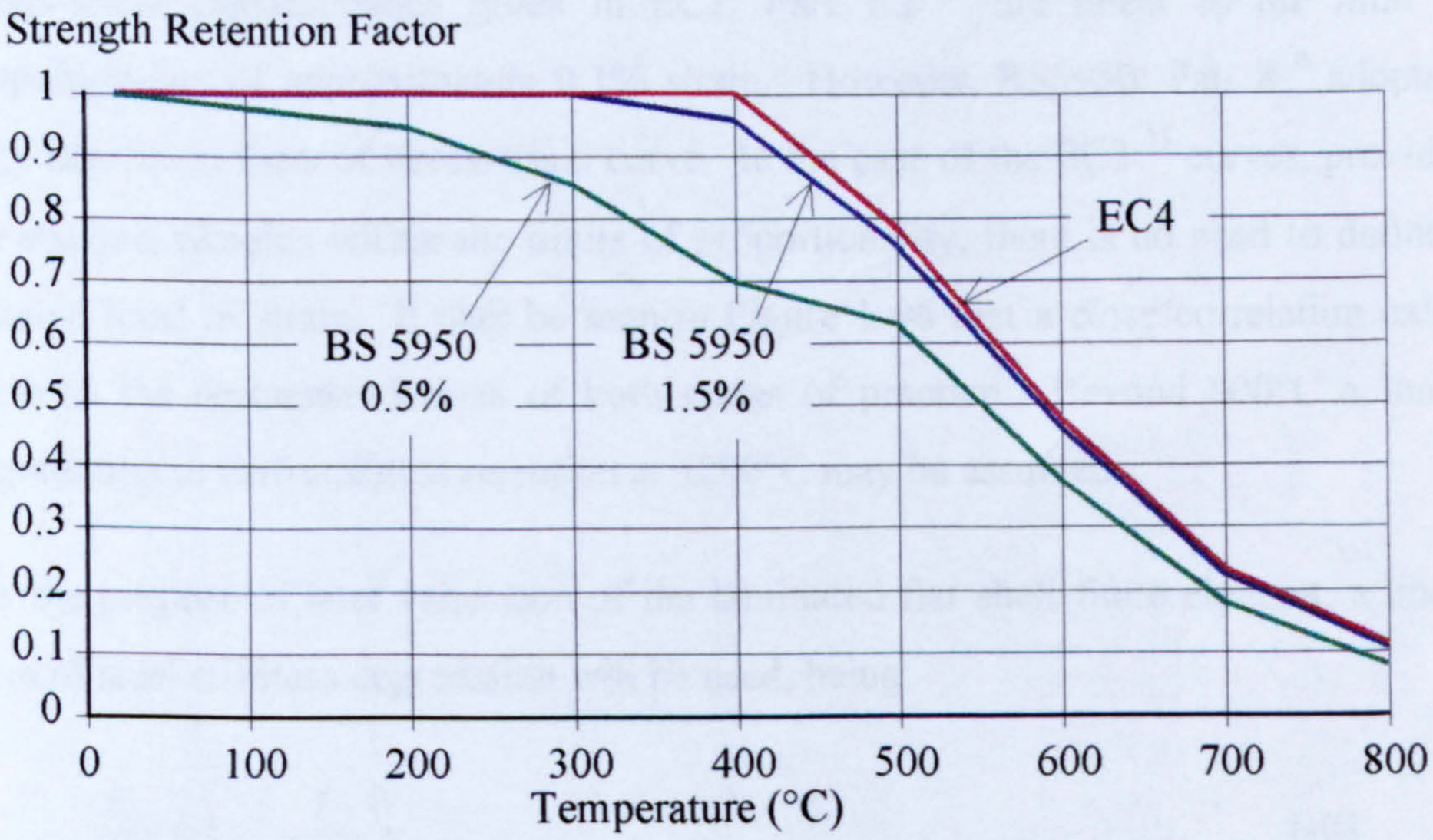

Figure 1-05. Degradation of steel strength with temperature

Steel begins to lose strength (yield stress) at temperatures above 300°C, continuing to weaken to approximately 10% of its original strength at 800°C. The degradation of this small residual strength then continues at a slower rate until melting begins at approximately 1500°C. The strain value at which the residual strength of steel should be measured when strength reduction factors are specified in the design codes is questionable. In this context, the strength reduction factor is defined as the residual strength of steel at a particular temperature, relative to its basic yield strength at room temperature. At ambient temperatures, mild steels have a yield stress that is defined

as the value consistent with a yield plateau. At elevated temperatures there is a gradual increase in stress with increasing strain. BS5950: Part 8 [9] adopts a strain limit of 1.5% for beams and 0.5% for columns, whereas EC3: Part 1.2 [11] uses a strain limit of 2.0% for all members. These strength reduction factors are shown in Figure 1-05.

Beyond 800°C, a linear steel degradation to zero strength retention at 1200°C may be assumed.

The stiffness of steel is defined by its elastic modulus, which is the tangent of the stress-strain curve at zero stress. It is known that increasing temperatures cause the elastic modulus of steel to deteriorate. As the stress-strain curves are curvilinear, it is difficult to define a consistent proof strain at which to assess the elastic modulus of structural steels at elevated temperatures.

Stress-strain characteristics given in EC3: Part 1.2 [11] are linear to the limit of proportionality of approximately 0.1% strain. However, BS5950: Part 8 [9] adopts a fully non-linear form of stress-strain curve. In the case of the EC3 [11] curves, provided the analysis remains within the limits of proportionality, there is no need to define a suitable level of strain. It may be seen in Figure 1-06 that a close correlation exists between the recommendations of both codes of practice. Beyond 800°C a linear degradation to zero stiffness retention at 1200°C may be assumed.

For the purpose of later validation of the laminated flat shell finite element, a linear form of steel stiffness degradation will be used, being:

$$\frac{E_T}{E_{20}} = 1 - \left(\frac{T}{1200}\right) \qquad 1\text{-}01$$

where,

T is the specified temperature,

E_T is the elastic modulus at the specified temperature,

E_{20} is the elastic modulus at the ambient temperature.

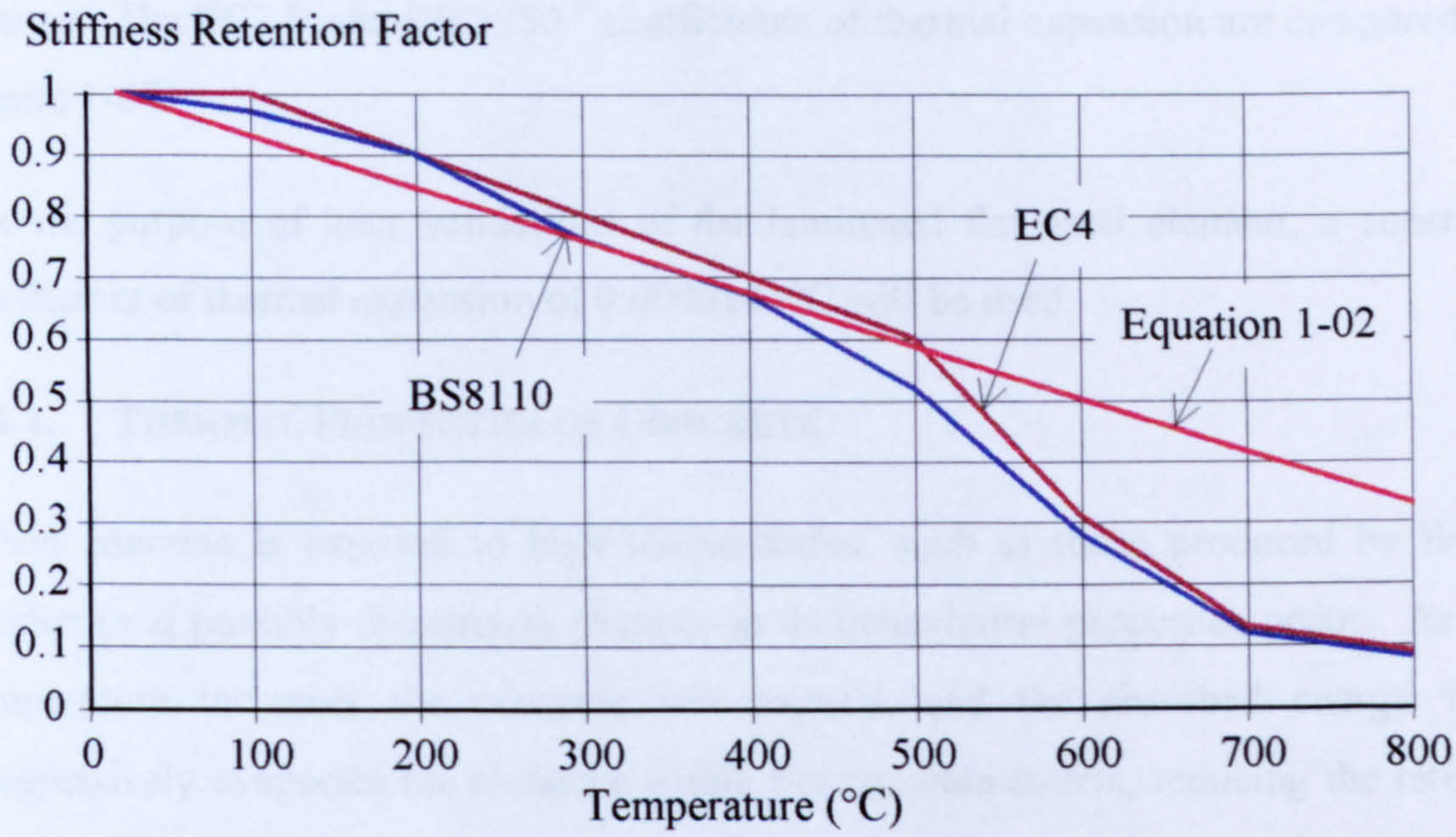

Figure 1-06. Degradation of steel stiffness with temperature

The thermal expansion of steel becomes significant at elevated temperatures. The coefficient of thermal expansion, α, for steel is typically assumed to be 12×10^{-6}/°C at low temperatures, increasing to 14×10^{-6}/°C at 600°C. At approximately 720°C, steel undergoes a phase change, producing a reduction in the rate of thermal expansion as energy is absorbed and the material adopts a denser internal structure.

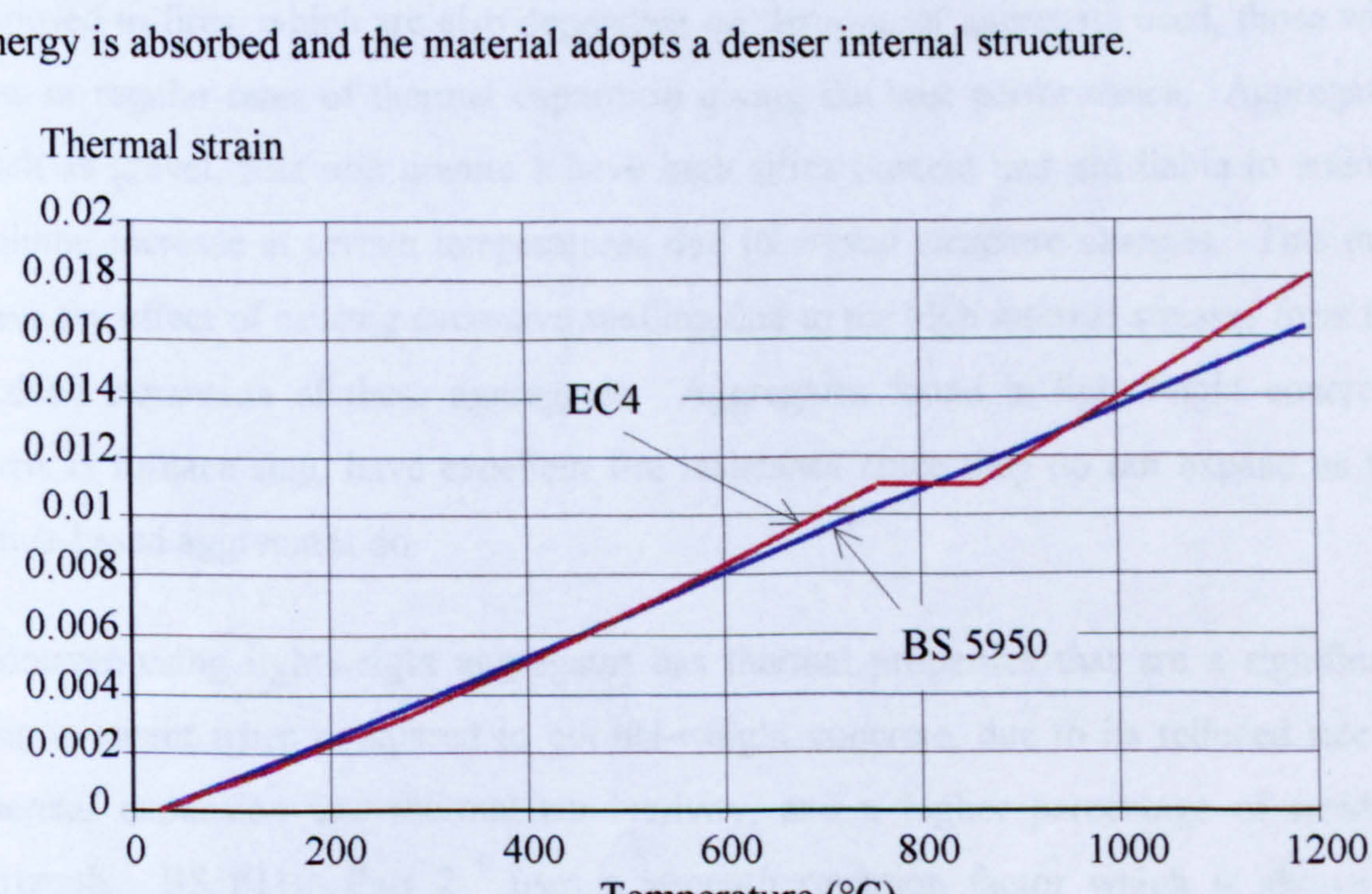

Figure 1-07. Steel thermal strain

In BS5950: Part 8[9], the assumption is made that the linear coefficient of thermal expansion continues with no account taken of the phase change and the consequent behaviour. EC3: Part 1.2 [11] uses a tri-linear relationship to account for this phase

change. The EC3 [11] and BS 5950 [9] coefficients of thermal expansion are compared in Figure 1-07.

For the purpose of later validations of the laminated flat shell element, a constant coefficient of thermal expansion of 0.000014 /°C will be used.

1.4.2. THERMAL PROPERTIES OF CONCRETE

When concrete is exposed to high temperatures, such as those produced by fires, sudden (and possibly disastrous) changes in its behavioural properties occur. As its temperature increases the concrete will expand, and the absorbed energy will progressively evaporate the moisture within the concrete matrix, reducing the rate of temperature increase. This loss of moisture will also cause shrinkage of the concrete, offsetting its rate of thermal expansion. Concrete has a low thermal conductivity, and thus a rise in the temperature of its surface will be transferred slowly throughout the section.

Different types of concrete possess different mechanical and thermal properties when exposed to fires, which are also dependent on the type of aggregate used, those with low or regular rates of thermal expansion giving the best performance. Aggregates such as gravel, flint and granite a have high silica content and are liable to sudden volume increase at certain temperatures due to crystal structure changes. This may have the effect of causing excessive spalling due to the high internal stresses from the sudden expansion of these aggregates. Aggregates found in lightweight concrete, such as furnace slag, have excellent fire resistance since they do not expand as the silica-based aggregates do.

Concrete using lightweight aggregates has thermal properties that are a significant improvement when compared to normal-weight concrete, due to its reduced rate of thermal expansion and thermal conductivity, and a higher percentage of residual strength. BS 8110: Part 2 [9] uses a strength retention factor which is shown in Figure 1-08, and this is compared to EC4: Part 1.2 [11].

Again the coefficient of thermal expansion for concrete is highly dependent on its mineralogical composition. If the aggregate is of a flint or quartzite type, producing normal-weight concrete, the coefficient of thermal expansion is greater than that due

to the lightweight aggregates. Figure 1-09 shows the variation of thermal expansion for both BS8110: Part 2 [9] and EC4: Part 1.2 [11]. When validating the laminated flat shell finite element, a coefficient of thermal expansion of 0.00001 /°C will be used.

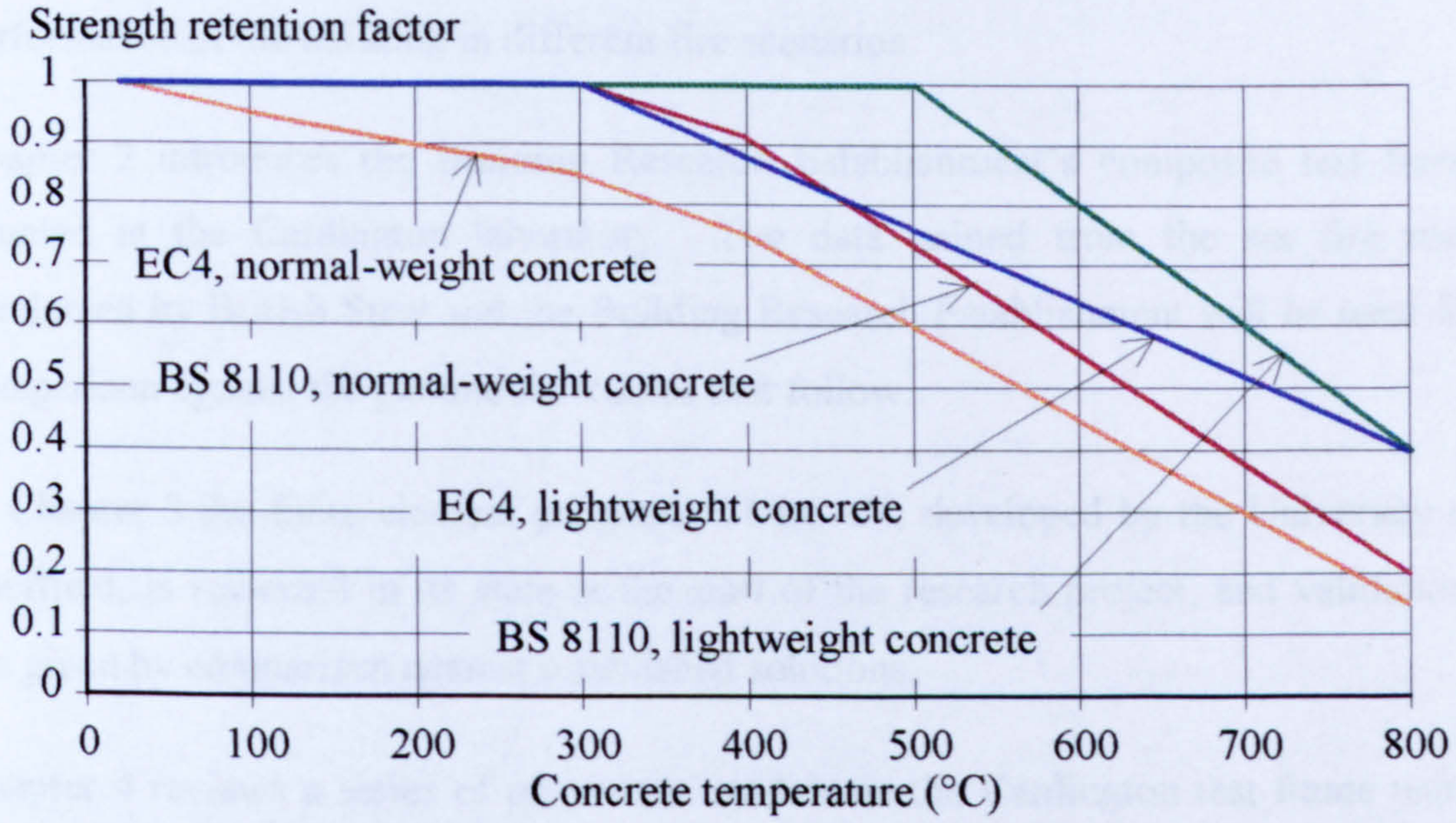

Figure 1-08. Strength retention factors of normal-weight and lightweight concrete at elevated temperatures.

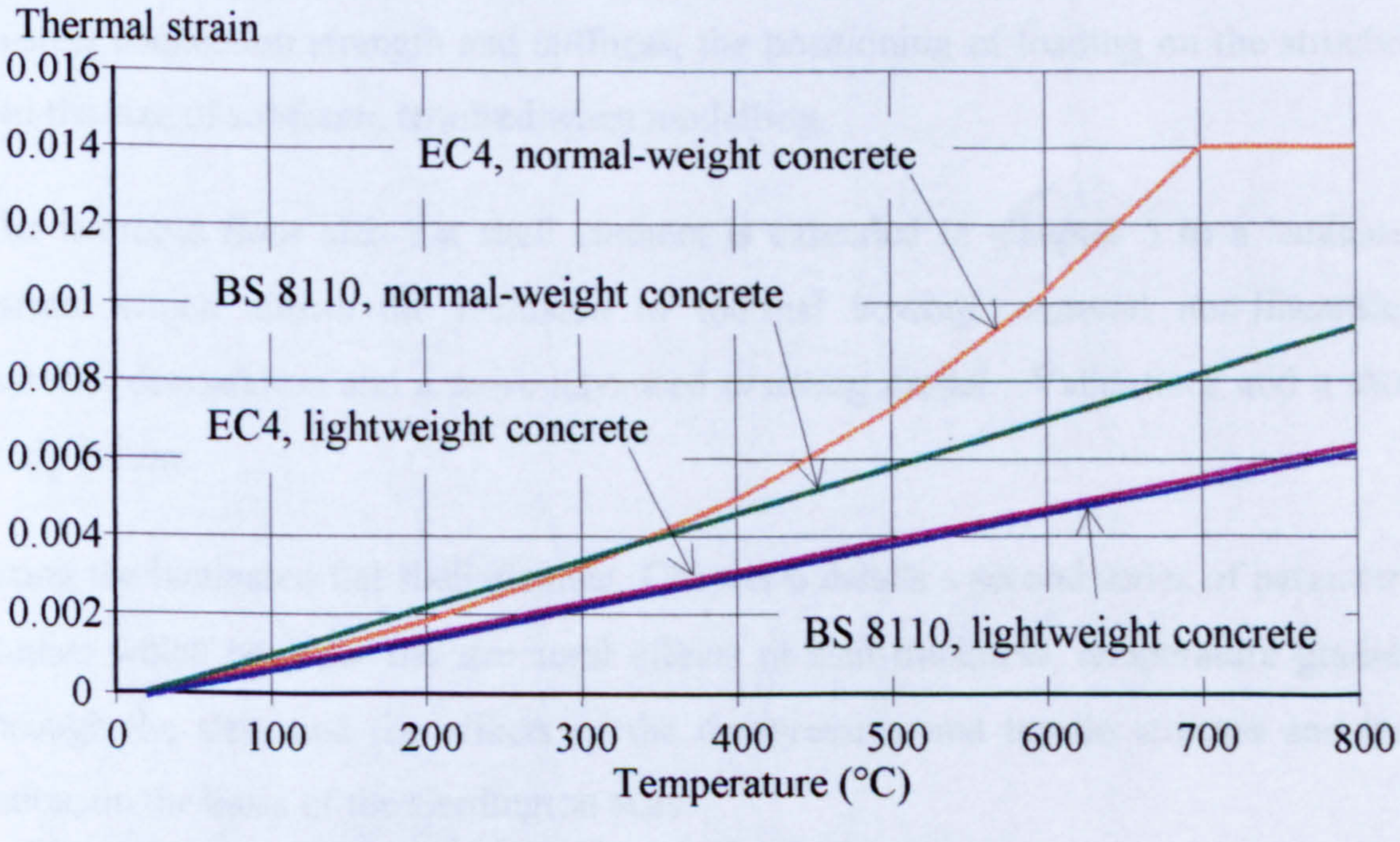

Figure 1-09. Thermal elongation of normal-weight and lightweight concrete at elevated temperatures

1.5. SCOPE AND LAYOUT OF RESEARCH

The primary aim of the present research is to investigate the effect of a fire on whole-structure behaviour and the predominant parameters that affect the structural performance of the building in different fire scenarios.

Chapter 2 introduces the Building Research Establishment's composite test frame situated at the Cardington laboratory. The data gained from the six fire tests conducted by British Steel and the Building Research Establishment will be used for comparison against the parametric studies that follow.

In Chapter 3 the finite element program, VULCAN, developed by the University of Sheffield, is reviewed in its state at the start of the research project, and validations are given by comparison against established solutions.

Chapter 4 reviews a series of parametric studies on the Cardington test frame using the isotropic flat shell element of Chapter 3 to simulate the composite floor slab. The parametric studies concern variation of the floor slab thickness, the influence of steel-to-steel connection strength and stiffness, the positioning of loading on the structure and the size of subframe required when modelling.

The isotropic floor slab flat shell element is extended in Chapter 5 to a laminated variant which allows the inclusion of thermal bowing, material non-linearities, material degradation and a more advanced cracking model. Validations and a short study follow.

Using the laminated flat shell element, Chapter 6 details a second series of parametric studies which consider the structural effects of slab thickness, temperature gradient through the slab, and the effects of the compressive and tensile stresses and load ratios, on the basis of the Cardington tests.

In Chapter 7 a qualitative analysis of the Cardington parametric studies is undertaken with particular reference to Chapters 4 and 6.

Finally, in Chapter 8 general conclusions are drawn and suggestions for further work are presented.

2 THE CARDINGTON TEST FRAME

Since the mid-eighteenth century, engineers have realised the need for large-scale fire tests to ensure that a fire is confined to the room of origin. Some tests were conducted using rather unorthodox methods such as David Hartley's test of 1776 in Putney Heath [2], where he stayed on the upper floor of a house, the floor of which had been protected with metal plates, with a fire burning in the room below. Fortunately, David Hartley remained unharmed.

Current fire tests are far safer than those of 1776 as many standard test procedures based on past experiences are now in circulation [14]. Assessment of the fire resistance of members relies heavily on the testing of isolated members under standard test procedures [14] as specified in BS 476:Part 20 [7] and ISO 834 [6]. The emphasis on testing isolated members means that the action of whole buildings in fire is not fully understood. This however was addressed in the concept of the Cardington test frame, in which whole building action in loading, vibration, fire and explosions was to be tested.

A full-scale, eight-storey building, of composite steel/concrete construction was erected at the Large Building Test Facility at the Cardington laboratory of BRE [15]. With a footprint of 45m by 21m and a total height of 35m, this structure was designed and built to resemble a typical modern city centre office block. 4m x 4.5m stairwells were placed at both ends and a 9m x 2.5m lift core was placed centrally within the building. An atrium is located in the reception area and two columns in the first two storeys were omitted to accommodate this. Above this level deep beams are incorporated to transfer loading from upper columns. A general arrangement of the Cardington building is shown in Figure 2-01. The beam sizes are as follows:

- 305 x 165 x 40 UB (Grade 43) for all secondary beams.
- 610 x 228 x 101 UB (Grade 50) for all 9m main beams.
- 356 x 171 x 45 UB (Grade 50) for all 6m main beams, perimeter beams and for all trimming beams (Around lift shaft voids etc.).

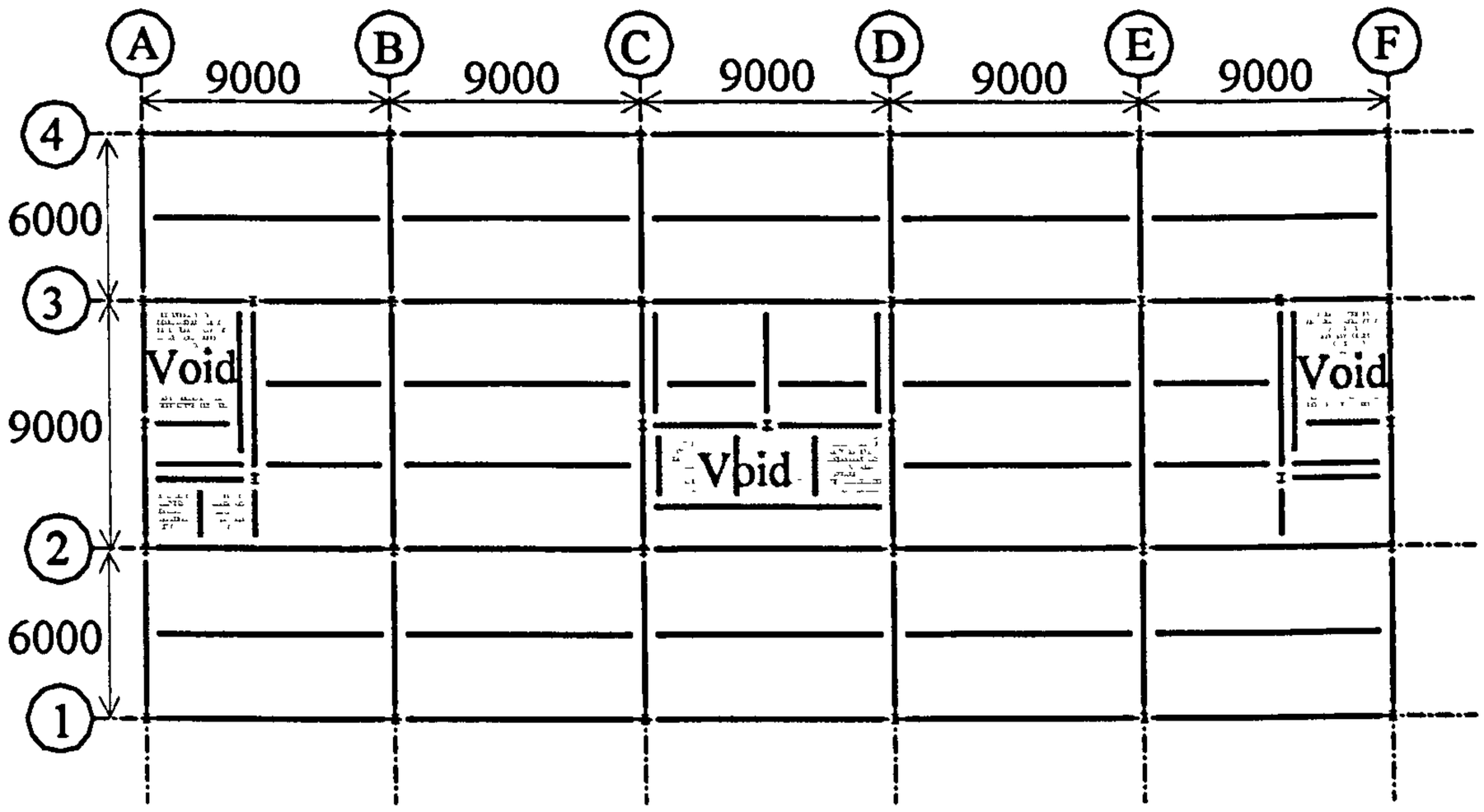

Figure 2-01. General arrangement of the Cardington Test Frame

Peter Brett Associates (Consultant engineers) conducted the structural design of the building to BS5950 [9]. The fabrication and building erection was carried out by Caunton Engineering Limited. This was completed in March 1993. All the steel members were shot-blasted, but left unpainted. The original intention was for the rolling of the steel to be conducted at one mill only, and each rolled bar to be tested three times. This was not possible as the rolling was split between three British Steel mills (Lackenby, Shelton and Scunthorpe), and some of the mills only carried out standard tests. Therefore the reported tensile test results of the steel members are not comprehensive. However, using the available data, it can be shown that for Grade 43 steel (S275) the yield strength ranged from 291 to 318 N/mm^2 and for Grade 50 steel (S355) the yield strength ranged from 371 to 413 N/mm^2.

The structural design concept was based on the assumption that the structural frame would be braced. This was effected by Grade 50 flat steel cross bracing down the three vertical access shafts. Grade 43 rolled steel angle windposts were positioned at 3m centres from ground to the fourth floor. Above this the windposts were positioned at 2.25m centres. Accidental damage must be localised – according to BS 5950 [9] – by the use of 'key elements'. This led to the transfer beams at second floor level, in conjunction with their supporting columns and restraining members, being designed for a blast load of 34kN/m^2, and hence the requirement for horizontal tying members to the columns at the level of the first and second floors.

An underlying principle at the design stage was that the building was to use a minimal amount of material and be inherently simple to manufacture. This had the effect of the secondary beams being designed as simply supported, whilst acting compositely with the floor slab through the use of 95mm x 19mm ∅ shear studs at 225mm spacing. A continuous composite flooring system with a nominal depth of 130mm was used, comprising 0.9mm steel decking (PMF CF70), lightweight concrete and A142 anti-crack mesh. A survey has shown the actual slab depths vary from 128mm to 175mm, as detailed in Section 2.8. A characteristic imposed load of 2.5kN/m^2 with an additional load of 1.0kN/m^2 to account for partitions was assumed for all floors, except the roof. The roof was assumed to support plant, and a characteristic imposed loading of 7.5kN/m^2 was used. In order to simulate the imposed serviceability loading sandbags, each weighing 11kN, were used.

Flexible end plates were used for beam-to-column connections and fin-plates for the beam-to-beam connections. Column splices consisted of cap and base plates. The perimeter columns and approximately 75% of those around the bracing cores were spliced once over the building height, whilst the heavier internal columns were spliced twice.

2.1 The Cardington Fire Tests

This test frame was subjected to a series of fire tests during 1995 and 1996 to investigate the importance of whole-structure behaviour under various types of compartment fires. The cost of such testing, and of fire tests in general, is extremely high, and one objective of the Cardington programme is to provide data over a range of fire scenarios in a real structure so that different computer modelling approaches may be tested and evaluated. A summary of the test programme is shown in Table 2-01.

The imposed serviceability loading applied to the test area and the surrounding structure was 3.5kN/m^2, and this remained constant during the fire tests. The load ratio applied to the beams (defined as the load applied at the fire limit state divided by the load causing the member to fail under normal conditions [16]) was 0.45 for the 9m secondary beams, 0.43 for the 6m primary beams and 0.29 for the 9m primary beams.

As these load levels are relatively low, there was an inherent reserve of strength that was utilised during the Cardington fire tests.

Test	Sponsor	Description	Date
1	ECSC	Restrained beam	January 1995
2	ECSC	Plane frame	May 1995
3	ECSC	1st Corner	July 1995
4	BRE	2nd Corner	October 1995
5	BRE	Large compartment	April 1996
6	ECSC	Large office compartment	June 1996

Table 2-01. Summary of the Cardington test programme

Figure 2-02 shows the extent of each of the Cardington fire tests. The tests were conducted on different floors and this will be detailed later in the chapter.

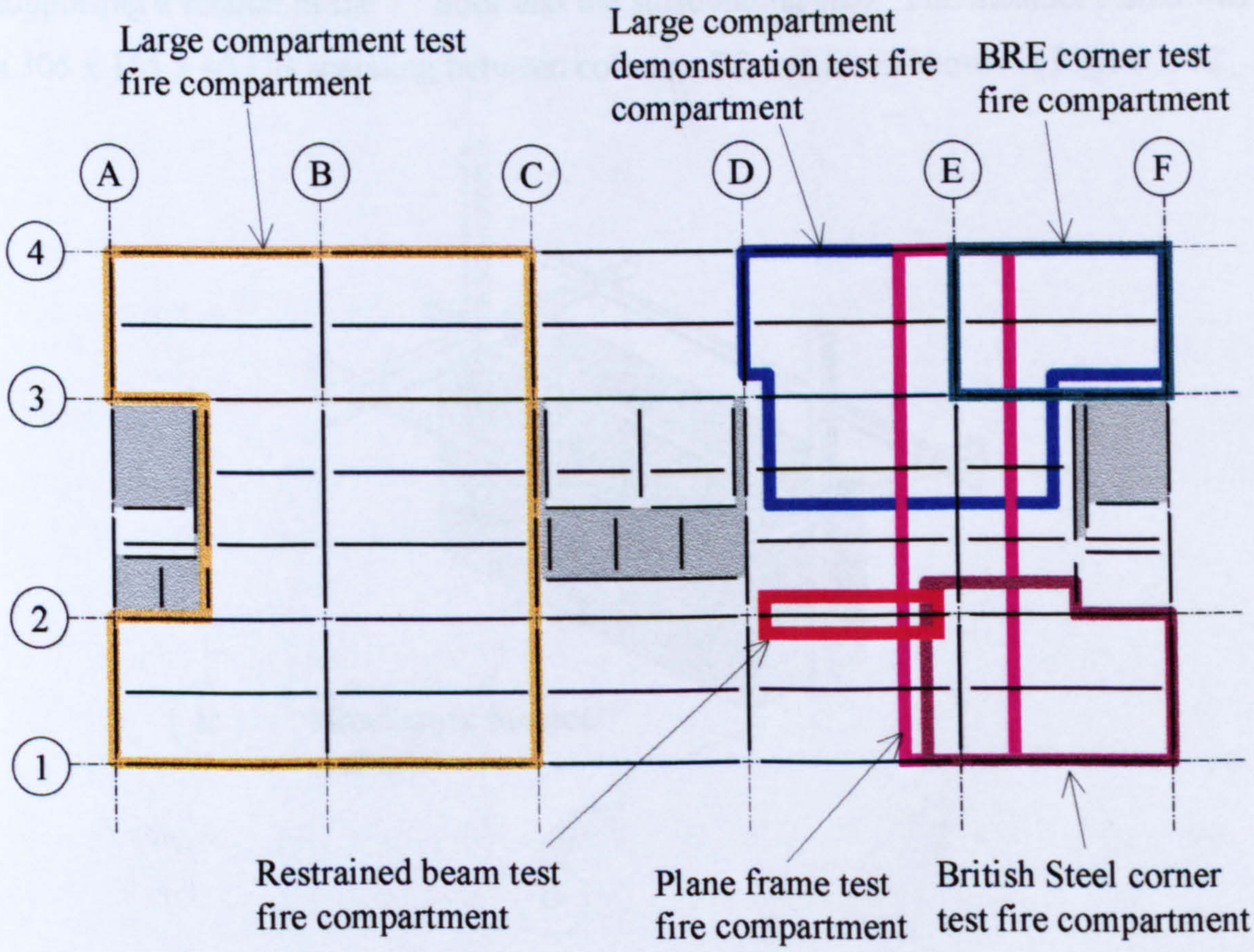

Figure 2-02. Schematic plan showing locations of the Cardington fire tests

The temperatures for each of the fire tests are recorded in this chapter, at the positions shown in Figure 2-03

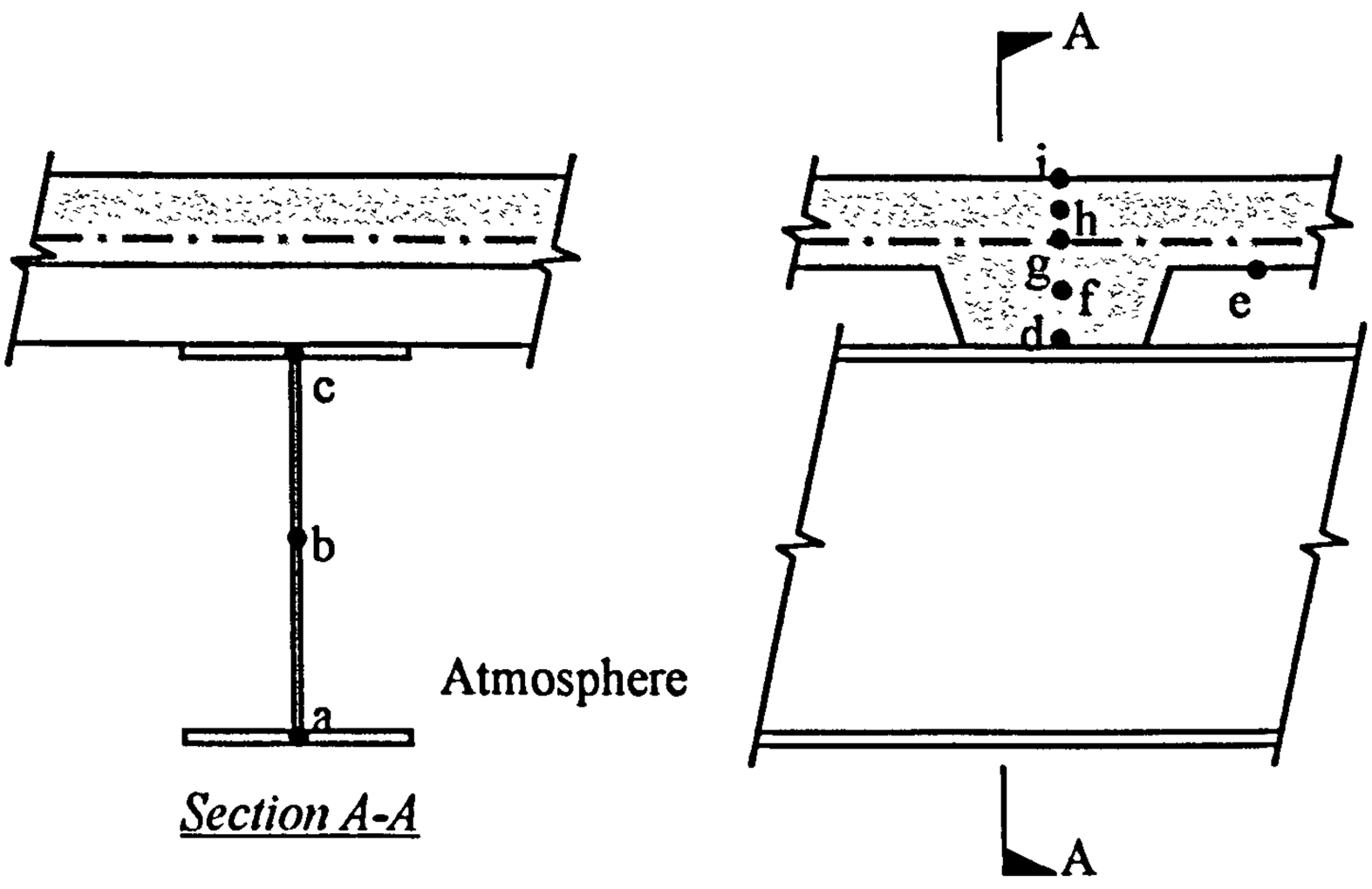

Figure 2-03. Location of restrained beam test sample temperatures.

2.2 RESTRAINED BEAM TEST

The restrained beam fire test involved the heating of a single secondary beam supporting a section of the 7th floor and the surrounding slab. The member tested was a 305 x 165 x 40 UB spanning between columns D2 and E2 as shown in Figure 2-02.

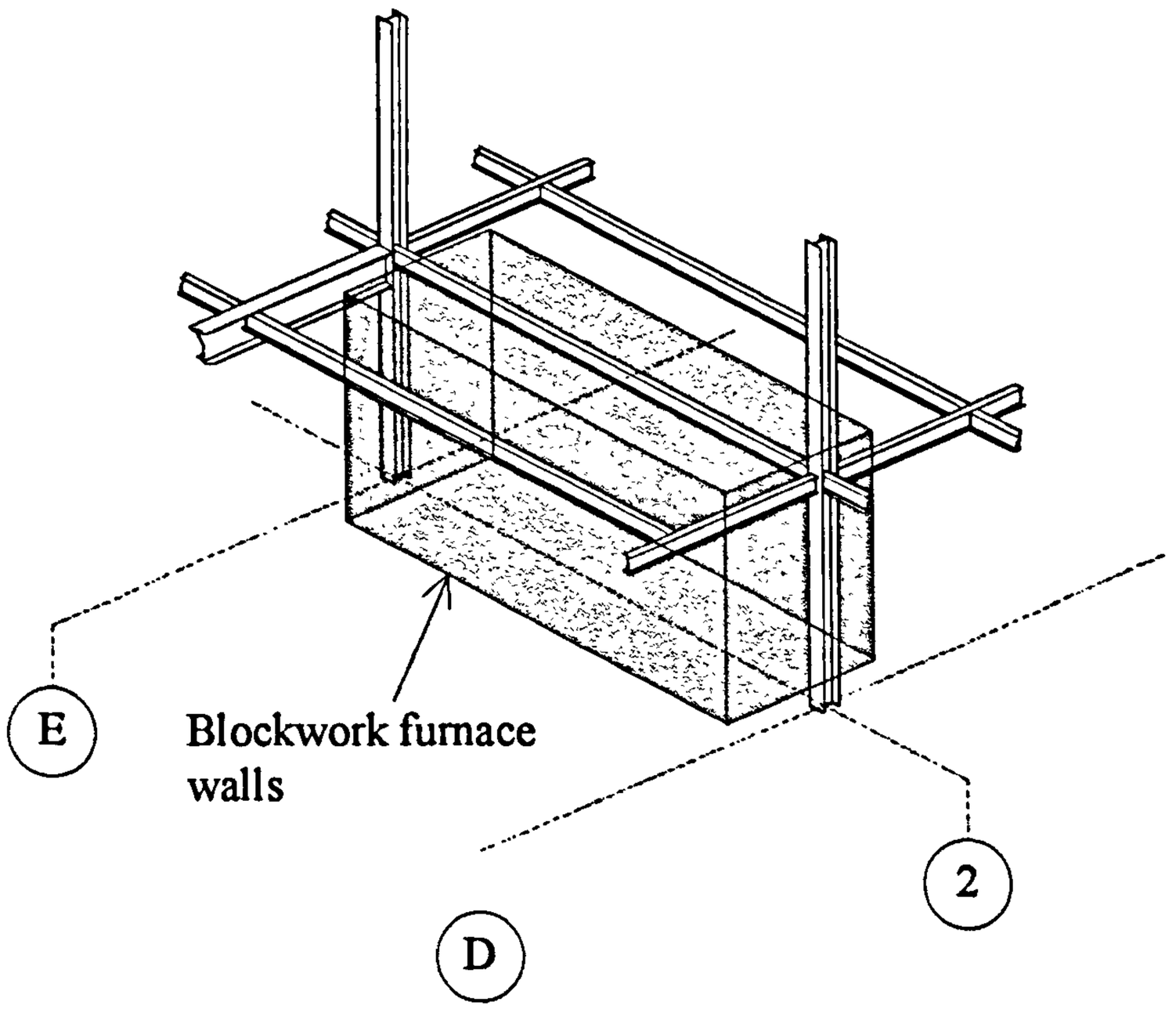

Figure 2-04. Restrained beam test fire compartment

The gas-fired furnace used in the test was built from the 6th floor with the capacity of heating a floor area of 8m x 3m. A flexible ceramic fibre fire barrier was fitted

between the metal decking soffit and the top of the furnace walls to prevent hot gases escaping the compartment whilst allowing unimpeded deflection of the beam and surrounding floor slab. The voids between the metal decking and steel beam upper flange were filled with mineral fibre in an attempt to reduce the thermal gradient through the heated beam; this was intended to simplify computer simulations. A schematic diagram of the restrained beam test fire compartment is shown in Figure 2-04.

A total of 300 channels of instrumentation were used on the restrained beam test. These measured:

1. Atmosphere, steel and concrete floor slab temperature profiles at specific locations within the test compartment [17].

2. Vertical and horizontal deflections of the test compartment [18, 19].

3. Rotation of the beams within the test compartment [20].

4. Structural movement of the floor slab immediately surrounding the test compartment [18, 19].

5. Strain re-distribution at the ends of the beams (outside the furnace) and the immediate surrounding structure [21].

The beam was heated at a rate between 3 to 10°C per minute until temperatures were recorded in the range 800 to 900°C within the beam section. A maximum bottom-flange steel temperature of 832°C was reached at the end of a 150-minute period.

Figure 2-05 shows the distribution of temperatures through the centre of the restrained beam and floor slab cross-section as shown in Figure 2-03. It will be noted that there is no temperature data for the atmosphere and beam for the first 5 minutes. Other data taken during the test shows that there is a rapid, approximately linear, increase up to 200°C in this time period, which indicates a lag in the beam and slab temperatures. It can also be noted that the temperatures of the bottom flange and the web are similar. The top flange temperature is lower, due to only being exposed to heat on the lower side and to the floor slab acting as a heat sink. The floor slab temperature increases more slowly than that of the beam. A 'plateau' in the slab temperature increase

occurs at 100°C. This is a consequence of the high water content (a normal characteristic of lightweight concrete) reaching boiling point and the energy requirement associated with latent heat of evaporation.

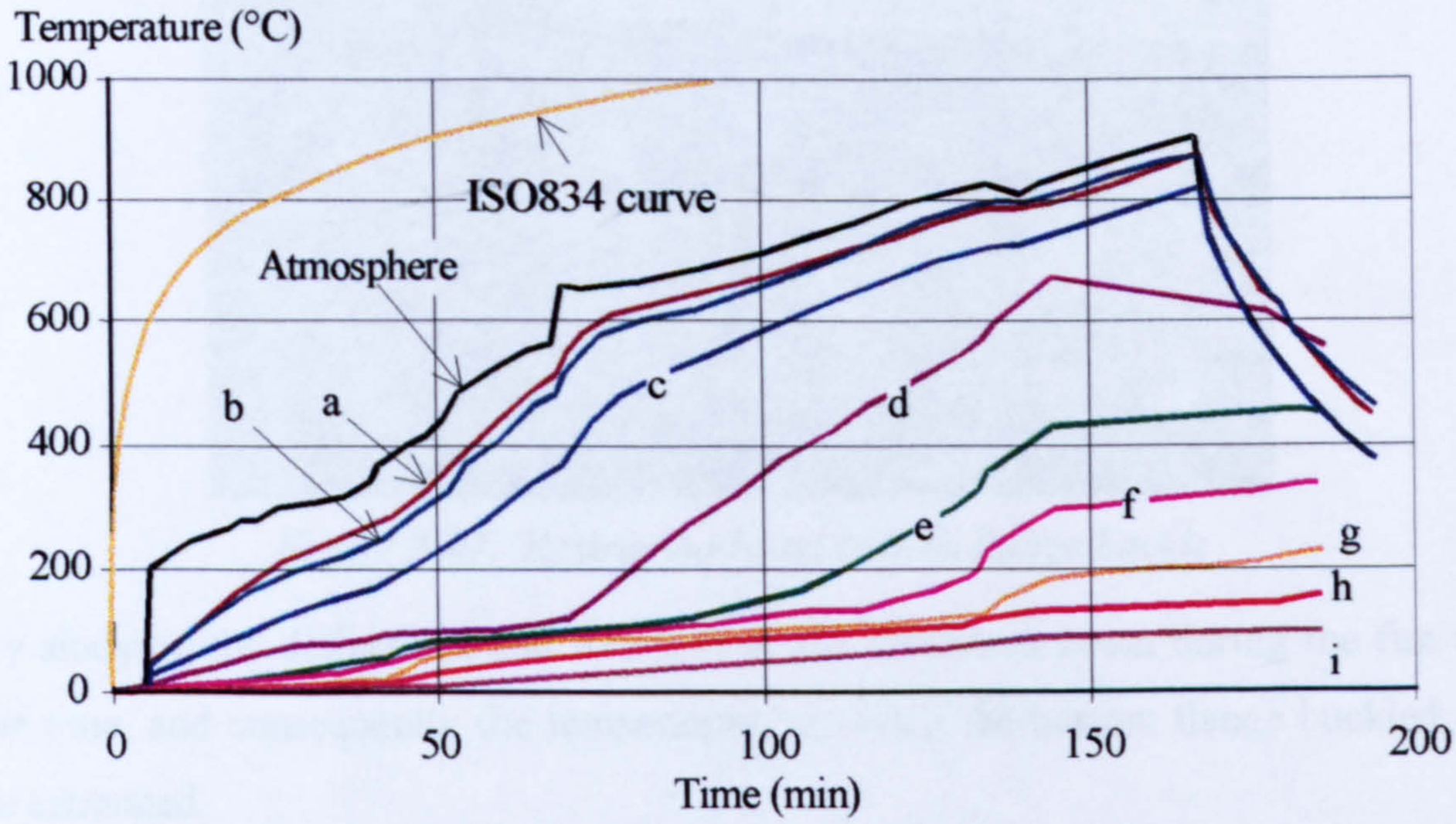

Figure 2-05. Temperature profile across the beam and concrete.

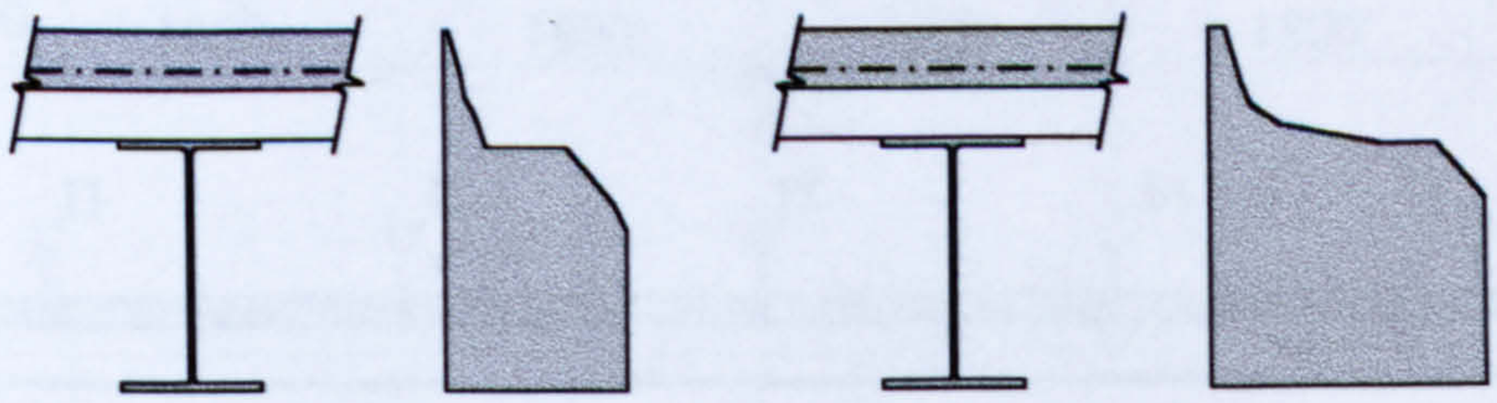

50 minutes *100 minutes*

Figure 2-06. Temperature profiles across the centre of the restrained beam test at 50 minutes and 100 minutes.

Figure 2-06 shows a temperature profile of the cross-section at the centre of the beam at times of 50 minutes and 100 minutes.

The test beam is highly restrained against thermal expansion due to the continuous nature of the slab over the beam and its position relative to the supporting columns and cross bracing. The principal aim of the test was to investigate the effect of this phenomenon locally. The lower flange did buckle at the ends of the furnace during the test, due to the large induced compressive forces, combined with the intrinsic hogging moment near the support, as shown by Figure 2-07. This is similar to local buckling found during the investigation of the Broadgate Phase 8 fire [22]. As Bailey [23] points out, this local buckling may not constitute failure, since formation of hinges at these locations would essentially create a simply-supported beam between them.

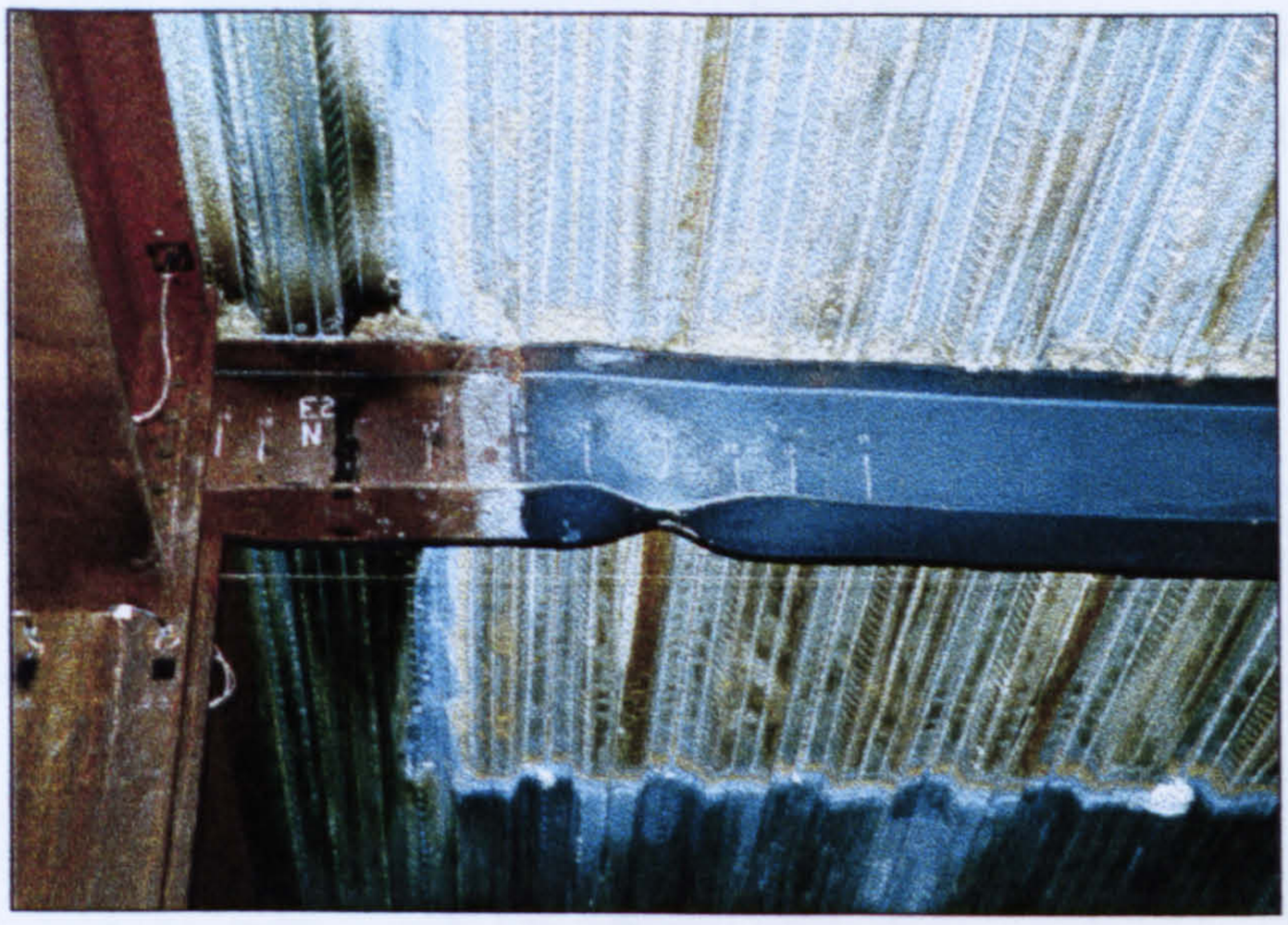

Figure 2-07. Restrained beam bottom flange buckle

By studying the deflections and rotations of the restrained beam during the fire test the time, and consequently the temperature, at which the bottom flange buckled can be estimated.

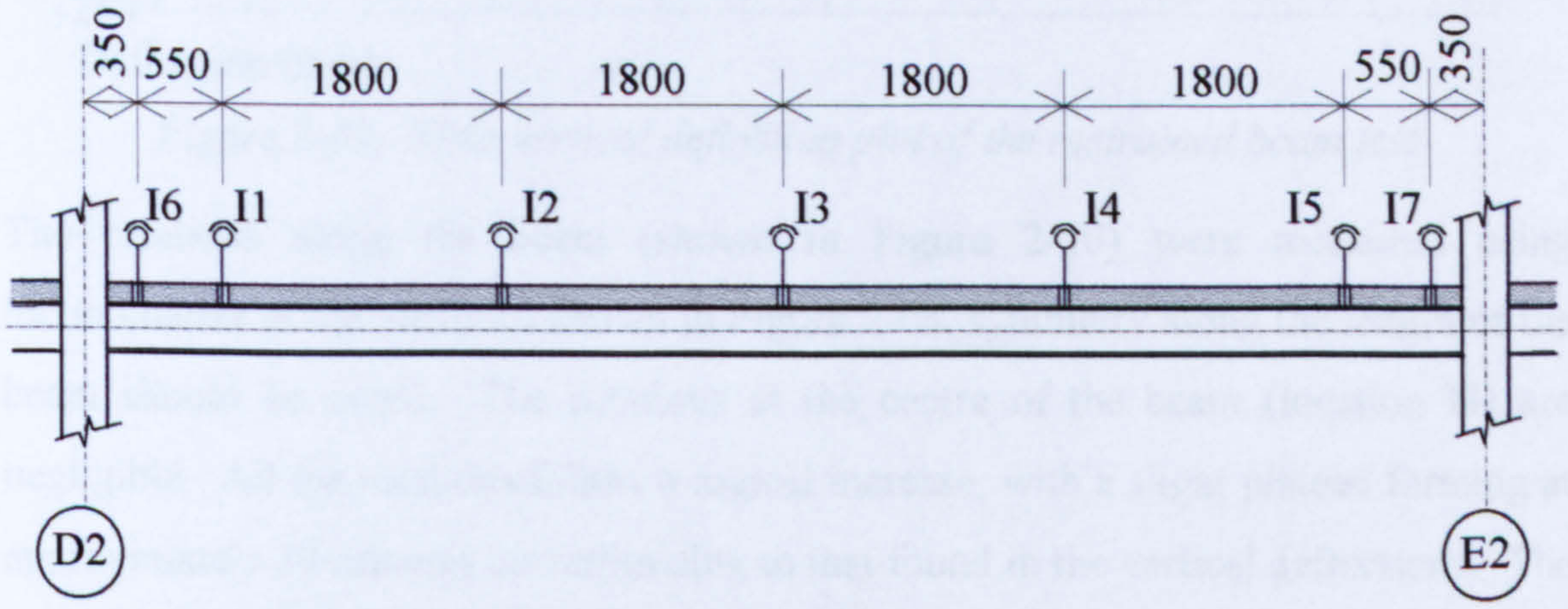

Figure 2-08. Location of measured deflections and inclinometers in the restrained beam test

Figure 2-09 shows a plot of the time and vertical deflection of the restrained beam test at the locations shown in Figure 2-08. Following Figure 2-09 it can be seen that for position I3 (the centre of the restrained beam), the beam deflects, easing gently at approximately 30 minutes, then continuing until approximately 70 minutes when there is a suddenly increase in deflection. The deflection then continues at an approximately linear rate until the end of the test. The beam follows a similar pattern to location I3 at locations I2 and I4. At locations I1, I5, I6 and I7 the beam has a similar action to that previously described until 70 minutes, at which stage there is a significant decrease in the rate of deflection. It will be noted that at positions I1 and

I5 the deflection slowly increases, whereas at positions I6 and I7 it remains constant. This indicates that a possible buckle has occurred between positions I1 and I6 and positions I5 to I7. Extra confirmation of the buckle at 70 minutes may be made using the rotational data from the test.

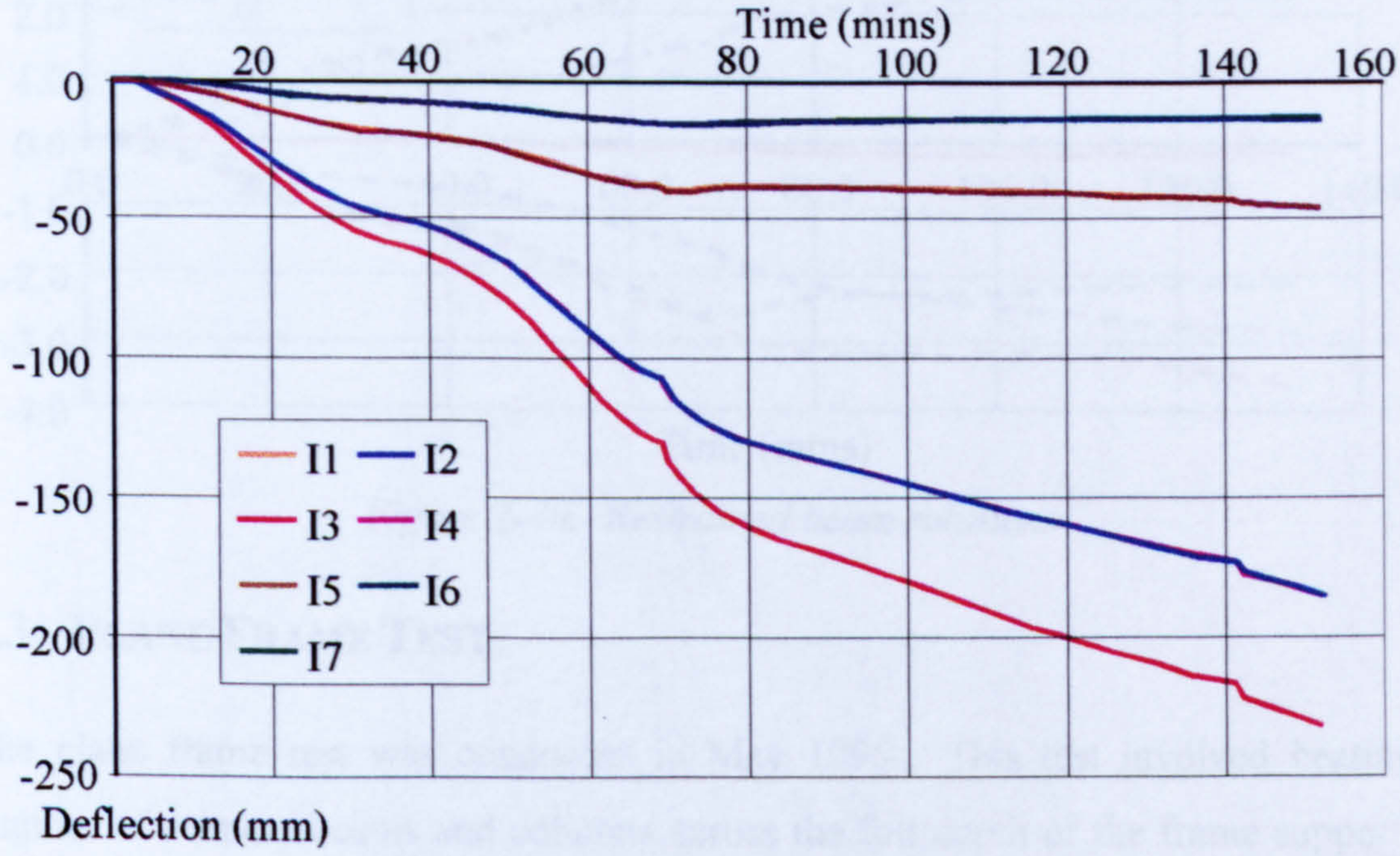

Figure 2-09. Time vertical deflection plot of the restrained beam test

The rotations along the beam (shown in Figure 2-10) were measured using inclinometers at the locations shown in Figure 2-08, symmetry along the length of the beam should be noted. The rotations at the centre of the beam (location I3) are negligible. All the rotations follow a logical increase, with a slight plateau forming at approximately 30 minutes corresponding to that found in the vertical deflections. The rotations increase until approximately 70 minutes, at which stage the rotations at locations I1, I2, I4 and I5 continue to increase. However, the inclinometers at locations I6 and I7 both record a small decrease in rotation at this point before stabilising at a constant value. This indicates that the beam is still rotating at locations I1, I2, I4 and I5, whereas at locations I6 and I7 rotations have stopped. This could be due to a hinge (such as a local buckle) forming.

Assuming that the 'hinge' formed at 70 minutes, this corresponds to a bottom flange temperature of 530°C.

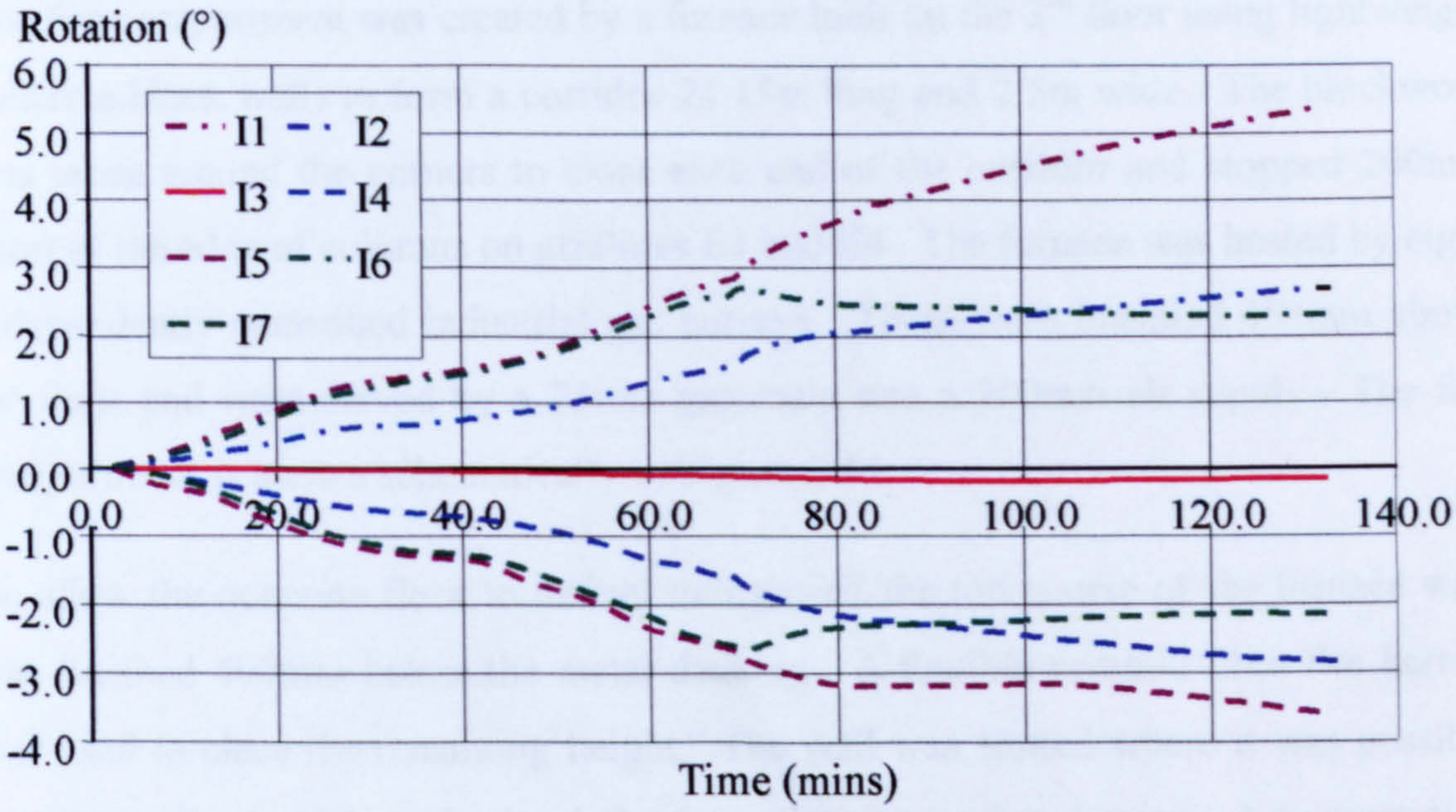

Figure 2-10. Restrained beam rotations

2.3 PLANE FRAME TEST

The plane frame test was conducted in May 1995. This test involved heating a number of primary beams and columns across the full depth of the frame supporting the fourth floor as shown on Figure 2-02. The aim of the test was to ascertain the influence of beam-column interaction.

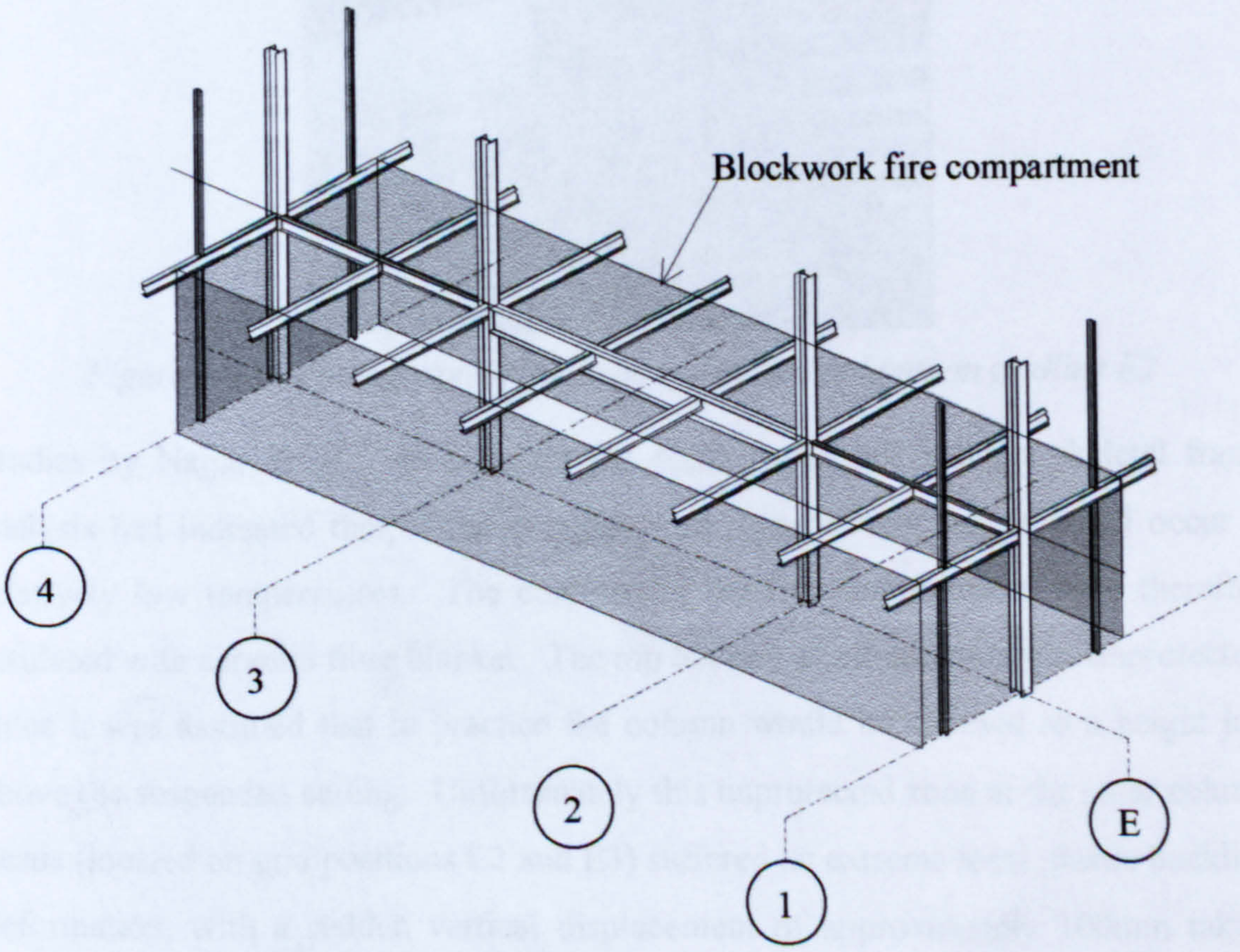

Figure 2-11. Plane frame test fire compartment

The fire compartment was created by a furnace built on the 3rd floor using lightweight concrete block walls to form a corridor 21.15m long and 2.5m wide. The blockwork was taken around the corners to close each end of the corridor and stopped 200mm short of the edge of columns on gridlines E1 and E4. The furnace was heated by eight independently controlled industrial gas burners. These were installed 450mm above the floor and were served by a 75mm gas main and a 200mm air supply. The fire compartment is shown schematically in Figure 2-11.

To allow the concrete floor to deflect unimpeded the top course of the furnace wall was finished 400mm below the metal decking. A flexible ceramic fibre fire barrier was used to close the remaining height. The wall was slotted where it was possible that the wall would impede the deflection of the secondary beams. Any remaining gaps in the blockwork were filled with ceramic fibre.

Figure 2-12. Photograph of the head of buckled column on gridline E2

Studies by Najjar *et al* [24] to simulate the plane frame test using a skeletal frame analysis had indicated that, if the columns were unprotected, failure could occur at relatively low temperatures. The columns in the fire compartment were therefore insulated with ceramic fibre blanket. The top 500mm of all columns was unprotected, since it was assumed that in practice the column would be encased to a height just above the suspended ceiling. Unfortunately this unprotected zone at the inner column heads (located on grid positions E2 and E3) suffered an extreme local plastic buckling deformation, with a sudden vertical displacement of approximately 100mm taking

place at a control temperature (the heated beam's lower flange temperature) of about 620°C. This is shown in Figure 2-12.

Instrumentation was installed on the plane frame test to measure:

1. Atmosphere, steel, concrete floor slab and connection (Beam to beam and beam to column) temperature profiles at specific locations within the test compartment [25, 26].

2. Vertical and horizontal deflections of the main beams [27].

3. Horizontal deflections of the columns [27].

4. Rotation of the columns and beams at the main connections within the test compartment [28].

5. Strain re-distribution in the columns and the immediate surrounding members [29].

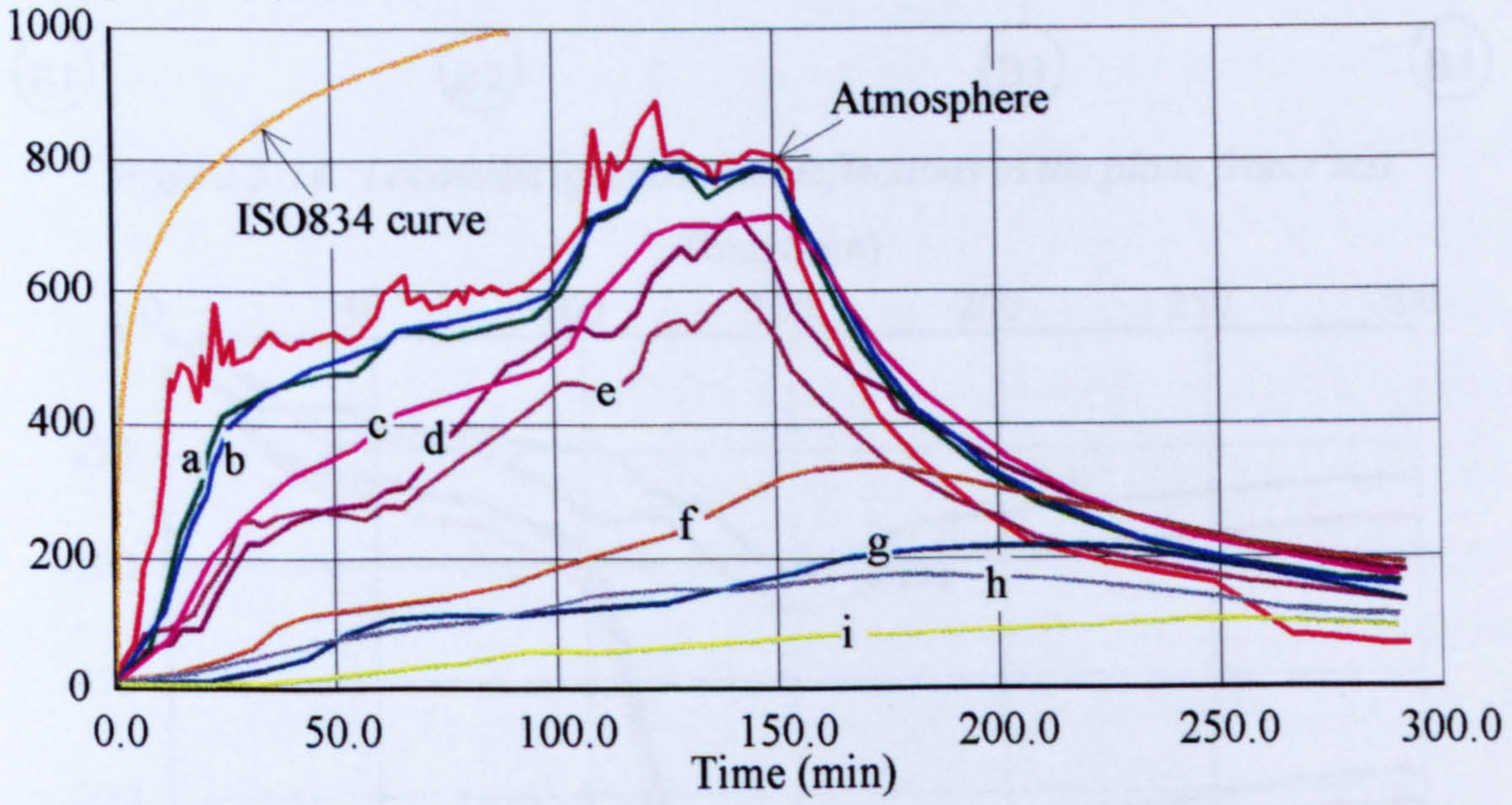

Figure 2-13. Plane frame test temperature profile across beam and slab at the centre of the furnace

The temperatures attained within the centre of the plane frame furnace are shown in Figure 2-13 and should be read in conjunction with Figure 2-03. This plot includes the standard ISO 834 [6] curve for comparison. The initial atmospheric temperatures within the test increase rapidly to approximately 500°C. The steel temperatures follow this with the bottom flange and web at approximately equal temperatures whilst the top flange is approximately 80% that of the bottom flange throughout the

test. The temperatures of the steel decking for both troughs and ridges increase rapidly following the atmospheric temperature rise. These are approximately 70% of the bottom flange temperature. The temperature of the concrete increases to 100°C at which stage the water contained within the concrete matrix begins to evaporate. This again causes a marked reduction in the rate of temperature gain. This stage could continue until all moisture had been removed. Following this the concrete would slowly increase in temperature.

The positions of the deflections recorded during the test are shown in Figure 2-14 and the corresponding test data in Figure 2-15.

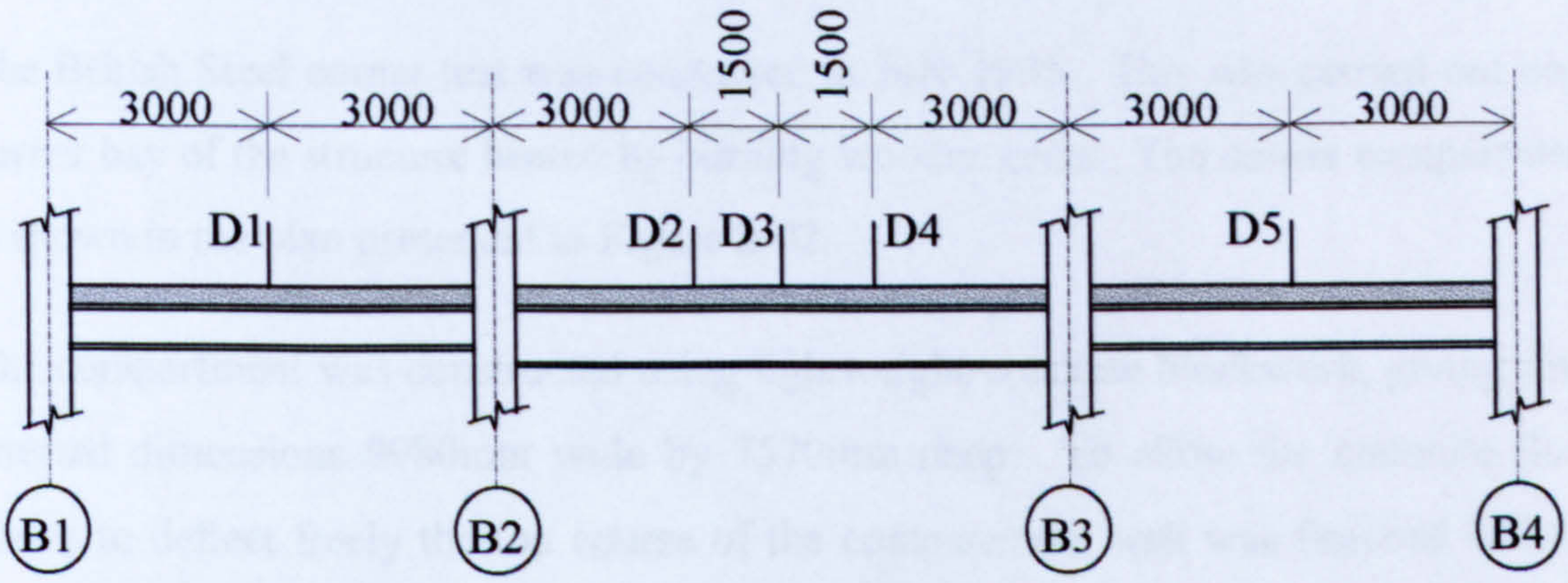

Figure 2-14. Locations of measured deflections in the plane frame test

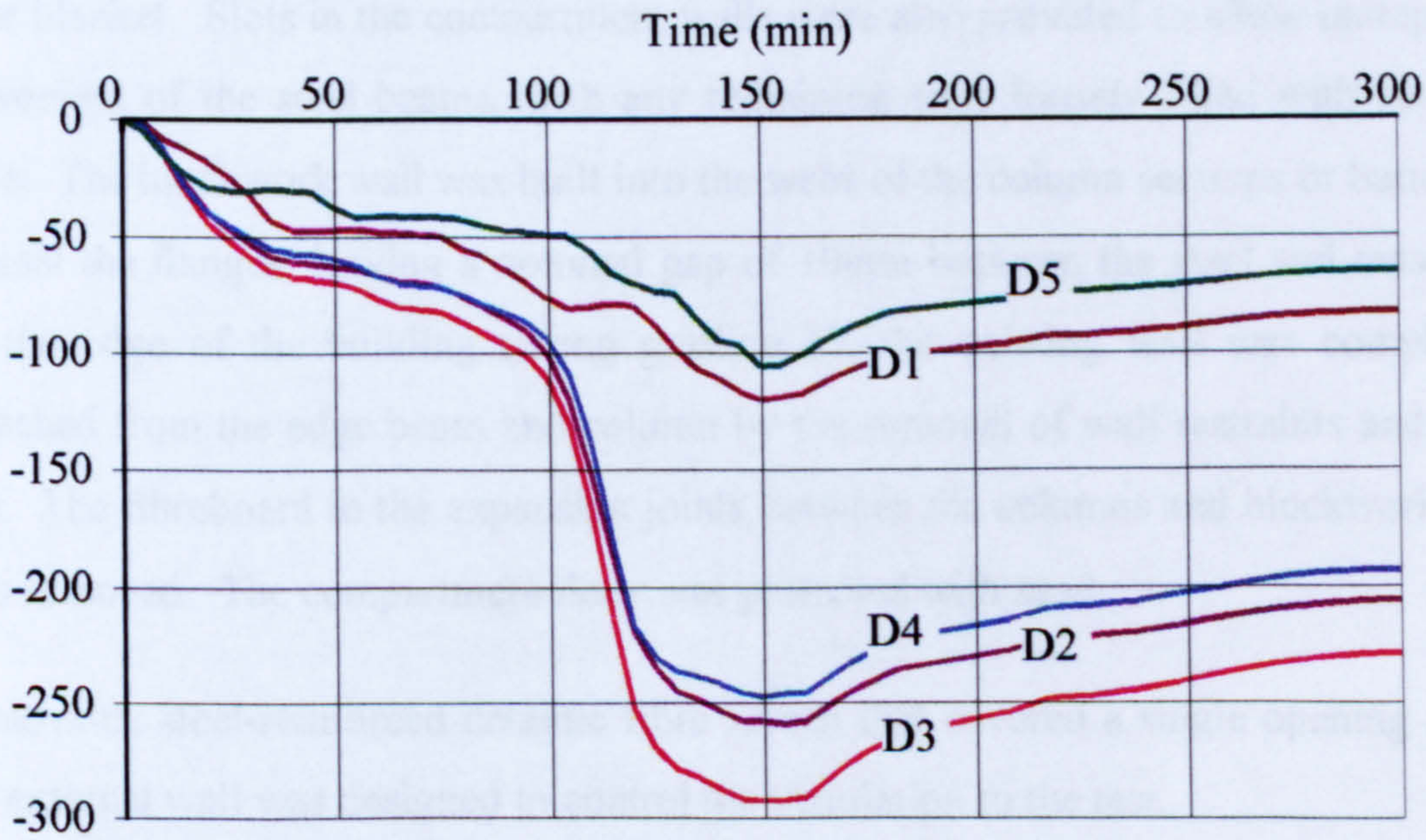

Figure 2-15. Plane frame test deflection plot

The initial increase is due to thermal bowing, where the temperature difference between the steel beam and the concrete slab causes different rates of expansion between the materials, causing curvature to occur. For temperatures higher than

approximately 550°C (80 minutes), the steel strength and stiffness reduces significantly causing the structure to deflect further. This continues until approximately 110 minutes when there is a sudden increase in the rate of deflection. This is probably a direct consequence of the plastic deformation at the head of the columns, although not due directly to vertical movement as the displacements were measured from the floor above and therefore all deflections are relative. However, the plastic deformation allows the head of the column to act as a hinge, dramatically reducing the rotational resistance of the column.

2.4 BRITISH STEEL CORNER TEST

The British Steel corner test was conducted in July 1995. This was carried out on a corner bay of the structure heated by burning wooden cribs. The corner compartment is shown in the plan presented in Figure 2-02.

The compartment was constructed using lightweight concrete blockwork, giving final internal dimensions 9980mm wide by 7570mm deep. To allow the concrete floor above to deflect freely the top course of the compartment wall was finished 400mm below the metal decking and the remaining height was completed by fitting ceramic fibre blanket. Slots in the compartment walls were also provided to allow unimpeded movement of the steel beams, with any remaining gaps loosely filled with ceramic fibre. The blockwork wall was built into the webs of the column sections or butted up against the flanges, leaving a nominal gap of 10mm between the steel and masonry. At the edge of the building (along gridline F), the existing wall was completely detached from the edge beam and column by the removal of wall restraints and steel ties. The fibreboard in the expansion joints between the columns and blockwork was also removed. The compartment floor was protected with sand.

A movable steel-reinforced ceramic fibre screen that covered a single opening along the external wall was designed to control the ventilation to the test.

Exposed surfaces of columns on gridlines E2, E1, F1 and F2, the connections and the perimeter beams were all protected using 25mm ceramic fibre blanket. However, all the internal primary and secondary beams were left fully exposed, and voids between

the upper flange and the metal decking were left unfilled. The fire compartment of the British Steel corner test is shown in Figure 2-16.

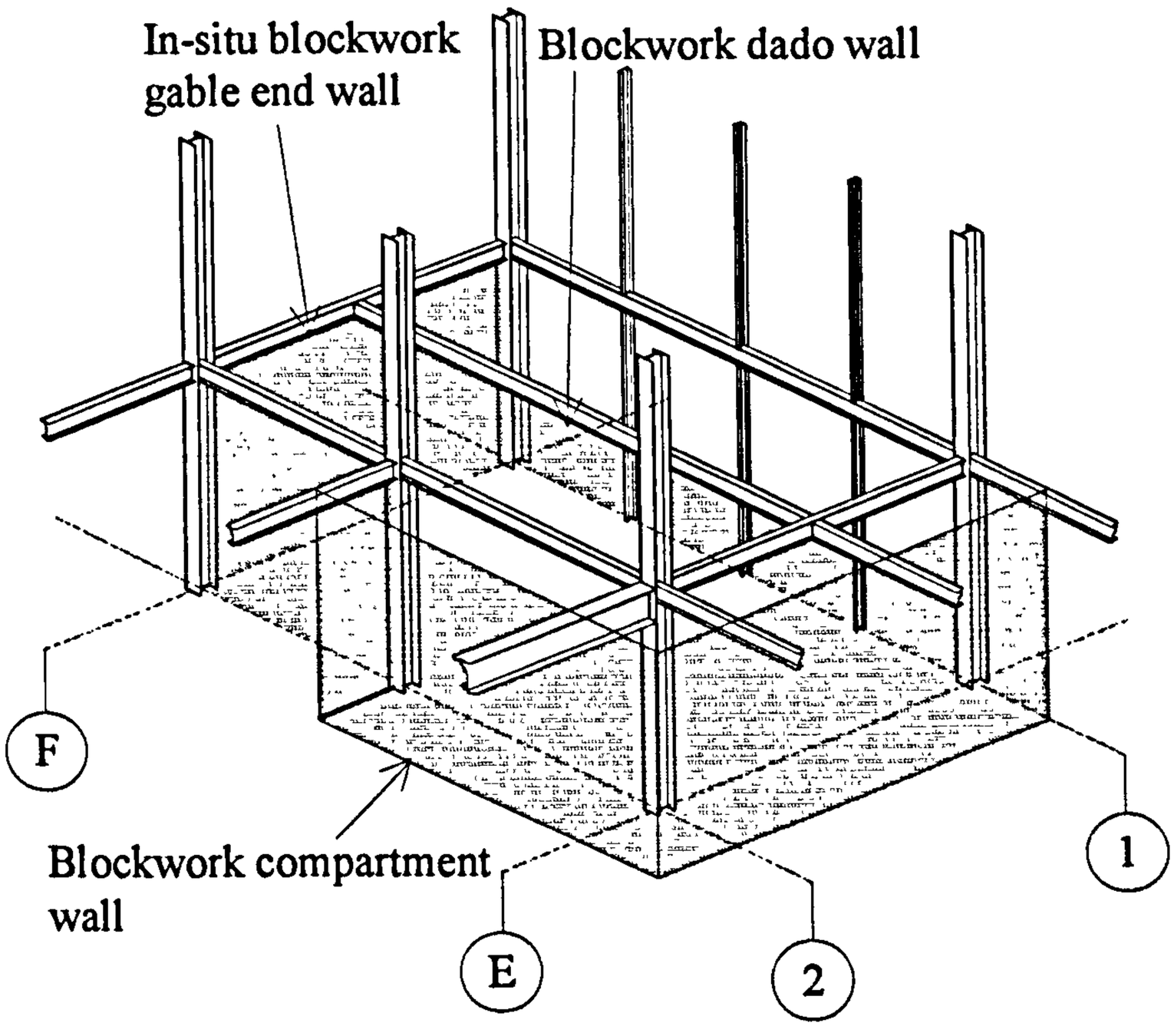

Figure 2-16. British Steel corner test fire compartment

Instrumentation was installed on the British Steel corner test to measure:

1. Steel temperature profiles at specific locations along the primary, secondary and edge beams [30, 31, 32].

2. Temperature profiles through the metal decking and concrete floor [30, 31, 32].

3. Steel temperature profiles around the beam-to-beam and beam-to-column connections [30, 31 and 32].

4. Steel temperature profiles at specific locations along the columns [30, 31 and 32].

5. Vertical and horizontal deflections of the beams, columns and the floor slab [33].

6. Beam and column rotations at the main connections [34].

7. Strain profiles across the columns within the compartment and the surrounding structural members [35].

8. Strain across the surface of the concrete slab [35].

The temperatures measured at the centre of the compartment are shown in Figure 2-17 and should be read in conjunction with Figure 2-03 which shows the positions of the thermocouples.

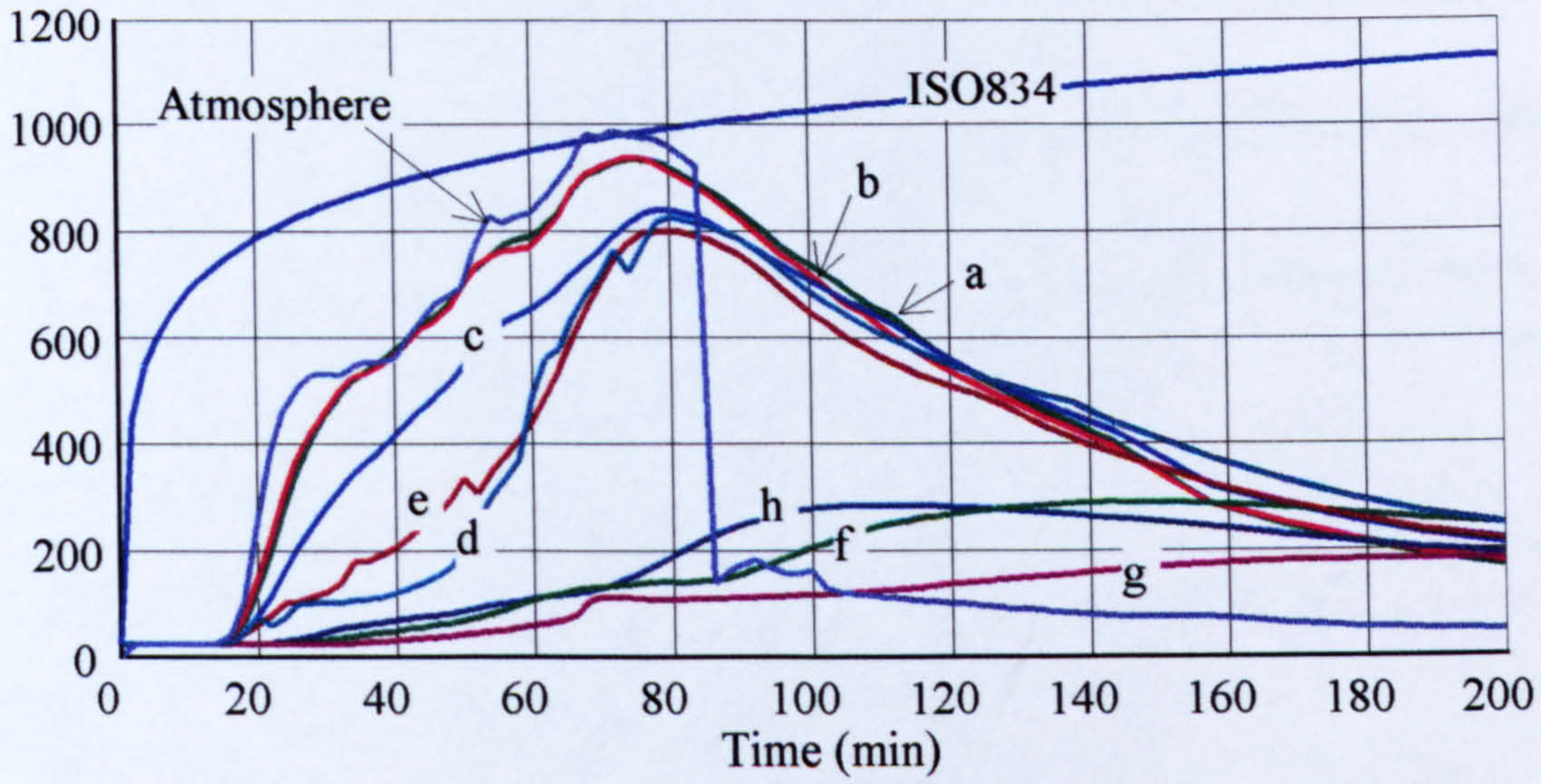

Figure 2-17. British Steel Corner Test Temperatures at centre of compartment

At the start of the test, the timber cribs burned but generated little increase in the compartment temperature, but at about 16 minutes flashover occurred. The temperatures of the beam at the bottom flange and web positions are similar throughout the test, and follow closely the atmospheric temperature with a lag of approximately 5 minutes. The top flange temperature is approximately 80% of that of the bottom flange. The temperature of the metal decking increases rapidly until it reaches 100°C. The metal decking then maintains a constant temperature for approximately 10 minutes while thermal energy is expended through the evaporation of the water held within the concrete. After this stage the metal decking quickly increases in temperature until it is approximately equal to the top flange temperature. The temperature within the concrete slowly increases due to its inherently low thermal conductivity. When the internal matrix of the concrete reaches 100°C, it remains at this temperature for approximately 20 minutes.

Deflections in this test were recorded at the locations shown in Figure 2-18 and the values are shown in Figure 2-19.

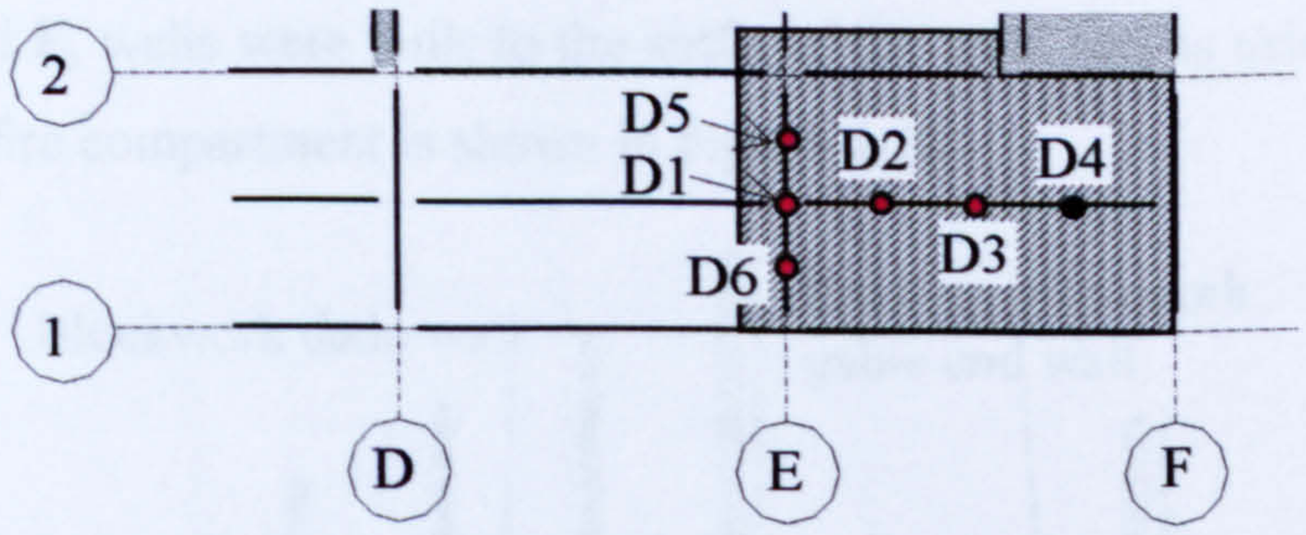

Figure 2-18. British Steel corner test position of measured deflections

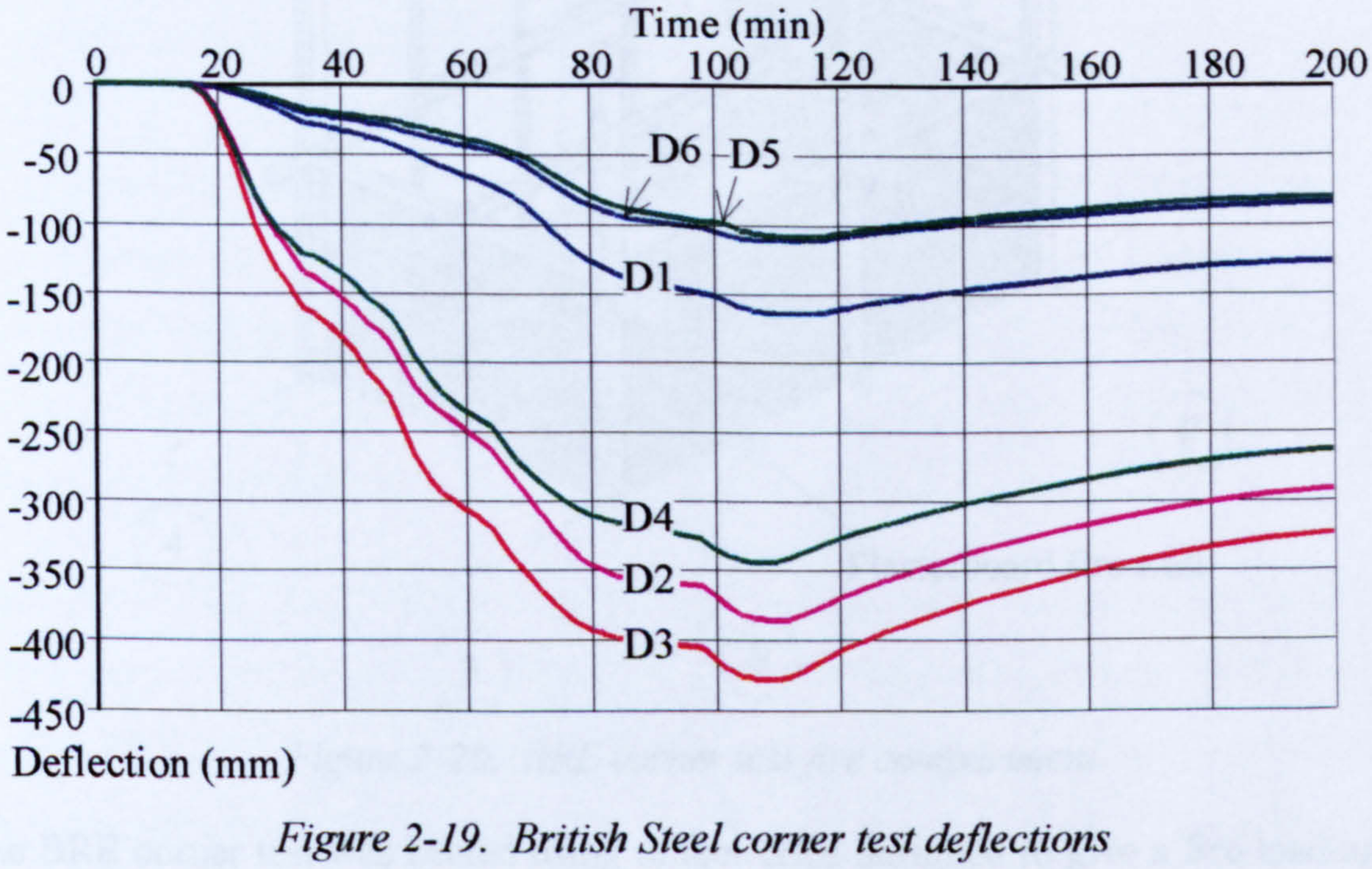

Figure 2-19. British Steel corner test deflections

For the first 16 minutes there was no increase in deflections as the fire was developing at this stage. The secondary and primary beams began deflecting at this stage due to thermal bowing. After approximately 35 minutes, the steel had lost significant strength and stiffness, increasing the deflections until approximately 100 minutes.

2.5 BRE Corner Test

The BRE corner test comprised a compartment 9m wide by 6m deep giving a total floor area of 54m^2. The test was conducted on the second storey, so that the floor under test was the floor above (i.e. the third floor). The position of the corner test is shown in Figure 2-02. The test took place during October 1995.

The fire compartment comprised a 1m high, blockwork, dado wall along gridline 4, this being where the windows would be positioned. Along gridline F the existing gable end wall was utilised as a boundary for the fire compartment. Finally on

gridlines 3 and E, walls were built to the soffit of the steel beams using plasterboard walling. The fire compartment is shown in Figure 2-20.

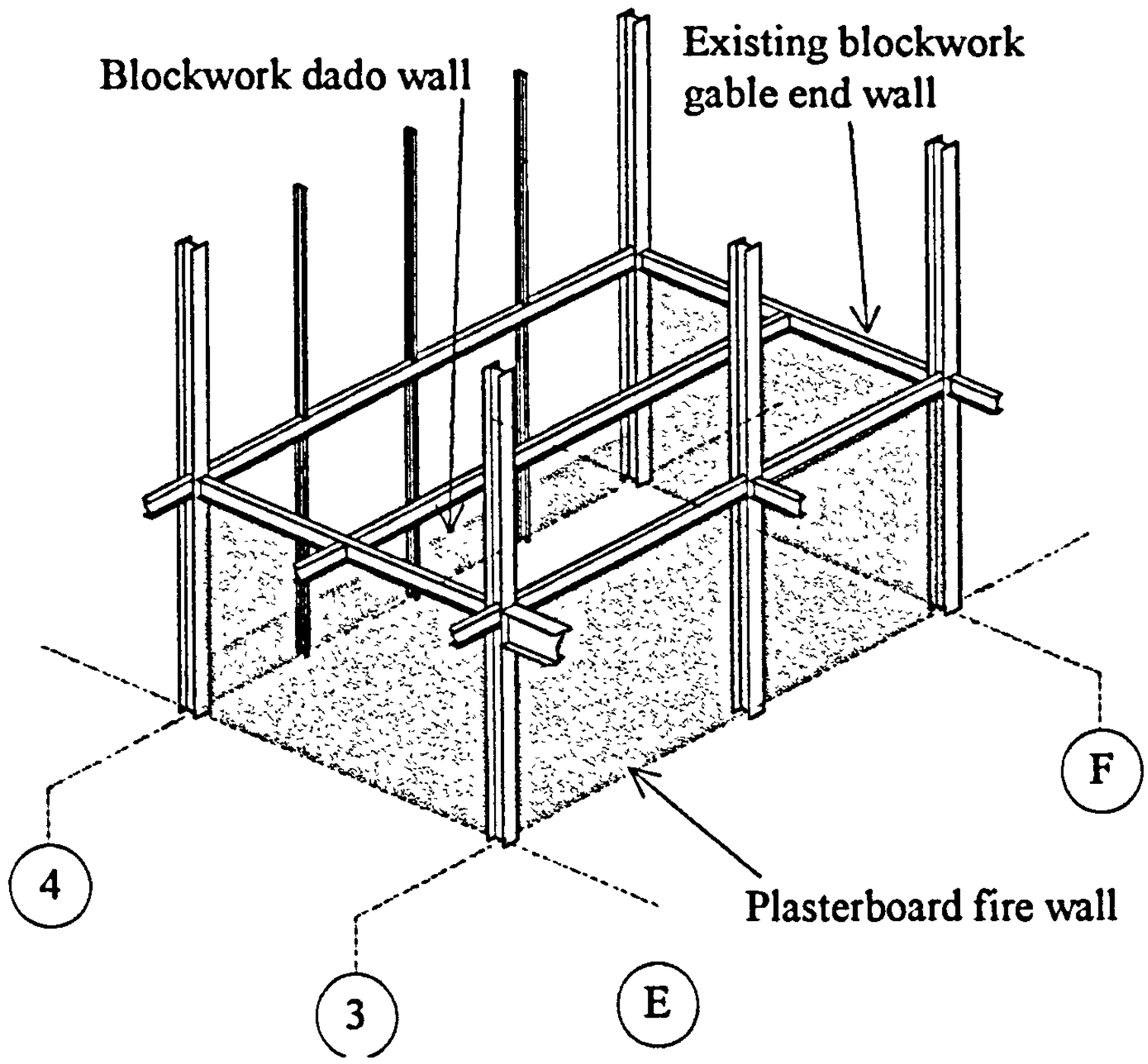

Figure 2-20. BRE corner test fire compartment

The BRE corner test was heated using timber cribs designed to give a fire loading in the compartment of 40 kg/m^2.

The following instrumentation was used on the BRE corner fire test:

1. Thermocouples were used to measure the temperatures within the compartment atmosphere, the concrete slab, columns, primary beams, secondary beams and the temperature of the environment outside the building [36].

2. Strain gauges were used to monitor the columns, beams and the concrete floor slab and its reinforcement mesh [36].

3. Displacement transducers were used to determine the deflection of the floor slab. The column deflections about the major and minor axes were also measured [36].

4. An innovative laser system was used to measure the movement of the masonry panels exposed to the fire placed on gridline F [36].

5. Inclinometers were used to record the rotations of the connections within the compartment [36].

6. Heat flux meters, steel billets and their associated thermocouples were also placed in the compartment [36].

7. Load cells were used to monitor the weight loss of three of the timber cribs [36].

As part of the experiment, support from a local double-glazing firm was procured who supplied three double-glazing units which were placed in the window opening of the fire compartment along gridline 4. These double-glazing units had a significant effect on the ventilation in that while they remained intact the temperature in the compartment did not seriously exceed approximately 200°C. The temperatures at the centre of the compartment are shown in Figure 2-21, which should be read in conjunction with the location plan, Figure 2-03.

After 60 minutes, the double-glazing was clearly contolling the fire, and so the middle of the three windows was broken to increase the ventilation so that the test might continue. This had the effect of increasing the temperature to approximately 350°C but then a steady state was again reached. One of the remaining two windows was then broken which allowed enough ventilation for flashover to be achieved at 95 minutes, leading to a maximum temperature in the centre of the compartment of 980°C. The steel bottom flange and web temperatures shown in Figure 2-21 closely follow the atmosphere temperature, with the top flange temperature lagging at approximately 80% that of the bottom flange temperature. The metal decking temperature follows closely, though slightly lower, than that of the top flange. This difference is due to the adjacent concrete having low thermal conductivity and acting as a heat sink. Temperatures on the reinforcement and on the top of the concrete slowly increase to 100°C, at which stage the moisture contained within the concrete begins to evaporate, causing the temperature to remain static. Once the moisture has been removed the temperature will begin to increase slowly.

The temperatures from the tests were not intended to follow the ISO 834 curve; however, this standard fire test curve is shown for the purpose of comparison.

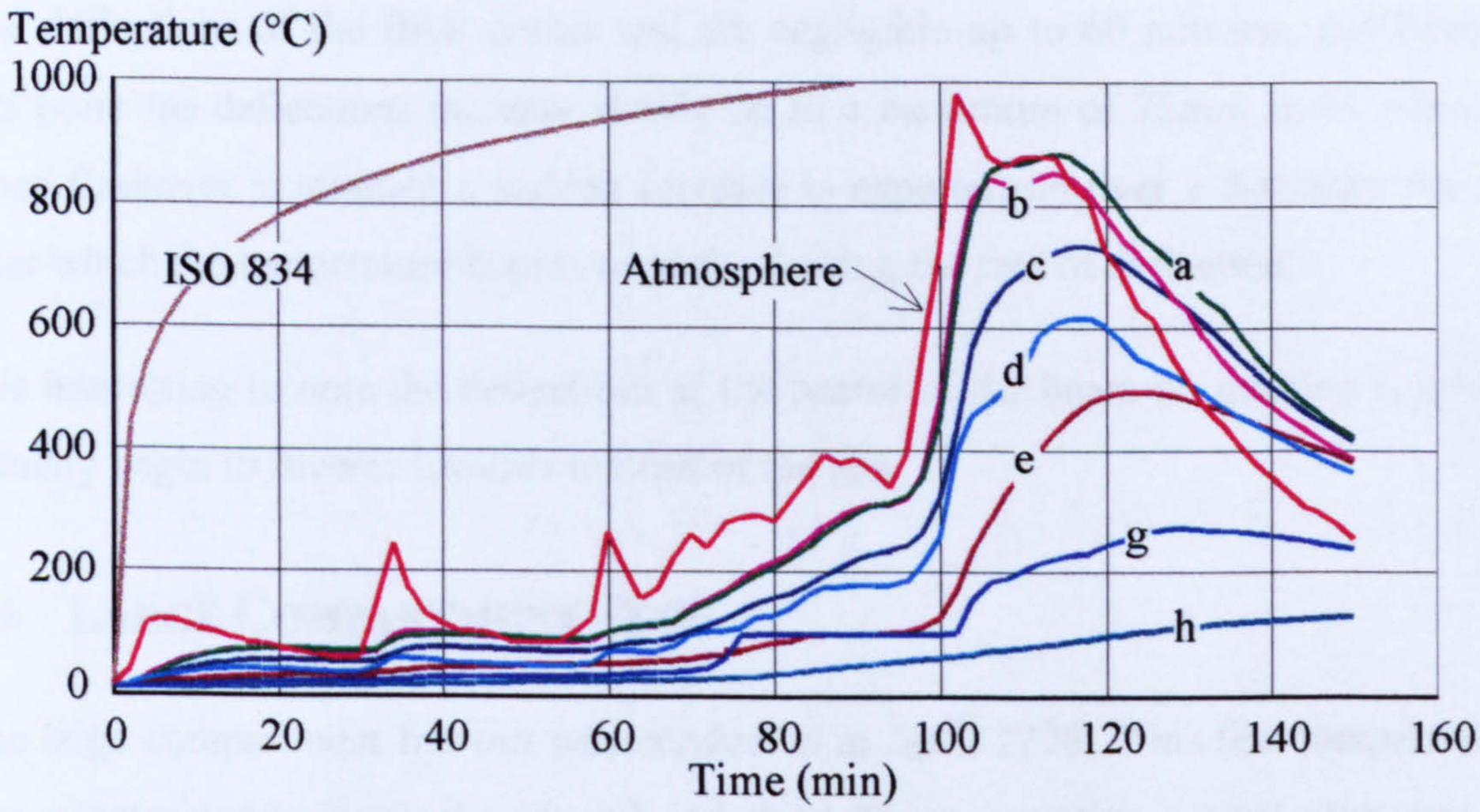

Figure 2-21. BRE corner test sample temperatures at centre of fire compartment

Deflections in the test have been measured at the locations shown in Figure 2-22, Figure 2-23 shows the corresponding deflection data.

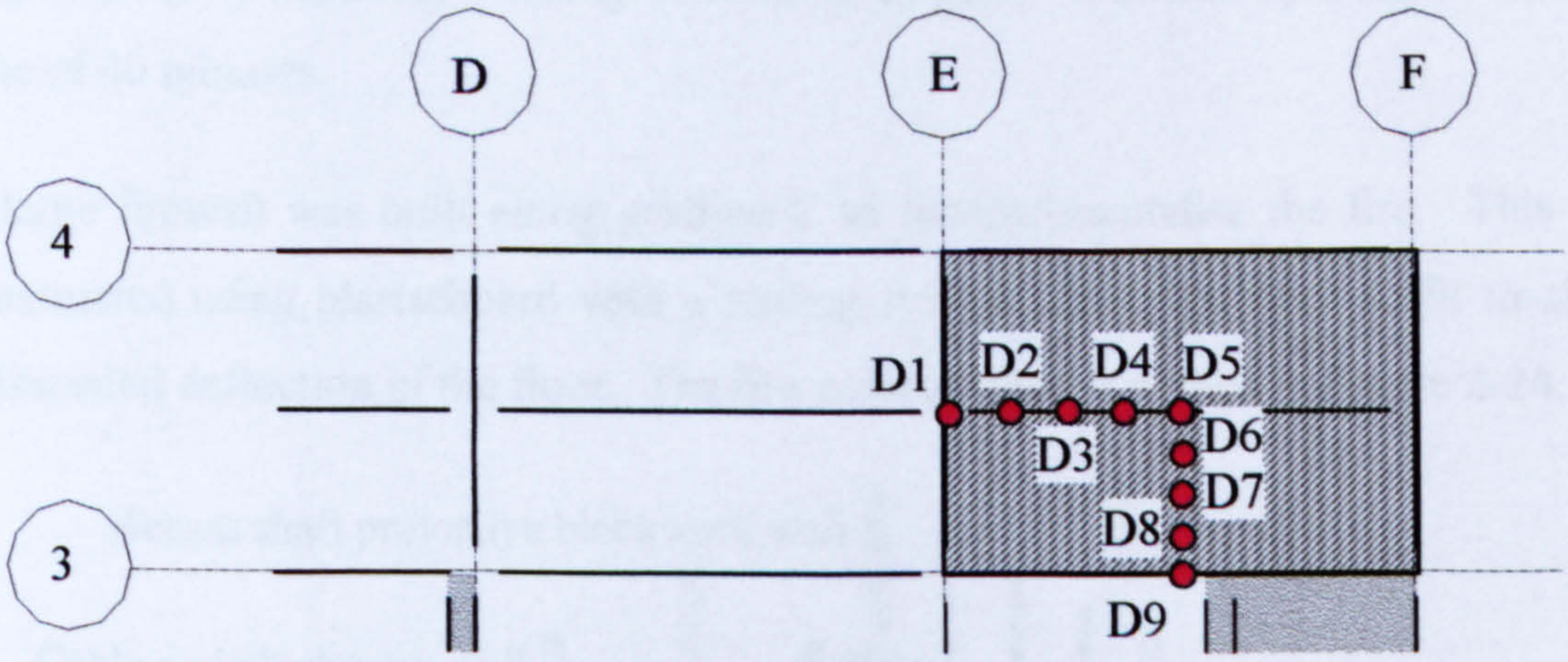

Figure 2-22. Location of the BRE corner measured deflections

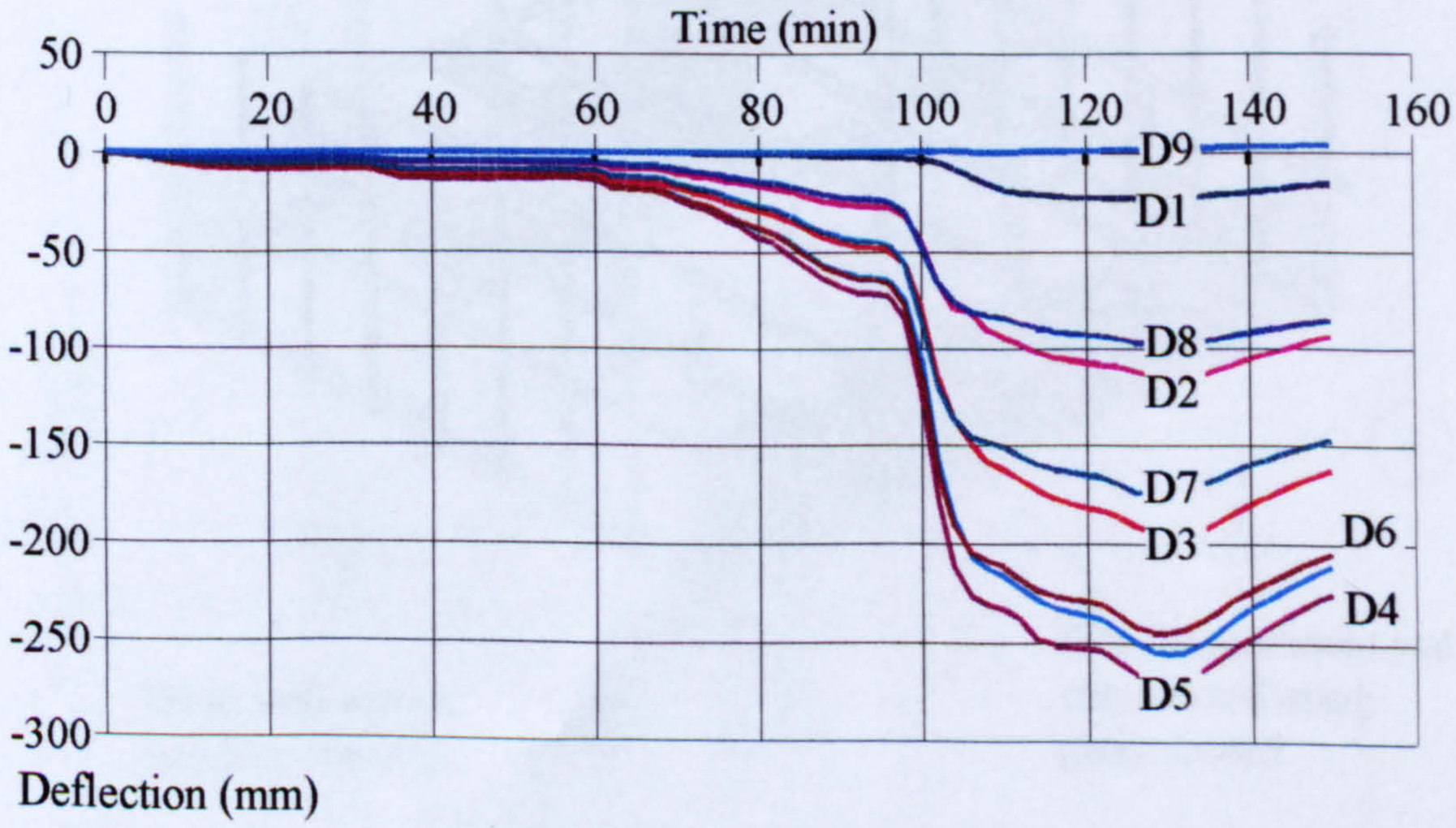

Figure 2-23. BRE corner test deflections

The deflections of the BRE corner test are negligible up to 60 minutes, and beyond this point the deflections increase slowly up to a maximum of 75mm at 95 minutes. Once flashover is attained a sudden increase is experienced over a 5-minute period, after which the temperature begins to peak, slowing the rate of deflection.

It is interesting to note the deflections at the centre of the beam on gridline 3, which actually begin to reverse towards the end of the test.

2.6 LARGE COMPARTMENT TEST

The large compartment fire test was conducted in April 1996. This fire compartment was constructed between the second and third floors, covering a total plan area of 342m^2. Figure 2-02 shows the location of the test.

In the test, timber cribs were used to heat the compartment. The cribs were designed to give an early flashover – taking 20 minutes to peak - followed by a steady burning time of 40 minutes.

A large firewall was built along gridline C to compartmentalise the fire. This was constructed using plasterboard with a sliding system under the floor soffit to allow unimpeded deflection of the floor. The fire compartment is shown in Figure 2-24.

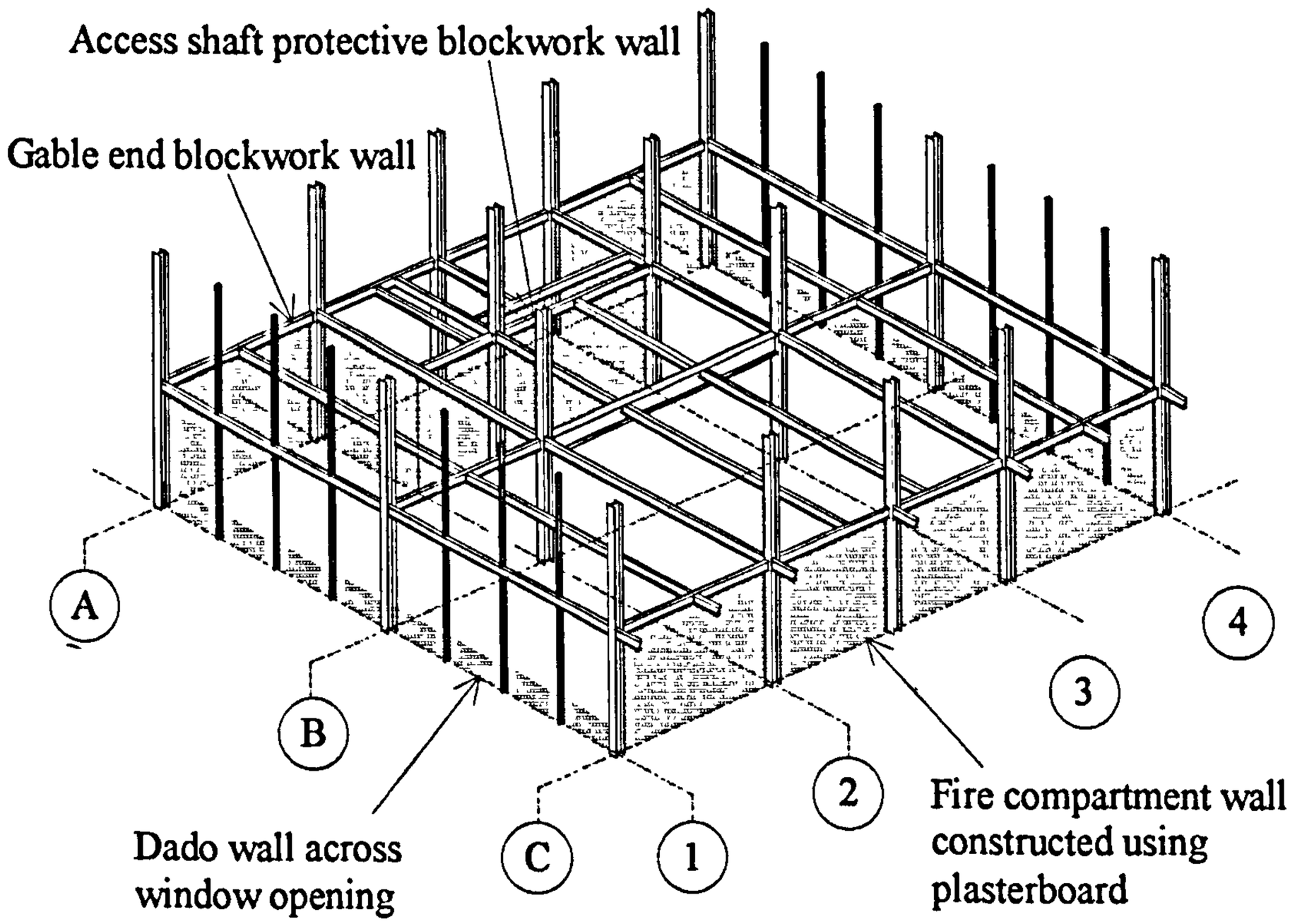

Figure 2-24. Large compartment test fire compartment

On a test of this scale it is not possible to instrument all members within and adjacent to the compartment, and so a balance of desirability against practicality must be made. The following instrumentation was used on the large compartment test:

1. Thermocouples were used to measure the atmospheric temperatures within the compartment [37].

2. Thermocouples measured the temperature of the concrete slab at different depths in 6 different locations [37].

3. The temperatures of columns, primary beams and secondary beams were recorded using thermocouples [37].

4. Thermocouples were also placed outside the building to measure the spread of temperatures outside the building and seven thermocouples were positioned to monitor the heat transferred through the fire resistant partition [37].

5. Strain gauges were used to monitor the columns throughout their cross-sections. No strain gauges were placed on beams in this test [37].

6. The concrete floor slab and its reinforcement mesh were both monitored using strain gauges [37].

7. 50 displacement transducers were used to determine the deflection of the floor slab. In order to ascertain the absolute movements of the 3rd floor, a number of additional displacement transducers were located on the 4^{th} floor [37].

8. The displacement of the firewall along gridline C was monitored by 6 displacement transducers placed along the length of the firewall [37].

9. An innovative laser system was used to measure the movement of the masonry panels on gridline A which were exposed to the fire [37].

In addition to the instrumentation listed above, a complete record using video and still photography was made of the large compartment fire test.

The temperatures presented in this thesis are taken from the centre of the fire compartment and are shown in Figure 2-25, which should be read in conjunction with the location plan, Figure 2-03.

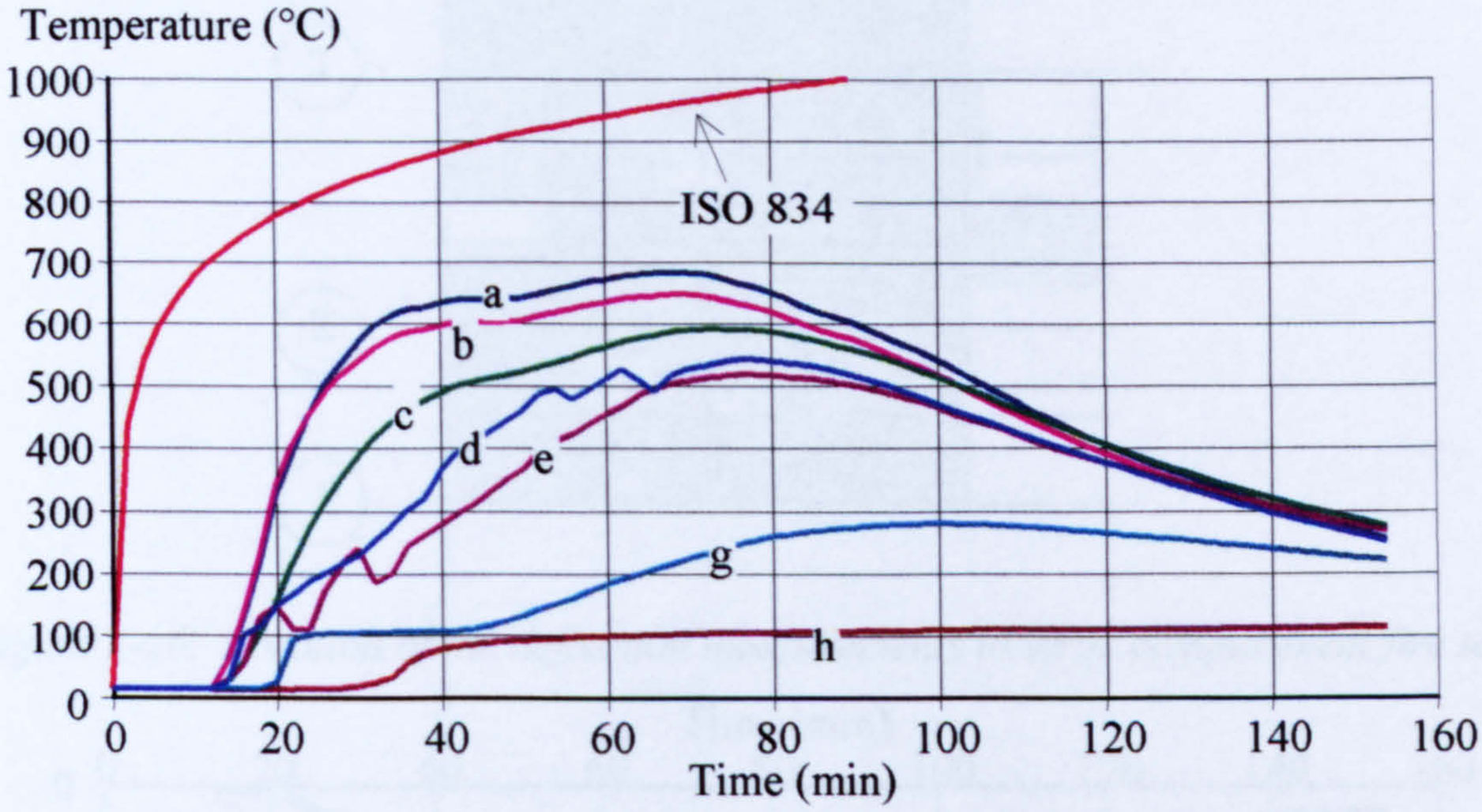

Figure 2-25. Large compartment demonstration test typical temperatures at the centre of the fire compartment

It may be seen that the bottom flange temperature is very close to that of the web, and these are 'shadowed' by the temperature of the top flange at approximately 80%. The temperatures of the metal decking both follow closely that of the top flange with the decking 'trough' logically slightly hotter than the decking 'ridge' due to its greater exposure to the fire. The temperatures within the floor slabs increase slowly until 100°C is reached. At 100°C the temperature remains constant as the water contained within the concrete matrix evaporates. At the centre of the concrete the constant temperature is slightly higher than 100°C due to the increased pressure, as the pores within the concrete through which the vapour must escape are small.

Deflections in the large compartment test were taken at points across the whole of the tested floor slab; the points illustrated within this thesis are presented in Figure 2-26.

Deflections around the structure are shown in Figure 2-27. Until approximately 16 minutes into the test no deflections were recorded, as at this stage the test fire was growing very slowly. The test beams then deflected due to the temperature difference between the steel beam and concrete slab causing thermal bowing. Beyond this (from approximately 30 minutes) the steel's loss of significant amounts of strength and stiffness increasingly produced the deflections.

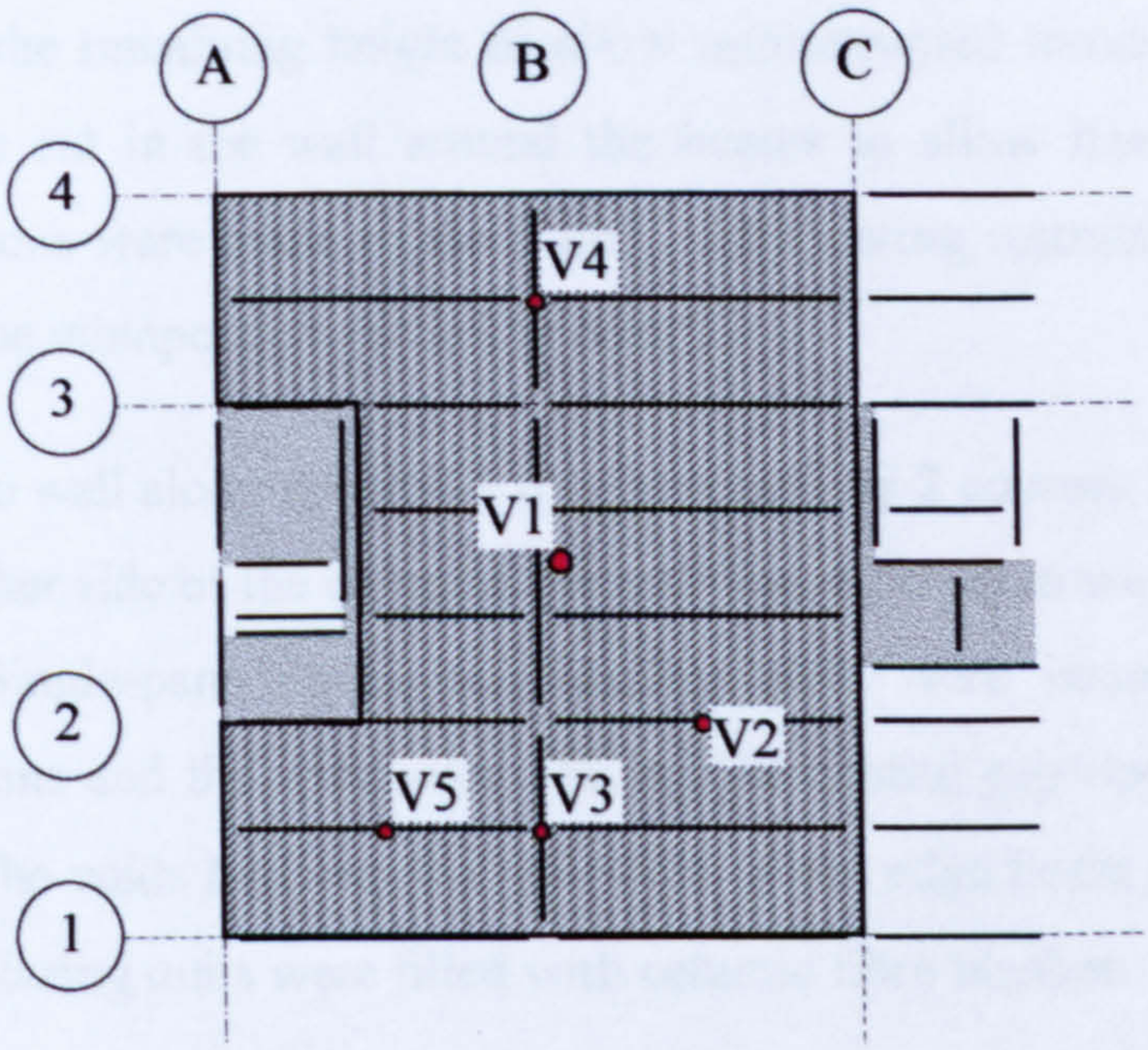

Figure 2-26. Location of the deflection measurements in large compartment fire test

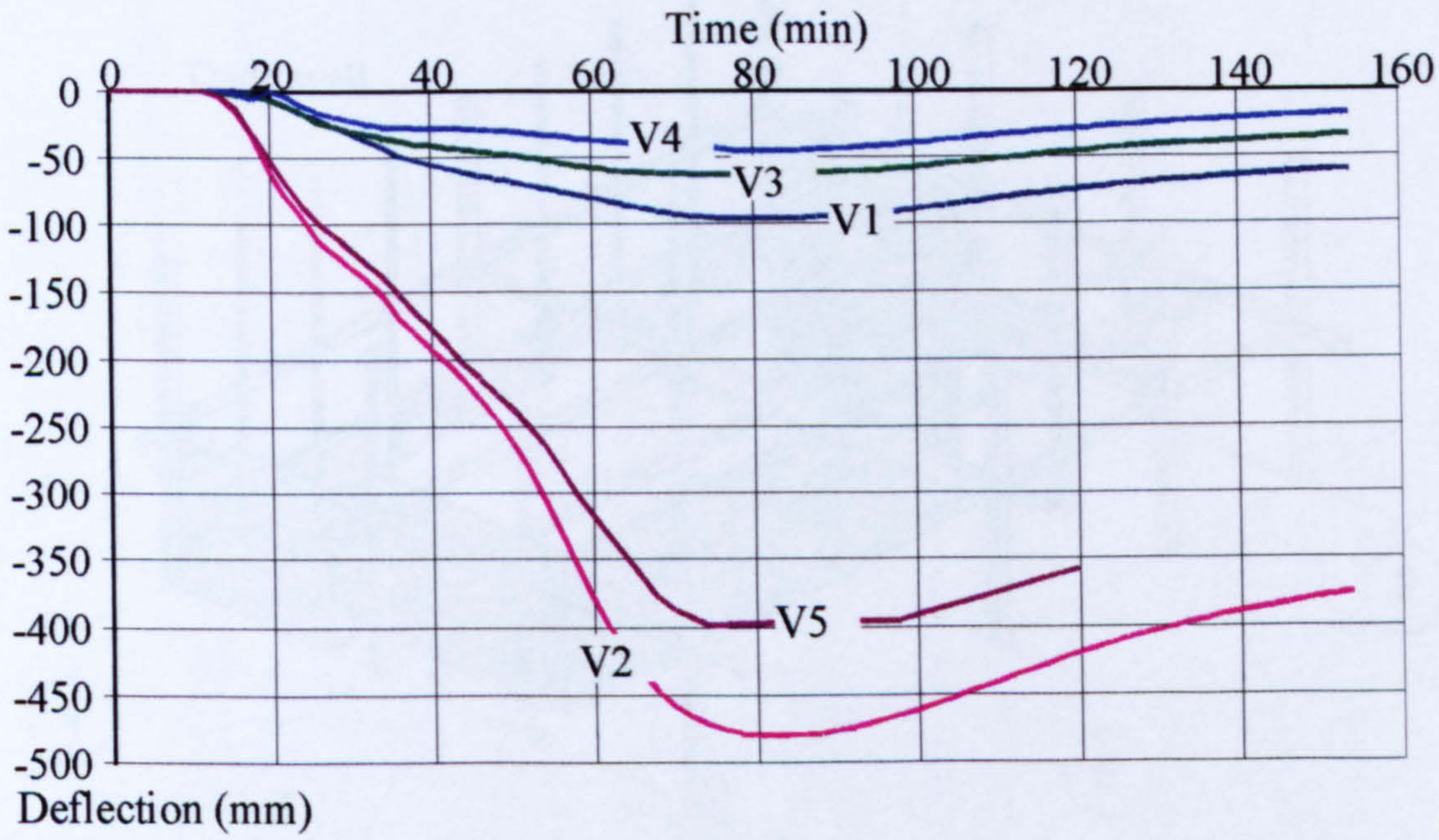

Figure 2-27. Deflections at centres of various secondary and main beams of the large compartment test

2.7 DEMONSTRATION TEST

The British Steel demonstration test was carried out during June 1996. The test was located between the first and second floors of the Cardington test frame as shown in Figure 2-02.

The fire compartment was built using lightweight blockwork to provide an open-plan office 18m wide and up to 10m deep, as shown in Figure 2-28. The wall was finished approximately 250mm below the soffit of the floor slab, and ceramic fibre blanket

was used to fill the remaining height to allow uninterrupted movement of the floor slab. Slots were cut in the wall around the beams to allow free movement. No structural alterations were made to the frame. All existing restraints and ties on the gable wall, and the windposts, were left in position.

The existing dado wall along gridline 4 was increased by 2 courses, and for a distance of 1.125m on either side of the columns the wall was built up to within 450mm of the edge beams. Single-pane aluminium glazing units were installed between the blocked-in columns and the windposts, leaving the central gap open to ventilate the compartment. The voids between the underside of the edge beam and the top of the blockwork and glazing units were filled with ceramic fibre blanket.

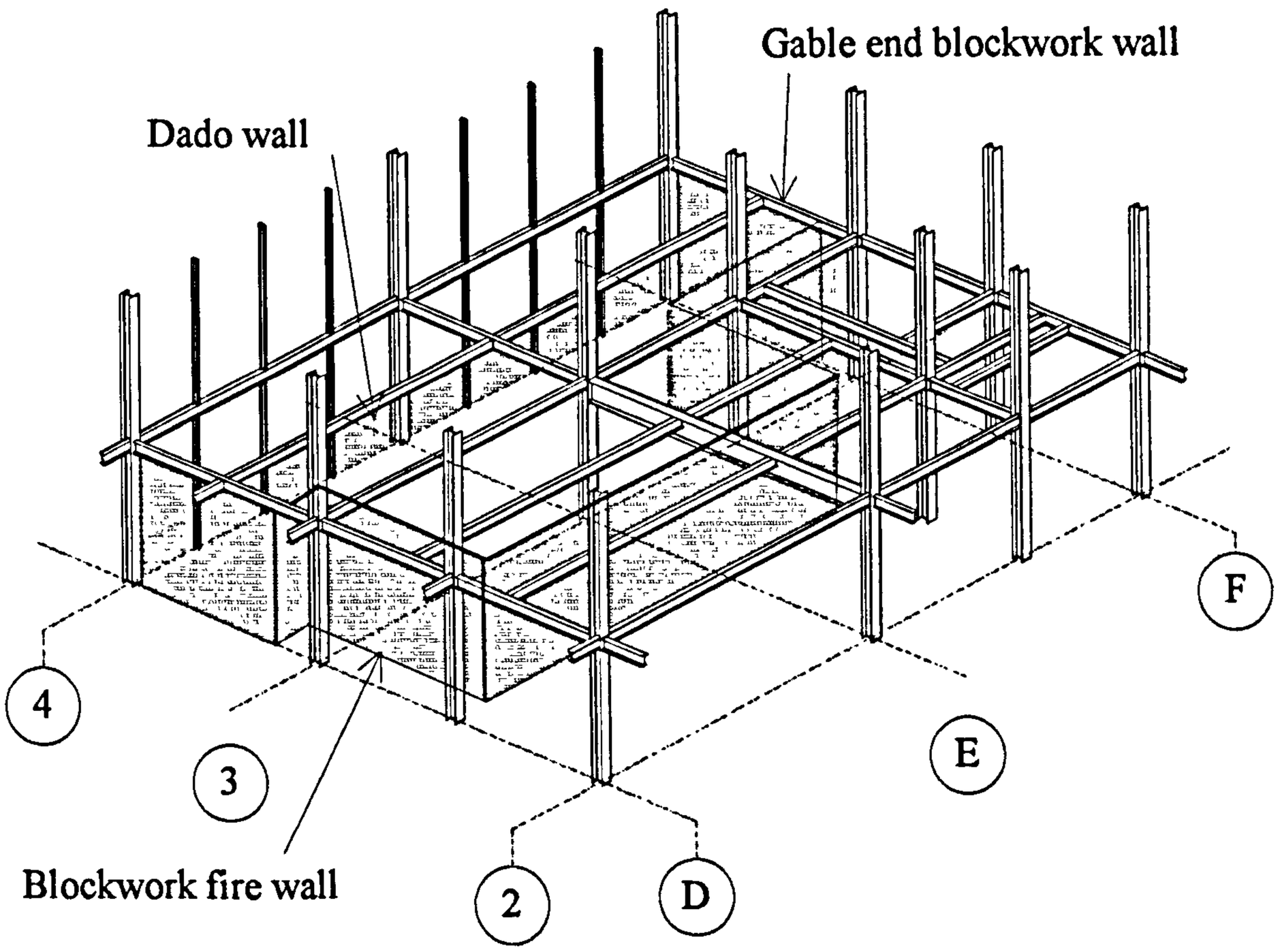

Figure 2-28. Demonstration test fire compartment

The internal column was protected to its full height, including the connections, with 25mm ceramic fibre; the columns on the perimeter of the fire compartment were treated similarly on their internal surfaces. All beams and beam-to-beam connections were left exposed.

Instrumentation for the demonstration test was installed to record:

1. Steel temperature profiles along the primary, secondary and edge beams [38, 39 and 40].

2. Steel temperature profiles at selected beam-to-beam and column-to-beam connections [38, 39 and 40].

3. Steel temperature profiles along the protected columns [38, 39 and 40].

4. Temperatures of the atmosphere gases [38, 39 and 40].

5. Vertical deflection of the floor beams [41].

6. Strain profiles across the columns within and above the compartment [42].

Temperatures found in the centre of the fire compartment during the test are shown in Figure 2-29 and should be read in conjunction with Figure 2-03. The standard ISO 834 curve has been included for comparison. After the fire was lit, the fuel smouldered for approximately 10 minutes, at which stage flashover occurred, with a maximum temperature of approximately 1100°C being reached at 30 minutes. The steel temperatures followed the atmosphere temperatures closely, with a bottom flange temperature lag of about 5 minutes over the preliminary stages of the fire. The top flange temperature was found to be 80% that of the bottom flange and the web.

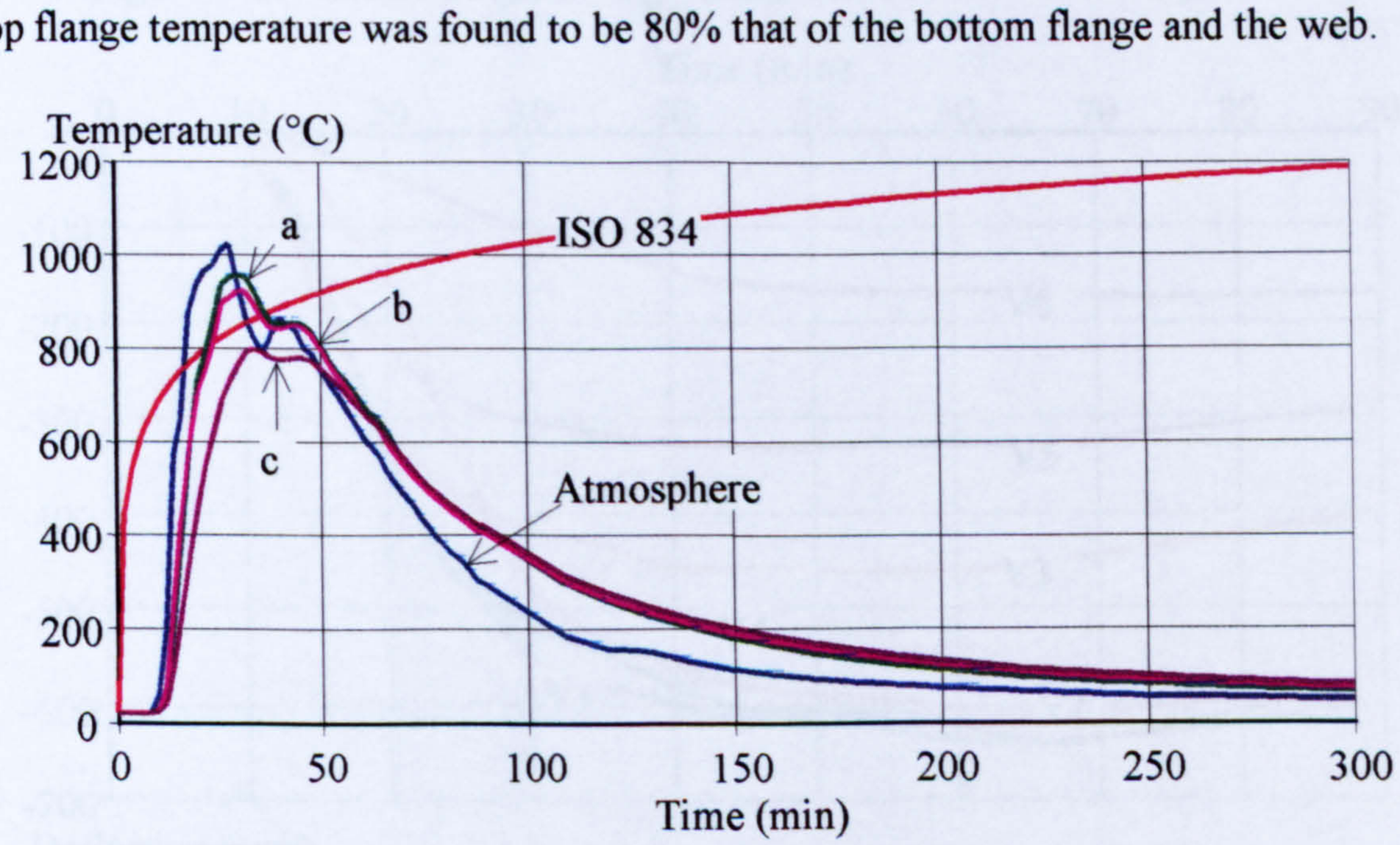

Figure 2-29. Temperatures at the centre of the large compartment demonstration test

Six of the key deflections - as located in Figure 2-30 – are shown in Figure 2-31. All six locations deflect nominally during the first 10 minutes whilst the fire smoulders. All members begin deflecting initially through thermal bowing due to the temperature differential between the steel beam and concrete slab. After approximately 20 minutes the compartment temperatures are sufficient for the steel members to begin to

lose strength and stiffness rapidly, therefore inducing greater deflections. The central deflection of the 6m main beam may be compared to the large compartment test, which has approximately the same deflections for the same temperature. The structure reached equilibrium after approximately 40 minutes.

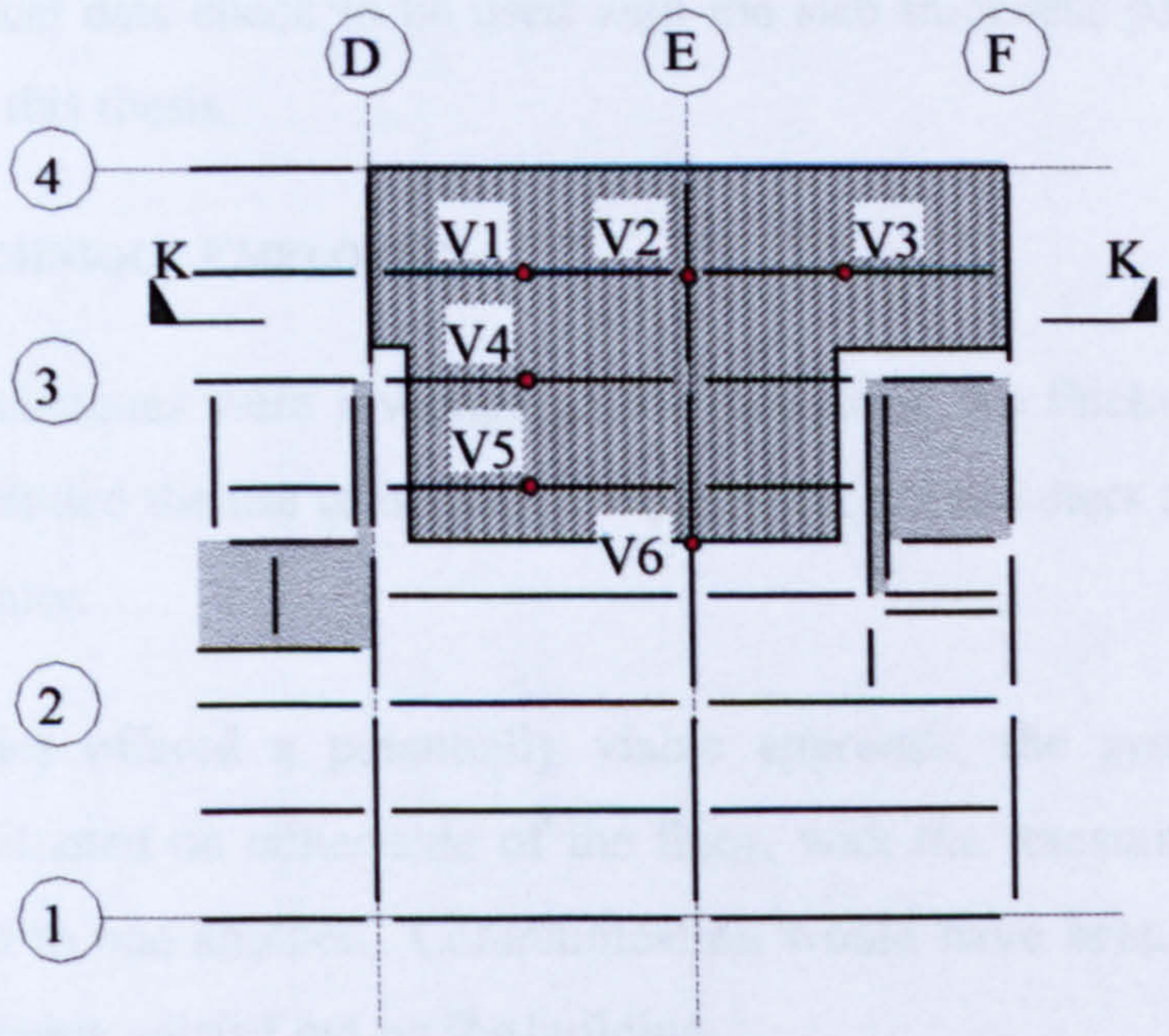

Figure 2-30. Location of the large compartment demonstration fire test

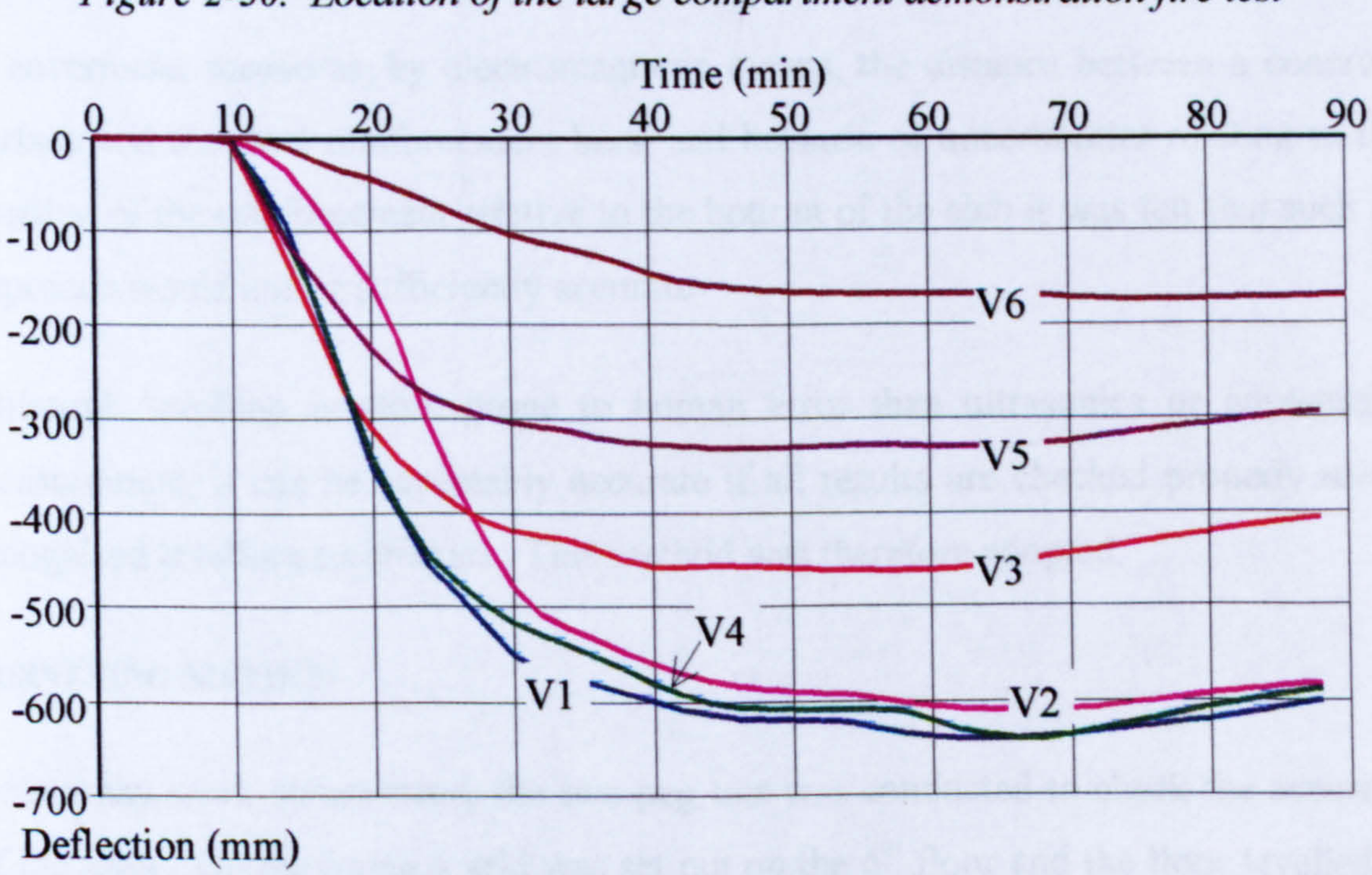

Figure 2-31. Beam deflections in large compartment demonstration test

2.8 Slab Thickness Survey of the Cardington Test Frame

Floor slab thicknesses in buildings of normal composite construction are known to vary significantly from those specified. This is normally due to 'ponding' as formwork (either permanent or temporary) supporting the setting concrete deflects

due to its self-weight. This was observed in a survey by the Building Research Establishment [43] covering an area of approximately 81m^2 of the composite test frame at Cardington. It was decided that a larger survey should be conducted covering half the test frame floor area, and on two adjacent floors. This was to provide a more extensive statistical data check to be used with the slab thickness parametric studies included later in this thesis.

SURVEYING TECHNIQUE EMPLOYED

A number of techniques were investigated for measuring the thickness of the floor slabs. These included the use of ultrasonic equipment, covermeters and conventional levelling techniques.

Whilst ultrasonics offered a potentially viable approach, the system requires an operator to be situated on either side of the floor, with the transmitter and receiver directly opposed to one another. Communication would have been difficult, due to extensive work being carried out on the building.

A covermeter measures, by electromagnetic means, the distance between a concrete surface and the steel reinforcement bars, and because of uncertainties relating to the position of the reinforcement relative to the bottom of the slab it was felt that such an approach would not be sufficiently accurate.

Although levelling is more prone to human error than ultrasonics or covermeter measurement, it can be acceptably accurate if all results are checked properly using recognised levelling techniques. This method was therefore adopted.

SURVEYING METHOD

Before any work commenced, the two-peg test was conducted to check the accuracy of the level. On the frame a grid was set out on the 6th floor and the floor levelled at all grid points, via a change-point in the lift shaft. The 6th floor soffit was surveyed at the corresponding grid points. The process was repeated for the top and bottom surfaces of the 5th floor. The survey was closed via the change-points in the lift shaft back to the datum point. The closing error was found to be negligible. Care had to be

taken to ensure that the levelling staff was at all times positioned on the ribs in the floor construction as shown in Figure 2-32.

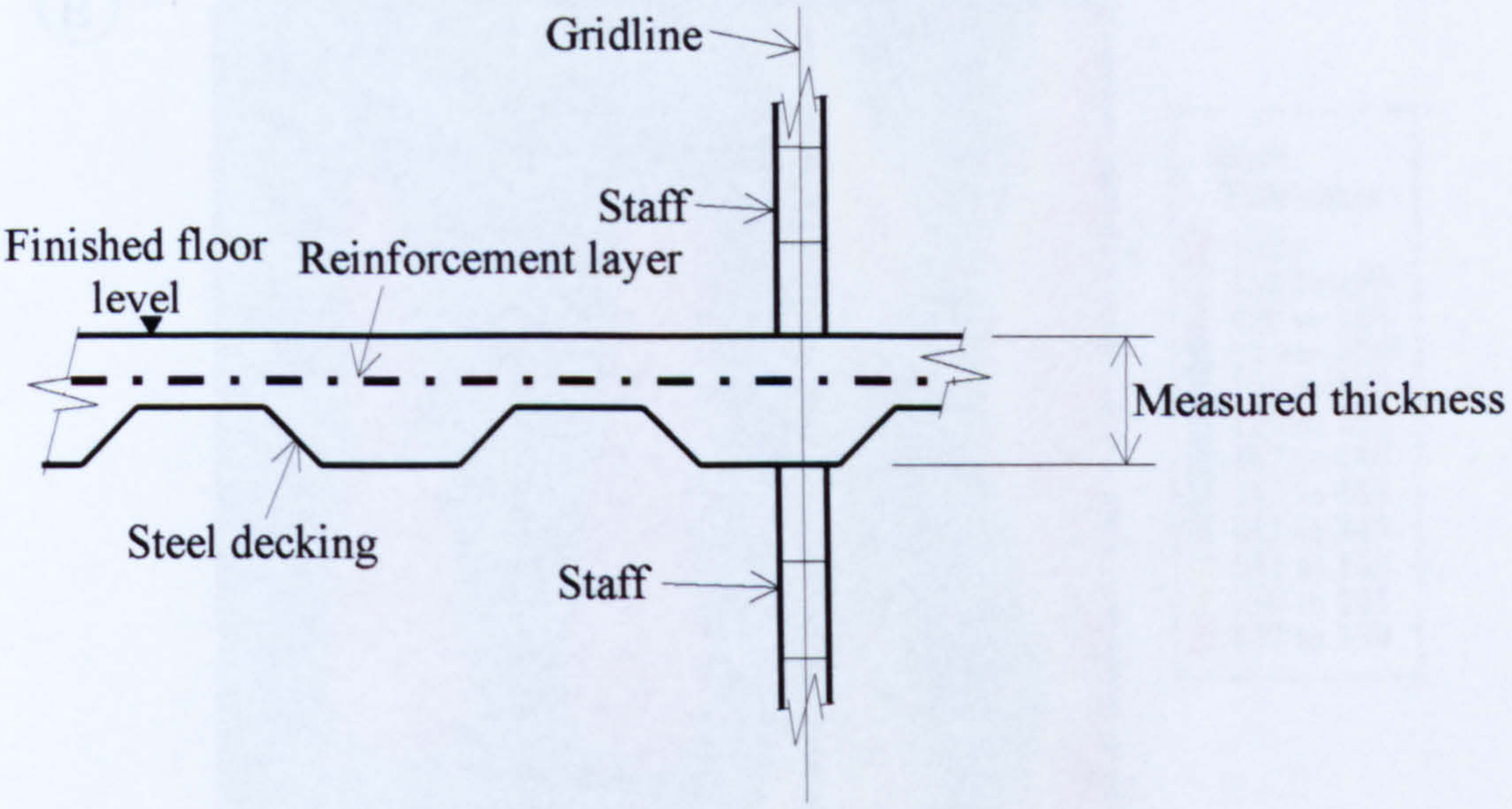

Figure 2-32. Cardington floor construction

SURVEY RESULTS

The areas surveyed on both the 5th and 6th floors are as shown in Figure 2-33.

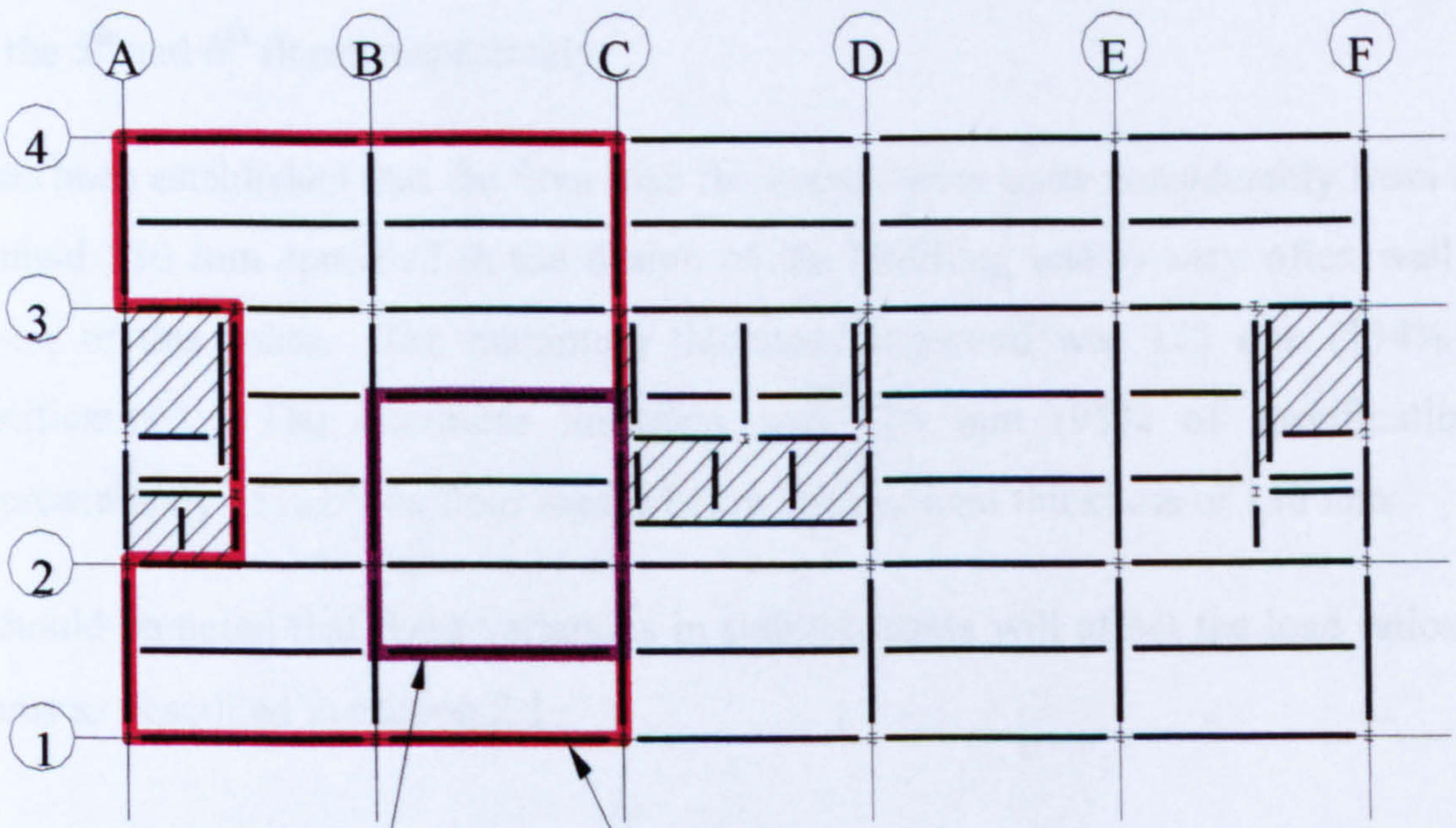

Figure 2-33. Cardington test frame plan showing floor area surveyed

B.R.E. had previously conducted a slab thickness survey of a small area of the Cardington test frame. The results from this survey are shown in Figure 2-34.

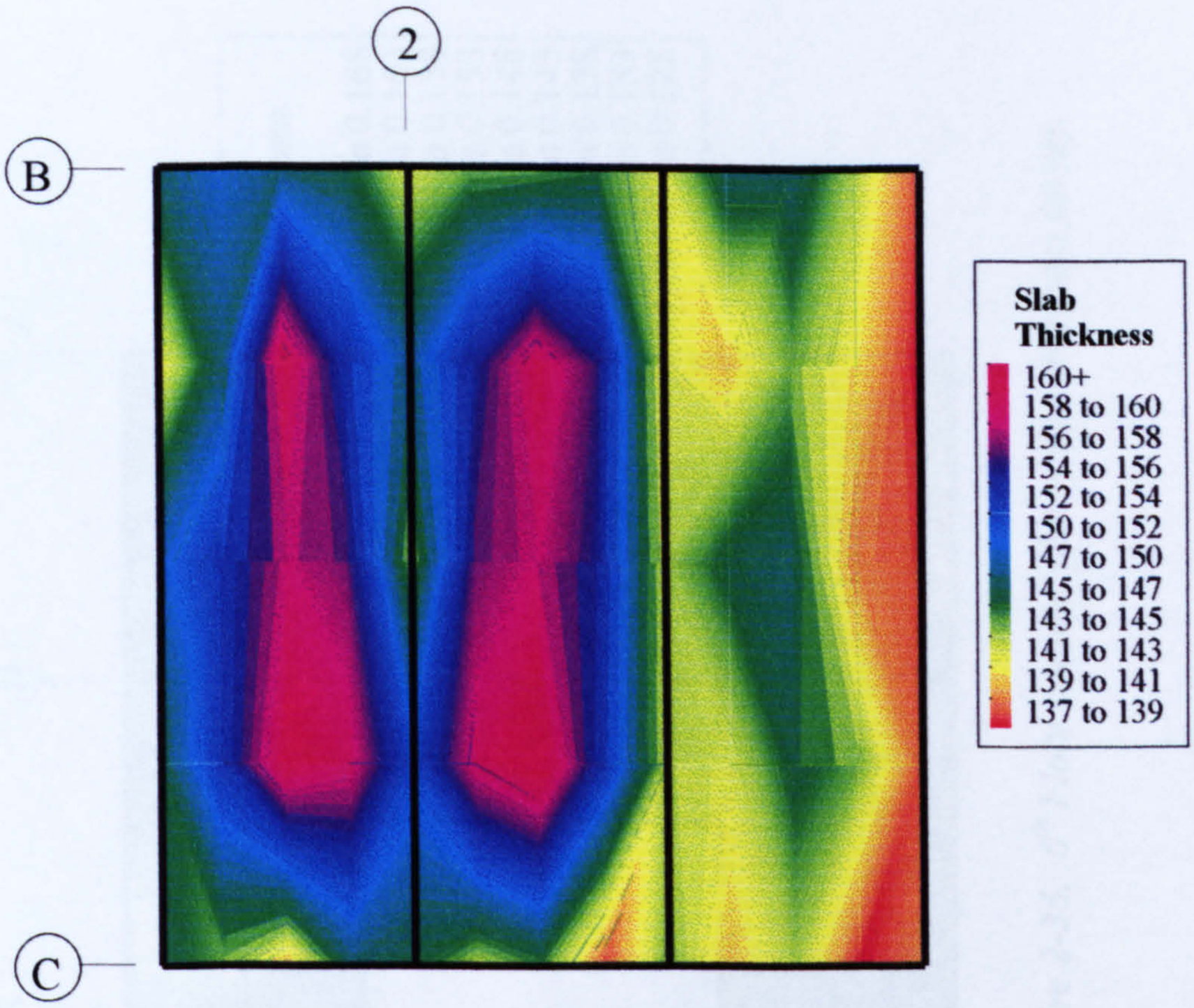

Figure 2-34. Contour plot of B.R.E. slab thickness survey on 5th floor [43]

The measured floor thicknesses are shown as contour plots in Figures 2-35 and 2-36 for the 5th and 6th floors respectively.

It has been established that the floor slab thickness varies quite considerably from the nominal 130 mm specified in the design of the building, and is very often well in excess of this value. The maximum thickness measured was 173 mm (134% of specification). The minimum thickness was 124 mm (95% of specification). Approximately 15% of the floor area is below the nominal thickness of 130 mm.

It should be noted that these variations in slab thickness will affect the load ratios to beams as described in section 2.1

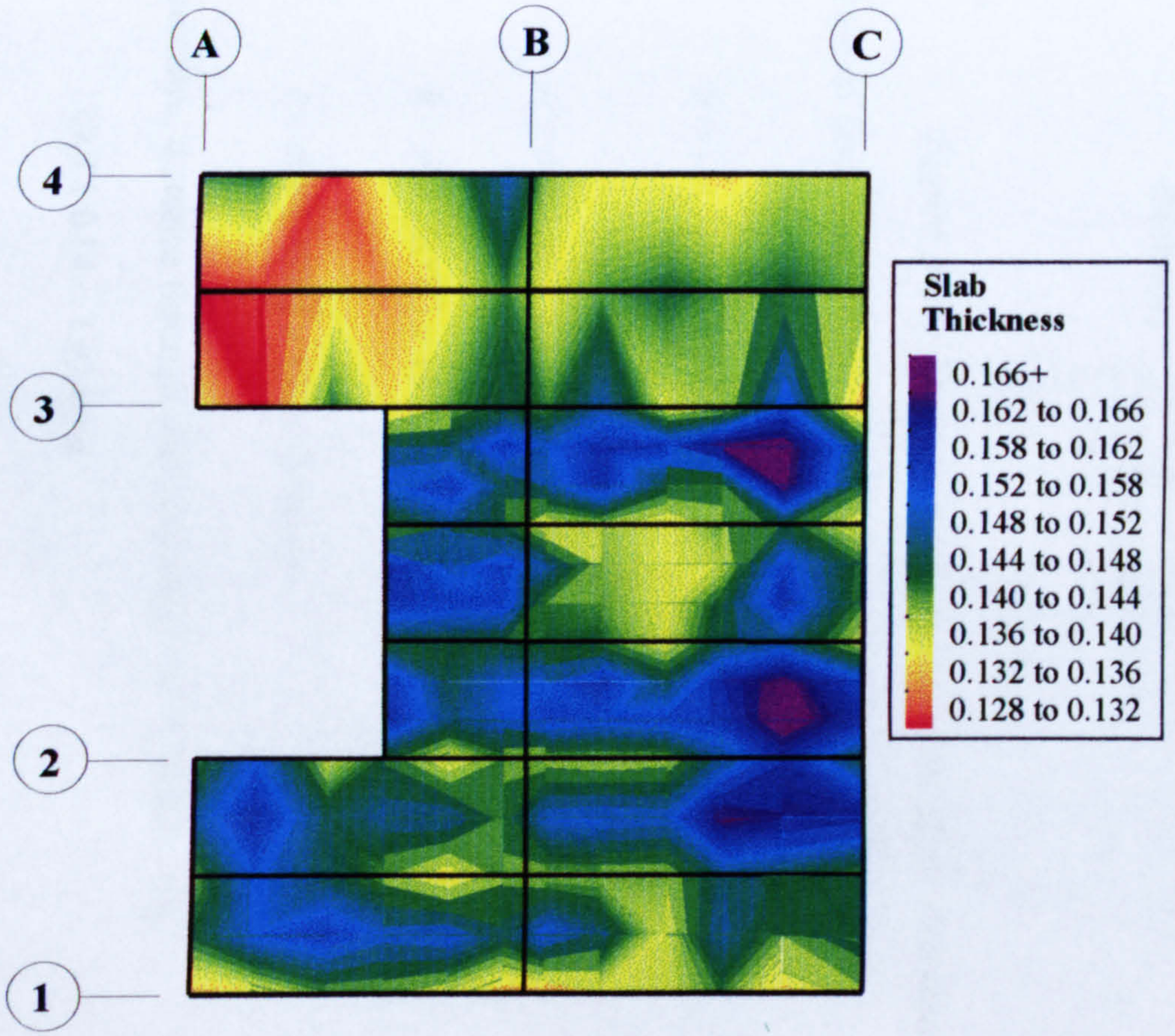

Figure 2-35. 5th Floor contour plot of slab thickness survey

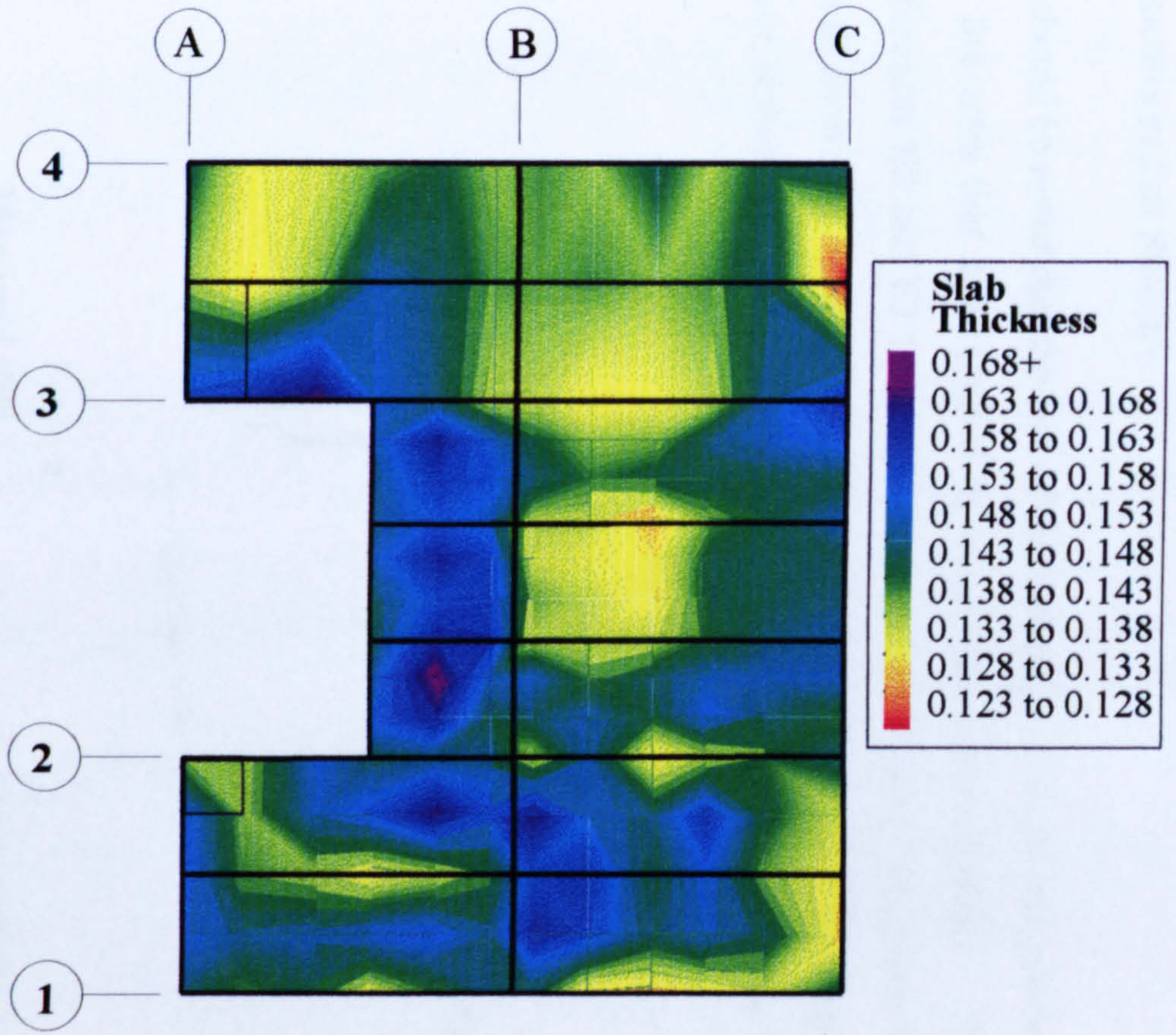

Figure 2-36. 6th Floor contour plot of slab thickness survey

ERRORS IN THE SURVEY

It should be noted that the end of the building surveyed had previously been subjected to fire tests that had resulted in large floor displacements. The columns on grid references E2 and E3 had 'squashed' locally (during the plane frame test) and as a result shortened by approximately 200 mm. This caused a change in the angle of the floor, influencing the apparent slab thickness, as shown in Figure 2-37.

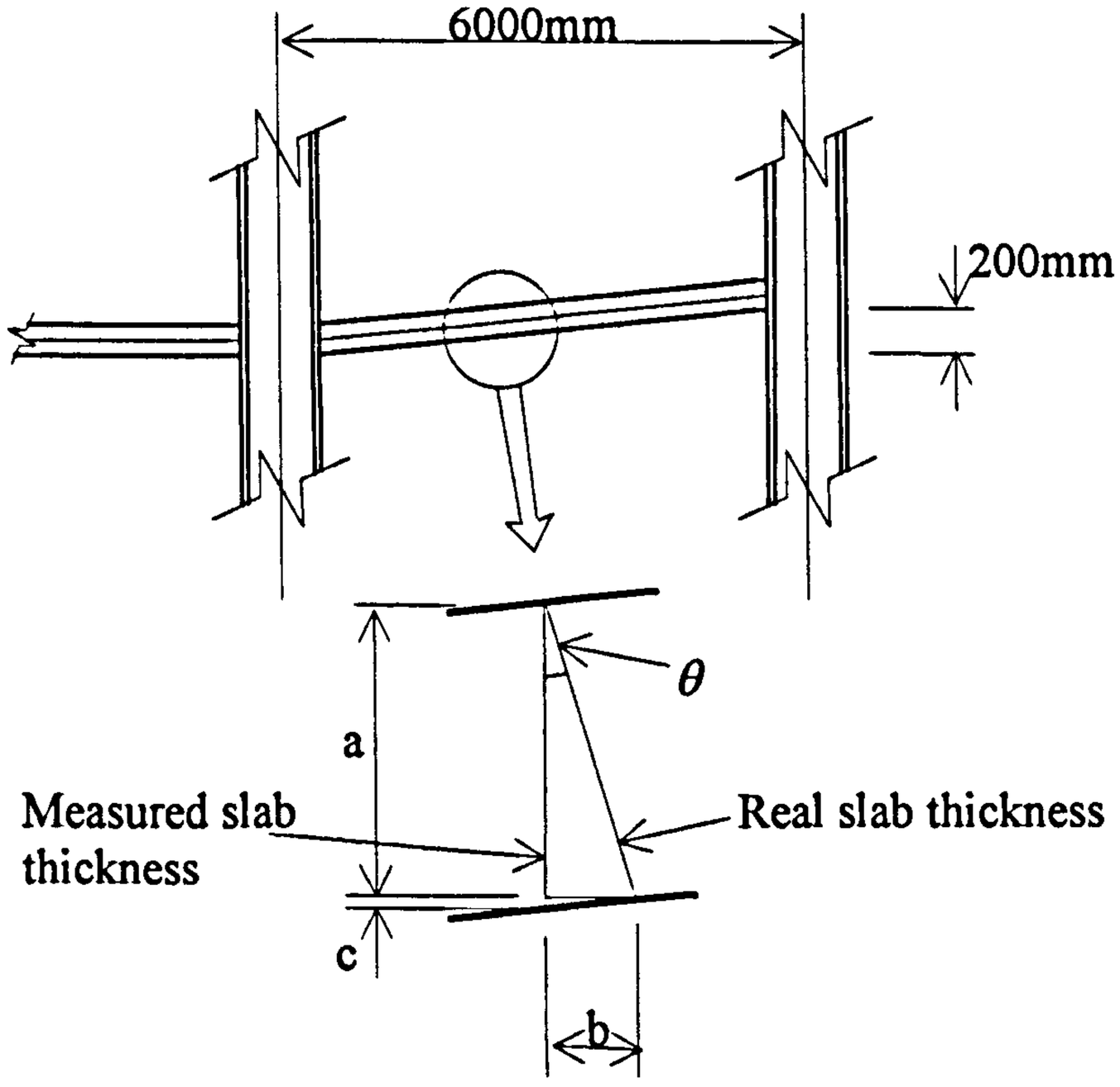

Figure 2-37. Error in the thickness of the floor slab due to slope

Angle of floor slab,

$$\theta = \tan^{-1}\left(\frac{200}{6000}\right) = 1.909°$$

$$a = \cos(1.909°) \times 130 = 129.93mm$$

$$b = \sin(1.909°) \times 130 = 4.33mm$$

$$c = \sin(1.909°) \times 130 = 0.14mm$$

Therefore, distance through slab is (Length 'a' + length 'c'),

$$129.9 + 0.14 = 130.4mm$$

The effect of the slope on the floor slab's measured thickness is deemed to be negligible.

This 'error' could be magnified if, when surveying the underside of the floor, the staff position did not correspond exactly with the survey point on the top of the slab. This could be caused simply by operator inaccuracy or by the staff having to be moved to avoid a trough in the composite decking. Assuming the point measured on the soffit is within 100 mm of the grid point, as shown by Figure 2-38, then the maximum error is,

$$D = \left(\frac{200}{6000}\right) \times 100 = 3.33mm$$

When considering the overall depth of the floor this error is again deemed to be negligible.

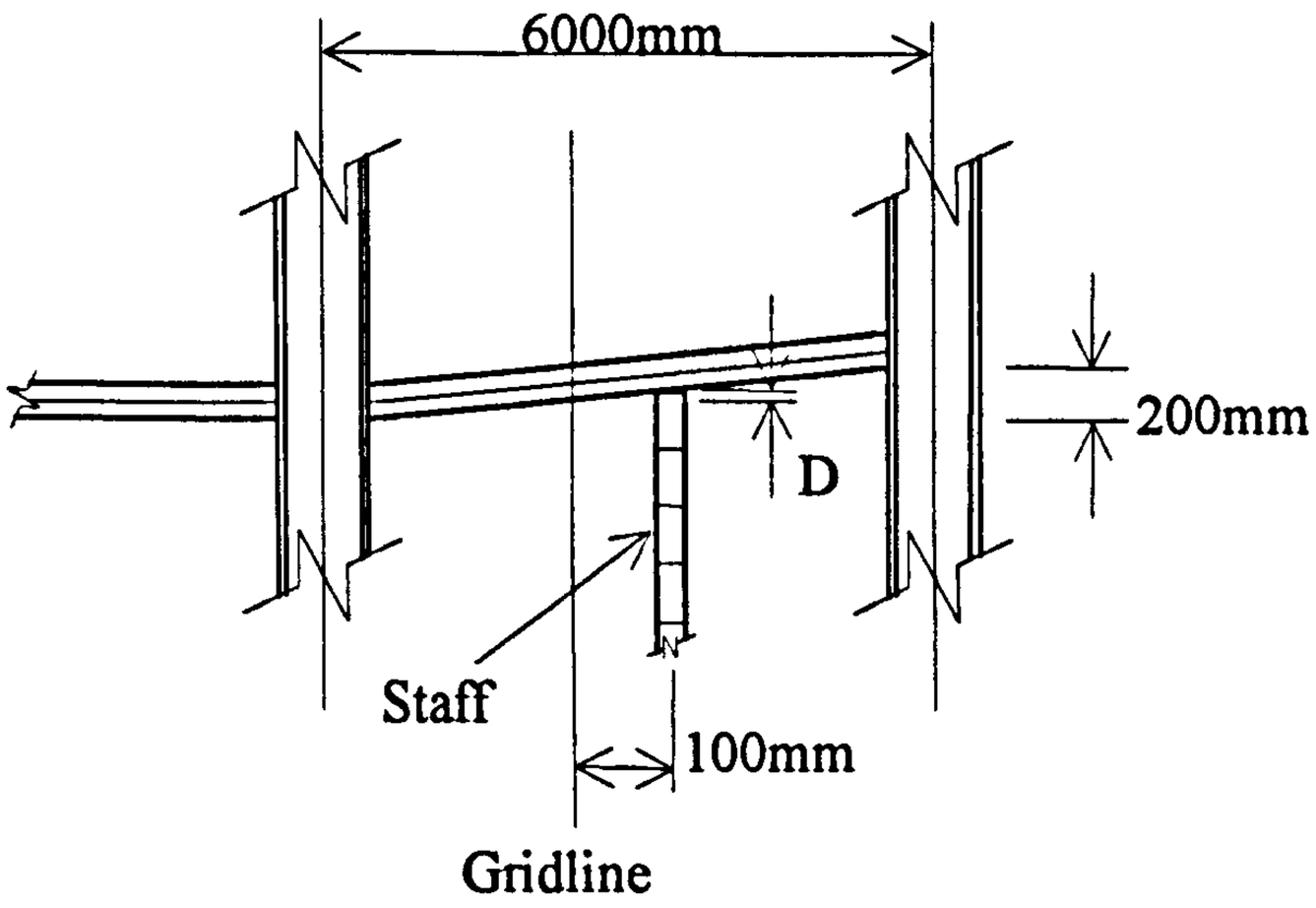

Figure 2-38. Error produced by misplacement of the staff whilst measuring the floor soffit.

3 DEVELOPMENT OF THE FINITE ELEMENT PROGRAM – VULCAN

3.1 INTRODUCTION

As was briefly outlined in Chapter 1, furnace testing is inherently limited by the physical size of the specimen and the financial costs involved. To continue with studies of the effects of fire action on steel structures, organisations have heavily invested time and money in developing reliable analytical models to reduce these costs and to gain an understanding of structures outside the capacity of a normal furnace. A brief history of the simulation of behaviour of steel structures in fire has been outlined by Bailey [44].

3.2 HISTORY AND FINITE ELEMENT PROCEDURE OF VULCAN

The finite element method is widely used in structural analysis, but can also be applied to a wide range of physical problems such as heat transfer, seepage and fluid flow. The finite element method idealises a continuum as an assemblage of elements (of finite size) with specified nodes, and hence specified unknowns at the nodes replace the infinite number of degrees of freedom across the continuum.

In the finite element program VULCAN, three different types of element have been used to represent various structural components, namely beam elements (for beams and columns), spring elements (for steel-to-steel semi-rigid connections) and flat shell elements (for floor slabs). These are described in the following sections.

3.2.1 BEAM ELEMENTS

El-Zanaty and Murray [45] of the University of Alberta originally developed their beam finite element model in the context of a frame program for large deflection analysis including spread-of-yield, in two-dimensional steel frames at ambient temperatures. This program was named INSTAF, an acronym for INelastic STability Analysis of Frames.

El-Zanaty and Murray[45] made three basic assumptions in the beam element formulation:

1. The element is straight, prismatic and symmetric about its axis, which coincides with the centroid of the cross-section.

2. Loads are applied only at the ends of an element, at nodes.

3. Only in-plane deformations occur, and cross-sections that are originally normal to the member longitudinal axis will remain undistorted and normal to the beam axis after deformation.

Nodal positions are assumed along the length of a beam, separating it into a number of elements. The nodes are positioned at the centroid of the beam section, the placement of which is determined at ambient temperature and remains constant throughout the analysis. The displacements of the nodal points are the basic unknown parameters of this problem. There are two different methods available to determine the solution, known as the displacement field and the stress field procedures, both of which are described by Zienkiewicz [46]. As the displacement field procedure is simpler to implement than the stress field procedure when accurate displacements are required, it has been adhered to throughout the formulation. The displacement of the reference axis within the element, bounded by the nodal points, is defined by interpolation (shape) functions. If the displacement of the reference axis is known, it is possible to determine the displacement anywhere within the cross-section of the beam, and using the large displacement-strain equation the state of strain may be obtained [47]. As the large displacement-strain equation retains higher-order terms within its formulation, geometrically non-linear behaviour may be introduced. As the constitutive properties of steel are known, the state of stress throughout the member may be calculated, together with the nodal stresses. Equilibrium is enforced between the boundary stresses and the externally applied loads.

Considering the work done by the steel element and the external loads, the Principle of Virtual Work may be used to enforce equilibrium by:

$$\delta W = \int_v \sigma_s \delta\varepsilon_s \, dv - \langle Q \rangle \{\delta q\} = 0 \qquad 3\text{-}01$$

where,

σ_z is the axial stress,

$\delta\varepsilon_z$ is the virtual axial strain (corresponding to the imposed virtual displacements),

$\langle Q \rangle$ is the row vector of external loads,

$\{\delta q\}$ is the column vector of imposed virtual displacements.

If the standard finite element procedure is followed [48, 46, 47] equation 3-01 results in a stiffness relationship,

$$[K]\{q\} = \{Q\} \qquad 3\text{-}02$$

where,

[K] is the tangent stiffness matrix,

{q} is the vector of nodal displacements,

{Q} is the vector of nodal forces.

If non-linear analysis is considered, an iterative procedure is required to find the solution, and so the above equation becomes

$$[K]\{\Delta q\} = \{\Delta Q\} \qquad 3\text{-}03$$

where,

$\{\Delta q\}$ is the vector of incremental nodal displacements,

$\{\Delta Q\}$ is the vector of out-of-balance forces, which on the first iteration is equal to the external loads.

As it is necessary to integrate equation 3-01 across the volume, Gaussian Integration is used to evaluate the integral over the cross-section at sampling (Gauss) points, in conjunction with weighting factors used to calculate the internal work by calculating along the element length. The accuracy of this process is dependent on the positions

of the Gauss points and the corresponding weighting factors, and the number of sampling points used. Within INSTAF, four Gauss points have been used on each element, and the positions of these (in conjunction with the weighting factors) can be obtained from textbooks by authors such as Bathe [48] and Zienkiewicz [46, 47].

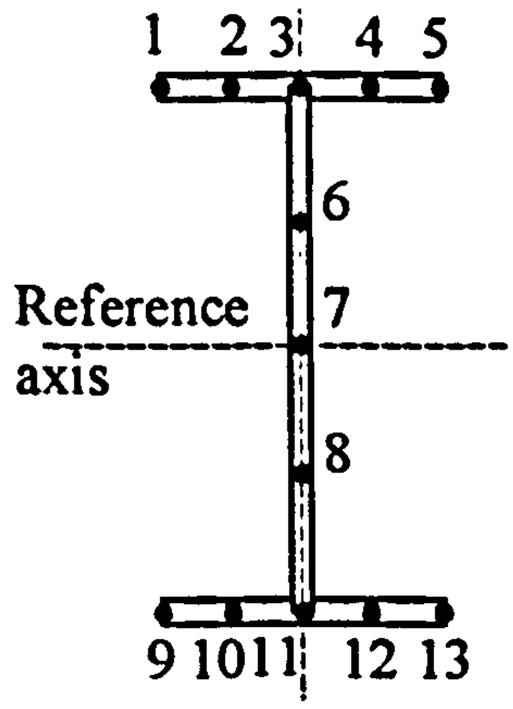

Figure 3-01. Cross-section positions at which displacements; strains and stresses are defined.

Stress resultants across the beam section are found by integration, either by the use of section properties or more easily in inelastic cases by direct numerical integration of the stresses. The cross-section is split into 12 segments, allowing the displacements and strains to be determined at 13 points as shown in Figure 3-01, which allows relatively accurate stress distribution across the section.

Basic structural mechanics reveals that yield of a member starts to occur where the bending moment forces the outer fibres of a section to exceed the yield stress of the material. This often occurs at the position of the maximum bending moment. As El-Zanaty and Murray [45] assumed that all loads are positioned at the nodal points of the beam elements, the maximum bending moment will typically occur at a node, although a few exceptional cases occur. Hence, in the initial INSTAF validations it was found that spread of yield in the areas local to nodes was not reflected in the element tangent stiffness due to the even distribution of the four Gauss points used in the numerical integration. The element length was therefore divided into three sub-elements with the central sub-element covering 80% of the element and the remaining two sub-elements 10% each. This resulted in the outer sub-elements containing four Gauss points clustered in the locality of the node; effectively incorporating the inelastic strains within the element stiffness matrix when necessary. Static condensation [48] is then used to eliminate the internal degrees of freedom created by the initial sub-division.

Saab [49, 50] developed this basic formulation of INSTAF and analysed two-dimensional steel frames in fire conditions. The thermal material non-linearities were included within the formulation using stress-strain-temperature relationships, and also by specifying the tangent modulus of the material at specific strain values by the use of the transformed section concept [45]. The method transforms the width of each of the twelve segments shown in Figure 3-01 based on the average tangent modulus of the material to find an equivalent elastic cross-section.

Thermal strains are included in the formulation by considering the temperature profile across the section, and these are added as mechanical strains of the opposite sign, as shown in Figure 3-02.

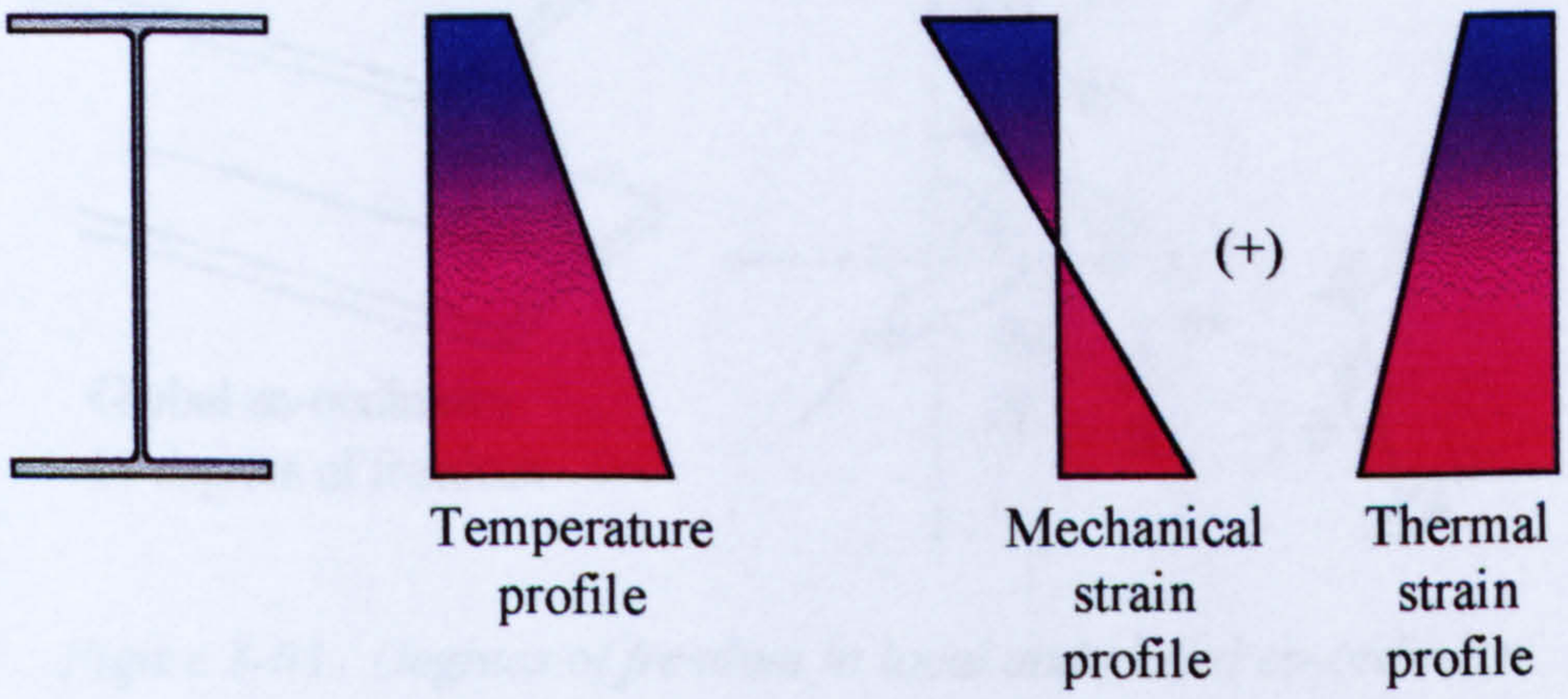

Figure 3-02. The addition of thermal strains in INSTAF

The unbalanced force in equation 3-03 now becomes,

$$\{\Delta Q\} = \{Q_{applied} - Q_{internal} - Q_{thermal}\} \qquad 3\text{-}04$$

This procedure is followed as the elements increase in temperature.

Najjar [51] further developed INSTAF to allow analysis of three-dimensional bare steel frame behaviour in fire conditions. In local three-dimensional co-ordinates each beam element node has eight degrees of freedom. These become eleven degrees of freedom when transformed to global co-ordinates as shown in Figure 3-03.

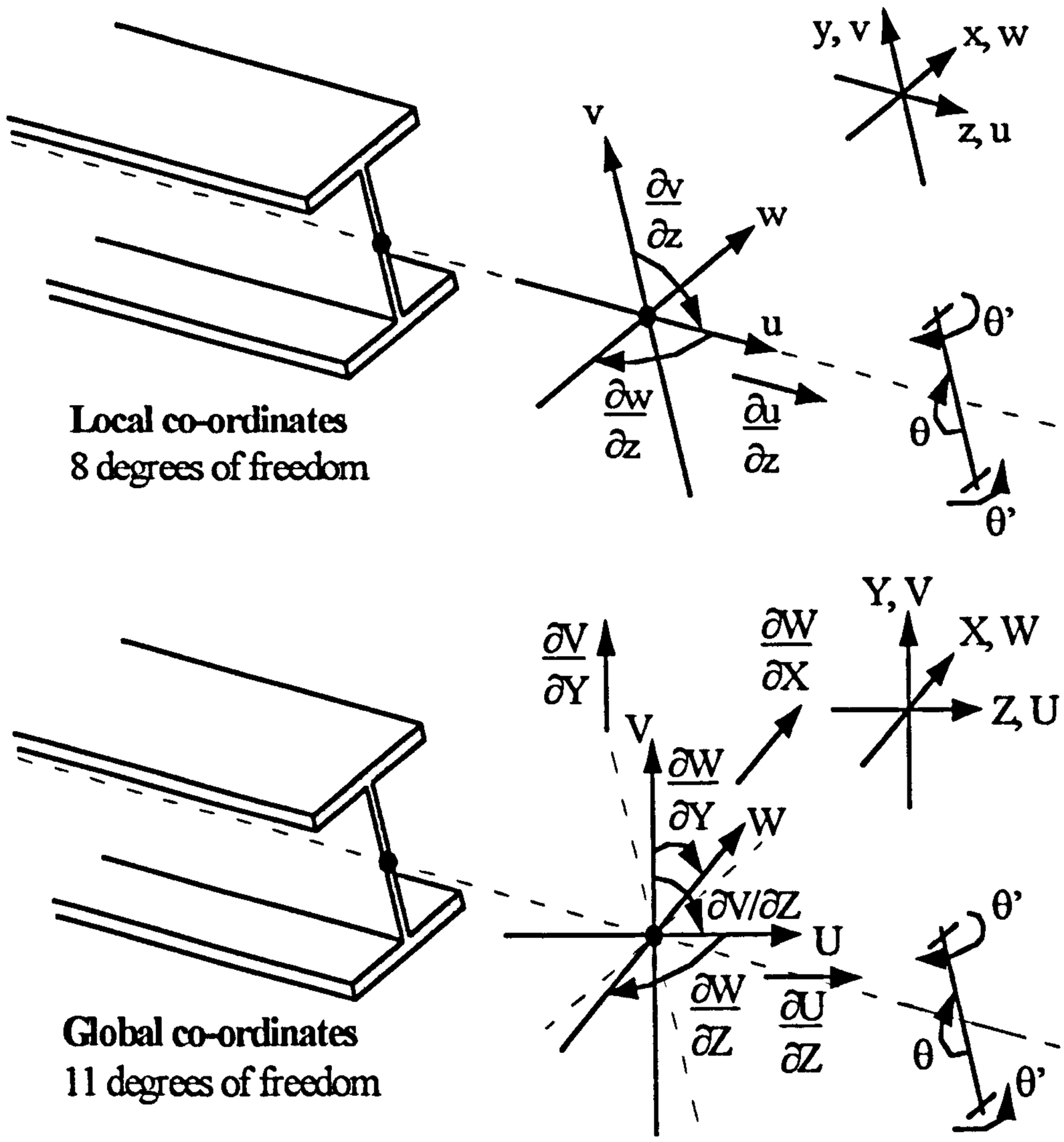

Figure 3-03. Degrees of freedom in local and global co-ordinates

The original formulation assumed a reference axis at the centroid of the steel section. Bailey [44] revised INSTAF so that it was possible to place the reference axis at any arbitrary point on the vertical axis. This was achieved by evaluating the sectional and sectorial properties, and the stress resultants required for the repositioning of the reference axis. It was necessary for the reference axis to be movable was so that the flat shell element could be 'attached' to the beam element nodes without the use of additional elements which are computationally expensive.

The final development of the steel beam element was also by Bailey [44], who included provision for lateral-torsional buckling. The analyses conducted within this thesis concern either beams restrained against lateral-torsional buckling, compression members or tension members, all of which are subject to negligible lateral-torsional buckling.

The finite element program INSTAF was renamed VULCAN during May 1997.

3.2.2 STEEL-TO-STEEL CONNECTIONS

Steel-to-steel connections within a structure are represented within the finite element code using zero-length non-linear spring elements that were added by Bailey [44]. The spring elements use the same eight degrees of freedom as the beam elements (in local co-ordinates), which when transformed to global co-ordinates become eleven degrees of freedom, as shown in Figure 3-03. The spring element is flexible in its use and may be placed at any position within the structure, as axial movement, rotations, strains, torsion and warping are all included within the formulation.

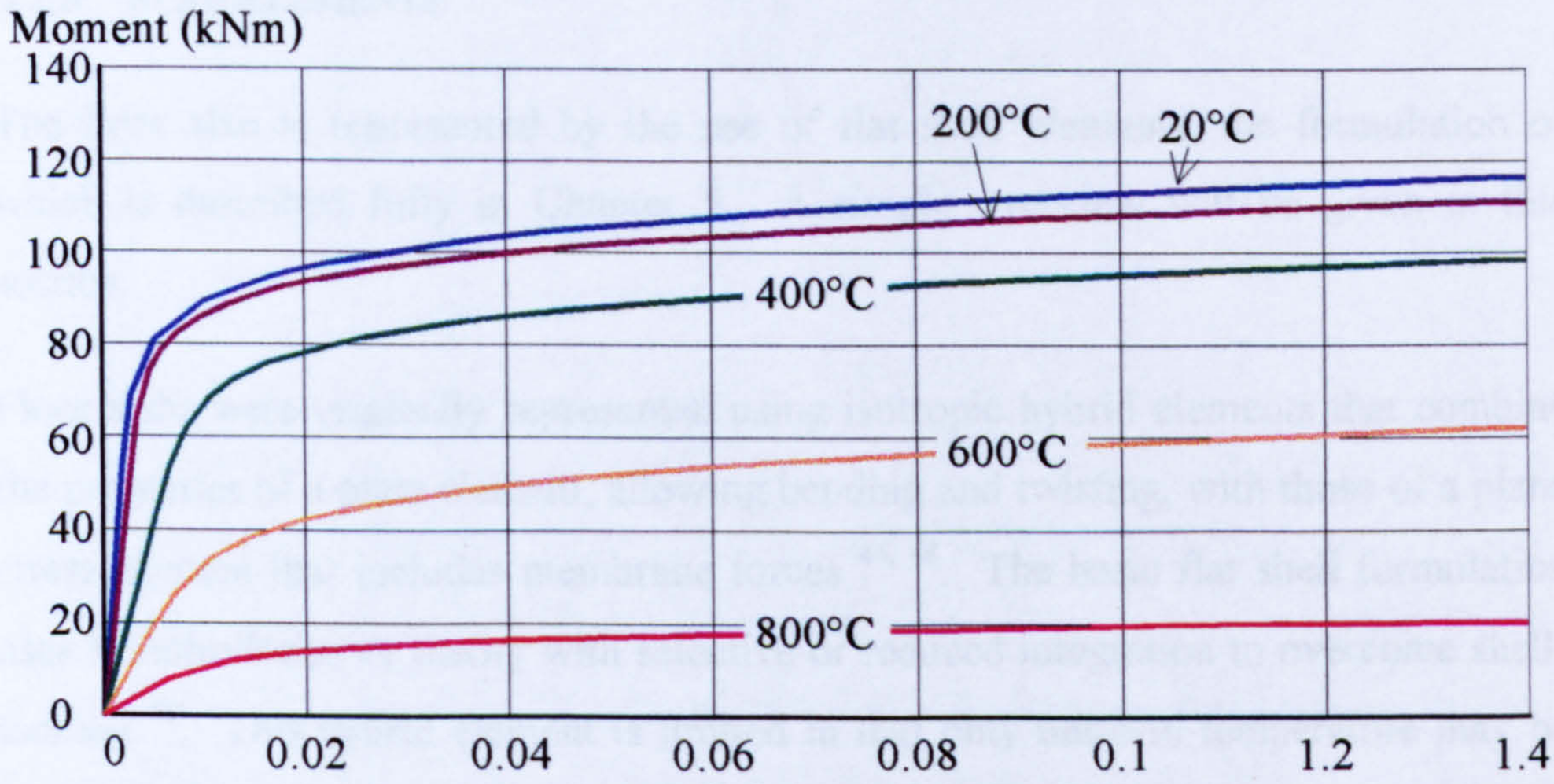

Figure 3-04. Postulated moment-rotation curves at increasing temperature based on an extended end plate used in one of the tests conducted by the Steel Construction Institute and British Steel [53].

To model the behaviour of steel-to-steel connections in fire, the moment-rotation characteristics for the connection are required at various temperatures. For bare steel connection behaviour at elevated temperature only twelve tests on different steel sections had been carried out [52]. This data was not sufficiently comprehensive enough to be used directly. However, El-Rimawi *et al* [53] postulated a family of in-plane moment-rotation curves at elevated temperatures on the basis of the extended end-plate connection test data by Lawson [52]. Although the spring model is capable of modelling axial and shearing displacements, no data exists for these actions, and they are considered to be of infinite stiffness. This seems a reasonable assumption since there is clearly less flexibility in these senses than in bending. The connection moment-rotation characteristics for a typical Cardington test frame secondary beam

connection is shown in Figure 3-04, and more information concerning them may be found from El-Rimawi *et al* [53] and Bailey [44].

More recent data concerning connection moment-rotation data is now available from Leston-Jones [53] who investigated the behaviour of bare steel connections at elevated temperature, and Al-Jabri *et al* [54, 55] who studied the behaviour of composite connections at elevated temperature. These results are very recent and have not been introduced into VULCAN at this time.

3.2.3 SLAB ELEMENTS

The floor slab is represented by the use of flat shell elements, the formulation of which is described fully in Chapter 5. A simple overview will be given in this section.

Floor slabs were originally represented using isotropic hybrid elements that combine the properties of a plate element, allowing bending and twisting, with those of a plane stress element that includes membrane forces [44, 48]. The basic flat shell formulation uses Mindlin/Reissner theory with selective or reduced integration to overcome shell-locking [56]. This hybrid element is limited in that only uniform temperature may be assumed across the thickness, and the slab must be isotropic.

The development of the VULCAN finite element program presented within this thesis embodies the development of a more sophisticated concrete slab model using a laminated flat shell element technique. This new approach for the slab will allow the inclusion of thermal gradients and hence thermal bowing, thermal material degradation, material non-linearities, orthotropic properties and a more sophisticated cracking arrangement than that formerly introduced by Bailey [44]. This extension will be discussed in greater detail in Chapter 5. The formulations used in VULCAN are not shown here, though a brief overview is given.

3.2.4 THE ITERATIVE (NEWTON-RAPHSON) PROCESS

As VULCAN is highly non-linear, to obtain equilibrium it is necessary to use an iterative process, this being the Newton-Raphson method.

If the structure is firstly considered at ambient temperature, the first iteration will give zero displacements throughout the structure, which results in zero internal forces and an elastic stiffness matrix based purely on the sectional properties. With reference to Figure 3-05, equation 3-03 is solved.

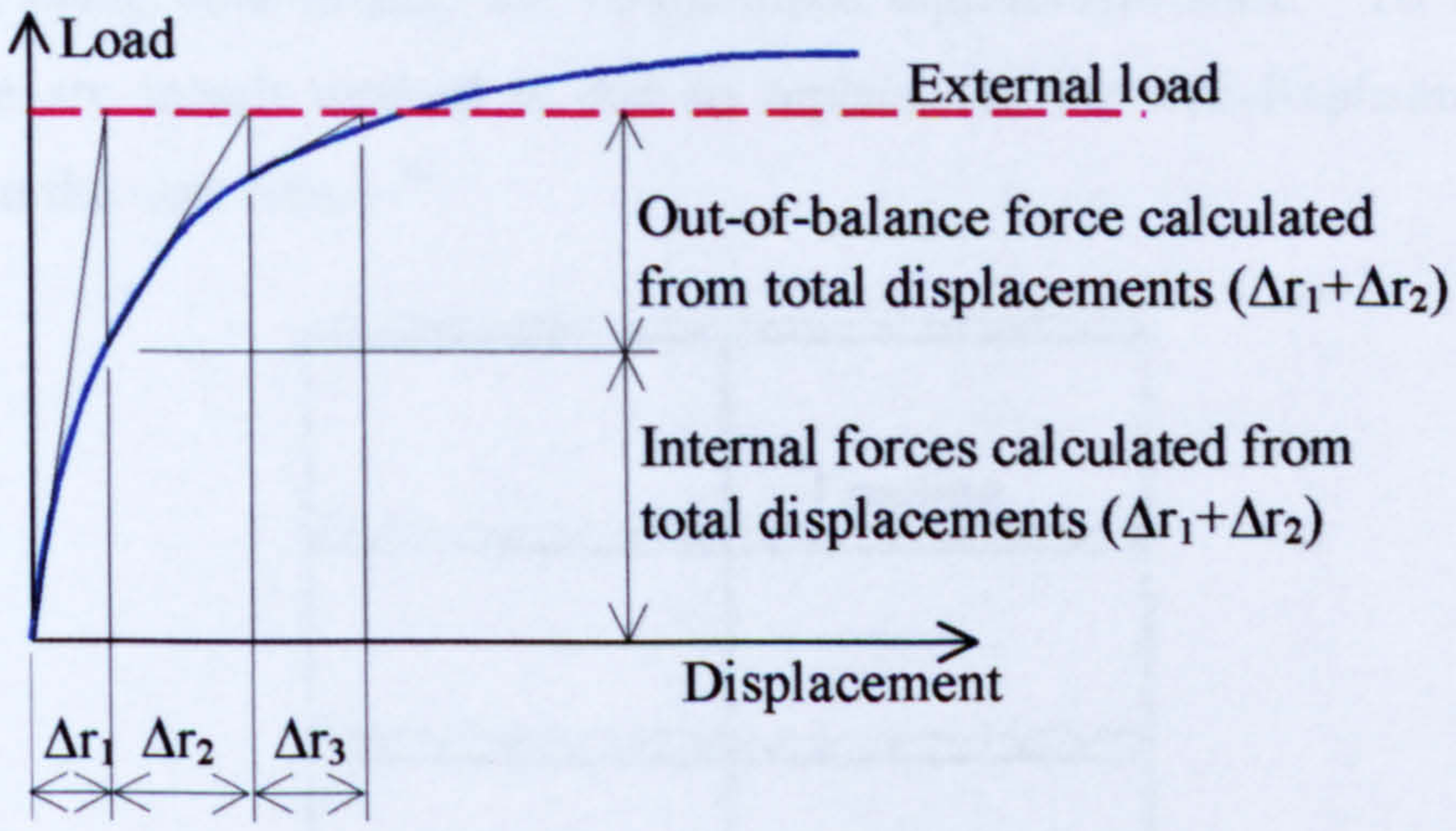

Figure 3-05. Newton-Raphson procedure

The displacements calculated for the increment are added to the total displacements, and this may be used to define the state of strain throughout the members. The out-of-balance forces are calculated with the new corresponding tangent stiffness matrix and equation 3-03 is again solved. The process is repeated until the incremental displacements and the unbalanced forces are within specified tolerances.

As temperature increases, the same procedure is adopted for all non-linearities excepting the inclusion of thermal effects, which is explained in Section 3.1.1. The displacements calculated for the previous temperature increment at equilibrium are used as a 'starting point' for the solution sequence.

Recently, problems have been encountered in the analysis of columns due to the Newton-Raphson procedure when 'snap-through' is encountered [57]. 'Snap-through' occurs when a highly stressed column forms a hinged mechanism. To illustrate an example of this, consider a heated column in a steel frame such as Figure 3-06.

As the column is exposed to fire, it will initially expand forcing the beam-ends framing into the centre column to deflect upwards. As the temperature increases, the steel material strength will reduce and the column will begin to fail in the manner of an Euler buckle with a plastic hinge forming at the top, center and bottom of the

column [58]. At this stage the structure is in a state of instability because of the loss of axial stiffness of the heated column, which the Newton-Raphson method cannot accommodate until stable equilibrium has again been reached. The Newton-Raphson procedure may be able to continue once stability has been regained although this depends on being able to find the re-stabilised equilibrium state. To remove this problem the arc length method is due to replace the Newton-Raphson method in VULCAN in the near future [59].

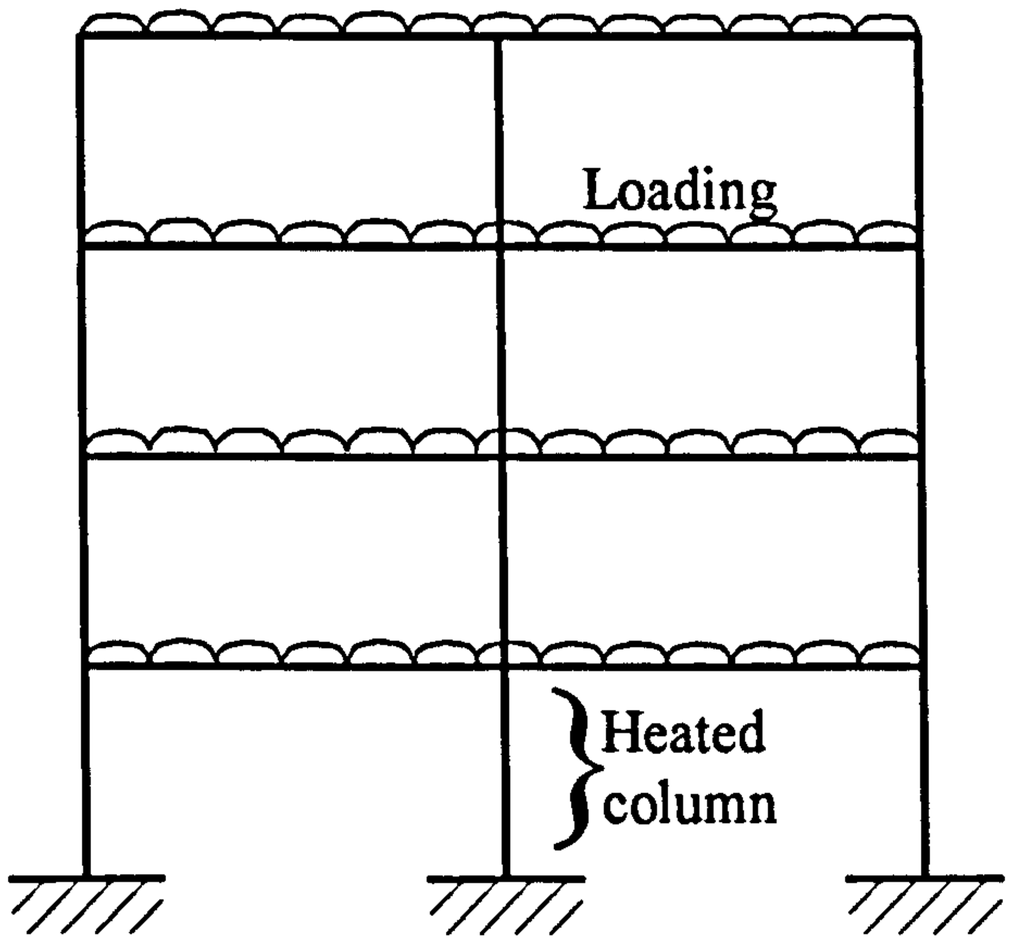

Figure 3-06. Example of where 'snap-through' may be encountered

3.2.5 IDENTIFICATION OF STRUCTURAL FAILURE

CONVERGENCE CONDITIONS

To check whether the equilibrium position has been reached by the Newton-Raphson procedure, VULCAN uses two convergence criteria to check that the incremental displacements and out-of-balance forces are within acceptable tolerances, so that the iteration process can be terminated. The first of these, based on the incremental displacements, is given [48, 60] by,

$$\frac{\|\Delta q\|_2}{\|q+\Delta q\|_2} \leq TOL \qquad 3\text{-}05$$

where,

$$\|\Delta q\| = \left(\sum_{i=1}^{n} \{q_i\}^2\right)^{1/2} \qquad 3\text{-}06$$

$$\|q+\Delta q\| = \left(\sum_{i=1}^{n} (\{q_i\}+\{\Delta q_i\})^2 \right)^{1/2} \qquad 3\text{-}07$$

n is the number of elements in the vector, which corresponds to the number of degrees of freedom.

TOL is the tolerance specified.

The second convergence criterion is obtained by measuring the out-of-balance force vector and is given by [48, 60],

$$\frac{\|\{Q_{external}\}-\{Q_{internal}\}\|_2}{\|\{Q_{external}\}\|_2} \leq TOL \qquad 3\text{-}08$$

where,

$$\|\{Q_{external}\}-\{Q_{internal}\}\|_2 = \left(\sum_{i=1}^{n} \left(\{Q_{i(external)}\}-\{Q_{i(internal)}\} \right)^2 \right)^{1/2} \qquad 3\text{-}09$$

$$\|\{Q_{external}\}\|_2 = \left(\sum_{i=1}^{n} \{Q_{i(external)}\}^2 \right)^{1/2} \qquad 3\text{-}10$$

Care must be taken when specifying the tolerance limits for the above convergence criteria. If the tolerance is too 'loose', inaccurate results will be obtained, and conversely if the tolerance is too 'tight' extra unnecessary iterations are performed to obtain an increase in accuracy which is unjustifiable.

TERMINATION OF THE MODEL DUE TO STRUCTURAL FAILURE

All iterations require the linear equation 3-03 to be solved for incremental displacements, and this is carried out using Gaussian Elimination. Physically, this means that each step of the Gaussian Elimination is the relaxation in turn of one degree of freedom and the carry-over of its effect to the remaining degrees of freedom. Therefore the remaining coefficient matrix at any stage is the tangent stiffness matrix of the structure, with the degrees of freedom corresponding to the eliminated equations relaxed. If any of the terms on the leading diagonal of the tangent stiffness matrix is zero or negative, the structure must be unstable. To ensure

that the correct failure point is attained, calculation of the tangent stiffness matrix must be correct and small changes in temperature adopted near the failure point.

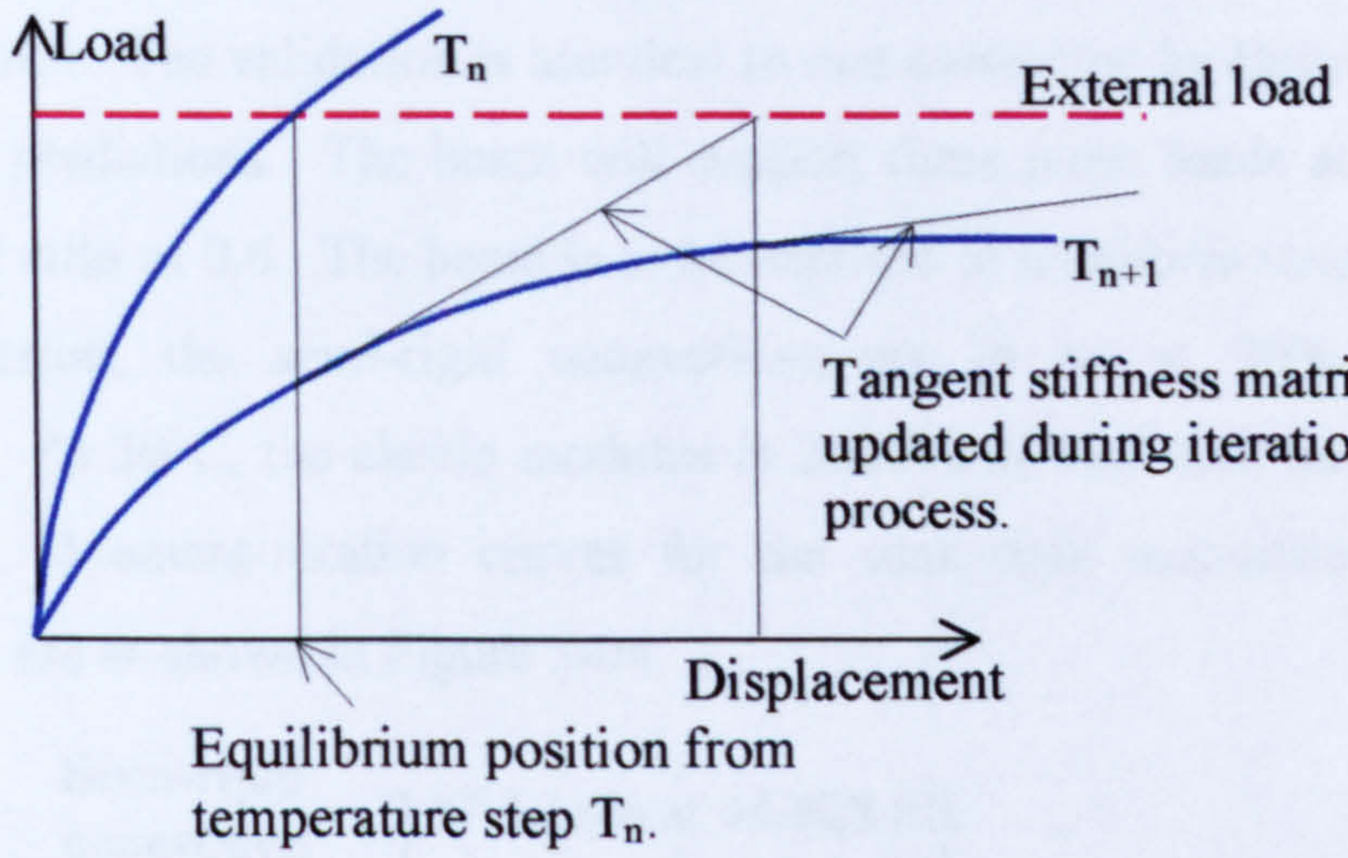

Figure 3-07. Newton-Raphson procedure in the proximity of structural failure

An automatic procedure is implemented internally in the model to refine the incremental temperature increase in the zone close to structural failure. This procedure is necessary to ensure that 'true' failure is identified, and that a termination of the analysis due to purely numerical failure is not encountered. During the initial stage of the analysis, the temperature is increased in increments specified by the user (normally 50°C or 100°C). At some stage the finite element program will show a negative number on the tangent stiffness matrix-leading diagonal. This is shown in Figure 3-07 as taking place at temperature T_{n+1}. Since a more accurate prediction of failure temperature is required, and to ensure that numerical instability does not occur at temperature T_{n+1}, the increment of temperature from the last recorded equilibrium position at T_n is reduced to 50% of the original increment. The analysis then continues from T_n until a negative again appears on the leading diagonal of the stiffness matrix. This process of bisection continues until the temperature increment is equal to or less than 0.1°C.

3.3 VALIDATION OF THE EXISTING VERSION OF VULCAN

The validation of the single-layer flat-shell slab elements is detailed in Chapter 5 and will not be covered in this section.

3.3.1 VALIDATION OF BEAM ELEMENTS

To validate the beam elements, a steel beam shown in Figure 3-08 will be analysed using VULCAN. The validation is identical to one conducted by Bailey [44] in order to compare the predictions. The beam will support three point loads at equal spacing giving a load ratio of 0.6. The beam is to be exposed to a uniform temperature across the cross-section; the semi-rigid connections are to be at 70% of the beam temperature. At 20°C, the elastic modulus is 205000 N/mm^2 and the yield stress is 275 N/mm^2. Moment-rotation curves for the semi-rigid connections at elevated temperatures are as shown in Figure 3-04.

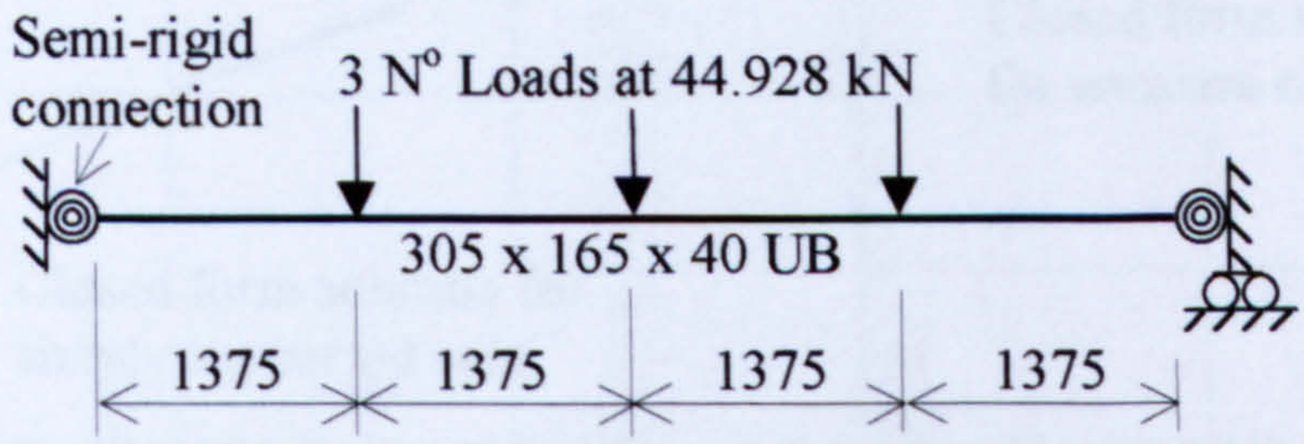

Figure 3-08. Simply supported beam validation

The beam has been analysed for completely rigid and simple cases, and for 25%, 50%, 75% and 100% of the standard semi-rigid connection strengths and stiffnesses. The deflections are shown in Figure 3-09. The deflections found are seen to be identical to those published by Bailey [44].

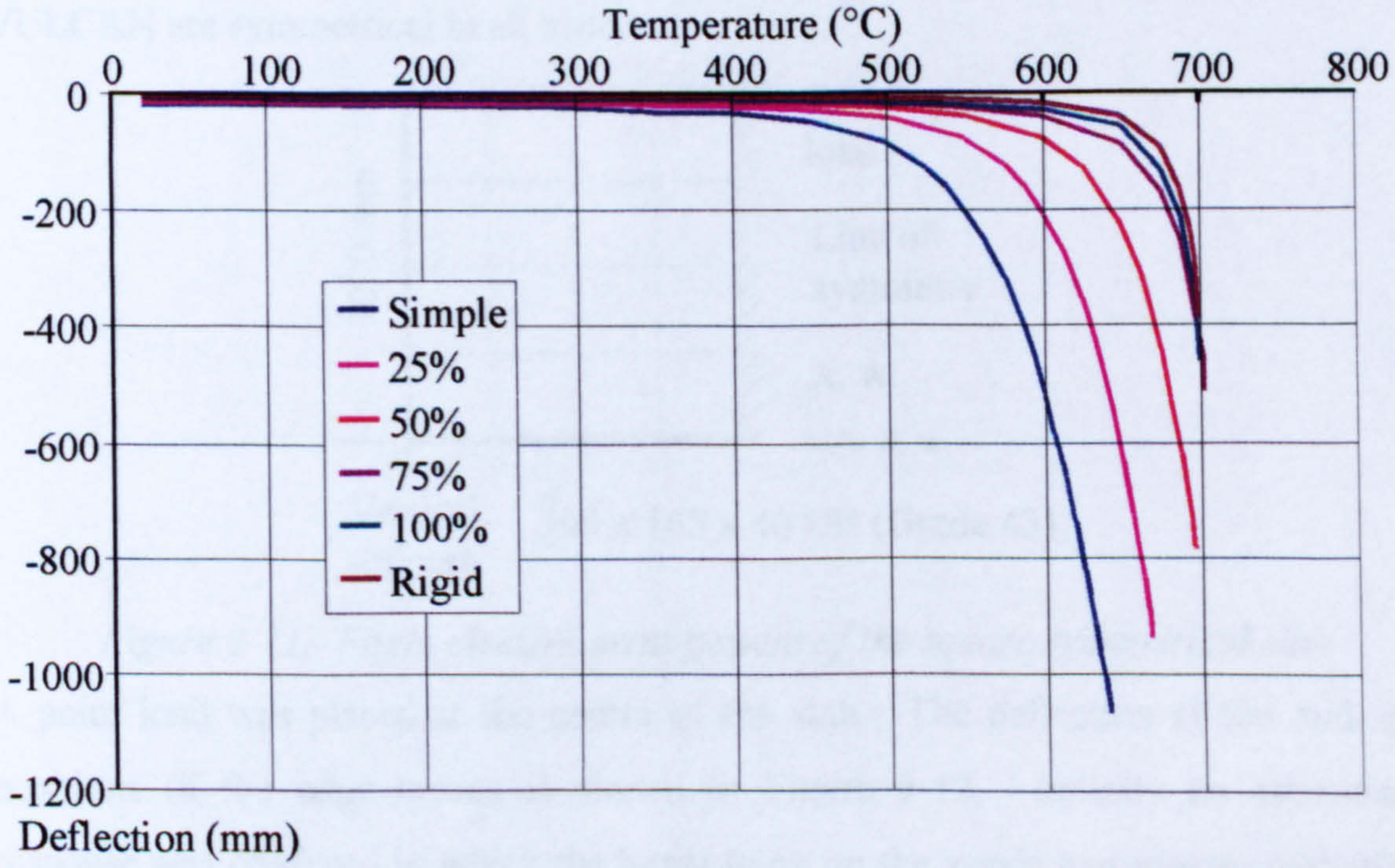

Figure 3-09. Effect of semi-rigid connections on a beam at elevated temperatures.

The sensitivity of the beam's deflection to connection stiffness at ambient temperature is shown in Figure 3-10. This allows comparisons to be made against closed-form solutions for the two extreme cases of simply supported and rigid connections.

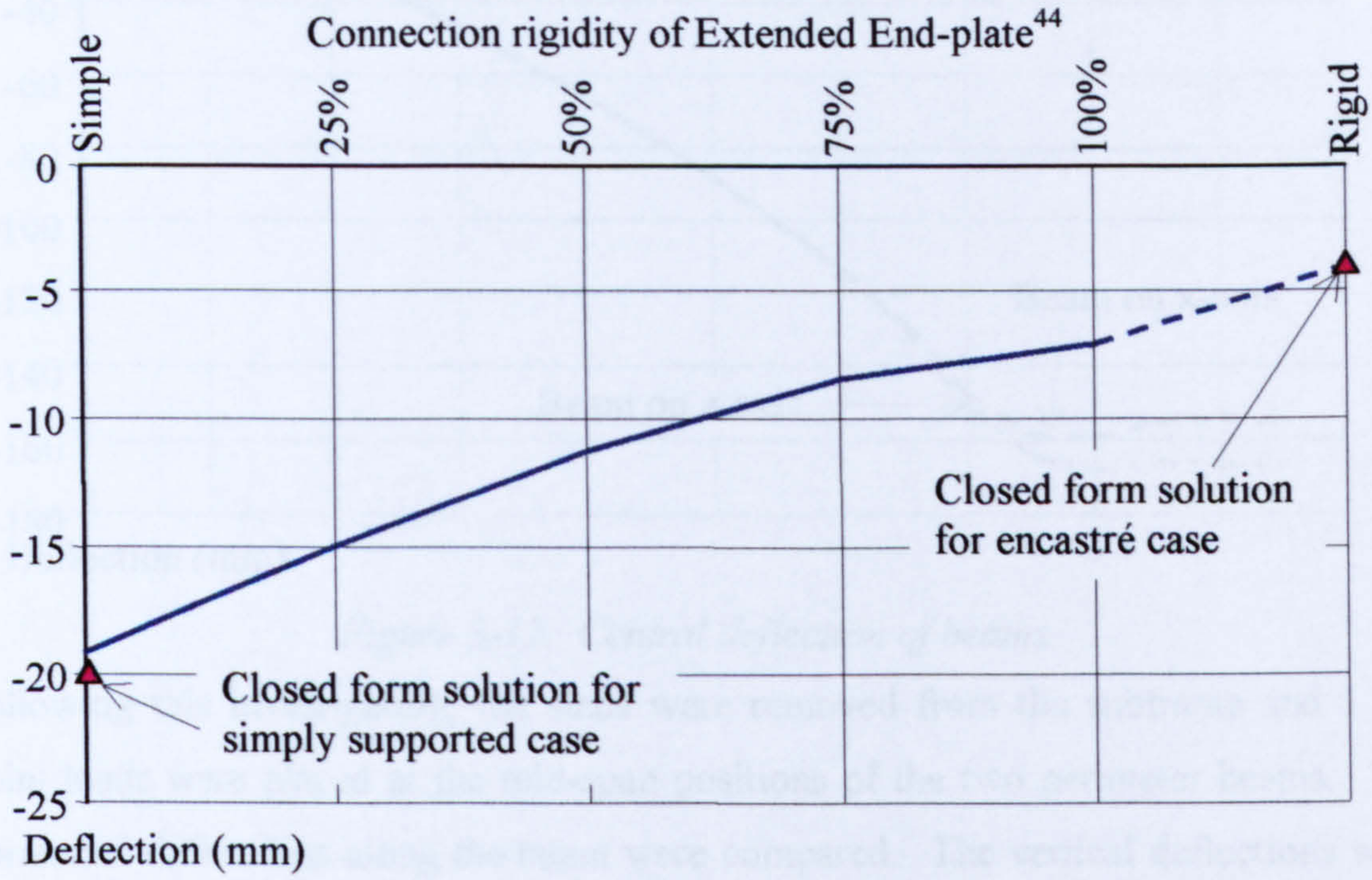

Figure 3-10. Sensitivity of beam deflections to semi-rigid connection stiffness at 20°C

3.3.2 SYMMETRY TEST

The square composite beam and slab with isotropic material properties, of which a quarter is shown in Figure 3-11, was heated to check that the results generated by VULCAN are symmetrical in all aspects.

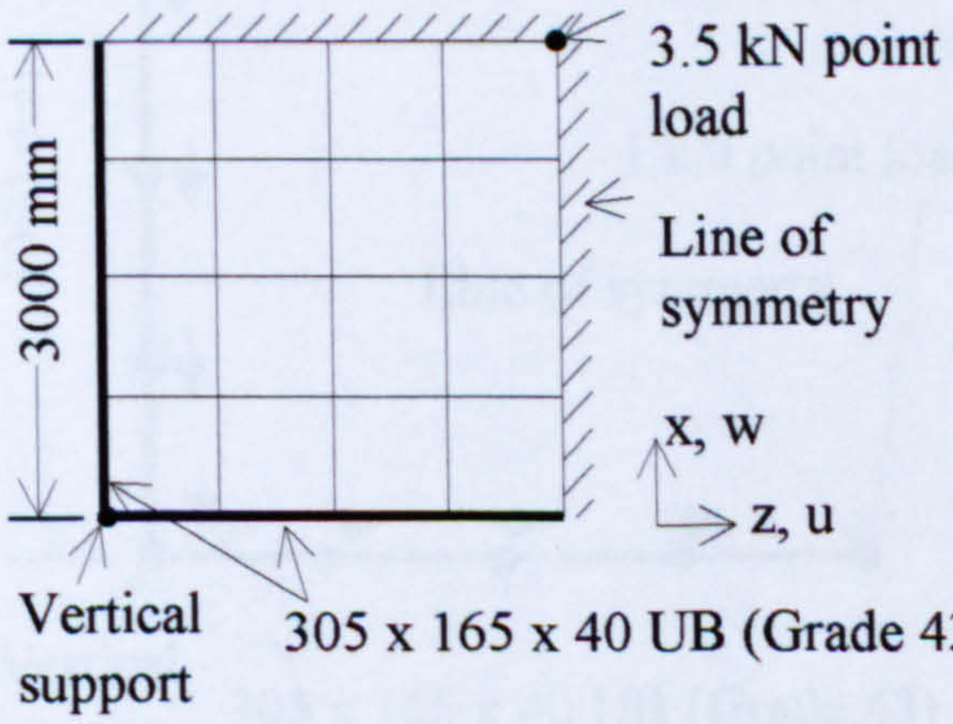

Figure 3-11. Finite element arrangement of the square symmetrical slab

A point load was placed at the centre of the slab. The deflection at the mid-span positions of the edge beams is shown in Figure 3-12. Initially an asymmetric response was observed in which the beam lying on the z-axis had greater deflections than that on the x-axis.

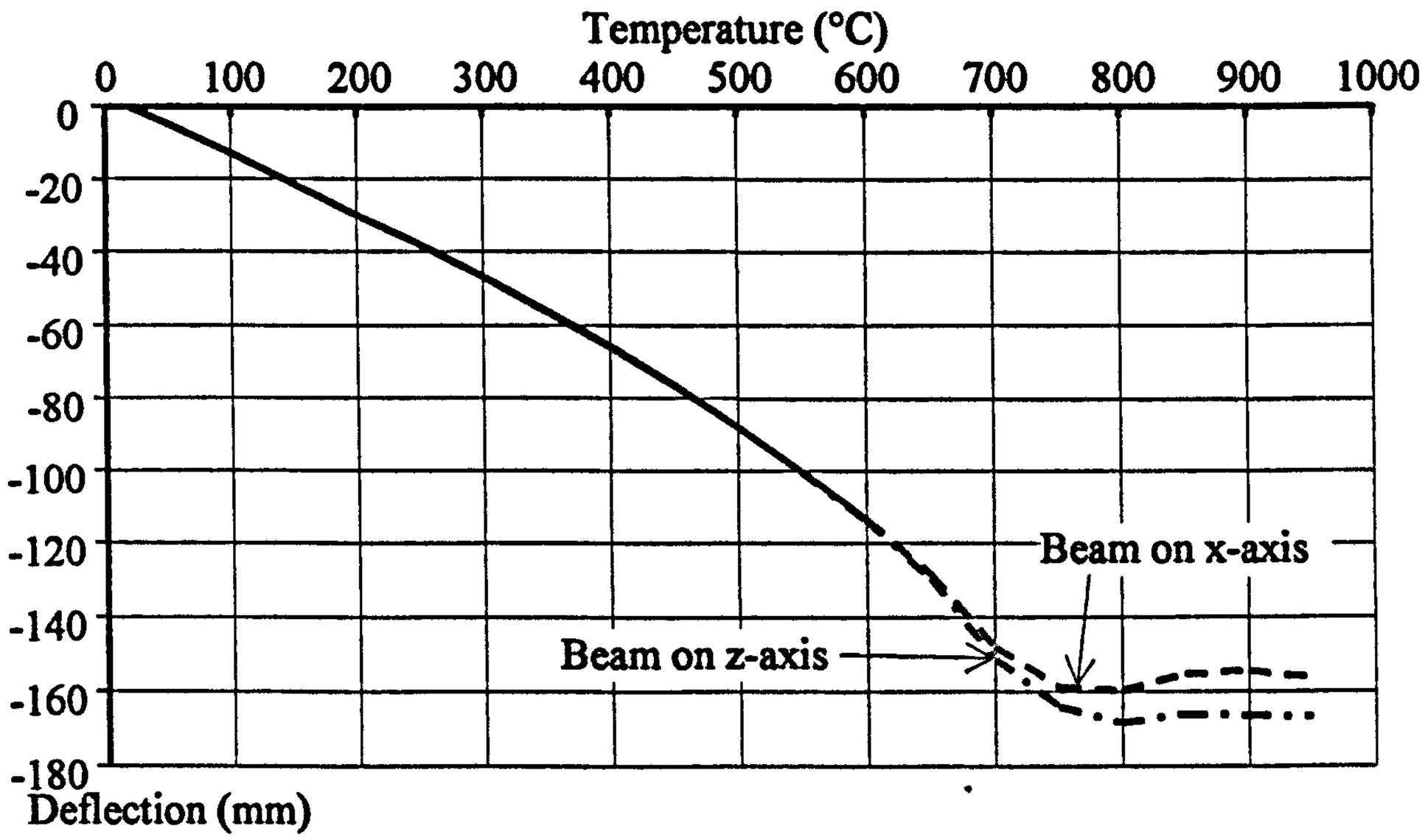

Figure 3-12. Central deflection of beams

Following this investigation, the slabs were removed from the subframe and 1 kN point loads were placed at the mid-span positions of the two perimeter beams. The horizontal deflections along the beam were compared. The vertical deflections were identical. Numerically, the horizontal movements were identical, but in opposing directions, as shown schematically in Figure 3-13. By this test the transformation matrix was found to be incorrect for the beam elements and required to be corrected.

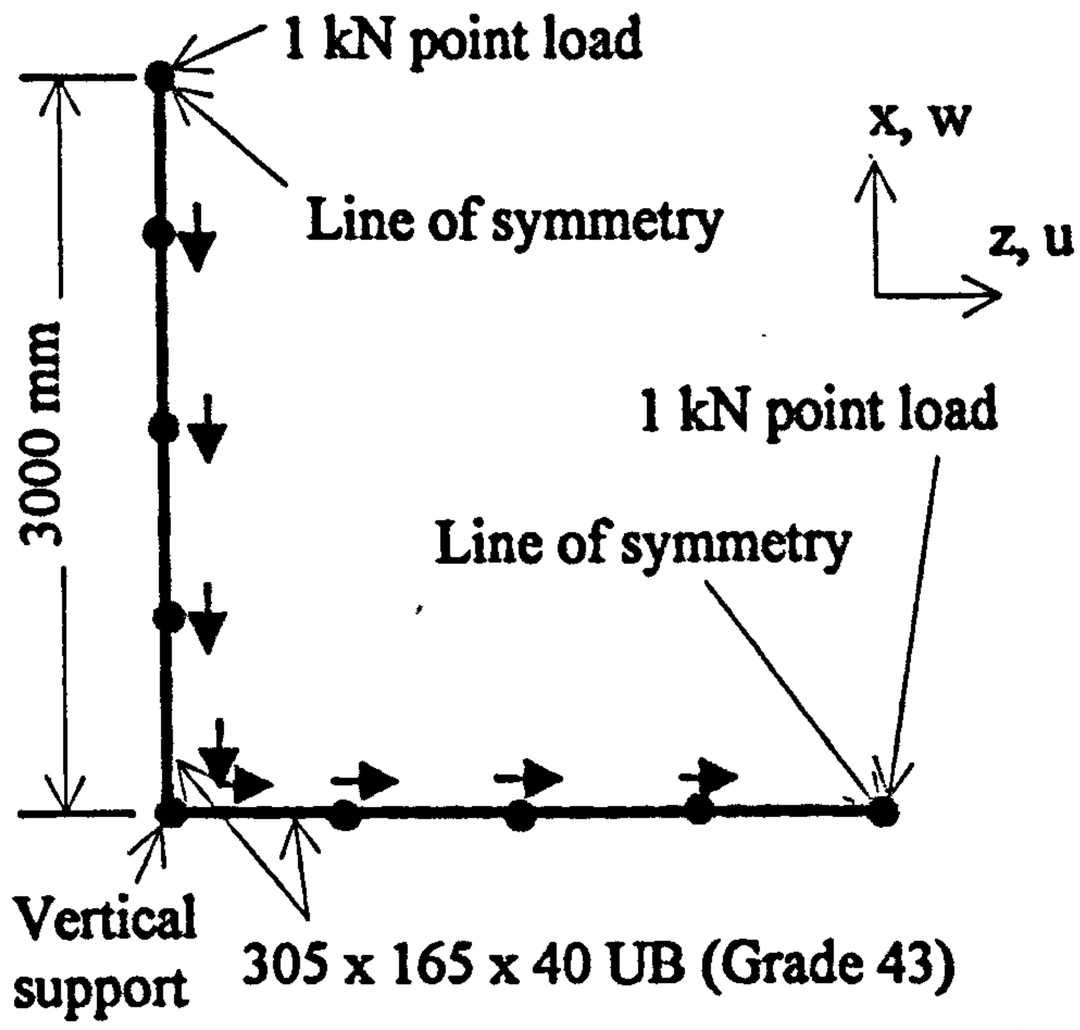

Figure 3-13. Horizontal direction of movement of the beams at 20°C

The effect of the error within the transformation matrix was a cause for concern; this was corrected and incorporated in all subsequent analyses. To assess the effect the error might have had on earlier analyses, comparisons were conducted on both the restrained beam test and the British Steel corner test, shown in Figures 3-14 and 3-15

respectively. (Subframes for these tests are shown later in Figures 4-03 and 4-26 respectively.) These tests were chosen because of the extremes of restraint imposed upon these subframes. The variation for both the Cardington tests between the analyses for the original and corrected transformation matrices is negligible.

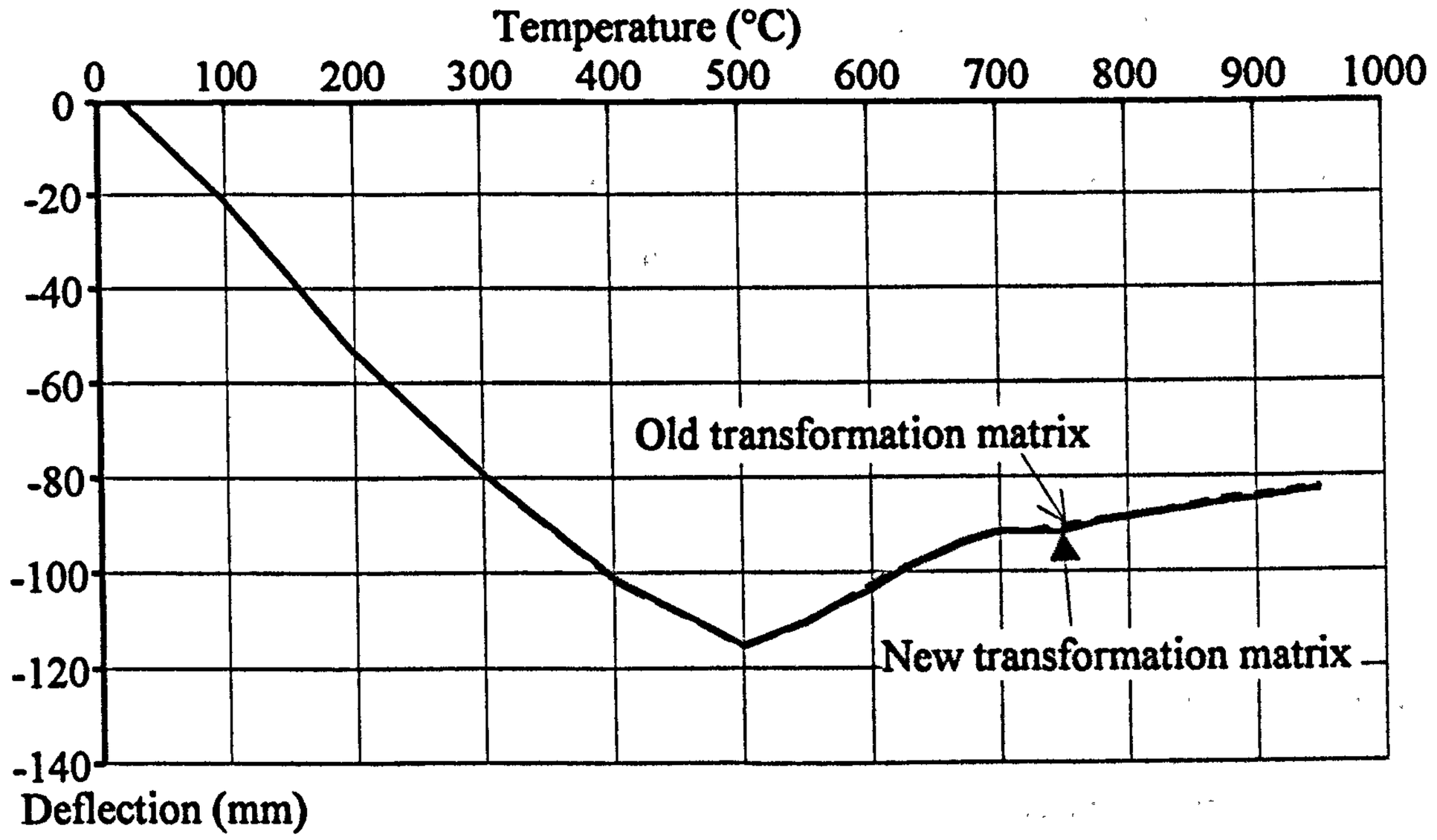

Figure 3-14. Restrained beam central deflection comparison between old and new transformation matrices

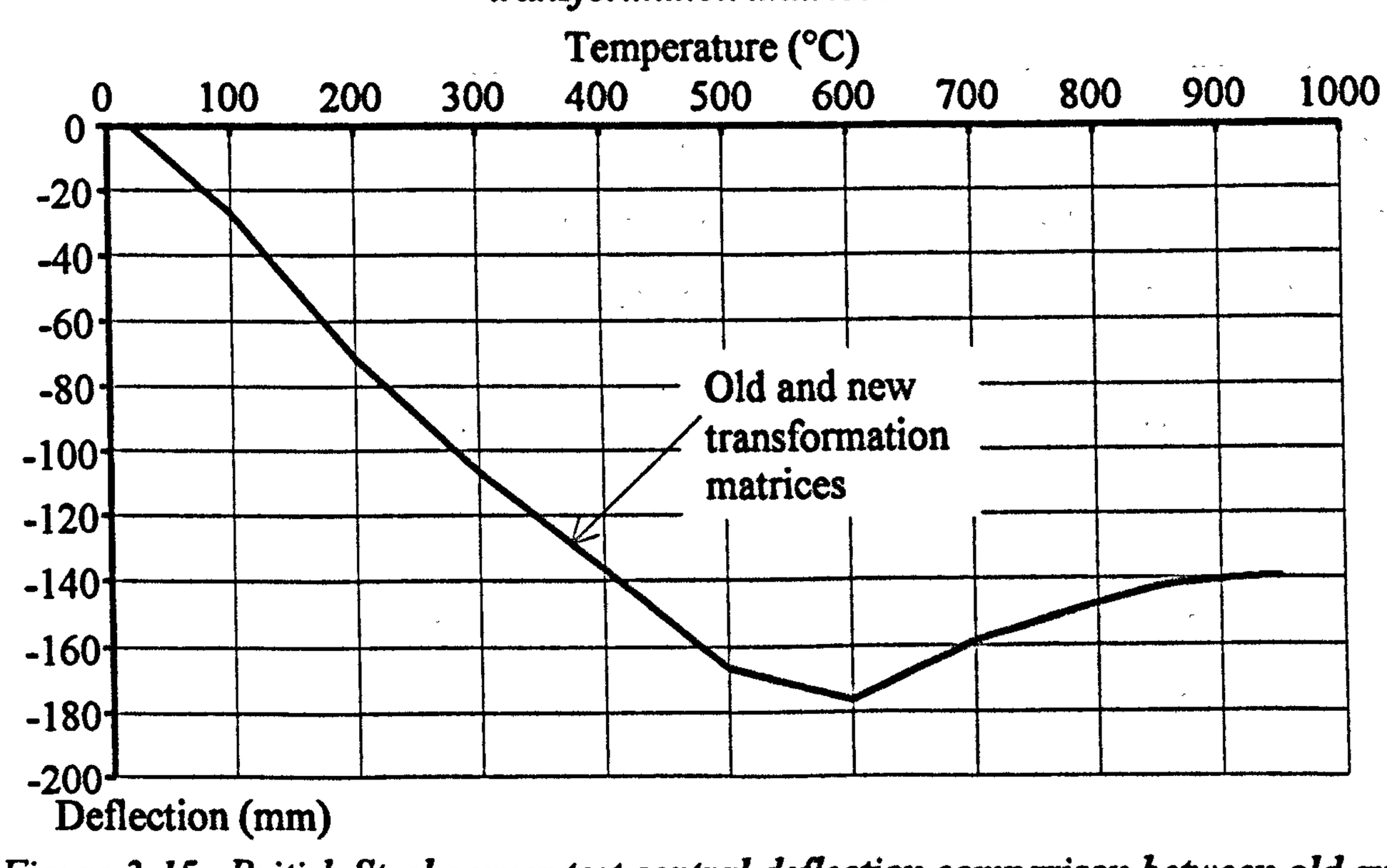

Figure 3-15. British Steel corner test central deflection comparison between old and new transformation matrices

3.3.3 SUBFRAME MESH CONVERGENCE STUDY

The objective of this convergence study was to vary the density of the finite element mesh to ensure adequate confidence that acceptable convergence may be obtained for

the parametric studies presented in Chapters 4, 6 and 7. To this end a standard structure, shown in Figure 3-16, was developed. Four 356 x 171 x 45 universal beams line the perimeter, with a longitudinal heated secondary beam (305 x 165 x 40 UB) placed centrally. All beams are grade 43 steel. The secondary beam was exposed to a constant temperature regime across its whole cross-section and the floor slab and perimeter beams were considered to be at ambient temperature. The floor slab was 65mm thick, and was laid directly onto the upper flanges of the steel beams, allowing the assumption of a fully composite beam-to-slab interface.

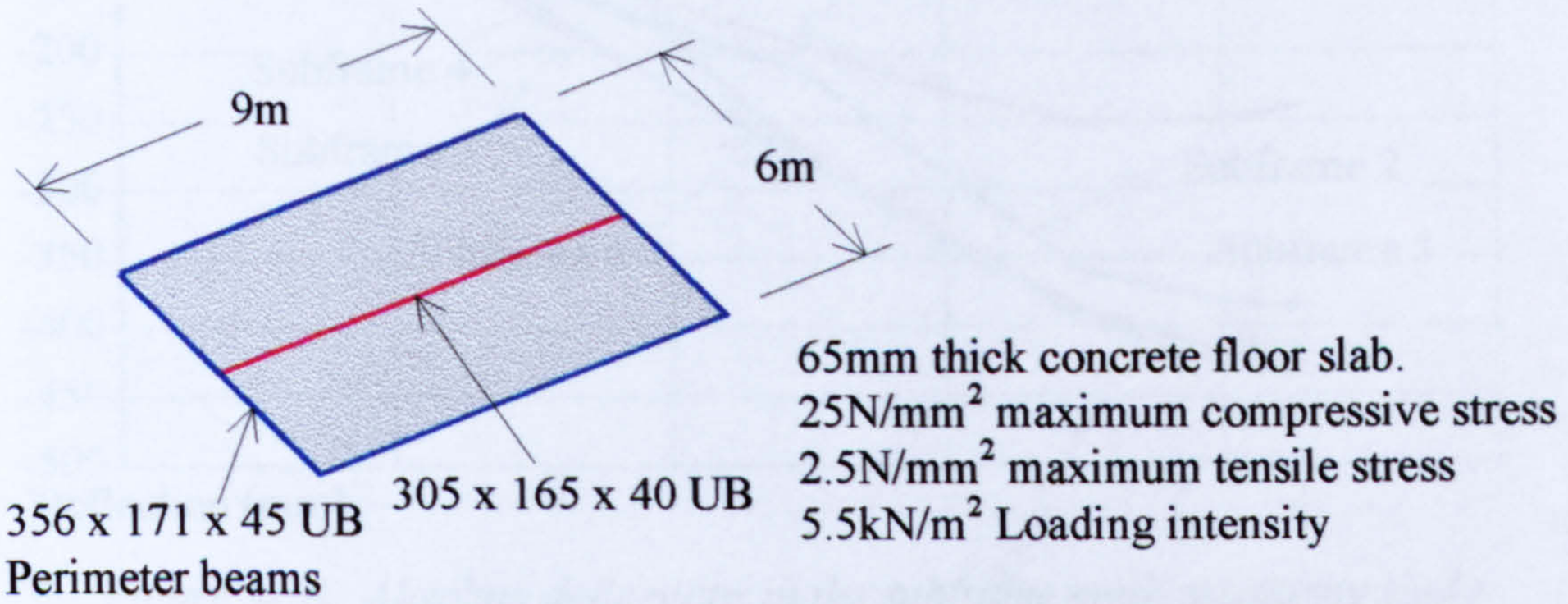

Figure 3-16. General details of the mesh convergence subframe

The maximum compressive stress of the concrete was 25N/mm^2 and the maximum tensile stress was 2.5N/mm^2. The loading intensity was 5.5kN/m^2, uniformly distributed. The subframe was supported vertically at its four corners and was free to expand in all directions. The different meshes used in this subframe are shown in Figure 3-17.

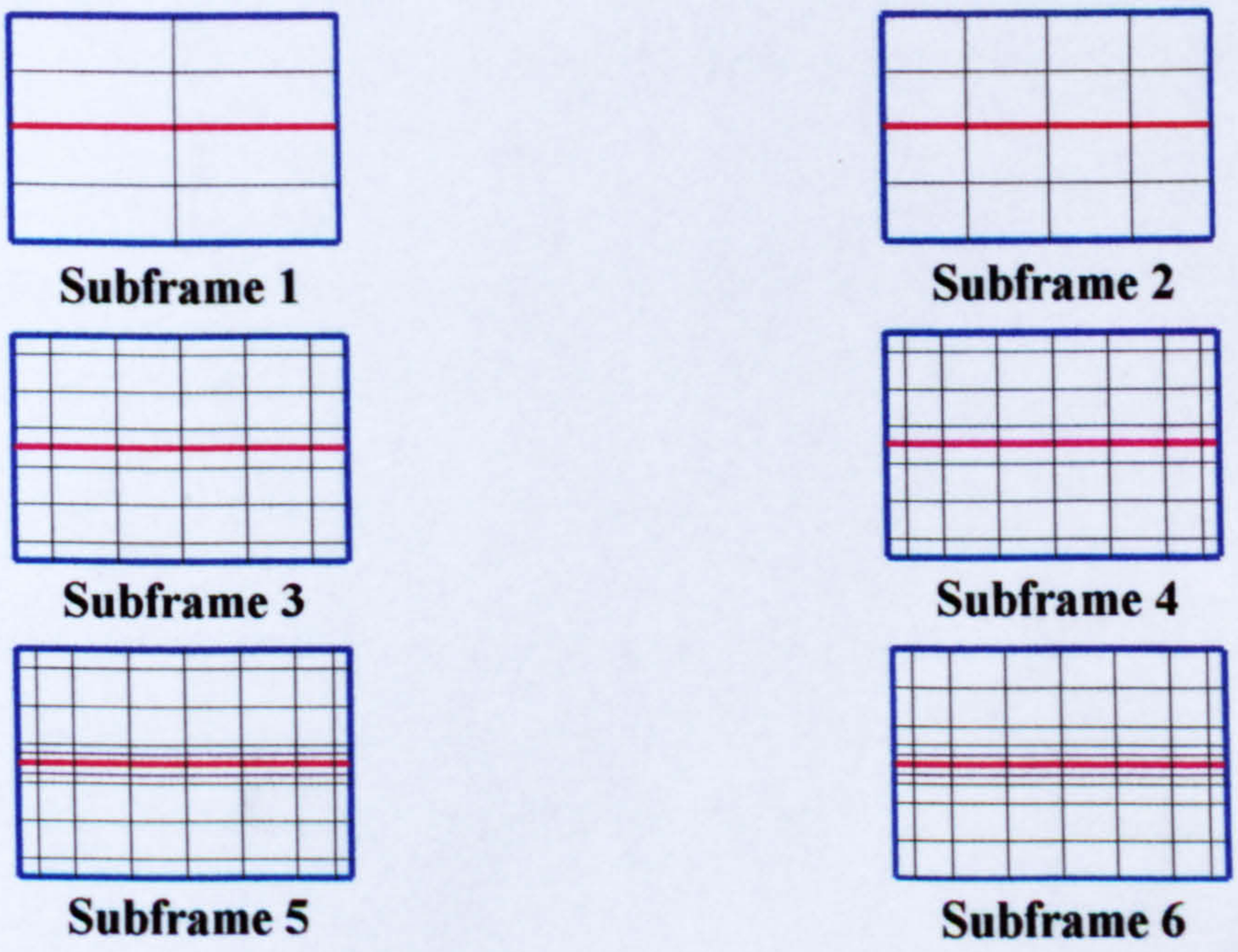

Figure 3-17. Varying subframe meshes

The results of the convergence study for the subframe mesh are shown in Figure 3-18. The coarser meshes tend to give lower deflections, whereas the finer meshes appear to converge onto a specific deflection path. The 'kinks' to subframes 3, 4 and 5 are produced by the crudity of the concrete cracking model.

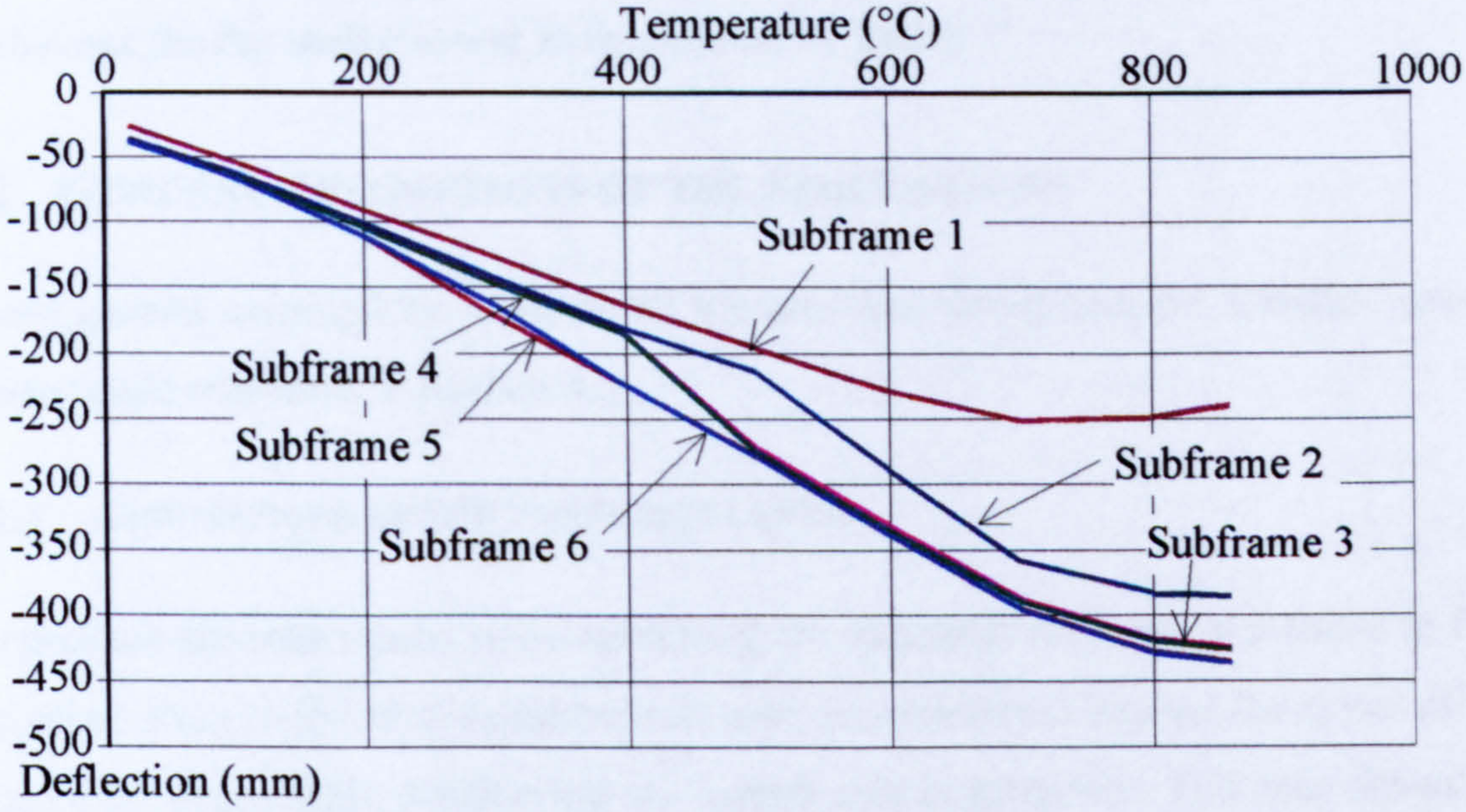

Figure 3-18. Absolute deflections in the subframe mesh sensitivity study

4 CARDINGTON PARAMETRIC STUDIES USING THE ISOTROPIC SLAB ELEMENT

The first set of parametric studies conducted on the Cardington test frame within this thesis uses the flat shell element as formulated by Bailey [44].

4.1 GENERAL ASSUMPTIONS OF THE SIMULATIONS

These general assumptions apply to all the analyses throughout the Chapter, except where noted otherwise in Section 4.2.

4.1.1 ASSUMPTIONS OF THE SUBFRAME LIMITS

To produce accurate results when modelling the structural response of a frame in fire, structural areas (referred to as subframes) must be considered beyond the extent of the fire, rather than simply considering the heated area in isolation. This was shown by Bailey *et al* [44] in previous analyses. For simplicity the subframe has generally been defined at least a beam or a bay half-span beyond the fire compartment. The assumption at these cut edges is that the concrete slab normal to the beam or bay half-span remains horizontal and with no horizontal lateral movement. This would be the normal condition across an axis of symmetry.

4.1.2 SIMULATION ASSUMPTIONS

For the computer simulations the following assumptions are made, following Bailey *et al* [23]:

1. The steel has a yield stress of 308 N/mm^2 for Grade 43 and 390 N/mm^2 for Grade 50, based on coupon test results provided by the supplier.

2. The elastic modulus of steel is 210 kN/mm^2.

3. The steel:concrete modular ratio at ambient temperature is 15. This figure is to be reduced by 30% over the heated area. This reduction is based on data given in EC4 [11], which indicates that the elastic modulus of concrete is reduced by 29% at 100°C.

4. The exposed (lower) flange and web of the steel section are heated uniformly with the upper flange being at 0.8 of this value. This is a simplification of the actual temperatures found in Chapter 2. Previous studies [53] have shown that varying this pattern has only a limited effect on the overall results.

5. The temperature of the concrete in the heated area is uniform throughout the slab, at 10% of that of the lower beam flange. As shown in Chapter 2 the slab temperatures are actually rather more complex than those assumed, due to the low thermal conduction and water evaporation.

6. Only the top 70mm of the slab is considered. This represents the continuous concrete thickness above the top of the trapezoidal steel deck, and is consistent with normal design assumptions for composite beams. Although this ignores the effect of the influence of the ribs in the transverse direction, a uniform thickness must be used, as Bailey's [44] formulation assumes that the slab elements are isotropic. Deflections obtained using the full depth of 130mm (i.e. a solid slab) were found to be very small and no cracking was evident.

7. The limiting bending stress difference in the slab in compressive regions is 25 N/mm^2.

8. The limiting bending stress difference in the slab in tensile regions is 2.5 N/mm^2.

9. All secondary and perimeter beams parallel to the secondary beams have fin-plate connections at either end. Details of these may be found in Section 3.2.2.

10. Unfactored loading across the structure is 5.48 kN/m^2 (including the slab dead load).

11. The concrete floor slab in the immediate vicinity of the secondary beam connections is assumed to have cracked and is therefore reduced to the thickness of the reinforcement.

4.1.3 Boundary Condition Assumptions

As detailed in Chapter 3, VULCAN uses eleven global degrees of freedom at each node. These are:

- Displacement in each of the three dimensions,
- Rotations about the three orthotropic axes,
- Strains along each of the three axes,
- Twisting,
- Warping.

Imposing either a fixed or free condition on each of the eleven degrees of freedom at a boundary node may simulate most boundary conditions. A description of the common cases where a subframe meets an external boundary follows.

- **Axis of symmetry**. An axis of symmetry is used where, in the full structure, the continuous floor slab or steel beam continues past the edge of the chosen subframe. This axis of symmetry is best located either halfway across a building bay or at the edge of a bay. Here the slab or beam is assumed to remain horizontal in the direction normal to the line of symmetry. Horizontal movement normal to the line of symmetry is assumed to be zero.

- **Column base**. At a column base, if the base is assumed rigid (i.e. capable of sustaining moments without rotation), then all degrees of freedom are fixed. If the column has a pinned base, then the degrees of freedom corresponding to displacements are fixed, together with axial rotation about the column centre-line, and the remaining rotations are left free.

- **Column head**. This (as for the column base) depends upon whether it is considered pinned or fixed. At a fixed column head, lateral and rotational movements are suppressed, allowing only vertical movement. At a pinned column head, lateral movements and rotation about the longitudinal axis are restrained, but vertical movement and all rotations are left free.

4.2 DESCRIPTIONS OF THE PARAMETRIC STUDIES CONDUCTED

All the parametric studies adopt the assumptions outlined in Section 4.1 unless noted in the following sections. All temperatures shown in the parametric studies are the bottom flange average temperatures.

4.2.1 PARAMETRIC STUDY 1: SLAB THICKNESS

The slab thickness parametric studies have been conducted by holding constant all parameters except the thickness of the slab. The thickness of the slab in these analyses represents the continuous top layer of concrete, with the slab corrugations in the decking region ignored, as illustrated in Figure 4-01. The temperature profile retained the same temperature ratios to the bottom flange average temperature regardless of thickness.

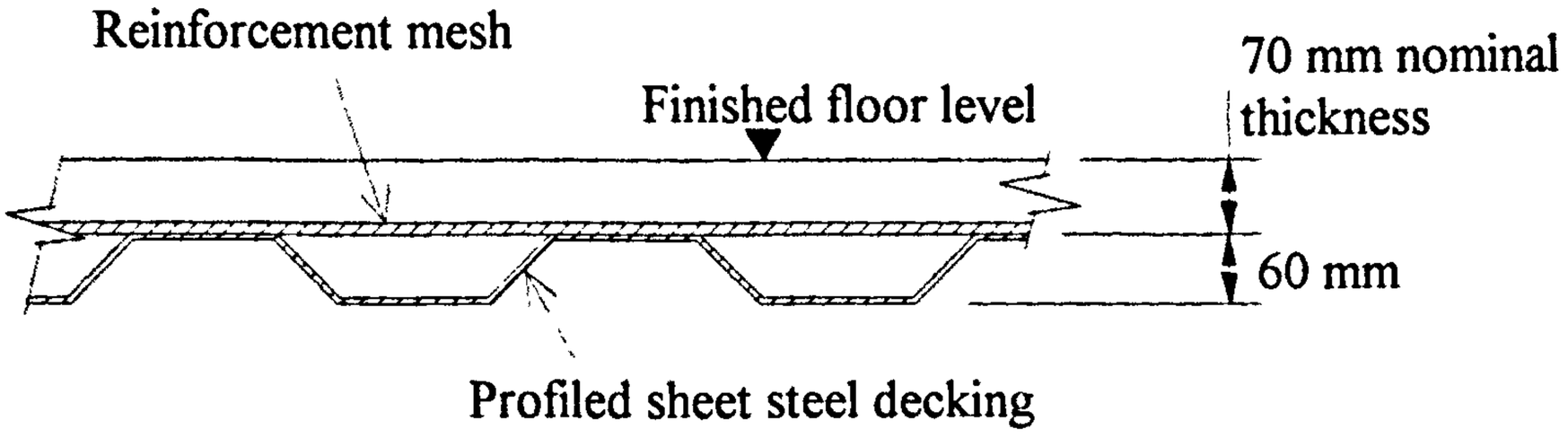

Figure 4-01. Floor slab arrangement

4.2.2 PARAMETRIC STUDY 2: SECONDARY BEAM CONNECTION STRENGTH AND STIFFNESS

The steel-to-steel secondary beam connection characteristics were varied from an almost pinned condition up to double the estimated strength and stiffness of the tab plate connections actually used. The rotational characteristics for a tab-plate connection (expressed as a Ramberg-Osgood equation) were multiplied by factors between 0 and 2 in increments of 0.2 for all four tests. The details of the assumed moment-rotation relationship for the Cardington tab-plate connection (secondary beam connections) at ambient temperature are given in Section 3.2.2. Semi-rigid joints have only been placed at the ends of the secondary beams in these studies and not at the ends of the primary beams, since the depth of these beams produces a much stiffer connection. All other parameters are held constant.

4.2.3 PARAMETRIC STUDY 3: SPACING OF SECONDARY BEAMS

This is a rather contrived parametric study, conducted only on the restrained beam test, in which the secondary beams adjacent to the restrained beam are moved by a small amount either towards or away from the restrained beam. This is done in increments of 100mm to a maximum displacement of 400mm.

4.2.4 PARAMETRIC STUDY 4: POSITIONING OF SANDBAGS

During some of the tests it was noticed that, in order to avoid interference with the displacement transducers, inclinometers and strain gauges, some of the sandbags were not in their pre-selected locations. This naturally leads to slightly changed load paths, and so it was decided to see how these new load paths would affect the overall performance of the structure.

4.2.5 PARAMETRIC STUDY 5: EXTENT OF SUBFRAME

This parametric study was conducted only on the restrained beam test. It involves performing a series of analyses using a number of different sizes of subframe to determine how much of the whole structure must be modelled in order to obtain sufficient accuracy.

4.3 RESTRAINED BEAM TEST PARAMETRIC STUDIES USING THE ISOTROPIC SLAB ELEMENT

A plan of the Cardington test frame is shown in Figure 4-02 detailing the location of the restrained beam test and the assumed subframe for studies 1 to 4.

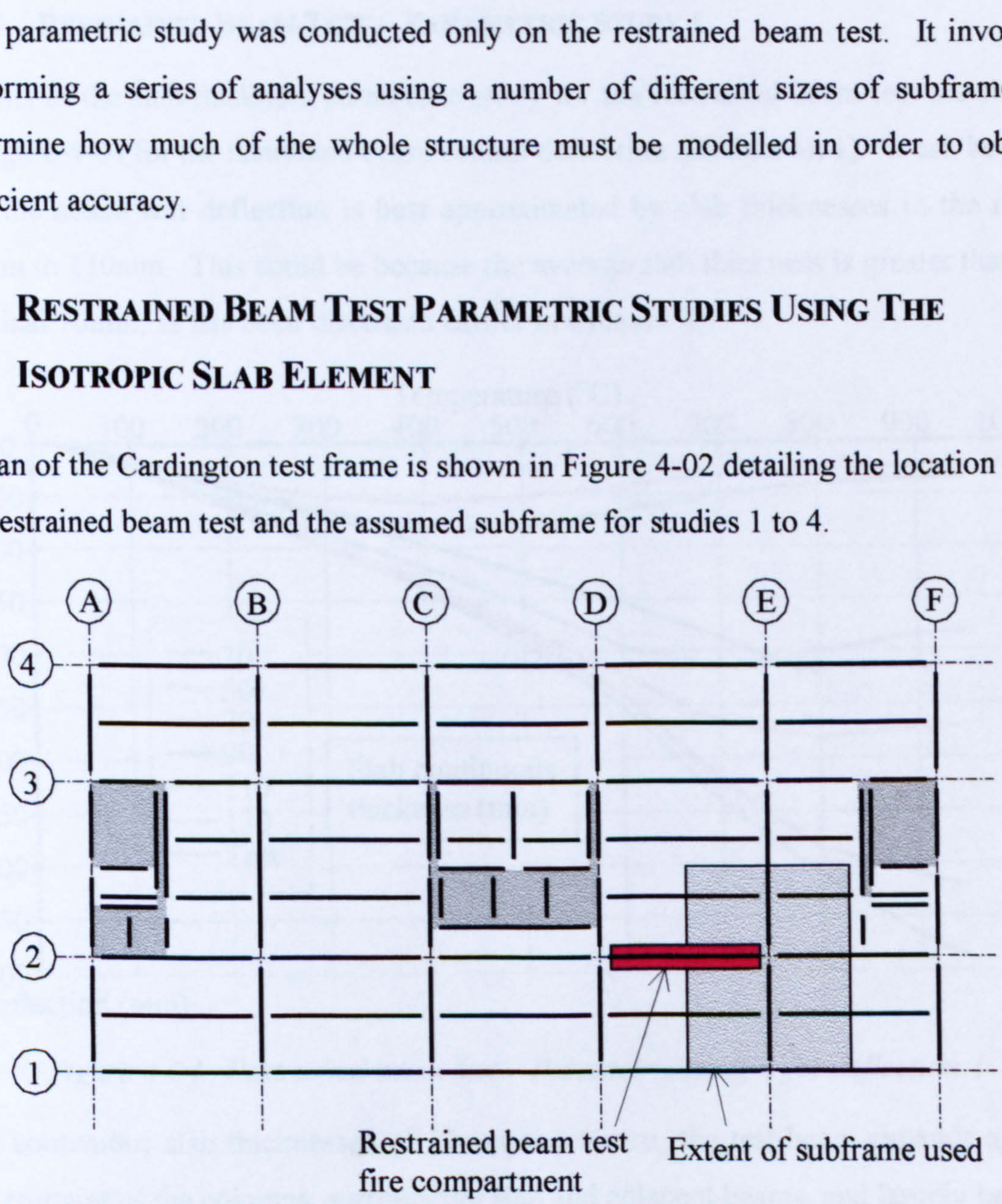

Figure 4-02. Location of the restrained beam test

The subframe and finite element mesh used for the parametric studies are shown in Figure 4-03, which also shows the position at which deflections are compared.

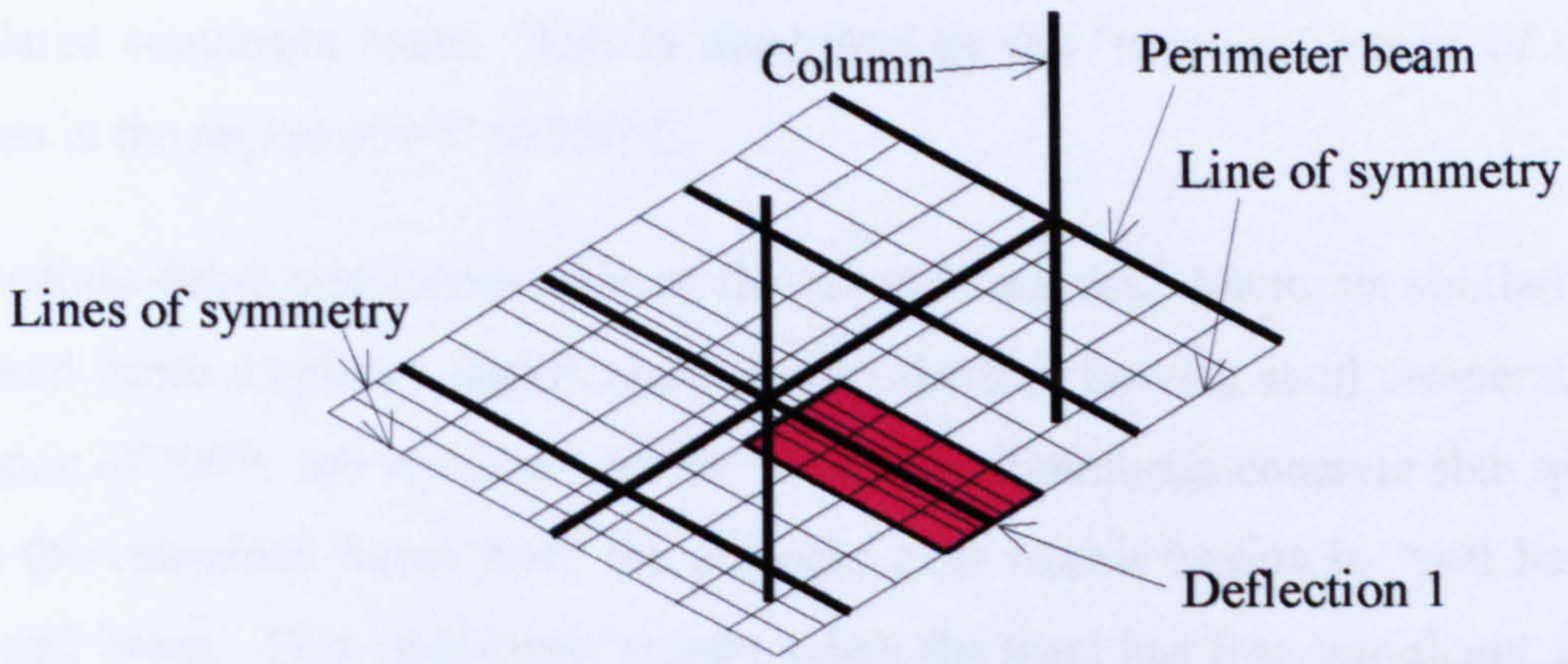

Figure 4-03. Restrained beam test subframe finite element mesh arrangement

4.3.1 RESTRAINED BEAM TEST – PARAMETRIC STUDY 1

Results of the slab thickness parametric study for the restrained beam test are shown in Figure 4-04 for the restrained beam central deflection (Deflection 1). It can be seen that the actual test deflection is best approximated by slab thicknesses in the range 90mm to 110mm. This could be because the average slab thickness is greater than the nominal 70mm, as has been discussed earlier in Chapter 2.

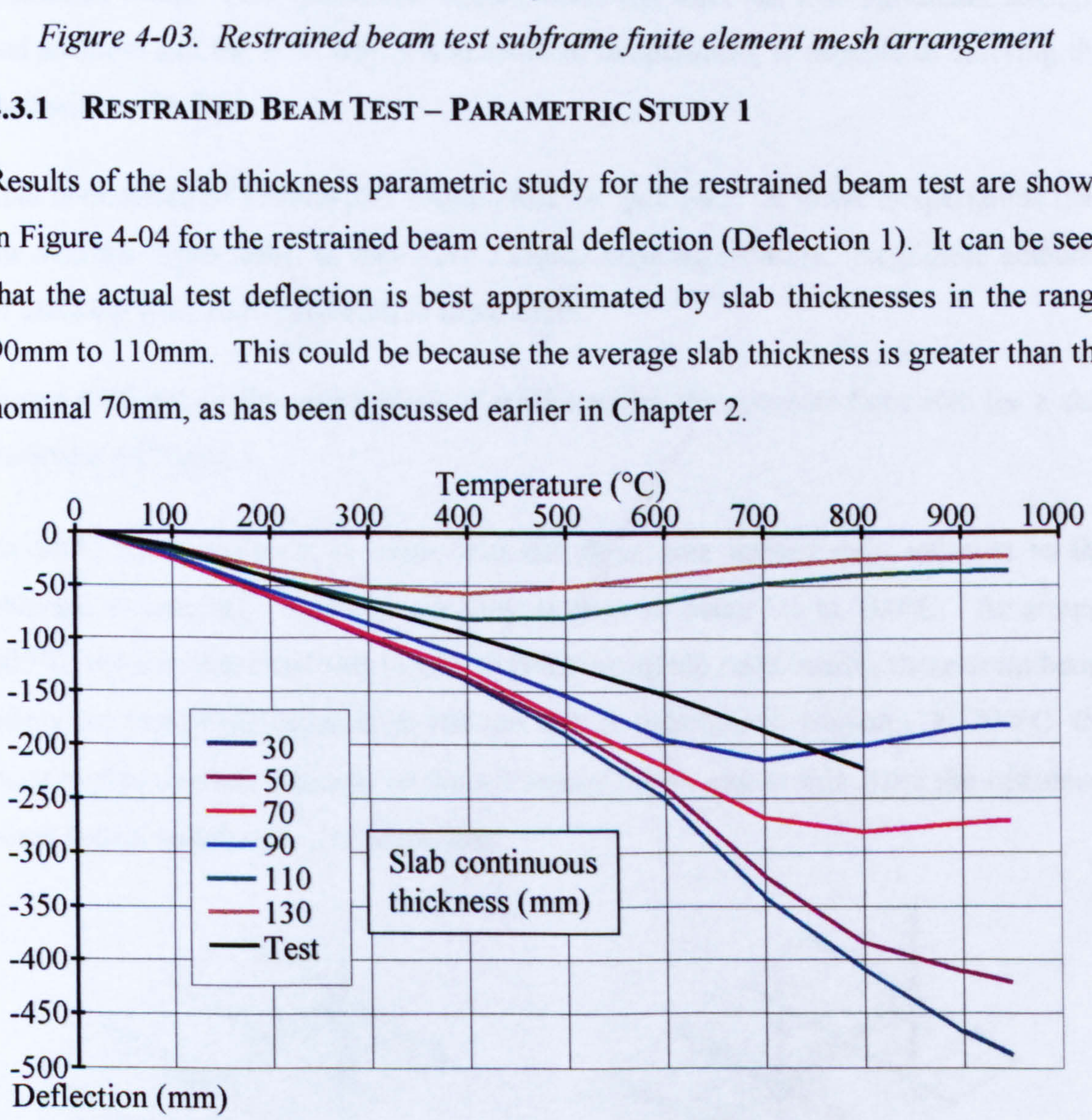

Figure 4-04. Restrained beam test – Parametric study 1 for deflection 1

For continuous slab thicknesses of 30mm and 50mm, the test beam expands against the restraint of the columns, surrounding slab and adjacent beams, and largely because of thermal bowing it begins to displace. Beyond approximately 500°C, the large deflections cause the slab to crack significantly, and the beam starts to act more like

an isolated composite beam. This is illustrated by the 'runaway' nature of the two analyses in the region 600°C to 950°C.

The medium-depth continuous slabs of thickness 70mm and 90mm act similarly. The restrained beam displaces significantly due to thermal bowing until temperatures in the region of 700°C are reached. Above 700°C the continuous concrete slab spanning across the restrained beam from the adjacent cold beams begins to 'pull back' the restrained beam. This 'pull-back' occurs when the steel has lost significant strength and stiffness and the slab, which is at uniform temperature, is capable of carrying the load without its help.

Slab thicknesses of 110mm and 130mm tend to 'pull back' at lower temperatures than the medium-depth slabs, as they have a higher bending stiffness. Negligible amounts of cracking have been predicted in these cases.

Figure 4-05 shows the propagation of cracks across the concrete floor slab for a slab thickness of 70mm.

At 20°C the assumption is made that the floor area immediately adjacent to the columns is cracked. Nominal cracking is seen to occur up to 500°C. At around 600°C, the concrete floor slab begins to crack along the main beams, these areas being where the composite beam hogs and the slab is therefore in tension. At 700°C, the floor begins to crack adjacent to the secondary beam, and at this stage the restrained beam begins to act as an isolated beam.

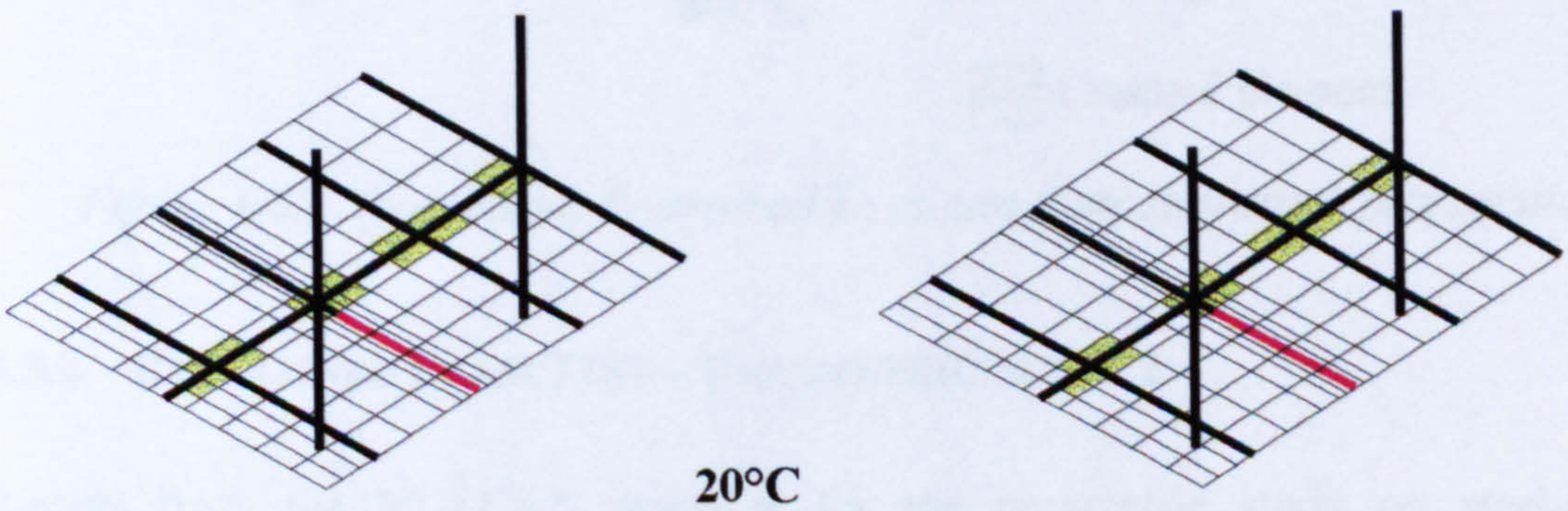

Figure 4-05. Restrained beam test floor slab crack propagation

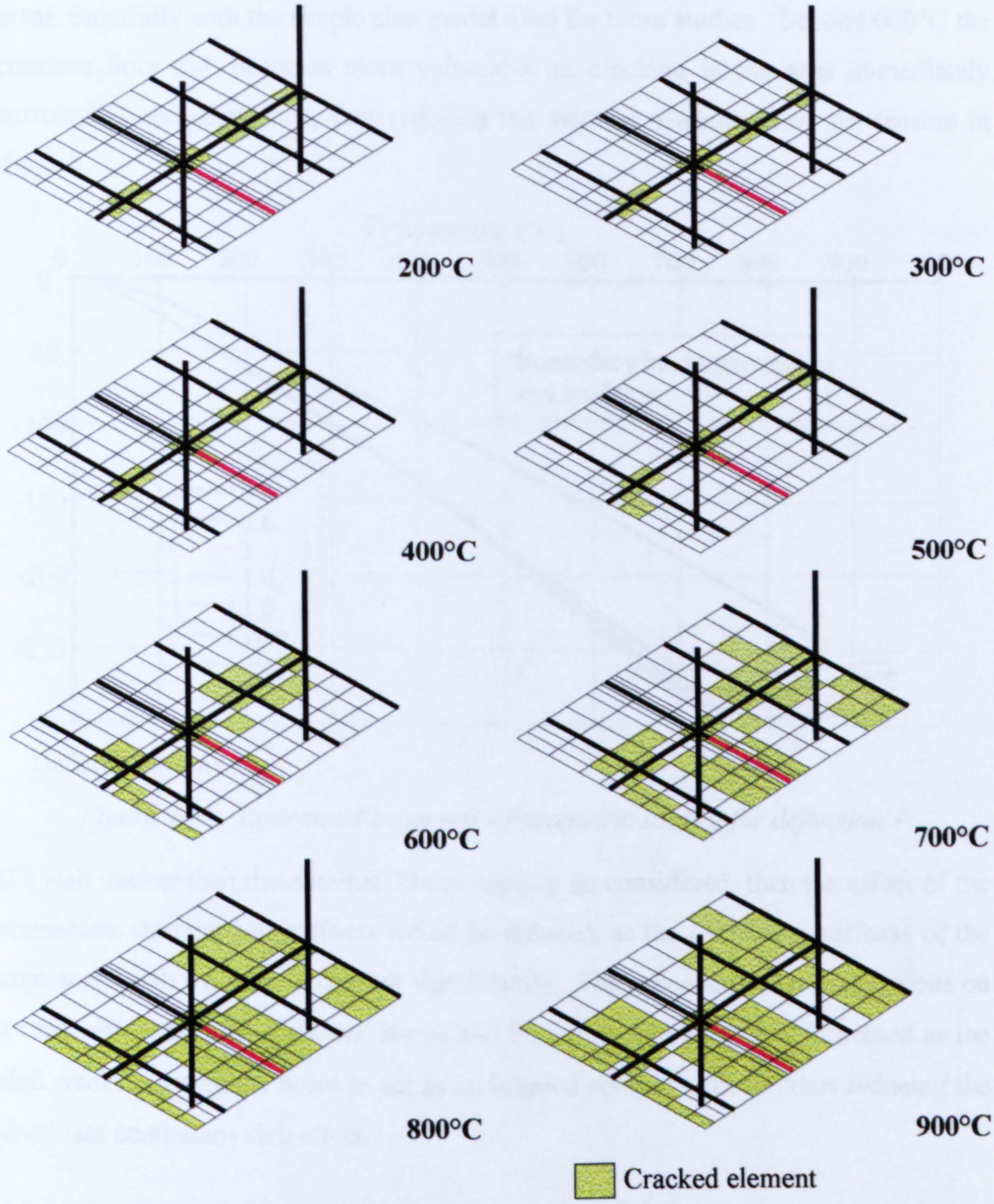

Figure 4-05. (contimued) Restrained beam test floor slab crack propagation

4.3.2 RESTRAINED BEAM TEST – PARAMETRIC STUDY 2

Results from the VULCAN analyses for the parametric study on steel-to-steel secondary beam connection strength and stiffness are shown in Figure 4-06. These show the effects of the rotational restraint of the connections to be negligible up to 600°C beyond which some small variation occurs. This apparent insensitivity to the characteristics of the semi-rigid joints is almost certainly attributable to the slab continuity across the connection, which dominates the bending resistance in these

areas, especially with the simple slab model used for these studies. Beyond 600°C the concrete floor slab becomes more vulnerable to cracking in the area immediately surrounding the connection, thus reducing the moment available from the tension in the slab.

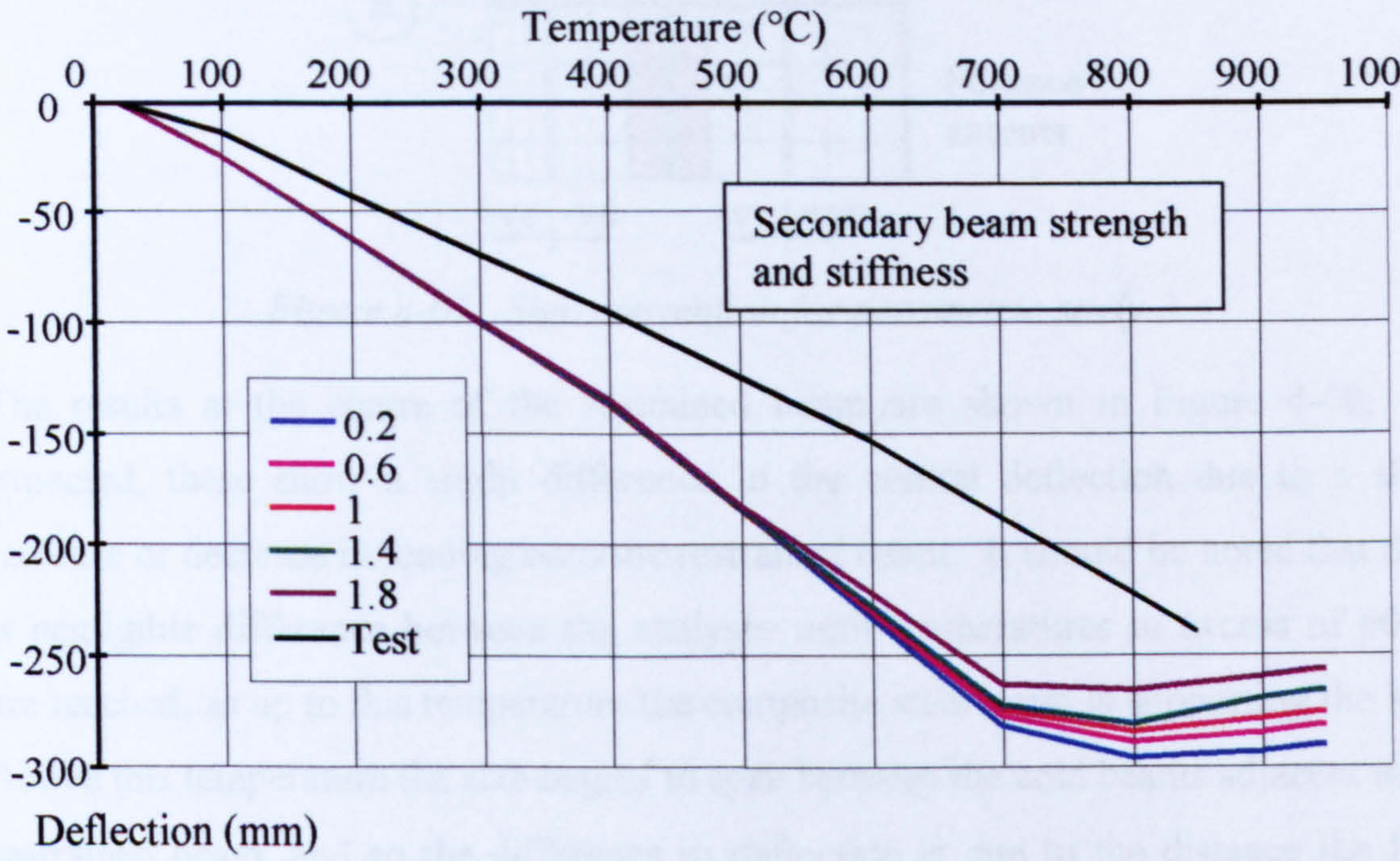

Figure 4-06. Restrained beam test - Parametric study 2 for deflection 1

If a slab thicker than the nominal 70mm were to be considered, then the effect of the connection strength and stiffness would be reduced, as the overriding stiffness of the continuous slab would be increased significantly. The influence of the connections on a case with a thin slab (between 30mm and 50mm) would be greatly increased as the slab cracks, causing the beam to act as an isolated composite beam, thus reducing the dominant continuous slab effect.

4.3.3 RESTRAINED BEAM TEST – PARAMETRIC STUDY 3

Figure 4-07 shows a plan view of the finite element mesh used for the restrained beam test, including the sign convention which indicates the direction in which the secondary beams have been moved.

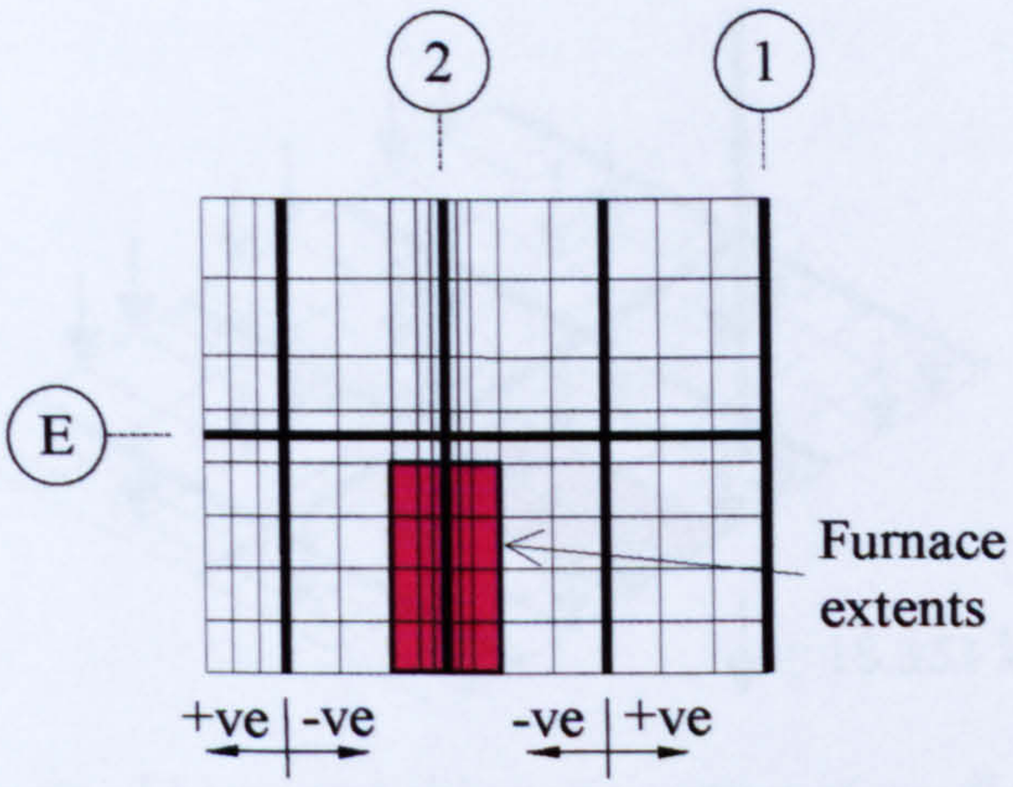

Figure 4-07. Sign convention for parametric study 3

The results at the centre of the restrained beam are shown in Figure 4-08. As expected, these show a slight difference in the central deflection due to a slight increase or decrease in loading onto the restrained beam. It should be noted that there is negligible difference between the analyses until temperatures in excess of 600°C are reached, as up to this temperature the composite steel beam is supporting the load. Above this temperature the slab begins to span between the cold beams adjacent to the restrained beam, and so the difference in deflection is due to the distance the floor slab is required to span.

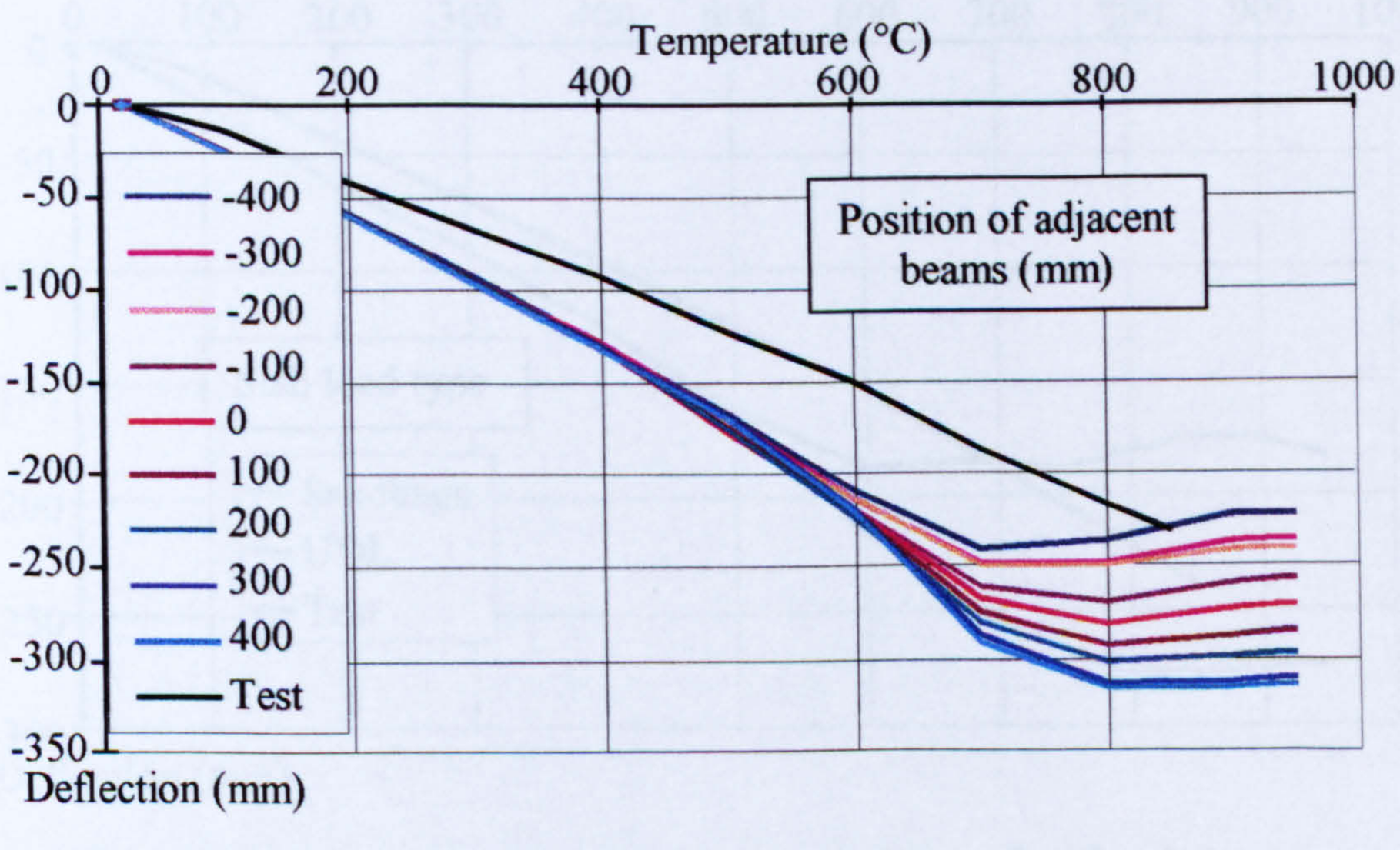

Figure 4-08. Restrained beam test - Parametric study 3 for deflection 1.

4.3.4 RESTRAINED BEAM TEST – PARAMETRIC STUDY 4

The actual positions of the sandbags are superimposed on the restrained beam finite element mesh in Figure 4-09.

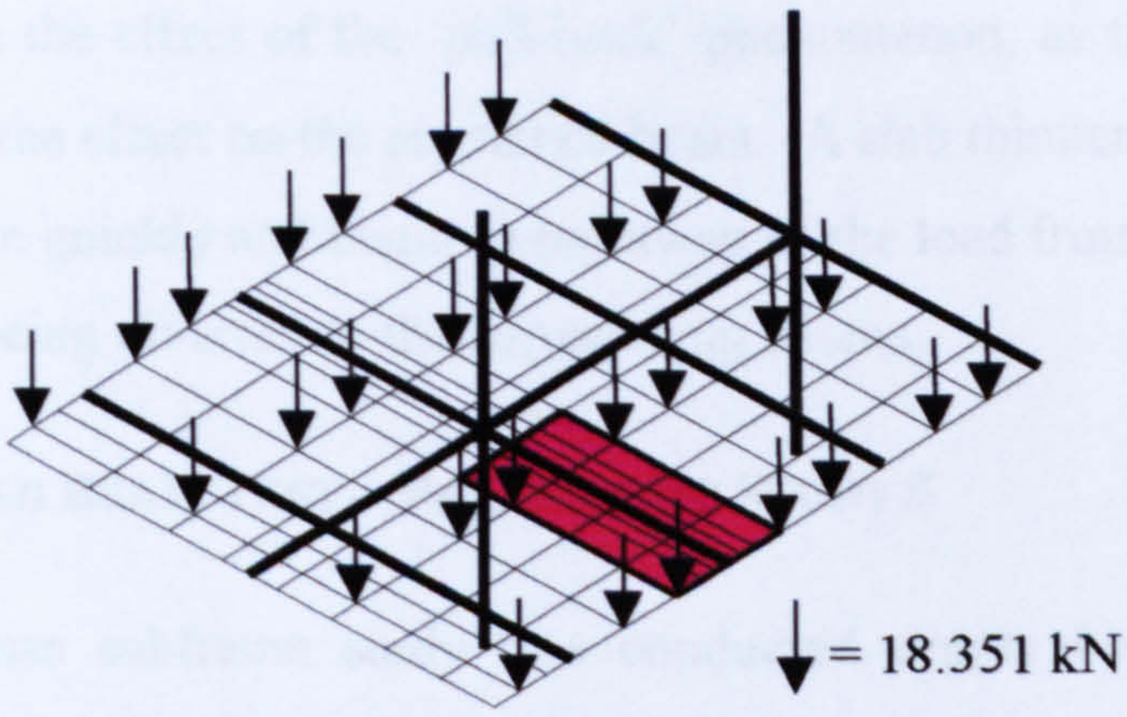

Figure 4-09. Restrained beam test showing position of sandbags (for parametric study 4)

Figure 4-10 shows the central deflection of the restrained beam test, comparing analyses for the assumed uniformly distributed load and the actual loading with the test results. The UDL and actual loading begin to diverge significantly at 500°C, as below this temperature the dominant actions are thermal bowing and restraint from the surrounding continuous structure. However, beyond 500°C the steel beam begins to lose strength and stiffness and so the less demanding load path of the actual loading causes less deflection than the UDL.

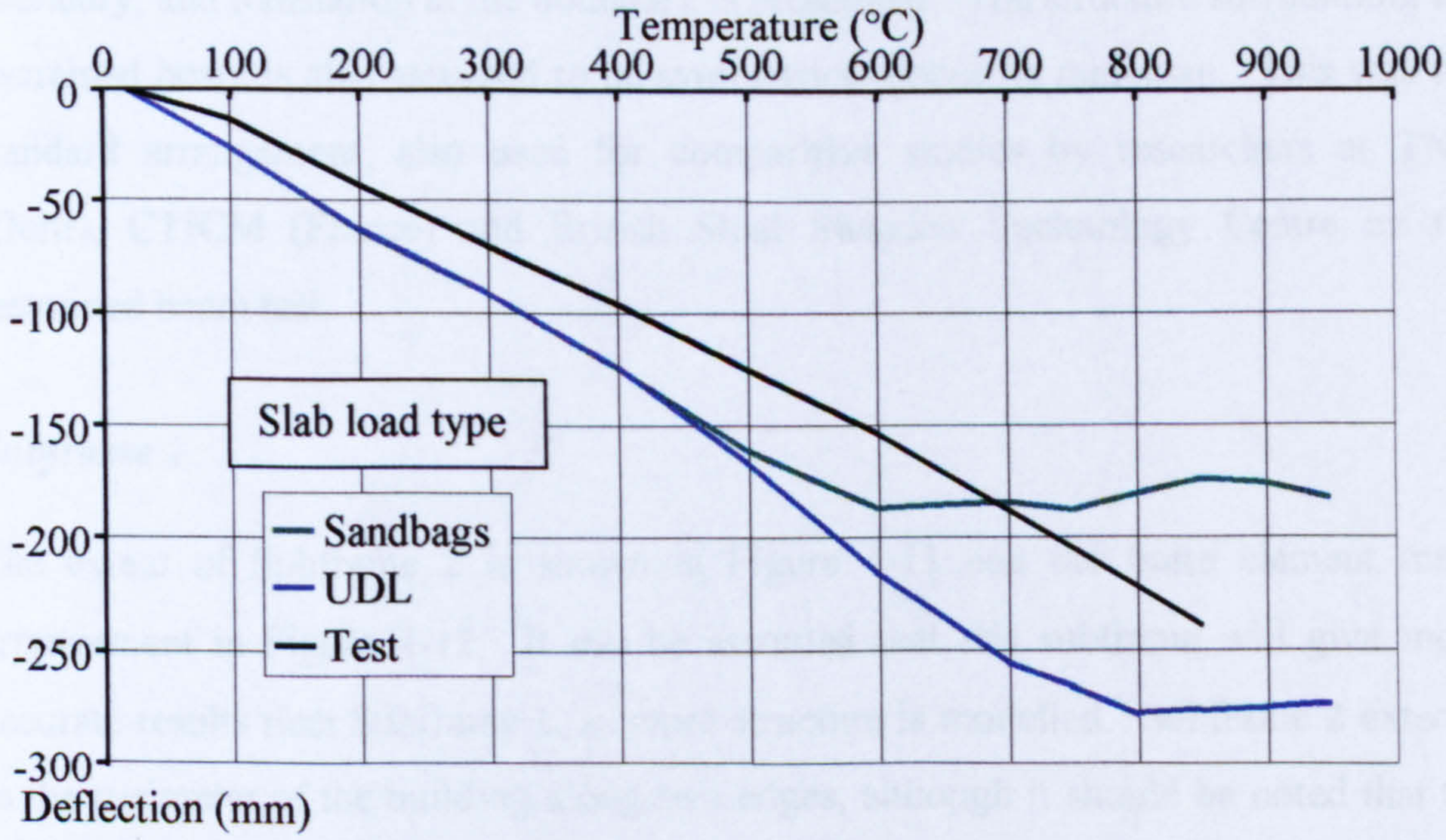

Figure 4-10. Restrained beam test - Parametric study 4 for deflection 1.

It is difficult to hypothesise about the potential effects of slab thickness on this parametric study, as little is known of the load paths in the structure from the point loads simulating the sandbags, although load paths similar to those for a UDL may be assumed. The effect of a slab thicker than the nominal 70mm on this parametric study

may be to increase the effect of the 'pull-back' phenomenon, as the load paths have changed to reduce the effect on the restrained beam. A slab thinner than 70mm would possibly crack more quickly and begin to run away as the load from the sandbags may not be capable of being diverted to the surrounding beams.

4.3.5 RESTRAINED BEAM TEST – PARAMETRIC STUDY 5

The restrained beam subframe study was conducted simply by taking the larger subframes used for other analyses, such as the large compartment demonstration fire test and the corner test, and modifying the finite element mesh to enable a reliable simulation.

Subframe 1

Subframe 1 is the basic subframe, as used in the previous four parametric studies, and is shown in Figure 4-02. The finite element layout has been shown in Figure 4-03. This layout makes several obvious approximations, as three of the external edges of the subframe are assumed in the analysis to be fixed against rotation about the boundary, and translation at the boundary is prohibited. The structure surrounding the restrained beam is also assumed to be symmetrical about its mid-span. This was the standard arrangement, also used for comparitive studies by researchers at TNO (Delft), CTICM (France) and British Steel Swinden Technology Centre on the restrained beam test.

Subframe 2

The extent of Subframe 2 is shown in Figure 4-11 and the finite element mesh arrangement in Figure 4-12. It can be assumed that this subframe will give more accurate results than Subframe 1, as more structure is modelled. Subframe 2 extends to the perimeter of the building along two edges, although it should be noted that the assumption is still made that the structure acts symmetrically about the mid-span of the 9m restrained beam by restraining horizontal movement and rotation about this axis of symmetry.

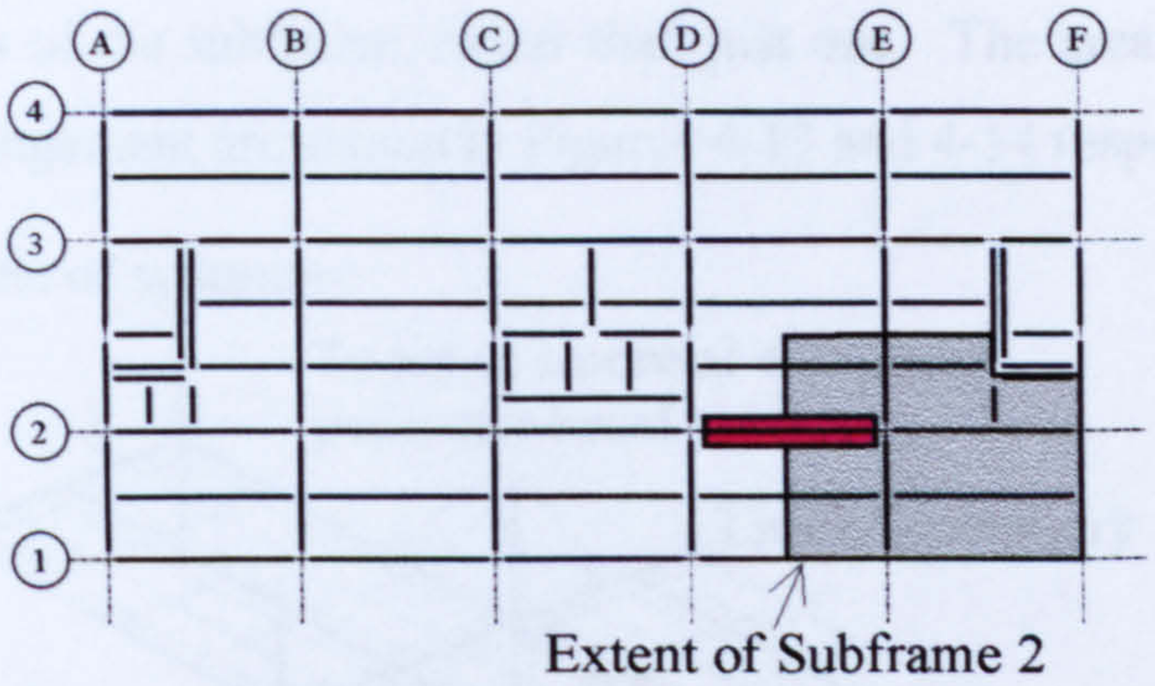

Figure 4-11. Restrained beam test - Subframe 2 location for parametric study 5

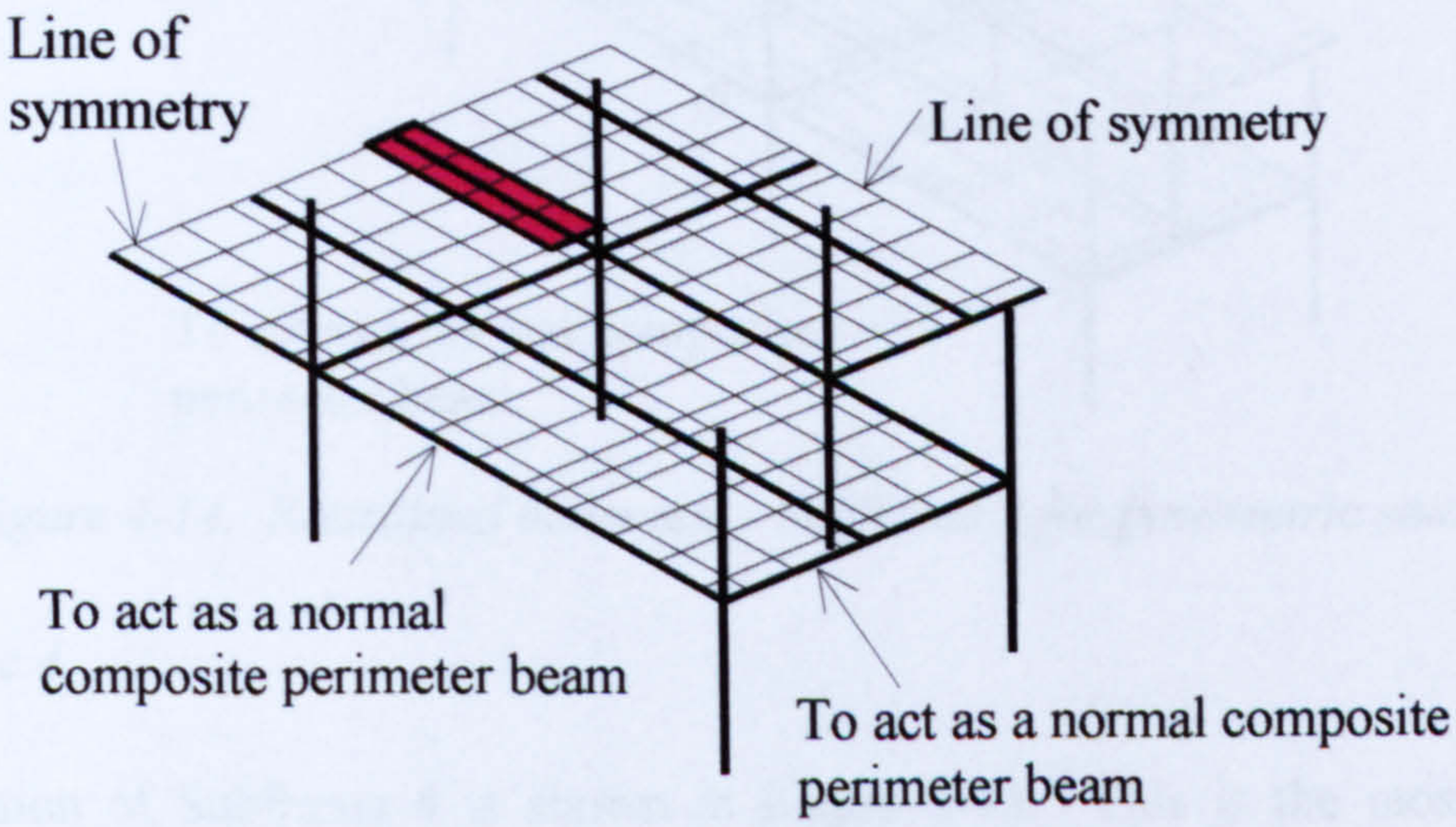

Figure 4-12. Restrained beam test - Subframe 2 for parametric study 5

Subframe 3

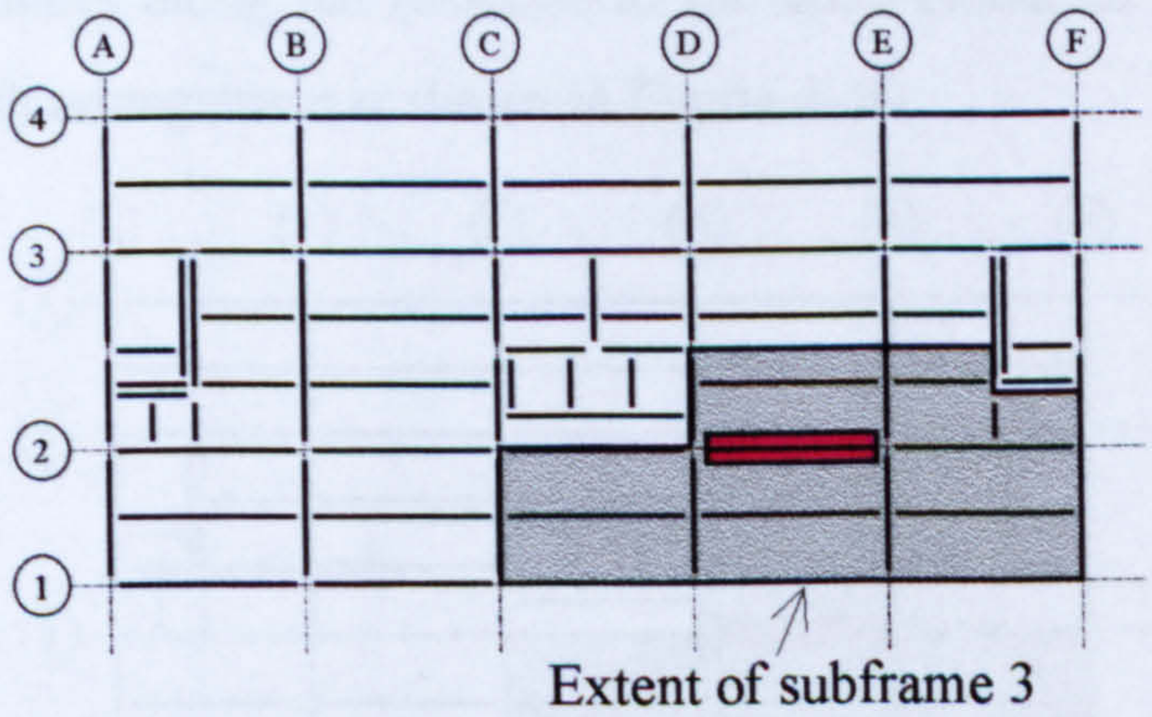

Figure 4-13. Restrained beam test - Subframe 3 location for parametric study 5

Subframe 3 is more extensive than the two previously discussed. It does not involve the implicit assumption that symmetry is maintained about the mid-span of the restrained beam. The subframe continues for a whole bay beyond the restrained beam to an area where it is assumed that the structure will act as continuous. This is again a more justifiable assumption than Subframe 1 as the building perimeter is included on

a number of edges of the subframe, rather than just one. The area modelled and the finite element arrangement are shown in Figures 4-13 and 4-14 respectively.

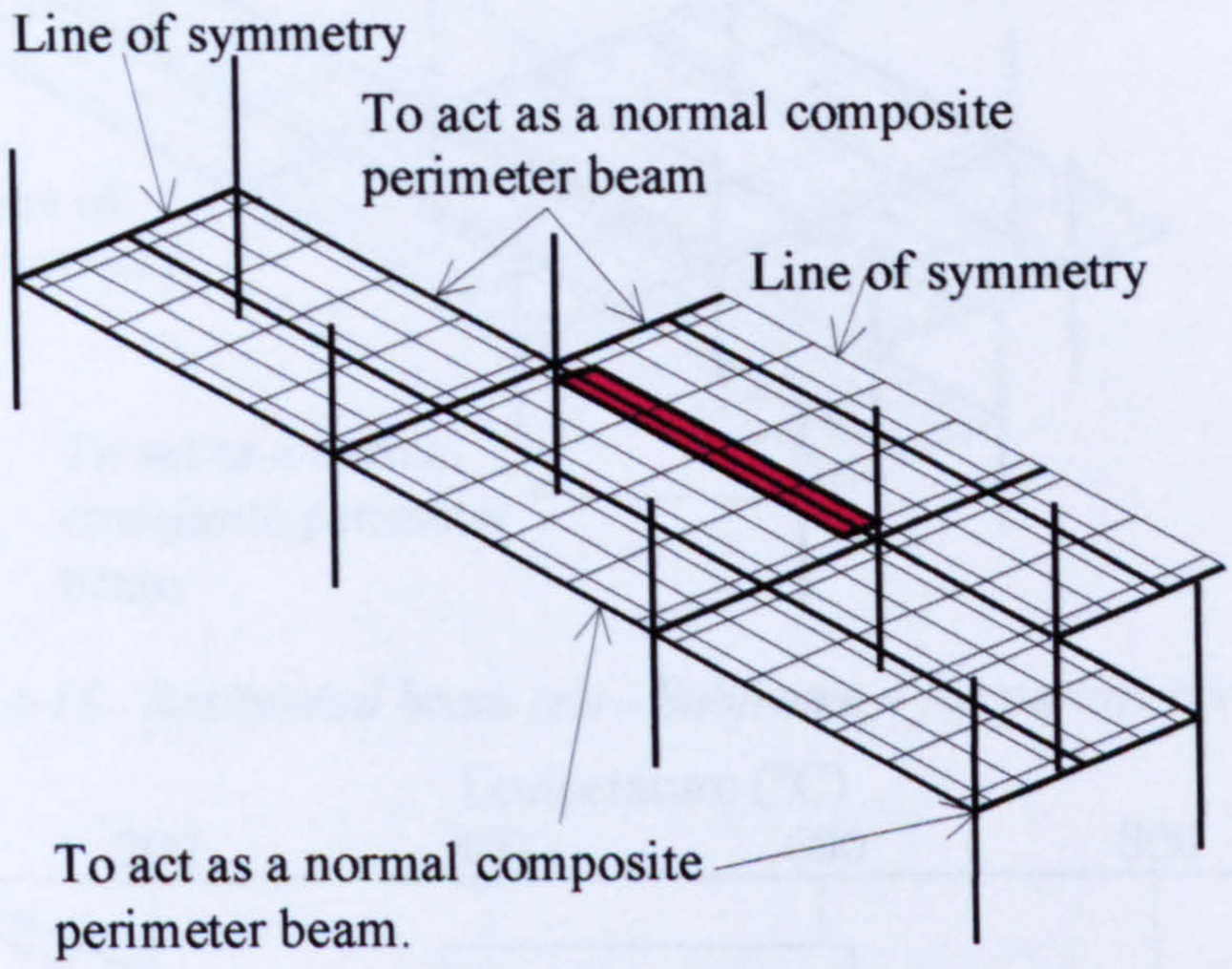

Figure 4-14. Restrained beam test - Subframe 3 for parametric study 5

Subframe 4

The location of Subframe 4 is shown in Figure 4-15. This is the most extensive subframe modelled to date, and improves on the majority of the assumptions made in the previous three subframes. The subframe extends across the structure for an extra half bay and continues along the structure to the same extent as Subframe 3. The finite element mesh arrangement is shown in Figure 4-16.

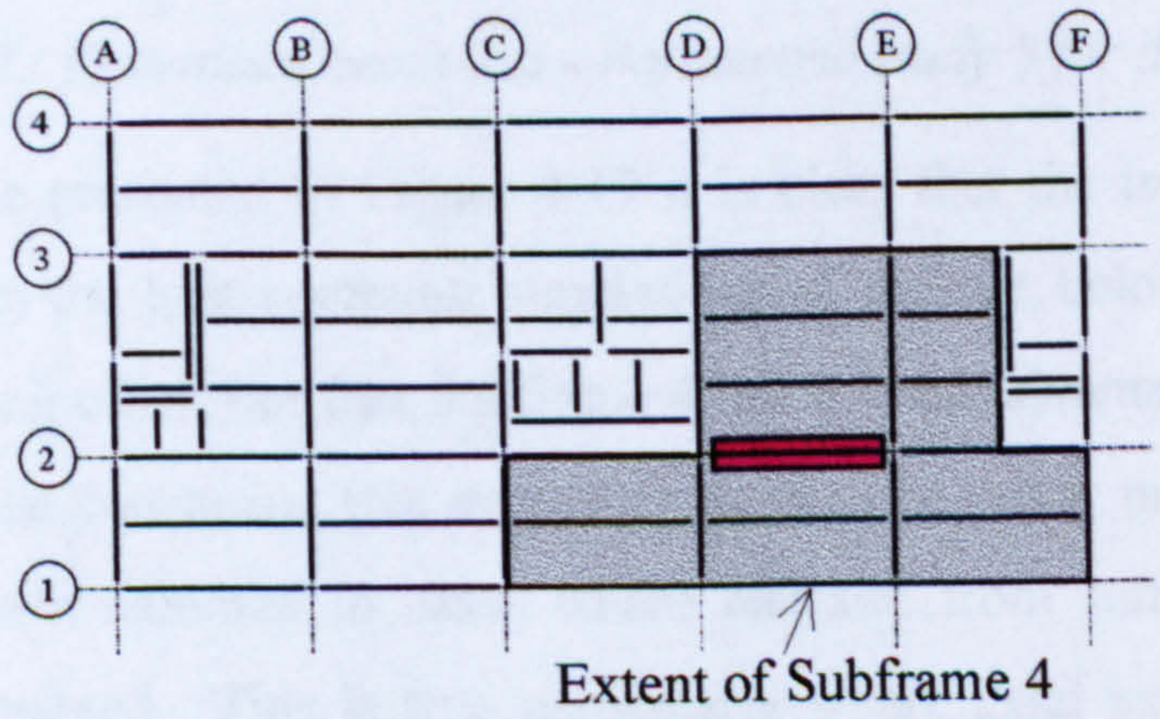

Figure 4-15. Restrained beam test - Subframe 4 location for parametric study 5

Figure 4-17 shows the mid-span deflection of the restrained beam relative to the column deflection at the beam-ends, recorded against the bottom flange temperature. The use of relative deflections also allows the actual test results to be compared with the model predictions.

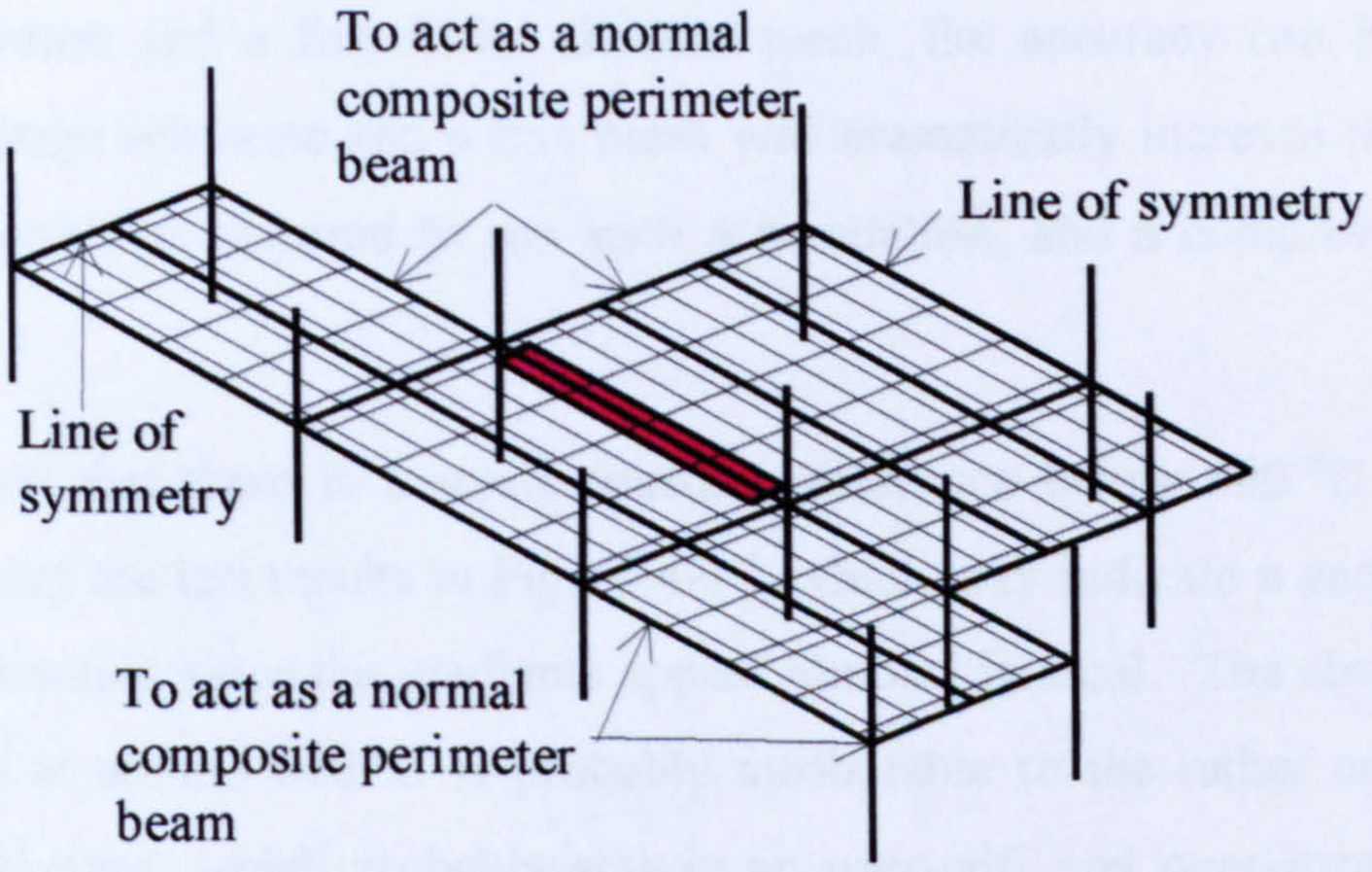

Figure 4-16. Restrained beam test - Subframe 4 for parametric study 5

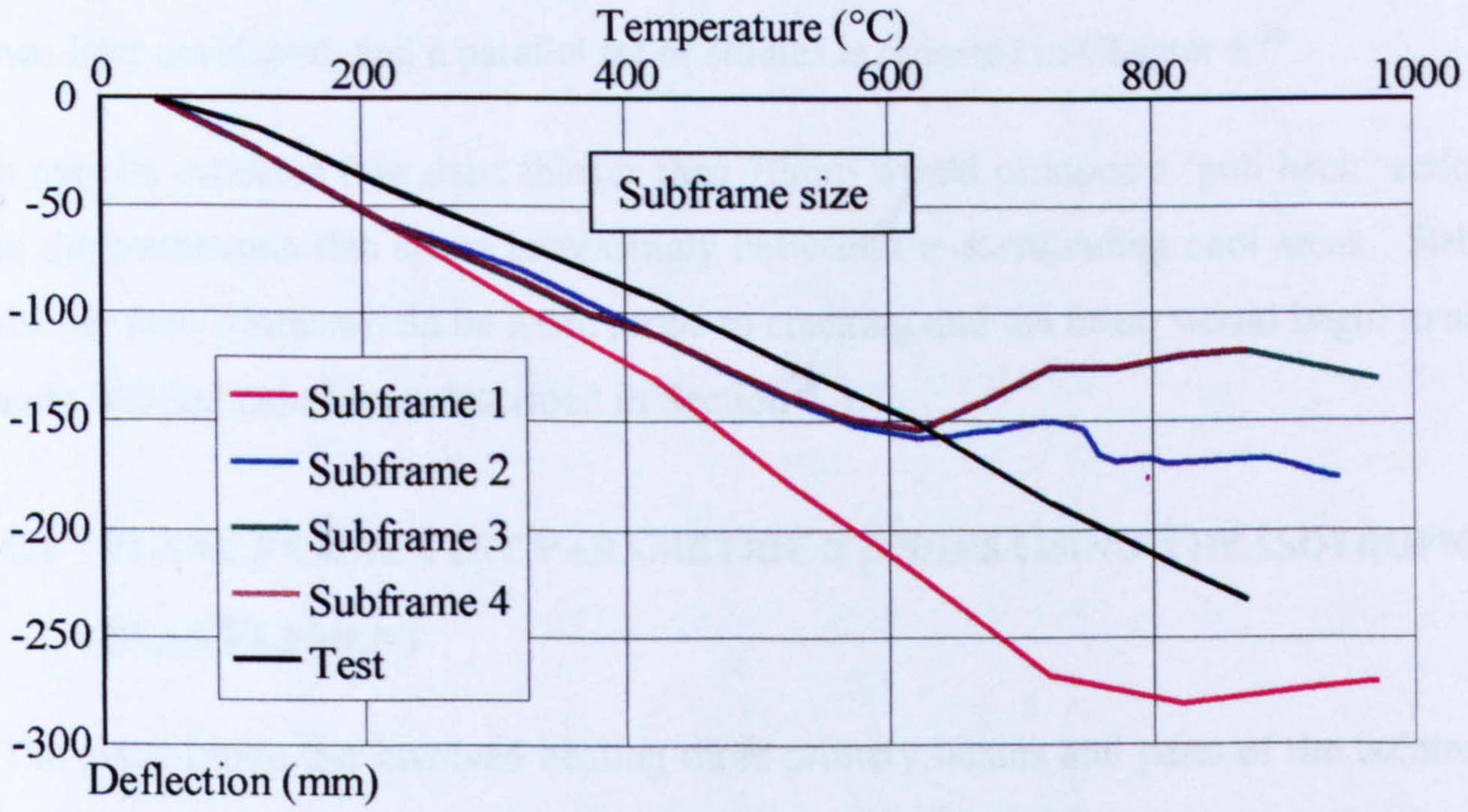

Figure 4-17. Restrained beam test - Parametric study 5 for deflection 1.

From the evidence presented in Figure 4-17 it is clear that the two most extensive subframes produce the best computer simulations of the test below 600°C, and are consistent with each other, but that Subframe 4 has no real advantage over Subframe 3. This leads to the conclusion that subframes need to be rather more extensive than had previously been assumed in cases where restraint from surrounding structure needs to be represented. This is true particularly where axial expansion of a steel member is directly resisted by boundary support conditions in line with the member, as is the case in Subframe 1. However, where there is simply restraint via membrane shear transmission to surrounding parallel areas of structure, the subframe need not be as extensive or as carefully chosen. It is well known that a finer finite element mesh will also increase accuracy, and hence it may be reasonably assumed that by choosing

a large subframe and a fine finite element mesh, the accuracy can be improved. However, a large subframe and a fine mesh will dramatically increase the amount of computing resources required to run such a simulation, and a compromise must be found.

It can be seen that there is a small constant difference below 600 °C between the simulations and the test results in Figure 4-17, which may indicate a zero error in the test instrumentation since the gradients appear almost identical. The abrupt reduction in deflection at around 600 °C is probably attributable to the rather crude concrete failure model used, which probably acts in an over-stiff and over-strong fashion in this region. This, along with the general nature of the slab formulation in VULCAN, was later developed, and a parallel set of studies is reported in Chapter 6 [66].

It may be expected that slabs thicker than 70mm would produce a 'pull back' action as the continuous slab spans increasingly between the surrounding cool areas. Slabs thinner than 70mm would be more prone to cracking and the beam would begin to act as an isolated member as described in Section 4.3.1.

4.4 PLANE FRAME TEST PARAMETRIC STUDIES USING THE ISOTROPIC SLAB ELEMENT

The plane frame test involved heating three primary beams and parts of the columns to which they were connected across the full-depth of the frame supporting the fourth floor, as shown in Figure 4-18. The aim of the test was to ascertain the influence of beam-column interaction using a two-dimensional cross-structure frame similar to that which a designer would use for analysis.

Pre-test design studies on skeletal frames using VULCAN [51] had indicated that, should the columns be left unprotected, failure could occur at relatively low temperatures due to a combination of column buckling and squashing. The columns in the fire compartment were therefore insulated with ceramic fibre blanket. The top 500mm of all columns was left unprotected, since it was assumed that in practice the column would be encased to a height just above the suspended ceiling. Unfortunately this unprotected zone at the inner column heads (located on grid positions E2 and E3 on Figure 4-18) suffered an extreme local plastic buckling deformation, with a sudden

vertical displacement of approximately 200mm taking place at a control temperature (the heated beam's lower flange temperature) of about 620°C.

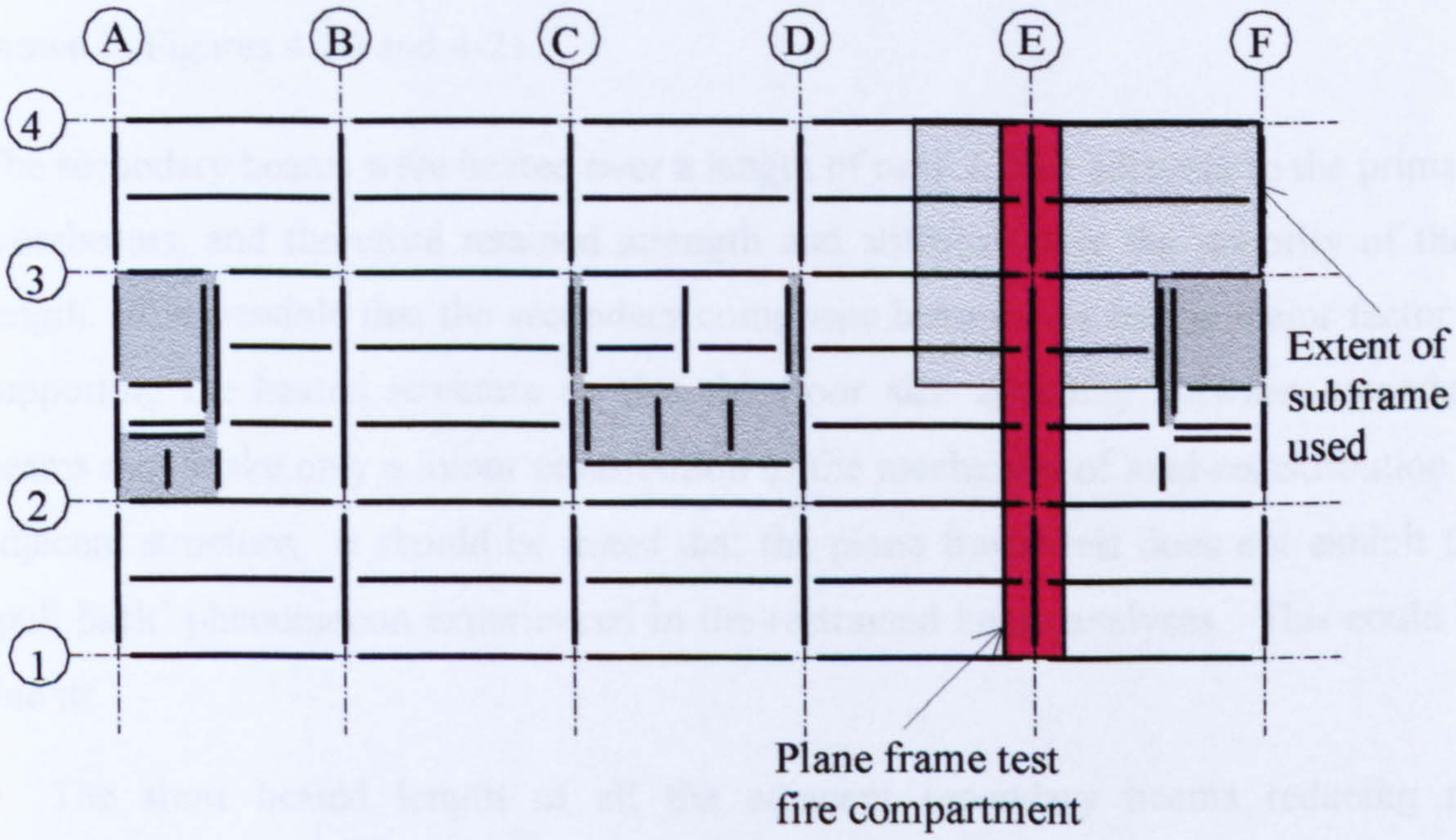

Figure 4-18. Location of the plane frame test.

The deflections in the plane frame test analyses are taken at two positions at the mid-spans of the 6m and 9m main beams of the test, as shown in Figure 4-19. In order to maintain compatibility with the test deflections, which were measured relative to the upper storey, these deflections are plotted relative to the mean of the member end-deflections.

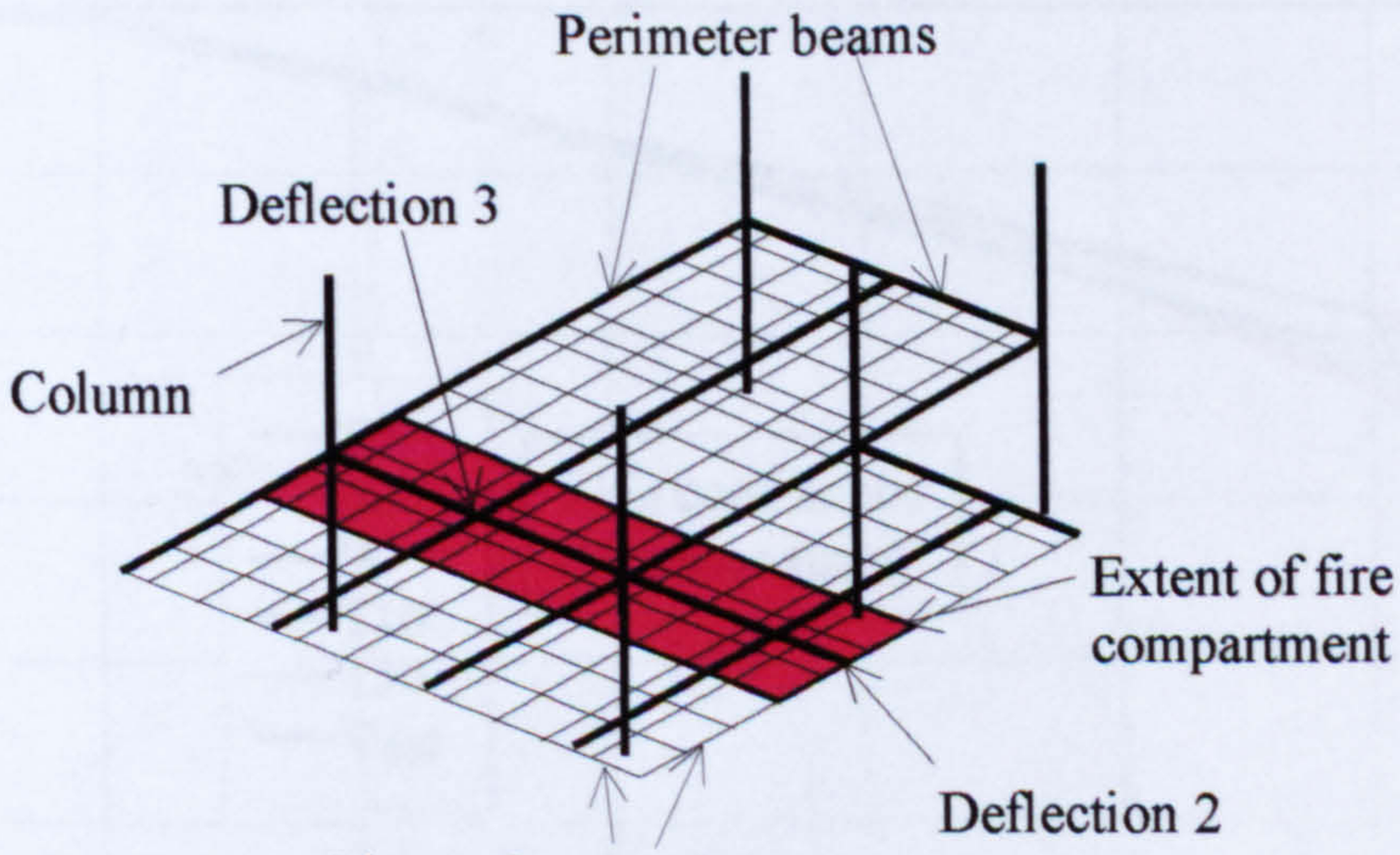

Figure 4-19. Finite element mesh arrangement for the plane frame test.

4.4.1 PLANE FRAME TEST – PARAMETRIC STUDY 1

Results of the analyses for the plane frame test parametric study on slab thickness are shown in Figures 4-20 and 4-21.

The secondary beams were heated over a length of only 1.25m adjacent to the primary crossbeams, and therefore retained strength and stiffness over the majority of their length. It is possible that the secondary composite beams may be the major factor in supporting the heated structure so that the floor slab spanning between secondary beams may make only a minor contribution to the mechanics of load-redistribution to adjacent structure. It should be noted that the plane frame test does not exhibit the 'pull back' phenomenon experienced in the restrained beam analyses. This could be due to:

- The short heated length of all the adjacent secondary beams reducing the rotational stiffness at the ends connected to the main beams.
- The secondary beam connections are of a tab-plate type that is not particularly resistant to rotation, even at ambient temperature.
- The concrete floor slab is in tension, and will therefore be susceptible to cracking parallel to the main test beams.

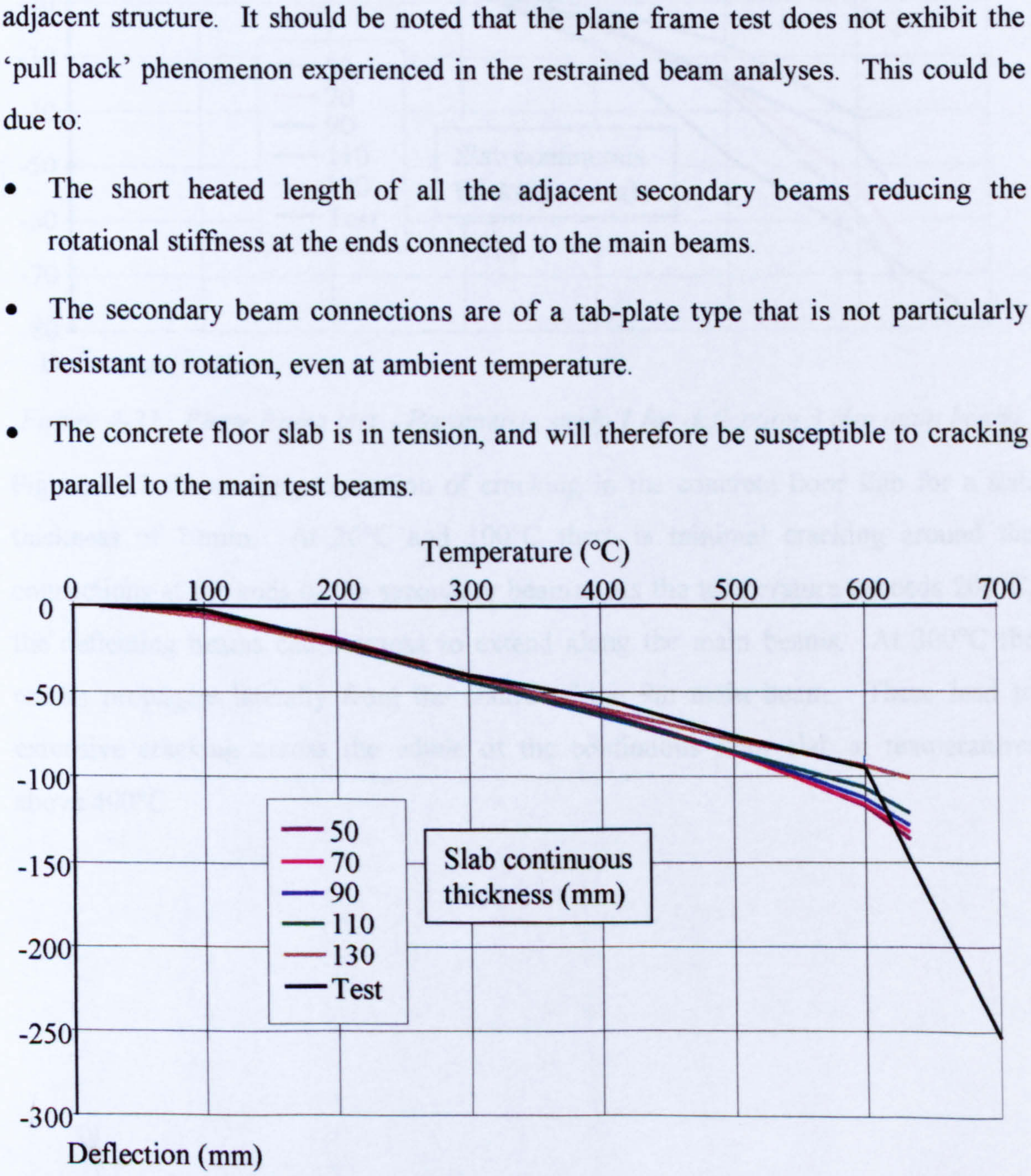

Figure 4-20. Plane frame test - Parametric study 1 for deflection 2 (9m main beam)

The VULCAN analysis ends at approximately 630°C, with a runaway deflection due to rapid softening of the elements exposed to heating over the top 500mm of the inner columns, which causes numerical instability. This is a fair representation of the high plasticity that resulted in a considerable distortion of the tops of each of these columns, starting at about 620°C.

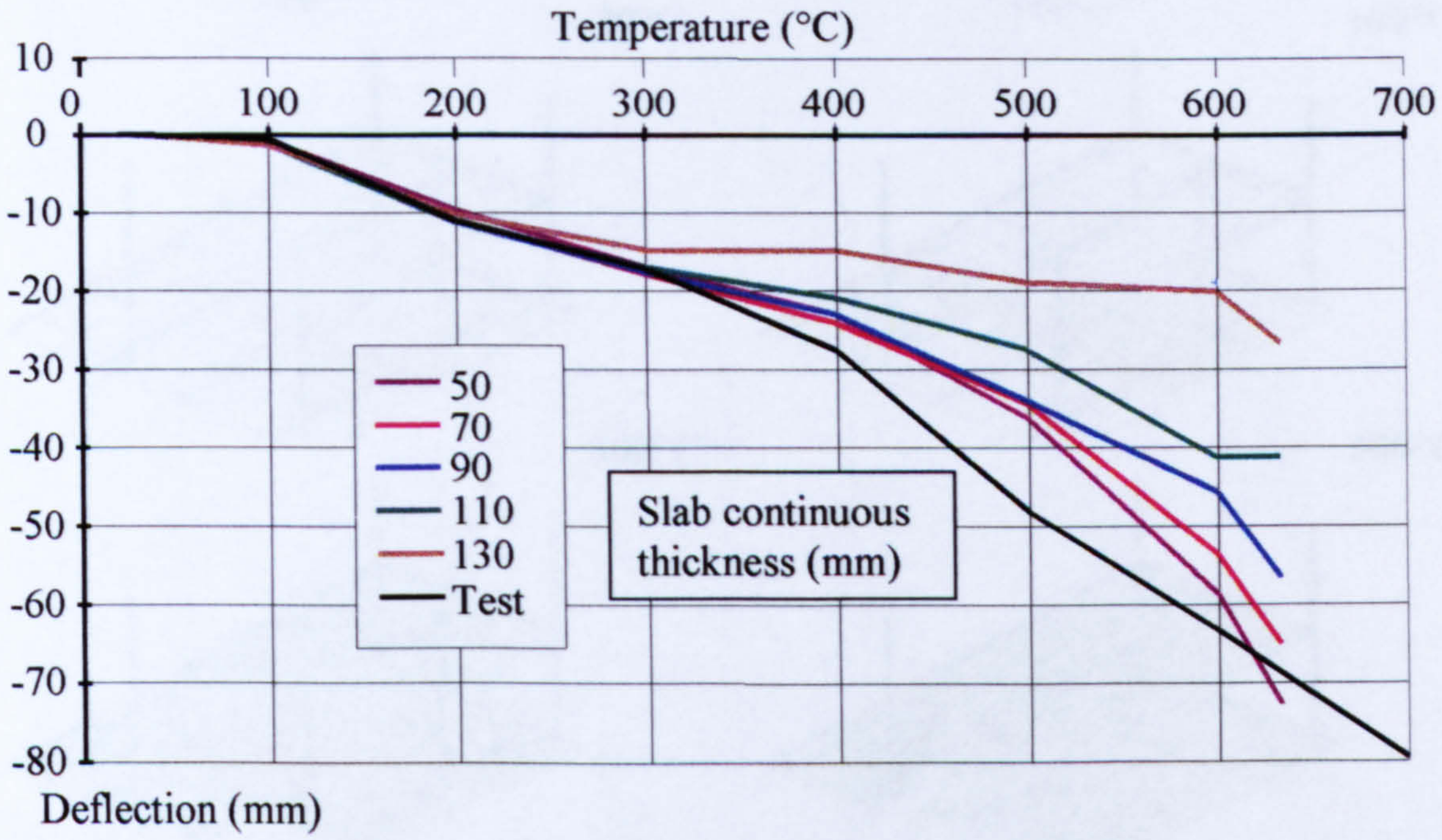

Figure 4-21. Plane frame test – Parametric study 1 for deflection 3 (6m main beam)

Figure 4-22 shows the progression of cracking in the concrete floor slab for a slab thickness of 70mm. At 20°C and 100°C there is minimal cracking around the connections at the ends of the secondary beams. As the temperature exceeds 200°C, the deflecting beams cause cracks to extend along the main beams. At 300°C the cracks propagate laterally from the centre of the 9m main beam. These lead to extensive cracking across the whole of the continuous floor slab at temperatures above 400°C.

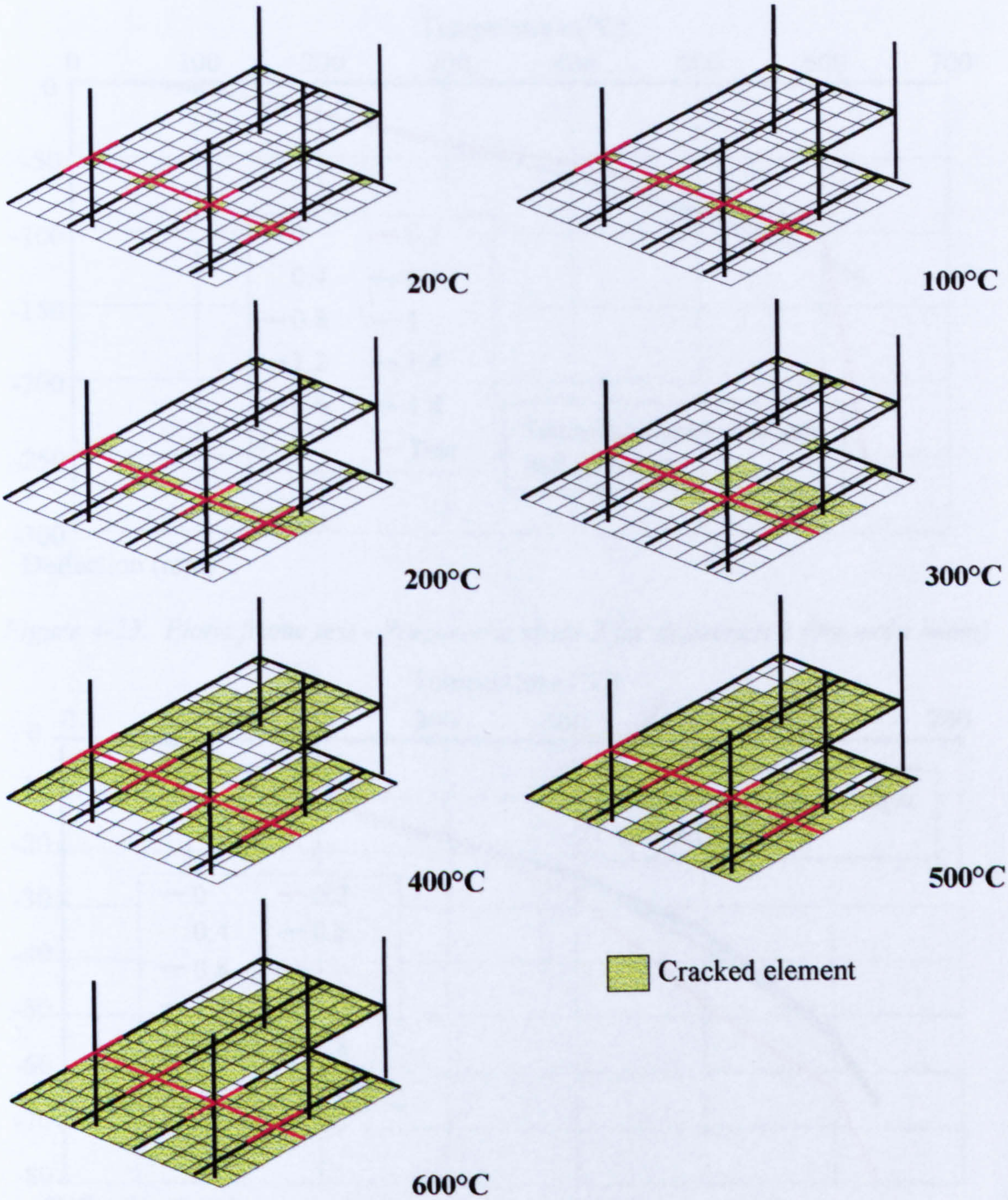

Figure 4-22. Plane frame test floor slab crack propagation

4.4.2 PLANE FRAME TEST – PARAMETRIC STUDY 2

The semi-rigid secondary beam joints can be seen from Figures 4-23 and 4-24 to have almost negligible effect on the performance of the plane frame. This provides some confirmation that the test is essentially of a plane frame with only minor support from the third dimension. As noted previously, the secondary beams and the slabs spanning them transversely are connected in very flexible fashion at both ends, and therefore resemble pinned linkages rather than beams in bending.

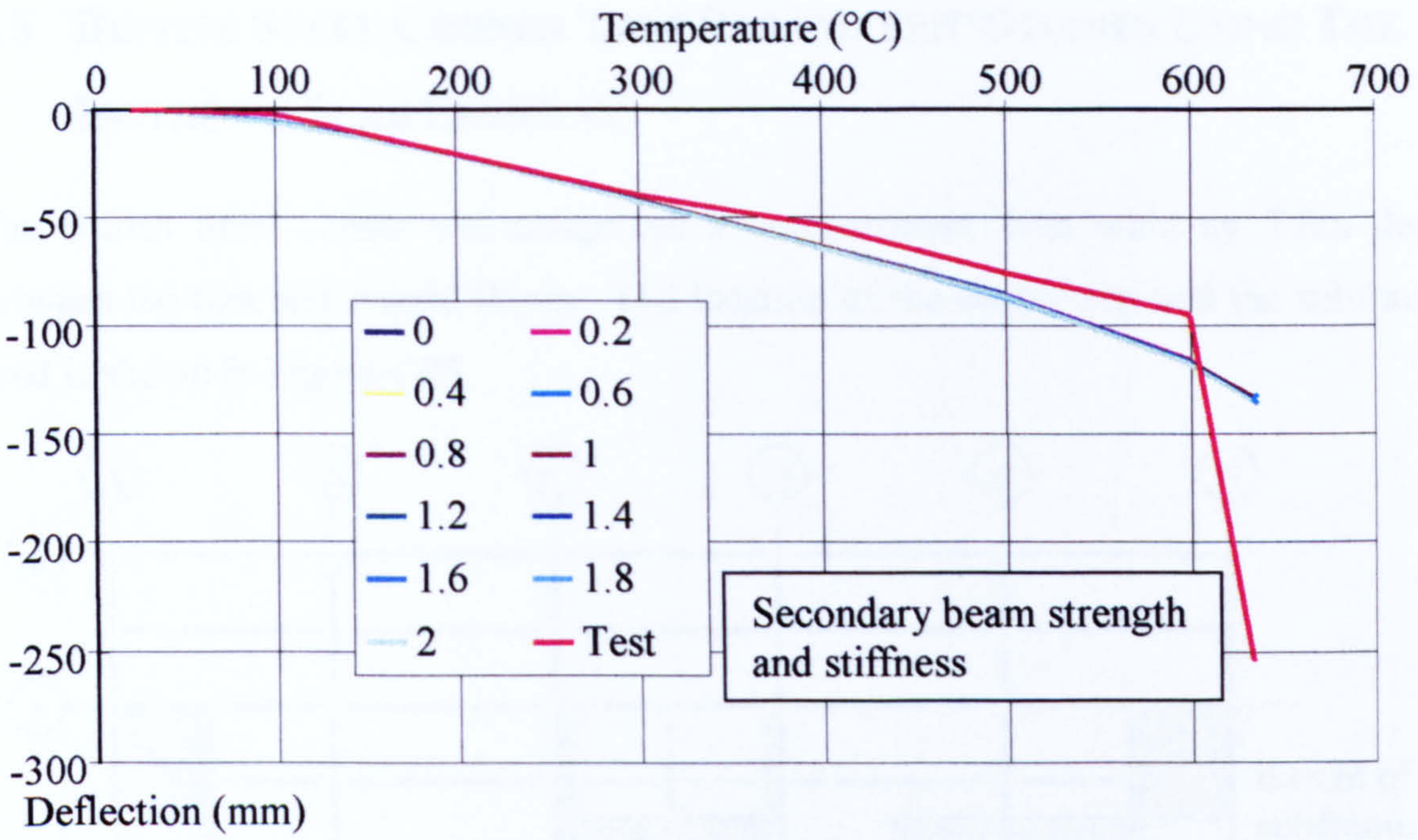

Figure 4-23. Plane frame test - Parametric study 2 for deflection 2 (9m main beam)

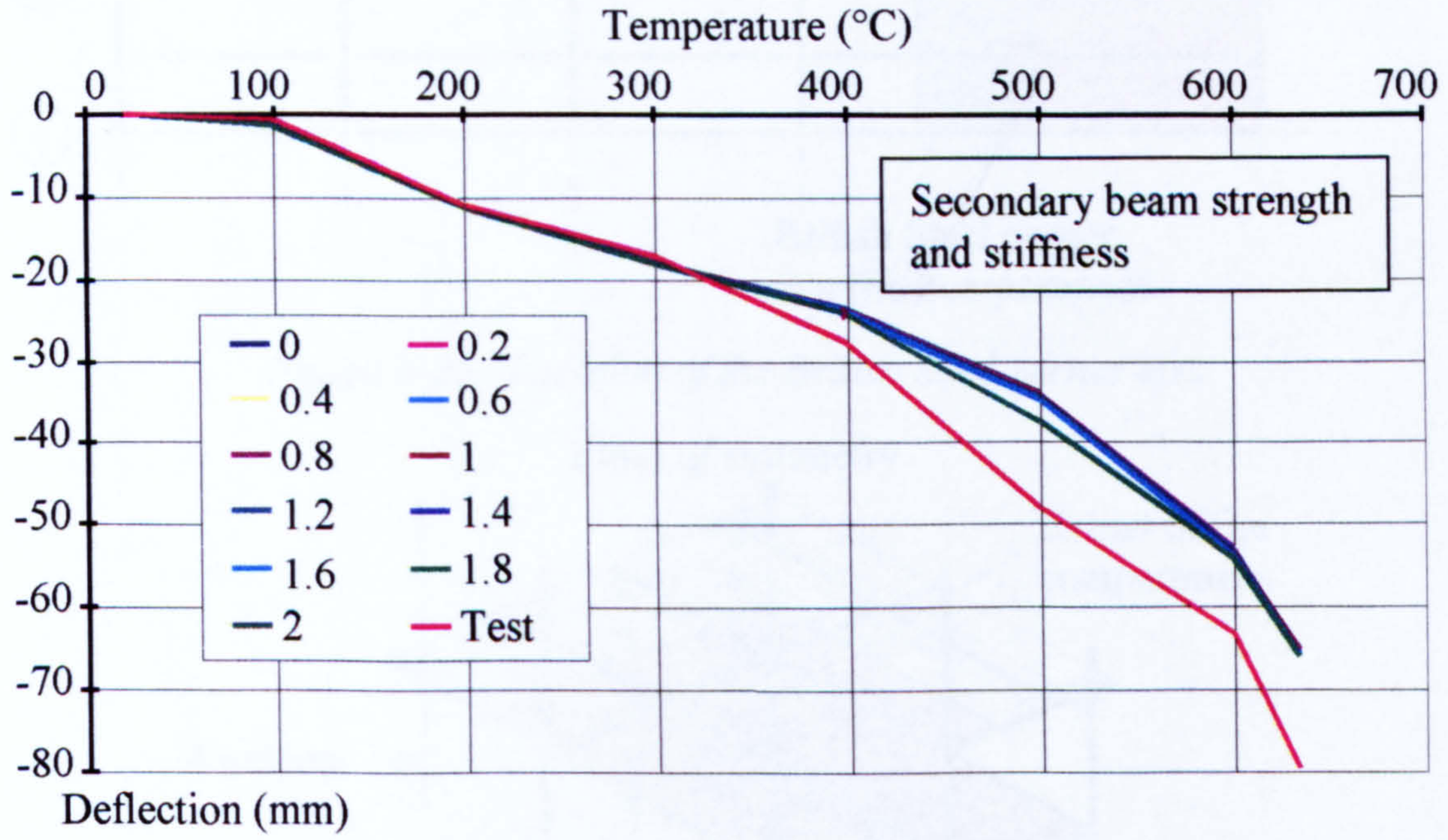

Figure 4-24. Plane frame test - Parametric study 2 for deflection 3 (6m main beam)

The analysis by VULCAN again ends at approximately 630°C in all cases due to the column elements being unprotected over the top 500mm, causing numerical instability to occur.

4.5 BRITISH STEEL CORNER TEST PARAMETRIC STUDIES USING THE ISOTROPIC SLAB ELEMENT

The British Steel corner test comprised a compartment 10m wide by 7.6m deep between the first and second floors. The location of the corner test and the subframe used is shown in Figure 4-25.

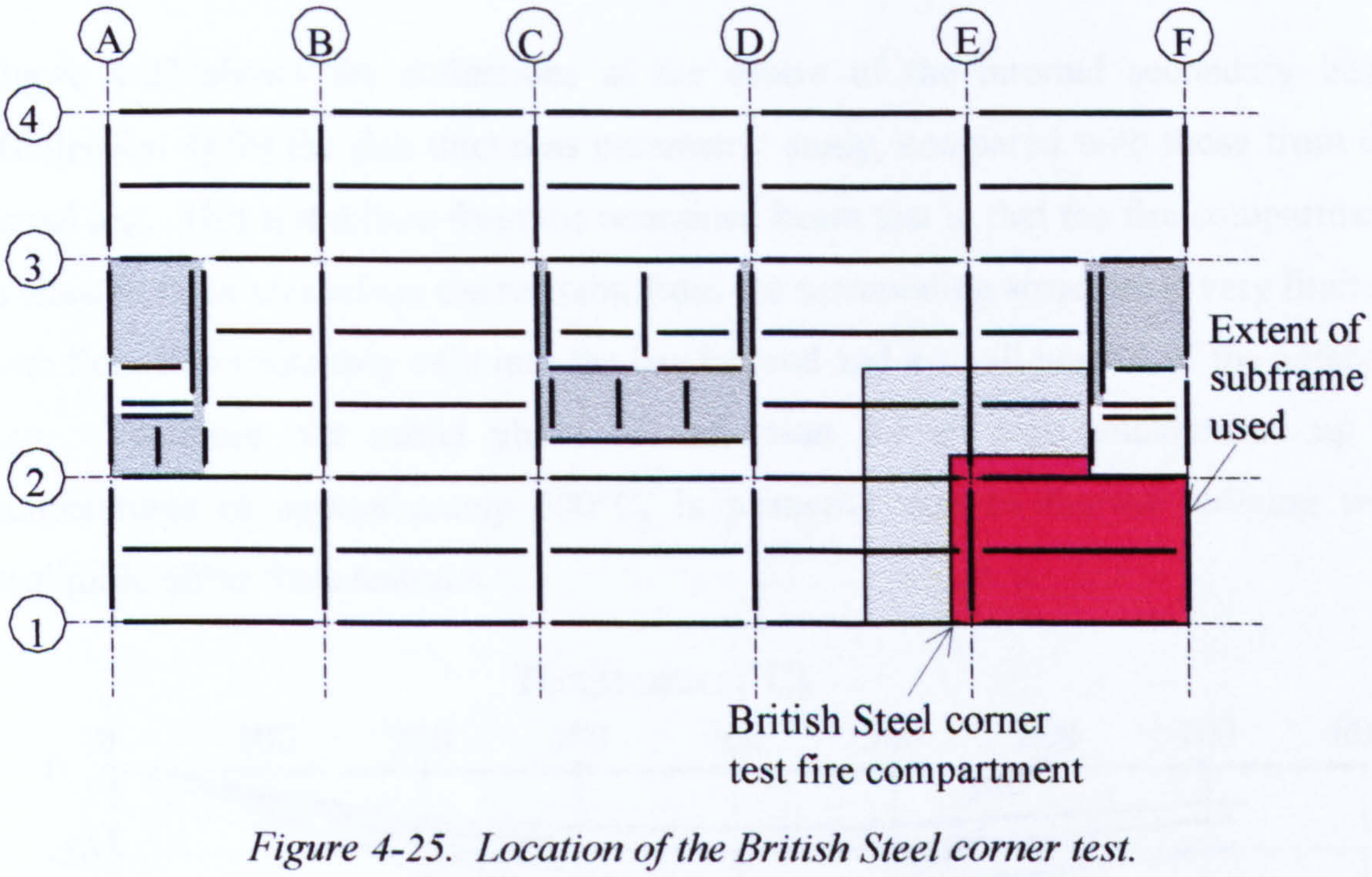

Figure 4-25. Location of the British Steel corner test.

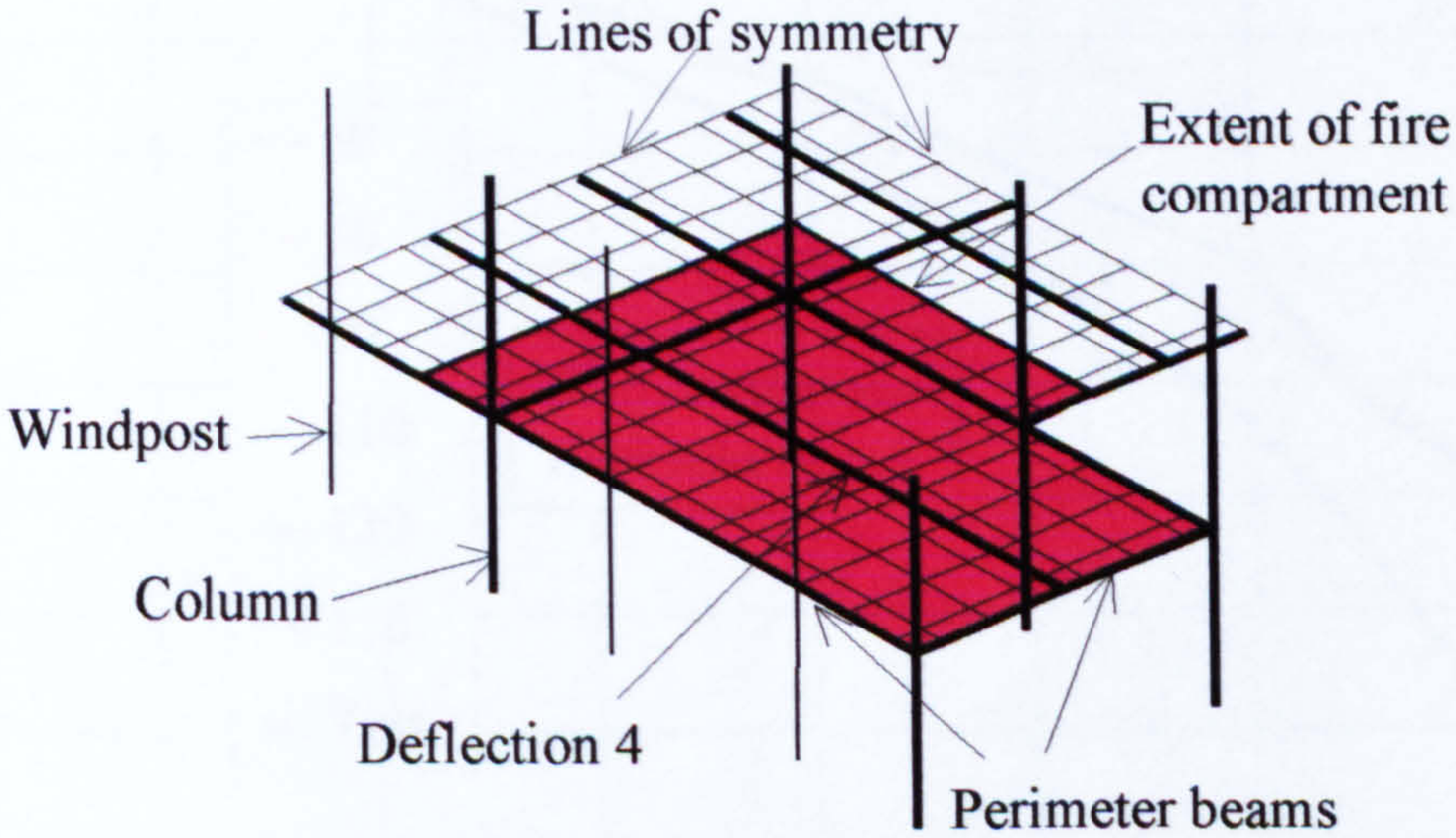

Figure 4-26. Finite element mesh arrangement for the British Steel corner test.

The columns within the compartment were protected to their full height. All perimeter beams were protected over their full length, and for the purpose of the analysis the perimeter beams were assumed to experience temperatures which were 50% of the internal secondary beam lower-flange temperature. Studies have shown that wind-posts along the perimeter beam affect the structural response of the

compartment because they act in tension as the beam deflects to the limit of the wind-post movement slots, hence supporting the edge beam [44].

Deflections are plotted at the mid-span of the internal secondary beam as shown on Figure 4-26. Once again, these are relative to the mean of the beam end deflections.

4.5.1 BRITISH STEEL CORNER TEST – PARAMETRIC STUDY 1

Figure 4-27 shows the deflections at the centre of the internal secondary beam (Deflection 4) for the slab thickness parametric study, compared with those from the actual test. This test differs from the restrained beam test in that the fire compartment is situated in an area where the restraint from the surrounding structure is very limited, with floor slab continuity only into the bay beyond and a small portion of the adjacent bay. Therefore, the initial phase of deflection for all slab thicknesses, up to temperatures of approximately 500°C, is primarily due to thermal bowing with negligible effect from restraint.

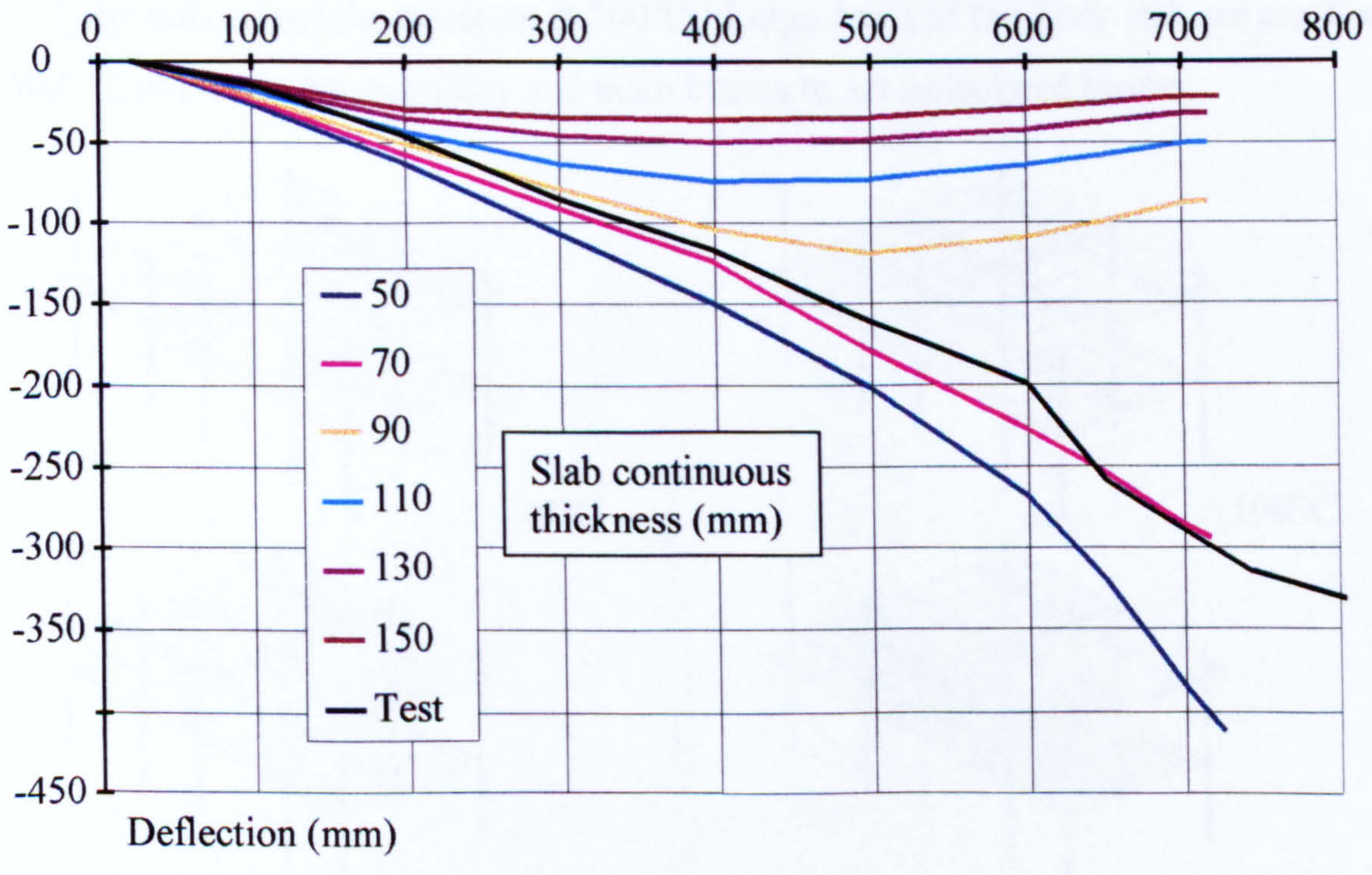

Figure 4-27. British Steel corner test - Parametric study 1 for deflection 4

The thinner concrete slabs of 50mm and 70mm continuous thickness continue deflecting beyond temperatures of approximately 500°C in a manner similar to an isolated beam which exhibits 'runaway'. This is due to the concrete cracking

(through tension on the bottom face) parallel to the secondary beam, producing something akin to an effective-width flange.

The concrete slab thicknesses between 90mm and 150mm all exhibit a general pattern of 'pull back' similar to that found in the restrained beam test. This is where the slab retains enough structural integrity to resist the continued bending of the beam. The support stiffness for the 'pull back' phenomenon is supplied by the perimeter beam (as previously discussed), which is supported by the windposts acting in tension from the cold floor above.

All the analyses finish at temperatures below that of the test due to simultaneous concrete cracking over the 6m main beam causing the finite element analysis to become numerically unstable as a result of the massive and sudden loss of stiffness.

The development of cracking for the British Steel corner test for a 70mm slab thickness is shown in Figure 4-28. Nominal cracking occurs at 20°C and 100°C. At 200°C the continuous floor slab begins to crack along the perimeter beam and this slowly spreads across the structure at 300°C. Large areas of the floor slab are cracked at 400°C, allowing the secondary and main beams to act as isolated beams.

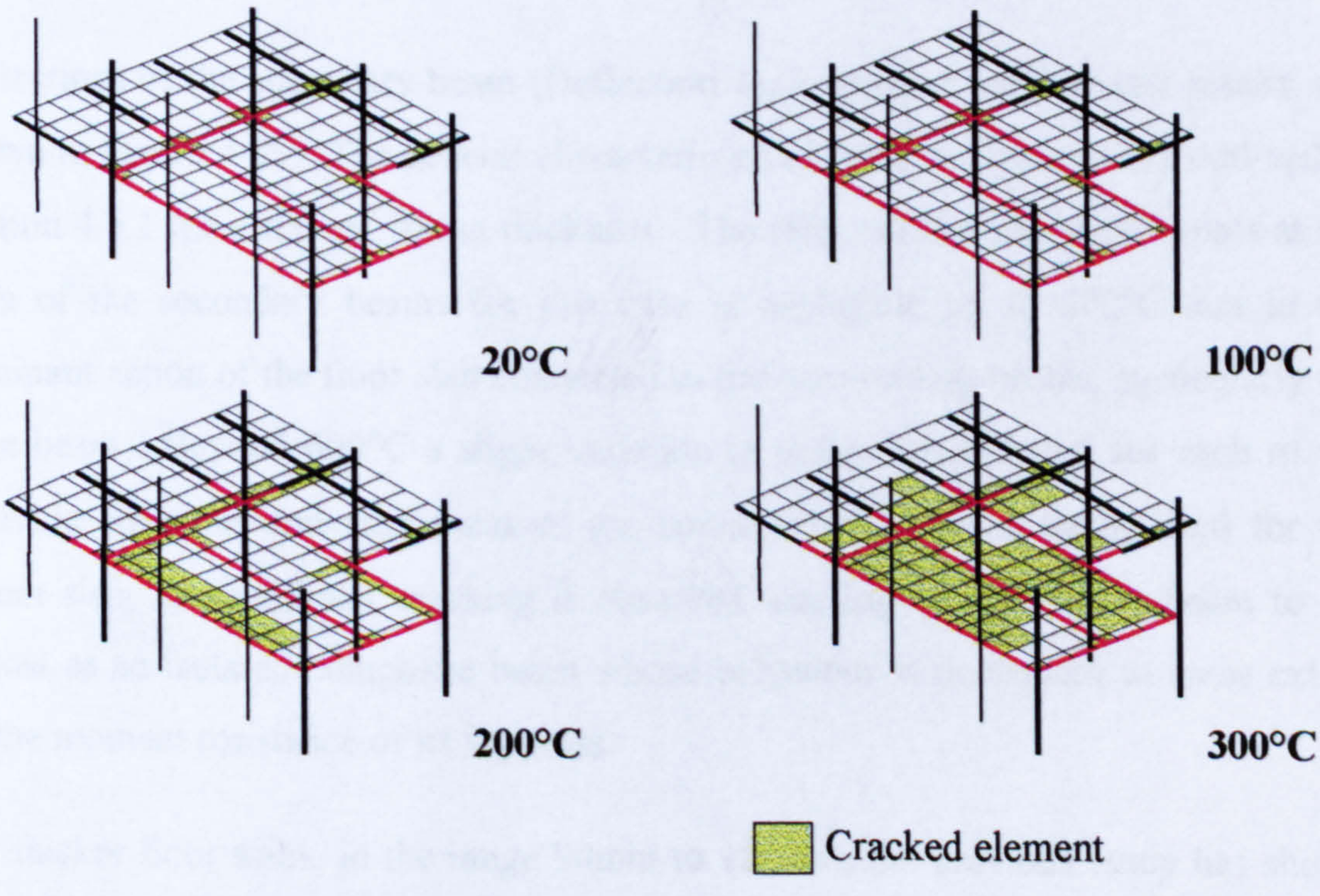

Figure 4-28. British Steel corner test floor slab crack propagation

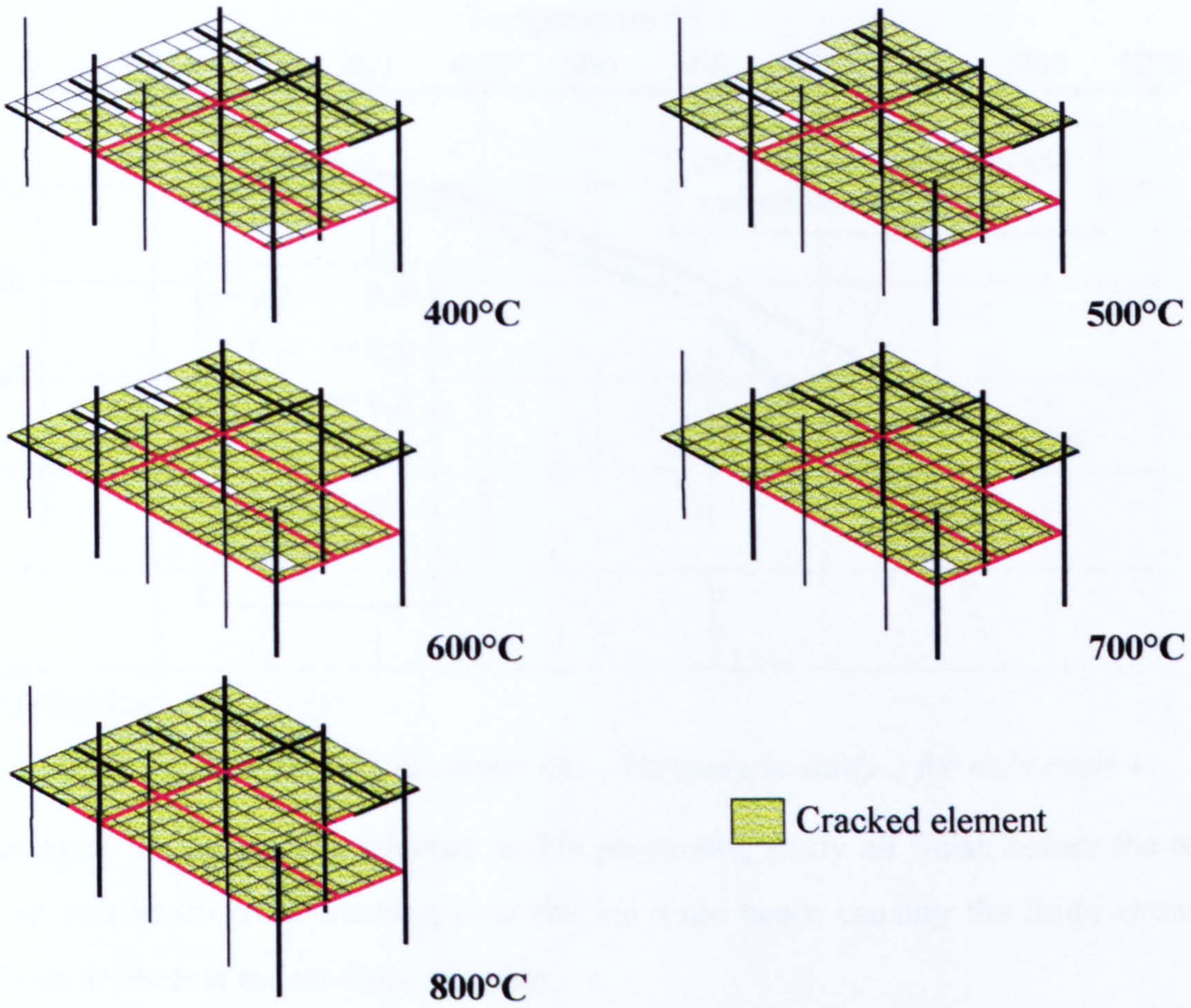

Figure 4-28. (continued) British Steel corner test floor slab crack propagation

4.5.2 BRITISH STEEL CORNER TEST – PARAMETRIC STUDY 2

Deflections of the secondary beam (Deflection 4), compared with the test results, are shown in Figure 4-29. The general characteristics of these analyses are as outlined in Section 4.5.1 for a slab of 70mm thickness. The effect of the semi-rigid joints at the ends of the secondary beams for this case is negligible up to 600°C due to the dominant action of the floor slab connected to the surrounding beams, particularly the edge beam. Beyond 600°C a slight variation in deflection is found for each of the differing strengths and stiffnesses of the connections. This is emphasised for the 70mm slab, as significant cracking is observed, causing the secondary beam to act almost as an isolated composite beam whose behaviour is dependent to some extent on the moment resistance of its supports.

For thicker floor slabs, in the range 90mm to 150mm, the previous study has shown that slabs of these thicknesses largely retain their integrity. This would override the small effect produced by the connections at the higher temperatures studied.

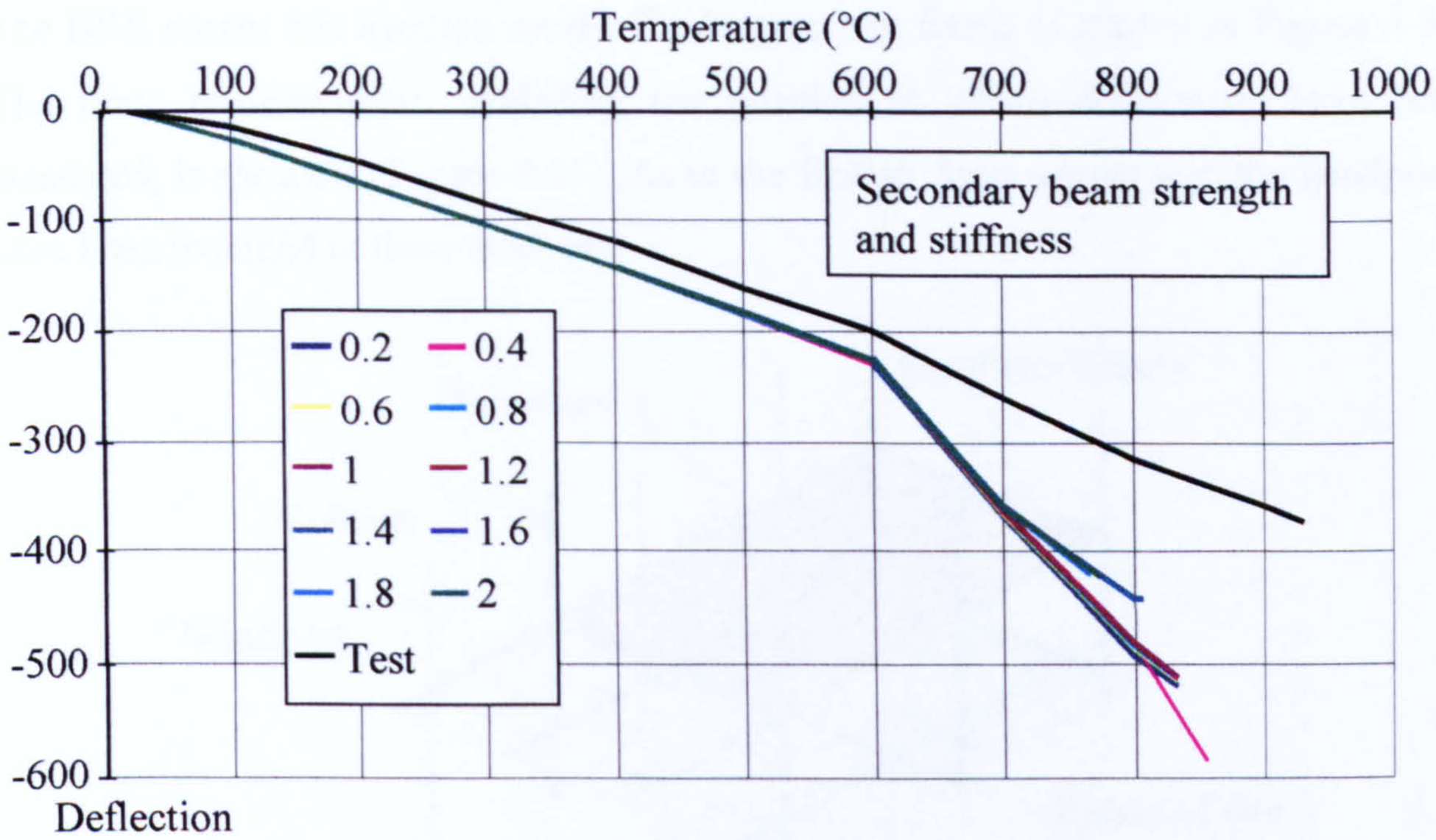

Figure 4-29. British Steel corner test - Parametric study 2 for deflection 4

Once again the analyses conducted in this parametric study all finish before the test, due to sudden concrete cracking over the 6m main beam causing the finite element analysis to become numerically unstable.

4.6 B.R.E. CORNER TEST PARAMETRIC STUDIES USING THE ISOTROPIC SLAB ELEMENT

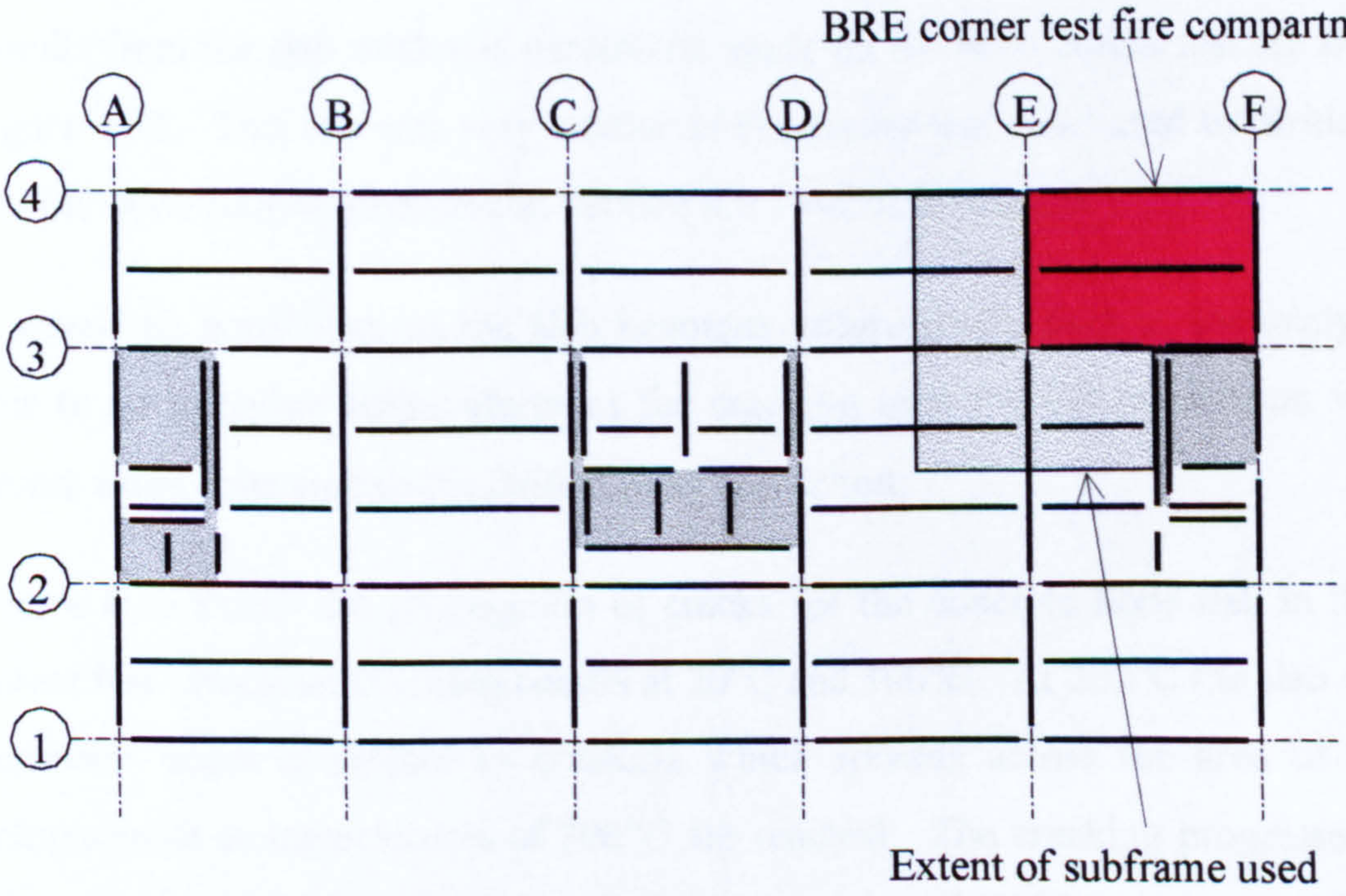

Figure 4-30. Location of the BRE corner test.

The BRE corner test location on the Cardington test frame is shown in Figure 4-30. The finite element mesh, including the position at which deflections have been measured, is shown in Figure 4-31. As in the British Steel corner test the windposts have been included in these analyses.

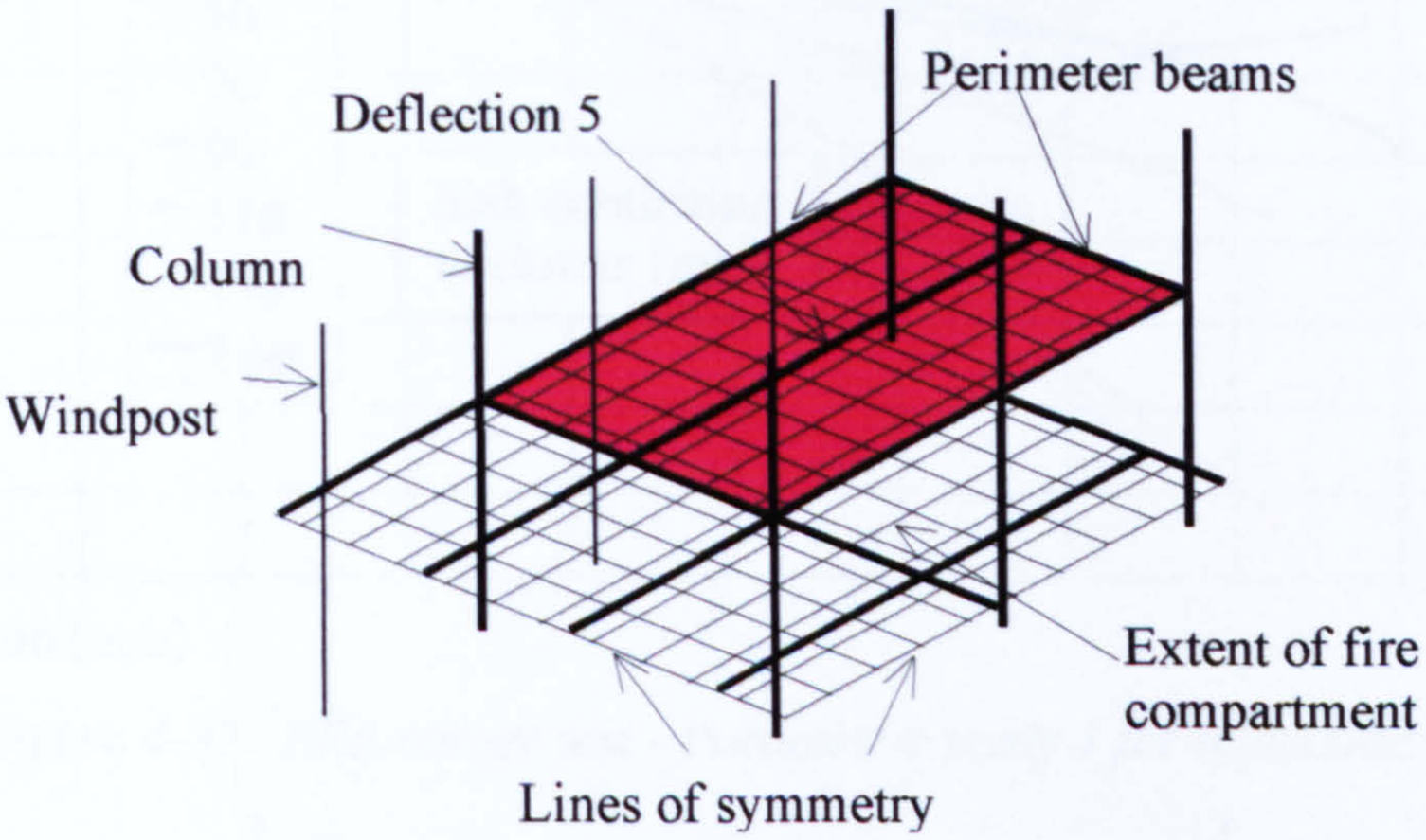

Figure 4-31. Finite element mesh arrangement for the BRE corner test.

The columns bounding the compartment were protected to their full height. The edge beams and the beams on the perimeter of the fire compartment were treated as being heated at 50% of the temperature of the lower flange of the internal beam.

4.6.1 B.R.E. Corner Test – Parametric Study 1

Results from the slab thickness parametric study on the BRE corner test are shown in Figure 4-32. This test was very similar to the corner test conducted by British Steel and the same actions discussed in Section 4.5.1 occur in this test.

It should be noted that, as the slab becomes progressively thicker, the analyses are able to go to higher temperatures as the cracking over the 6m main beam was less severe when compared to the British Steel corner test.

Figure 4-33 shows the propagation of cracks for the concrete floor slab in the BRE corner test. Nominal cracking occurs at 20°C and 100°C. At 200°C the slab over the perimeter beam is subject to cracking which spreads across the area of the test compartment as temperatures of 300°C are reached. The cracking progresses across the area outside the fire compartment as temperatures of 400°C are exceeded.

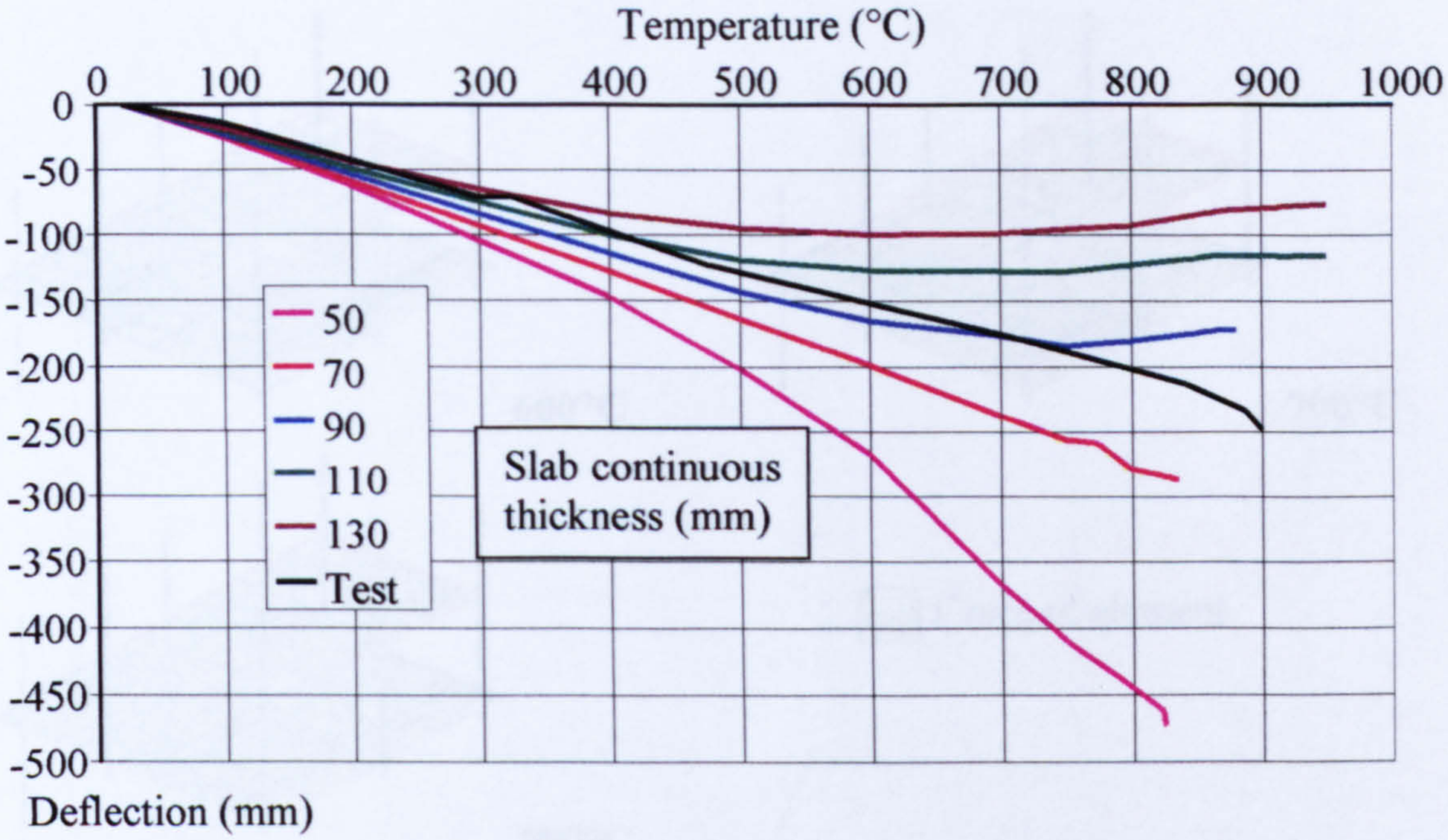

Figure 4-32. BRE corner test - Parametric study 1 for deflection 5

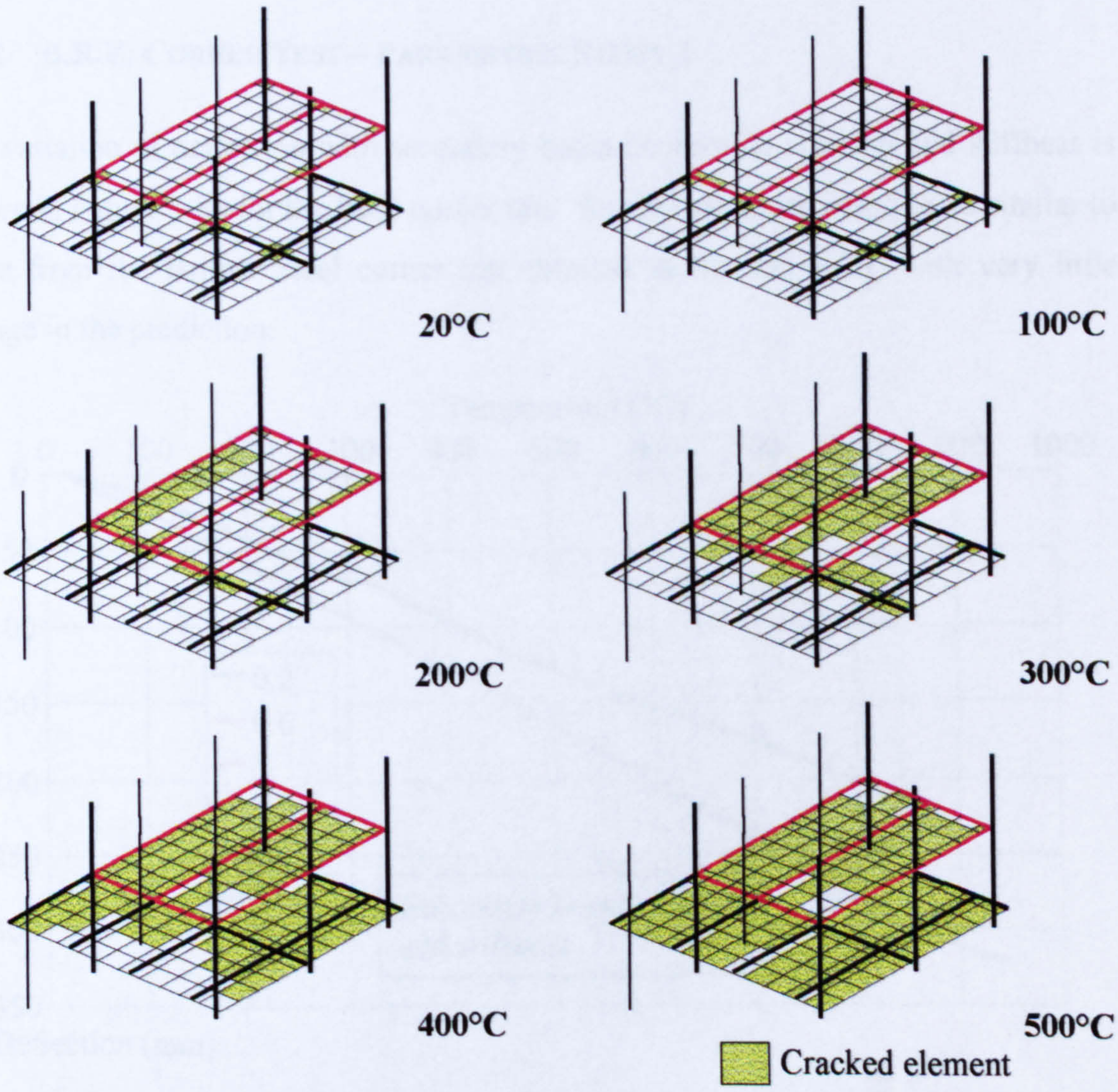

Figure 4-33. BRE corner test floor slab crack propagation

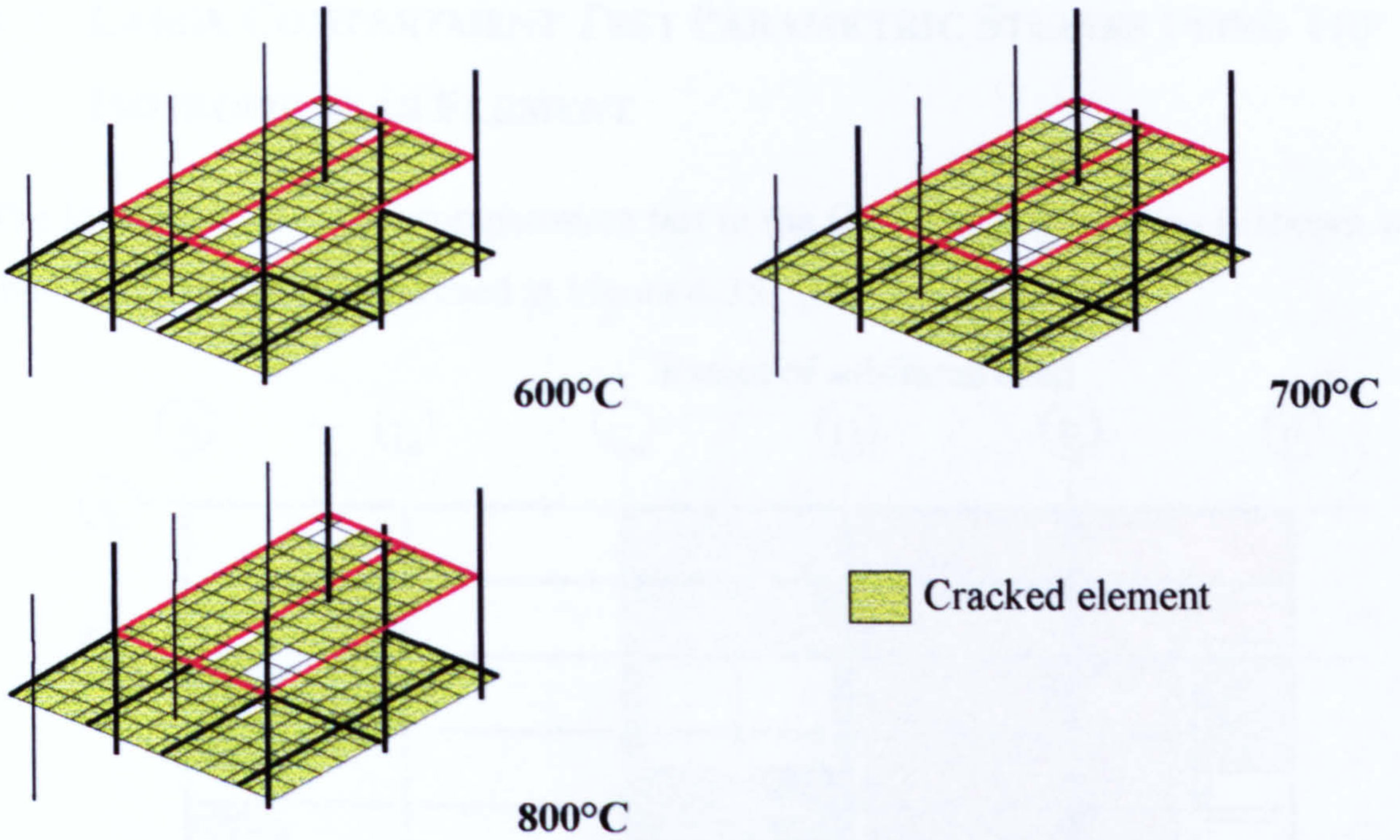

Figure 4-33. (continued) BRE corner test floor slab crack propagation

4.6.2 B.R.E. CORNER TEST – PARAMETRIC STUDY 2

The variation of deflection with secondary beam connection strength and stiffness is shown in Figure 4-34 for the BRE corner test. Results are again found to be similar to those from the British Steel corner test detailed in Section 4.5.2, with very little change in the prediction.

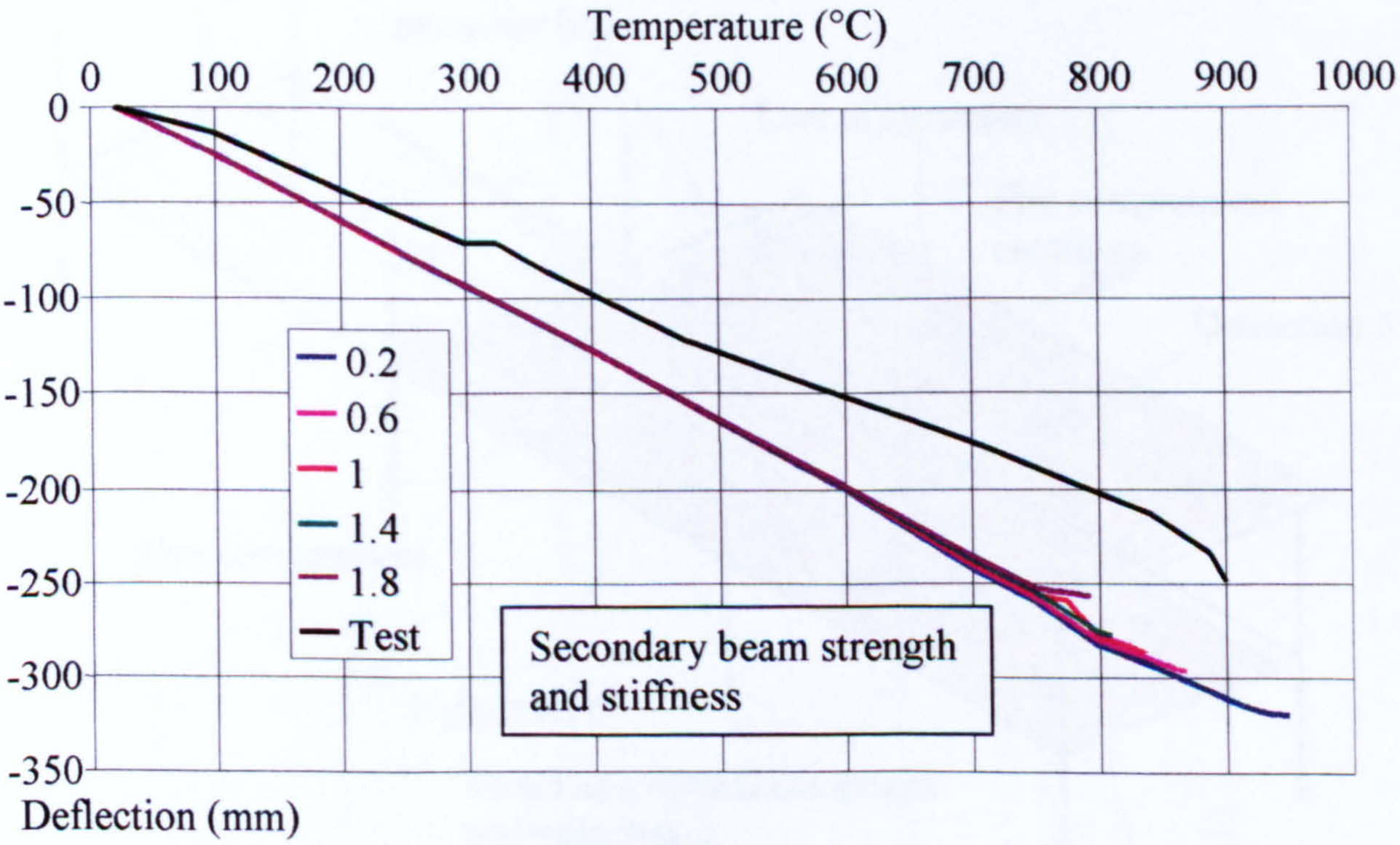

Figure 4-34. BRE corner test - Parametric study 2 for deflection 5

4.7 LARGE COMPARTMENT TEST PARAMETRIC STUDIES USING THE ISOTROPIC SLAB ELEMENT

The location of the large compartment test in the Cardington test frame is shown with the extent of the subframe used in Figure 4-35.

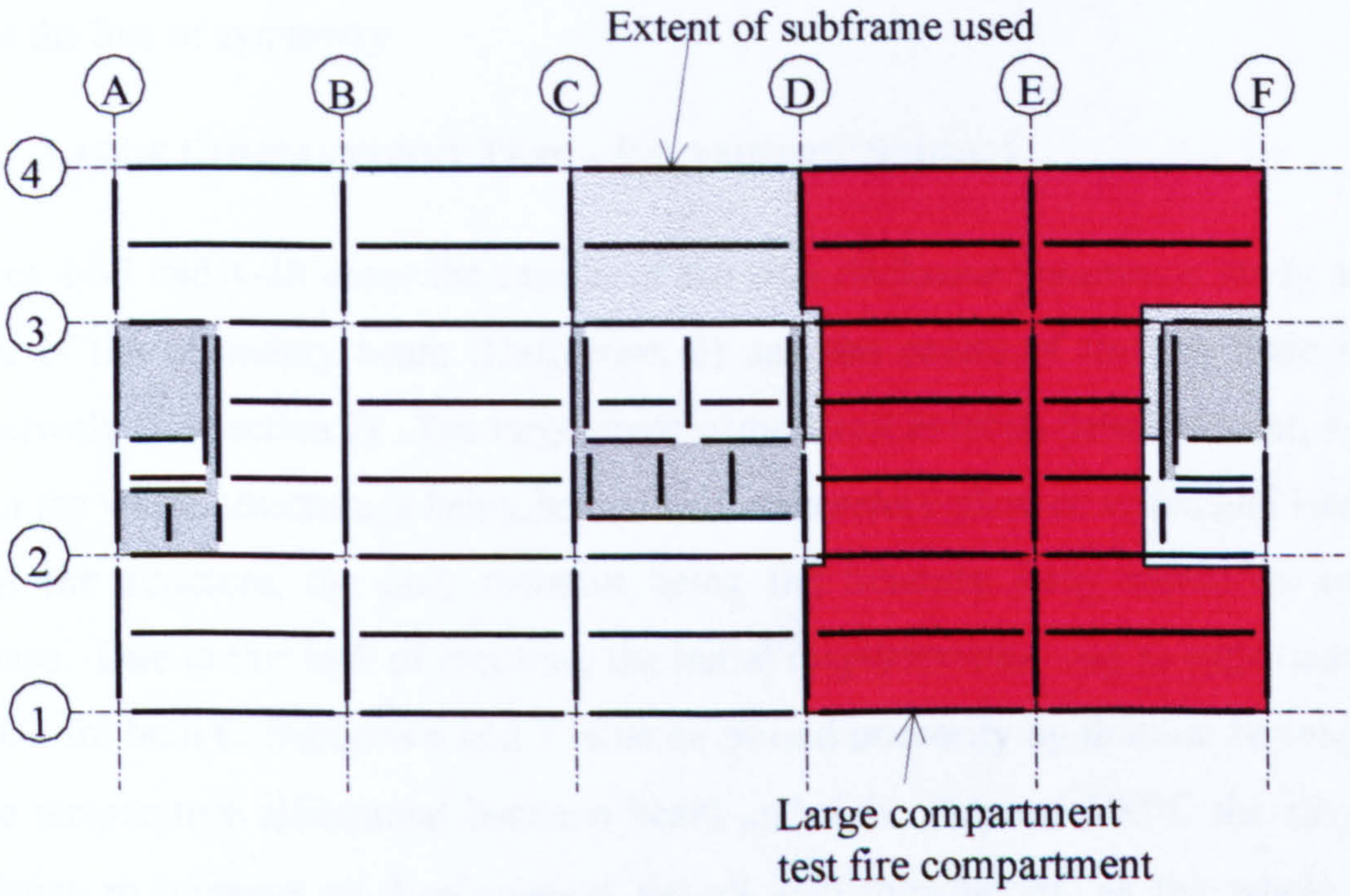

Figure 4-35. Location of the large compartment test.

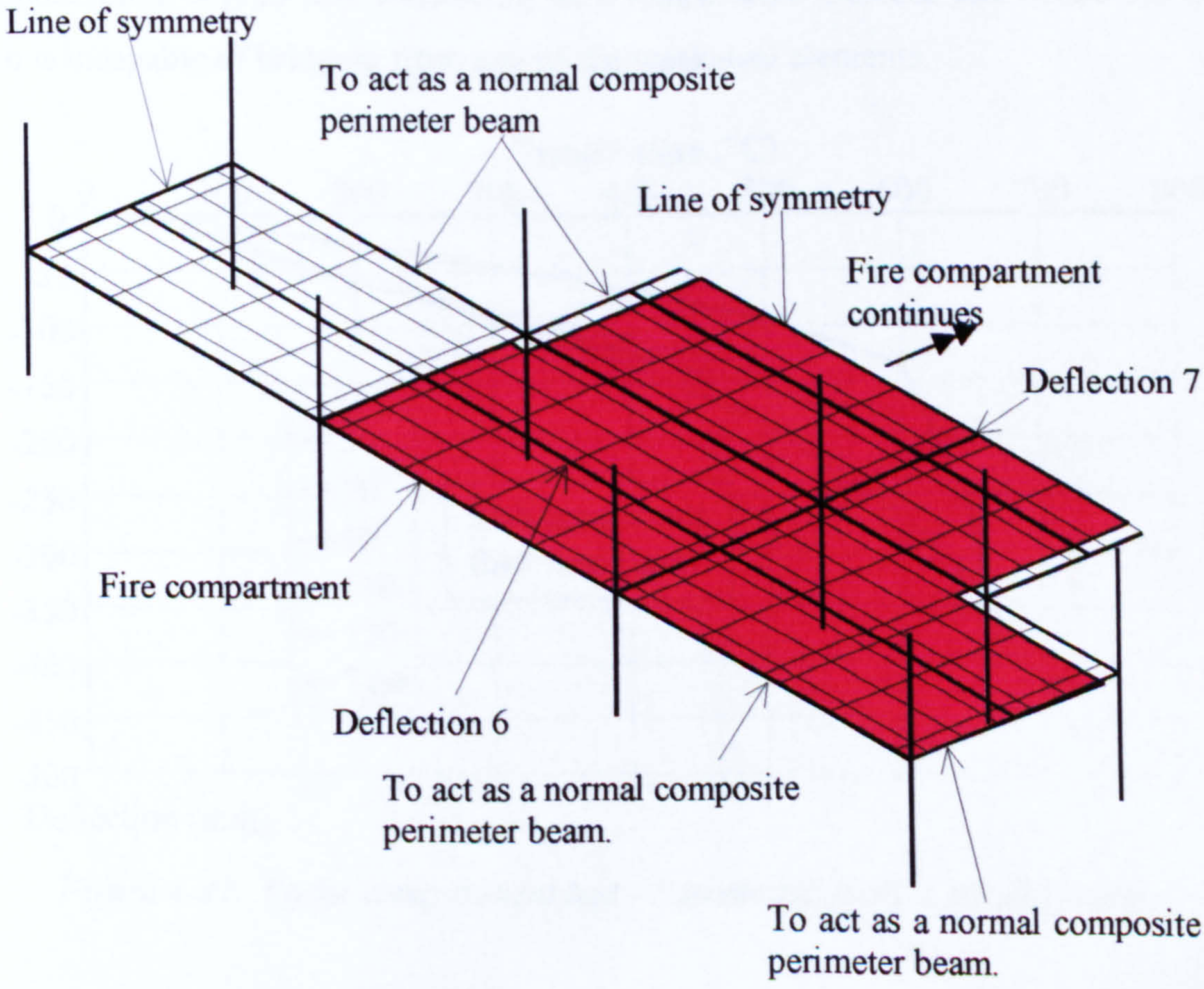

Figure 4-36. Finite Element Arrangement of large compartment test

Figure 4-36 shows the subframe and external boundary conditions used for the large compartment test. The positions at which deflections are studied are also shown, being the centre of the 9m main beam (deflection 7) and the centre of the marked secondary beam (deflection 6). It should also be remembered in studying the results for this subframe that the entire fire compartment is not modelled, but continues across the line of symmetry.

4.7.1 LARGE COMPARTMENT TEST – PARAMETRIC STUDY 1

Figures 4-37 and 4-38 show the results of the slab thickness parametric study at the centre of the secondary beam (Deflection 6) and the centre of the 9m main beam respectively (Deflection 7). The large compartment test exhibits little restraint, as one end of the whole structure is being heated and is therefore allowed to expand laterally across the structure, the only restraint being the inherent sway resistance of the columns. Due to this lack of restraint, the initial displacements - up to approximately 500°C - for both Deflections 6 and 7 must be caused primarily by thermal bowing due to the temperature differential between beam and slab. Beyond 500°C the structure continues to increase its displacement for all slab thicknesses, as the whole steel support frame is gradually weakening with temperature increase and hence the floor slab is incapable of bridging from any of the weakened elements.

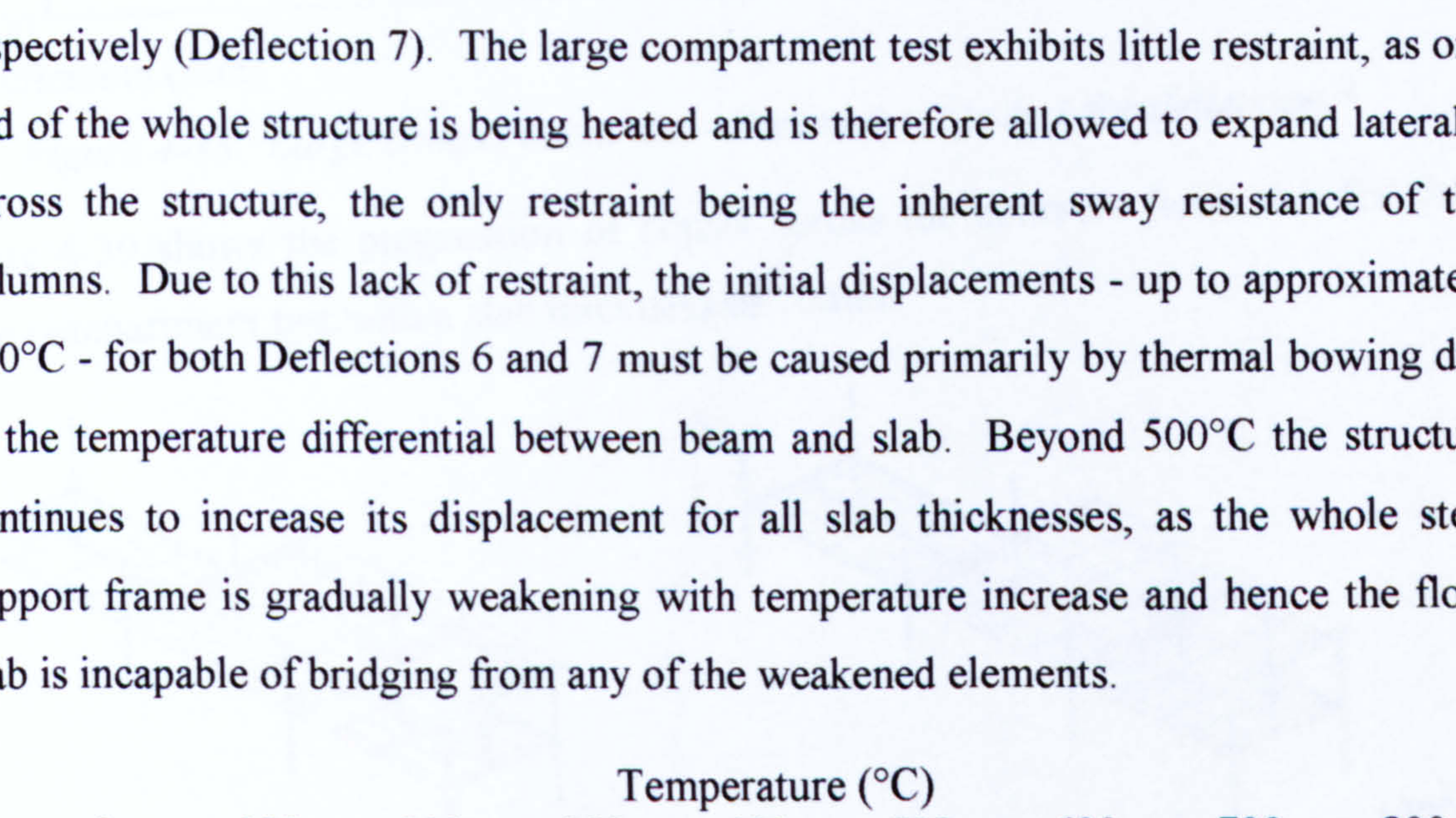

Figure 4-37. Large compartment test - Parametric study 1 for deflection 6

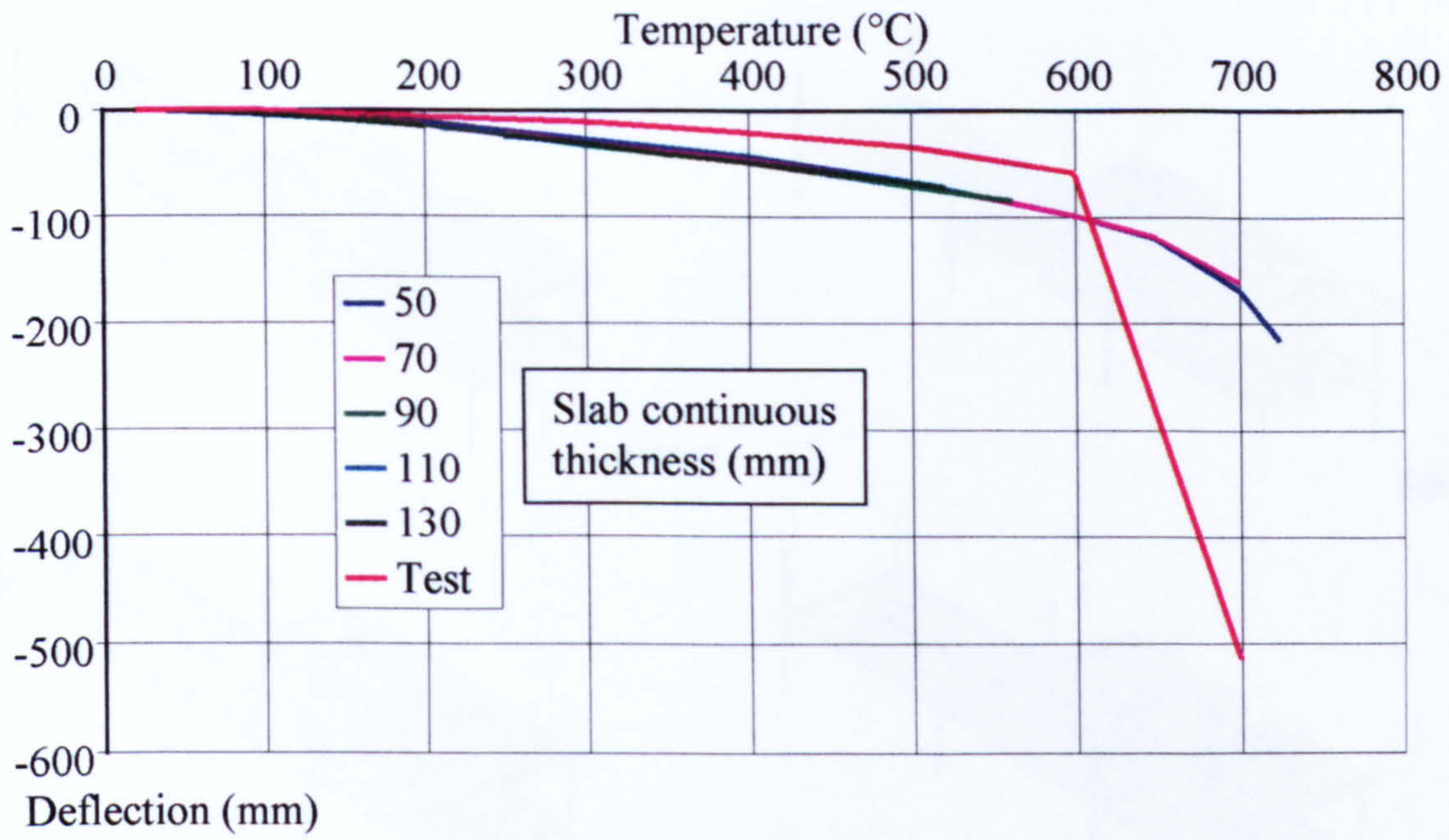

Figure 4-38. Large compartment test - Parametric study 1 for deflection 7

Figure 4-39 shows the progression of cracks across the concrete floor slab for the large compartment test with a slab thickness of 70mm.

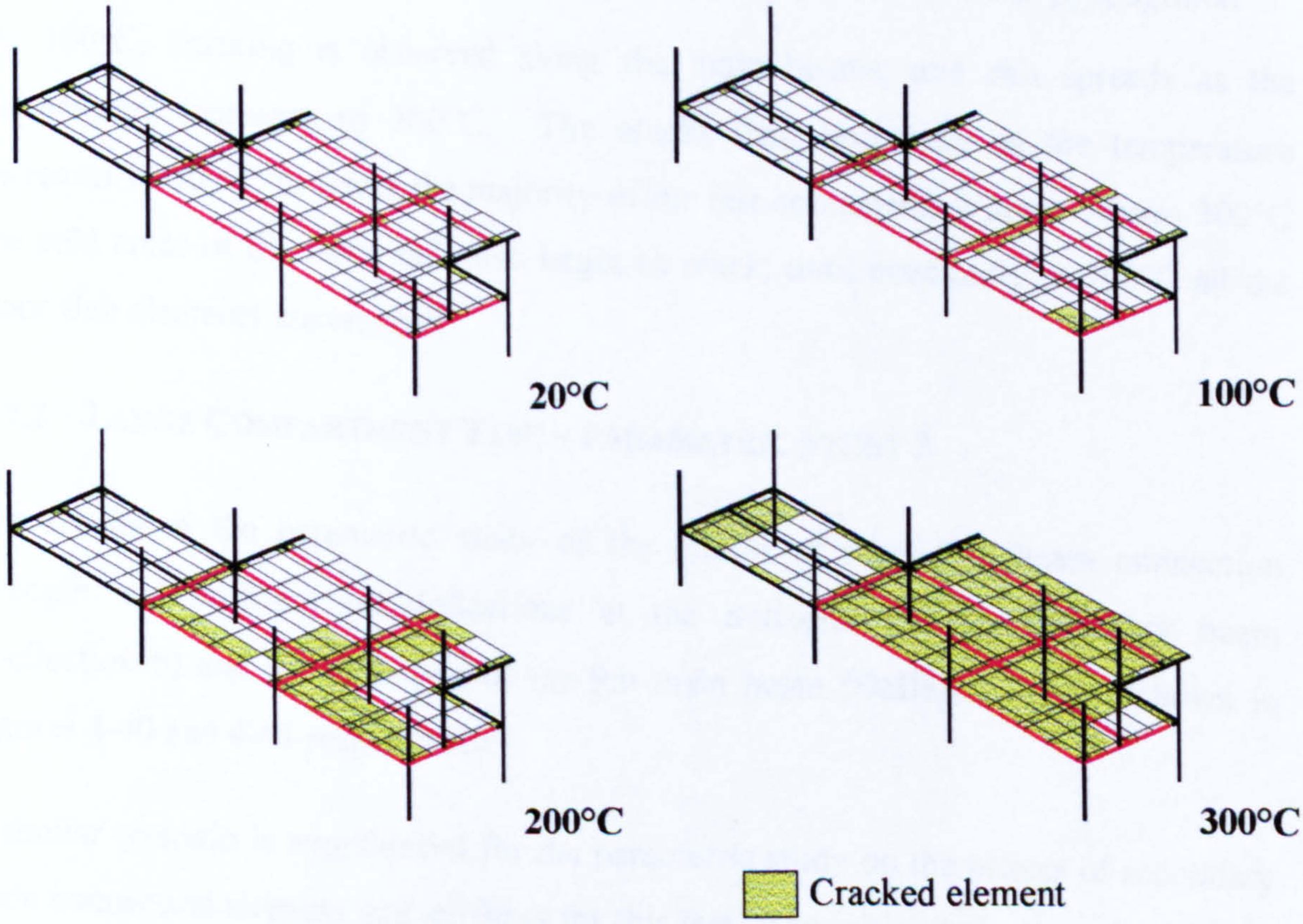

Figure 4-39. Large compartment test floor slab crack propagation

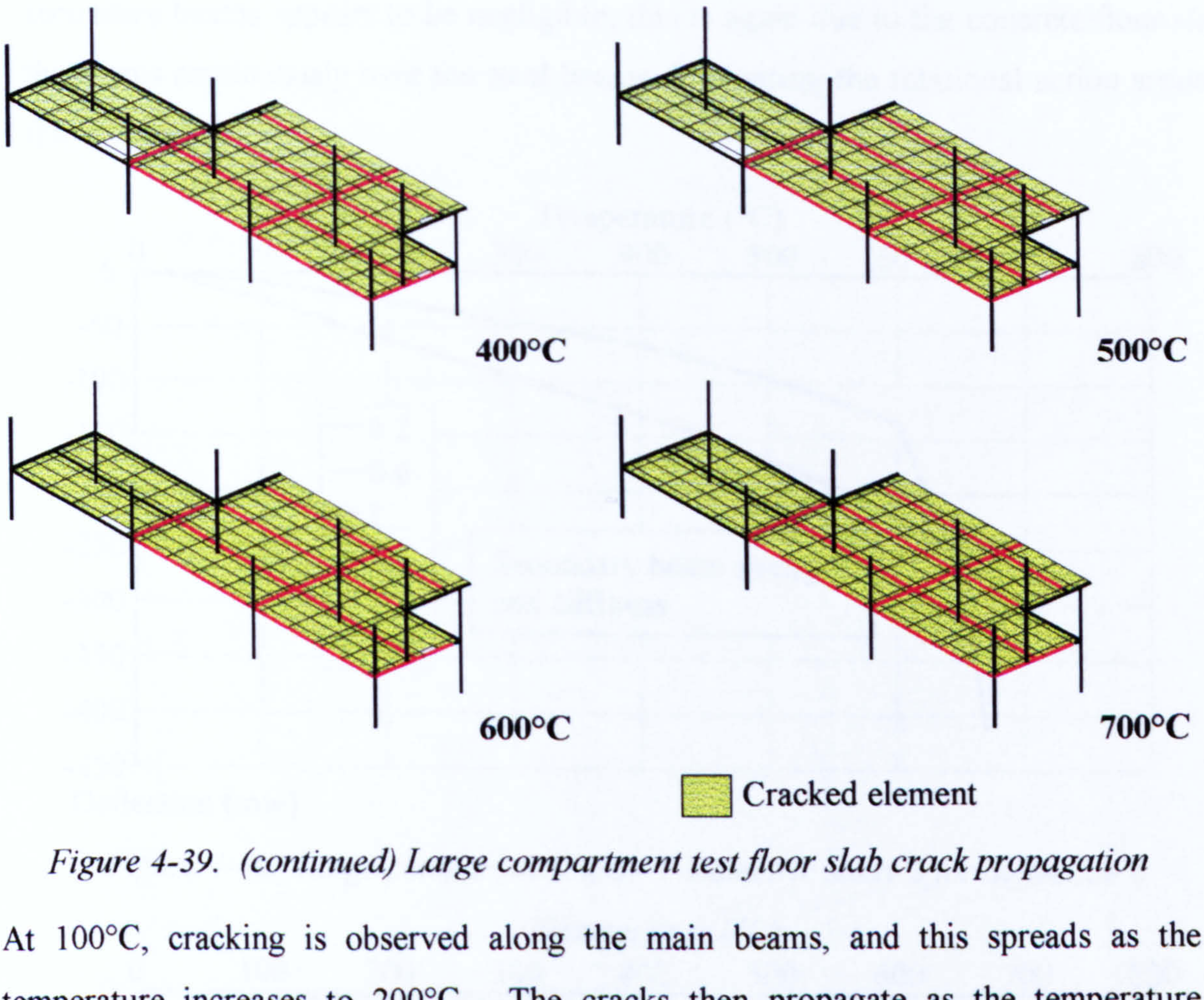

Figure 4-39. (continued) Large compartment test floor slab crack propagation

At 100°C, cracking is observed along the main beams, and this spreads as the temperature increases to 200°C. The cracks then propagate as the temperature increases to 300°C to cover the majority of the test compartment area. Above 300°C the cold areas of the floor slab also begin to crack, until eventually at 700°C all the floor slab elements are cracked.

4.7.2 LARGE COMPARTMENT TEST – PARAMETRIC STUDY 2

The results of the parametric study of the effects of secondary beam connection strength and stiffness on deflections at the mid-span of the secondary beam (Deflection 6) and the mid-span of the 9m main beam (Deflection 7) are shown in Figures 4-40 and 4-41 respectively.

A similar scenario is experienced for the parametric study on the effects of secondary beam connection strength and stiffness for this test. The initial deflections (to 500°C) are mainly due to thermal bowing as this test lacks external restraint. Beyond 500°C the steel strength begins to decrease significantly, and hence members throughout the whole test area deflect with no possibility of the floor slab bridging from any cool areas of the building. The effect of the strength and stiffness of the connections on the

secondary beams appears to be negligible; this is again due to the concrete floor slab that spans continuously over the steel beams dominating the rotational action around the connections.

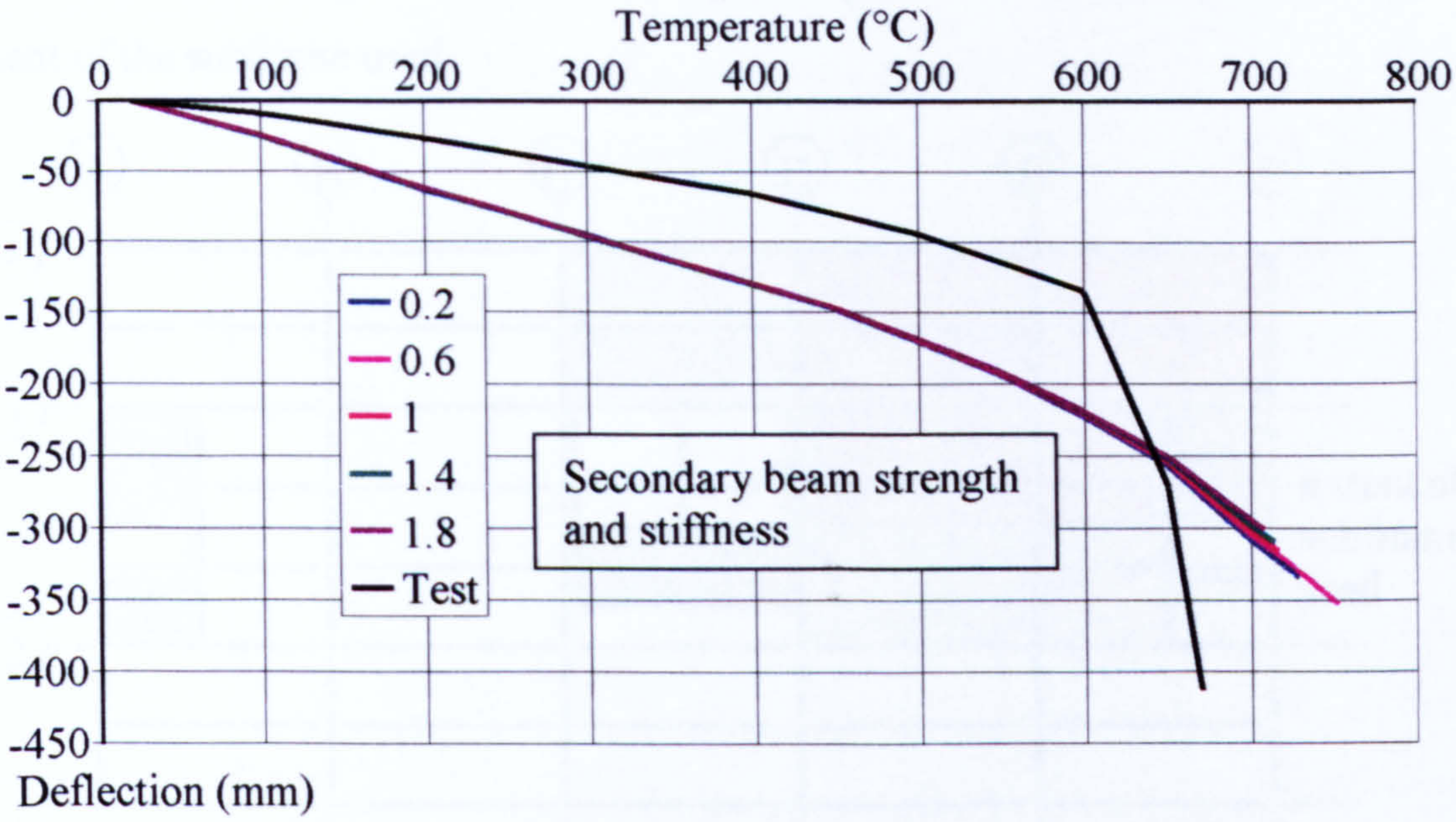

Figure 4-40. Large compartment test - Parametric study 2 for deflection 6

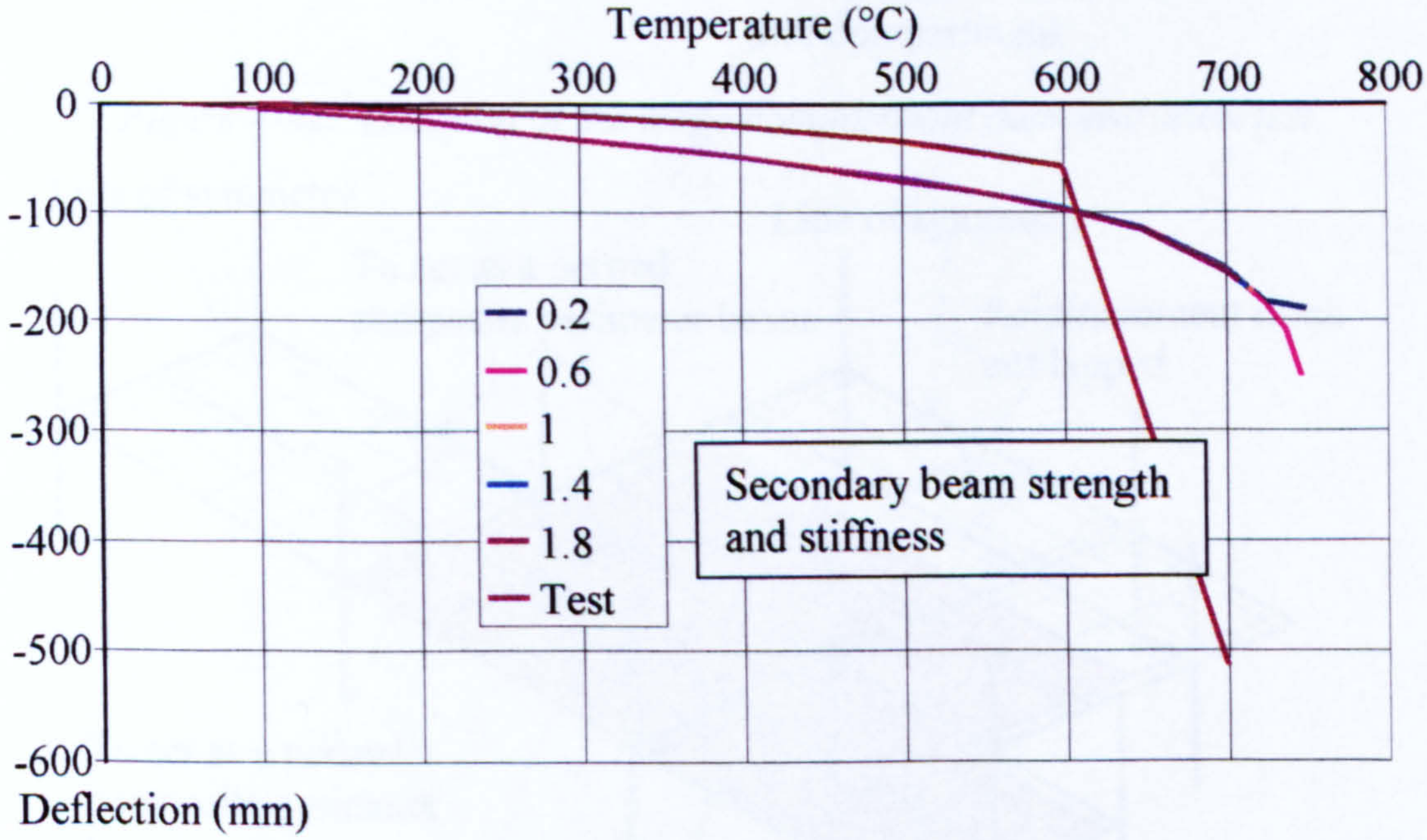

Figure 4-41. Large compartment test - Parametric study 2 for deflection 7

As in the slab thickness parametric study, when the analyses reach temperatures in the region of 700°C the beam deflections begin to 'run away' as exhibited by the test.

4.8 LARGE COMPARTMENT DEMONSTRATION TEST PARAMETRIC STUDIES USING THE ISOTROPIC SLAB ELEMENT

Figure 4-42 shows the location of the large compartment demonstration test and the extent of the subframe used.

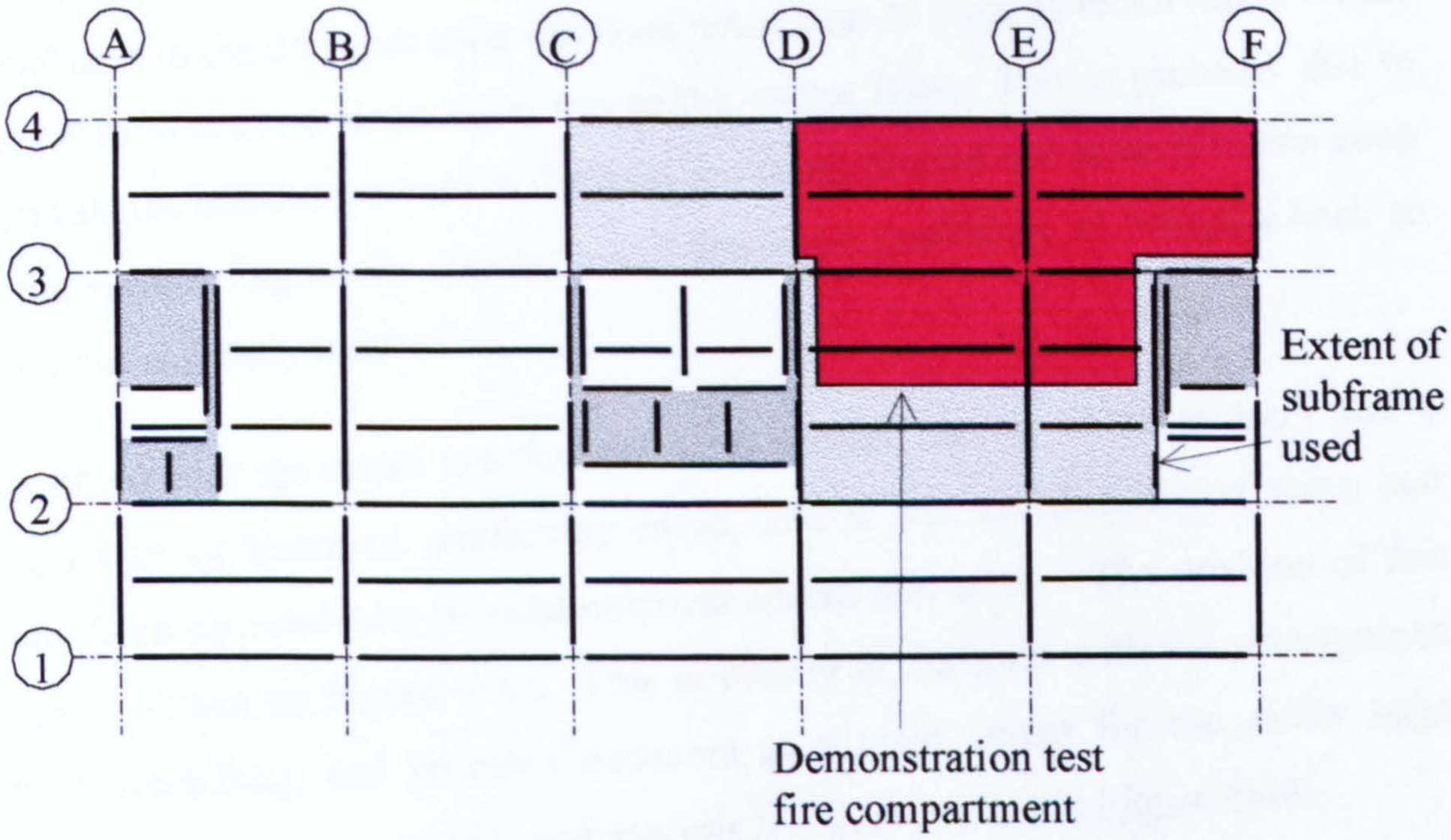

Figure 4-42. Location of the large compartment demonstration test.

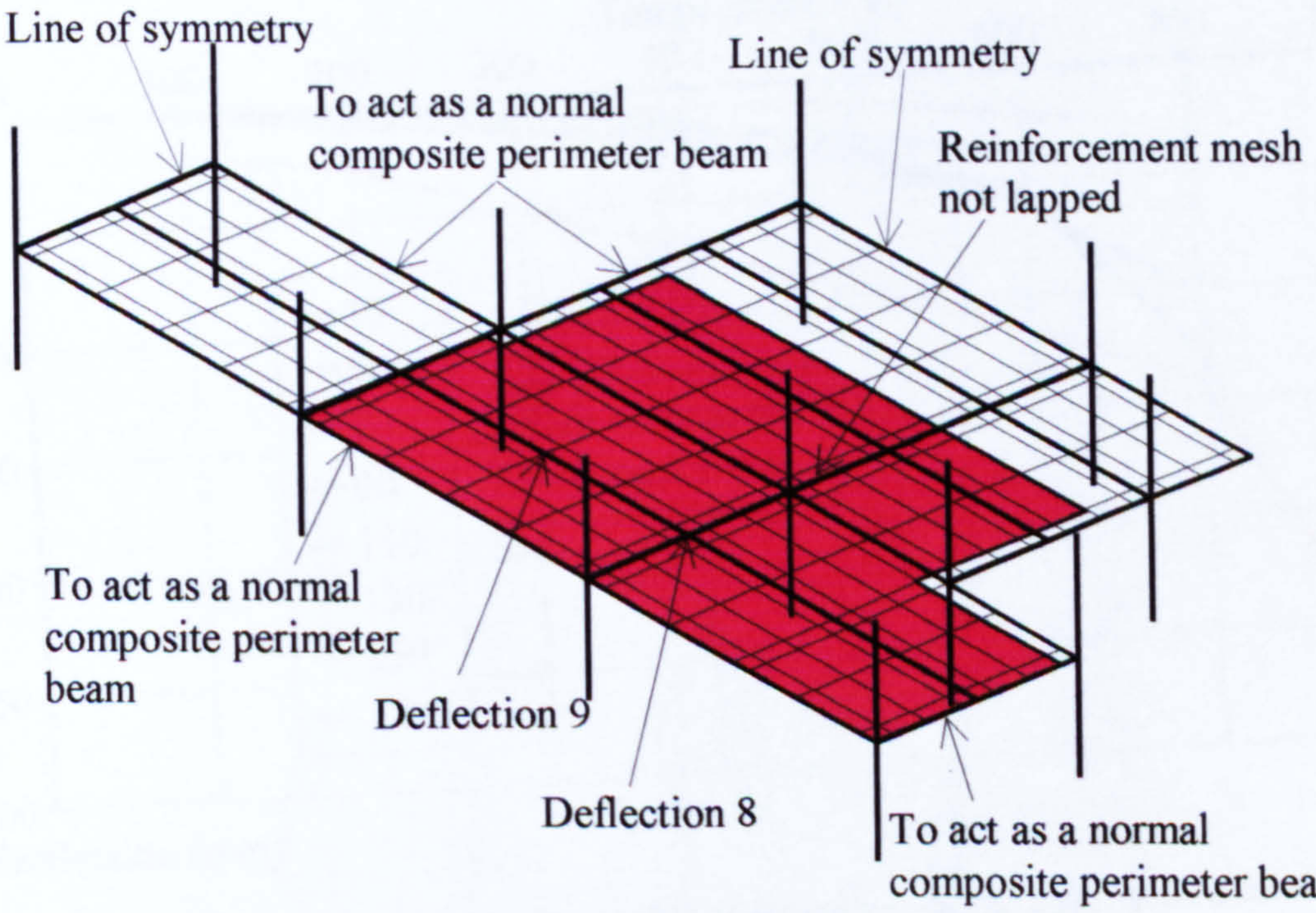

Figure 4-43. Finite element mesh arrangement for the large compartment demonstration test.

Figure 4-43 shows the subframe used to simulate the large compartment demonstration test. Also shown are the positions where deflections were measured in

the subsequent analyses, being the mid-span of a secondary beam (deflection 9) and the mid-span of the 6m main beam (deflection 8).

4.8.1 LARGE COMPARTMENT DEMONSTRATION TEST – PARAMETRIC STUDY 1

The results from the VULCAN analyses are shown in Figures 4-44 and 4-45. The slab thickness in the demonstration test does not appear to have as much effect on the behaviour as in the restrained beam test or the corner tests. This is probably due to the fact that the members whose deflections are being plotted are some distance away from the surrounding cooler structure, and hence the possibility of bridging back to stiff support is greatly reduced.

It was noted after the actual test that slabs had sheared cleanly at the primary beam, with no sign of fractured reinforcing mesh, and it was concluded that there had actually been no continuity of reinforcement across this beam. The position of this fracture is shown on Figure 4-43. This is clearly at variance with the assumptions made in modelling, and probably accounts to a great extent for the rather large discrepancy between experiment and analysis which is evident in Figure 4-44.

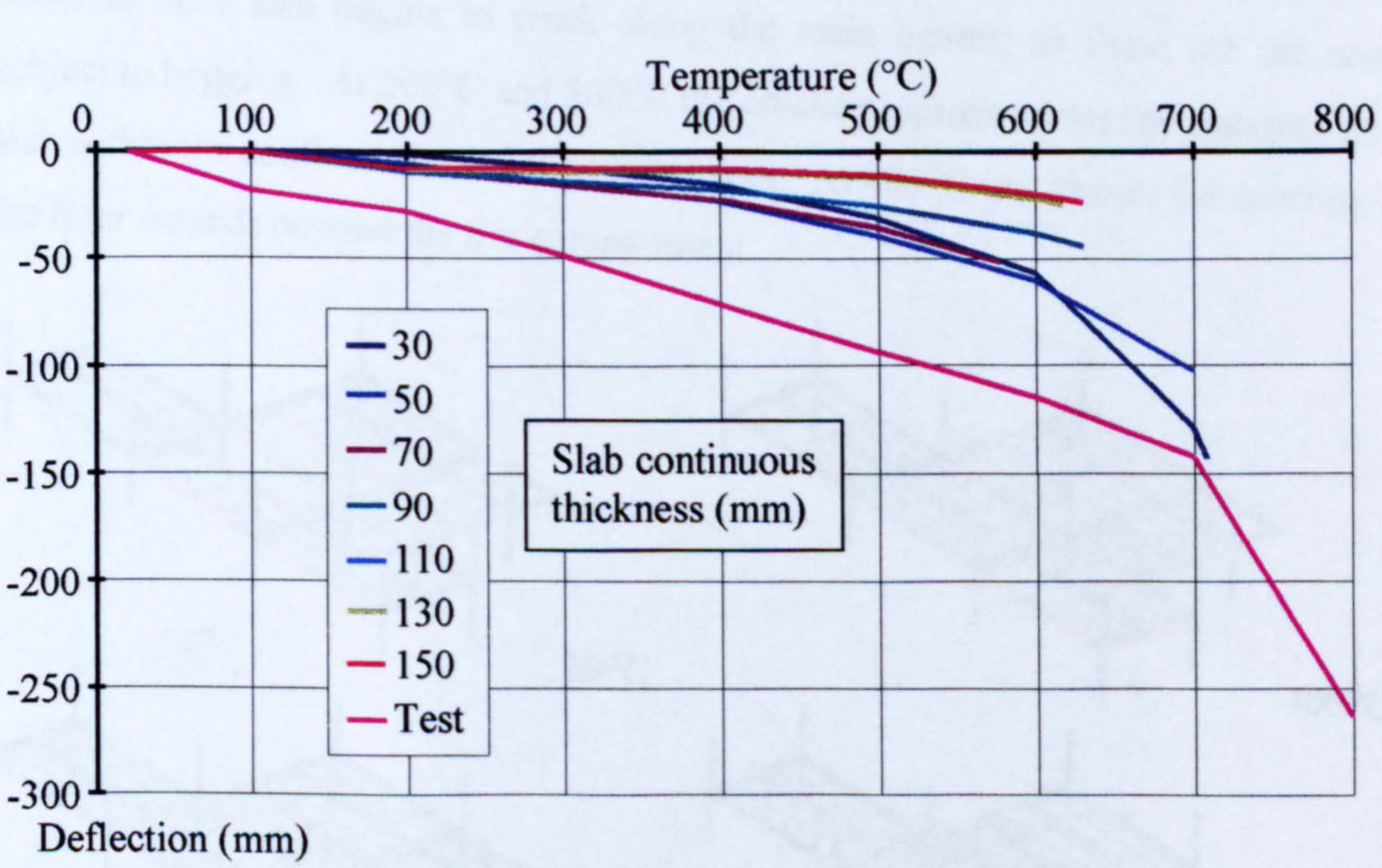

Figure 4-44. Demonstration test - Parametric study 1 for deflection 8

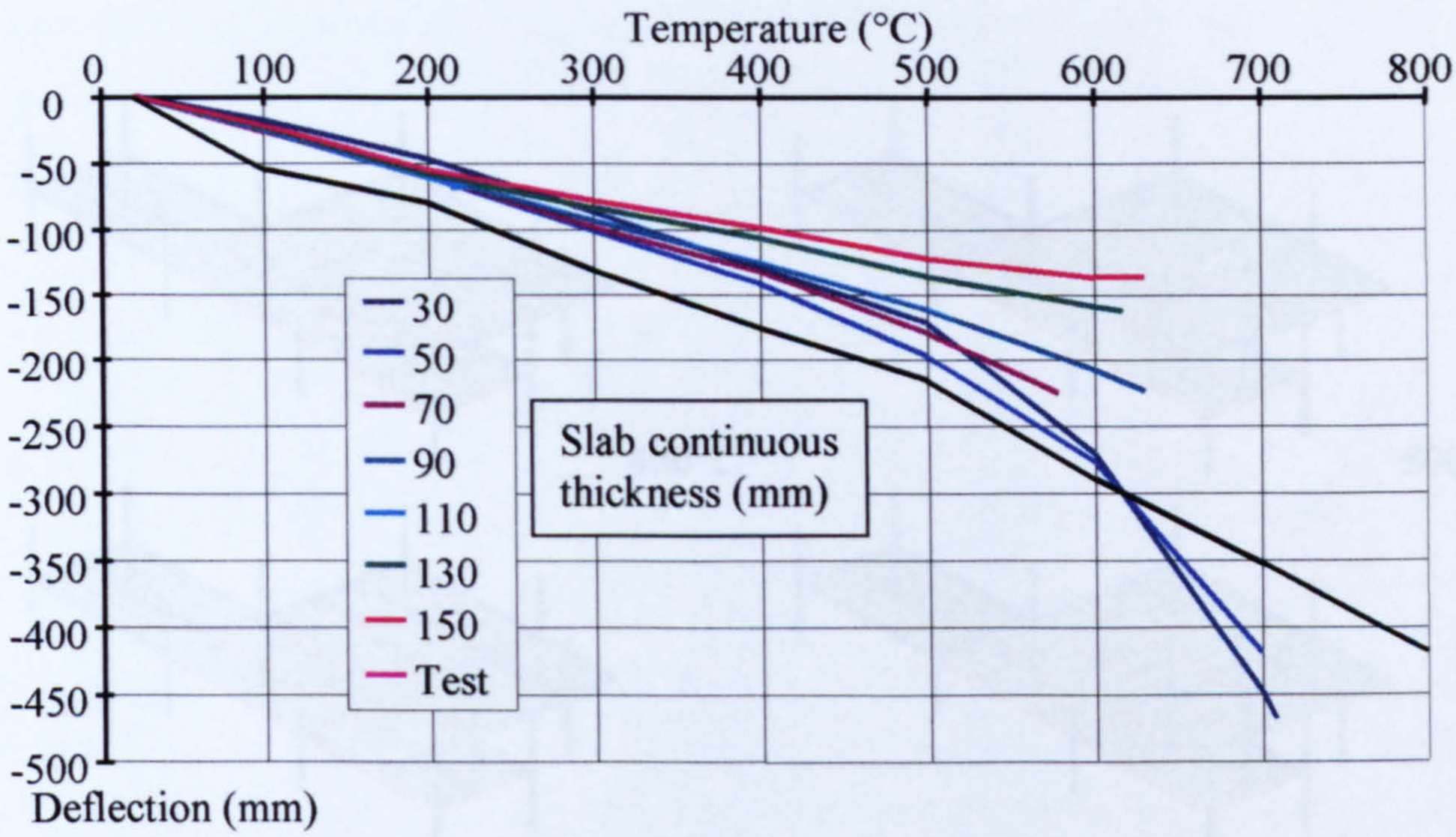

Figure 4-45. Demonstration test - Parametric study 1 for deflection 9

Figure 4-46 shows the propagation of cracks predicted by the analysis in the demonstration test for a floor slab thickness of 70mm.

At 20°C there is nominal cracking at the ends of the secondary beams. At 100°C the concrete floor slab begins to crack along the main beams, as these are the zones subject to hogging. At 200°C and 300°C the cracks progress across the concrete floor slab within the confines of the fire compartment. At 400°C and above, the cracking of the floor extends beyond the fire compartment.

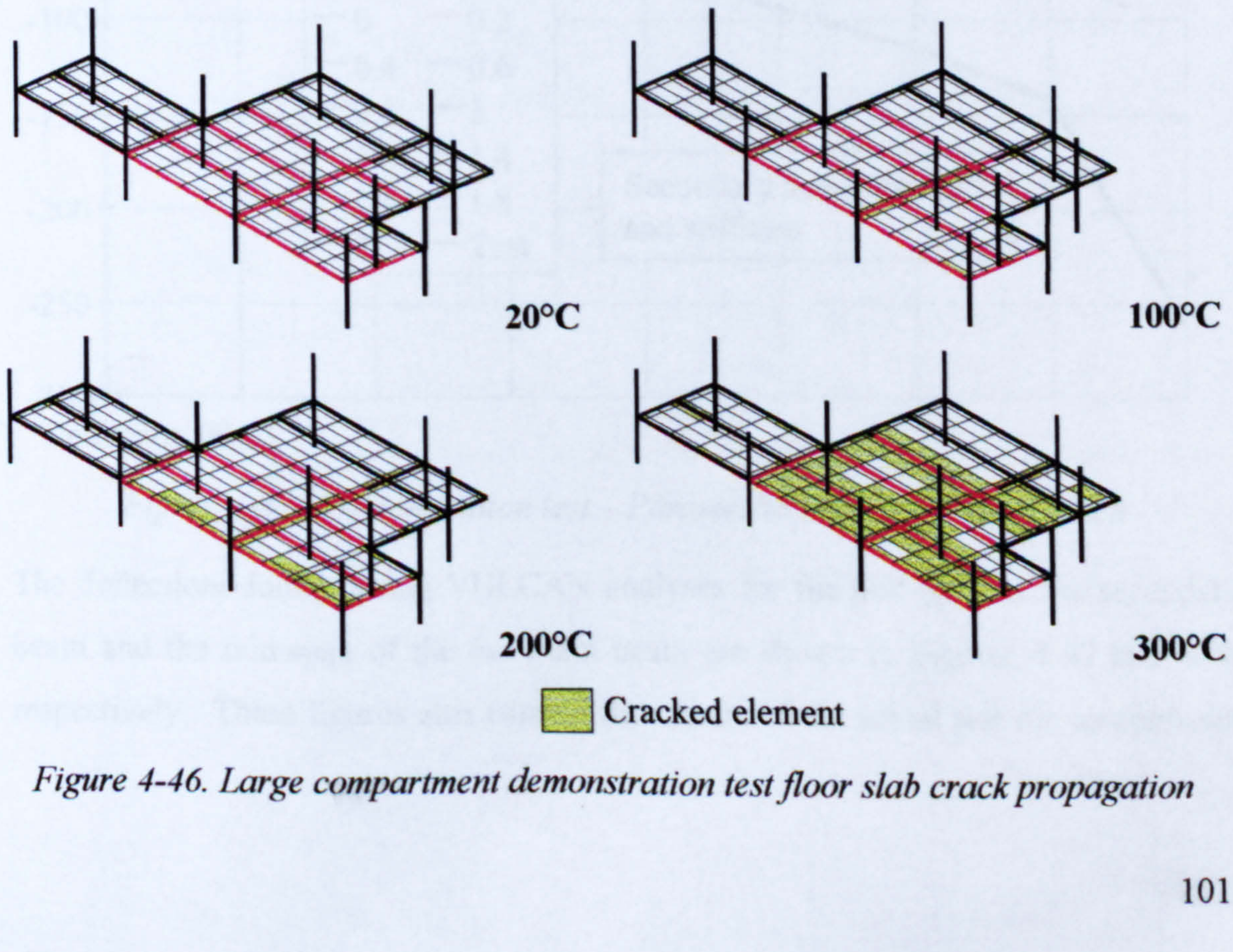

Figure 4-46. Large compartment demonstration test floor slab crack propagation

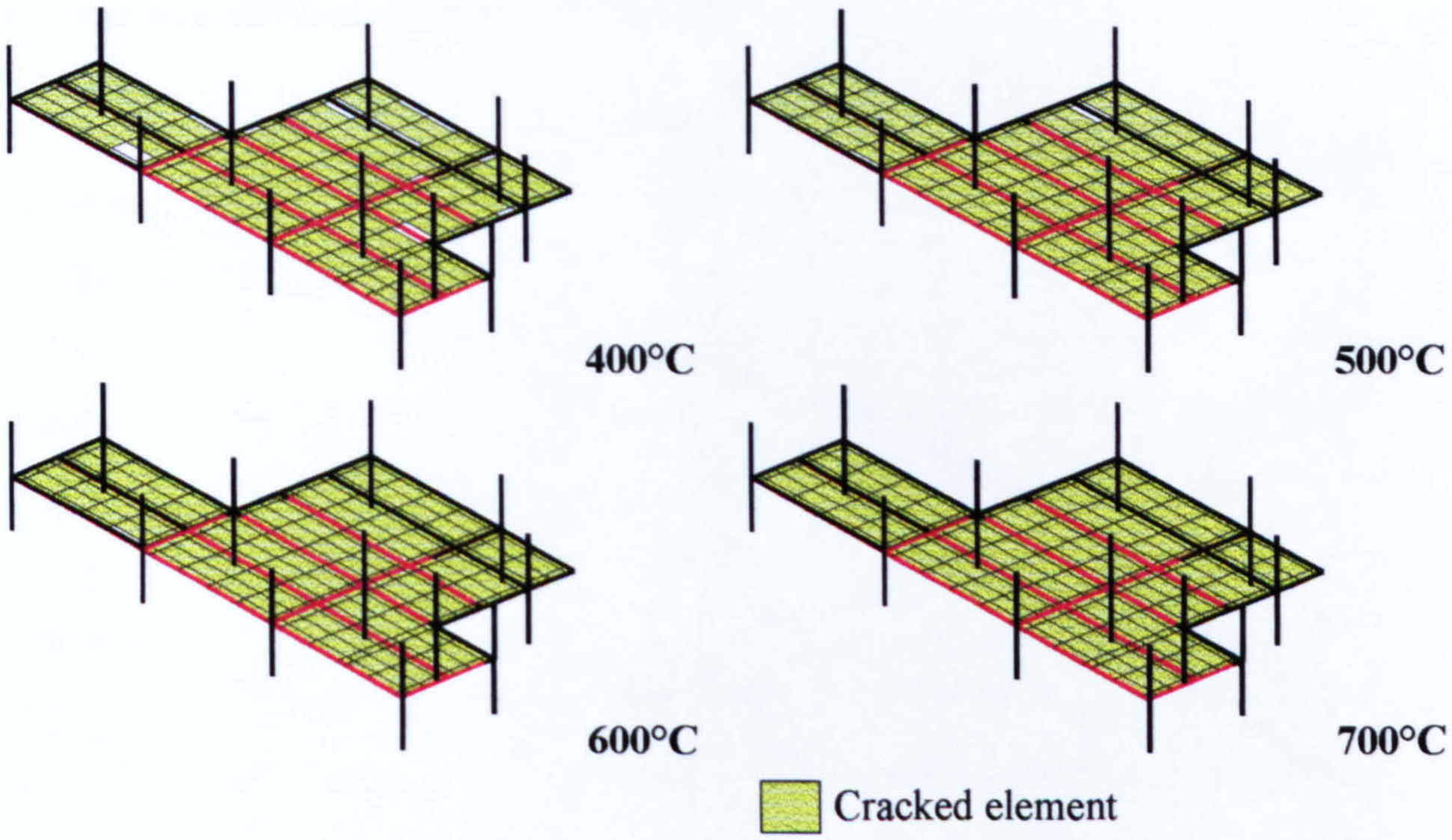

Figure 4-46. (continued) Large compartment demonstration test floor slab crack propagation

4.8.2 LARGE COMPARTMENT DEMONSTRATION TEST – PARAMETRIC STUDY 2

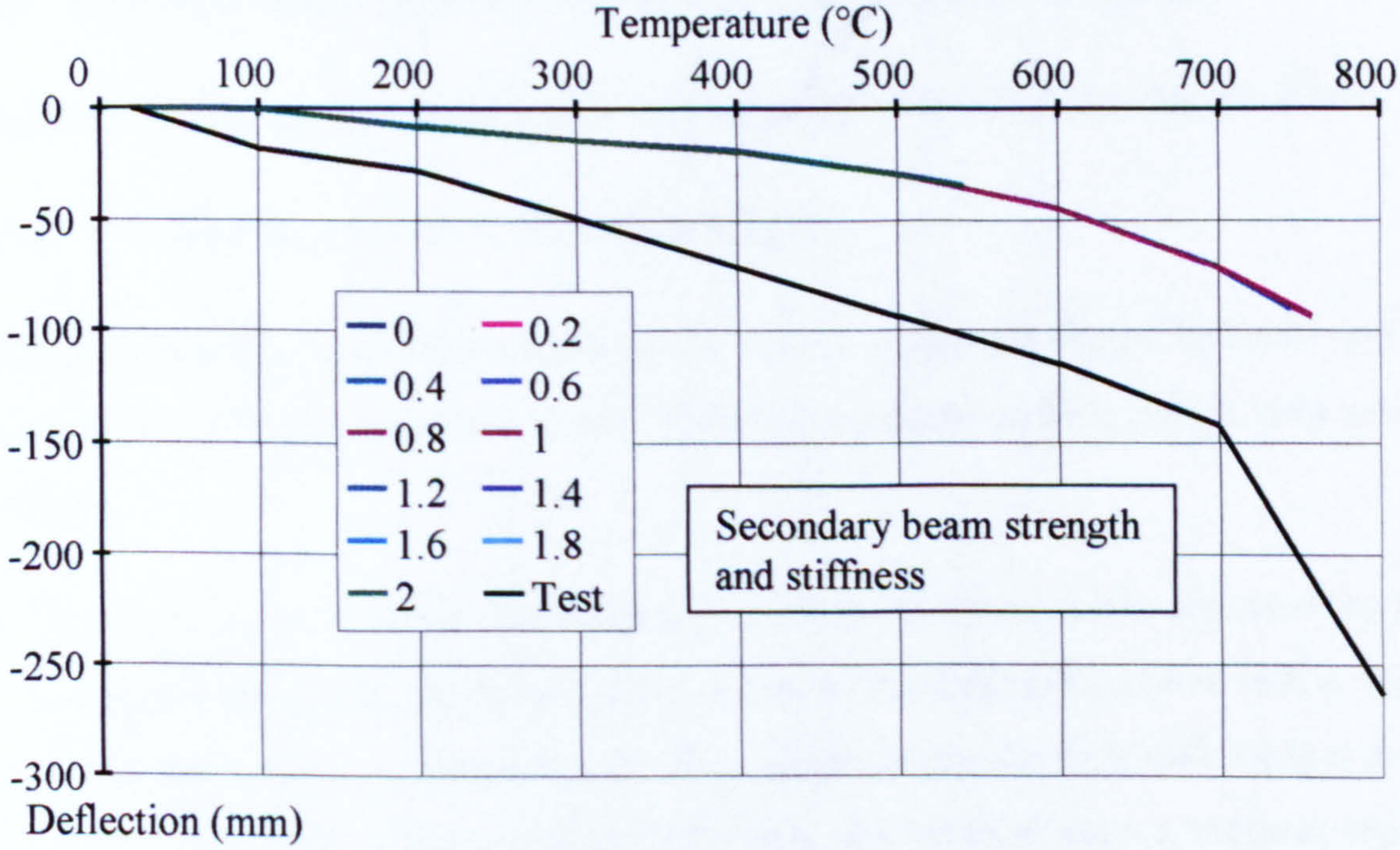

Figure 4-47. Demonstration test – Parametric study 2 for deflection 8

The deflections found during VULCAN analyses for the mid-span of the secondary beam and the mid-span of the 6m main beam are shown in Figures 4-47 and 4-48 respectively. These figures also contain the results of the actual test for comparison.

Once again the influence of secondary beam joint stiffness on the structural behaviour within the compartment appears to be negligible.

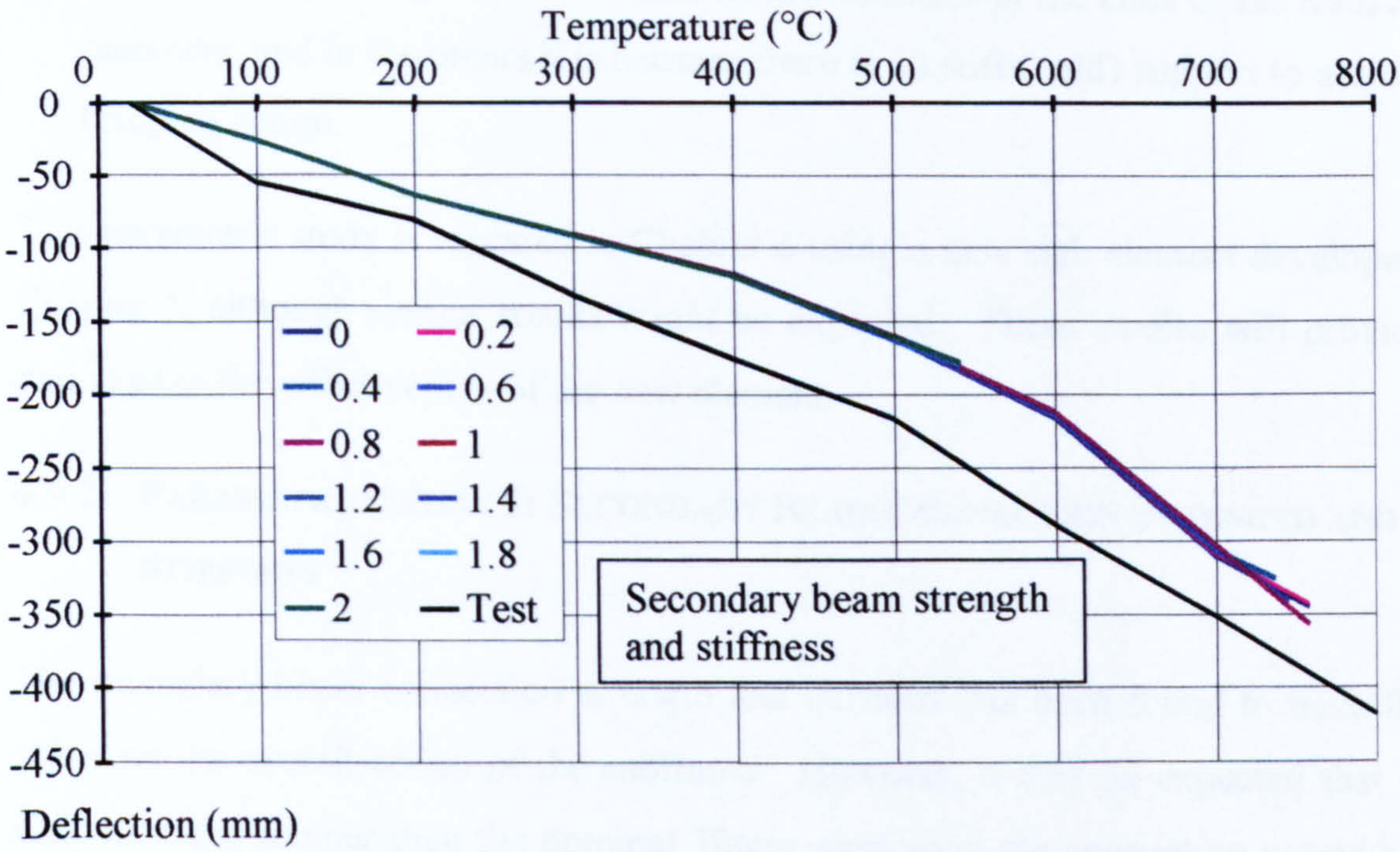

Figure 4-48. Demonstration test – Parametric study 2 for deflection 9

4.9 CONCLUSIONS DRAWN FROM THE PARAMETRIC STUDIES

General conclusions for the parametric studies conducted within this chapter follow.

4.9.1 PARAMETRIC STUDY 1: SLAB THICKNESS

The slab thickness has been shown to be a very important factor influencing the performance of composite slabs in fire. General observations from the six tests are as follows:

- When there is restraint from the surrounding structure, as is the case in the restrained beam test, the British Steel corner test and the BRE corner test, a 'pull-back' phenomenon is experienced. This occurs where the floor slab bridges from the hot beams to cooler sections of structure. As the steel beam's stiffness begins to decrease rapidly, the slab's stiffness begins to dominate, attempting to return the slab to its original shape. This is a very pronounced effect with the slab model used in this set of analyses, since it does not allow a temperature distribution across the slab thickness, and thus prohibits thermal bowing of the slab.

- When there is little restraint, for example in the plane frame test, large compartment test and the demonstration test, the slab thickness is less crucial. In the first case this is probably because of low stiffness at the ends of the transverse members, and in the others it is because there is no stiff (cold) support to assist the bridging action.

This parametric study is repeated in Chapter 6 using a new slab element developed in Chapter 5, although similar results might be expected. These studies will provide a datum as to the effectiveness of the new element.

4.9.2 Parametric Study 2: Secondary Beam Connection Strength and Stiffness

The secondary beam connection strength and stiffness has been found to have little effect on the overall action of the subframe. However, it may be expected that if a slab thickness thinner than the nominal 70mm were used the connection would have more effect, as the concrete would then crack causing the beams to act more as isolated composite beams. Conversely, if the thickness of the slab were to be increased the effect of the connections would decrease, as the slab would dominate the structural action.

The secondary beam connection strength and stiffness parametric study will not be repeated in the following set of parametric studies in Chapter 6 because of the low sensitivity of the behaviour to this parameter.

4.9.3 Parametric Study 3: Spacing of Secondary Beams

The third parametric study, considering the spacing of the secondary beams has limited scope for generalisation as this study could only reasonably be conducted on the restrained beam test due to the relative complexity of the other tests.

4.9.4 Parametric Study 4: Positioning of Sandbags

The positioning of the actual loading of the structure is clearly important in a test of limited area, such as the restrained beam test. Unfortunately difficulties arise when trying to analyse the test qualitatively as the load paths change. The following

parametric studies in Chapter 6 will continue to assume a uniformly distributed load at all times.

4.9.5 PARAMETRIC STUDY 5: EXTENT OF SUBFRAME

The extent of a subframe is clearly important, and thus the largest practical subframes will be used in the following set of parametric studies using the new slab element in Chapter 6. Some general rules for the selection of a subframe follow:

- The subframe should extend for at least one bay beyond the fire compartment in the direction of the continuous structure.

- If possible, the subframe should extend to any nearby free edges of the structure, as the boundary conditions at this point are easily definable.

- Artificial rigid restraint to axial expansion of a steel member should be avoided as this may have an extreme effect on the internal forces, and thus give an incorrect view of the structural mechanics in the fire condition.

5 MODELLING FLOOR SLABS USING LAMINATED FLAT SHELL ELEMENTS

A hybrid flat shell element may be formed by superimposing a plate bending stiffness matrix and a plane stress membrane stiffness matrix, as shown in Figure 5-01.

Figure 5-01. Flat shell element

The basic shell formulation is similar to that used by Bathe [48]. Bailey [44] also incorporates this formulation in the VULCAN finite element code. The laminated flat shell element consists of a series of laminae so that different material properties may be allocated to each lamina within the shell depth (as opposed to a normal flat shell element in which the material properties are assumed to be uniform throughout). This will also allow temperature gradients, thermal bowing, modulus of elasticity degradation relative to temperature, and a greater accuracy in the estimation of stresses throughout the element. The laminated flat shell element therefore offers a potential improvement for the modelling of reinforced concrete floor slabs compared with the flat shell element adopted by Bailey in representing concrete slabs exposed to fire.

5.1 PLATE ELEMENT FORMULATION

The following assumptions are made within the plate element formulation (after Bailey):

1. The stress normal to the surface of the plate is zero.

2. Any points within a plate that were originally in a straight line normal to the mid-surface of the plate remain in a straight line as the plate deforms. The Kirchhoff (thin plate) theory [47, 48] excludes shear deformations, and therefore straight lines originally perpendicular to the mid-surface remain perpendicular during

deformation. The Mindlin/Reissner (thick plate) theory [47, 48] includes shear deformations and therefore lines originally normal to the mid-surface will, in general, not remain perpendicular to the mid-surface during deformation. A physical comparison between the Mindlin/Reissner and the Kirchhoff theories is shown in Figure 5-02.

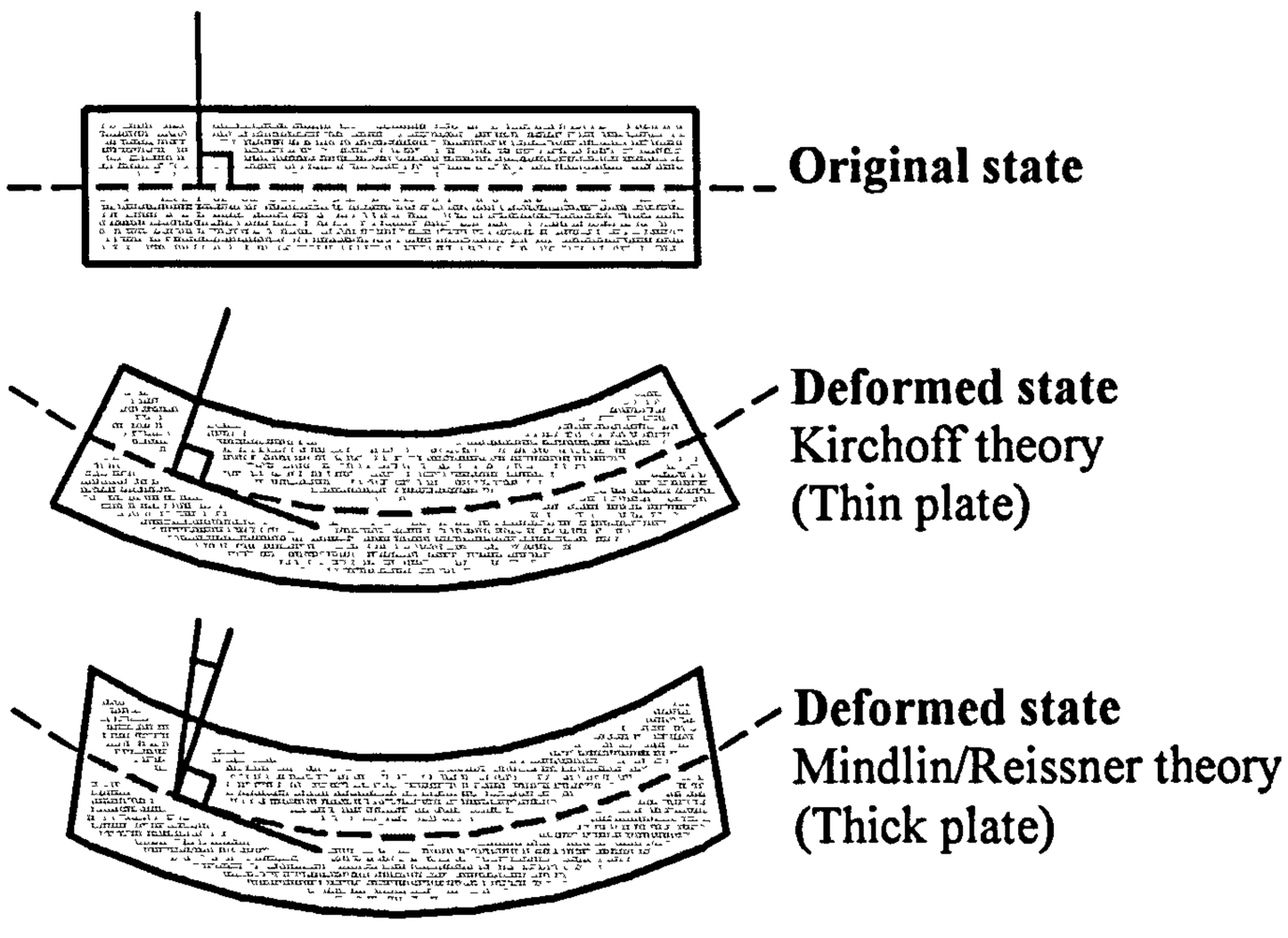

Figure 5-02. Comparison of Kirchhoff and Mindlin/Reissner shear assumptions

The Kirchhoff theory [47, 48] uses a single variable (v) to represent out-of-plane deformation; this corresponds to the lateral displacement of the mid-plane of the plate. The generalised strains are represented by the second derivatives of the lateral displacement. The lateral displacement and the slope (the first derivative of v) must be continuous between element boundaries to ensure finite values for the strains. This continuity requirement is known as C_1 continuity, and causes mathematical and computational difficulties in defining shape functions for the plate elements.

The Mindlin/Reissner theory [47, 48] uses different variables to define the lateral displacement and the slope, each with independent shape functions. The first derivatives of the slope represent the generalised strains, and therefore the slope and lateral displacement must be continuous at the element boundaries. This continuity criterion is referred to as C_0 continuity [47] and is easier to implement than C_1 continuity. The Mindlin/ Reissner theory may normally only be used for thin plates if higher-order elements (elements with 9 or 16 nodes) are used. Lower-order elements, when used to model thin plates, tend to become artificially stiff, causing a phenomenon called shell locking. Methods have been developed to overcome shell

locking by the use of selective or reduced integration, or the use of discrete Kirchhoff theory [47, 48].

It has been shown that these approaches may be integrated into a more general formulation to approximate the shear and bending deformations independently (a method known as mixed interpolation). It was decided to adopt the Mindlin/Reissner theory with mixed interpolation so that;

1. Lower-order elements (mainly four-noded) can be used when modelling thin shells.

2. Any form of thick or thin shell or plate can be modelled.

3. The formulation can be extended to geometric and material non-linearity.

The basic isoparametric finite element (as defined by Bailey [44] and Bathe [48]) has a predefined relationship between displacements at any point within the element and the element nodal displacements, by the use of interpolation (shape) functions. These interpolations express the element co-ordinates and displacements in the form of the natural co-ordinate system of the element, which has variables r, s and t, which vary from -1 to +1, as shown in Figure 5-03.

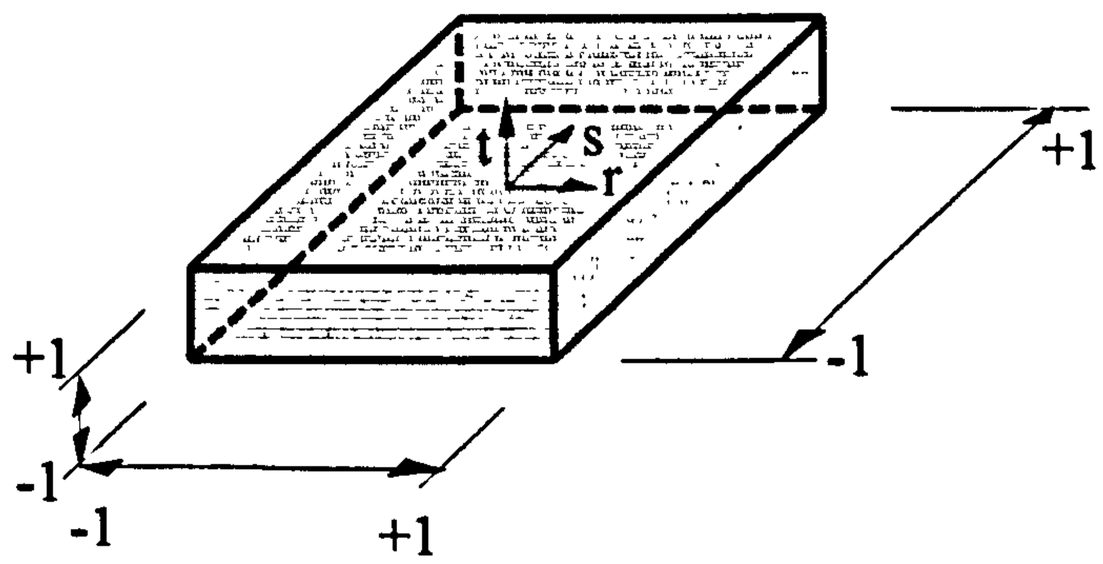

Figure 5-03. Natural co-ordinate system of the element

The general three-dimensional element co-ordinate interpolations are,

$$x = \sum_{i=1}^{q} h_i x_i \qquad y = \sum_{i=1}^{q} h_i y_i \qquad z = \sum_{i=1}^{q} h_i z_i \qquad \text{5-01}$$

where,

x, y and z are the local co-ordinates of any point within the element,

x_i, y_i and z_i (i = 1, 2, 3.... q) are the co-ordinates of the element nodes,

h_i (i = 1, 2, 3.... q) are the shape functions (or interpolation functions) defined in the natural co-ordinate system relating to the global co-ordinates [48].

The element displacements are interpolated in a similar way to give

$$u = \sum_{i=1}^{q} h_i u_i \qquad v = \sum_{i=1}^{q} h_i v_i \qquad w = \sum_{i=1}^{q} h_i w_i \qquad \text{5-02}$$

where

u, v and w are the local element displacements at any point within the element,

u_i, v_i and w_i (i = 1, 2, 3.... q) are the element nodal displacements.

In the formulation of the element stiffness matrix, elemental strains are required. These are obtained in terms of the derivatives of element displacements with respect to the local co-ordinates. Since the element displacements are defined in the natural co-ordinate system, the x, y and z derivatives must be related to the r, s and t derivatives. Let

$$x = f_1(r,s,t) \qquad y = f_2(r,s,t) \qquad z = f_3(r,s,t) \qquad \text{5-03}$$

which implies also that

$$r = f_4(x,y,z) \qquad s = f_5(x,y,z) \qquad t = f_6(x,y,z) \qquad \text{5-04}$$

To obtain the derivatives $\partial/\partial x$, $\partial/\partial y$ and $\partial/\partial z$, the product rule is used:

$$\frac{\partial}{\partial x} = \frac{\partial}{\partial r}\frac{\partial r}{\partial x} + \frac{\partial}{\partial s}\frac{\partial s}{\partial x} + \frac{\partial}{\partial t}\frac{\partial t}{\partial x} \qquad \text{5-05}$$

The derivatives $\partial/\partial y$ and $\partial/\partial z$ are performed similarly.

To obtain $\partial/\partial x$, the value $\partial r/\partial x$ is needed, which requires the relationship defined in equations 5-04 to be evaluated. However, these relationships are generally difficult to establish explicitly, and so the required derivatives are obtained in the following way.

Using the product rule, the following relationship may be formed:

$$\begin{Bmatrix} \frac{\partial}{\partial r} \\ \frac{\partial}{\partial s} \\ \frac{\partial}{\partial t} \end{Bmatrix} = \begin{bmatrix} \frac{\partial x}{\partial r} & \frac{\partial y}{\partial r} & \frac{\partial z}{\partial r} \\ \frac{\partial x}{\partial s} & \frac{\partial y}{\partial s} & \frac{\partial z}{\partial s} \\ \frac{\partial x}{\partial t} & \frac{\partial y}{\partial t} & \frac{\partial z}{\partial t} \end{bmatrix} \begin{Bmatrix} \frac{\partial}{\partial x} \\ \frac{\partial}{\partial y} \\ \frac{\partial}{\partial z} \end{Bmatrix} \qquad 5\text{-}06$$

which can also be expressed in matrix form as

$$\frac{\partial}{\partial r} = \mathbf{J}\frac{\partial}{\partial x} \qquad 5\text{-}07$$

where **J** is the Jacobian operator, relating the natural co-ordinate derivatives to the local co-ordinates derivatives. Since $\partial/\partial x$ is required we obtain

$$\frac{\partial}{\partial x} = \mathbf{J}^{-1}\frac{\partial}{\partial r} \qquad 5\text{-}08$$

which requires that the inverse of **J** exists. This will be the case provided that there is a one-to-one correspondence between the natural and local co-ordinates of the element. Once the derivatives are obtained, the strain-displacement transformation matrix $\boldsymbol{B}$ can be obtained, which allows the strains at any point within the element to be calculated using

$$\varepsilon = \boldsymbol{B}\hat{u} \qquad 5\text{-}09$$

where

ε is the strain vector,

$\boldsymbol{B}$ is the strain-displacement matrix,

$\hat{u}$ is the vector of displacements at nodal positions.

It should be noted that the formulation presented up to this stage is for a general three-dimensional element; this will be simplified for the following two-dimensional elements.

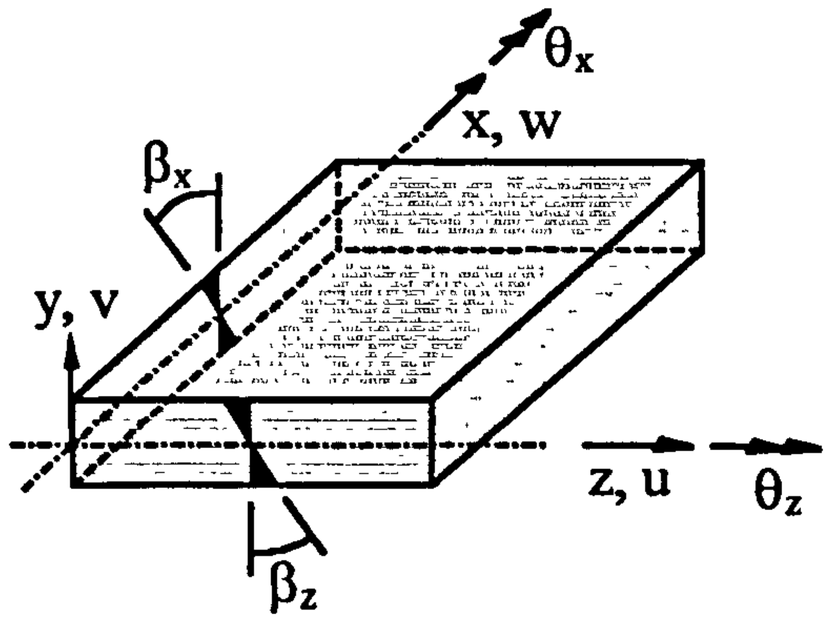

Figure 5-04. Plate element

Considering the plate element shown in Figure 5-04, and following the sign convention of the existing model, the displacement components of a point having co-ordinates x, y, z (assuming small-displacement bending theory) are

$$u = -y\beta_z(x,y) \qquad w = -y\beta_x(x,y) \qquad v = v(x,y) \qquad \text{5-10}$$

The bending strains, ε_{zz}, ε_{xx}, γ_{zx}, vary linearly throughout the plate thickness and are given by the curvatures of the plate

$$\begin{Bmatrix} \varepsilon_{zz} \\ \varepsilon_{xx} \\ \gamma_{zx} \end{Bmatrix} = y \begin{Bmatrix} -\dfrac{\partial \beta_z}{\partial z} \\ -\dfrac{\partial \beta_x}{\partial x} \\ -\dfrac{\partial \beta_z}{\partial x} - \dfrac{\partial \beta_x}{\partial z} \end{Bmatrix} \qquad \text{5-11}$$

The transverse shear strains are assumed to be constant throughout the thickness and are given by

$$\begin{bmatrix} \gamma_{zy} \\ \gamma_{xy} \end{bmatrix} = \begin{Bmatrix} \dfrac{\partial v}{\partial z} - \beta_z \\ \dfrac{\partial v}{\partial x} - \beta_x \end{Bmatrix} \qquad \text{5-12}$$

Considering an isotropic material, the stress gradient can be obtained from

$$\begin{Bmatrix} \tau_{zz} \\ \tau_{xx} \\ \tau_{zx} \end{Bmatrix} = y \frac{E}{1-\nu^2} \begin{bmatrix} 1 & \nu & 0 \\ \nu & 1 & 0 \\ 0 & 0 & \dfrac{1-\nu}{2} \end{bmatrix} \begin{Bmatrix} -\dfrac{\partial \beta_z}{\partial z} \\ -\dfrac{\partial \beta_x}{\partial x} \\ -\dfrac{\partial \beta_z}{\partial z} - \dfrac{\partial \beta_x}{\partial x} \end{Bmatrix} \qquad \text{5-13}$$

and

$$\begin{Bmatrix}\tau_{zy}\\ \tau_{xy}\end{Bmatrix}=\frac{E}{2(1+\nu)}\begin{Bmatrix}\dfrac{\partial v}{\partial z}-\beta_z\\ \dfrac{\partial v}{\partial x}-\beta_x\end{Bmatrix} \qquad 5\text{-}14$$

The expression for the total potential energy (Π) of the plate element is given by

$$\Pi=\frac{1}{2}\int_A\int_{-h/2}^{+h/2}\{\varepsilon_{zz}\quad \varepsilon_{xx}\quad \gamma_{zx}\}\begin{Bmatrix}\tau_{zz}\\ \tau_{xx}\\ \tau_{zx}\end{Bmatrix}dy\,dA+\frac{k}{2}\int_A\int_{-h/2}^{+h/2}\{\gamma_{zy}\quad \gamma_{xy}\}\begin{Bmatrix}\tau_{zy}\\ \tau_{xy}\end{Bmatrix}dy\,dA-\int_A wp\,dA$$

5-15

where

p is the transverse loading per unit area,

k is a constant shear stress correction factor (generally set to 5/6) [48].

Substituting equations 5-11 to 5-14 into 5-15 and integrating with respect to y over the thickness produces,

$$\Pi=\frac{1}{2}\int_A \kappa^T C_b \kappa dA+\frac{1}{2}\int_A \gamma^T C_s \gamma dA-\int_A wpdA \qquad 5\text{-}16$$

where

$$\kappa=\begin{Bmatrix}-\dfrac{\partial\beta_z}{\partial z}\\ -\dfrac{\partial\beta_x}{\partial x}\\ -\dfrac{\partial\beta_z}{\partial z}-\dfrac{\partial\beta_x}{\partial x}\end{Bmatrix} \qquad 5\text{-}17$$

$$\gamma=\begin{Bmatrix}\dfrac{\partial v}{\partial z}-\beta_z\\ \dfrac{\partial v}{\partial x}-\beta_x\end{Bmatrix} \qquad 5\text{-}18$$

$$C_b = \frac{Eh^3}{12(1-\nu^2)}\begin{bmatrix} 1 & \nu & 0 \\ \nu & 1 & 0 \\ 0 & 0 & \frac{1-\nu}{2} \end{bmatrix} \qquad 5\text{-}19$$

$$C_s = \frac{Ehk}{2(1+\nu)}\begin{bmatrix} 1 & 0 \\ 0 & 1 \end{bmatrix} \qquad 5\text{-}20$$

Since the normal stress in the plate has been integrated, C_b is the generalised stress-strain matrix relating moments per unit length to bending strains

$$\begin{Bmatrix} M_{zz} \\ M_{xx} \\ M_{zx} \end{Bmatrix} = C_b \begin{Bmatrix} -\frac{\partial \beta_z}{\partial z} \\ -\frac{\partial \beta_x}{\partial x} \\ -\frac{\partial \beta_z}{\partial z} - \frac{\partial \beta_x}{\partial x} \end{Bmatrix} \qquad 5\text{-}21$$

Similarly, C_s is the generalised stress-strain matrix relating shear force per unit length to shear strains

$$\begin{Bmatrix} V_{zy} \\ V_{xy} \end{Bmatrix} = C_s \begin{Bmatrix} \gamma_{zy} \\ \gamma_{xy} \end{Bmatrix} \qquad 5\text{-}22$$

For equilibrium $\delta\Pi=0$, and since C is symmetrical we obtain from equation 5-16

$$\int_A \delta\kappa^T C_b \kappa \; dA + \int_A \delta\gamma^T C_s \gamma \; dA - \int_A \delta w p \; dA = 0 \qquad 5\text{-}23$$

This is the Principle of Virtual Displacements for a plate element based on the Mindlin/Reissner theory [48]. The first two terms represent internal work due to virtual strains (corresponding to the imposed virtual displacements due to bending (C_b) and shear (C_s)) and the last term represents external work due to nodal loads subject to virtual displacements.

In finite element analysis we use

$$v = \sum_{i=1}^{q} h_i v_i \qquad \beta_z = \sum_{i=1}^{q} h_i \theta_x^i \qquad \beta_x = \sum_{i=1}^{q} h_i \theta_z^i$$

$$z = \sum_{i=1}^{q} h_i z_i \qquad x = \sum_{i=1}^{q} h_i x_i \qquad 5\text{-}24$$

and adopt the following notation:

$$\kappa(r,s) = B_\kappa \hat{u} \qquad \gamma(r,s) = B_\gamma \hat{u} \qquad v(r,s) = H_w \hat{u} \qquad 5\text{-}25$$

where

B_κ and B_γ are generalised strain-displacement matrices,

H_w is a matrix of the shape functions,

$\hat{u}$ is a matrix of nodal displacements.

Substituting the notation of equation 5-25 into equation 5-23, and letting the imposed virtual nodal displacements be $\bar{\hat{u}}$, gives

$$\bar{\hat{u}}^T \left[\int_A B_\kappa^T C_b B_\kappa \, dA + \int_A B_\gamma^T C_s B_\gamma \, dA \right] \hat{u} = \bar{\hat{u}}^T \int_A H_w^T p \, dA \qquad 5\text{-}26$$

To solve equation 5-26 for unknown nodal displacements, a unit virtual displacement is applied in turn for all the displacement components used. Therefore, $\bar{\hat{u}}$ is an identity matrix, which allows equation 5-26 to be expressed as

$$K\hat{u} = R \qquad 5\text{-}27$$

where

$$K = \int_A \left(B_\kappa^T C_b B_\kappa + B_\gamma^T C_b B_\gamma \right) dA \qquad 5\text{-}28$$

and

$$R = \int_A H_w^T p \, dA \qquad 5\text{-}29$$

Equations 5-28 and 5-29 have to be converted to natural co-ordinates (r and s) which requires the area derivative to be expressed as

$$dA = \det \mathbf{J}\ drds \qquad 5\text{-}30$$

where detJ is the determinant of the Jacobian operator. Therefore, equation 5-28 may be written as

$$K = \det \mathbf{J} \int_{-1}^{+1}\int_{-1}^{+1} \left(B_\kappa^T C_b B_\kappa + B_\gamma^T C_s B_\gamma \right) dr\, ds \qquad 5\text{-}31$$

and equation 5-29 may be expressed as

$$R = \det \mathbf{J} \int_{-1}^{+1}\int_{-1}^{+1} H_w^T p\ dr\, ds \qquad 5\text{-}32$$

The shape functions are

$$h_1 = \frac{1}{4}(1+r)(1+s) \qquad h_2 = \frac{1}{4}(1-r)(1+s)$$

$$h_3 = \frac{1}{4}(1-r)(1-s) \qquad h_4 = \frac{1}{4}(1+r)(1-s) \qquad 5\text{-}33$$

Therefore, the co-ordinate interpolations are given by

$$z = \frac{1}{4}(1+r)(1+s)z_1 + \frac{1}{4}(1-r)(1+s)z_2 + \frac{1}{4}(1-r)(1-s)z_3 + \frac{1}{4}(1+r)(1-s)z_4$$

5-34

$$x = \frac{1}{4}(1+r)(1+s)x_1 + \frac{1}{4}(1-r)(1+s)x_2 + \frac{1}{4}(1-r)(1-s)x_3 + \frac{1}{4}(1+r)(1-s)x_4$$

5-35

and the displacement interpolations are given by

$$v = \frac{1}{4}(1+r)(1+s)v_1 + \frac{1}{4}(1-r)(1+s)v_2 + \frac{1}{4}(1-r)(1-s)v_3 + \frac{1}{4}(1+r)(1-s)v_4$$

5-36

$$\beta_x = \frac{1}{4}(1+r)(1+s)\theta_x^1 + \frac{1}{4}(1-r)(1+s)\theta_x^2 + \frac{1}{4}(1-r)(1-s)\theta_x^3 + \frac{1}{4}(1+r)(1-s)\theta_x^4$$

5-37

$$\beta_y = \frac{1}{4}(1+r)(1+s)\theta_y^1 + \frac{1}{4}(1-r)(1+s)\theta_y^2 + \frac{1}{4}(1-r)(1-s)\theta_y^3 + \frac{1}{4}(1+r)(1-s)\theta_y^4$$

5-38

To evaluate the displacement derivatives we need to calculate

$$\begin{Bmatrix} \frac{\partial}{\partial r} \\ \frac{\partial}{\partial s} \end{Bmatrix} = \begin{bmatrix} \frac{\partial z}{\partial r} & \frac{\partial x}{\partial r} \\ \frac{\partial z}{\partial s} & \frac{\partial x}{\partial s} \end{bmatrix} \begin{Bmatrix} \frac{\partial}{\partial z} \\ \frac{\partial}{\partial x} \end{Bmatrix}$$

5-39

which may be expressed as

$$\frac{\partial}{\partial r} = \mathbf{J}\frac{\partial}{\partial z}$$

5-40

Now

$$\frac{\partial z}{\partial r} = \frac{1}{4}(1+s)z_1 - \frac{1}{4}(1+s)z_2 - \frac{1}{4}(1-s)z_3 + \frac{1}{4}(1-s)z_4$$

5-41

$$\frac{\partial z}{\partial s} = \frac{1}{4}(1+r)z_1 - \frac{1}{4}(1+r)z_2 - \frac{1}{4}(1-r)z_3 + \frac{1}{4}(1-r)z_4$$

5-42

$$\frac{\partial x}{\partial r} = \frac{1}{4}(1+s)x_1 - \frac{1}{4}(1+s)x_2 - \frac{1}{4}(1-s)x_3 + \frac{1}{4}(1-s)x_4$$

5-43

$$\frac{\partial x}{\partial s} = \frac{1}{4}(1+r)x_1 - \frac{1}{4}(1+r)x_2 - \frac{1}{4}(1-r)x_3 + \frac{1}{4}(1-r)x_4$$

5-44

Therefore the Jacobian operator can be obtained for any values of r and s ($-1 \le r \le +1$ and $-1 \le s \le +1$), which allows the displacement derivatives to be evaluated for any value of r and s using

$$\begin{Bmatrix} \dfrac{\partial}{\partial z} \\ \dfrac{\partial}{\partial x} \end{Bmatrix}_{r,=r_i \,\&\, s=s_j} = \mathbf{J}_{ij}^{-1} \begin{Bmatrix} \dfrac{\partial}{\partial r} \\ \dfrac{\partial}{\partial s} \end{Bmatrix}_{r=r_i \,\&\, s=s_j} \qquad 5\text{-}45$$

Now

$$\frac{\partial \beta_z}{\partial r} = \frac{1}{4}(1+s)\theta_x^1 - \frac{1}{4}(1+s)\theta_x^2 - \frac{1}{4}(1-s)\theta_x^3 + \frac{1}{4}(1-s)\theta_x^4 \qquad 5\text{-}46$$

$$\frac{\partial \beta_z}{\partial s} = \frac{1}{4}(1+r)\theta_x^1 - \frac{1}{4}(1+r)\theta_x^2 - \frac{1}{4}(1-r)\theta_x^3 + \frac{1}{4}(1-r)\theta_x^4 \qquad 5\text{-}47$$

$$\frac{\partial \beta_x}{\partial r} = \frac{1}{4}(1+s)\theta_y^1 - \frac{1}{4}(1+s)\theta_y^2 - \frac{1}{4}(1-s)\theta_y^3 + \frac{1}{4}(1-s)\theta_y^4 \qquad 5\text{-}48$$

$$\frac{\partial \beta_x}{\partial s} = \frac{1}{4}(1+r)\theta_y^1 - \frac{1}{4}(1+r)\theta_y^2 - \frac{1}{4}(1-r)\theta_y^3 + \frac{1}{4}(1-r)\theta_y^4 \qquad 5\text{-}49$$

Therefore the displacement derivatives are given by

$$\begin{Bmatrix} \dfrac{\partial \beta_z}{\partial z} \\ \dfrac{\partial \beta_z}{\partial x} \end{Bmatrix} = \frac{1}{4}\mathbf{J}^{-1} \begin{bmatrix} 0 & 0 & -(1+s) & 0 & 0 & (1+s) & 0 & 0 & (1-s) & 0 & 0 & -(1-s) \\ 0 & 0 & -(1+r) & 0 & 0 & -(1-r) & 0 & 0 & -(1-r) & 0 & 0 & -(1+r) \end{bmatrix} \{\hat{u}\} \qquad 5\text{-}50$$

$$\begin{Bmatrix} \dfrac{\partial \beta_x}{\partial z} \\ \dfrac{\partial \beta_x}{\partial x} \end{Bmatrix} = \frac{1}{4}\mathbf{J}^{-1} \begin{bmatrix} 0 & -(1+s) & 0 & 0 & (1+s) & 0 & 0 & (1-s) & 0 & 0 & -(1-s) & 0 \\ 0 & -(1+r) & 0 & 0 & -(1-r) & 0 & 0 & (1-r) & 0 & 0 & (1+r) & 0 \end{bmatrix} \{\hat{u}\} \qquad 5\text{-}51$$

where,

$$\{\hat{u}\} = \langle v_1 \quad \theta_z^1 \quad \theta_x^1 \quad v_2 \quad \theta_z^2 \quad \theta_x^2 \quad v_3 \quad \theta_z^3 \quad \theta_x^3 \quad v_4 \quad \theta_z^4 \quad \theta_x^4 \rangle^T$$

Therefore, from equation 5-25, the generalised strain-displacement, B_κ, is given by

$$B_\kappa = \frac{1}{4}\mathbf{J}^{-1}\begin{bmatrix} 0 & 0 & 0 \\ 0 & -(1+r) & -(1+s) \\ -(1+s) & 0 & -(1+r) \\ 0 & 0 & 0 \\ 0 & -(1-r) & (1+s) \\ (1+s) & 0 & -(1-r) \\ 0 & 0 & 0 \\ 0 & (1-r) & (1-s) \\ (1-s) & 0 & -(1-r) \\ 0 & 0 & 0 \\ 0 & (1+r) & -(1-s) \\ -(1-s) & 0 & -(1+r) \end{bmatrix}^T \qquad 5\text{-}52$$

To obtain the generalised stress-displacement matrix for shear strains, the derivation by Bathe and Dvorkin [56] was adopted. This expresses the shear strains as

$$\gamma_{xy} = \gamma_{ry}\sin\beta - \gamma_{sy}\sin\alpha$$

$$\gamma_{xy} = -\gamma_{ry}\cos\beta + \gamma_{sy}\cos\alpha \qquad 5\text{-}53$$

Where, α and β are the angles between the r and x-axes, and the s and x-axes respectively. In this formulation it is assumed that the plate is not originally deformed. Therefore

$$\alpha = 0° \qquad \beta = 90°$$

Using the derivation by Bathe and Dvorkin [56] the following expressions are used:

$$\gamma_{ry} = \frac{\sqrt{\left[\left(C_z + r\beta_z\right)^2 + \left(C_x + r\beta_x\right)^2\right]}}{8\det\mathbf{J}}\left\{\begin{aligned}&(1+s)\begin{bmatrix}\dfrac{v_1 - v_2}{2} + \dfrac{z_1 - z_2}{4}\left(\theta_x^1 + \theta_x^2\right) \\ -\dfrac{\left(x_1 - x_2\right)}{4}\left(\theta_z^1 + \theta_z^2\right)\end{bmatrix} \\ &+(1-s)\begin{bmatrix}\dfrac{v_4 - v_3}{2} + \dfrac{z_4 - z_3}{4}\left(\theta_z^4 + \theta_z^3\right) \\ -\dfrac{x_4 - x_3}{4}\left(\theta_z^4 - \theta_z^3\right)\end{bmatrix}\end{aligned}\right\}$$

5-54

and

$$\gamma_{sy} = \frac{\sqrt{\left[\left(A_z + r\beta_z\right)^2 + \left(A_x + r\beta_x\right)^2\right]}}{8\det \mathbf{J}} \left\{ \begin{array}{l} (1+r)\left[\begin{array}{l} \dfrac{v_1 - v_4}{2} + \dfrac{z_1 - z_4}{4}\left(\theta_x^1 + \theta_x^4\right) \\ -\dfrac{\left(x_1 - x_4\right)}{4}\left(\theta_z^1 + \theta_z^4\right) \end{array} \right] \\ +(1-s)\left[\begin{array}{l} \dfrac{v_2 - v_3}{2} + \dfrac{z_1 - z_3}{4}\left(\theta_x^2 + \theta_x^3\right) \\ -\dfrac{x_2 - x_3}{4}\left(\theta_z^2 - \theta_z^3\right) \end{array} \right] \end{array} \right\}$$

where

$$A_z = z_1 - z_2 - z_3 + z_4 \qquad A_x = x_1 - x_2 - x_3 + x_4$$

$$B_z = z_1 - z_2 + z_3 - z_4 \qquad B_x = x_1 - x_2 + x_3 - x_4$$

$$C_z = z_1 + z_2 - z_3 - z_4 \qquad C_z = x_1 + x_2 - x_3 - x_4$$

when

z_i (i=1, 2, 3, 4) are the nodal z co-ordinates,

x_i (i=1, 2, 3, 4) are the nodal x co-ordinates.

Now

$$\left\{ \begin{array}{l} \gamma_{zy} \\ \gamma_{xy} \end{array} \right\} = \boldsymbol{B}_\gamma \hat{\boldsymbol{u}}$$

using the notation

$$\boldsymbol{B}_\gamma = \left\{ \begin{array}{l} \boldsymbol{B}_{\gamma ry} \\ \boldsymbol{B}_{\gamma sy} \end{array} \right\}$$

where

$$B_{\gamma_{ry}} = Tr_1 \left\langle \begin{array}{c} \frac{1}{2}(1+s) \\ \frac{1}{4}(-x_1+x_2)(1+s) \\ \frac{1}{4}(z_1-z_2)(1+s) \\ -\frac{1}{2}(1+s) \\ \frac{1}{4}(-x_1+x_2)(1+s) \\ \frac{1}{4}(z_1-z_2)(1+s) \\ -\frac{1}{2}(1-s) \\ \frac{1}{4}(x_4+x_3)(1-s) \\ \frac{1}{4}(z_4-z_3)(1-s) \\ \frac{1}{2}(1-s) \\ \frac{1}{4}(-x_4+x_3)(1-s) \\ \frac{1}{4}(z_4-z_3)(1-s) \end{array} \right\rangle^T \qquad 5\text{-}56$$

in which

$$Tr_1 = \frac{\sqrt{\left[(C_z+r\beta_z)^2+(C_x+r\beta_x)^2\right]}}{8\det \mathbf{J}}$$

and

$$B_{\gamma_{sr}} = Tr_2 \left\langle \begin{array}{c} \frac{1}{2}(1+r) \\ \frac{1}{4}(-x_1+x_4)(1+r) \\ \frac{1}{4}(z_1-z_4)(1+r) \\ -\frac{1}{2}(1+r) \\ \frac{1}{4}(-x_2+x_3)(1+r) \\ \frac{1}{4}(z_2-z_3)(1+r) \\ -\frac{1}{2}(1-r) \\ \frac{1}{4}(x_2+x_3)(1-r) \\ \frac{1}{4}(z_2-z_3)(1-r) \\ \frac{1}{2}(1-r) \\ \frac{1}{4}(-x_1+x_4)(1-r) \\ \frac{1}{4}(z_1-z_4)(1-r) \end{array} \right\rangle^T \qquad 5\text{-}57$$

in which

$$Tr_2 = \frac{\sqrt{\left[(A_z+rB_z)^2+(A_x+rB_x)^2\right]}}{8\det \mathbf{J}}$$

Obtaining the generalised strain-displacement matrices B_κ and B_γ allows the element stiffness matrix to be obtained from

$$K = \det \mathbf{J} \int_{-1}^{+1}\int_{-1}^{+1} \left(B_\kappa^T C_b B_\kappa + B_\gamma^T C_b B_\kappa \right) dr\, ds \qquad 5\text{-}58$$

Gaussian numerical integration is used to evaluate the expression 5-58. Let

$$K = \int_{-1}^{+1}\int_{-1}^{+1} f\, dr\, ds \qquad 5\text{-}59$$

where

$$f = \det \mathbf{J} \left(B_\kappa^T C_b B_\kappa + B_\gamma^T C_b B_\kappa \right)$$

Using numerical integration

$$K = \sum_{ij} \alpha_{ij} f_{ij} t_{ij} \qquad 5\text{-}60$$

where f_{ij} is the matrix f evaluated at points r_i and s_j, t_{ij} is the thickness at this point and α_{ij} is a constant known as a weighting factor which depends on the positions of r_i and s_i.

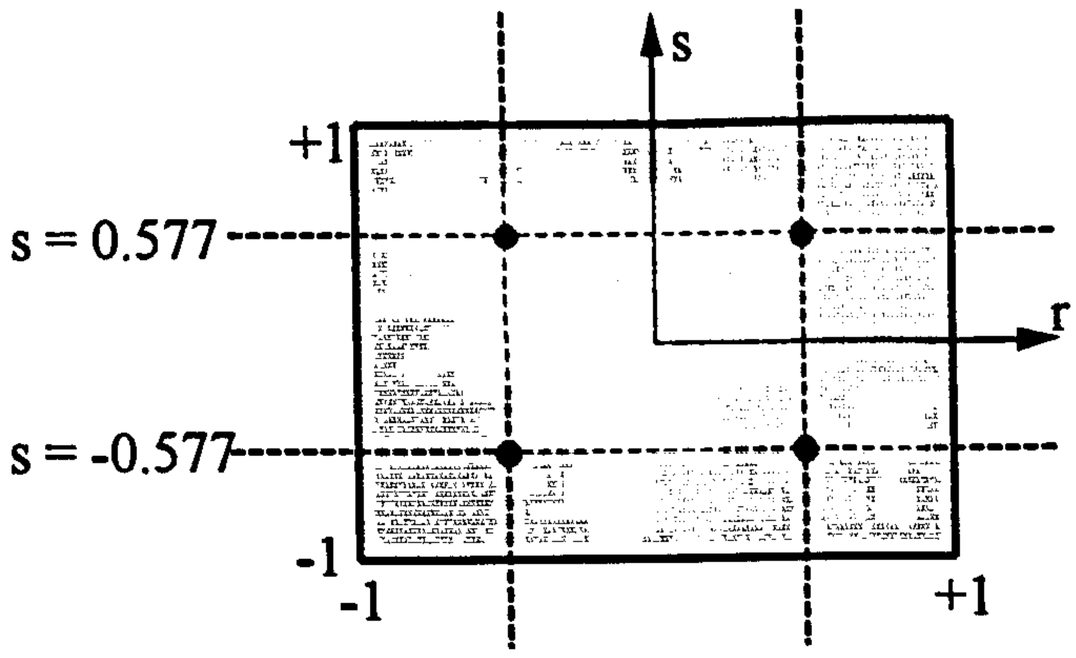

Figure 5-05. Position of Gauss points in the element

The positions of r_i and s_j, together with the values of the weighting factors, are such as to give maximum integration accuracy for the number of Gauss points (i.e. r_i and s_j) used. In this formulation 2-point Gauss integration is employed, which means that the matrix f_{ij} is calculated at four points as shown in Figure 5-05. The weighting factors

corresponding to the positions of these Gauss points can be found in many textbooks on numerical methods, for example those by Zienkiewicz [47] and Bathe [48].

5.2 PLATE ELEMENT FORMULATION EXTENDED TO ACCOMMODATE LAMINATIONS

The laminated shell formulation is an extension of that found in Section 5.1 for the simple plate formulation.

A sequential numbering system is adopted, starting at the top surface of the flat shell, as shown in Figure 5-06. Stress points are taken at the mid-surface of each lamina. The stress components are computed at these stress points and are assumed to vary linearly over the thickness of each lamina. These are then transposed accordingly (or condensed) to form an element stiffness matrix in the manner of the static condensation method [48].

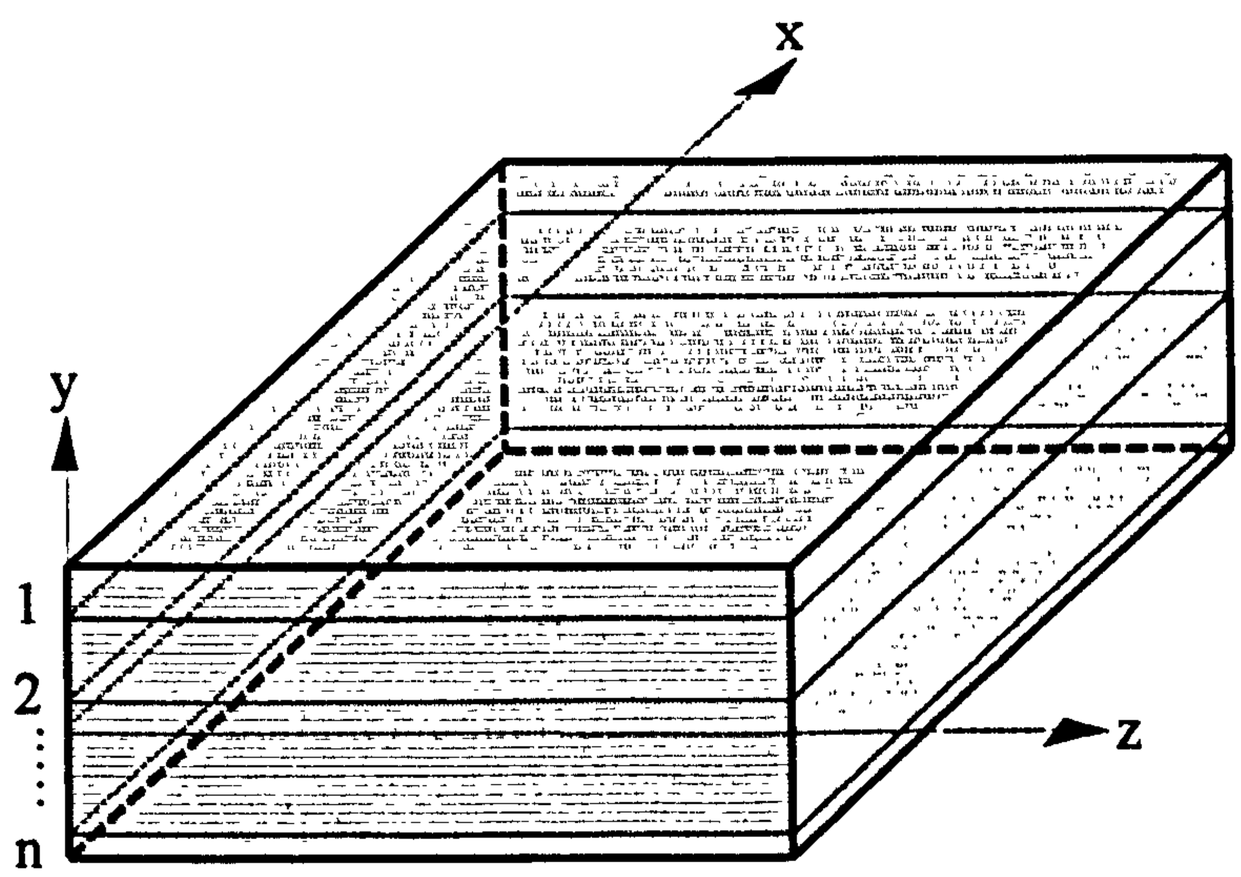

Figure 5-06. Layered shell element

First consider the element as a plate element allowing bending. The Principle of Virtual displacements (equation 5-23) states that

$$\int_A \delta\kappa^T C_b \kappa \; dA + \int_A \delta\gamma^T C_s \gamma \; dA - \int_A \delta w p \; dA = 0$$

As stated in Section 5.1, the first term is the effect of bending on the plate, the second term is the effect of shear, and the final term is the external work due to nodal loads subject to virtual displacements.

First consider the shell element in bending. For a single lamina of thickness h the bending stiffness corresponds to that of a simple non-laminated element and is defined by equation 5-19

$$C_b = \frac{Eh^3}{12(1-\nu^2)}\begin{bmatrix} 1 & \nu & 0 \\ \nu & 1 & 0 \\ 0 & 0 & \frac{1-\nu}{2} \end{bmatrix}$$

When considering a laminated system, it is important that we take into account the position of the overall reference axis. By definition, the second moment of area for a strip of unit width, can be found using

$$I = \int y^2 \, dv = \frac{y^3}{3} \qquad 5\text{-}61$$

evaluated between limits on y representing the two faces of the strip.

Inserting this into the bending stiffness matrix, with reference to Figure 5-07, produces for each lamina about the element mid-surface (as Howlett *et al* [61])

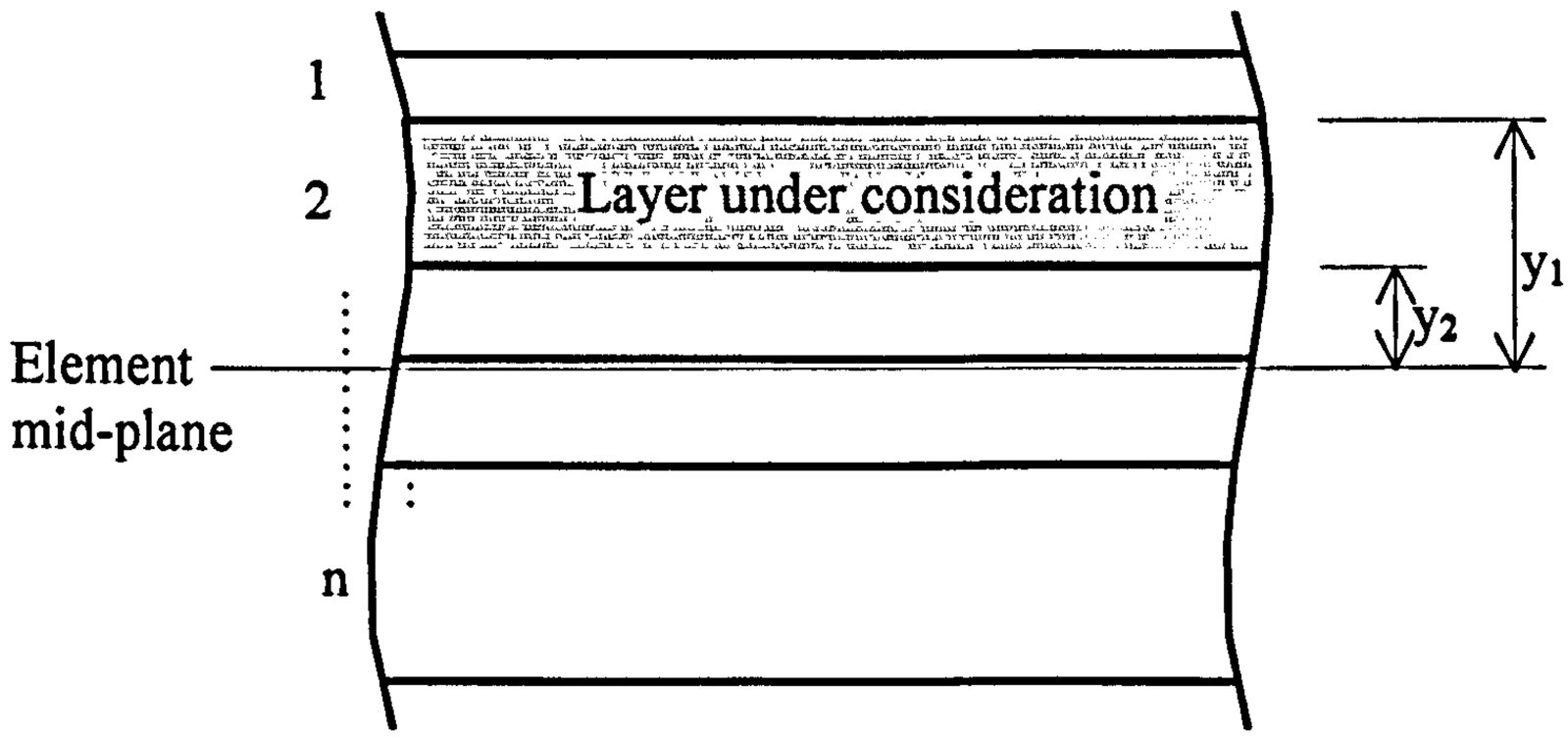

Figure 5-07. Plate element divided into layers

$$C_b = \frac{E\left((y_1)^3 - (y_2)^3\right)}{3(1-\nu^2)}\begin{bmatrix} 1 & \nu & 0 \\ \nu & 1 & 0 \\ 0 & 0 & \frac{1-\nu}{2} \end{bmatrix} \qquad 5\text{-}62$$

Summing this over the full plate thickness to form the elemental stiffness matrix

$$C_b = \sum_1^n \frac{E_i\left((y_1)^3 - (y_2)^3\right)}{3(1-\nu^2)} \begin{bmatrix} 1 & \nu & 0 \\ \nu & 1 & 0 \\ 0 & 0 & \frac{1-\nu}{2} \end{bmatrix} \qquad 5\text{-}63$$

The shear stiffness matrix (with reference to equation 5-23) is summed to find the total shear stiffness along the edge of each lamina

$$C_s = \sum_1^n \frac{Eh_i k}{2(1+\nu)} \begin{bmatrix} 1 & 0 \\ 0 & 1 \end{bmatrix} \qquad 5\text{-}64$$

where k is the shear coefficient,

The number of laminae which are necessary for discretizing and integrating in the thickness direction depends on the particular problem. Hinton and Owen [62] have suggested that between 6 and 10 laminae should be acceptable to represent non-linear behaviour in moderately thin structures.

5.3 Plane Stress Element Formulation

For the plane stress membrane stiffness, consider the element in Figure 5-08.

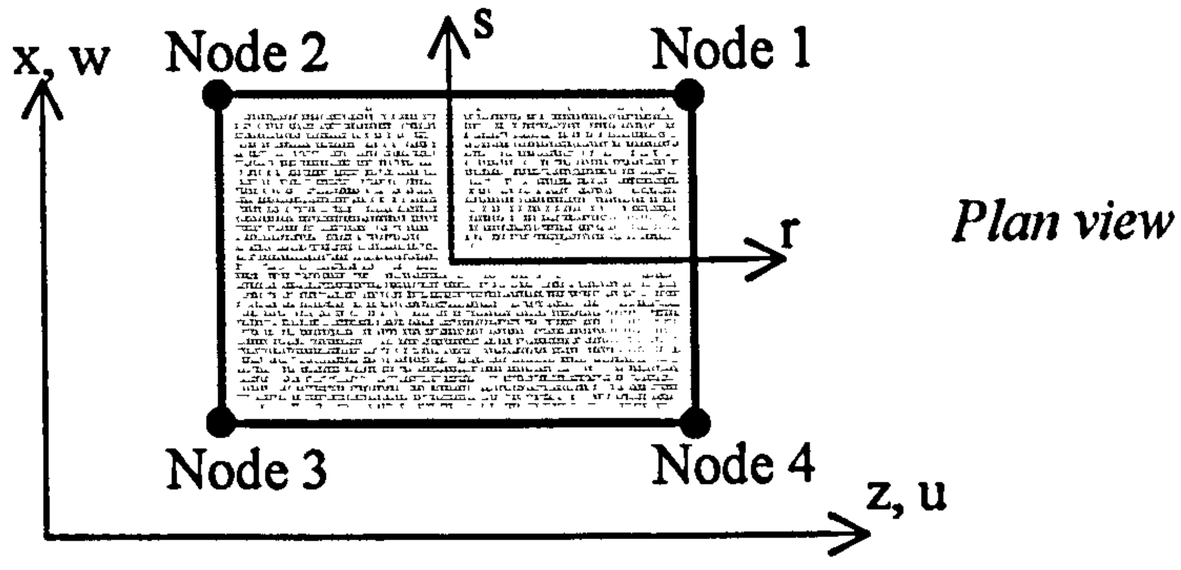

Figure 5-08. Plane stress element

As for the plate formulation, the Principle of Virtual Displacements gives

$$\int_A \delta\varepsilon^T \tau \, dA = \sum_i \delta\hat{u}^{iT} F^i \qquad 5\text{-}65$$

where

F^i is the concentrated external force at node i,

$\hat{u}^i$ is the nodal displacement at node i.

Using $\varepsilon = B\hat{u}$ and letting the imposed virtual displacements equal $\bar{\hat{u}}$ gives,

$$\bar{\hat{u}}^T \left[\int_A B^T C B \, dA \right] \hat{u} = \bar{\hat{u}}^T \{F\} \qquad 5\text{-}66$$

where

$\{F\}$ is the vector of externally applied nodal forces.

Using the virtual nodal displacement method of applying a unit virtual displacement in turn to all displacement components gives $\bar{\hat{u}}$ as an identity matrix, allowing equation 5-68 to be expressed as

$$K\hat{u} = F \qquad 5\text{-}67$$

where the stiffness matrix K, is given by

$$K = \int_A B^T C B \, dA \qquad 5\text{-}68$$

Converting this equation to the natural co-ordinate system (as shown in the derivation of the plate element) produces

$$K = \det \mathrm{J} \int_{-1}^{+1} \int_{-1}^{+1} \left(B^T C B \right) dr \, ds \qquad 5\text{-}69$$

Considering Figure 5-08, the co-ordinate and displacement interpolations are given by

$$x = \sum_{i=1}^{q} h_i x_i \qquad z = \sum_{i=1}^{q} h_i z_i \qquad w = \sum_{i=1}^{q} h_i w_i \qquad u = \sum_{i=1}^{q} h_i u_i \qquad 5\text{-}70$$

where

x and z are the local co-ordinates at any point within the element,

x_i and z_i are the local co-ordinates at the i^{th} node,

w and u are the local displacements at any point within the element,

w_i and u_i are the local displacements at the i^{th} node,

h_i are the interpolation functions, which are the same used for the plate element (equation 5-33), and are shown again below.

$$h_1 = \frac{1}{4}(1+r)(1+s) \qquad h_2 = \frac{1}{4}(1-r)(1+s)$$

$$h_3 = \frac{1}{4}(1-r)(1-s) \qquad h_4 = \frac{1}{4}(1+r)(1-s) \qquad \text{5-71}$$

Therefore the local co-ordinates at any position within the element are given by

$$z = \frac{1}{4}(1+r)(1+s)z_1 + \frac{1}{4}(1-r)(1+s)z_2 + \frac{1}{4}(1-r)(1-s)z_3 + \frac{1}{4}(1+r)(1-s)z_4$$

5-72

$$x = \frac{1}{4}(1+r)(1+s)x_1 + \frac{1}{4}(1-r)(1+s)x_2 + \frac{1}{4}(1-r)(1-s)x_3 + \frac{1}{4}(1+r)(1-s)x_4$$

5-73

and the local displacements at any position within the element are given by

$$u = \frac{1}{4}(1+r)(1+s)u_1 + \frac{1}{4}(1-r)(1+s)u_2 + \frac{1}{4}(1-r)(1-s)u_3 + \frac{1}{4}(1+r)(1-s)u_4$$

5-74

$$w = \frac{1}{4}(1+r)(1+s)w_1 + \frac{1}{4}(1-r)(1+s)w_2 + \frac{1}{4}(1-r)(1-s)w_3 + \frac{1}{4}(1+r)(1-s)w_4$$

5-75

The element strains in a plane stress element are given by

$$\varepsilon = \begin{Bmatrix} \varepsilon_{zz} \\ \varepsilon_{xx} \\ \gamma_{zx} \end{Bmatrix}$$

where

$$\varepsilon_{zz} = \frac{\partial u}{\partial z} \qquad \varepsilon_{xx} = \frac{\partial w}{\partial x} \qquad \gamma_{zx} = \frac{\partial u}{\partial z} + \frac{\partial w}{\partial z} \qquad 5\text{-}76$$

The displacement derivatives can be evaluated at any values of r and s using

$$\begin{Bmatrix} \frac{\partial}{\partial z} \\ \frac{\partial}{\partial x} \end{Bmatrix}_{\text{at } r=r_i \text{ and } s=s_j} = \mathbf{J}_{ij}^{-1} \begin{Bmatrix} \frac{\partial}{\partial z} \\ \frac{\partial}{\partial x} \end{Bmatrix}_{\text{at } r=r_i \text{ and } s=s_j} \qquad 5\text{-}77$$

The formulation of the Jacobian matrix **J** has been shown in the derivation of the plate element. Now

$$\frac{\partial u}{\partial r} = \frac{1}{4}(1+s)u_1 - \frac{1}{4}(1+s)u_2 - \frac{1}{4}(1-s)u_3 + \frac{1}{4}(1-s)u_4 \qquad 5\text{-}78$$

$$\frac{\partial u}{\partial s} = \frac{1}{4}(1+r)u_1 + \frac{1}{4}(1+r)u_2 - \frac{1}{4}(1-r)u_3 + \frac{1}{4}(1-r)u_4 \qquad 5\text{-}79$$

$$\frac{\partial w}{\partial r} = \frac{1}{4}(1+s)w_1 - \frac{1}{4}(1+s)w_2 - \frac{1}{4}(1-s)w_3 + \frac{1}{4}(1-s)w_4 \qquad 5\text{-}80$$

$$\frac{\partial w}{\partial s} = \frac{1}{4}(1+r)u_1 + \frac{1}{4}(1+r)u_2 - \frac{1}{4}(1-r)u_3 - \frac{1}{4}(1-r)u_4 \qquad 5\text{-}81$$

Therefore the displacement derivatives are given by

$$\begin{Bmatrix} \frac{\partial u}{\partial z} \\ \frac{\partial u}{\partial x} \end{Bmatrix} = \frac{1}{4}\mathbf{J}^{-1} \begin{bmatrix} (1+s) & 0 & -(1+s) & 0 & -(1-s) & 0 & (1-s) & 0 \\ (1+r) & 0 & (1-r) & 0 & -(1-r) & 0 & -(1+r) & 0 \end{bmatrix} \{\hat{u}\}$$

5-82

$$\begin{Bmatrix} \frac{\partial w}{\partial z} \\ \frac{\partial w}{\partial x} \end{Bmatrix} = \frac{1}{4}\mathbf{J}^{-1}\begin{bmatrix} 0 & (1+s) & 0 & -(1+s) & 0 & -(1-s) & 0 & (1-s) \\ 0 & (1+r) & 0 & (1-r) & 0 & -(1-r) & 0 & -(1+r) \end{bmatrix}\{\hat{u}\}$$

5-83

where

$$\{\hat{u}\} = \langle z_1 \quad x_1 \quad z_2 \quad x_2 \quad z_3 \quad x_3 \quad z_4 \quad x_4 \rangle^T$$

Therefore, using

$$\varepsilon = B\hat{u}$$

the strain-displacement matrix B is given by

$$B = \frac{1}{4}\mathbf{J}^{-1}\begin{bmatrix} (1+s) & 0 & -(1+s) & 0 & -(1-s) & 0 & (1-s) & 0 \\ 0 & (1+r) & 0 & (1-r) & 0 & -(1-r) & 0 & -(1+r) \\ (1+r) & (1+s) & (1-r) & -(1+s) & -(1-r) & -(1-s) & -(1+r) & (1-s) \end{bmatrix}$$

5-84

Therefore the element stiffness matrix can be formed using

$$K = \det \mathbf{J} \int_{-1}^{+1}\int_{-1}^{+1} \left(B^T C B\right)\, dr\, ds$$

5-85

where C is the stress-strain matrix given by

$$C = \frac{E}{1-\nu^2}\begin{bmatrix} 1 & \nu & 0 \\ \nu & 1 & 0 \\ 0 & 0 & \frac{1-\nu}{2} \end{bmatrix}$$

5-86

Gaussian numerical integration is used to evaluate the member stiffness matrix; this method has been explained previously in the derivation of the single-layer plate stiffness matrix.

5.4 Extension of Plane Stress Element Formulation to Accommodate Laminations

The formulation for a laminated element follows that for the virtual nodal displacement method. Equation 5-67 is

$$K\hat{u} = F$$

in which

F is the vector of externally applied nodal force,

$\hat{u}$ is the nodal displacement.

K is the tangent stiffness matrix defined by equation 5-85.

In the laminated plate element formulation, the average in-plane stiffness is calculated assuming that the thicknesses of the layers used are equal.

$$C = \frac{\sum_{i=1}^{n} \frac{E}{1-\nu^2} \begin{bmatrix} 1 & \nu & 0 \\ \nu & 1 & 0 \\ 0 & 0 & \frac{1-\nu}{2} \end{bmatrix}}{n} \qquad 5\text{-}87$$

For situations where the thicknesses of the layers are not equal, it would perhaps be more appropriate to apportion the stiffness of each layer accordingly into the stress-strain matrix.

5.5 Calculation of Stress Values

After the nodal displacements of the element have been found it is possible to determine the stress values at any position throughout the element using

$$\tau = \mathbf{CB}\hat{u} \qquad 5\text{-}88$$

where

τ is the generalised stress,

C is the generalised stress-strain matrix,

B is the generalised strain-displacement matrix,

$\hat{\boldsymbol{u}}$ is the matrix of nodal displacements.

The accuracy of stress values within a displacement-field finite element formulation is dependent upon the positions at which they are calculated within an element. Under normal circumstances, convergence of all criteria ensures that all displacements across an element will be continuous. However, continuity across boundaries does not generally apply to stress values unless the formulation is based on stress fields, which has the effect of 'slower' convergence of the stresses than displacements. Previous research [44, 47, 48] has been conducted into the accuracy of predicted stress values for displacement-field formulations in relation to their locations within the element. These conclude that the most accurate stress values are obtained at the Gauss integration points. It is therefore logical that a dense-mesh finite element model will give more accurate results for stress distribution than those for a sparse mesh. This will be demonstrated in the following sections. It was decided to take the stress values at each of the four Gauss points and to average them across the whole element. From the geometric properties of the element, the stress gradient due to bending, and the shear and in-plane stresses for each layer may be calculated.

5.6 Validation of the Laminated Flat Shell Element

The validation of the laminated flat shell element is intended to begin with simple elastic, single-lamina examples, and to proceed in logical steps to more complicated composite beams with slabs, including cracking, reinforcement and full thermal effects. The planned progression is shown in Figure 5-09.

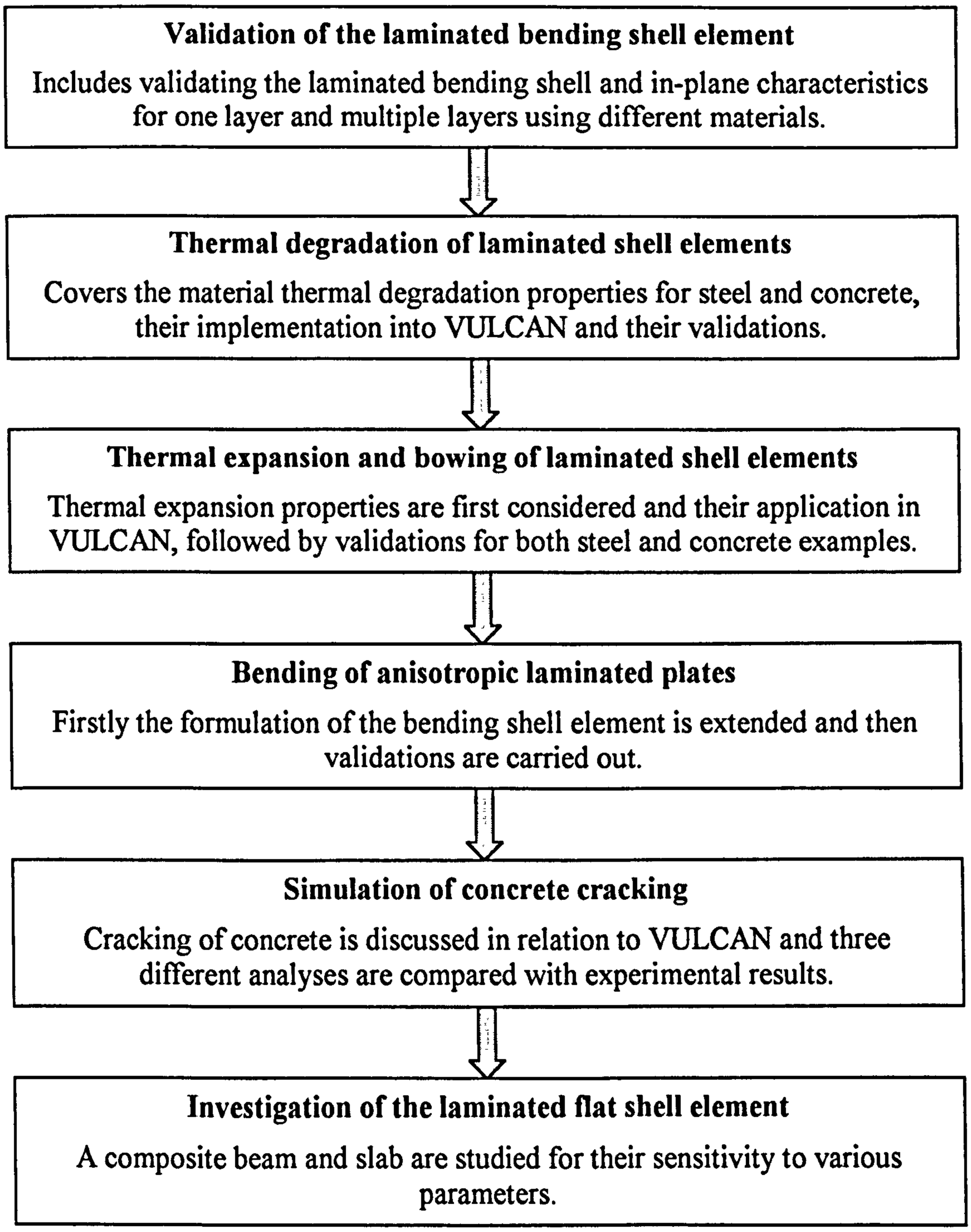

Figure 5-09. Validation sequence for laminated, flat-shell elements.

The validations will, where possible, involve three different cases with established closed-form solutions for both deflections and stresses. Case 1 is a concrete cantilever beam, Case 2 is a simply supported steel plate and Case 3 is a deep steel beam. Cases 2 and 3 were previously used by Bailey [44] for his simpler validations.

During the validations differences will occur in comparisons between the closed form solutions for stresses and the finite element analyses. These have two main causes:

1. The finite element method used is concerned with the displacement field and not the stress field, as was discussed in Section 5.5.

2. The stresses calculated during the analyses are averaged across the elemental Gauss points, which are themselves a short distance from the nodes.

5.6.1. CASE 1 – CONCRETE CANTILEVER BEAM

The concrete cantilever beam is 2000mm long, 300mm deep and 300mm wide with a point load of 2kN at its free end. The boundary conditions at the built-in end of the cantilever are fully fixed, (i.e. no rotation, movement or strain is allowed at this position). The assumed elastic modulus at 20°C is $E_{20} = 14\ 000\ N/mm^2$ and Poisson's ratio at 20°C is $\nu = 0.3$. The load is positioned at the tip of the cantilever; and is distributed uniformly between the nodes at this point. Case 1 will be used to study the bending properties of the flat shell elements.

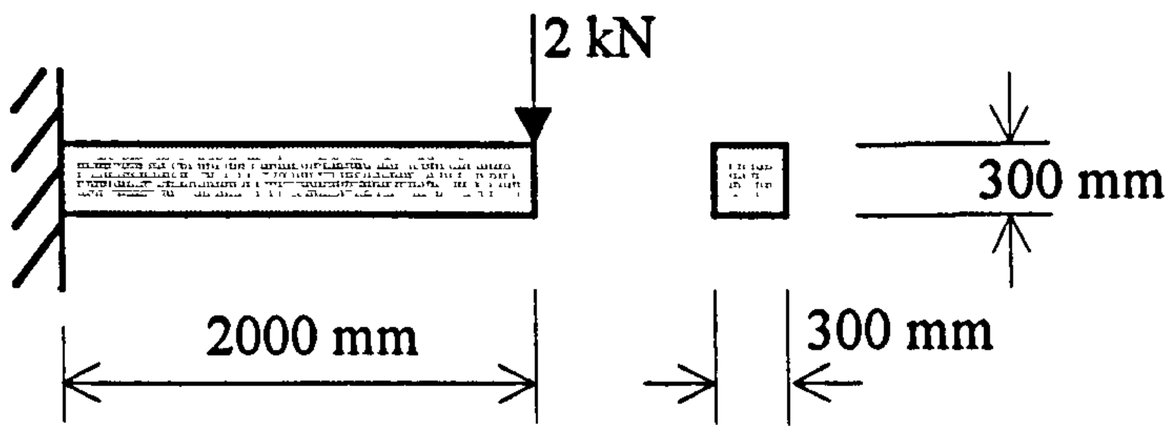

Figure 5-10. Case 1 – Concrete cantilever beam

The closed form linear elastic theoretical solution for the deflection caused by a point load at the end of a cantilever beam is given by

$$\Delta = \frac{PL^3}{3EI} \qquad 5\text{-}89$$

The second moment of area is given by

$$I_{xx} = \frac{BD^3}{12} = \frac{300 \times 300^3}{12} = 6.75 \times 10^8\, mm^4 \qquad 5\text{-}90$$

Therefore using equation 5-89 gives a total deflection of

$$\Delta = \frac{2000 \times 2000^3}{3 \times (14 \times 10^3) \times (6.75 \times 10^8)} = 0.5644 mm$$

The stress gradient at the support of the cantilever may be found using classic bending theory, which gives

$$\sigma = \frac{My}{I_{xx}} \qquad 5\text{-}91$$

where

M is the bending moment at the point where the stress is required,

y is the dimension from the neutral axis to the outermost fibres of the beam,

For the cantilever beam example, the bending moment at the support will be

$$M = 2000 \times 2000 = 4000000 Nmm$$

Therefore the stress at the outermost fibres of the beam at the support is

$$\sigma = \frac{4000000 \times 150}{6.75 \times 10^8} = 0.889 \text{N/mm}^2$$

5.6.2. Case 2 – Steel Simply Supported Plate

A 2000mm square steel plate with a thickness of 8mm has been used in many of the validations; this is shown in Figure 5-11. Poisson's ratio at 20°C is ν=0.3 and the elastic modulus at 20°C is E_{20} = 205000 N/mm^2. Case 2 will be used to validate the plate bending properties.

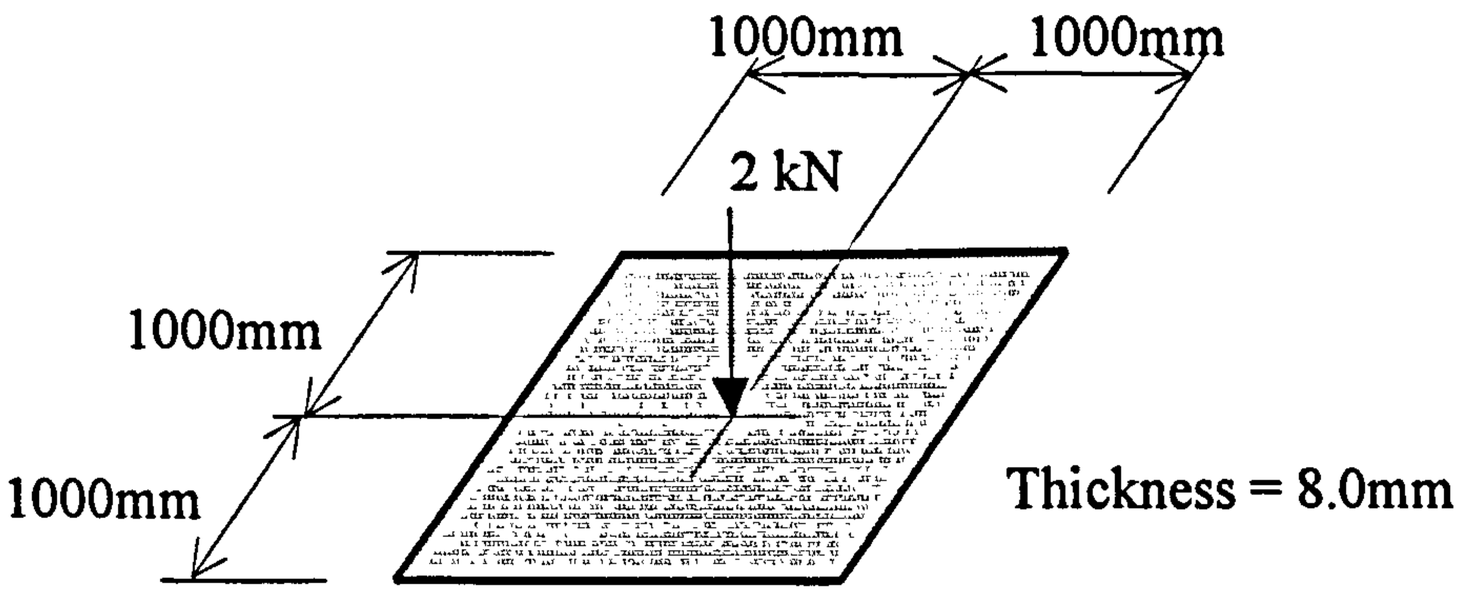

Figure 5-11. Steel simply supported plate

Using the symmetry inherently found within this type of plate example, it is possible to model only a quarter of the plate provided the correct boundary conditions are implemented. These are shown in Figure 5-12.

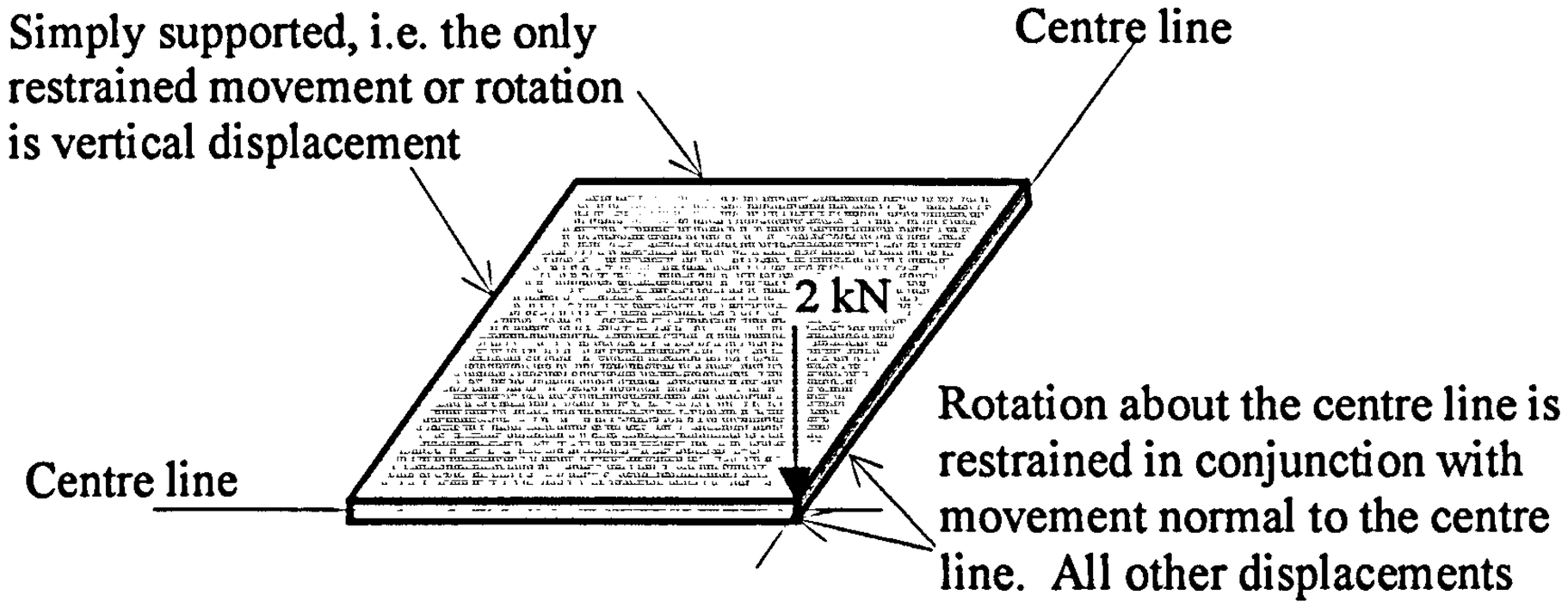

Figure 5-12. Boundary conditions for modelling one quarter of a simply supported plate using symmetry

Timoshenko [63] gives the linear elastic theoretical solution for the central deflection as

$$\Delta_c = 0.0116\frac{PL^2}{D} \qquad 5\text{-}92$$

where

P is the central point load

L is the side length of the square plate

$$D = \frac{Et^3}{12(1-\nu^2)} \qquad 5\text{-}93$$

Therefore

$$D = \frac{205\times10^3(8.0)^3}{12(1-0.3^2)} = 9.6\times10^6\,Nmm$$

Giving a central deflection of

$$\Delta_c = \frac{0.0116\times(2.0\times10^3)\times2000^2}{96117\,21.6} = 9.65mm$$

An approximation by Timoshenko [63] gives the bending moment per unit width at the centre of the elastic square plate subject to a point load as

$$M_{xx} = 0.298P = 0.298\times2000 = 596Nmm \qquad 5\text{-}94$$

Timoshenko [63] gives the solution for the maximum stress at the extreme fibres of an elastic plate as

$$\sigma = \frac{6M_{xx}}{h^2} = \frac{6 \times 596}{8^2} = 56N/mm^2 \qquad 5\text{-}95$$

5.6.3. CASE 3 – DEEP STEEL BEAM

To validate the plane stress membrane characteristics, a deep beam analysis is carried out. The material is steel with an assumed elastic modulus of 205000N/mm^2 and Poisson's ratio of 0.3.

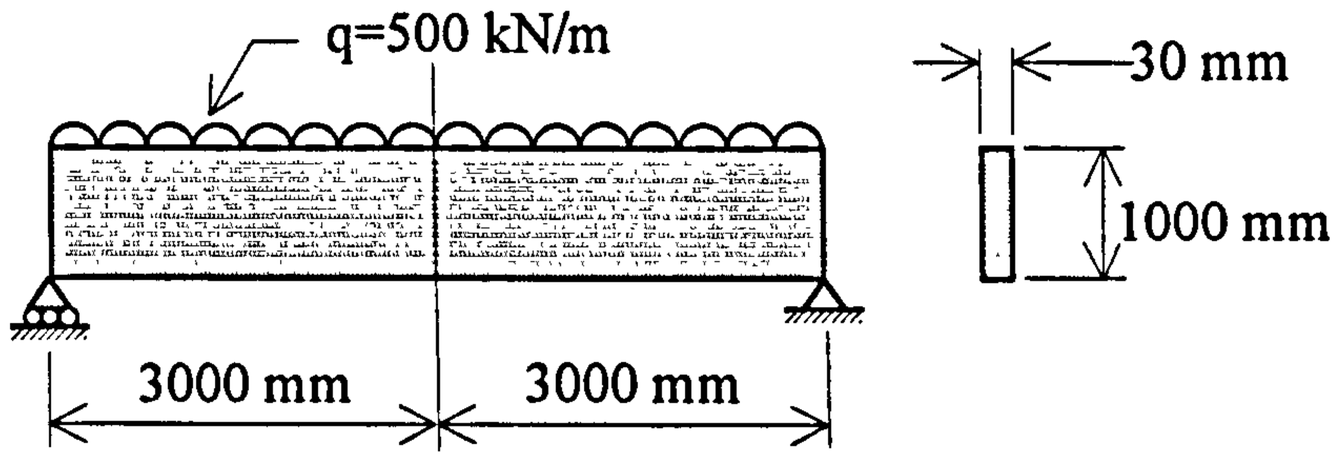

Figure 5-13. Deep steel beam

In elementary beam bending theory it is assumed that plane sections remain plane during bending, with no account taken of the presence of shear deformation. Shear stresses cause plane cross-sections to distort during bending, and significantly affect the stresses and displacements of the beam when the depth of the beam is a substantial proportion of its length. To validate the membrane characteristics of the flat shell element, the deep beam shown in Figure 5-13 was analysed. Timoshenko [64] gives the theoretical solution for the central deflection; this method takes into account the effect of the shearing force.

$$\Delta_c = \frac{5}{24}\frac{qL^4}{EI}\left[1 + \frac{12}{5}\frac{c^2}{L^2}\left(\frac{4}{5} + \frac{\nu}{2}\right)\right] \qquad 5\text{-}96$$

where notation is shown in Figure 5-14

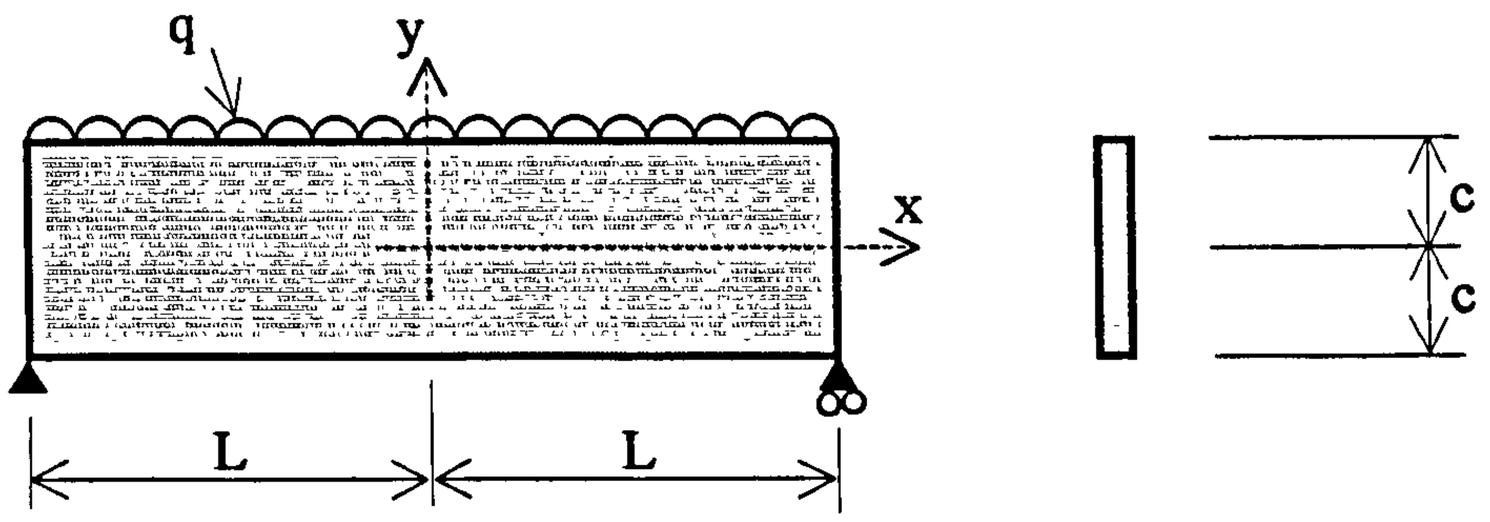

Figure 5-14. Deep beam deflection and stress equation notation

The central deflection is given by

$$\Delta_c = \frac{5}{24}\frac{500\times 3000^4}{205\times 10^3\times 2.5\times 10^9}\left[1+\frac{12}{5}\frac{(500)^2}{(3000)^2}\left(\frac{4}{5}+\frac{0.3}{2}\right)\right] = 17.51mm$$

Timoshenko also provides a calculation for stress gradients across a deep beam:

$$\sigma_x = \frac{q}{2I}\left(L^2-x^2\right)y+\frac{q}{2I}\left(\frac{2}{3}y^3-\frac{2}{5}c^2y\right) \qquad 5\text{-}97$$

Therefore the central extreme-fibre stresses are

$$\sigma_{max} = \frac{500}{2\times\left(2.5\times 10^9\right)}\left(3000^2-0^2\right)500+$$
$$\frac{500}{2\times\left(2.5\times 10^9\right)}\left(\frac{2}{3}500^3-\frac{2}{5}500^2\times 500\right) = 453.3 \ \ N/mm^2$$

Symmetry was utilised for the computer model predictions, and the boundary conditions were as shown in Figure 5-15.

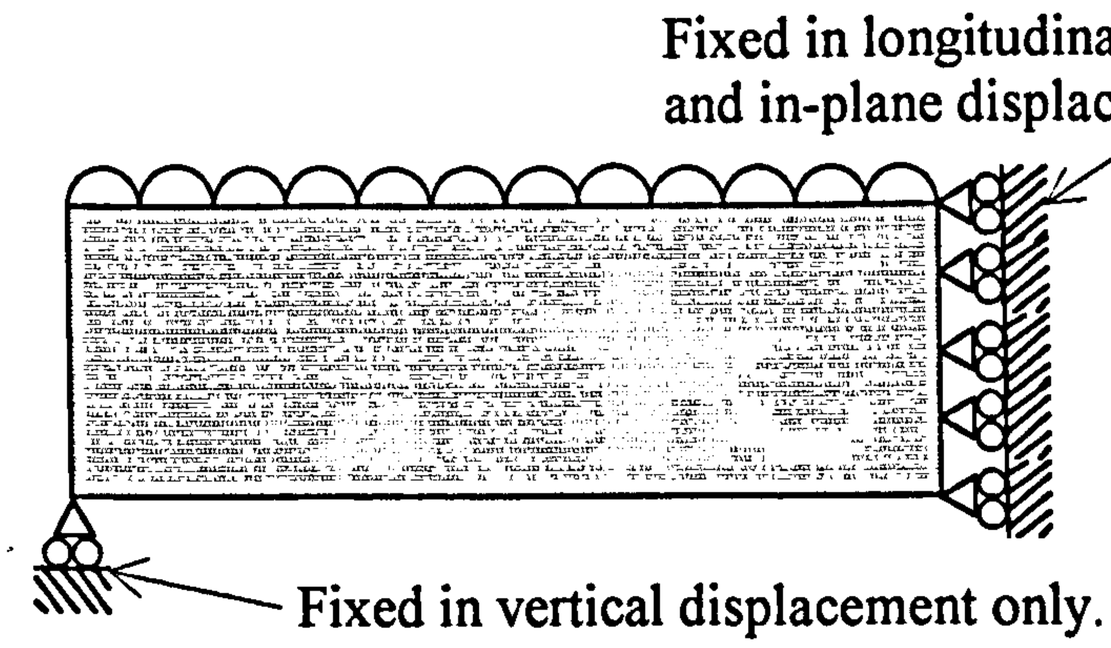

Figure 5-15. Boundary conditions for modelling deep steel beam using symmetry

5.7 VALIDATION OF A SINGLE-LAMINA, ELASTIC, FLAT SHELL ELEMENT

The single-lamina, elastic, flat shell element is now tested against the three cases defined in Section 5.6.

5.7.1 VALIDATION OF THE SINGLE-LAMINA, ELASTIC, FLAT SHELL ELEMENT IN BENDING

The validation of the cantilever example, Case 1, uses a conventional convergence test in which the number of elements along the beam is progressively increased, as shown in Figure 5-16.

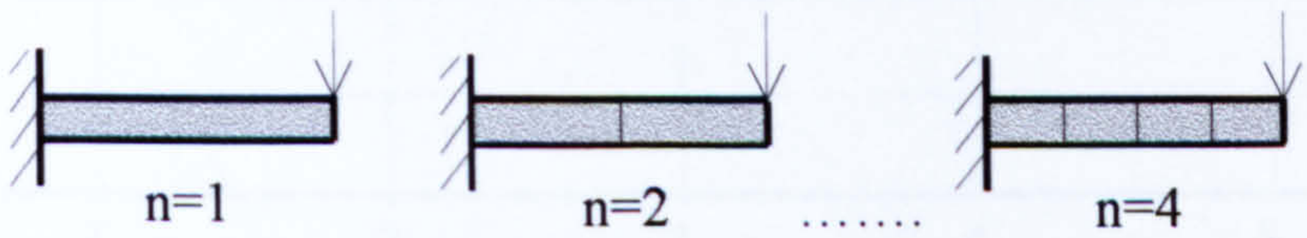

Figure 5-16. Convergence study for the cantilever beam

Figure 5-17 shows the results of the convergence study of the cantilever beam in terms of deflection. It will be noted that the finite element analysis quickly converges to a satisfactory result of less than 1% error from the closed form solution when five elements are used.

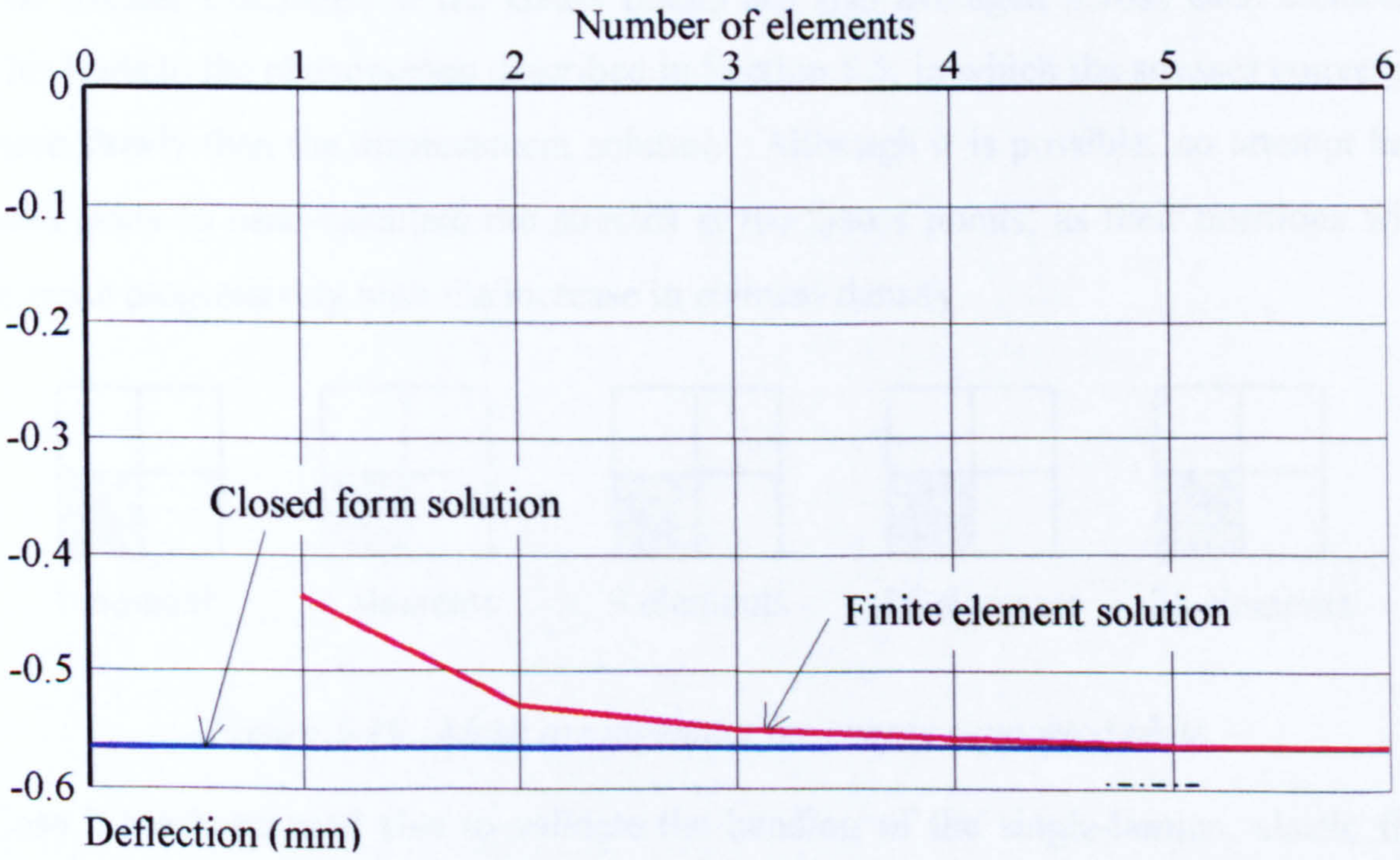

Figure 5-17. Convergence study of a cantilever beam

Figure 5-18 shows a convergence curve for the extreme stress given by the finite element solution for the cantilever beam at its built-in support compared to the closed form solution.

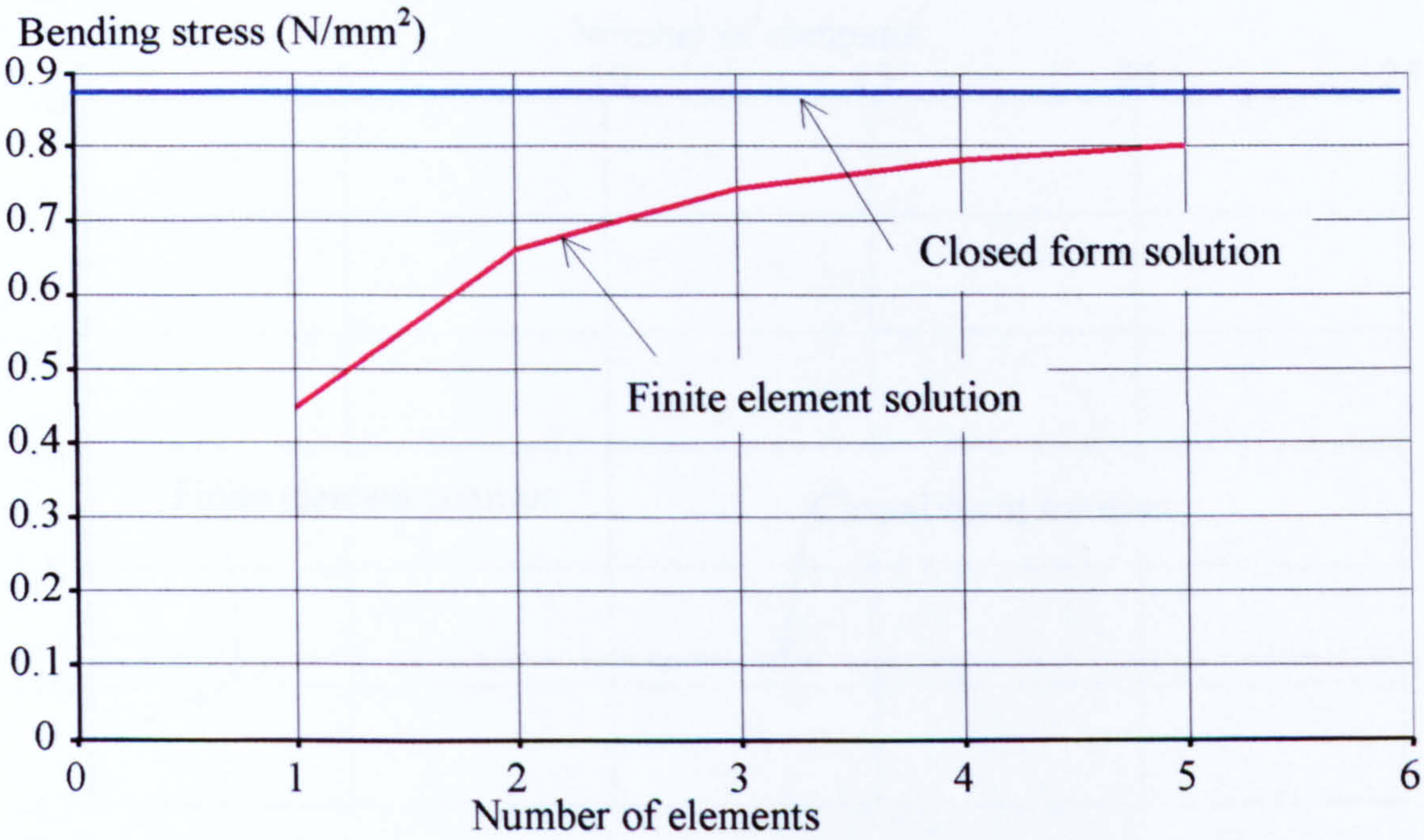

Figure 5-18. Convergence of stress gradient at support of cantilever beam

There is an expected variation within the results because the closed form solution gives the stress at the support point whilst the finite element procedure gives an approximation at the Gauss points, which are situated away from the built-in end. The stresses calculated at the Gauss points are also averaged across each element. This leads to the phenomenon described in Section 5.5, in which the stresses converge more slowly than the displacement solution. Although it is possible, no attempt has been made to hand-calculate the stresses at the Gauss points, as their positions will relocate progressively with the increase in element density.

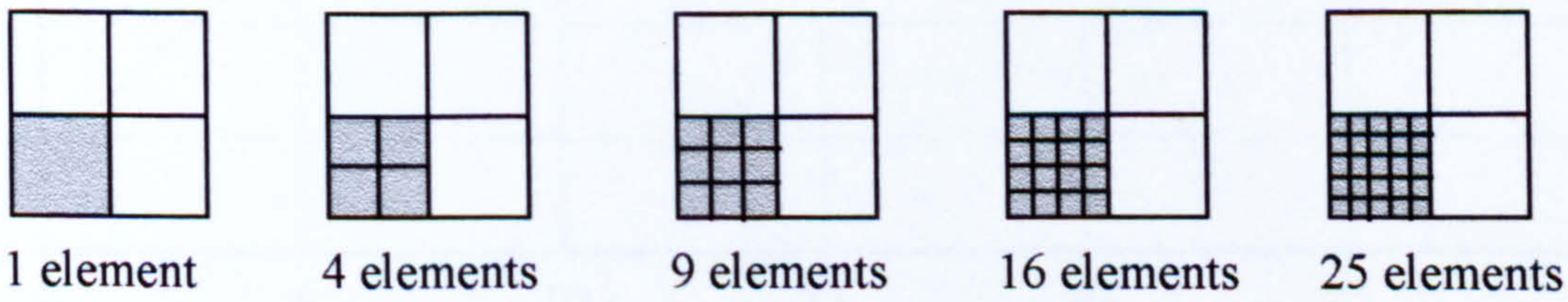

Figure 5-19. Mesh arrangement for simply supported plate

Case 2 has been used also to validate the bending of the single-lamina, elastic flat shell element. A convergence study was carried out using different meshes, as shown in Figure 5-19, to determine the number of elements required for an accurate result.

Figure 5-20 shows the convergence study for deflection. The result converges quickly as the number of elements increases, and even a sparse mesh of just four elements gives an acceptable error of below 1%.

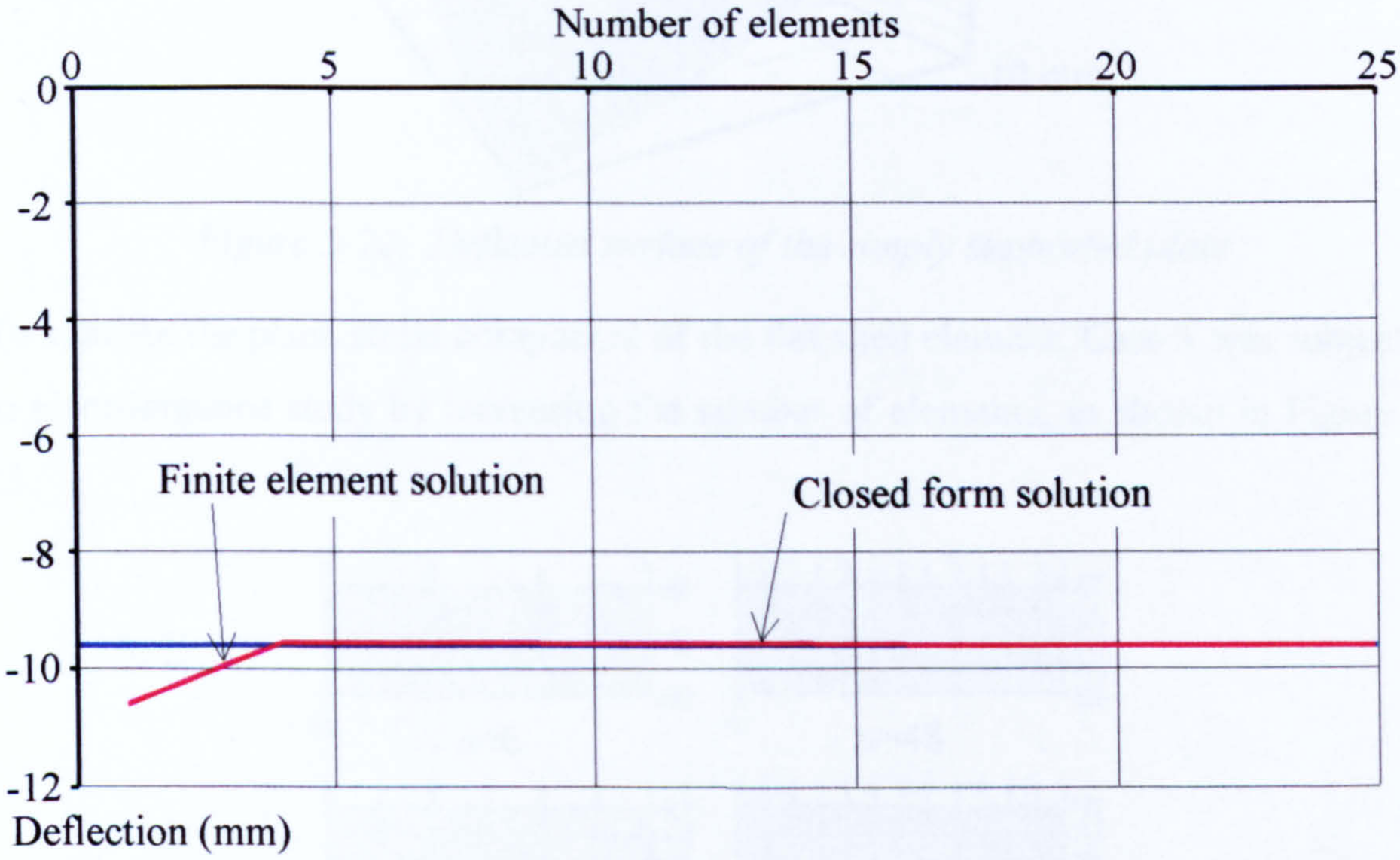

Figure 5-20. Convergence study for the single layer plate example

Figure 5-21 shows the corresponding results for the convergence study in terms of the stress at the centre of the steel plate.

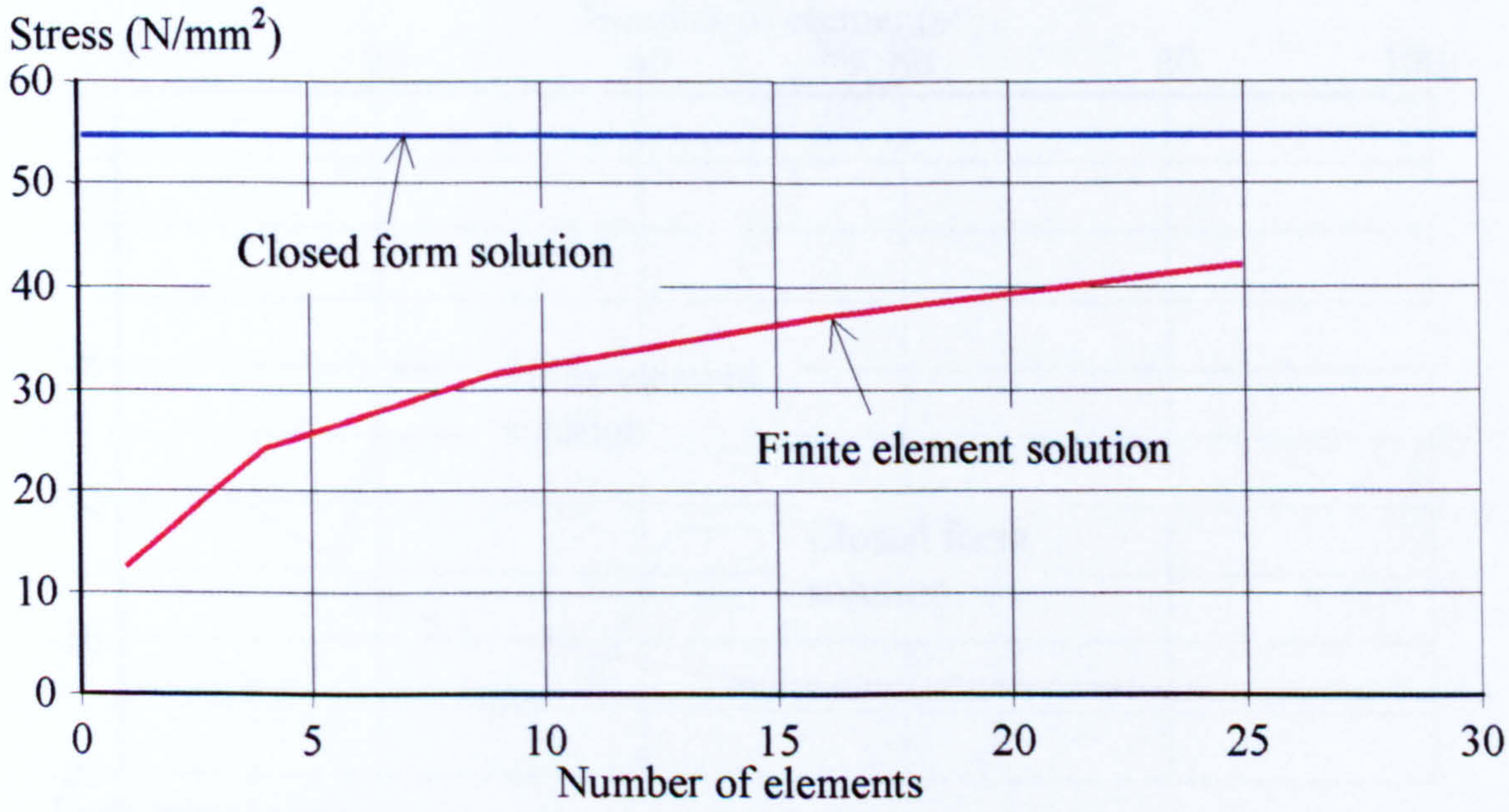

Figure 5-21. Stress convergence of a simply supported plate

A surface deflection plot for the plate is shown in Figure 5-22, which exhibits a synclastic curvature at the supporting corner.

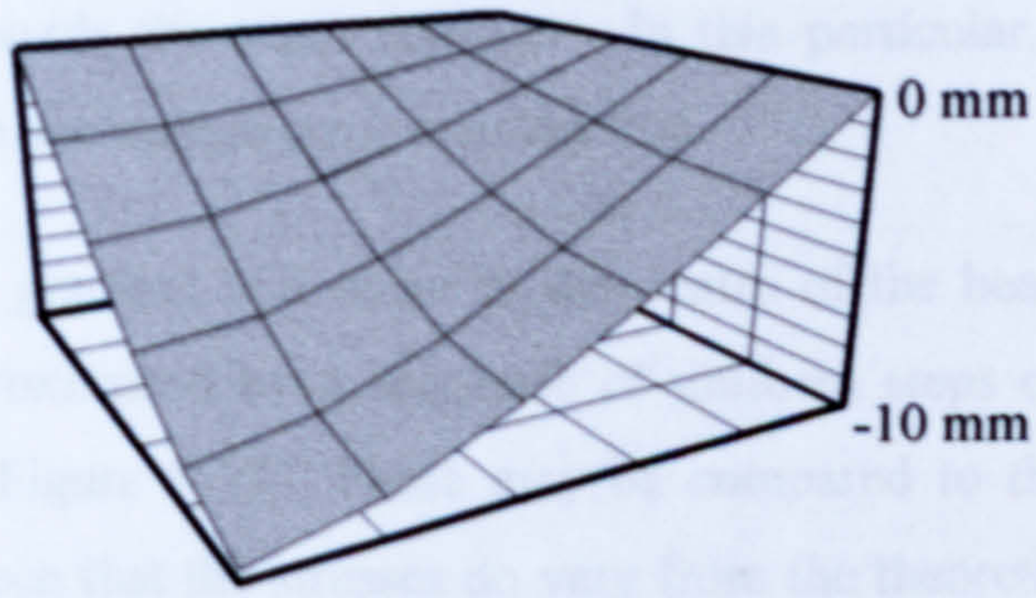

Figure 5-22. Deflected surface of the simply supported plate

To validate the plane stress component of the flat shell element, Case 3 was subjected to a convergence study by increasing the number of elements, as shown in Figure 5-23.

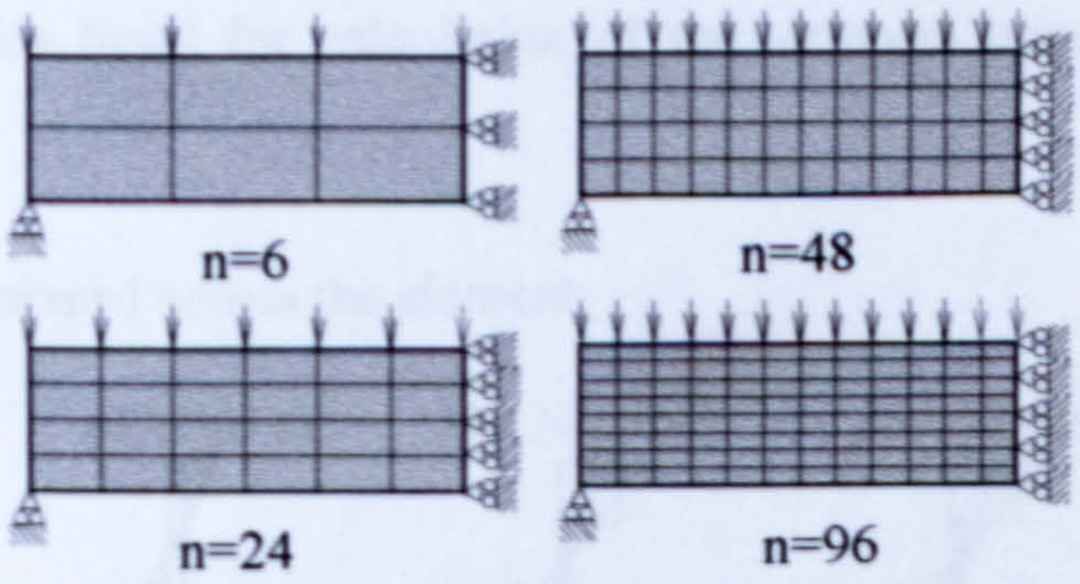

Figure 5-23. Mesh configurations used for convergence study for plane stress characteristics of the laminated flat shell element

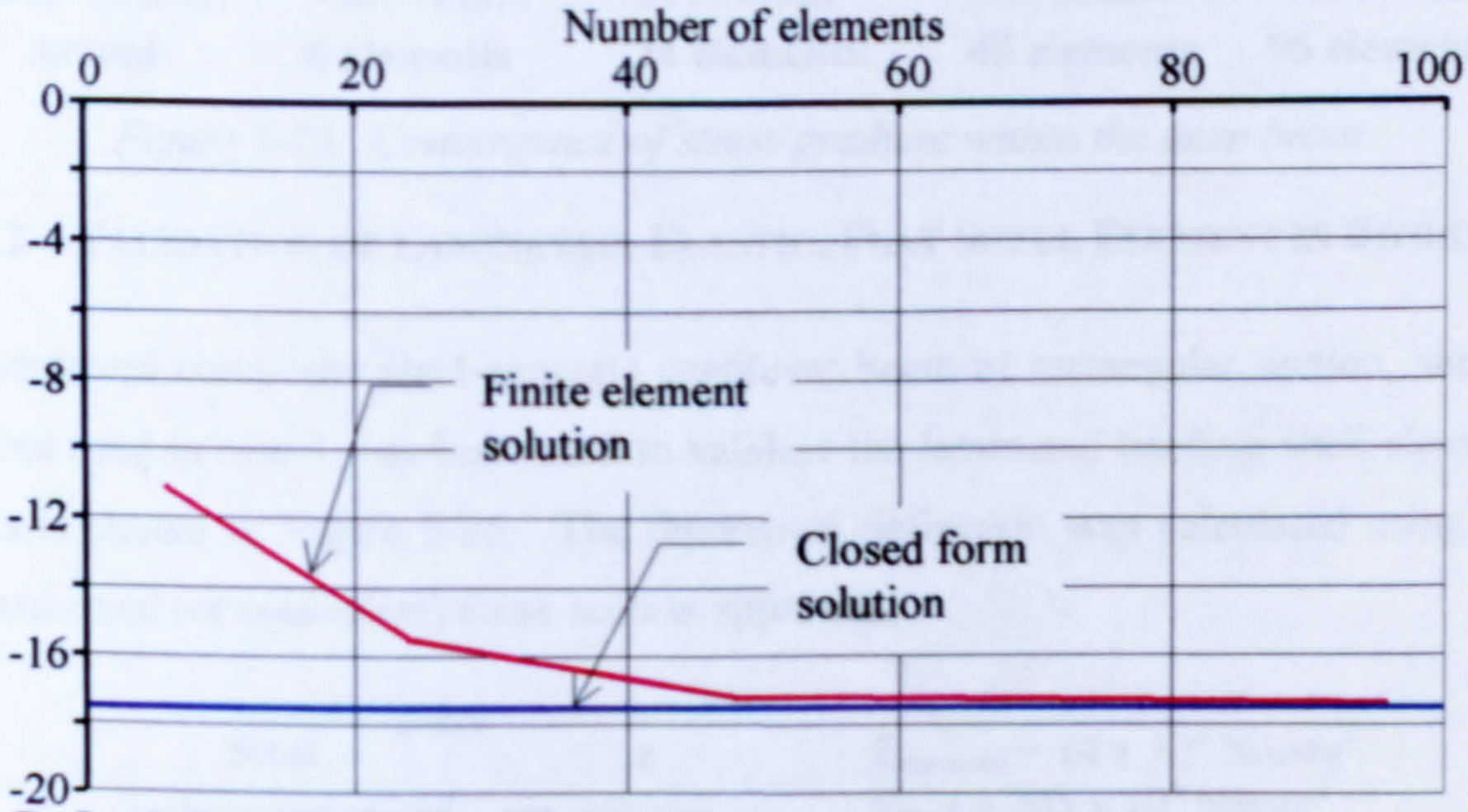

Figure 5-24. Deflection convergence study for plane stress characteristics of a single laminated flat shell element

The results for the deflection convergence test are shown in Figure 5-24. Once again this test shows that as the number of elements is increased the computed results

converge quickly towards the exact solution. In this particular solution, when 48 elements are used, the percentage error is below 1%.

The maximum stress gradient will occur at the centre of the beam span; this stress gradient will be approximated by a sequence of uniform steps of stress across the section as shown in Figure 5-25. These may be compared to the calculated stress gradient. It can be seen that the stresses do vary from the theoretical stress gradient. This will be due a combination of:

- The finite element code working in convergence criteria relative to a displacement field (as opposed to stress field criteria).

- The gauss points (used for calculation of the stresses) being remote from the nodes.

- The stresses averaged across the element.

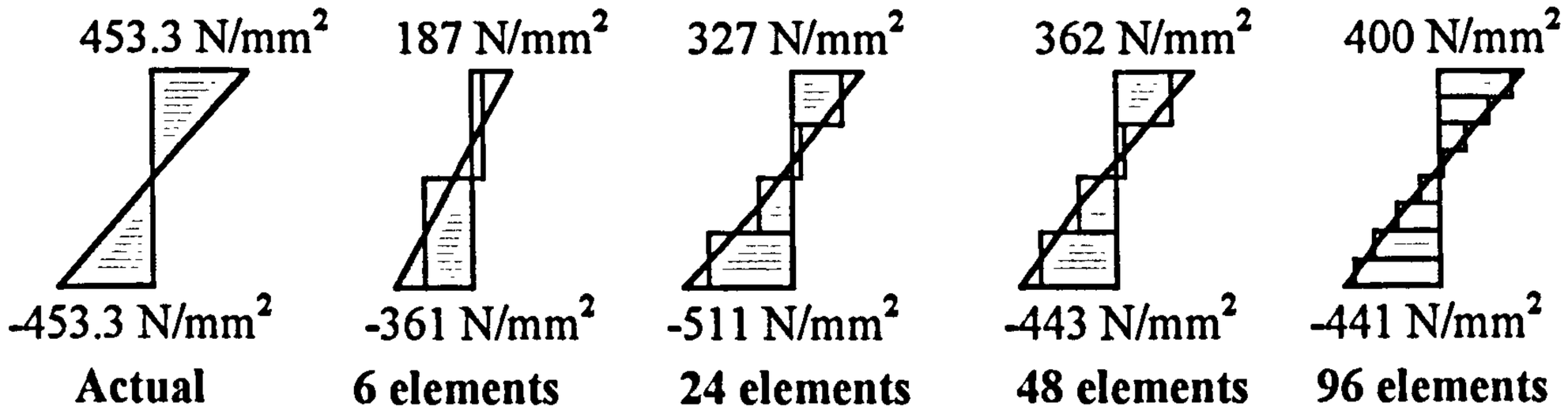

Figure 5-25. Convergence of stress gradient within the deep beam

5.7.2 VALIDATION OF LAMINATED, ELASTIC, FLAT SHELL ELEMENT IN BENDING

A contrived composite steel-concrete cantilever beam of rectangular section, similar to that used in case 1, has been used to validate the laminated bending shell element. This is shown in Figure 5-26. The theoretical deflection was calculated using the transformed (or equivalent) cross-section approach.

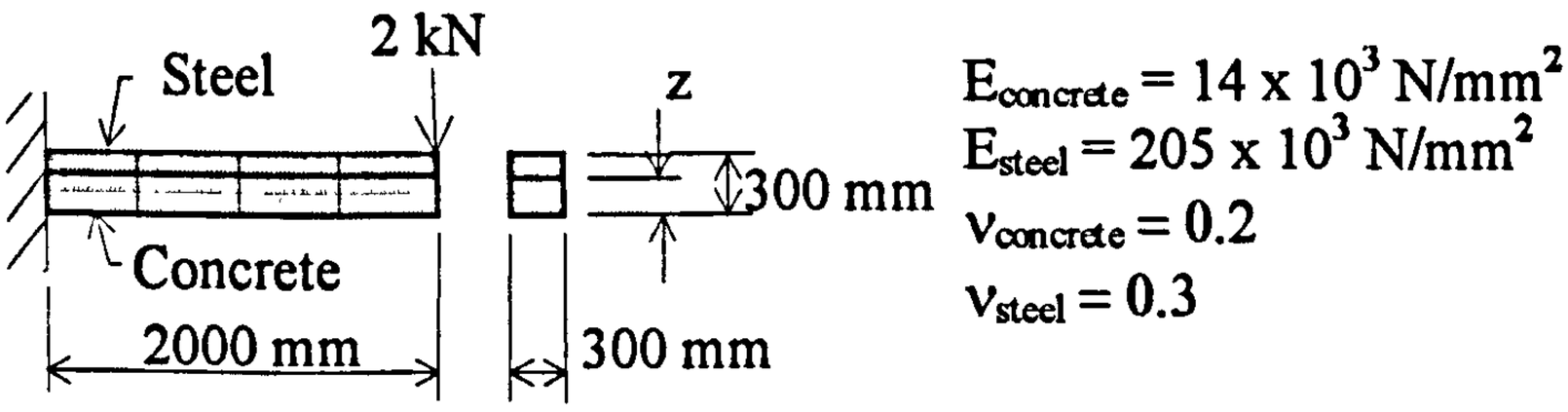

Figure 5-26. Composite material cantilever beam (Two layers)

The interface between the steel and concrete (dimension 'z') has been increased in 10mm intervals through the depth of the section, in order to check that the contribution to the element stiffness matrix for each layer is correct.

A typical closed form solution for the case where the steel/concrete interface (z) is at a depth of 150mm is given below.

The position of the neutral axis (plane of zero strain) is found by taking moments about the beam soffit.

$$NA = \frac{(150 \times 225) + (150 \times 75 \times (14000/205000))}{(150) + (150 \times (14000/205000))} = 215.41mm$$

Therefore the second moments of area of the steel and concrete portions of the beam are

$$I_{Steel} = \frac{300 \times (300 - 215.41)^3}{3} + \frac{300 \times (215.41 - 150)^3}{3} = 8.85 \times 10^7 mm^4$$

$$I_{Concrete} = \frac{300 \times 215.41^3}{3} - \frac{300 \times (215.41 - 150)^3}{3} = 9.72 \times 10^8 mm^4$$

Hence the deflection is (equation (5-89))

$$\Delta = \frac{PL^3}{3((E_{Steel} I_{Steel}) + (E_{Concrete} I_{Concrete}))}$$

$$\Delta = \frac{2000 \times 2000^3}{3 \times ((205000 \times (8.85 \times 10^7)) + (14000 \times) \times (9.72 \times 10^8))} = 0.168mm$$

Figure 5-27 shows the deflection of the computer model compared to the deflection found by hand calculations. The maximum percentage error found is 1.78%.

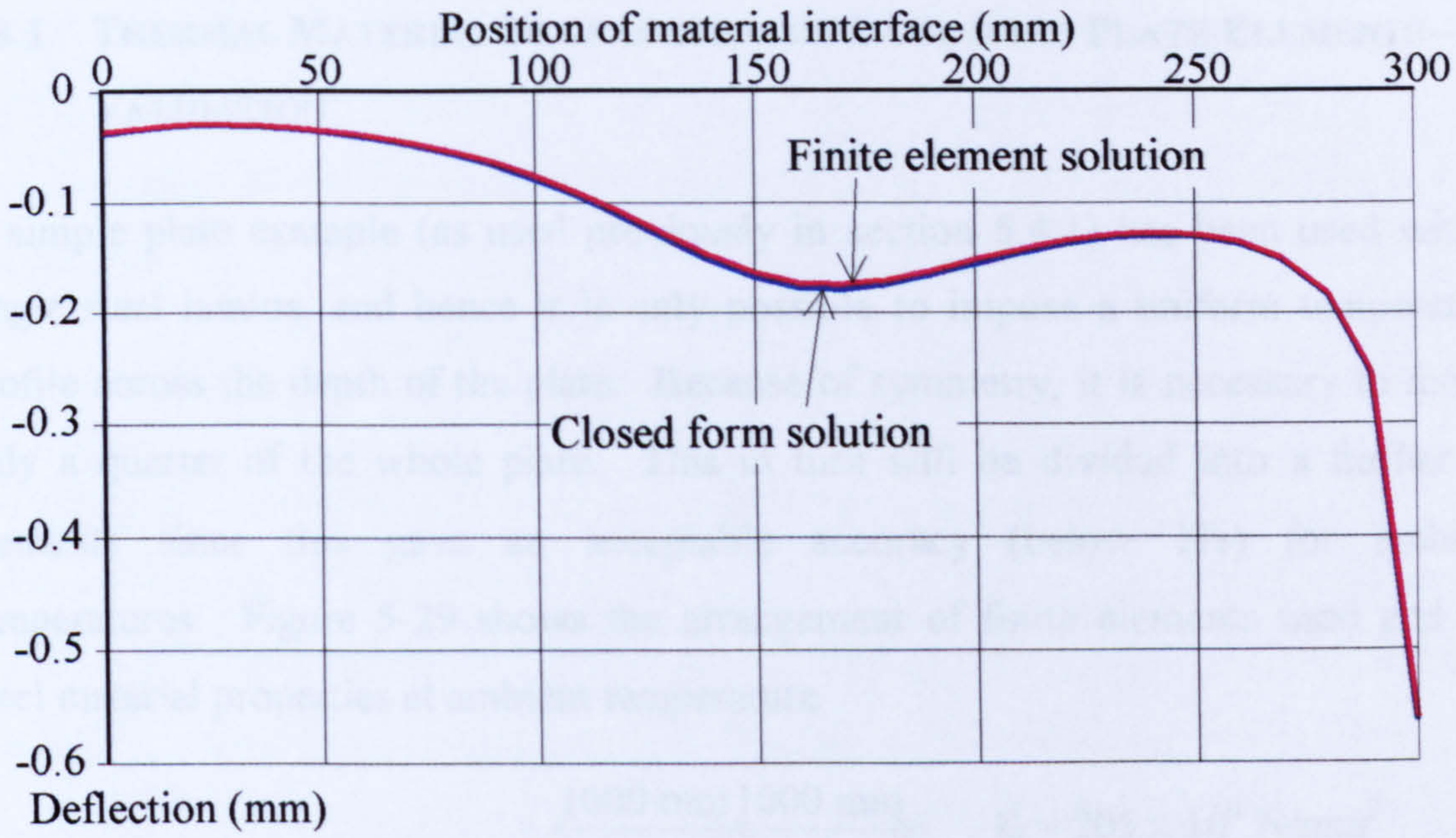

Figure 5-27. Convergence study of a two layer composite cantilever

Figure 5-28 shows the bending stress found in each of the layers. These are satisfactory.

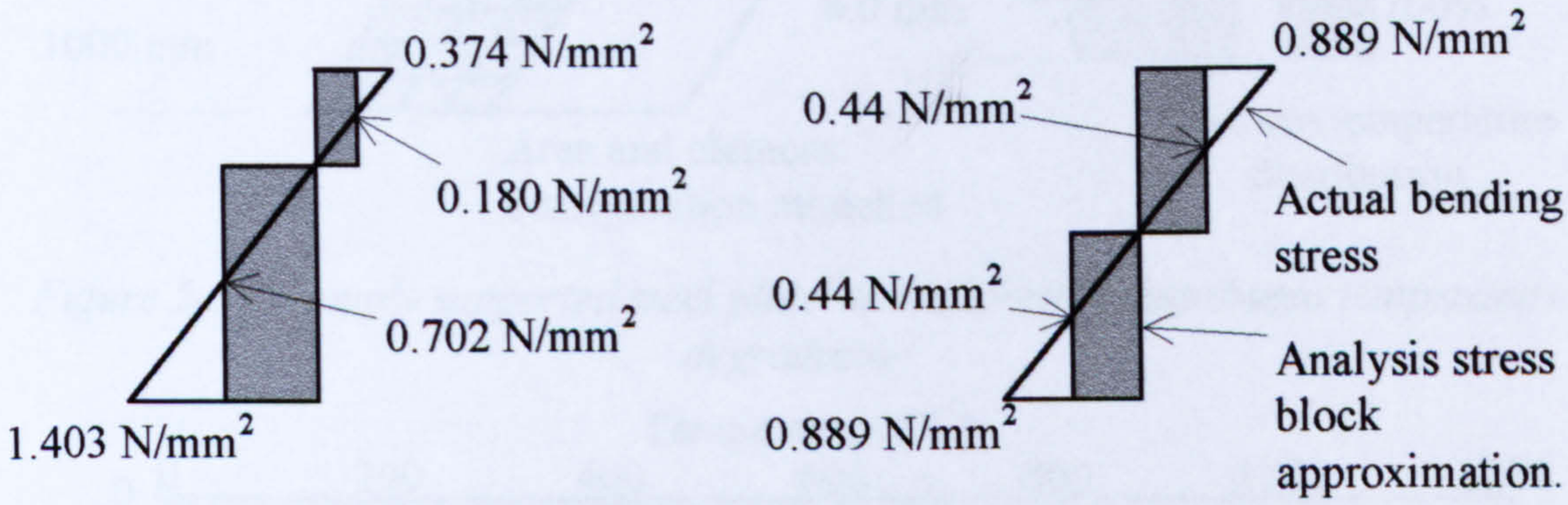

Interface at 50mm from top face *Interface at bottom of element*

Figure 5-28. Layer stress blocks at intervals through the cantilever

5.8 Elastic Thermal Material Degradation of Laminated Shell Elements

The material degradation of laminated shell elements due to increase in temperature can be achieved simply by reducing the elastic modulus of the material. For the degradation of steel and concrete Eurocode 4 provides a way of modelling the stress-strain characteristics.

5.8.1 THERMAL MATERIAL DEGRADATION OF LAMINATED PLATE ELEMENTS – VALIDATION

A simple plate example (as used previously in section 5.4.1) has been used with a single steel lamina, and hence it is only possible to impose a uniform temperature profile across the depth of the plate. Because of symmetry, it is necessary to model only a quarter of the whole plate. This in turn will be divided into a further 16 elements since this gave an acceptable accuracy (below 1%) for ambient temperatures. Figure 5-29 shows the arrangement of finite elements used and the steel material properties at ambient temperature.

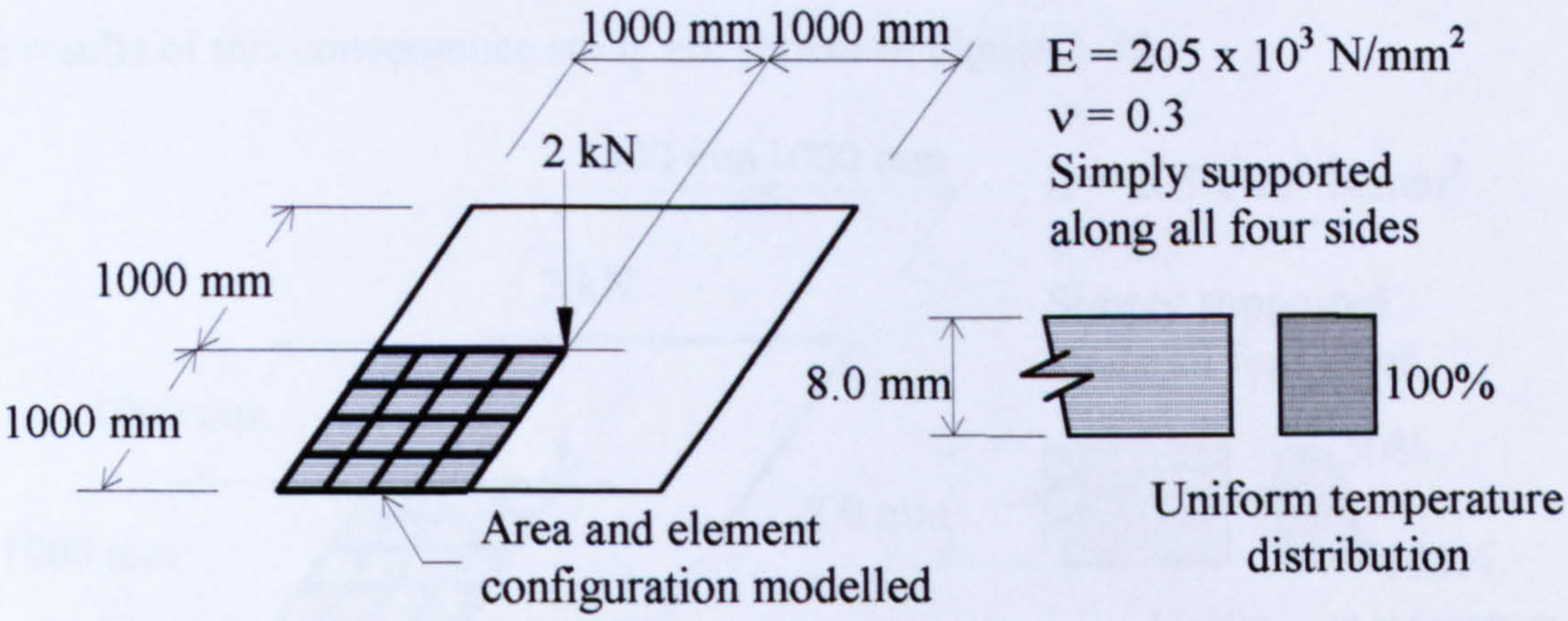

Figure 5-29. Simply supported steel plate with uniformly distributed temperature degradation

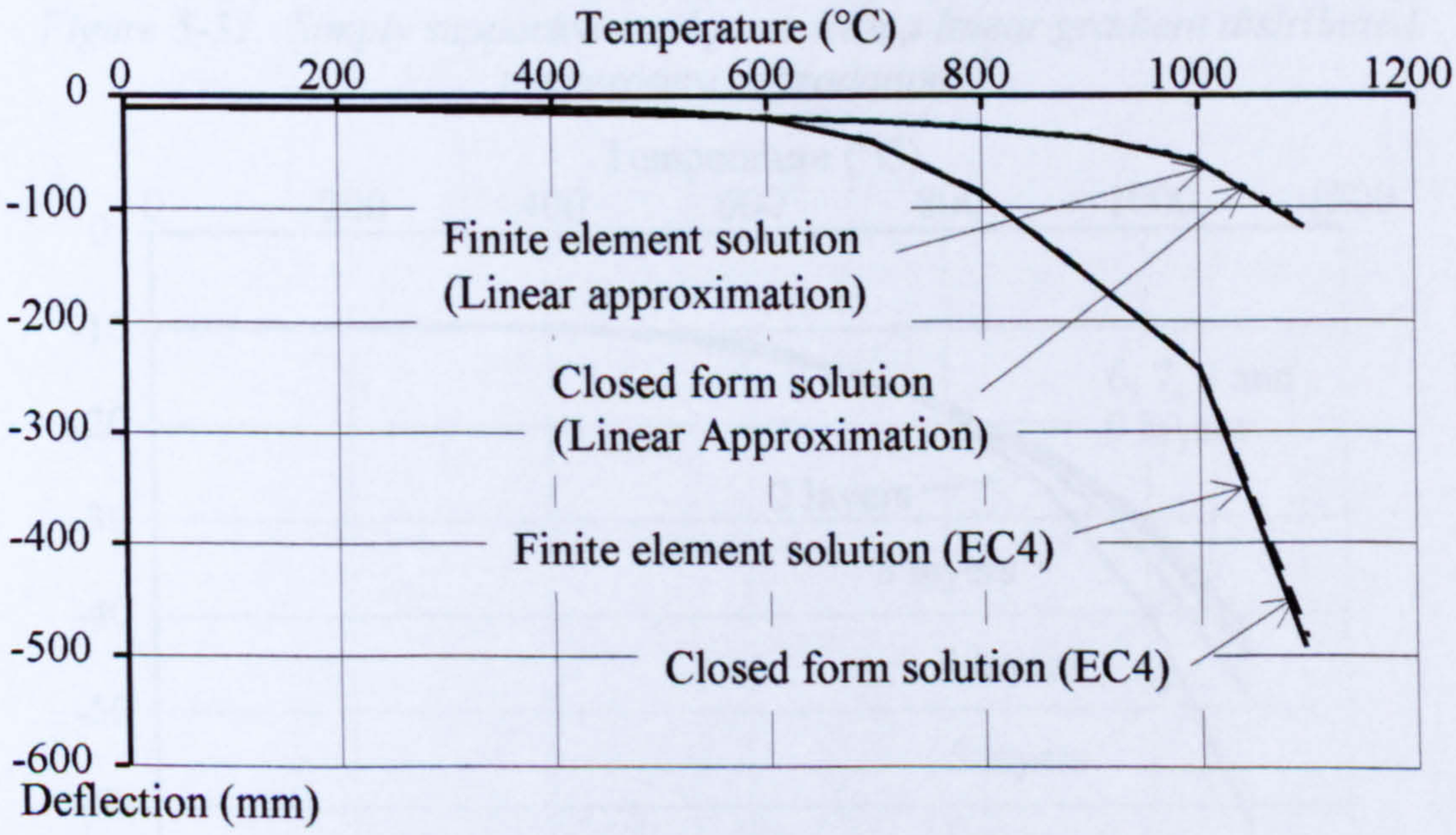

Figure 5-30. Central deflection of a simply supported plate subject to thermal material degradation from EC4 and a linear representation of EC4 degradation

Finite element analyses have been carried out using both the linear approximation and the EC4 non-linear approximation. Calculated deflections in relation to temperature

are shown in Figure 5-30. A comparison is made between the closed form solution and the finite element solution for both the linear and non-linear approximations and it can be noted that the correlation is excellent with the maximum percentage error being 1.1%.

5.8.2 NON-UNIFORM TEMPERATURE DISTRIBUTION

A convergence test was carried out on the steel plate shown in Figure 5-31. A linear temperature gradient was assumed between bottom and top face temperatures of 100% and 50% respectively. All thermal bowing effects were restrained. The number of laminae used to represent the plate was then varied between two and nine. The results of this convergence study are shown in Figure 5-32.

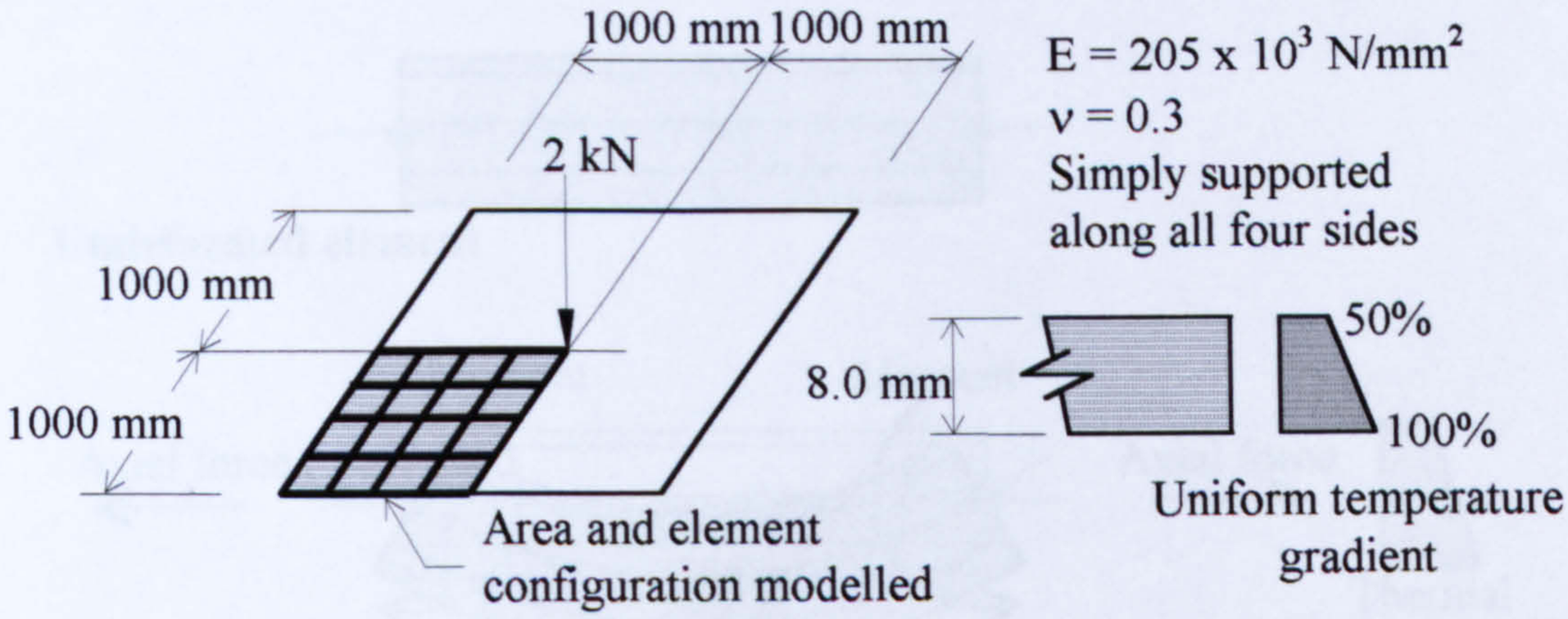

Figure 5-31. Simply supported steel plate with a linear gradient distributed temperature degradation

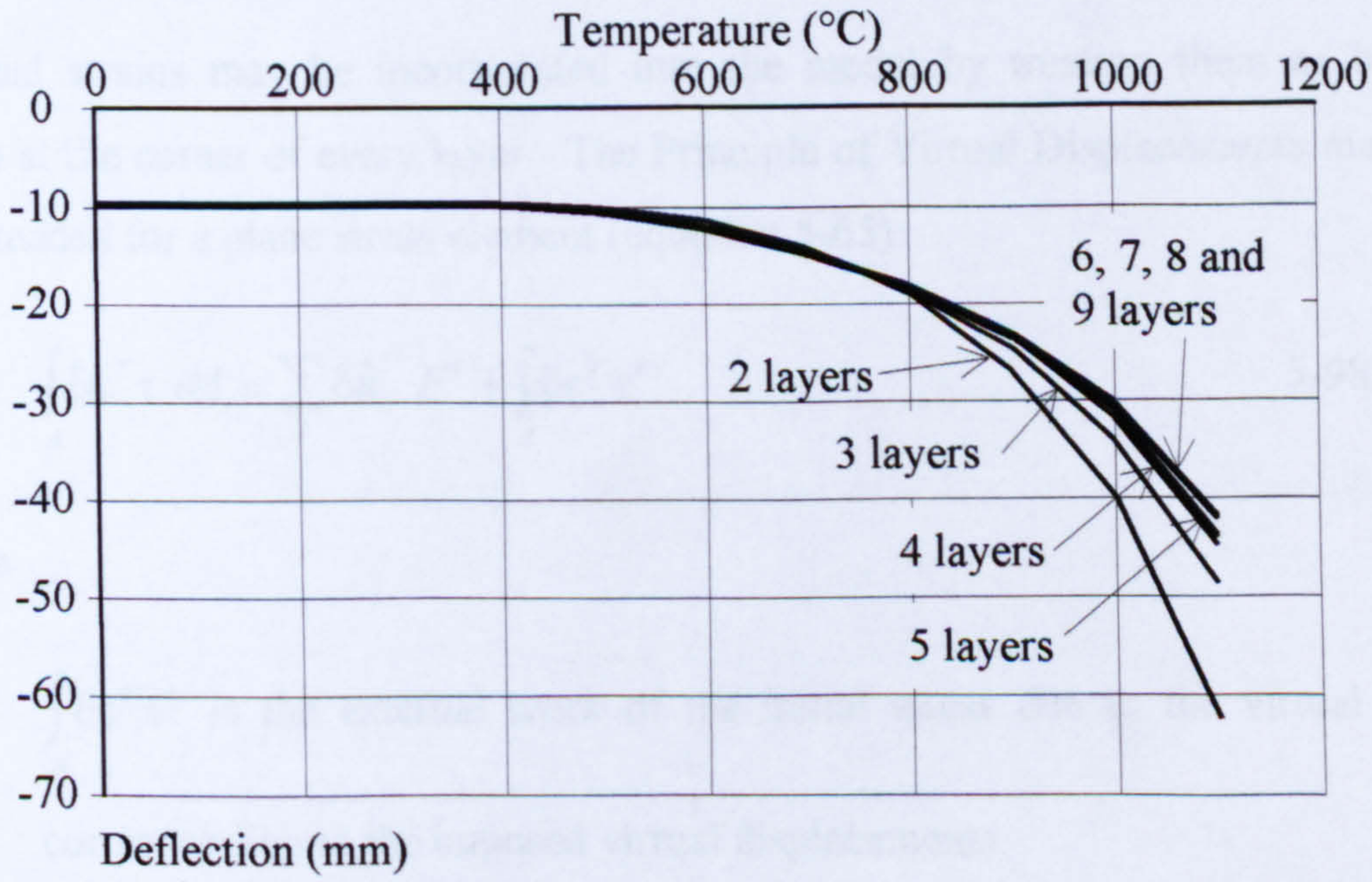

Figure 5-32. Convergence study of the number of layers required for the simulation of an irregular temperature gradient.

5.9 THERMAL EXPANSION AND BOWING OF LAMINATED SHELL ELEMENTS

If it is assumed that the lower surface of a plate has a temperature that exceeds that of the upper surface, the plate will have a tendency to bow downwards due to the non-uniform heating pattern. Within a laminated plate element, a thermal gradient is represented as previously, with each lamina having a different uniform temperature across its depth. The free strain of each lamina is computed and applied as an axial force at the mid-plane of the lamina. The equivalent moments and axial forces necessary for restraint may then be calculated about the reference plane of the element and applied implicitly to the initial force vector. This is shown schematically in Figure 5-33.

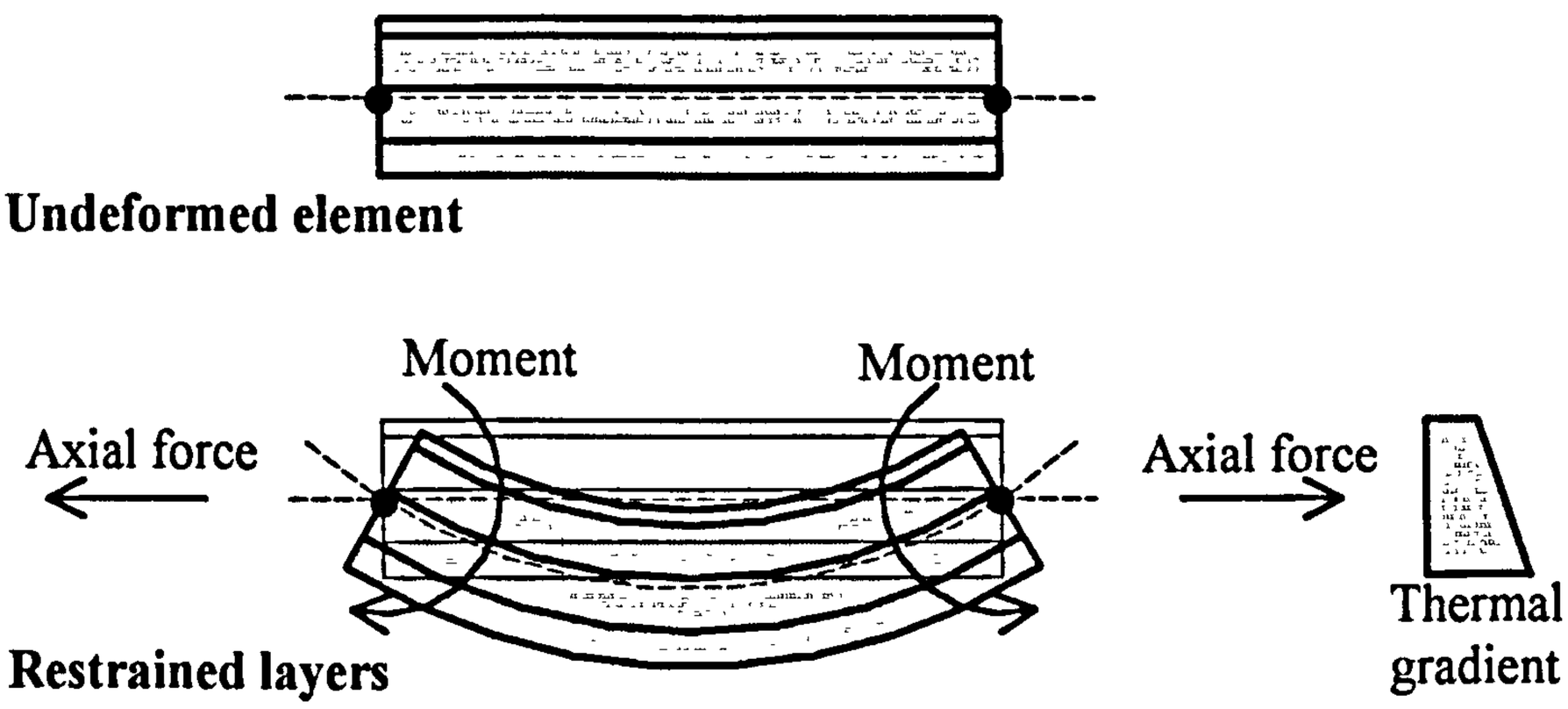

Figure 5-33. Thermal bowing of a laminated plate element

Thermal strains may be incorporated into the model by treating them as bi-axial forces at the corner of every layer. The Principle of Virtual Displacements may then be extended for a plane stress element (equation 5-65)

$$\int_A \delta\varepsilon^T \tau \, dA = \sum_i \delta\hat{u}^{iT} F^i + \int_A \delta\varepsilon^T \tau^i \qquad 5\text{-}98$$

where

$\int_A \delta\varepsilon^T \tau^i$ is the external work of the initial stress due to the virtual strains corresponding to the imposed virtual displacements.

Equation (5-68) can therefore be extended to

$$\bar{\hat{u}}^T\left[\int_A B^T C B \, dA\right]\hat{u} = \bar{\hat{u}}^T[F] + \bar{\hat{u}}^T\int_A B^T \tau^i \, dA \qquad 5\text{-}99$$

Since $\bar{\hat{u}}^T$ is an identity matrix, then the axial forces for each layer are given by

$$R_i = \int_A B^T \tau^i \, dA \qquad 5\text{-}100$$

where

$$\tau^i = -\frac{E\alpha}{1-\nu^2}\begin{bmatrix} 1 & \nu & 0 \\ \nu & 1 & 0 \\ 0 & 0 & \frac{1-\nu}{2} \end{bmatrix}\begin{bmatrix} 1 \\ 1 \\ 0 \end{bmatrix}\{T - T_o\} \qquad 5\text{-}101$$

in which

T_o is the initial temperature,

T is the temperature of the lamina.

α is its coefficient of thermal expansion,

These axial laminar forces may then be added into the analysis by calculating their resultant moments and forces about the mid-surface.

5.9.1 Thermal Expansion and Bowing of Laminated Shell Elements – Validations

The square steel plate used in previous validations has also been utilised to validate the thermal bowing within the finite element analysis (Figure 5-34). A convergence study was conducted in which the number of layers within the depth of the plate was increased from 2 to 9, to approximate the temperature gradient shown in Figure 5-34. At this stage of validation, thermal material degradation has been ignored. The plate is not loaded.

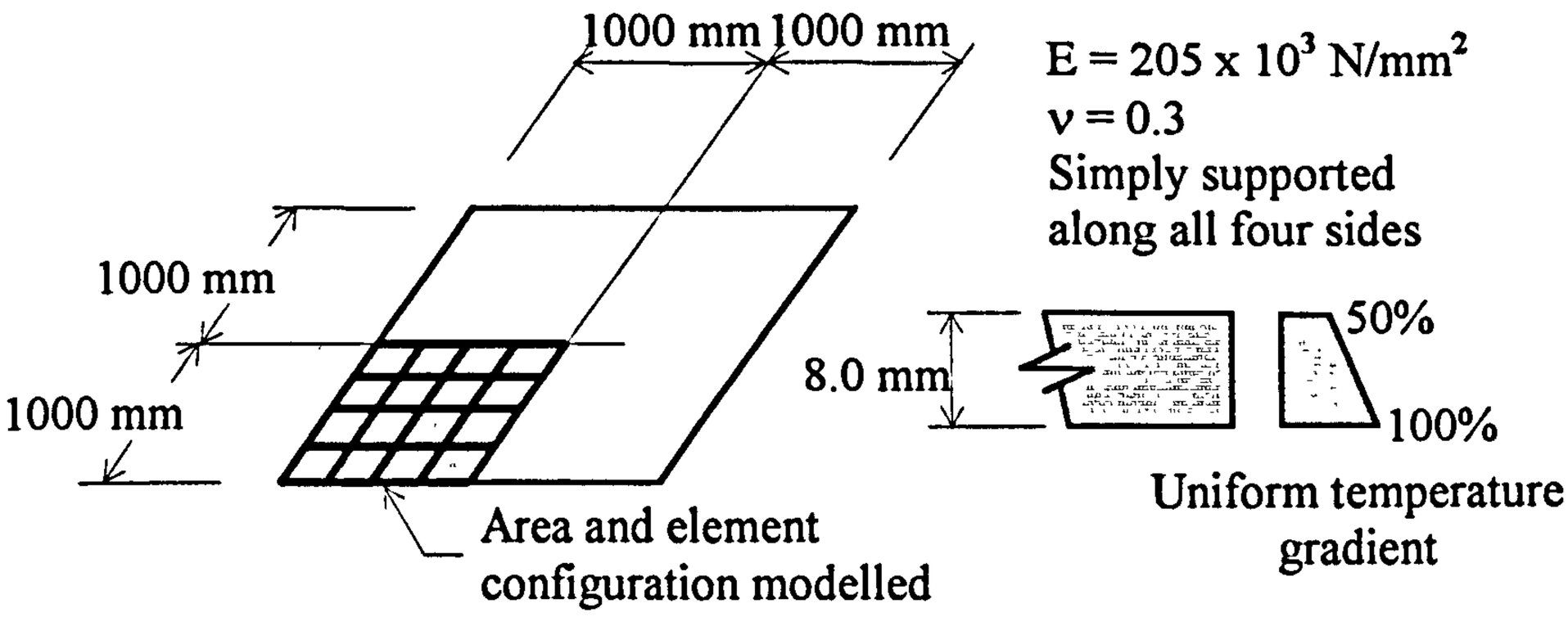

Figure 5-34. Thermal bowing of a simply supported steel plate with a linear temperature gradient

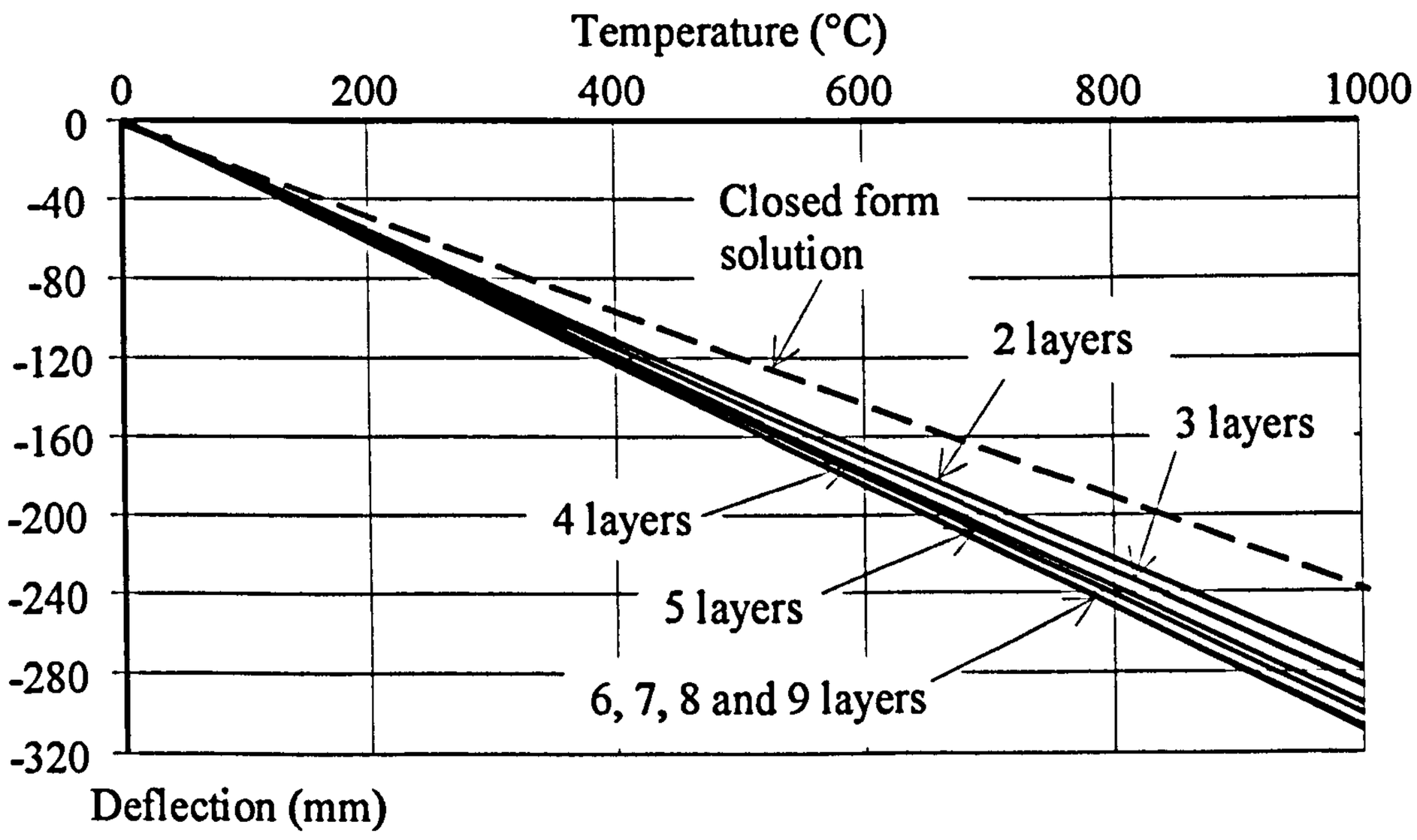

Figure 5-35. Convergence study of thermal bowing of a steel plate with a constant coefficient of thermal expansion

Figure 5-35 shows the results of the thermal bowing of the plate for a constant coefficient of thermal expansion of 0.000014; the temperature shown on the horizontal axis is that of the bottom face. The temperature has been limited to 1000°C as a linear relationship between temperature and deflection is found. This is due to not including material degradation at this stage of the analyses, and to assuming a constant temperature gradient and a constant coefficient of thermal expansion. It will be seen that a solution has converged from the finite element analysis when 6 layers or more are used; this is at a constant percentage error of 23.73% when compared to the closed form solution [63]. This is possibly due to Timoshenko's [63] solution being an approximation in that it is not able to take shear

into account. A convergence using 6 or more layers confirms Hinton and Owen's [62] statement that 6 to 10 layers will give acceptable results.

5.10 BENDING OF ANISOTROPIC LAMINATED SHELL ELEMENTS

The formulation described in Sections 5.1 and 5.2 is general for isotropic plates; this can easily be advanced to allow orthotropic materials to be considered within the finite element formulation. This is necessary for the modelling of cracking within the plate elements, the uni-axial nature of reinforcement layers, and in situations where the floor is cast on a profiled sheet decking. Timoshenko [63] advises that, for reinforced concrete, the rigidity of the laminae should be calculated using the following approximation.

First, consider the shell element in bending. For a single lamina (or a simple unlaminated element) it is known that the bending stiffness is defined by equation 5-19,

$$C_b = \begin{bmatrix} D(1,1) & D(2,1) & 0 \\ D(1,2) & D(2,2) & 0 \\ 0 & 0 & D(3,3) \end{bmatrix} \qquad 5\text{-}102$$

where

$$D(1,1) = \frac{E_x h^3}{12\left(1-\nu_x{}^2\right)}$$

$$D(2,1) = \nu_x \frac{E_x h^3}{12\left(1-\nu_x{}^2\right)}$$

$$D(1,2) = \nu_z \frac{E_z h^3}{12\left(1-\nu_z{}^2\right)}$$

$$D(2,2) = \frac{E_z h^3}{12\left(1-\nu_z{}^2\right)}$$

$$D(3,3) = \left(\frac{1-\left((\nu+\nu)/2\right)}{2}\right)\sqrt{D(1,1)\times D(2,2)}$$

This may then be applied within the finite element program using the methods described in Section 5.2.

5.10.1 BENDING OF ANISOTROPIC LAMINATED SHELL ELEMENTS – VALIDATIONS

To validate the anisotropic laminated shell elements, the same steel plate as used in previous validations has been utilised; this is shown in Figure 5-36. The validation is conducted by holding all material properties constant, except the elastic modulus in the z-direction.

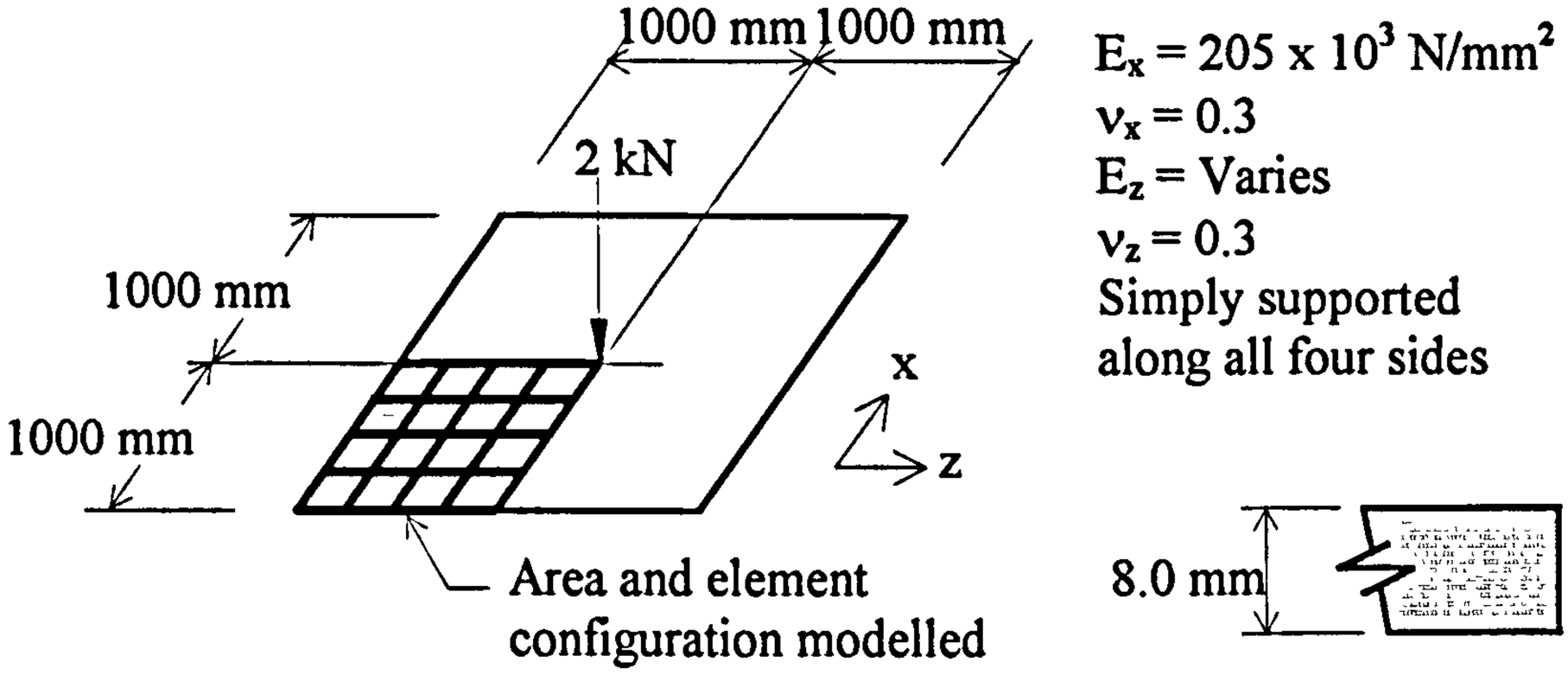

Figure 5-36. Simply supported steel plate with a varying elastic modulus in one direction

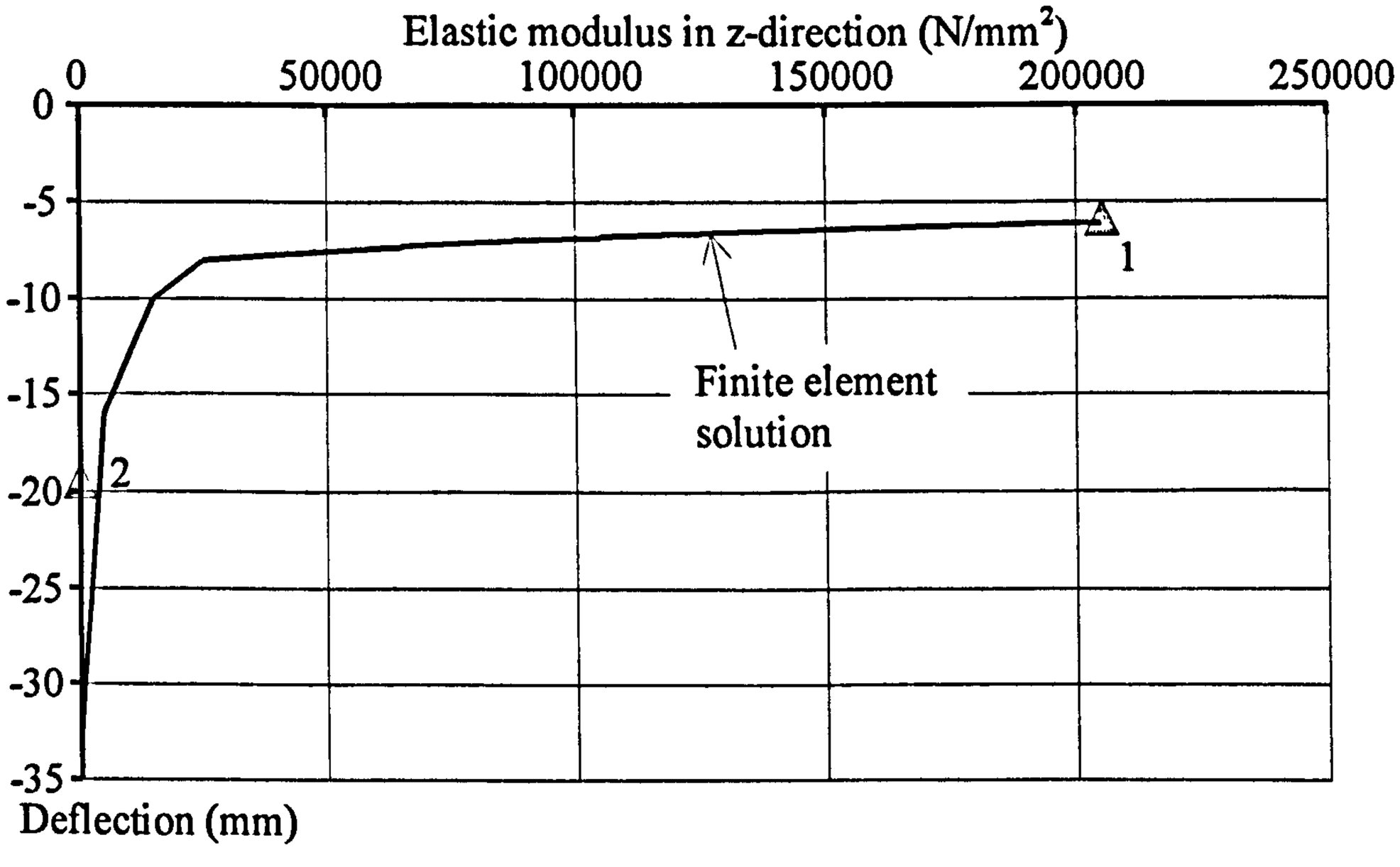

Figure 5-37. Central deflection of a simply supported plate where the elastic modulus in the z direction has been varied

Validation of this ambient temperature anisotropic plate in bending against analytical solutions is impossible except through the use of the finite element method, because the variation in torsional properties cannot be accounted for in closed-form or finite difference solutions. The logical limits to this are shown on the figure. These are:

1. When the elastic modulus is equal in both directions, this can be treated as a simple isotropic plate.

2. When the elastic modulus in one direction is equal to zero, this can be likened to a simply-supported steel beam, although this will not allow for the synclastic action that is normally associated with this type of deflection.

These bounds are shown respectively on Figure 5-37, and are comparable to the results from the finite element analysis.

5.11 Simulation of Concrete Cracking

At the start of the current project, the program VULCAN contained flat shell elements to simulate the effect of the floor slab on a structure during fire. The cracking model used within this formulation measured the membrane stress within the plate element and the stress gradient between its extreme fibres. Where individual calculated orthogonal stresses exceeded those specified by the user, the element was reduced to a thickness of 6mm to simulate the A142 anti-crack mesh within the Cardington test frame floor slab.

VULCAN has since been modified to accommodate the laminated flat shell element. The general approach for the cracking model is similar to that for the single-layer flat shell elements used by Bailey [44]. The laminated flat shell elements are formulated together with any beam or spring elements within the structure. These are used to assemble the global stiffness matrix, and the displacement field is calculated. The displacements are then used to determine the membrane stresses and stress gradient within the flat shell elements, and these stresses are used to find the orthogonal stresses within each lamina. The stresses are compared to limiting compression and tension stresses, and if these are exceeded the corresponding lamina is considered as cracked. On the next Newton-Raphson iteration of the finite element solution process the 'cracked' laminae are ignored in the subsequent formulation of the flat shell element, and the stiffness of the element is calculated on the basis of a newly located centroid. The subsequent displacements are then evaluated for the cracked element in the following Newton-Raphson iteration.

In-plane shear stresses within the elements can also be considered for cracking. Taking account of the in-plane shear stress makes it possible to obtain the principal stresses within the element. This method was not used because during an iteration of the solution process the principal stresses may be resolved in a direction causing a crack. The crack can then influence the formulation of the principal stresses in the next iteration causing them to rotate and cause another series of cracks. The process may not be convergent, and can prevent solutions from being reached.

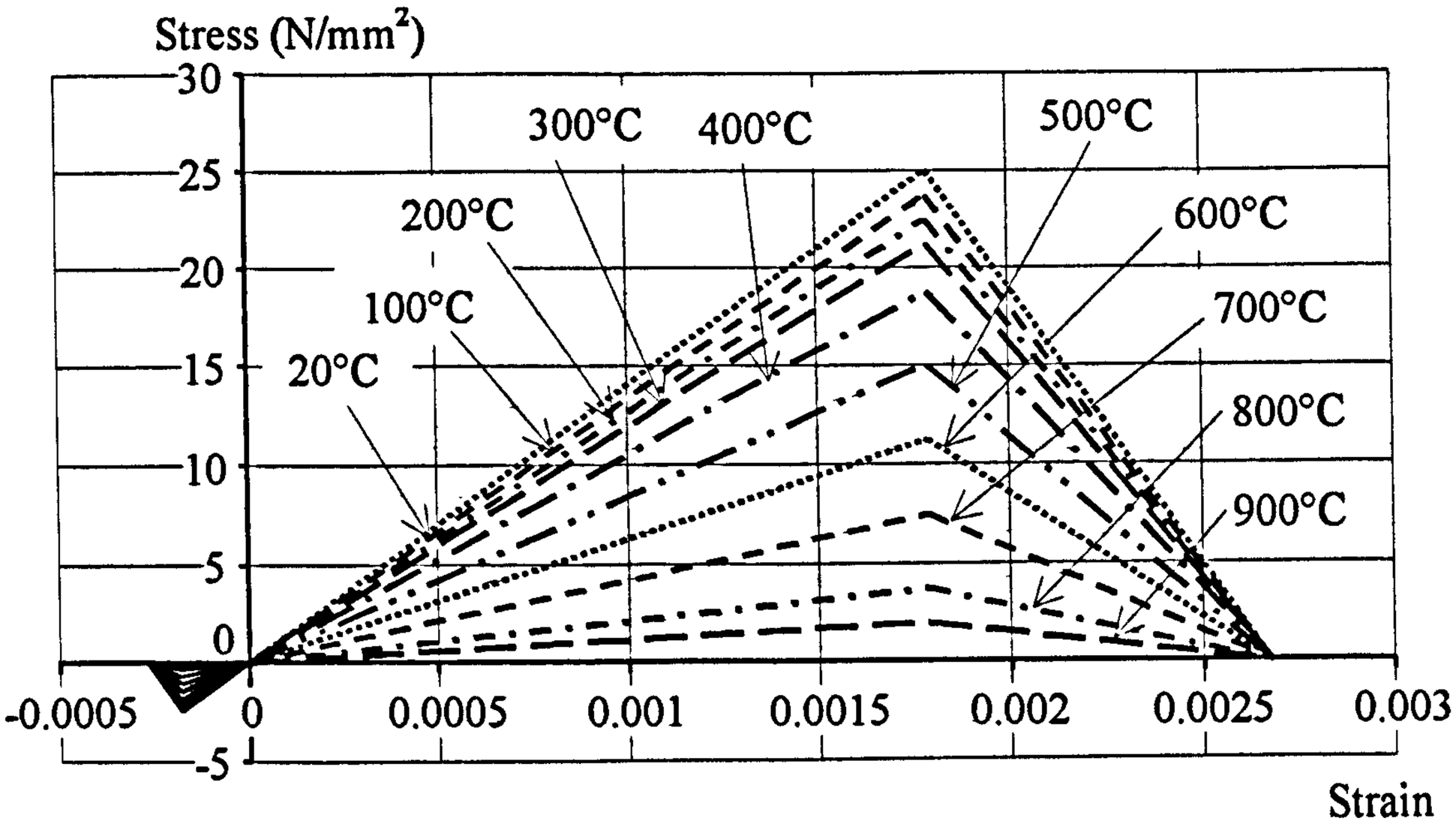

Figure 5-38. Stress-strain relationship of concrete at elevated temperatures

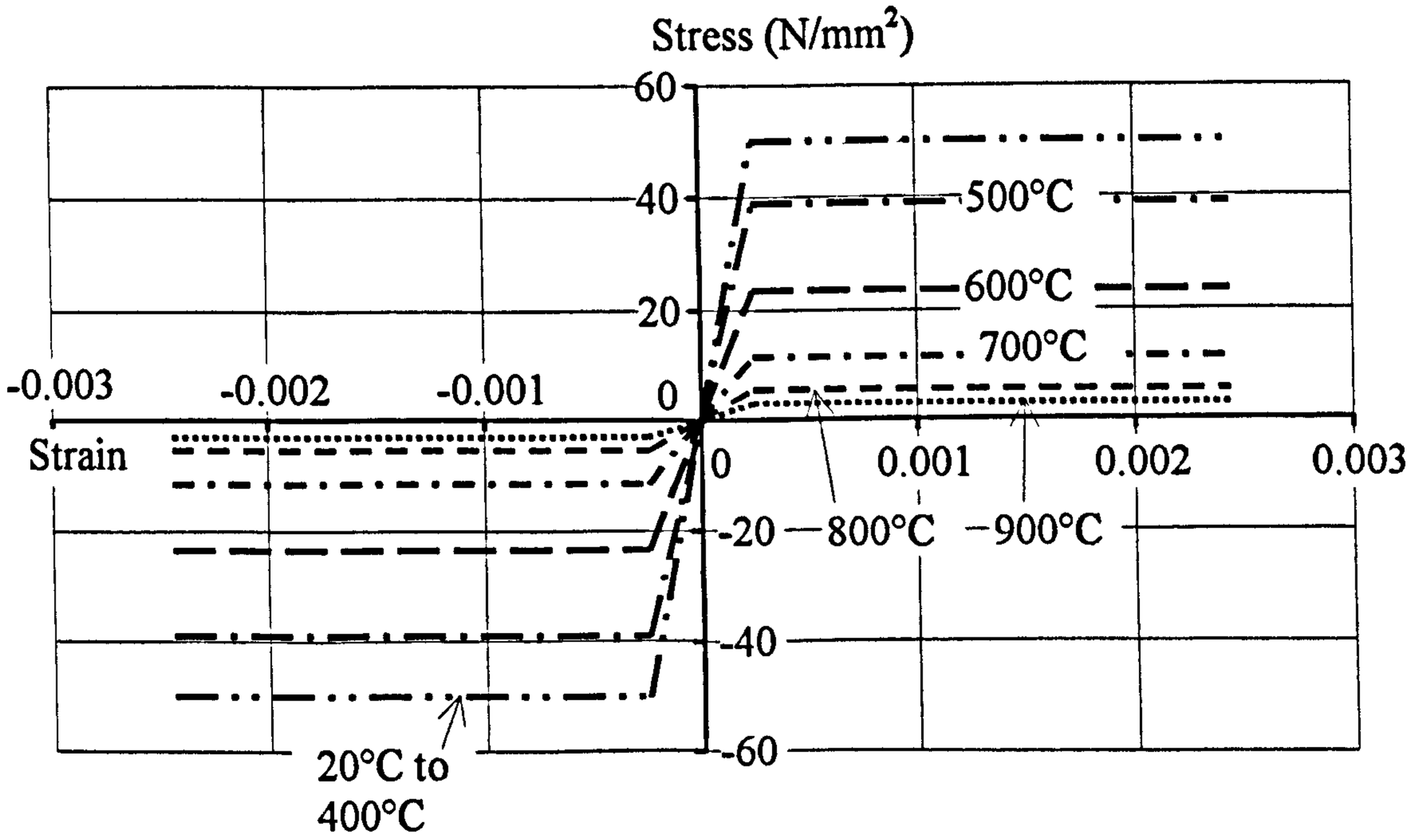

Figure 5-39. Stress-strain relationship of reinforcing steel at elevated temperatures

The stress-strain model for concrete is a bi-linear representation containing a cracking regime that continues down a non-returnable path to zero, as shown in Figure 5-38.

The gradient of the non-returnable descending path may be varied. A bi-linear characteristic is also used to represent the constitutive relationship for the steel reinforcement; this is shown in Figure 5-39.

5.11.1 SIMULATION OF CONCRETE CRACKING – VALIDATIONS

A number of validations have been conducted on the cracking model, of which four are included here. These are: a restrained concrete beam subjected to thermal forces, a simply supported slab at ambient temperature [65], and two fire tests carried out by British Steel on composite beams [14].

Concrete Restrained Beam Subjected to Thermal Forces

A simple concrete prism with a limiting compressive stress of 35 N/mm^2 and restrained against all longitudinal movement was subjected to uniform temperature increase. Assuming an elastic modulus (E) of 14000 N/mm^2 and a constant coefficient of thermal expansion (α) of 0.0000108, the temperature (T) at which the concrete beam reached a stress of 35 N/mm^2 was calculated using:

$$\sigma = \alpha T E$$
$$35 = 0.0000108 \times T \times 14000 \qquad \text{5-103}$$
$$\therefore T = 231.48\ ^{\circ}C$$

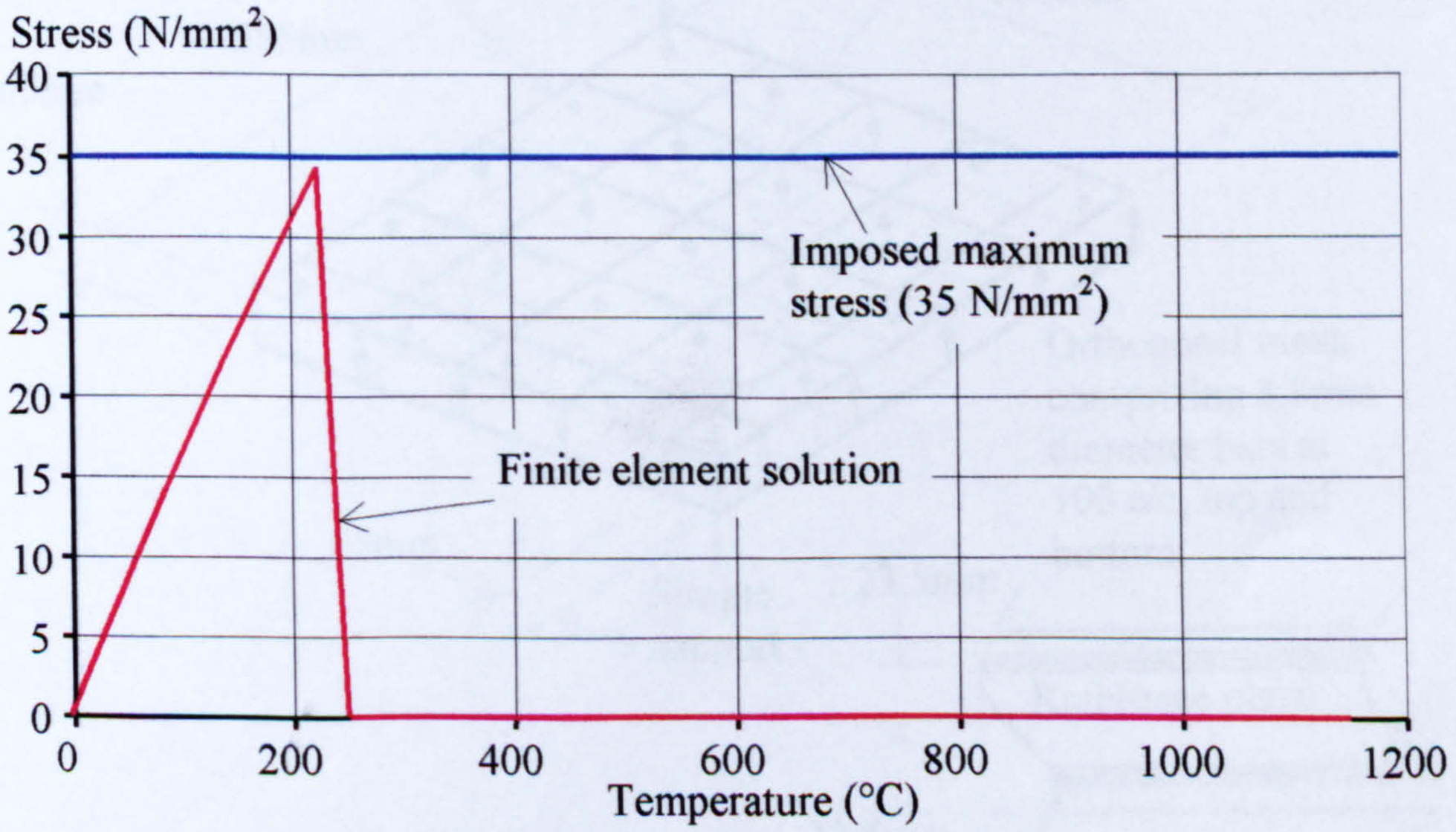

Figure 5-40. Internal forces of restrained concrete beam

The prism used for this validation was encastré at both ends, 2000mm long, 300mm deep and 300mm wide, externally unloaded, and split into 5 equal elements along the length. Figure 5-40 shows the longitudinal stress given by finite element analysis within the restrained beam. It can be seen that the beam does not appear to crack at exactly 35 N/mm^2. This is due to the difficulty of using temperature increments that coincide with the temperature that gives the specified stress (231.48 °C as calculated previously). If simple visual extrapolation is applied to Figure 5-40 it may be determined that the beam stress will be 35 N/mm^2 at approximately 230 °C.

Reinforced Concrete Simply Supported Slab at Ambient Temperature

Hinton and Owen [62] detail a series of tests (conducted by Duddeck *et al* [65]) on the cracking of concrete slabs at ambient temperature. One of these tests consisted of a corner-supported square slab (1170mm square) with a central point load. This slab was constructed from lightweight concrete and has the advantage of having well defined boundary conditions, being horizontally free. Reinforcing steel within the slab is positioned as shown in Figure 5-41, together with the dimensions of the slab and its finite element idealisation. The material properties of the concrete slab found from test samples are detailed in Table 5-01.

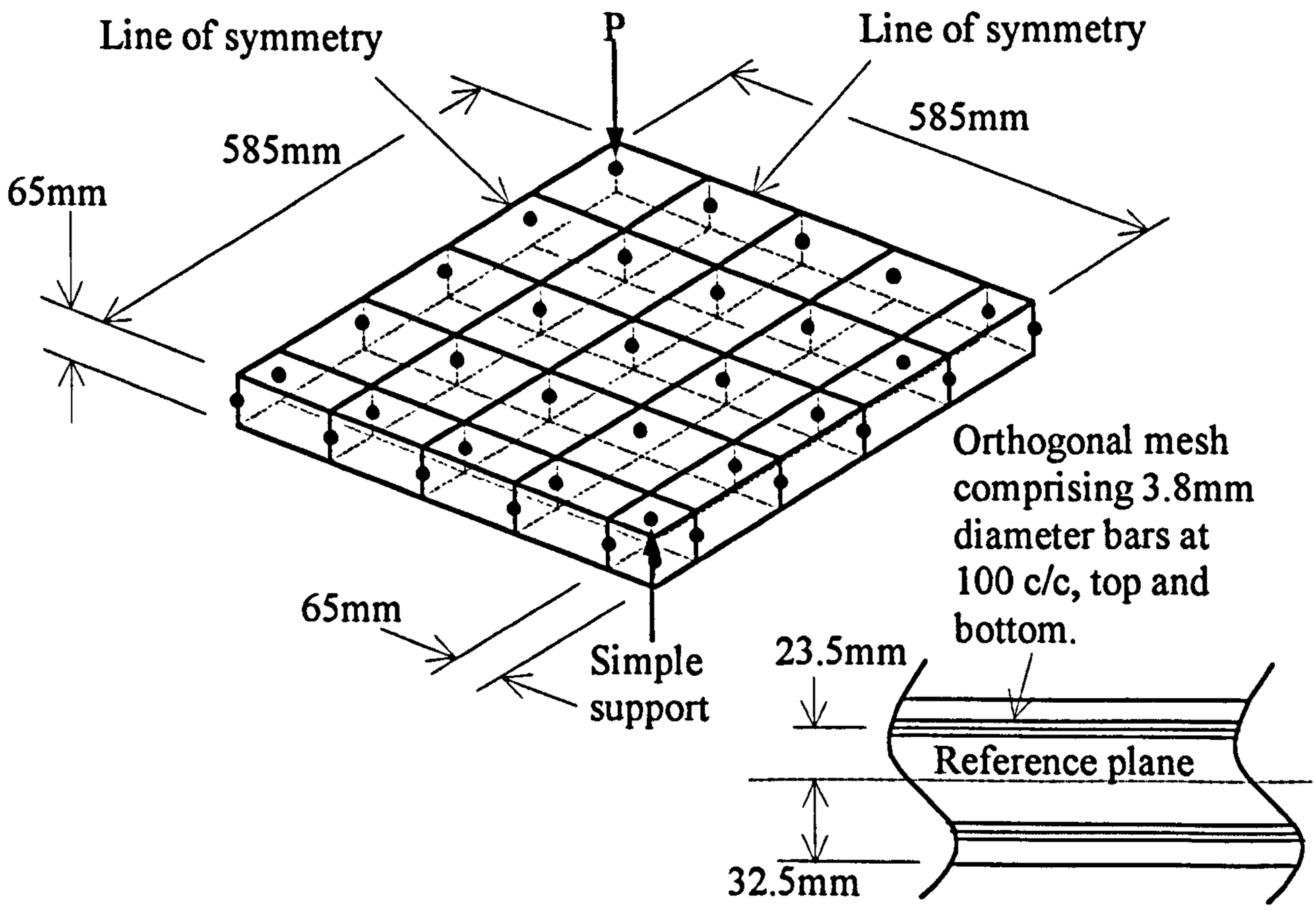

Figure 5-41. Corner supported concrete slab

CONCRETE	STEEL
Elastic modulus (E_c)=16400N/mm^2	Elastic modulus (E_s)=201000N/mm^2
Poisson's ratio (ν_c)=0.2	Yield stress (f_y)=600N/mm^2
Ultimate compressive stress (f'_c)=43N/mm^2	Ultimate stress (f'_s)=700N/mm^2
Ultimate tensile stress (f_t)=3.0N/mm^2	Angle x-axis (θ_x)=0.0
Ultimate compressive strain (ε_u)=0.0035	Angle x-axis (θ_x)=1.57
Tension stiffening coefficient (α)=0.7	
Tension stiffening coefficient (ε_m)=0.0020	

Table 5-01. Material properties of corner supported concrete slab.

To simulate the layers of reinforcement within the concrete slab, it is necessary to utilise the orthotropic formulation. For a lamina of reinforcement within the mesh a value for the elastic modulus in one direction is assigned, whilst for the perpendicular direction the elastic modulus is set to zero. As it is not possible to model the separate reinforcing bars, the elastic modulus is effectively smeared across the width and depth of the reinforcement to give an equivalent elastic modulus value. This method is also applied to the yield stress.

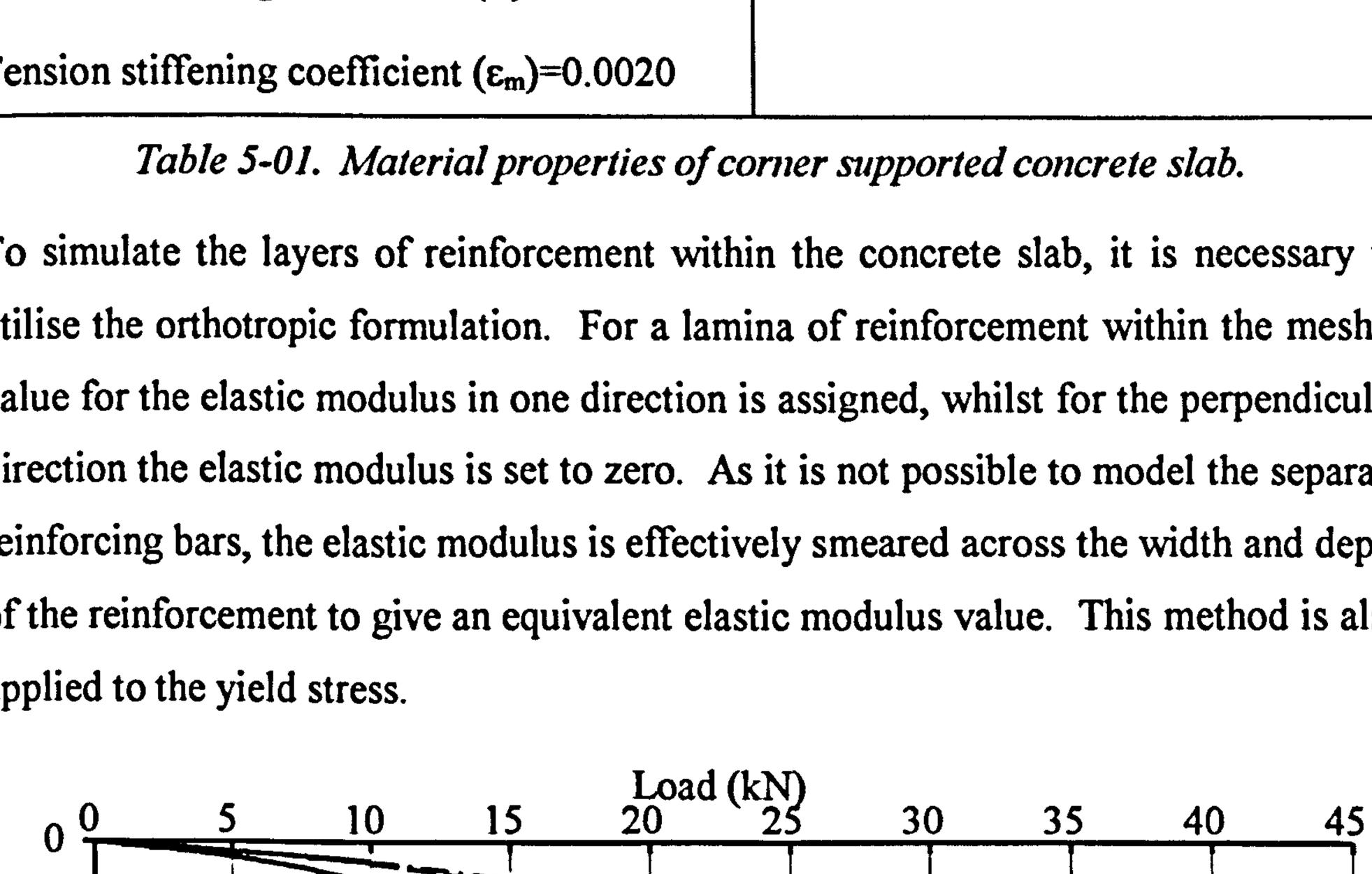

Figure 5-42. Central deflection of corner supported concrete slab

Figure 5-42 shows a comparison of the central deflection comparing the present analyses, test deflections, and the results of an alternative finite element analysis

(Huang *et al* [66]). It will be noted from the figure that Huang's cracking method gives a more accurate representation of the test than the author's finite element solution, although the author's finite element solution is deemed to be acceptable. This difference in results between Huang's [66] finite element solution and the present approach may be due to the more sophisticated cracking model used by Huang [66].

To check that the finite element analysis begins to crack at approximately the correct loading, a yield line analysis has been conducted on the corner supported concrete slab. Before a slab cracks, the distribution of bending moments is given by elastic plate theory. As the tension steel reaches its yield stress, a collapse mechanism will start to form along the lines on which the slab yields.

All calculations have been made with reference to Figure 5-43.

In yielding, the work done by the external forces must equal the work done by the internal forces. Therefore, using small angle theory,

Work done by external forces = Work done by internal forces

$$W.\theta.d = \frac{4MD\theta}{\sqrt{2}}$$

$$W = \frac{2.83DM}{d}$$

5-104

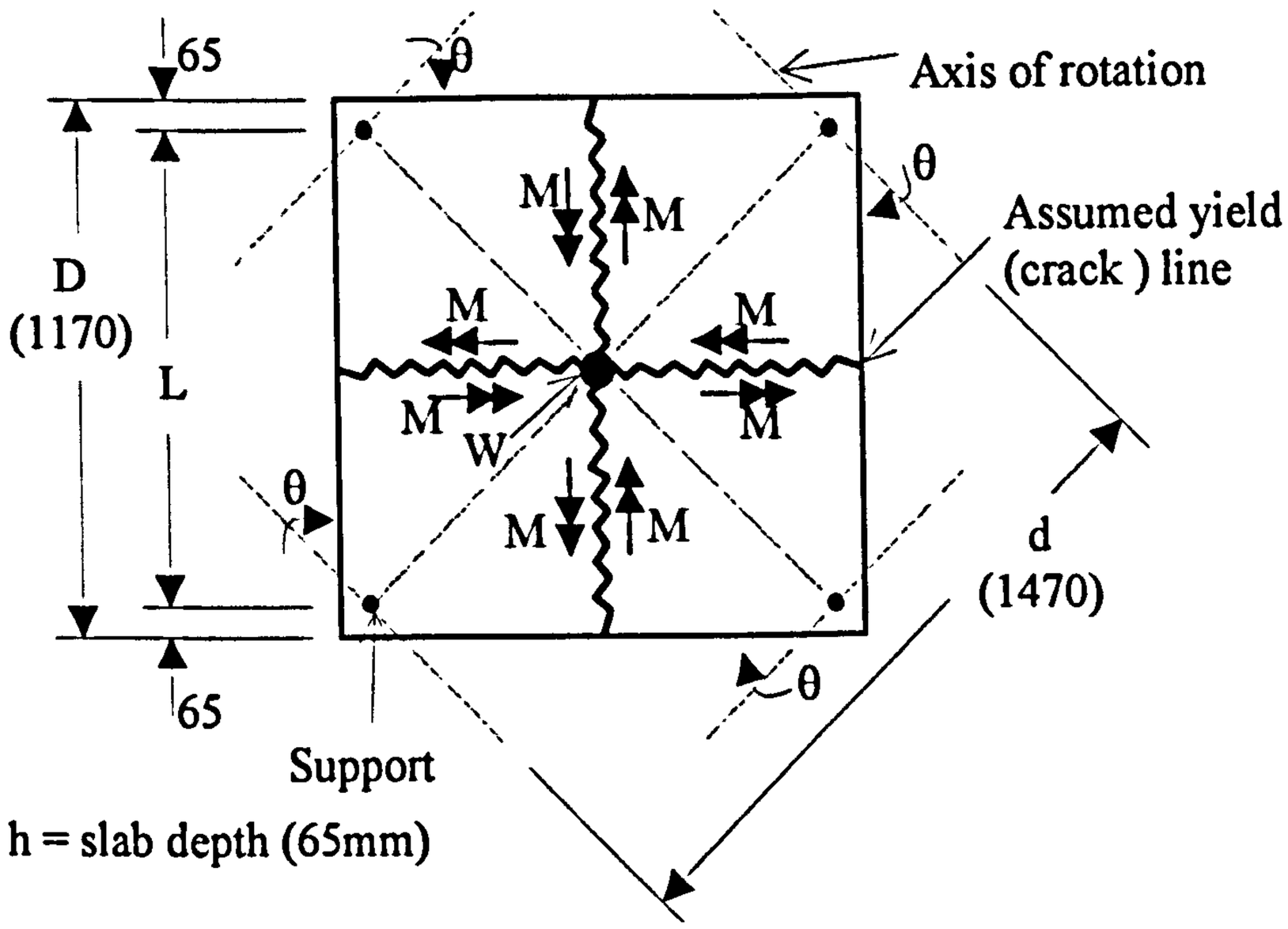

Figure 5-43. Equilibrium condition for the yield line analysis of the corner supported square slab.

Using the stress blocks shown in Figure 5-44, the force capable of being sustained by the slab in compression is

$$F = \frac{0.67 \times 43}{1.5} \times 34.6 = 664.5N \qquad 5\text{-}105$$

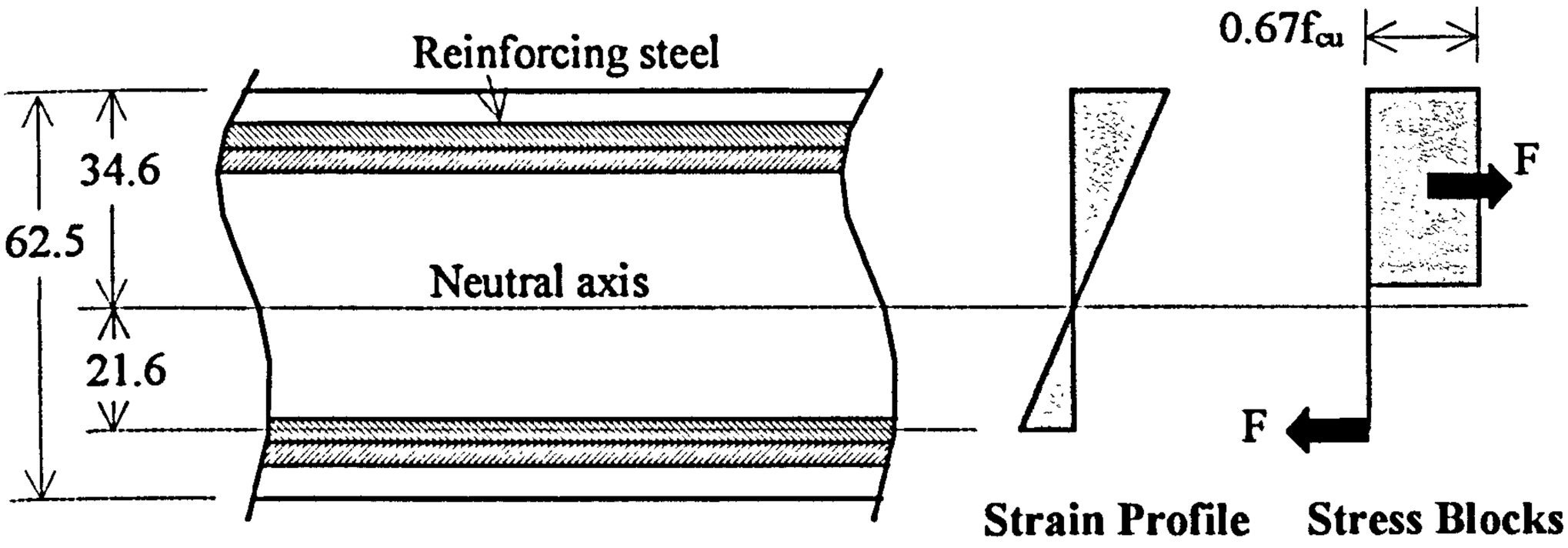

Figure 5-44. Stress block profile for the corner supported square slab.

The ultimate moment that the slab may support is therefore

$$M = 664.5 \times \left(\frac{34.6}{2} + 19.5 \right) = 24454Nmm \qquad 5\text{-}106$$

The maximum load that the slab can support is

$$W = \frac{2.83 \times 1170 \times 24454}{1470} = 55.1kN \qquad 5\text{-}107$$

This method of predicting the ultimate moment of slabs is an upper bound solution.

The tension cracks shown in Figure 5-45 all developed in the bottom face of the concrete through to the reinforcement. The compressive cracks in the centre of the top face began appearing at approximately 28kN and continued as deep as the reinforcement. The slab then retained its structural integrity until a load of approximately 35kN was exerted upon the slab. Beyond 35kN the yield lines of the slab act as hinges where the majority of the central area of the slab is under tension.

An assumption that has been made within this analysis is that there is no restraint given by the simple supports and point load. Even low-levels of restraint from the simple supports and the point load (which is exerted onto a 100mm square steel pad on the top surface of the slab) could affect the results considerably.

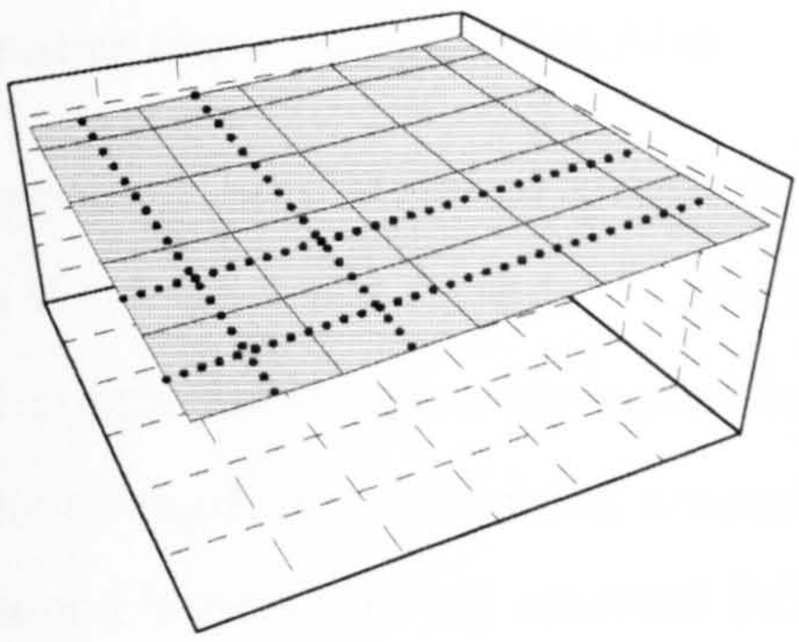

a_1. 10 kN – Bottom face

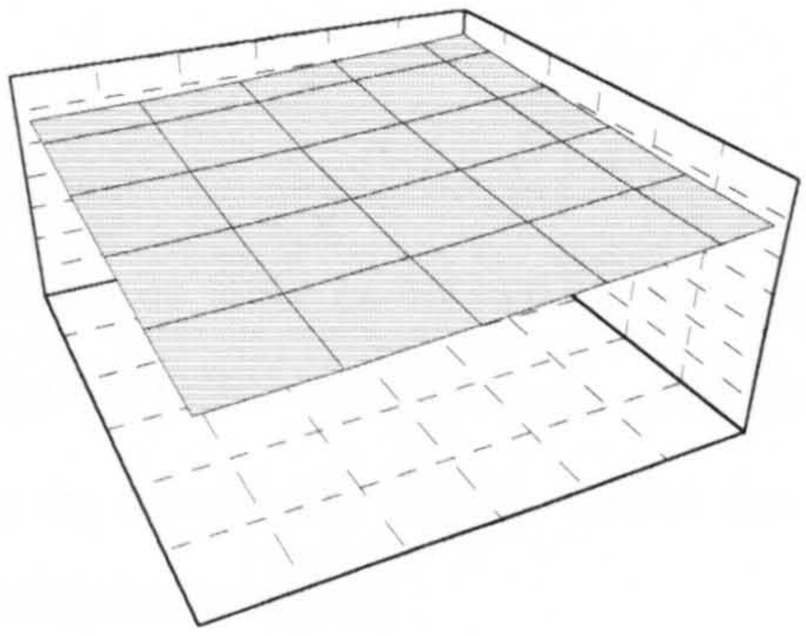

a_2. 10 kN – Top face

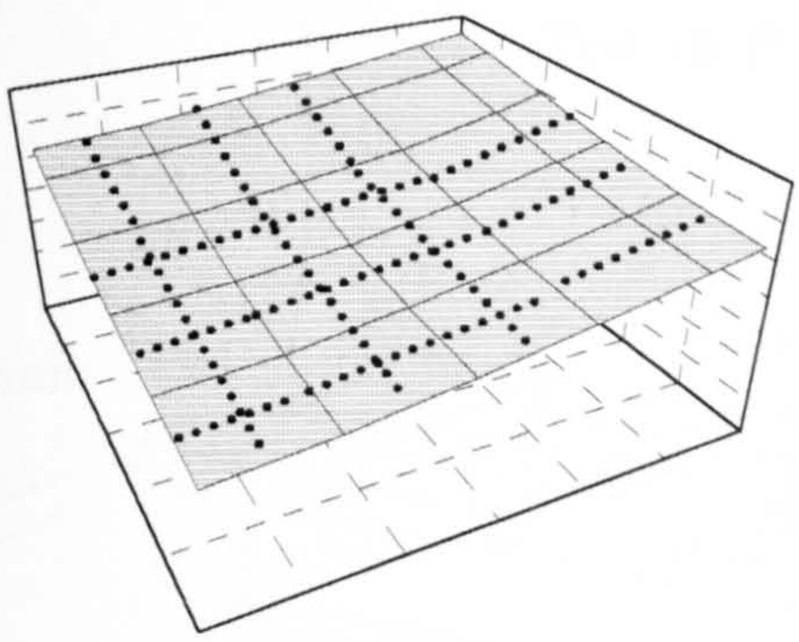

b_1. 20 kN – Bottom face

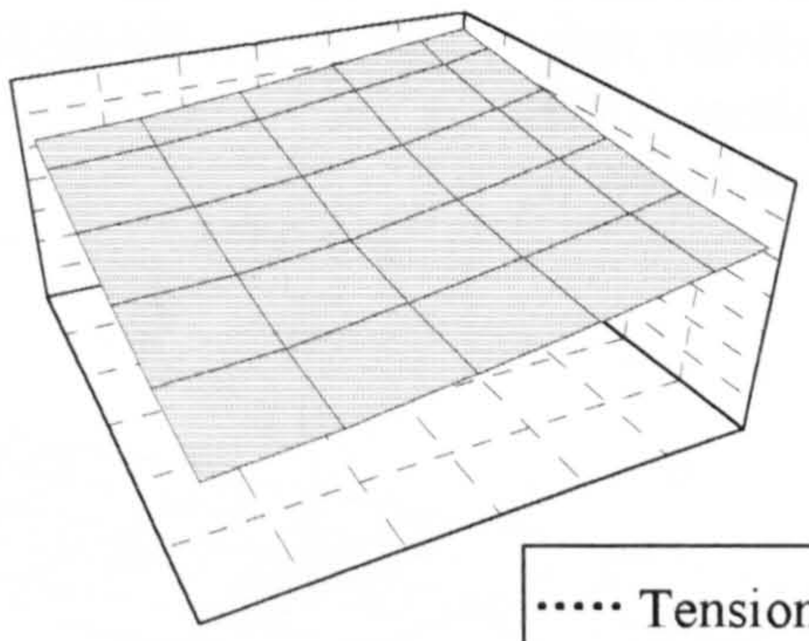

b_2. 20 kN – Top face

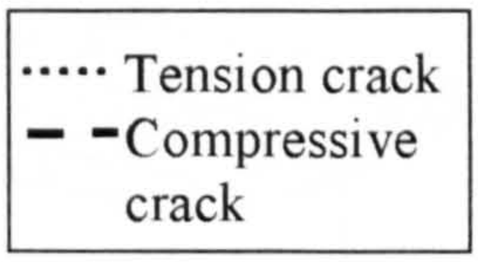

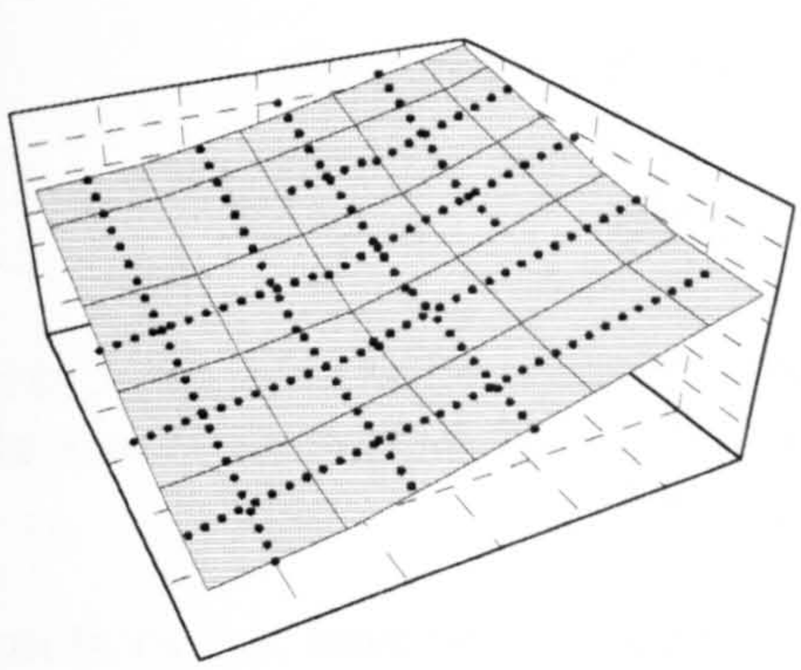

c_1. 30 kN – Bottom face

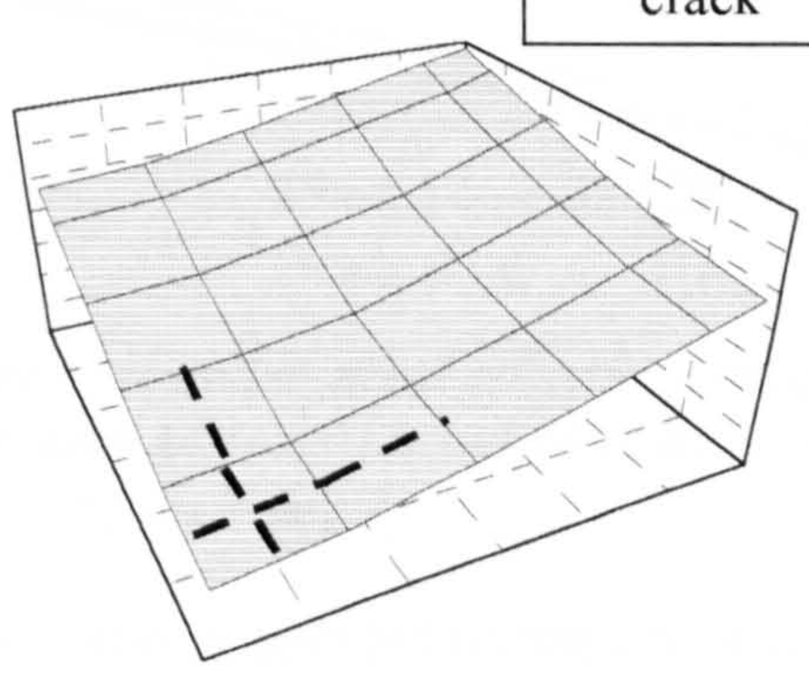

c_2. 30 kN – Top face

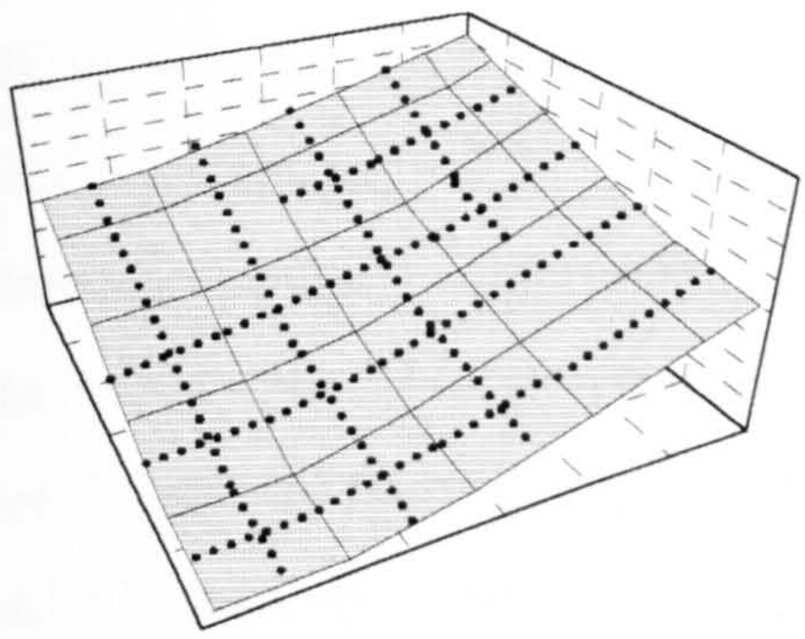

d_1. 40 kN – Bottom face

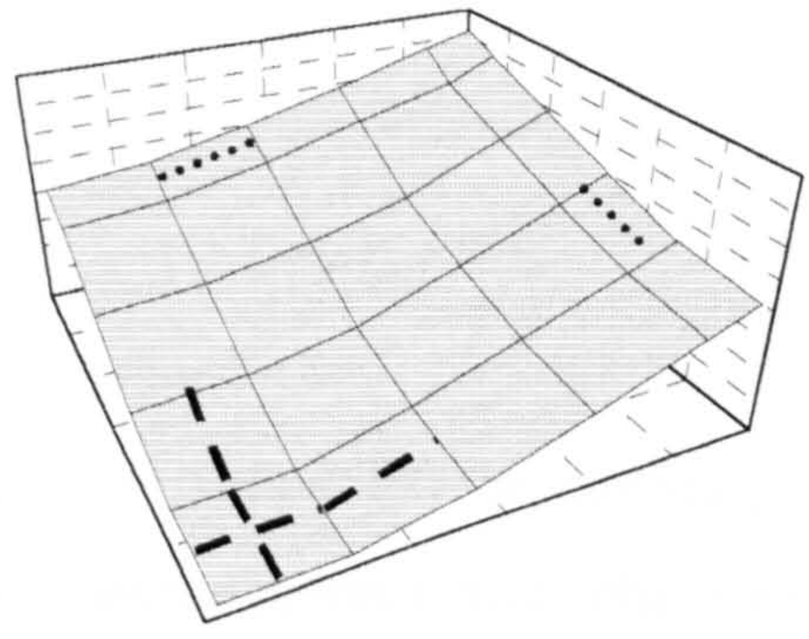

d_2. 40 kN – Top face

Figure 5-45. Deflected shape and cracking patterns of the corner supported concrete slab

Composite Beam Subjected to Fire

Two geometrically identical simply supported composite beams were tested in 1982 in the Warrington test furnace [14]. The specimens were as shown in Figure 5-46. Both of the composite beams were loaded to the CP117 [67] design loads. For the first (Test 15) the strength was calculated assuming no composite action, whilst the loading on the second beam (Test 16) assumed full composite action.

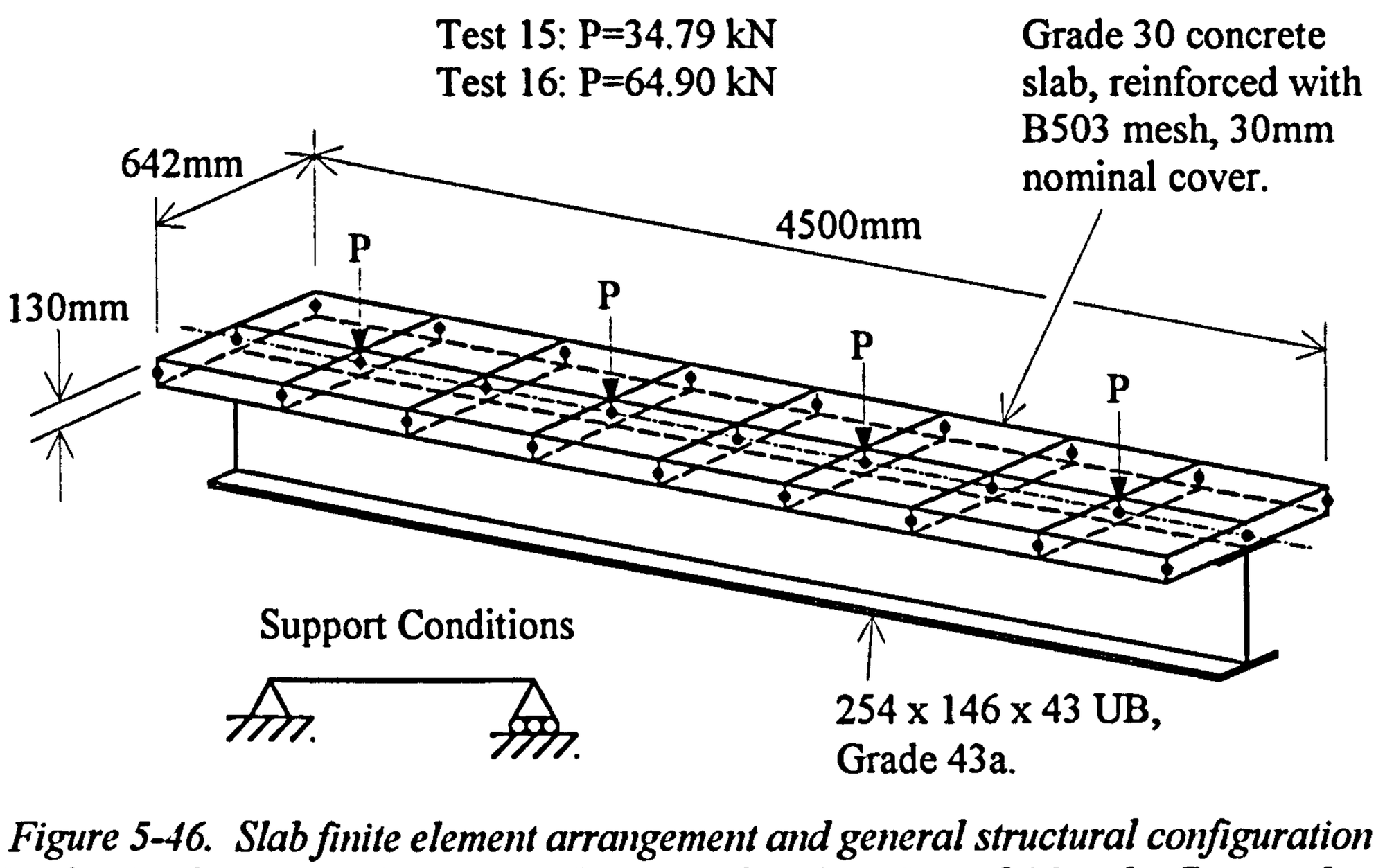

Figure 5-46. Slab finite element arrangement and general structural configuration for the simply supported composite beam used in Tests 15 and 16 in the Compendium of UK Standard Fire Tests [14]

Assumptions that have been made for the simply supported composite beams are:

1. The material properties of the concrete are

- Elastic modulus (E) = 14000 N/mm^2
- Poisson's ratio (ν) = 0.2
- Maximum stress in compression ($\sigma_{compression}$) = 30 N/mm^2
- Maximum stress in tension ($\sigma_{tension}$) = 3 N/mm^2
- Coefficient of thermal expansion (α) = 0.0000108 for analysis when using Bailey's cracking method. The author uses the thermal strain characteristics given by EC4.

2. The composite beam was assumed to be simply supported.

3. The temperature profiles across the steel beam were approximated as a two-step form, with the upper flange being at 80% of the temperature of the web and lower flange. No data was recorded for the temperature profile in the slab, and it has therefore been assumed that the temperatures of the lower and upper faces of the concrete slab are 50% and 10% respectively that of the lower flange. This concrete temperature profile is in keeping with that measured in the Cardington restrained beam test.

The results of the analyses for both cases, including a comparison with the original slab element, are shown in Figures 5-47 and 5-48.

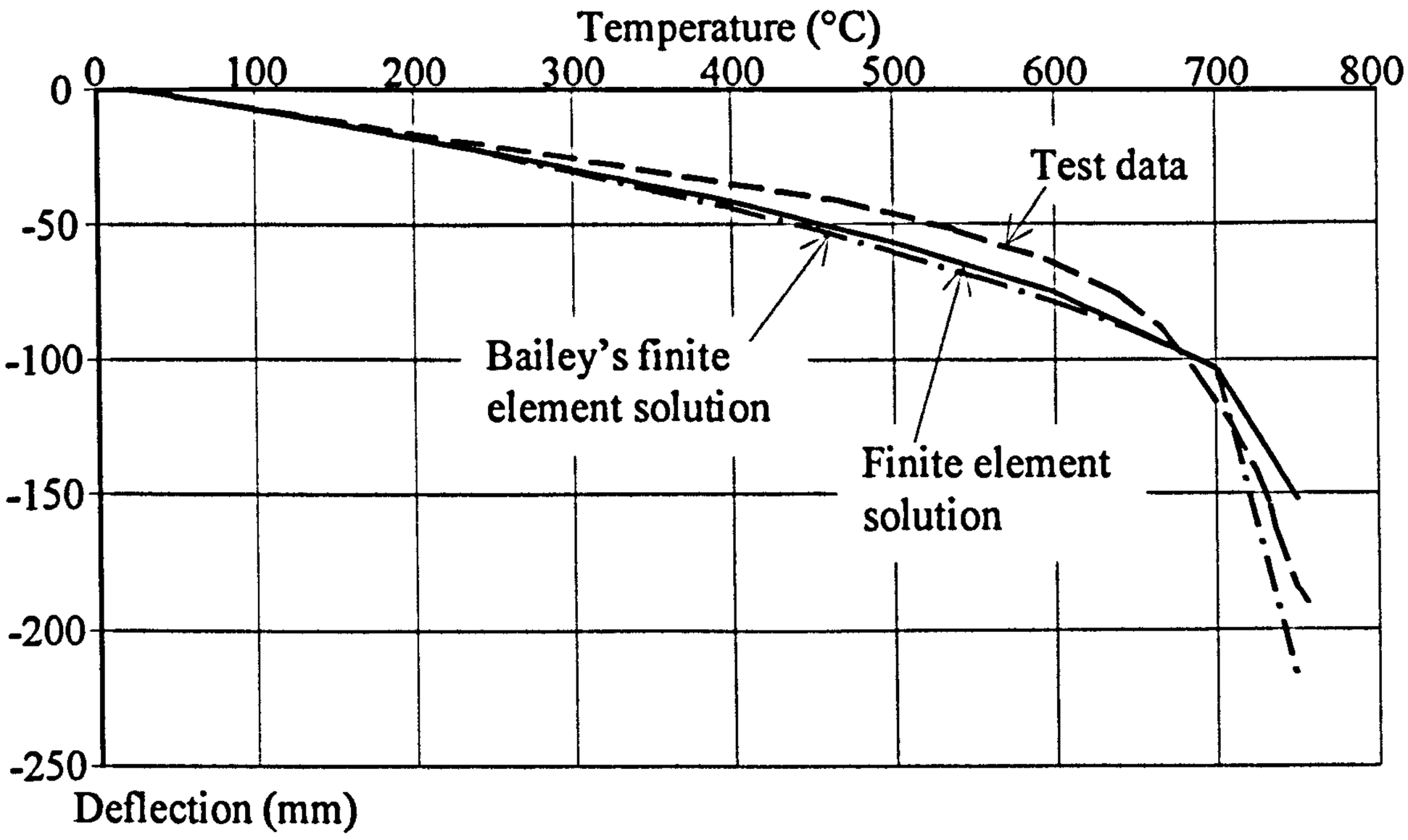

Figure 5-47. Comparison between the finite element solution, Bailey's slab assumptions and the test results for Test 15

It can be seen from the figures that the analysis predicts slightly greater deflections than those found in the tests and slightly higher load capacity, although the correlation is generally good. These differences could be due to many assumptions, for example, the support conditions, the assumed concrete properties, the slab temperature profile, the beam temperature profile, temperature lag of the concrete at the beginning of the analysis, slip between the concrete and the slab, or spalling of the concrete.

The fact that the more highly loaded test (Test 16) deflected less for the first 13 minutes must cast doubt on the reference positions from which the deflections were measured. The basic correlation for Test 16 is good, and if the datum were adjusted accordingly the agreement would be much improved for both Bailey's [44] and the

author's slab model. Test 15 (Figure 5-44) can be clearly seen to be running away at temperatures over 650°C and test 16 (Figure 5-45) similarly runs away past 600°C. The modelling of this run-away is modelled well by Bailey's isotropic element, though the author's appears to retain excessive stiffness due to the different cracking model.

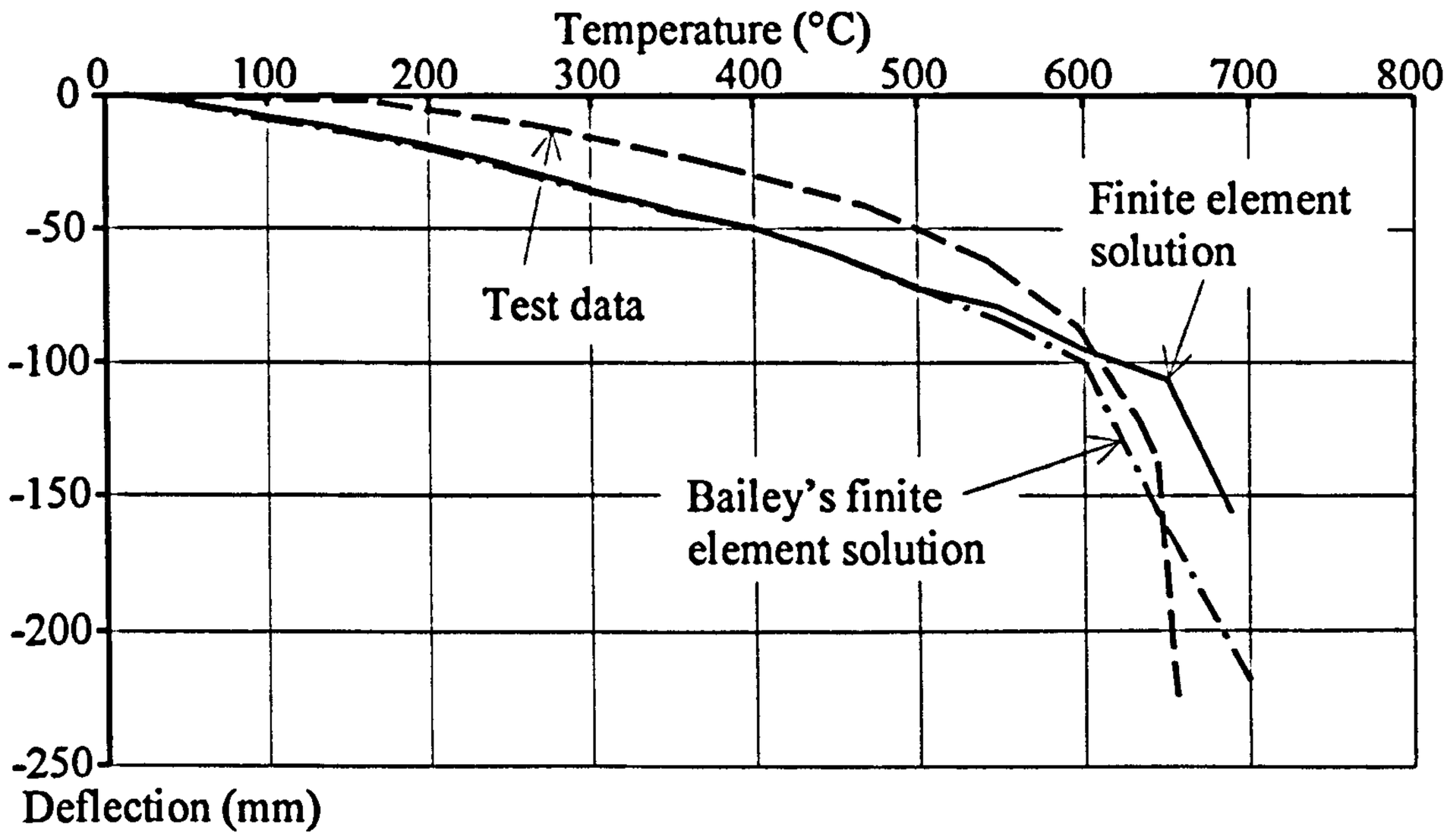

Figure 5-48. Comparison between the finite element solution, Bailey's slab assumptions and the test results for Test 16

Effects of the Laminated Shell Element on a Small Subframe

To ascertain the effects that may now be included within the slab depth, a study has been conducted on a contrived composite beam and slab arrangement. The supporting beam is a 9000mm long 305 x 165 x 40 UB which is attached with full interaction to the concrete slab. The concrete slab is 9000mm long by 6000mm wide and 120mm thick, and lies on top of the upper flange of the supporting beam. All edges of the concrete slab are supported only in the vertical plane. For computational efficiency, only a quarter of the structure has been modelled, and the finite element mesh and subframe are shown in Figure 5-49. A constant uniform load of 5.48 kN/m^2 has been used at all times throughout the analyses.

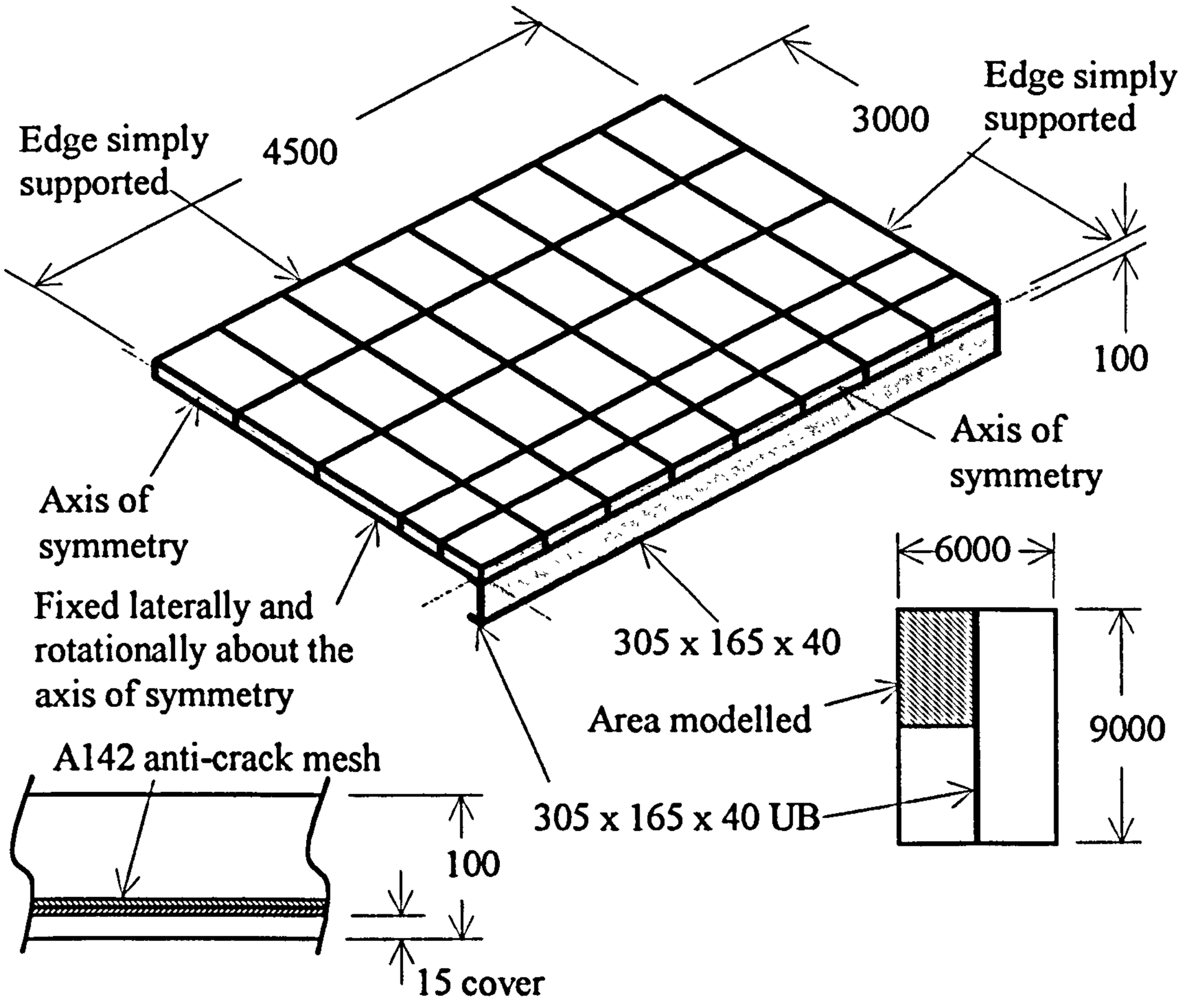

Figure 5-49. Beam and slab general arrangement

This beam and slab arrangement has been analysed for a number of different scenarios:

1. A cold slab with no supporting beams underneath.
2. A heated slab with no supporting beams underneath.
3. A cold slab with the beam heated using a uniform temperature profile.
4. A heated slab where the bottom face of the slab is heated to 30% of the uniform beam temperature and the top face to 10 % of the same.

The concrete compressive strength used is 25 N/mm^2 in conjunction with a tensile strength of 2.5 N/mm^2. The reinforcement is assumed to be A142, which is the equivalent of 6mm bars at 200mm spacing. The yield strength of the steel reinforcement layer is 50 N/mm^2.

Figure 5-50 shows the central deflections of the supporting beam with a cold slab compared to the cold slab with no supporting beam. All temperatures refer to the bottom flange of the beam. This analysis has been conducted using the concrete

model with orthogonal cracking in response to maximum tensile and compressive normal stresses.

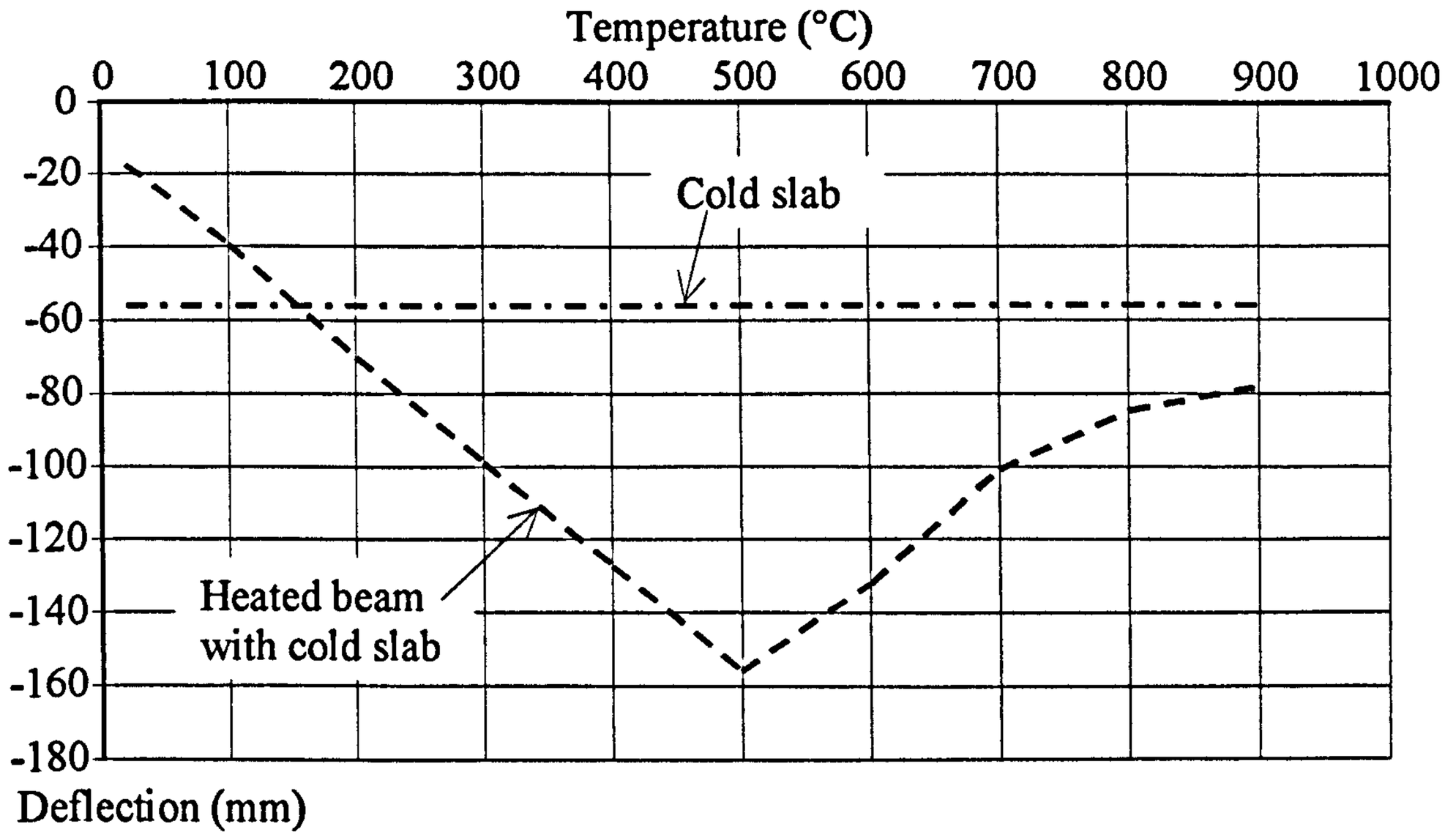

Figure 5-50. Central deflection of the heated beam and cold slab as compared to a cold slab with no secondary beam

As expected the initial deflection at the centre of the beam is less than that of the unsupported slab, and this changes as the temperature increases, causing thermal bowing to occur between the beam and the cold slab, acting approximately linearly until 500°C when the steel begins to soften. Above 500°C the strength of the slab begins to dominate the behaviour, forcing the beam back towards the original state of deflection of the slab. The force in the slab that causes this 'pull back' phenomenon is due entirely to bending strength of the slab because its edges are allowed to move laterally. The structure does not reach its original shape due to the weakening of the slab caused by cracking. In larger, continuous structures the attempts of the slab to return to its original shape may also be affected by catenary action in combination with the bending action of the slab.

A similar comparison is made in Figure 5-51 where the central deflection of the heated beam and slab is compared to a heated slab with no beam. The composite beam deflects initially due predominantly to thermal bowing. Beyond approximately 500°C the continued deflection is caused by deterioration in strength and stiffness of the steel beam. The heated slab deflects quickly because of thermal bowing, but then begins to 'relax' at 300°C as extensive cracking and softening of the concrete material

allows redistribution of the loads, the effect of which is to allow the centre of the slab to rise vertically. As in the previous example, it will be noted that, as the composite beam loses appreciable strength and stiffness, the slab (through bending resistance) attempts to pull back to the shape that it would have had the beam not been part of the original structure. The fact that the deflections at 900°C are nearly identical indicates that the cracking in the two cases is very similar.

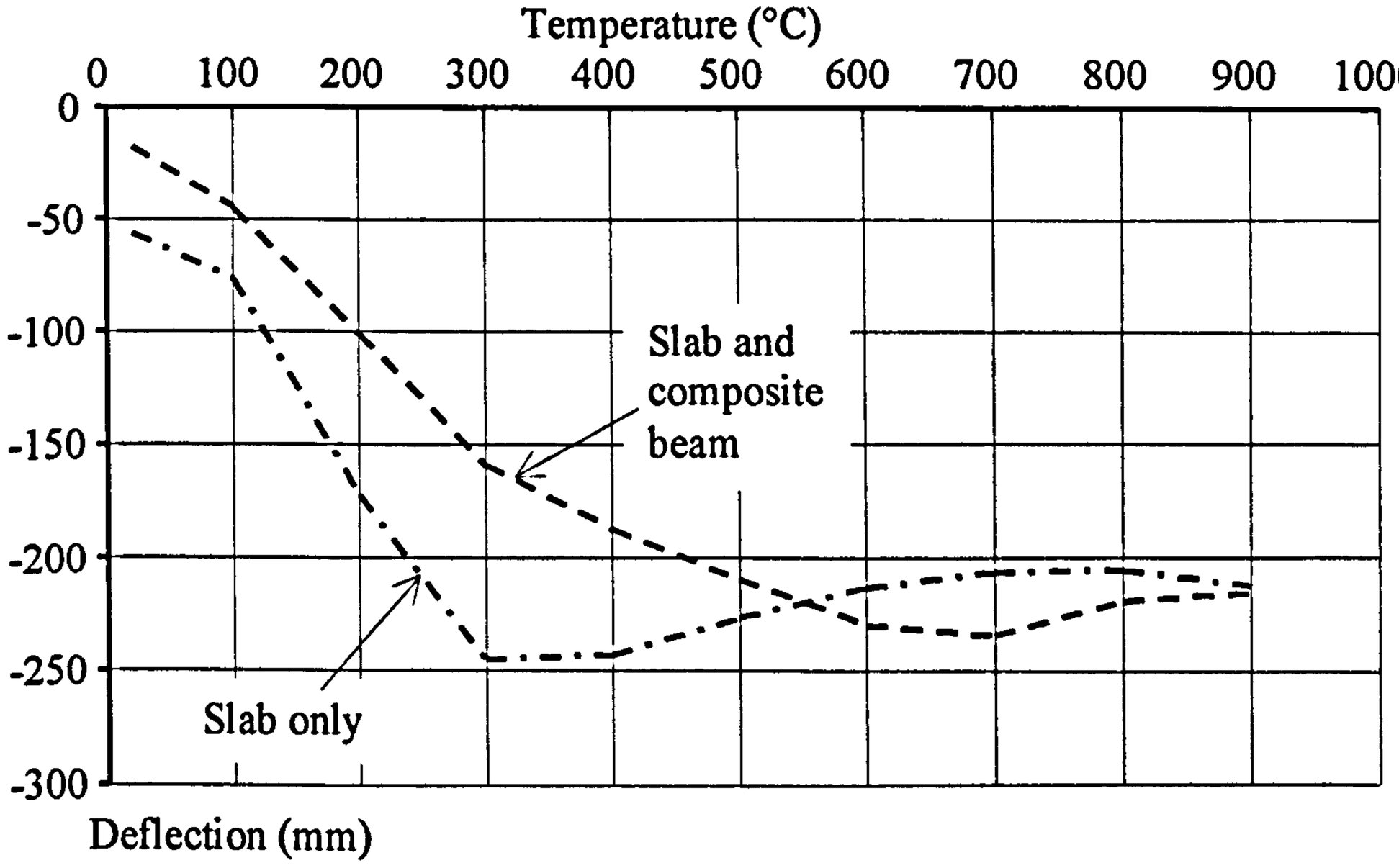

Figure 5-51. Central deflection of the heated beam and slab as compared to a heated slab with no supporting beam

Figure 5-52 shows a sequence of deflected surfaces of the heated slab and beam (Case 4) at increasing temperatures, on which are superimposed the crack patterns for the top and bottom faces. It can be noted that the bottom face of the concrete floor slab cracks extensively up to approximately 200°C. These cracks occur in the bottom 15mm of the slab and do not cause yield of the reinforcing mesh. The upper surface of the concrete floor slab is seen to form a tension crack at 400°C parallel to the beam. Above this temperature the slab continues deflecting and forms two compression cracks near the centre of the beam.

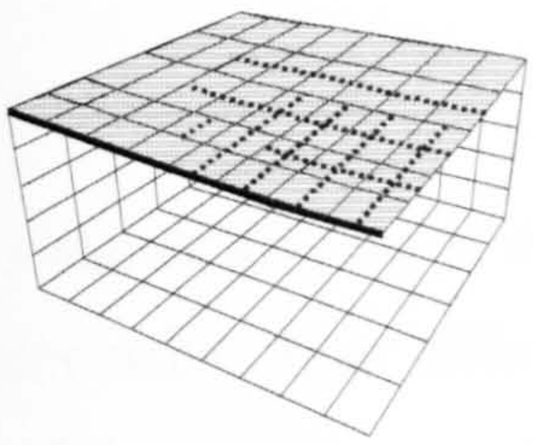

Bottom Face 20°C

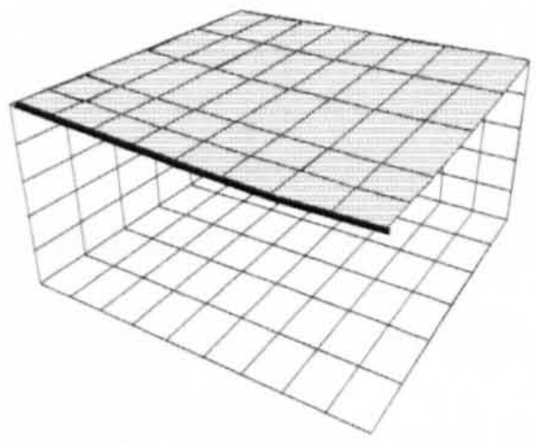

Top Face 20°C

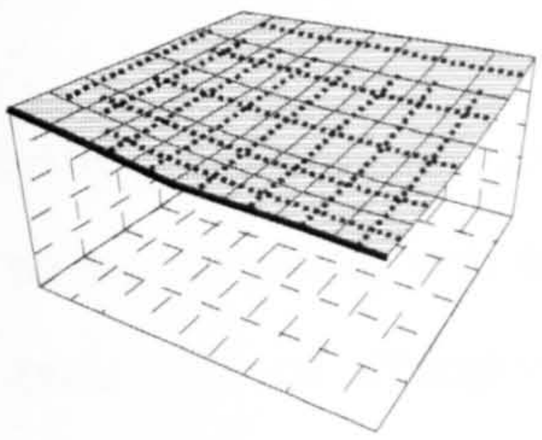

Bottom Face 100°C

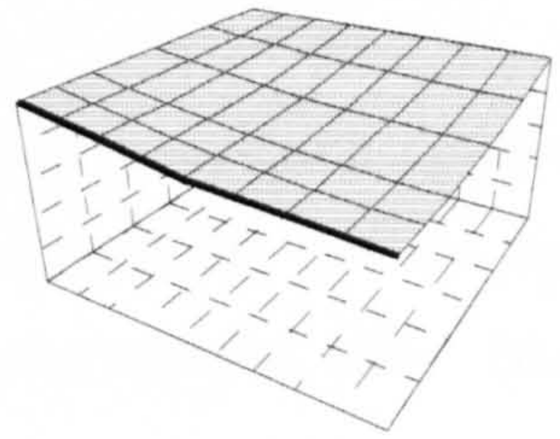

Top Face 100°C

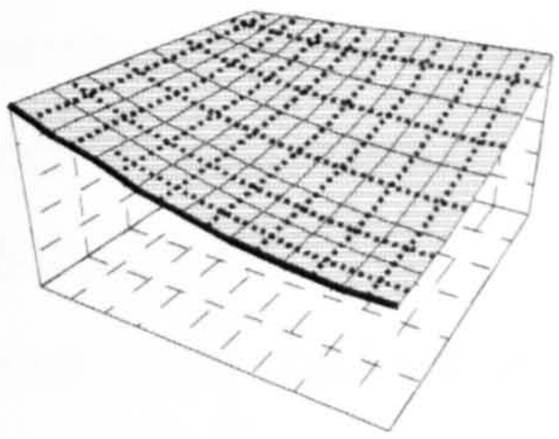

Bottom Face 200°C

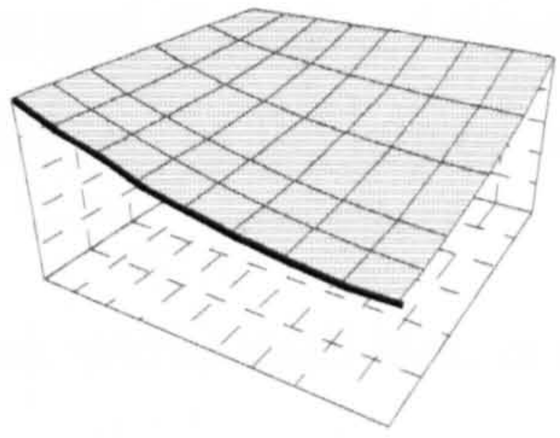

Top Face 200°C

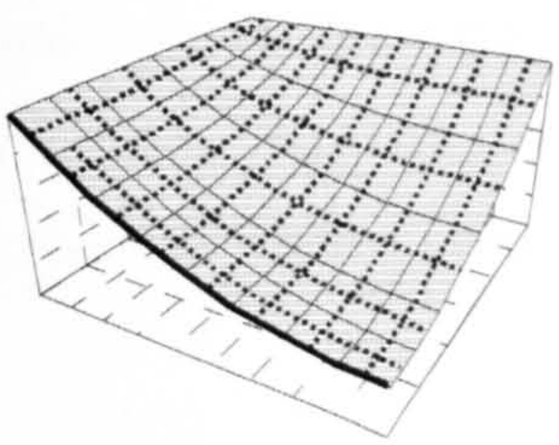

Bottom Face 400°C

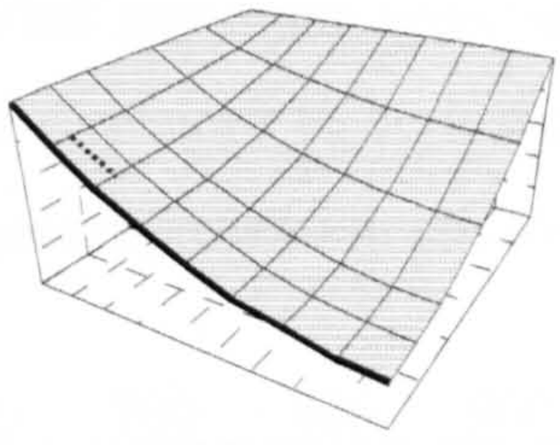

Top Face 400°C

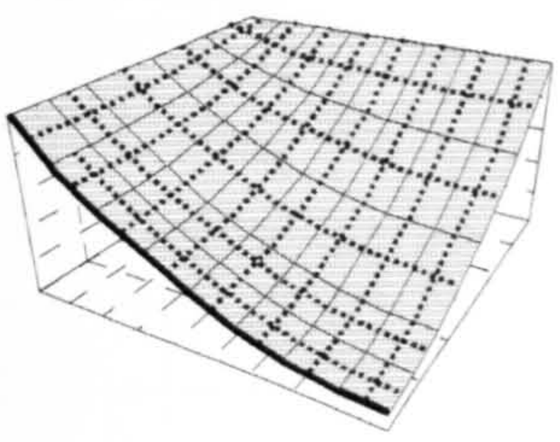

Bottom Face 600°C

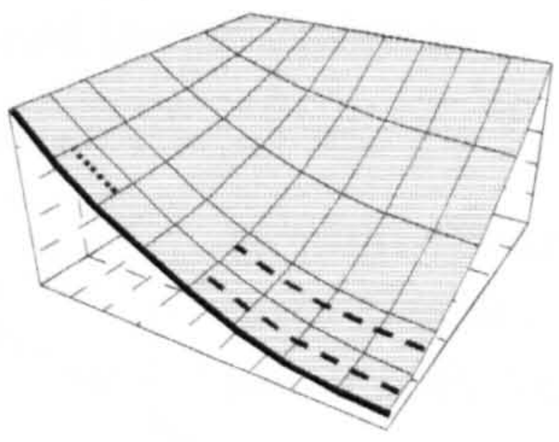

Top Face 600°C

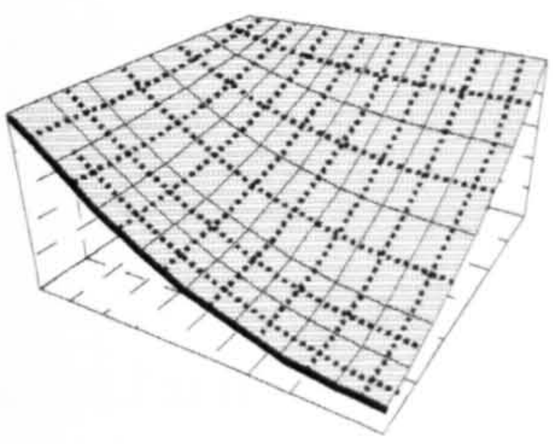

Bottom Face 800°C

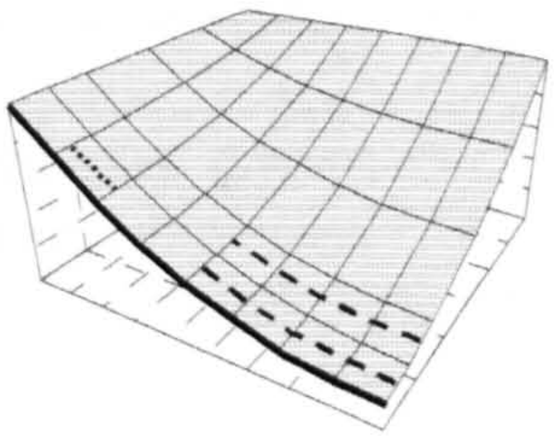

Top Face 800°C

------ Compression crack

..... Tension crack

Figure 5-52. Sequential cracking patterns of the heated beam and slab

Study of Cracking Models

Figure 5-53 shows a study of the effect of using different cracking models for the concrete floor slabs. Four different cracking models have been chosen to assess the suitability of the cracking model described in section 5.8. These are defined as follows:

1. If the orthogonal stresses on each lamina exceed the maximum compressive or tensile stress, cracking will occur in one direction across the element represented by the reduction of strength and stiffness along the relevant axis. (As used in section 5.8)
2. The normal stresses on each lamina are calculated and if either of these exceeds the specified maximum stress, the strength and stiffness of the lamina is reduced in both directions.
3. Two-directional cracking occurs if a principal stress within each lamina is greater than the maximum compressive or tensile stresses.
4. Principal stresses in excess of either of the specified maximum compressive and tensile stresses cause all concrete strength in both directions to be lost across the whole element when a crack occurs, excepting layers representing reinforcement.

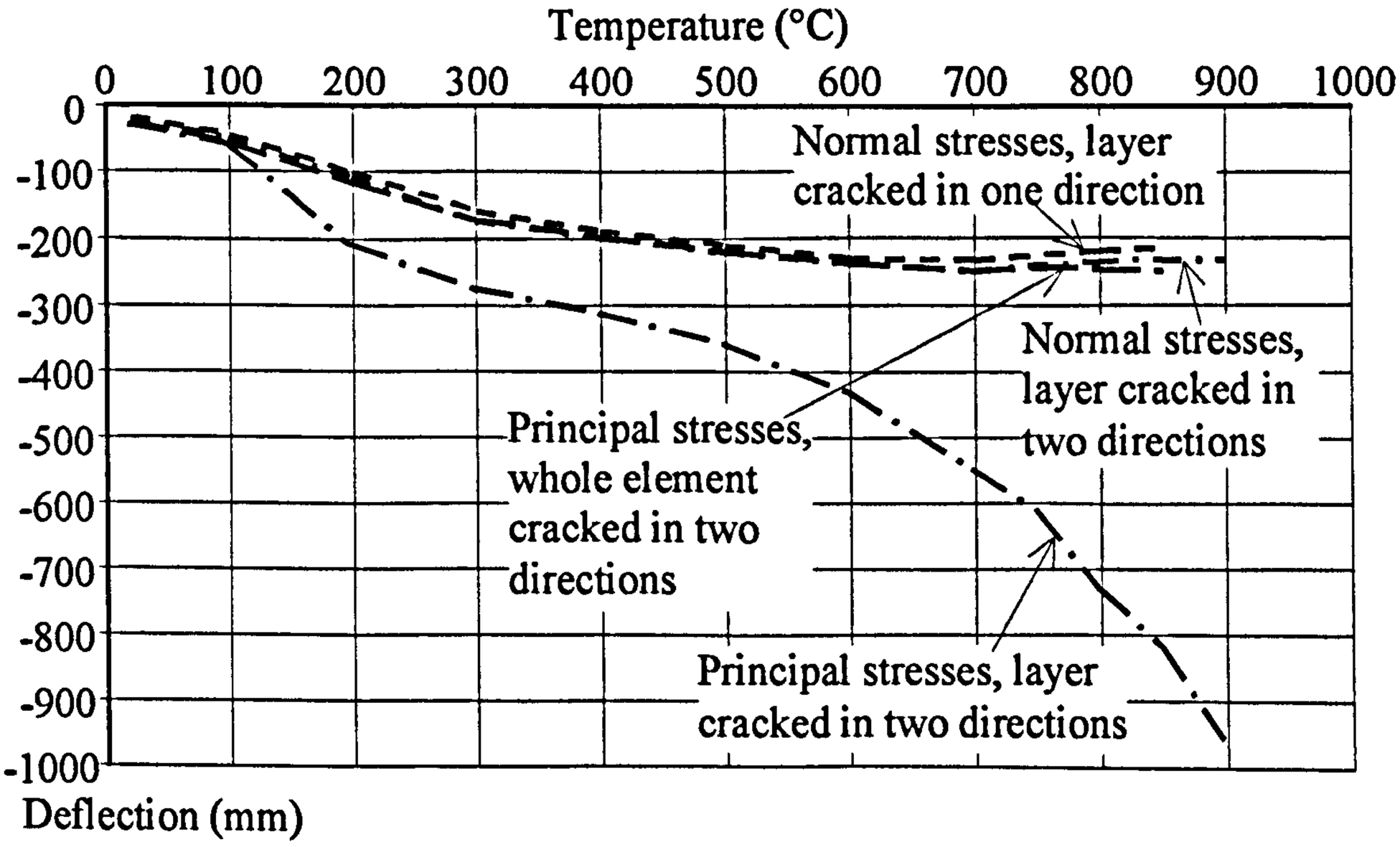

Figure 5-53. Central deflection of the heated beam and slab for different cracking assumptions.

Uni-directional cracking is not applicable when principal stresses are used, as this leads to a phenomenon called 'crack rotation', as outlined in Section 5.8.

This analysis has been conducted on the beam and slab with both components at elevated temperatures. Again the maximum concrete tensile stress is assumed to be 2.5 N/mm^2, the maximum concrete compressive stress 25 N/mm^2 and the steel yield stress is 50 N/mm^2.

The cracking method where principal stresses on each layer crack in two directions leads to excessive cracking of the tension face of the concrete occurring at between 100°C and 200°C. At between 500°C and 600°C the reinforcement layer begins to yield and the deflection begins to progressively run-away. The other three cracking methods all behave in a similar manner, producing patterns that reflect those in Figure 5-53.

Effect of Edge Restraint

A study was then conducted on the heated beam and slab to ascertain the effects of the boundary conditions. Along the two free edges the boundary conditions were methodically fixed according to the process indicated in Figure 5-54. The results may be seen in Figure 5-55.

It will be noted that Cases 1, 2 and 3 all follow the simply supported case to approximately 200°C, after which the restrained thermal expansion of the steel section and the concrete floor slab begin to dominate the action, forcing a rapid increase in deflection. The restraint against thermal expansion in Case 1 comes from the floor slab expanding against a support where lateral movement is restrained. In Case 2 the restraint against thermal expansion will occur due to the combination of thermal expansion of the floor slab and steel beam against a support where lateral movement is restrained. Case 3 is restrained against all lateral movement at the supports. In all three cases the concrete begins to crack rapidly on the underside of the slab at 300°C. These tension cracks (caused by bending) extend to the reinforcement layer. From this stage, the position of the neutral axis rises and the slab bending stiffness is still sufficient to maintain integrity, hence the reinforcement begins to act in tension and the upper layer of concrete in compression. As the slab continues to sag, compression cracks begin to appear on the upper face of the slab, reducing the bending stiffness. The slab then supports the load through catenary action, and continues to sag due to material degradation.

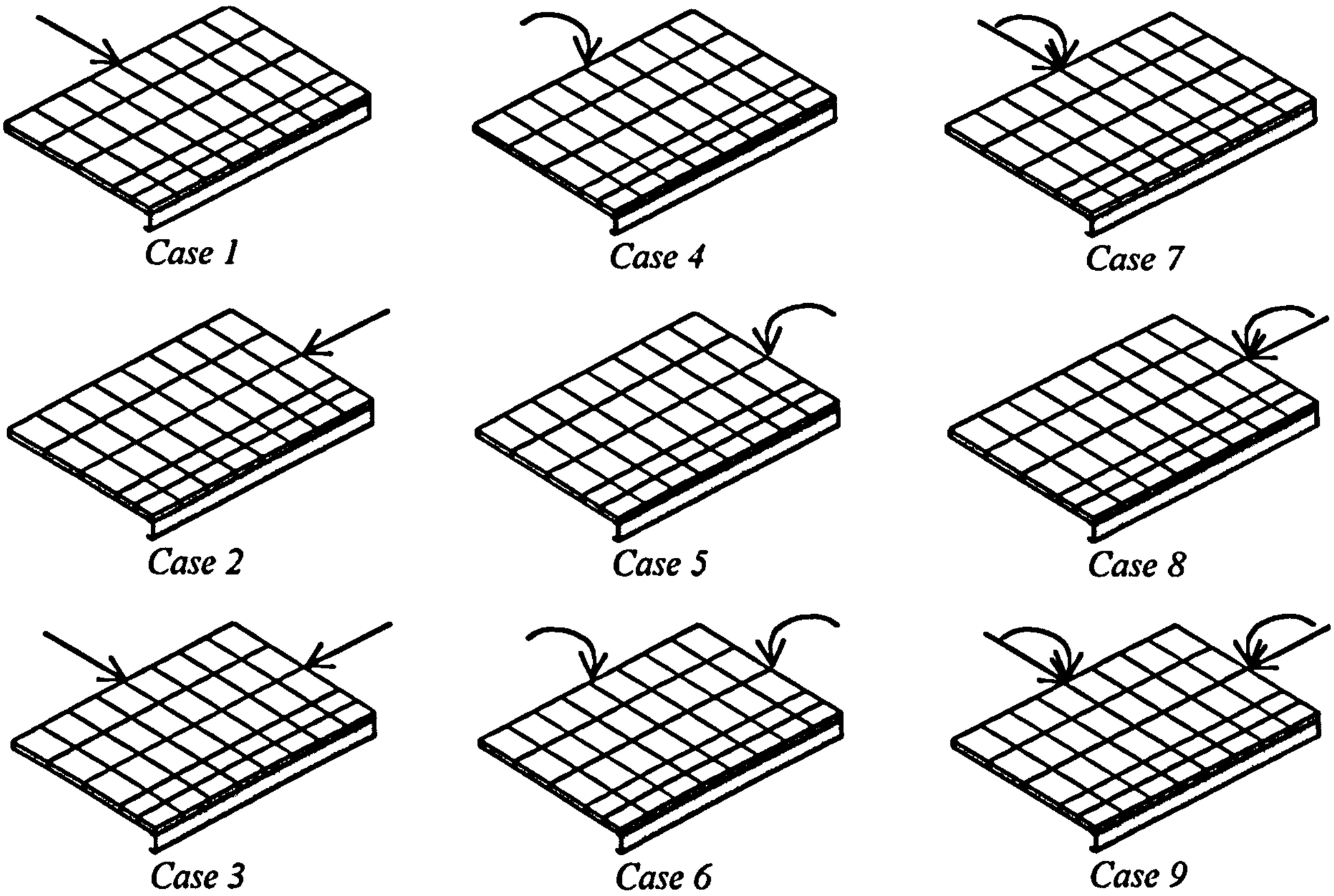

Figure 5-54. Different boundary condition cases for the heated slab and beam.

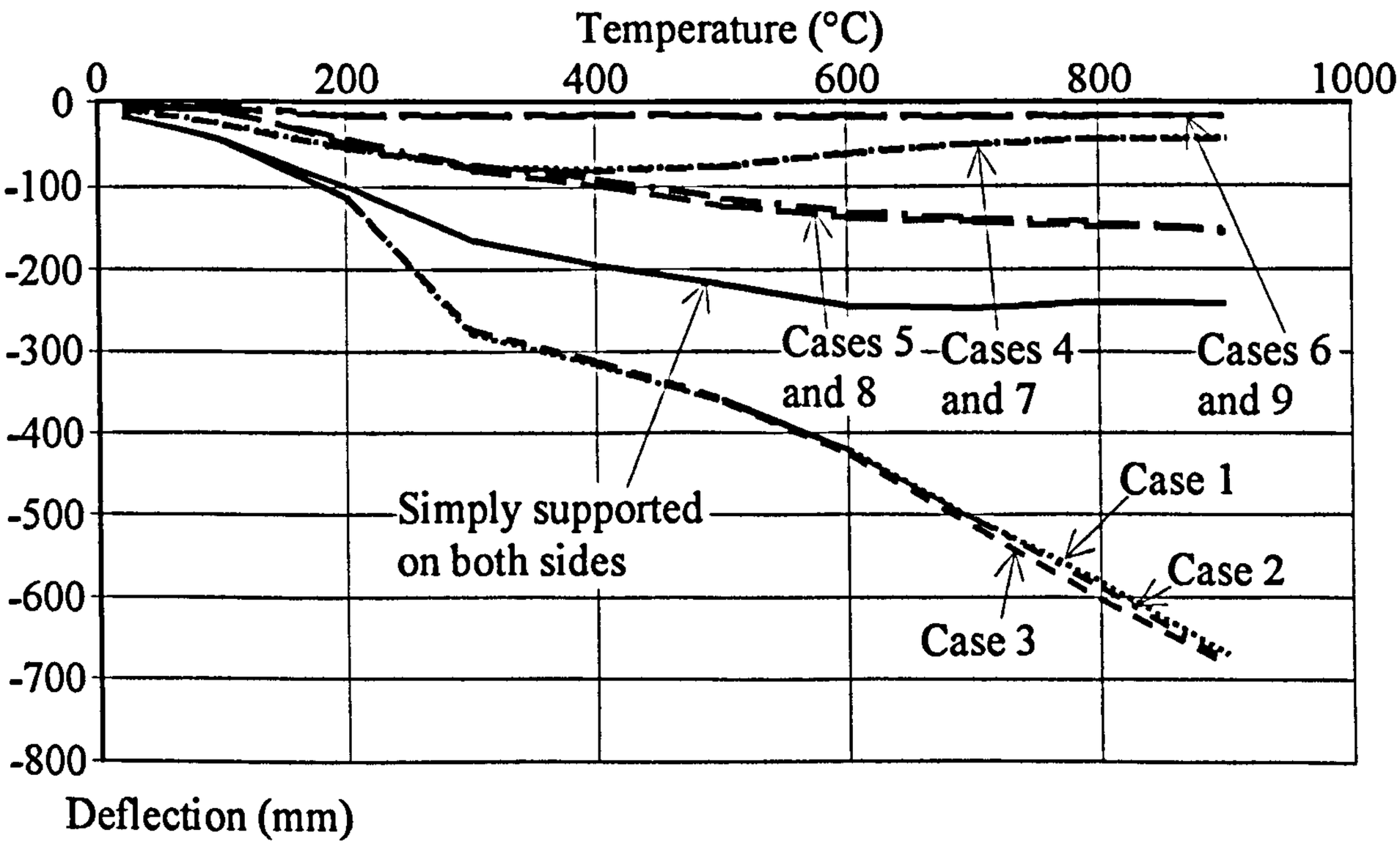

Figure 5-55. Central deflection of heated slab and beam for differing boundary conditions.

The other 6 cases do not crack to the same extent as cases 1, 2 and 3. When Cases 1, 4 and 7 are compared, it will be noted that 4 and 7 give very similar results. This leads to the simple conclusion that the overriding effect is the rotational fixity of the boundary conditions. This is confirmed by comparison of Cases 2, 5 and 8, against 3, 6 and 9 respectively. Cases 5 and 8 - at all temperatures - deflect to approximately two thirds as much as the simply supported case. This is logical as the effective span has been reduced by the introduction of the end rigidity.

It may also be noted from comparison of Cases 4 and 5, against Cases 7 and 8 that transverse restraint against rotation has a larger effect than rotational restraint about the end of the beam when temperatures exceed 400°C. For Cases 4 and 7 a bridging action is clearly taking place, attempting to return the beam to its original shape, whereas Cases 5 and 8 continue to deflect.

Effect of Slab Thickness

A parametric study concerning the effect of the thickness of the concrete slab was conducted on the beam and slab arrangement illustrated in Figure 5-49. All parameters were held constant except the thickness of the slab, which was varied from the extremes of 50mm to 120mm.

The results of the slab thickness parametric study are shown in Figure 5-56. All the slab thicknesses are seen to be acting in the same manner up to 300°C. This is due to the steel beam dominating the action of the beam and slab by thermal bowing. Beyond this temperature the steel beam begins to weaken and the slab begins to dominate the overall behaviour of the subframe.

The thinnest slab (50mm) cracks extensively across both the top and bottom faces at 20°C due to the loading. At 212.5°C the reinforcement in the slab begins to yield, and this increases the spread of cracking as the temperature increases, so that the deflections begin to 'run-away' in the manner of an isolated beam at high temperature. For thicknesses of 60mm and 70mm a similar action is taking place, albeit at higher temperatures. Thicknesses of 80mm and above crack nominally, and this range of thicknesses (beyond approximately 300°C) dominates the structural action of the subframe, reaching a steady state in the later stages of the temperature development.

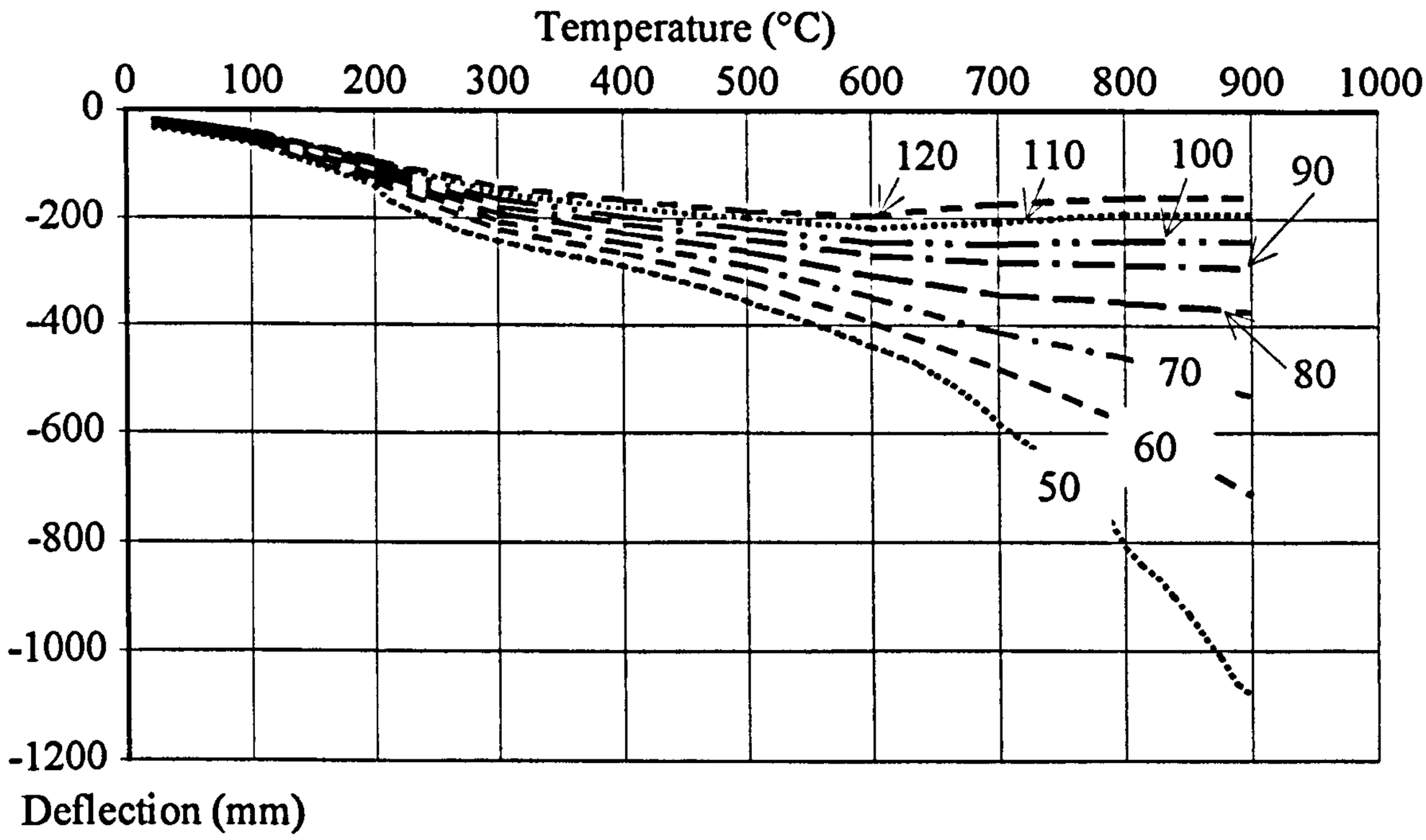

Figure 5-56. Slab thickness parametric study of the heated slab and beam

Effect of Slab Temperature Gradient

The beam and slab arrangement shown in Figure 5-46 was also subjected to different slab temperature gradients to ascertain the combined effects of thermal bowing and thermal material degradation in such a situation. At all times the concrete model uses the normal stress and uni-directional cracking failure criterion, with a compressive strength of 25 N/mm^2 and a tensile strength of 2.5 N/mm^2. The slab is 120mm thick and its edges are all assumed to be free to rotate and move laterally.

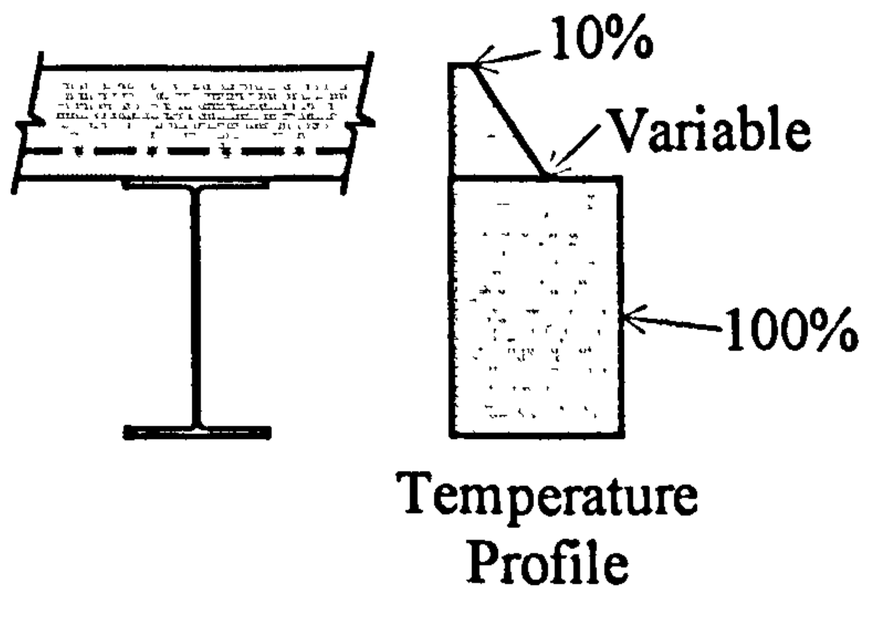

Figure 5-57. Temperature profile of beam and slab

The temperature on the upper concrete face is at 10% of the temperature of the beam; the soffit of the concrete slab varies in temperature proportionately to the beam. This is illustrated in Figure 5-57.

The parametric study results are shown in Figure 5-58.

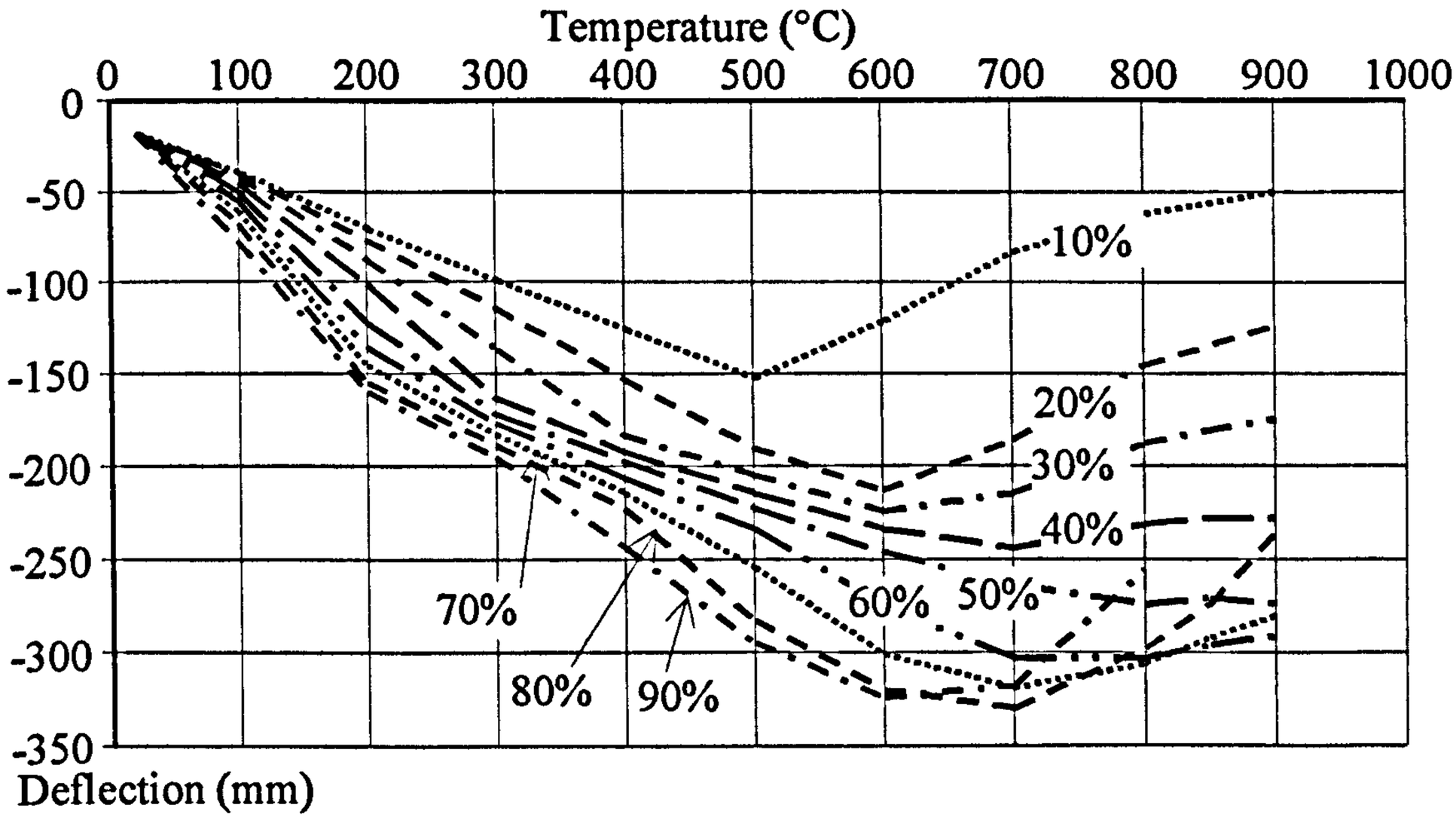

Figure 5-58. Slab temperature gradient parametric study of the heated slab and beam

The deflection of the slab whose lower face is subjected to 10% of the beam temperature is comparable to that of the unheated slab in Figure 5-47. The unheated slab has a greater deflection than the heated slab because the thermal bowing effects reduce due to the thermal expansion of the heated slab.

Conclusions

The beam and slab arrangement studied in section 5.9 has produced the following conclusions:

- A 'continuous' beam and slab arrangement will try to pull back to its original position, the transverse restraint in bending having the highest effect on this. However the original state will not be regained because of the action of cracking of the slab.

- The study of the four different methods of modelling cracking concrete show that the three less rigorous models give approximately the same results.

- Thin slab thicknesses produce greater cracking around the beam. This causes the beam to act as if isolated, causing run-away to occur. Thicker slabs dominate the behaviour of the subframe, causing the beam to return to the vicinity of its original position.

- A severe temperature gradient will produce large deflections.

6 SIMULATION OF THE CARDINGTON TESTS USING THE LAMINATED SHELL ELEMENT FLOOR SLAB

Using the laminated shell element described in Chapter 5 a series of parametric studies has been conducted on the six Cardington tests and, where possible, analysis output has been plotted against test data. This has been done to attempt to improve the understanding of the crucial parameters for the ultimate survival of the structure in fire.

6.1 GENERAL MODELLING ASSUMPTIONS

A number of assumptions have been adhered to for all the analyses unless noted otherwise. These are described in the following sections, and refer to certain slab characteristics and temperature distributions.

6.1.1 STRUCTURE TEMPERATURES

The beam bottom flange temperature is assumed to be the 'key temperature' (100%), and all other temperatures are described relative to this. For the elements of the steel beam, the temperature of the web is be assumed to be the same as that of the bottom flange with the top flange at 80% of this value. The temperatures of the top and bottom faces of the concrete floor slab are assumed to be 10% and 50% respectively of the key temperature, with a linear gradient between the two. This temperature pattern is shown in Figure 6-01.

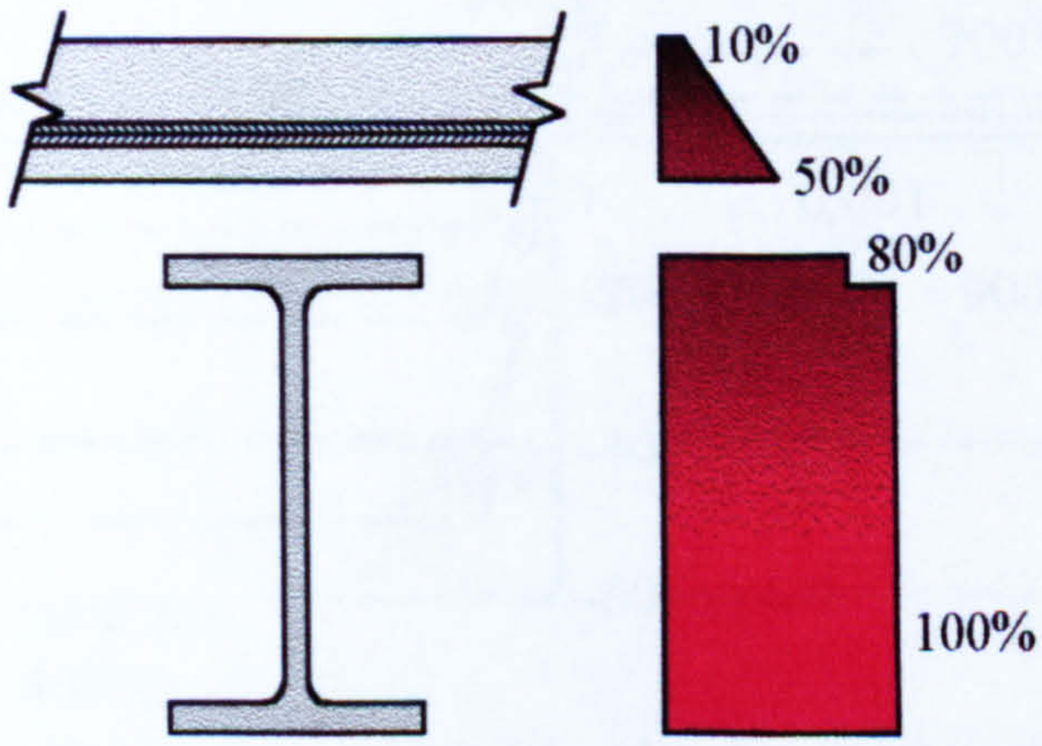

Figure 6-01. Assumed slab and beam temperatures

These approximations were based on the real Cardington temperature distributions described in Chapter 2.

6.1.2 SLAB CONSTANT PARAMETERS

Except where otherwise stated the slab thickness is assumed to be a constant 80mm for the continuous top section of the slab. This is based on the slab thickness survey described in Chapter 2. The concrete compressive strength is 25N/mm^2 and its tensile strength is 2.5N/mm^2 at ambient temperature. The elastic modulus at ambient temperature is 14000 N/mm^2. The stress-strain-temperature curves for concrete are based on EC4 [11] and are shown in Figure 6-02.

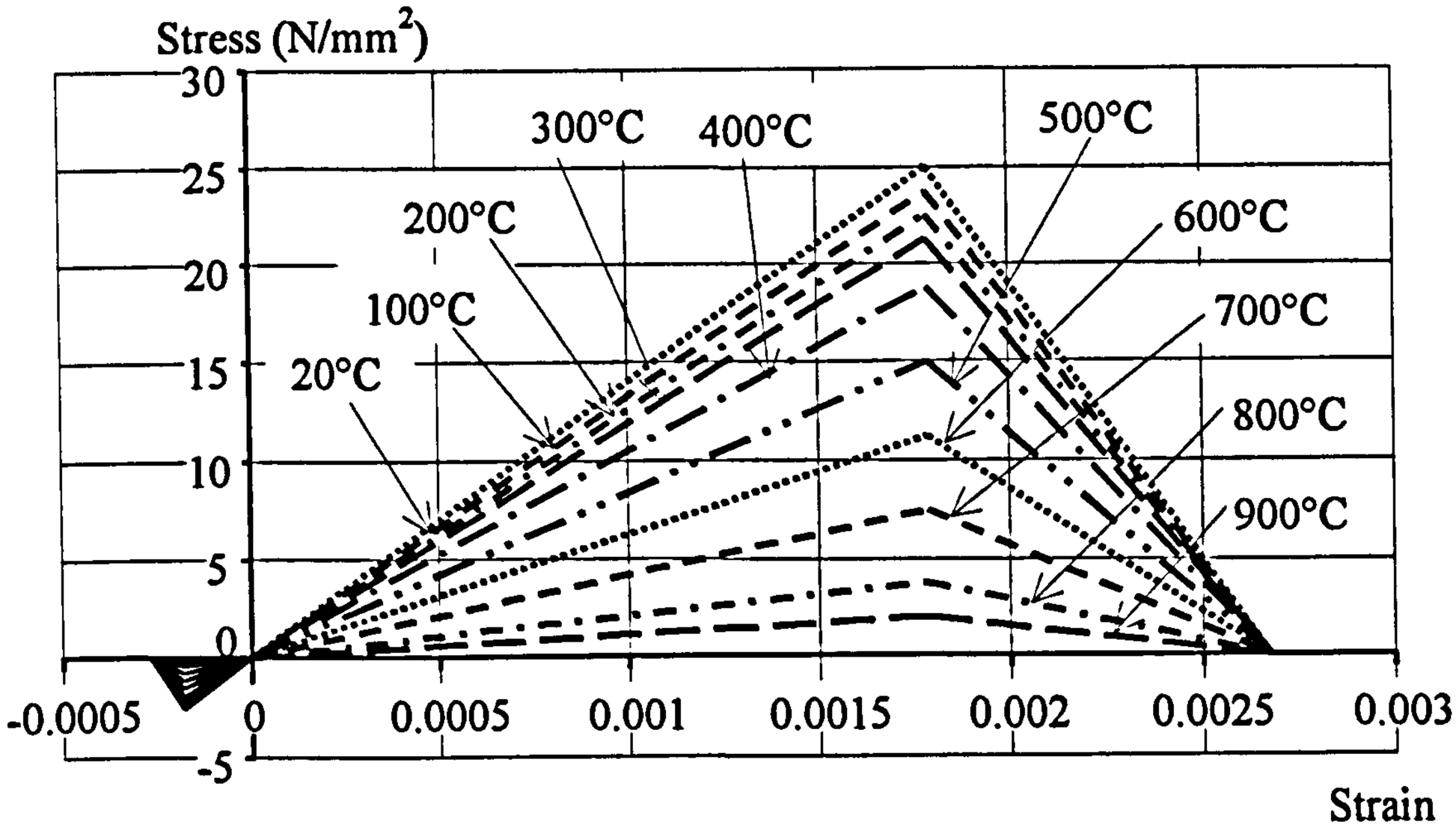

Figure 6-02. Stress-strain relationship of concrete at elevated temperatures

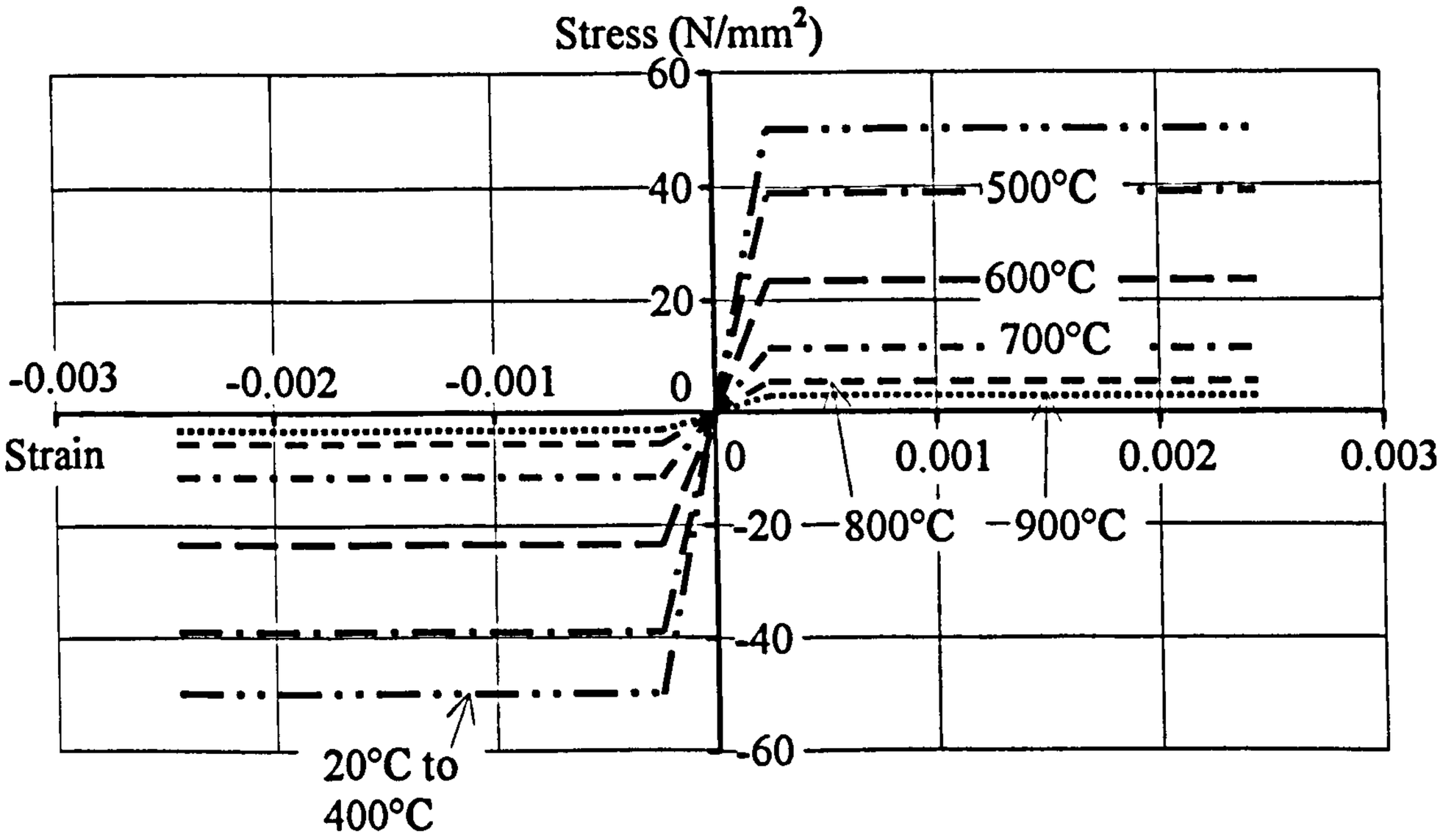

Figure 6-03. Stress-strain relationship of reinforcing steel at elevated temperatures

The A142 slab reinforcement has been modelled as a continuous smeared layer with maximum ambient temperature compression and tension strengths of 50 N/mm^2

across the reinforcement layers. The yield stresses for the steel were reduced in accordance with EC4 [11], as shown in Figure 6-03.

As the number of layers within a slab element does not greatly affect the computing time, their thickness has been maintained at a depth of 1mm throughout. This is advantageous, as the cracking model will be more accurate than if thicker layers are used.

The ambient-temperature material properties and dimensions are summarised in Figure 6-04

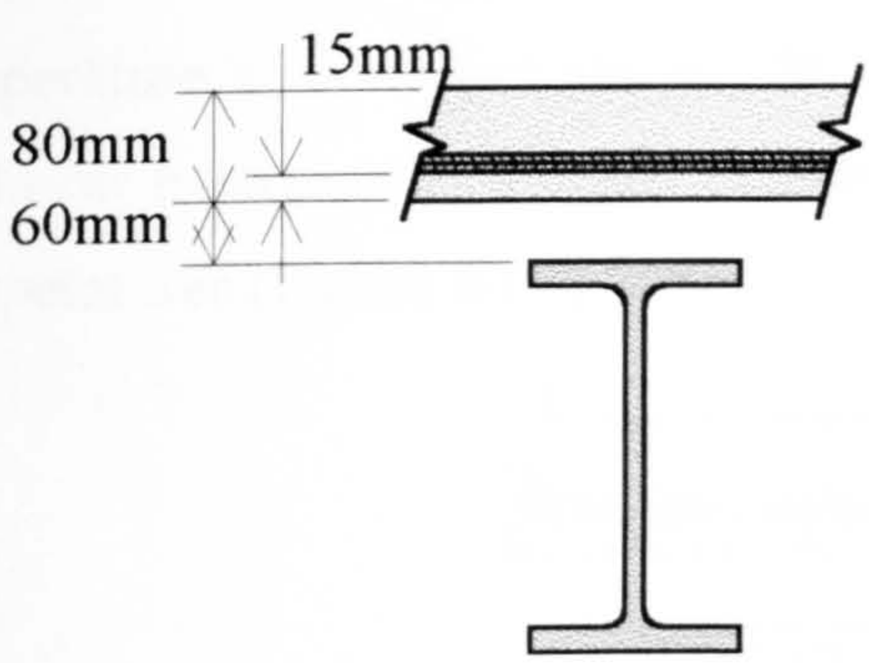

Figure 6-04 Assumed slab and beam material properties

6.2 Description of the Parametric Studies

Five types of parametric studies have been conducted on the six Cardington fire tests. The general details of the studies are described in the following sections.

6.2.1 Parametric Study 1 - Slab Thickness

The continuous slab thickness was varied throughout these parametric studies in 5mm increments between extremes of 70mm and 90mm. These limits are based on the slab thickness survey discussed in Section 2.

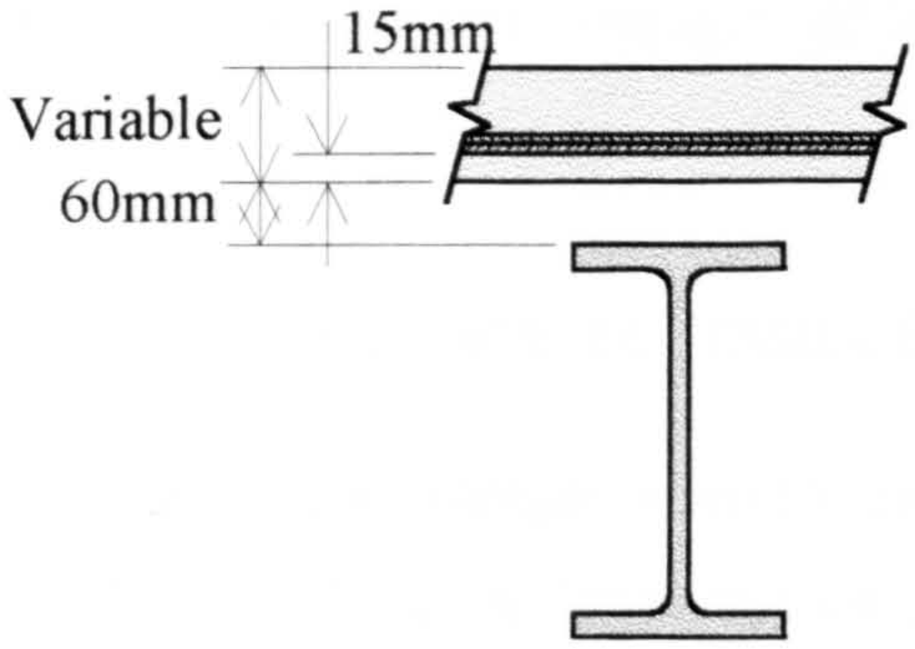

Figure 6-05. Parametric study 1 – Slab thickness

All other variables were held constant throughout the analyses including the position of the concrete reinforcement (Figure 6-05).

This parametric study was previously conducted using the isotropic elements defined in Chapter 4 and is repeated to give a comparison between the two slab models.

6.2.2 PARAMETRIC STUDY 2 - SLAB TEMPERATURE GRADIENT

In studying the influence of the temperature in the concrete slab, the bottom face temperature was varied between the extremes of 10% to 80% of the bottom flange temperature. The temperature of the top face is 10% of that of the bottom flange temperature as described above. At all times the temperature gradient is assumed to be linear between the top and bottom faces, and this also defines the reinforcement temperatures (Figure 6-06).

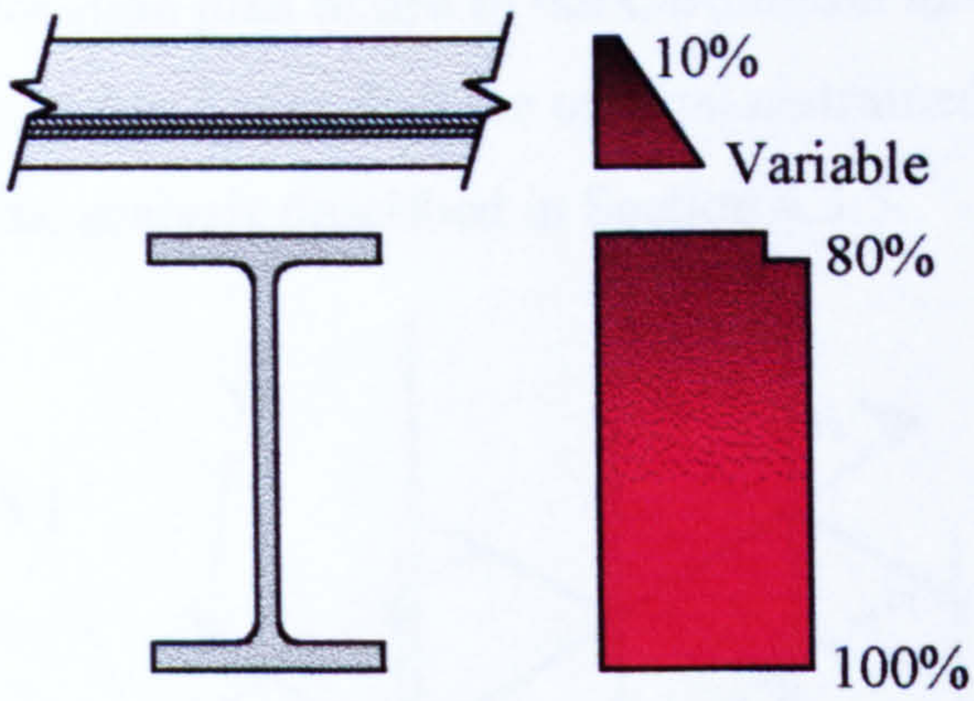

Figure 6-06. Parametric study 2 - slab and beam temperatures

6.2.3 PARAMETRIC STUDY 3 - SLAB CONCRETE COMPRESSIVE STRENGTH

The actual compressive strength of concrete within a structural element is generally variable, and differs from that found in a standard cube crushing test. BS8110 [68] suggests a figure of 67% of the cube strength. To study the influence of the compressive strength on the overall performance of the structure, a parametric study has been conducted with the compressive strength of concrete varied between $10N/mm^2$ and $30N/mm^2$.

6.2.4 PARAMETRIC STUDY 4 - SLAB CONCRETE TENSILE STRESS

BS8110 [68] also suggests that the tensile strength of concrete may be taken as 10% of the compressive strength. This is of course dependent on many factors such as the amount and type of aggregate and cement, the moisture content, air voids and the age

of the concrete. In this parametric study the tensile strength of concrete with a compressive strength of 25N/mm^2 has been varied between 5% and 15% in increments of 2.5%.

6.2.5 PARAMETRIC STUDY 5 - LOAD RATIO

As outlined previously in Section 2.1, the load ratio of a typical secondary beam in the Cardington test frame is 0.45 according to the normal design assumptions. This parametric study involved varying the load ratio from 0.33 to 0.57 in increments of 0.06 to study the effect of the load ratio on a full structure in fire.

6.3 RESTRAINED BEAM TEST PARAMETRIC STUDIES

The subframe used in the VULCAN restrained beam test analyses is shown in Figure 6-07, which includes a location plan of test in the Cardington test frame. Note that the extent of the subframe is rather larger than the original restrained beam subframe used in Chapter 4, based on the analysis described in Section 4.3.5.

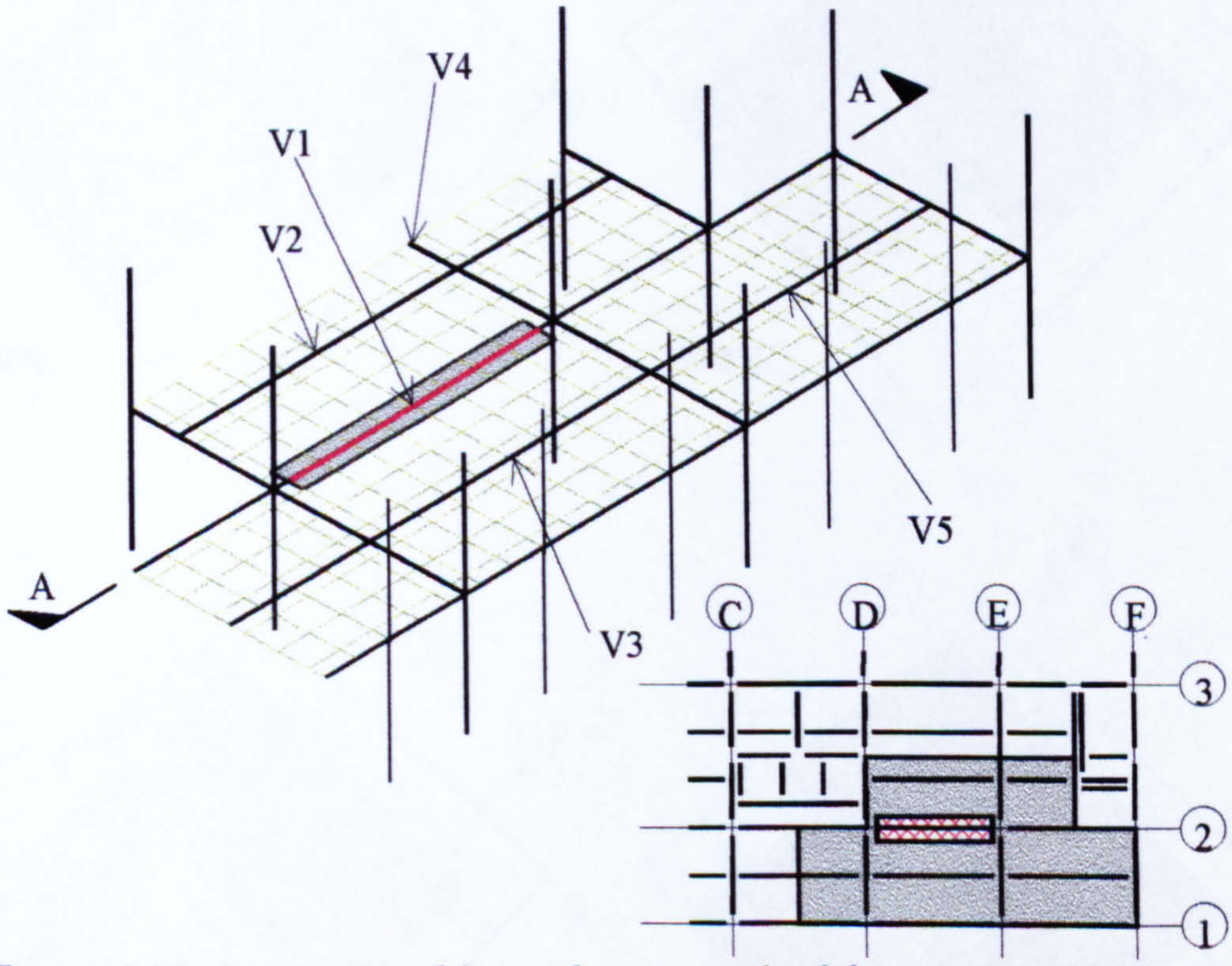

Figure 6-07. Location and finite element mesh of the restrained beam test.

Using the standard assumptions detailed in Section 6.1, a detailed analysis has been made for the restrained beam test to assist the understanding of the following parametric studies.

Figure 6-08 shows the progressive deflections within the subframe.

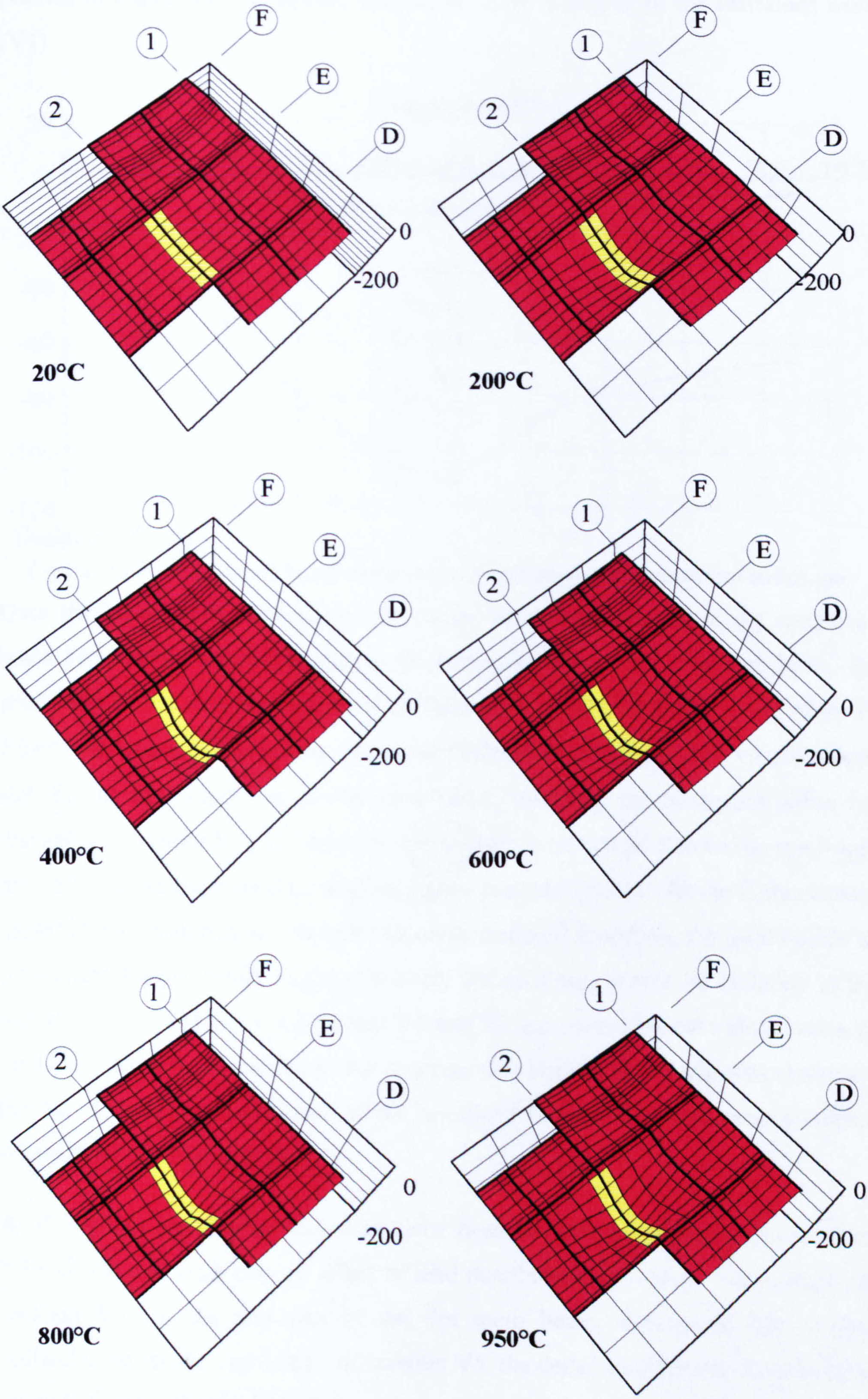

Figure 6-08. Progressive deflection of the restrained beam test

Figure 6-09 shows deflections determined at different locations across the subframe (shown in Figure 6-07) compared with those at the mid-span of the restrained beam (V1).

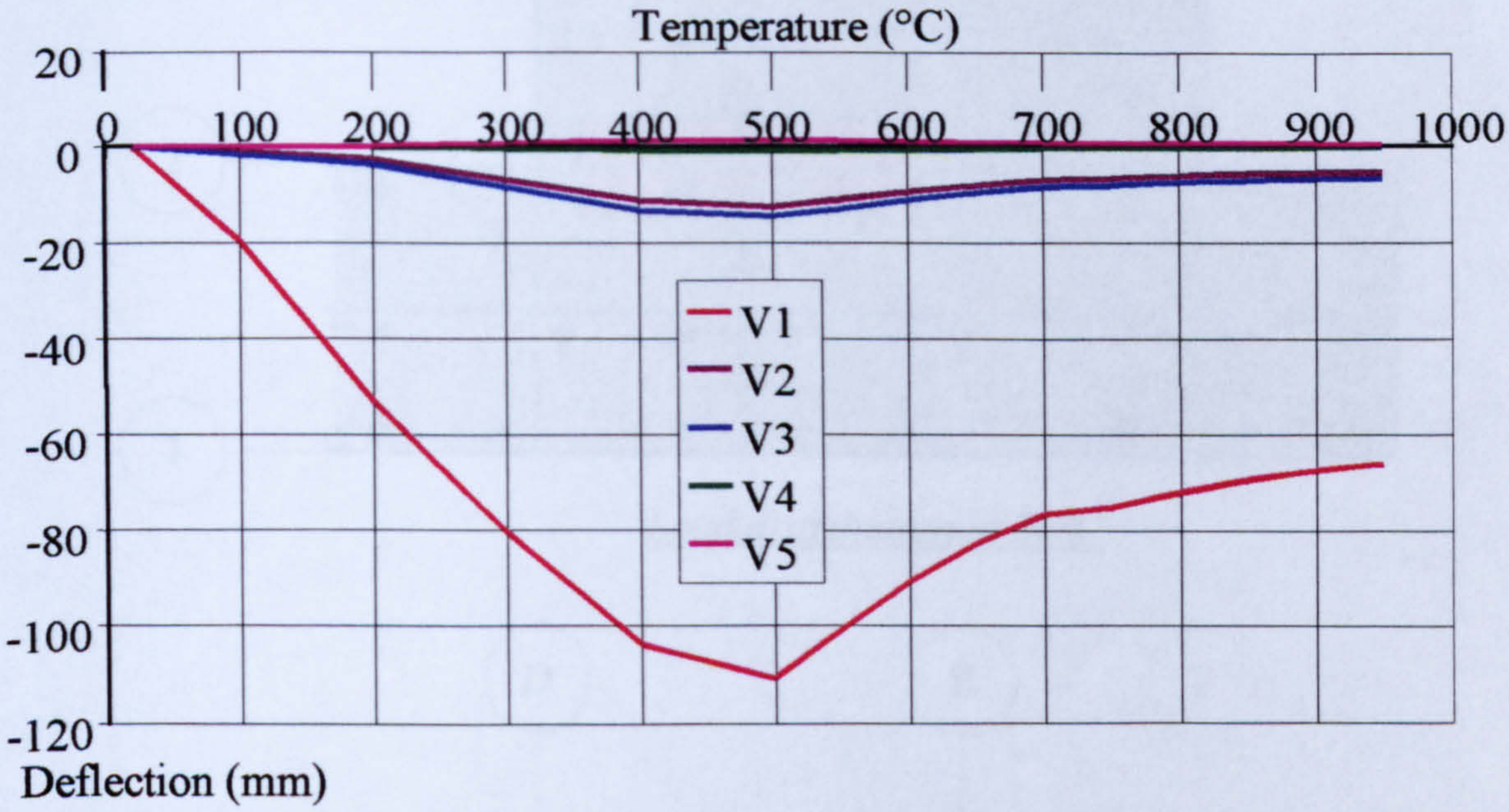

Figure 6-09. Restrained beam deflections at various locations around subframe.

Over the initial 500°C, deflections are caused by thermal bowing of the composite beam and thermal expansion against the surrounding structure. Beyond 500°C the steel beam begins to lose strength and stiffness significantly, leading to relief of the P-Δ bending deflection component. The effect of bending stiffness of the concrete floor slab begins to exceed that of the steel beam, reversing the beam deflection (as discussed in Section 5.12.1). Another contributory factor could also be the semi-rigid nature of the beam connections dominating the secondary beam. As the finite element model is not capable of accommodating cross-sectional distortion, the local buckle of the bottom flange, which might effectively act as a pin, cannot be included in the analysis. The deflections at locations V2 and V3 are caused by the redistribution of load away from the test beam as the concrete slab bridges to the adjacent secondary beams. This load redistribution of the restrained beam test compartment is shown schematically in Figure 6-10.

As deflections are considered further away from the test compartment (in locations V4 and V5) it is clear that the effect of load distribution decreases. For example, at location V4 –at the mid-span of the 9m main beam, deflections due to load redistribution increase by 1mm. At location V5, the deflections actually reverse by as much as 5mm as the test beam sags.

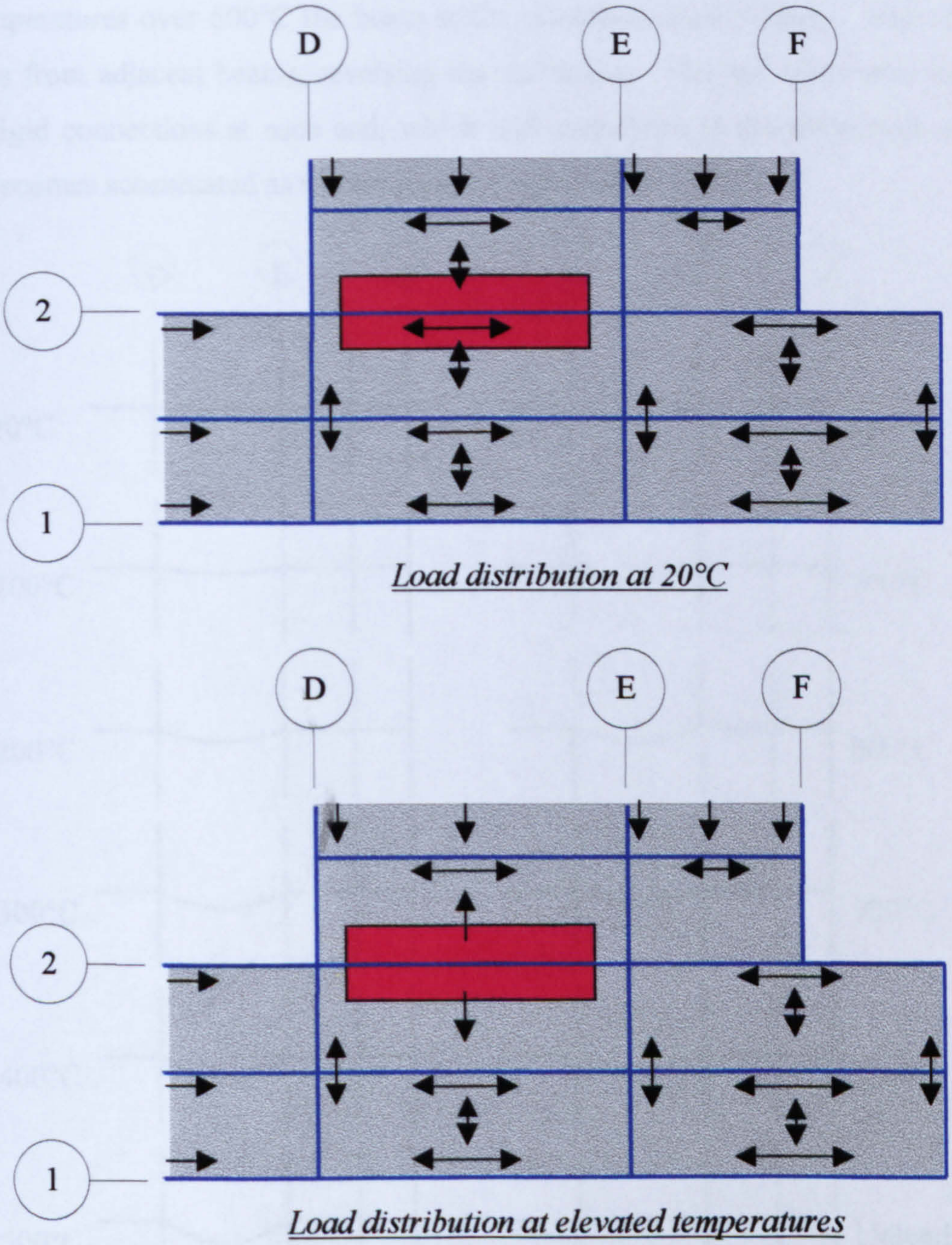

Figure 6-10. Redistribution of loads in the restrained beam test

Figure 6-11 shows the progressively deflecting shape of the restrained beam and adjoining subframe along the same section line (shown as Section A-A on Figure 6-07). Deflections have been scaled by a factor of 10.

At 20°C the restrained beam deflects under normal loading. This causes the supporting columns to deflect horizontally at mid-height between floors by 1mm.

Between 100°C and 500°C the beam expands against the surrounding structure; this movement is redistributed to the beams beyond the restrained beam, forcing them to hog. The horizontal deflection of the columns increases to a maximum of 8mm.

At temperatures over 600°C the beam stiffness reduces significantly. The concrete bridges from adjacent beams, reversing the deflection. The test beam also has cool semi-rigid connections at each end, which will contribute to the deflection reversal. This becomes accentuated as the temperature increases to 950°C.

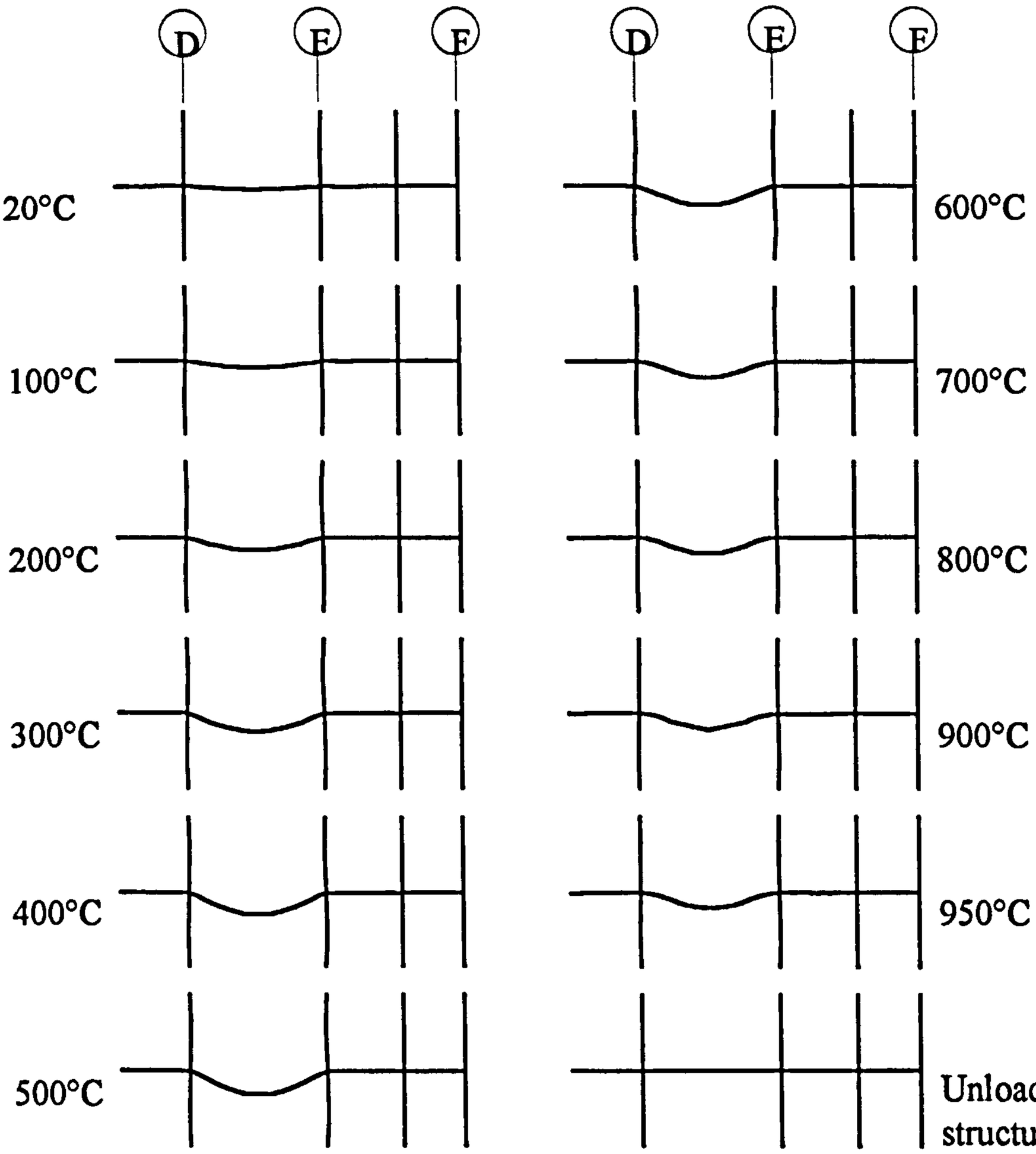

Figure 6-11. Restrained beam progressive deflections along the restrained beam

The propagation of cracking found from the finite element analysis conducted on the restrained beam test is shown in Figure 6-12 for both top and bottom faces. At 20°C a nominal amount of cracking may be seen at various locations across the structure on both faces. The cracking at 100°C is localised around the restrained beam as it begins to expand against the surrounding structure. This expansion forces the beam to sag, causing the bottom face of the slab to change from compression to tension. As the temperature rises to between 200°C and 400°C, the slab continues cracking in tension on its lower face. At this stage, the slab bridging from the secondary beams either side of the test beam begins to crack across its upper face as the slab hogs in this locality. Beyond this phase – at approximately 500°C – the strength and stiffness of

the test beam is reduced, so that the bending stiffness of the concrete slab attempts to return the test beam to its original shape, as discussed in Chapter 5.

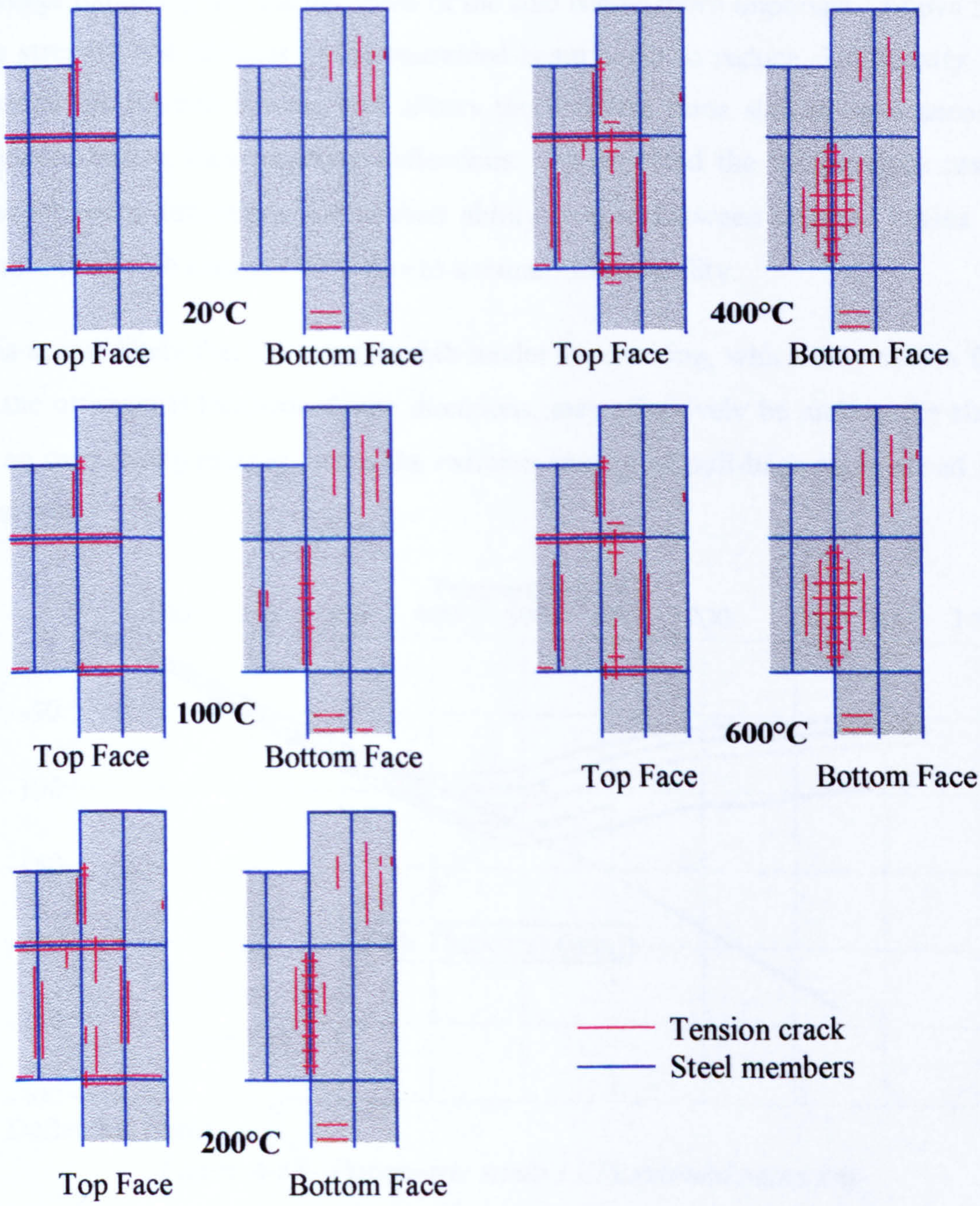

Figure 6-12. Propagation of cracks during the restrained beam test analyses

6.3.1 PARAMETRIC STUDY 1 - RESTRAINED BEAM TEST

The effect of varying slab thickness on the deflection of the test beam is shown in Figure 6-13. The analyses give a very good correlation with the test results up to 400°C. It will be noted that the effect of thickness of the floor slab at this stage is very small. The dominant action here is thermal bowing due to the temperature differential within the steel beam, and between the restrained beam and the concrete floor slab. Another factor contributing to the initial beam deflection is the restraint of

the surrounding structure. This effectively holds the ends of the beam stationary, so that as it tries to expand it is forced to sag. Beyond 400°C, the deflections begin to diverge indicating that the thickness of the slab is now more important. Above 500°C the strength and stiffness of the restrained beam begin to reduce significantly. This lessens the thermal bowing and allows the concrete floor slab to span across the adjacent beams, thus reversing deflections. As expected the thicker slabs result in smaller beam deflections due to their ability to span between adjacent beams. The 80mm thick slab ends at 600°C due to a numerical instability.

It is seems likely that the concrete slab model for cracking, which only allows failure in the orthogonal local-coordinate directions, may effectively be making the slab act in an over-strong manner, hence the extreme amount of pull-back experienced in the analyses.

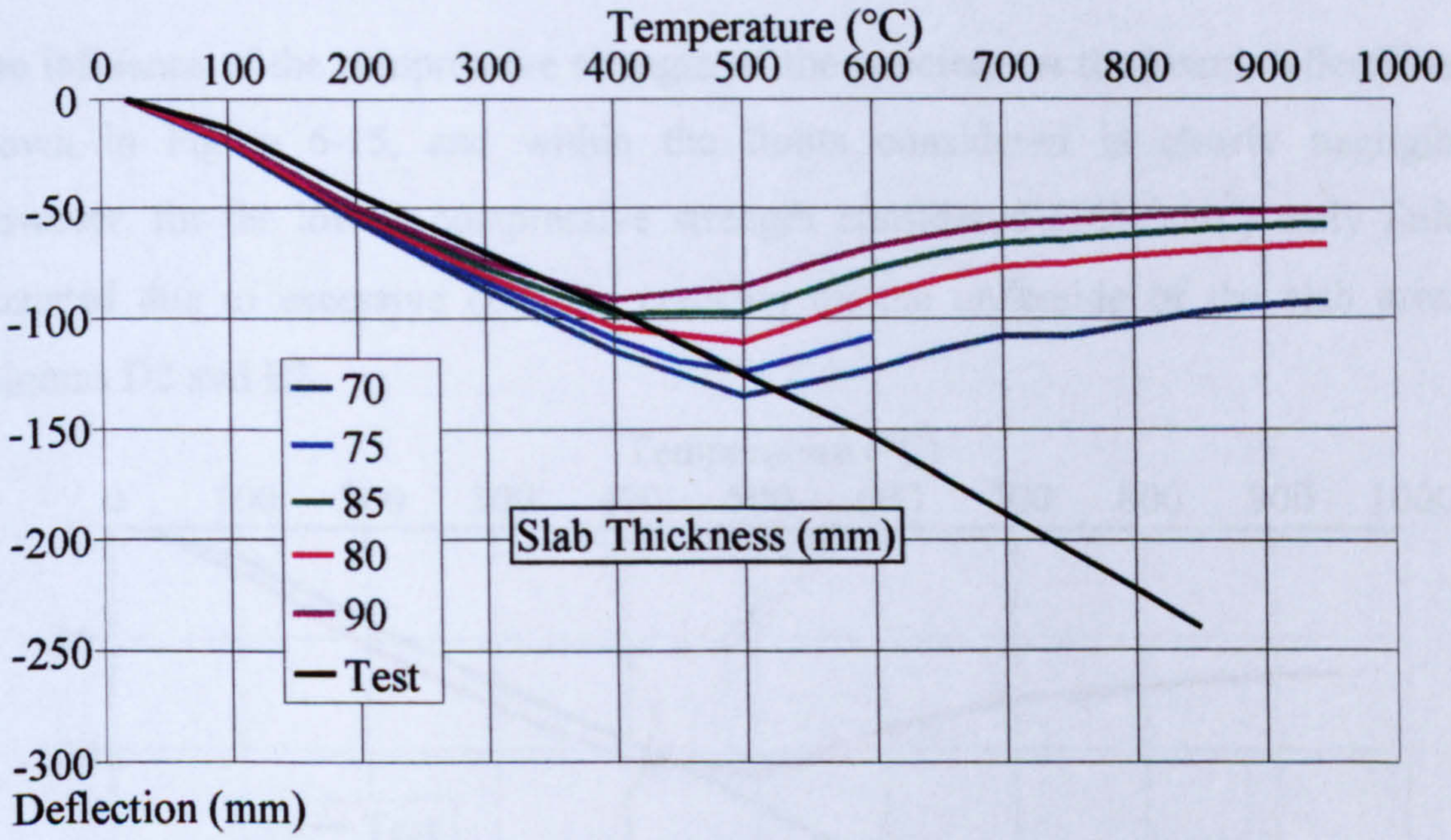

Figure 6-13. Parametric study 1 - Restrained beam test

6.3.2 PARAMETRIC STUDY 2 - RESTRAINED BEAM TEST

The second parametric study is concerned with the effect of the slab temperature gradient in the restrained beam test. The effects of this on the test beam deflections are shown in Figure 6-14. The parametric study follows a similar pattern to that discussed for the general restrained beam test in Section 6.3.

The fact that up to 400°C the curves are almost identical suggests that thermal bowing be principally due to temperature variations in the beam, and not to the difference between the beam and the floor slab temperatures.

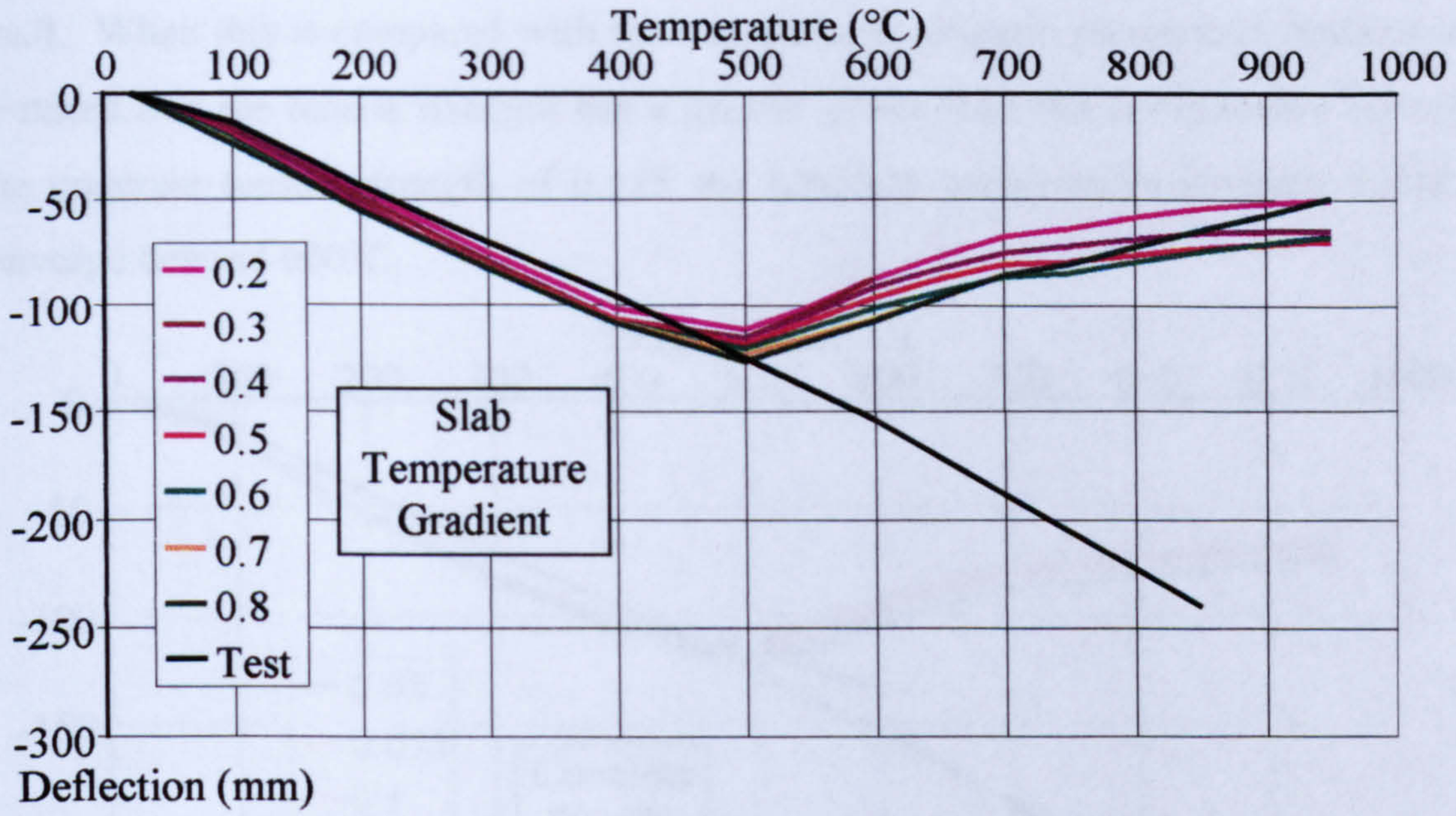

Figure 6-14. Parametric study 2 - Restrained beam test

6.3.3 PARAMETRIC STUDY 3 - RESTRAINED BEAM TEST

The influence of the compressive strength of the concrete on the beam deflections is shown in Figure 6-15, and within the limits considered is clearly negligible. However, for the lowest compressive strength considered (10N/mm^2) early failure occurred due to excessive concrete cracking on the underside of the slab around columns D2 and E2.

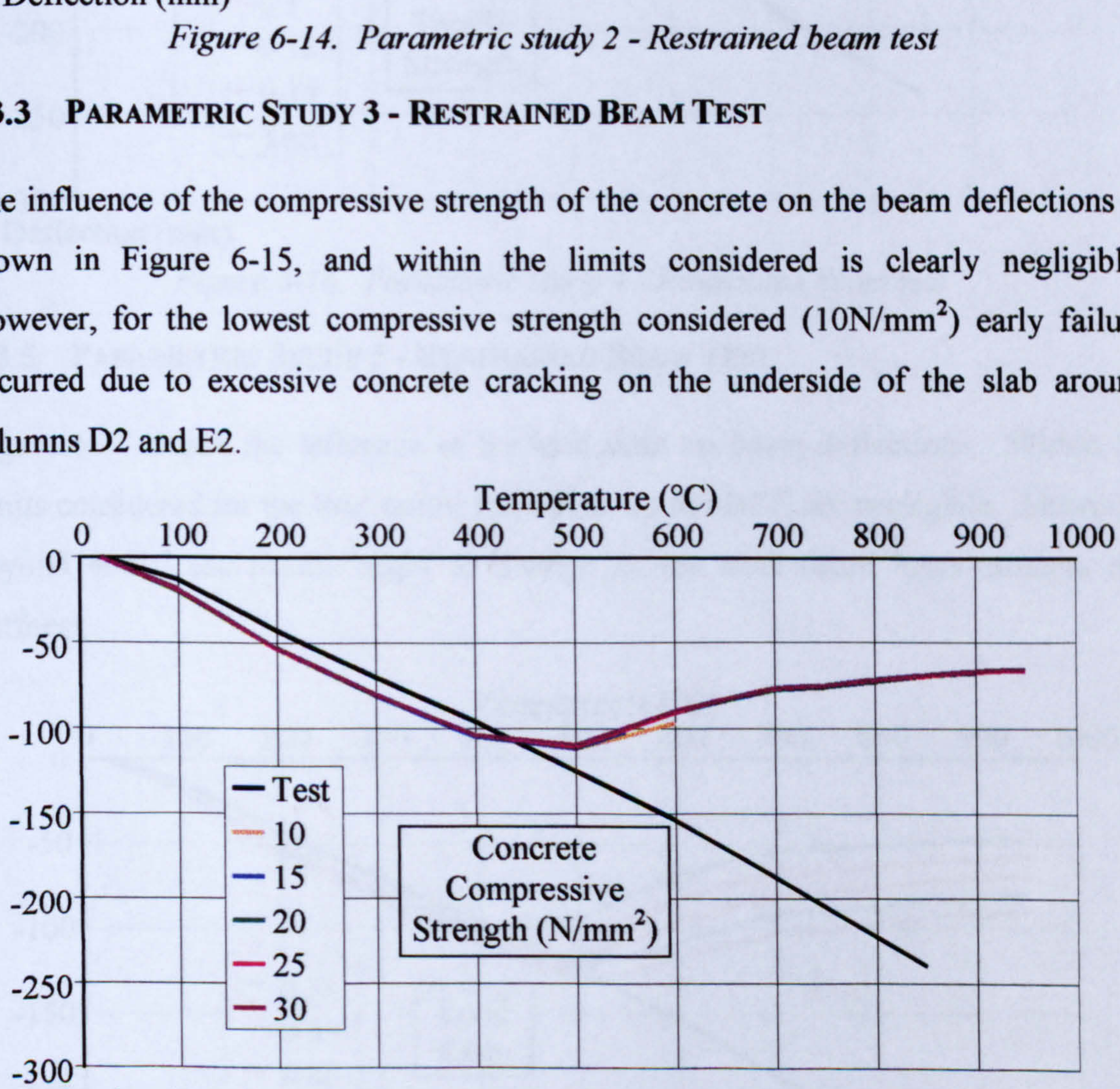

Figure 6-15. Parametric study 3 - Restrained beam test

6.3.4 PARAMETRIC STUDY 4 - RESTRAINED BEAM TEST

The effect of the concrete tensile strength on the beam deflection is shown in Figure 6-16. As expected the weaker concrete results in greater deflections, but the effect is

small. When this is compared with the compressive strength parametric study, it will be noted that the tensile strength has a greater effect than the compressive strength. The concrete tensile strength of 0.125 the concrete compressive strength failed to converge beyond 600°C.

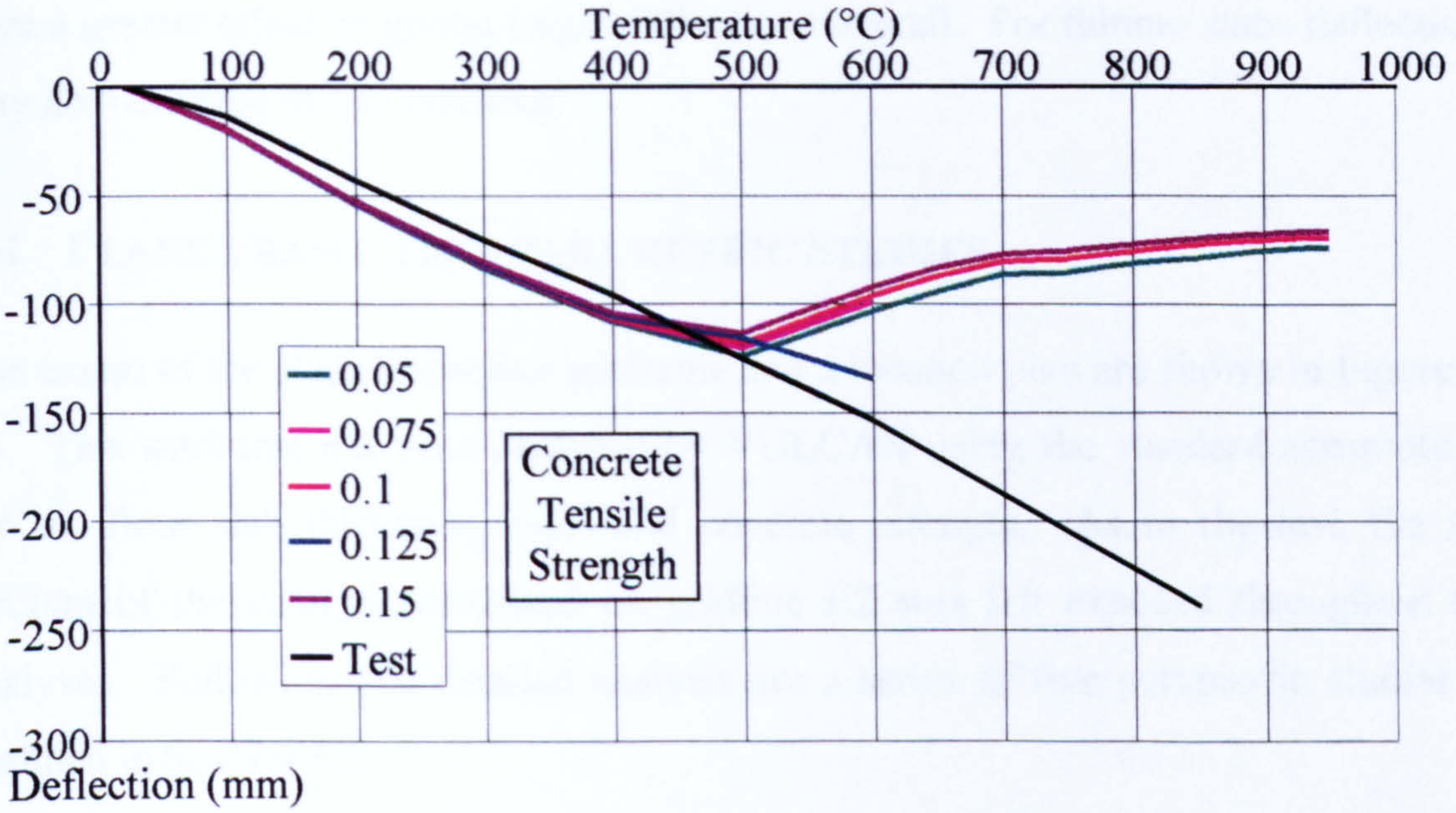

Figure 6-16. Parametric study 4 - Restrained beam test

6.3.5 PARAMETRIC STUDY 5 - RESTRAINED BEAM TEST

Figure 6-17 shows the influence of the load ratio on beam deflections. Within the limits considered for the load ratios, the results up to 400°C are negligible. However, beyond 400°C the results begin to diverge as the steel beam loses strength and stiffness.

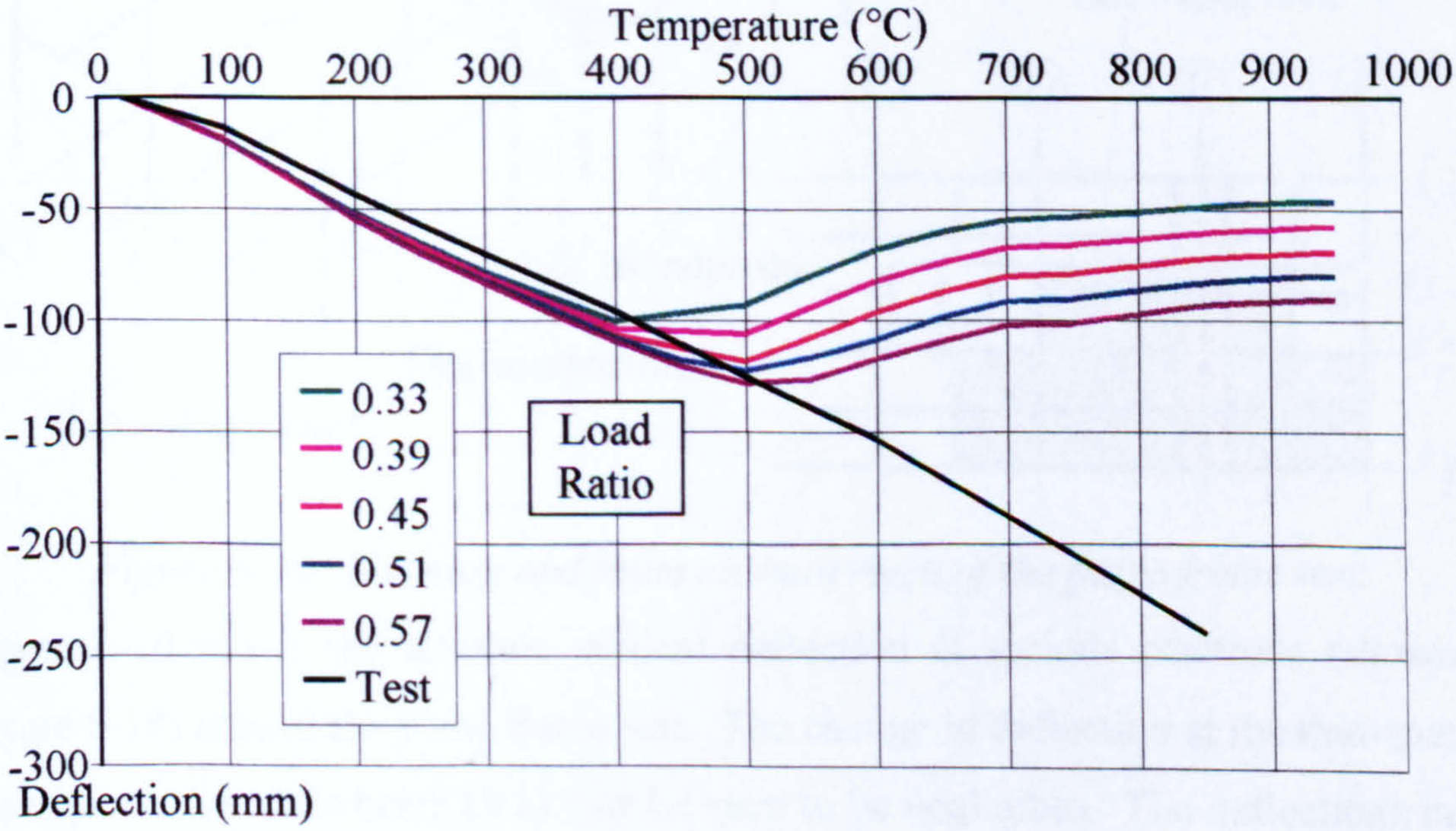

Figure 6-17. Parametric study 5 – Restrained beam test

It may be speculated that, if a thicker slab were to be applied to the load ratio parametric study, the effect of the load parameter would reduce due to the enhanced bending stiffness inherently found in thick slabs. Conversely, should a thinner slab be used in the parametric study, the reduced bending stiffness would allow the load to have a greater effect by giving larger deflections overall. For thinner slabs deflections may also increase due to cracking.

6.4 PLANE FRAME TEST PARAMETRIC STUDIES

The extent of the plane frame test subframe and a location plan are shown in Figure 6-18. This subframe has been analysed by VULCAN using the standard assumptions for the floor slab thickness, loads and concrete strength. As in the test, the top 500mm of the column positioned on gridline E2 was left exposed throughout the analyses. Following this detailed analysis are a series of five parametric studies as outlined in Section 6.2.

The plane frame test has significantly less inherent restraint than the restrained beam test, provided only by the column stiffness and slab shear across the structure.

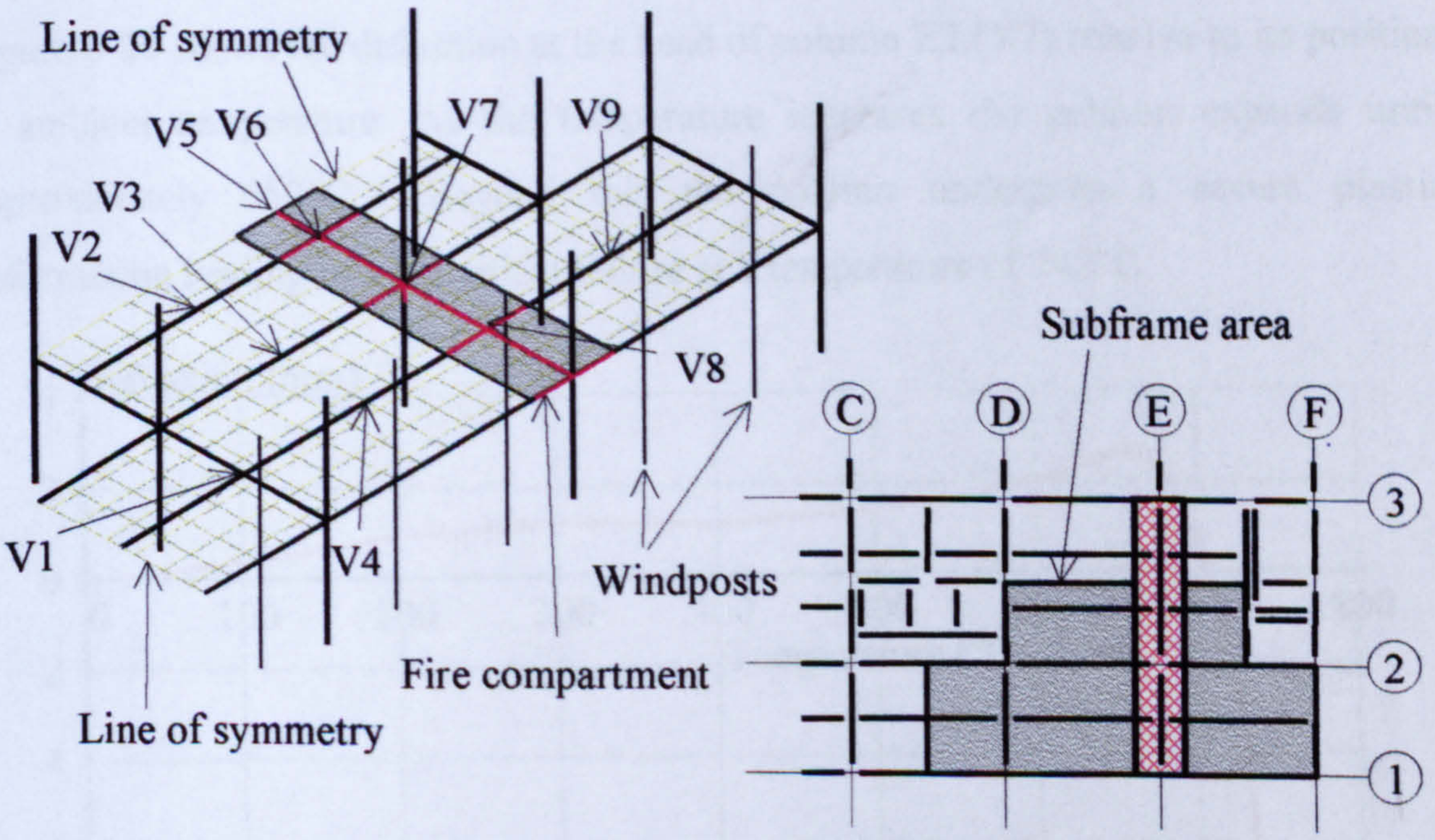

Figure 6-18. Location and finite element mesh of the plane frame test.

Figure 6-19 shows the absolute vertical deflection at various positions (shown in Figure 6-18) around the plane frame test. The change in deflection at the mid-span of the adjacent 6m main beam (V1) may be seen to be negligible. The deflections taken at the mid-spans of secondary beams that frame into the plane frame test (V2, V3, V4

and V9) start at 20°C with deflections between 18mm and 25mm and slowly increase as the corresponding supporting beam or column deflects. Deflections along the primary beams (V5, V6 and V8) increase initially due to thermal bowing. At temperatures of approximately 500°C the steel beams have lost significant strength and stiffness, thus causing continued deflections.

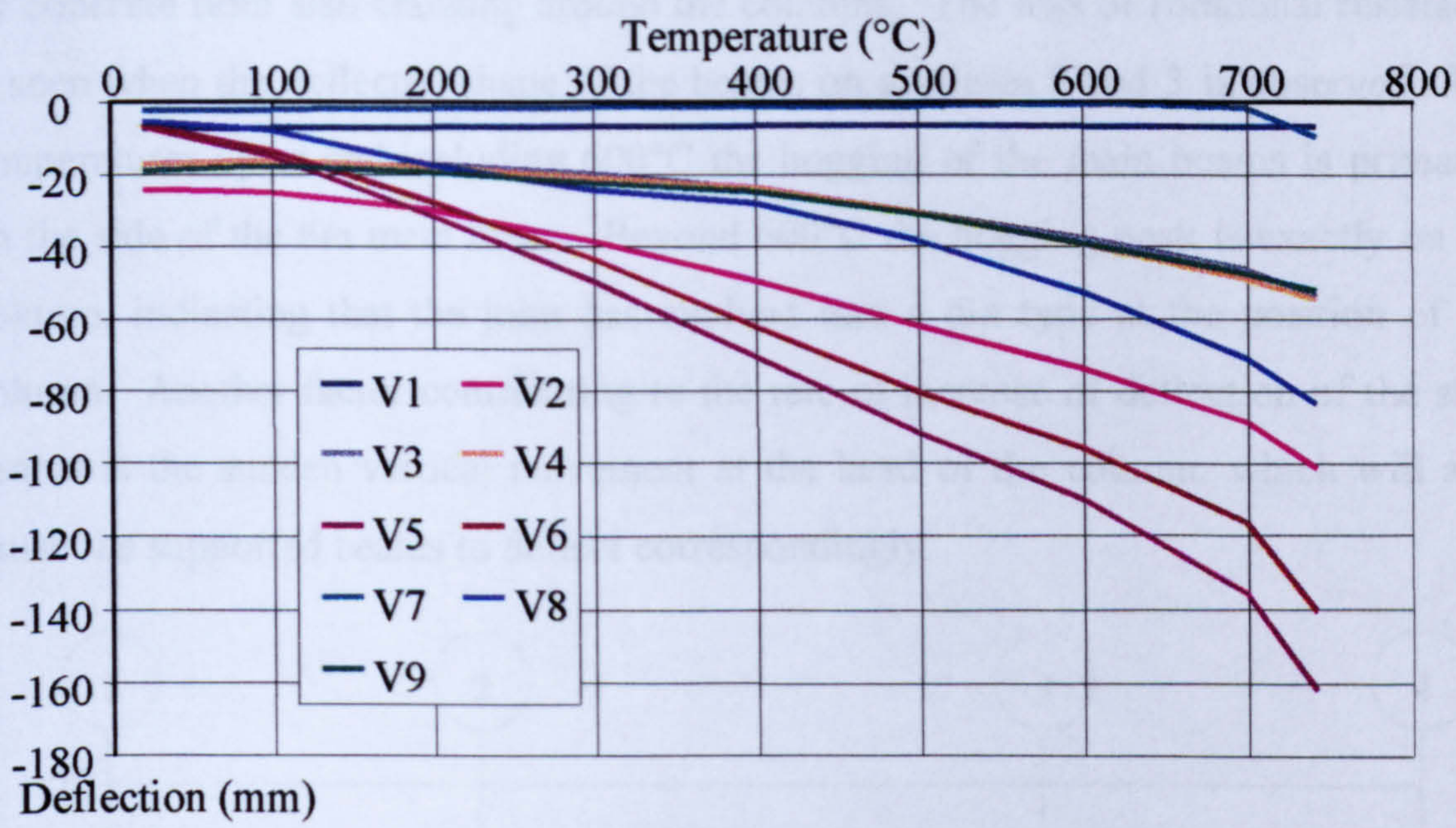

Figure 6-19. Plane frame test analysis deflections at various locations around the subframe

Figure 6-20 shows the deflection at the head of column E2 (V7) relative to its position at ambient temperature. As the temperature increases the column expands until approximately 650°C. Beyond this the column undergoes a severe plastic deformation leading to a numerical failure at a temperature of 742°C.

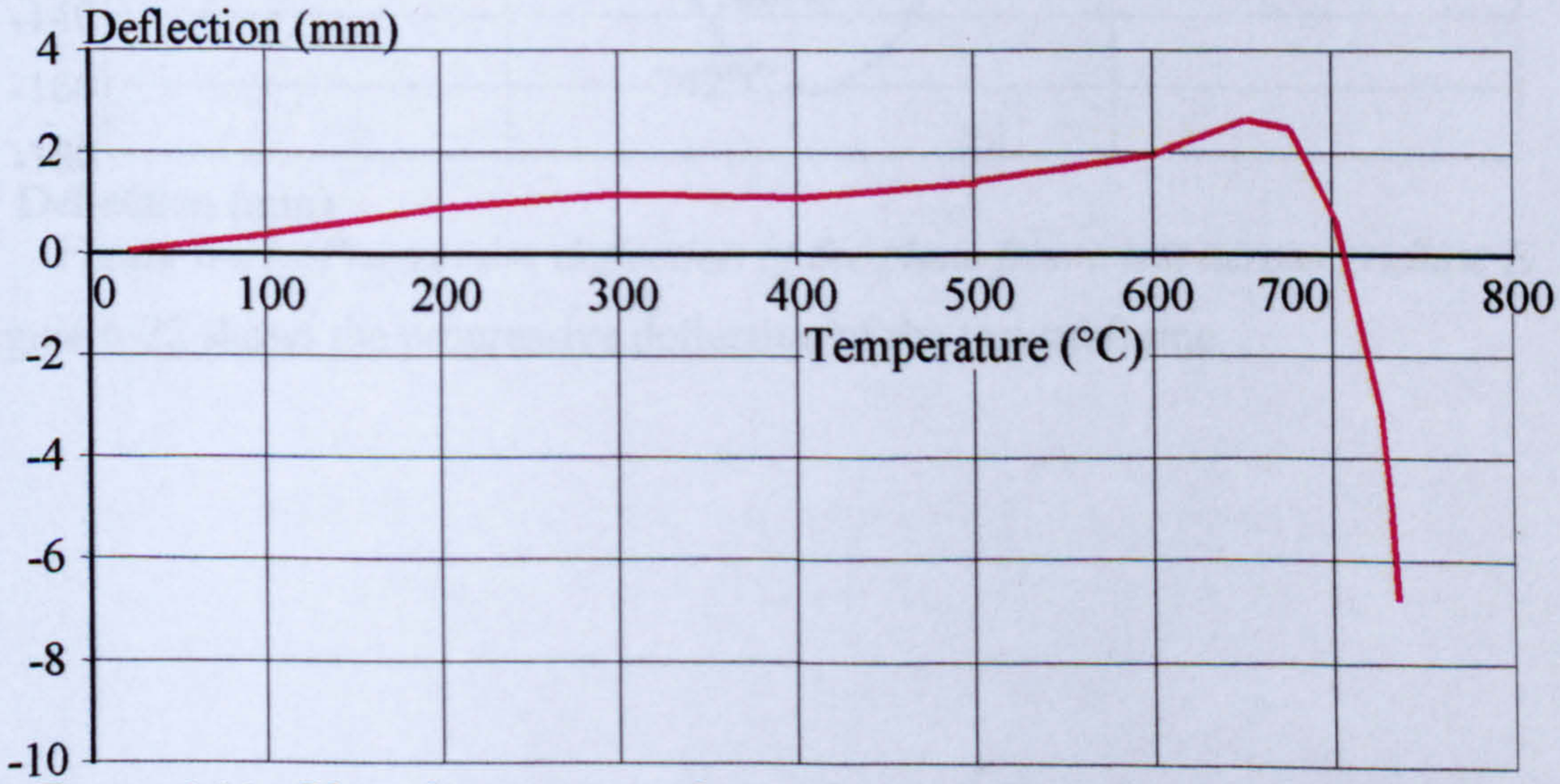

Figure 6-20. Plane frame test analysis relative deflection at head of column E2

Figure 6-21 shows the absolute deflection profile of the plane frame along the main beams as the temperature increases. The rate of deflection is approximately constant up to 700°C, after which it increases markedly. This is caused partly by the sudden plastic deformations at the heads of the two inner columns which effectively act as pinned supports, removing the rotational resistance of the lower columns, and partly by concrete floor slab cracking around the columns. The loss of rotational resistance is seen when the deflected shape of the beams on gridlines 2 and 3 is observed. For temperatures up to and including 600°C the hogging of the main beams is primarily on the side of the 6m main beam. Beyond 600°C the hogging peak is exactly on the column, indicating that the joint has evolved into a pin type at the position of the column. Another factor contributing to the rate of increase of deflection of the steel beams is the sudden vertical movement at the head of the column, which will also cause the supported beams to deflect correspondingly.

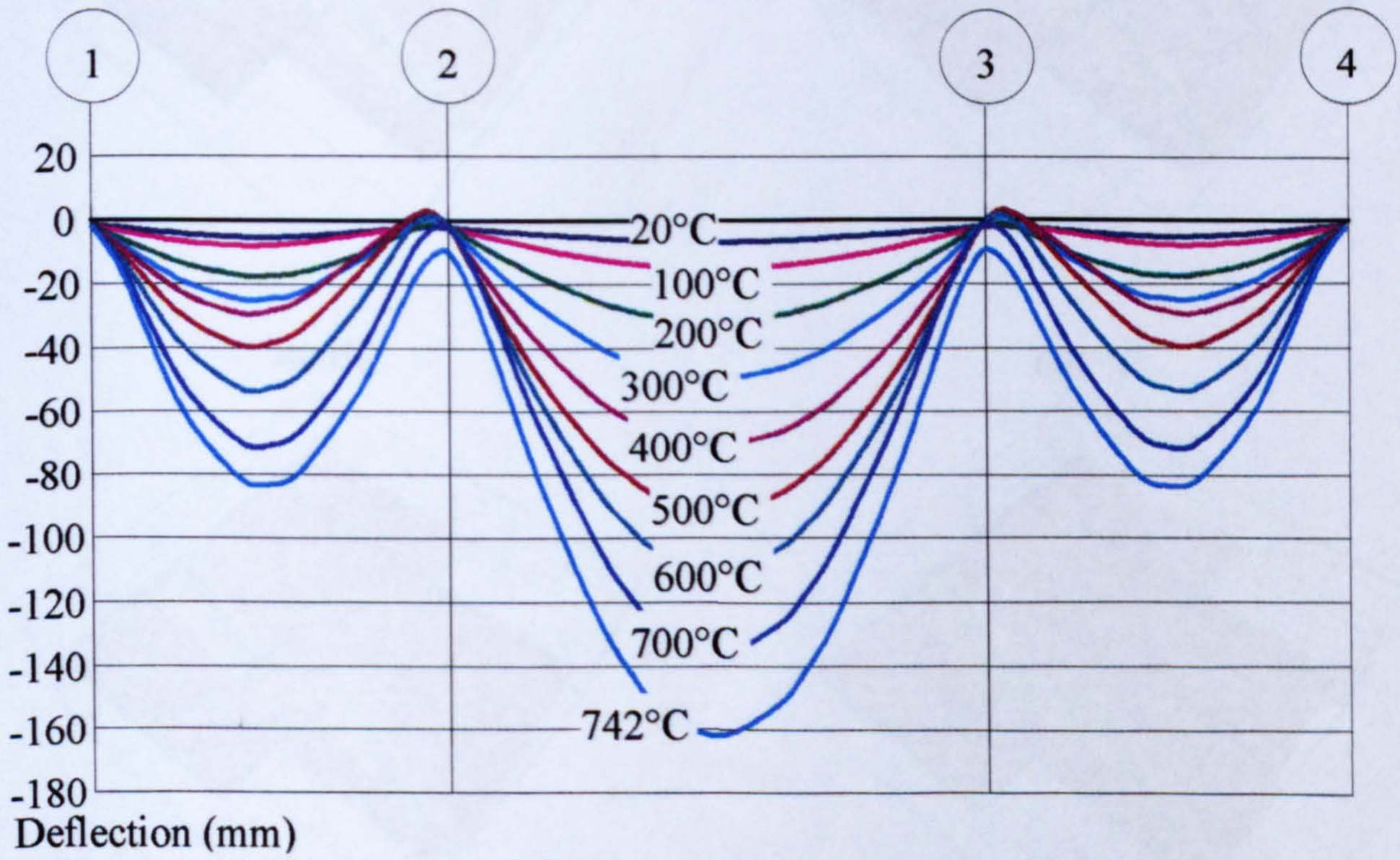

Figure 6-21. Progressive deflection of the plane frame test across gridline E

Figure 6-22 shows the progressive deflection of the test subframe.

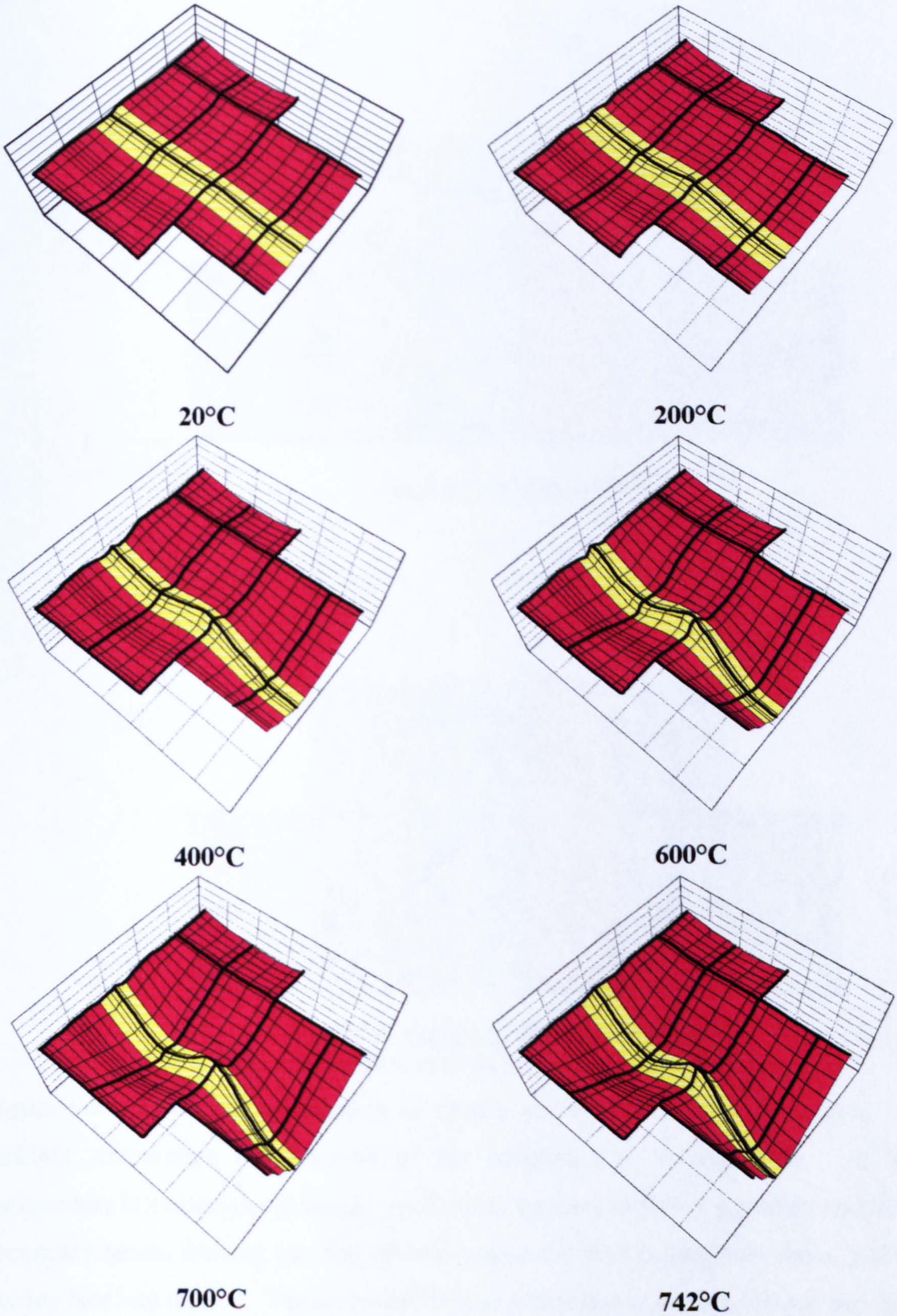

Figure 6-22. Progressive deflection of the plane frame test

Figure 6-23 shows a schematic drawing of the load paths at the two extremes of the test; 20°C and after the column deforms plastically at 742°C.

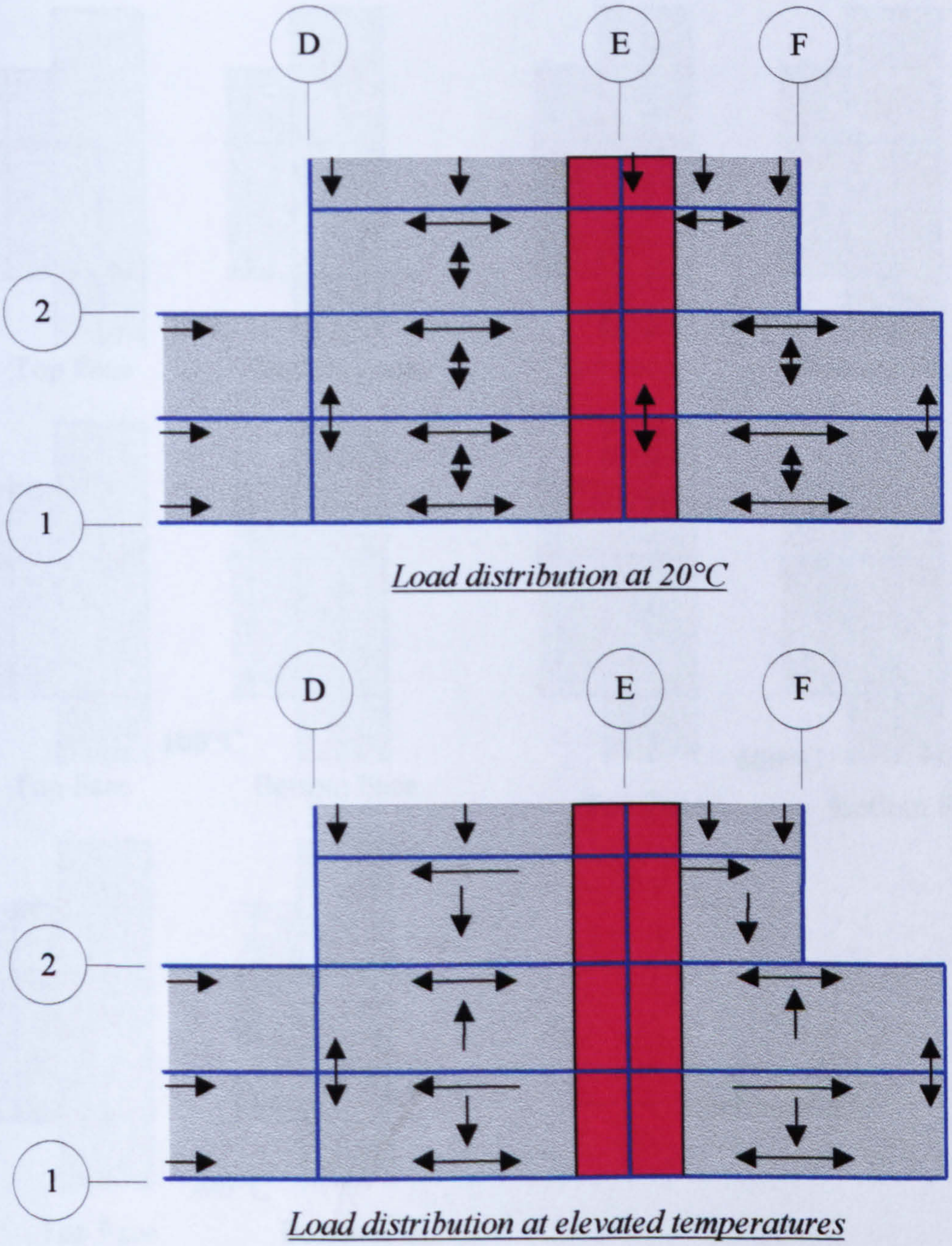

Figure 6-23. Redistribution of loads in the plane frame test

Figure 6-24 shows the propagation of cracks across the concrete floor slab. At ambient temperature the cracking of the concrete slab is negligible. As the temperature increases, the propagation of cracks appears to follow a pattern where the secondary beams framing into the columns cause the slab to hog over them, forcing the top face into tension. The secondary beams which frame into the 6m and 9m main beams sag, causing tension in the bottom face of the concrete slab, therefore causing cracking along these lines. Along gridline 1, a cracking pattern is shown which indicates that the edge beam is alternating between sagging and hogging. This is caused by the windposts supporting the edge beam by acting in tension from the floor above. The maximum stress due to bending was $15N/mm^2$. No compression cracks were found to appear in the analysis.

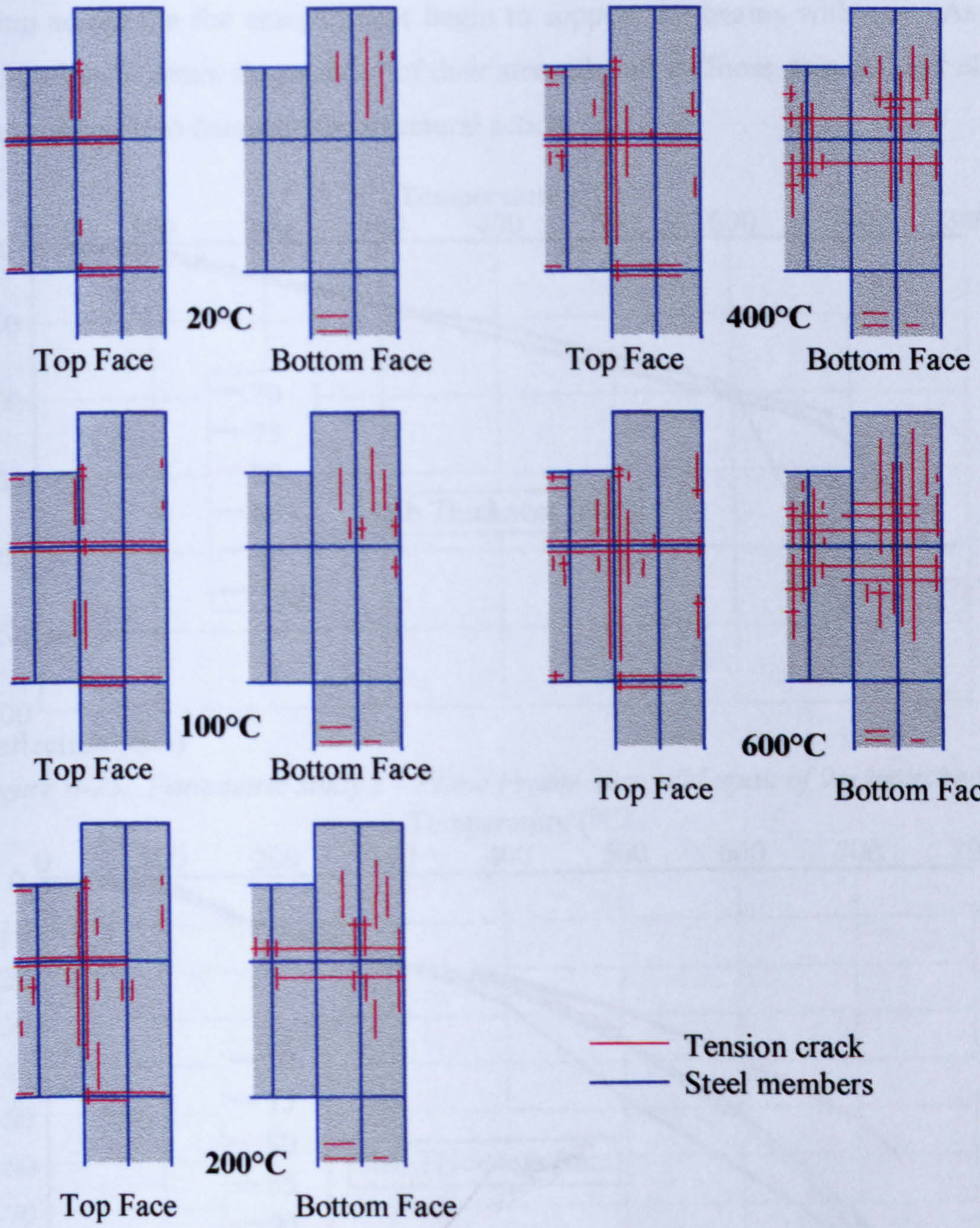

Figure 6-24. Propagation of cracks during the plane frame test analyses

6.4.1 PARAMETRIC STUDY 1 - PLANE FRAME TEST

Figures 6-25 and 6-26 show the central deflections of the 9m and 6m main beam respectively for different slab thicknesses, and demonstrate a very good correlation with the test results.

The thickness of the concrete slab appears to have little influence over the beam deflections. From this it may be deduced that the initial deflections up to 500°C are largely due to thermal bowing for both the 6m and 9m beams, as in-plane restraint is predominantly due to the stiffness of the columns. Beyond 500°C, the strength and stiffness of the steel beam is reduced significantly, so that the secondary beams

spanning across the fire compartment begin to support the beams within it. As the secondary beams retain the majority of their strength and stiffness, this will not allow the slab thickness to dominate the structural action.

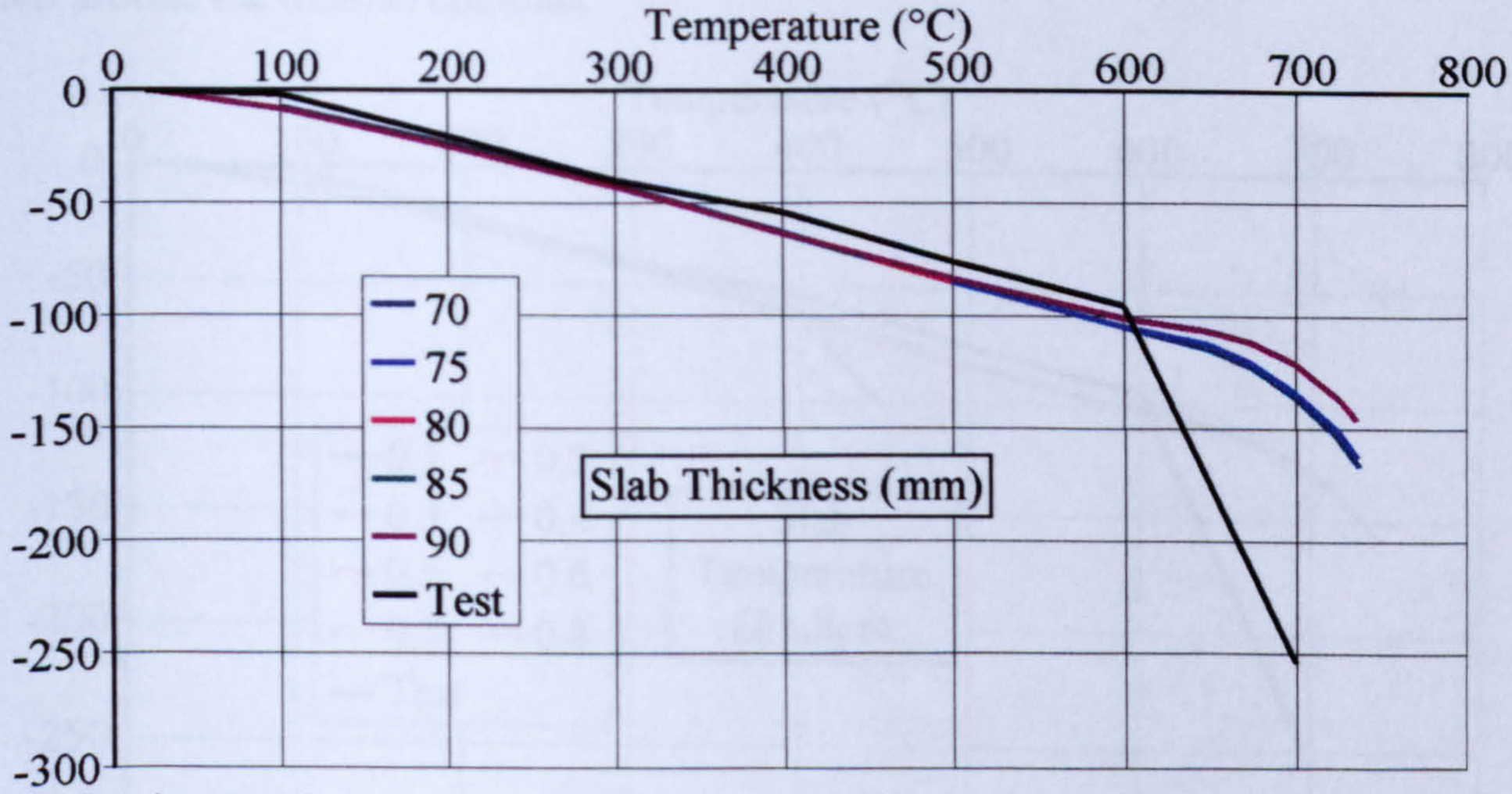

Figure 6-25. Parametric study 1 - Plane Frame Test, mid-span of 9m main beam

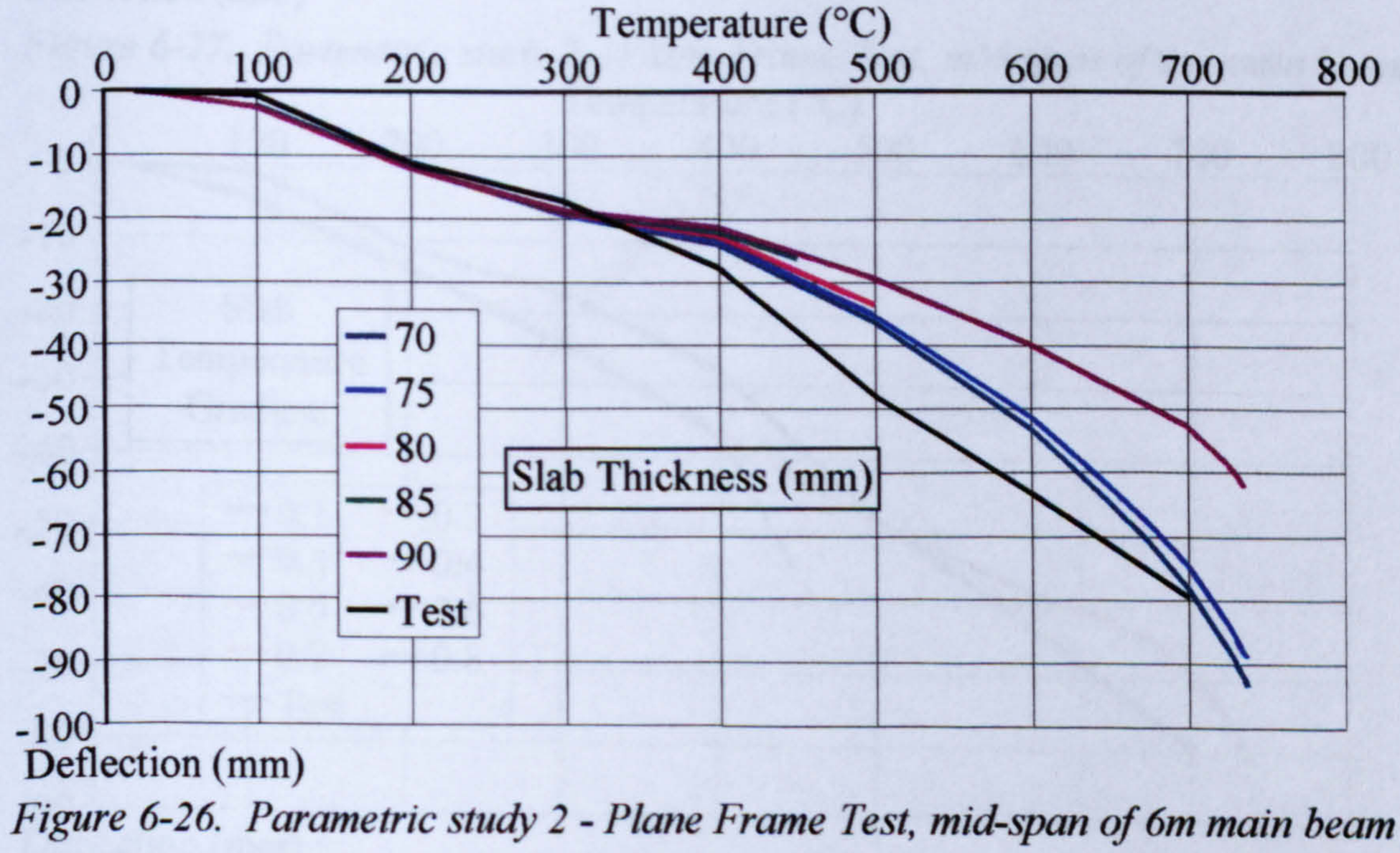

Figure 6-26. Parametric study 2 - Plane Frame Test, mid-span of 6m main beam

6.4.2 PARAMETRIC STUDY 2 - PLANE FRAME TEST

The influence of the floor slab temperature gradient for the 9m and 6m main beams is shown in Figures 6-27 and 6-28 respectively.

The lack of variation in the deflections indicates that the thermal bowing is dependent on the temperature differential across the beams rather than the temperature differential between the floor slab and the steel beam.

When the temperature gradient is severe, for example a bottom face temperature of 0.8 or 0.7 that of the bottom flange temperature, the analysis is seen to fail early. This is due to sudden loss of concrete strength, allowing excessive cracking of the floor slab around the internal columns.

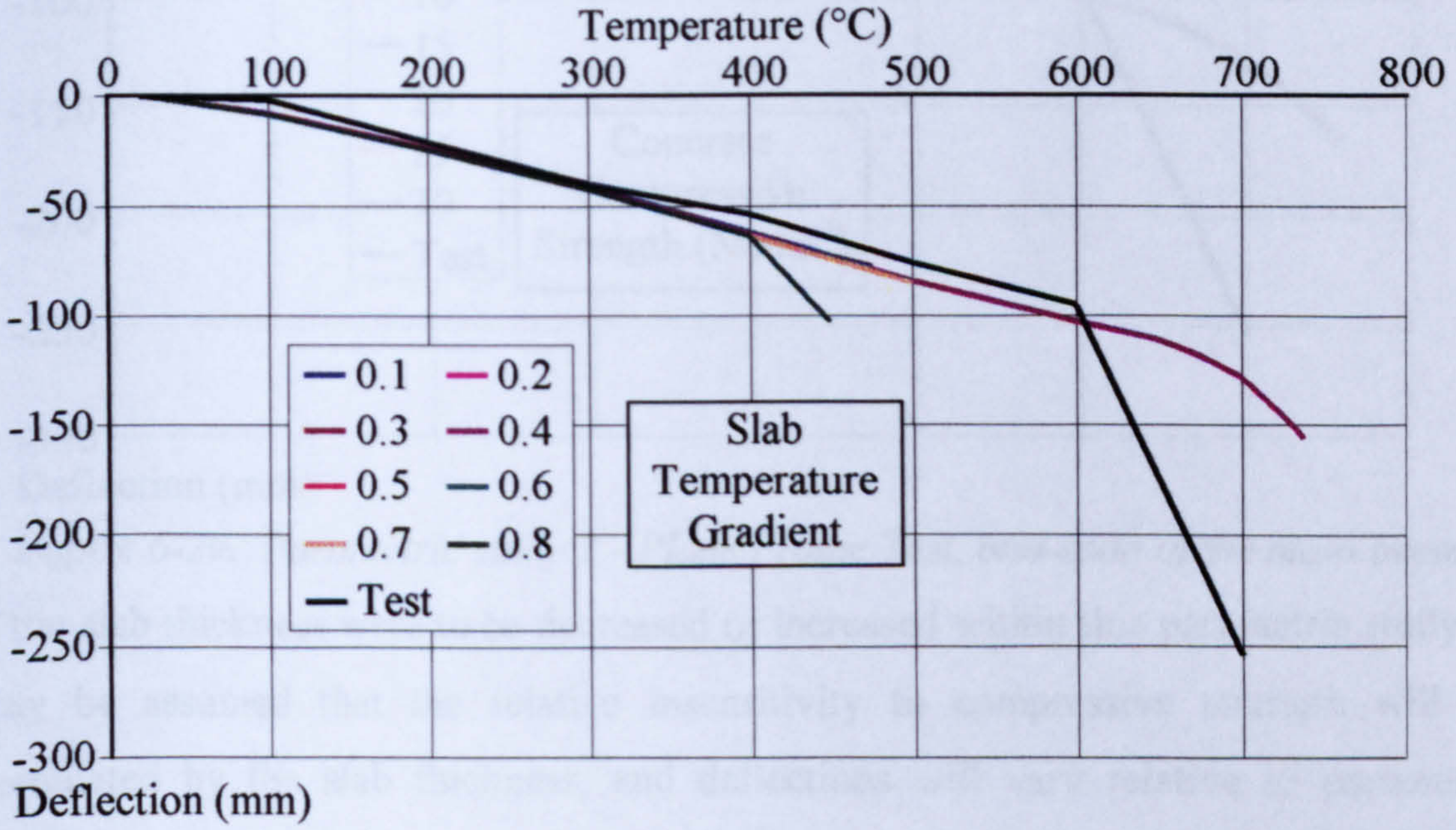

Figure 6-27. Parametric study 2 - Plane Frame Test, mid-span of 9m main beam

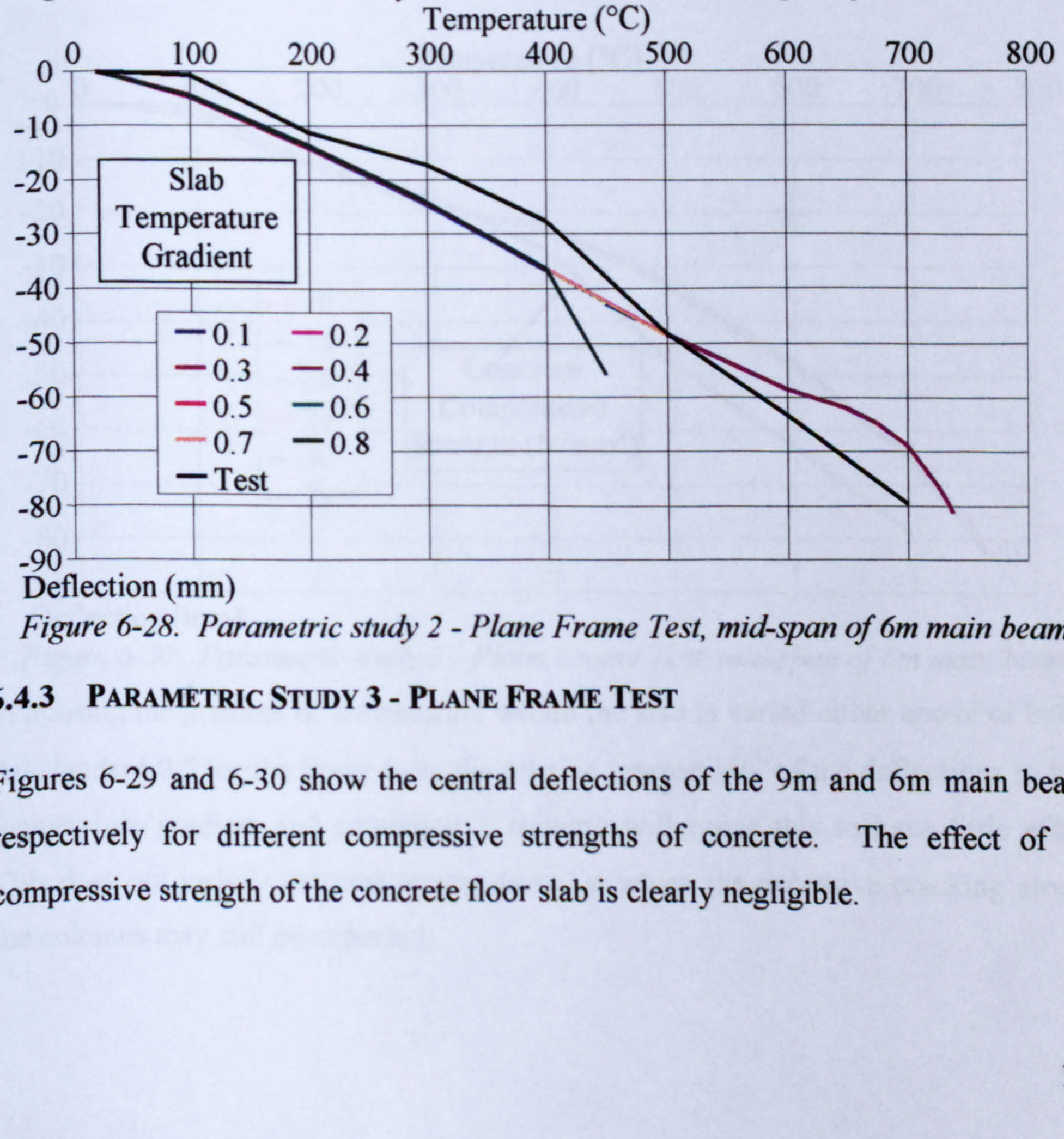

Figure 6-28. Parametric study 2 - Plane Frame Test, mid-span of 6m main beam

6.4.3 PARAMETRIC STUDY 3 - PLANE FRAME TEST

Figures 6-29 and 6-30 show the central deflections of the 9m and 6m main beams respectively for different compressive strengths of concrete. The effect of the compressive strength of the concrete floor slab is clearly negligible.

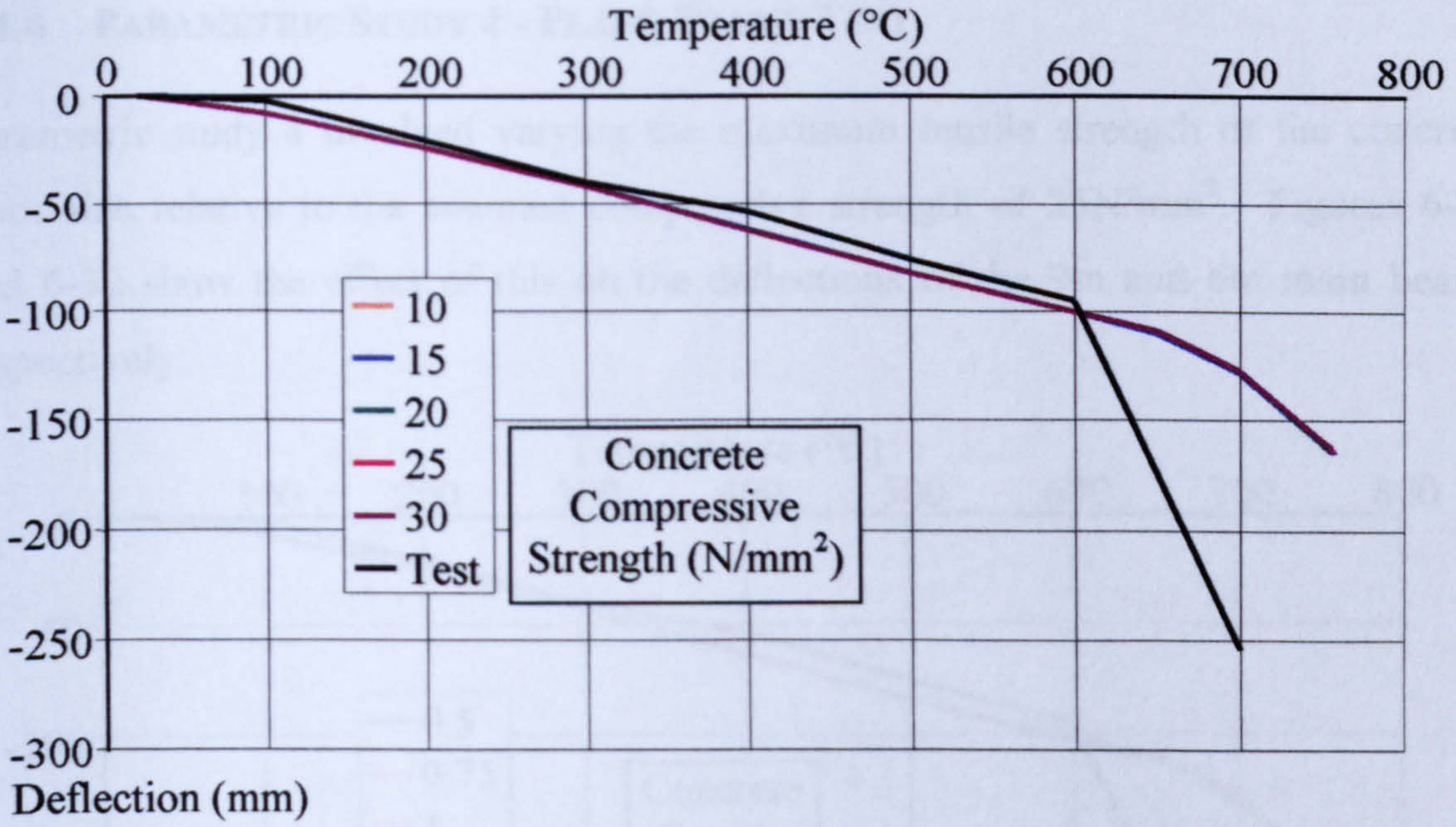

Figure 6-29. Parametric study 3 - Plane Frame Test, mid-span of 9m main beam

If the slab thickness were to be decreased or increased within this parametric study, it may be assumed that the relative insensitivity to compressive strength will be dominated by the slab thickness, and deflections will vary relative to parametric study 1.

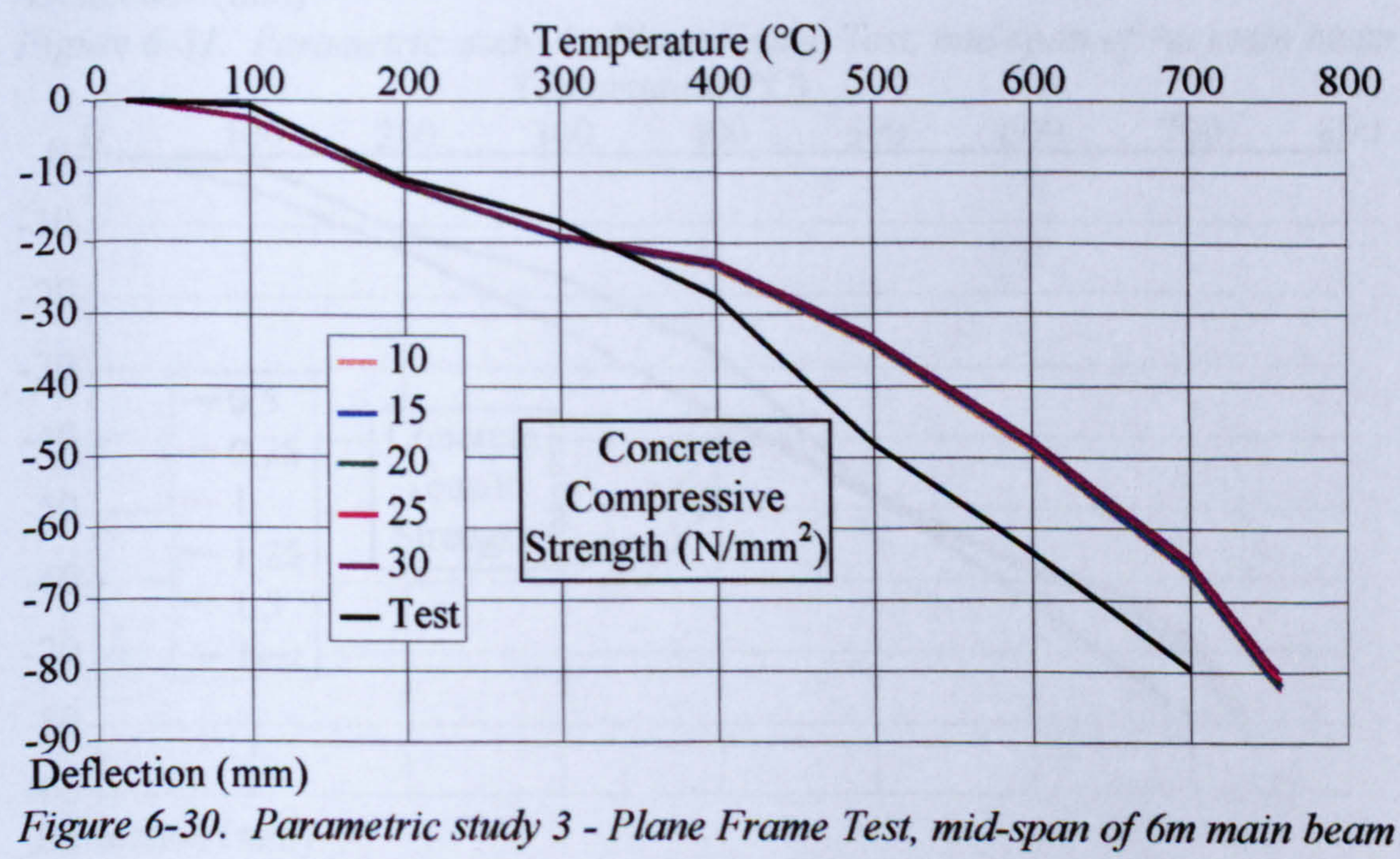

Figure 6-30. Parametric study 3 - Plane Frame Test, mid-span of 6m main beam

Supposing the gradient of temperature within the slab is varied either above or below the standard 0.5 for the lower face, the relative insensitivity of the deflections to both temperature gradient and compressive strength will cause this to have little effect. This does not include extreme temperatures, at which the excessive cracking around the columns may still be expected.

6.4.4 PARAMETRIC STUDY 4 - PLANE FRAME TEST

Parametric study 4 involved varying the maximum tensile strength of the concrete floor slab relative to the assumed compressive strength of 25N/mm^2. Figures 6-31 and 6-32 show the effect of this on the deflections of the 9m and 6m main beams respectively.

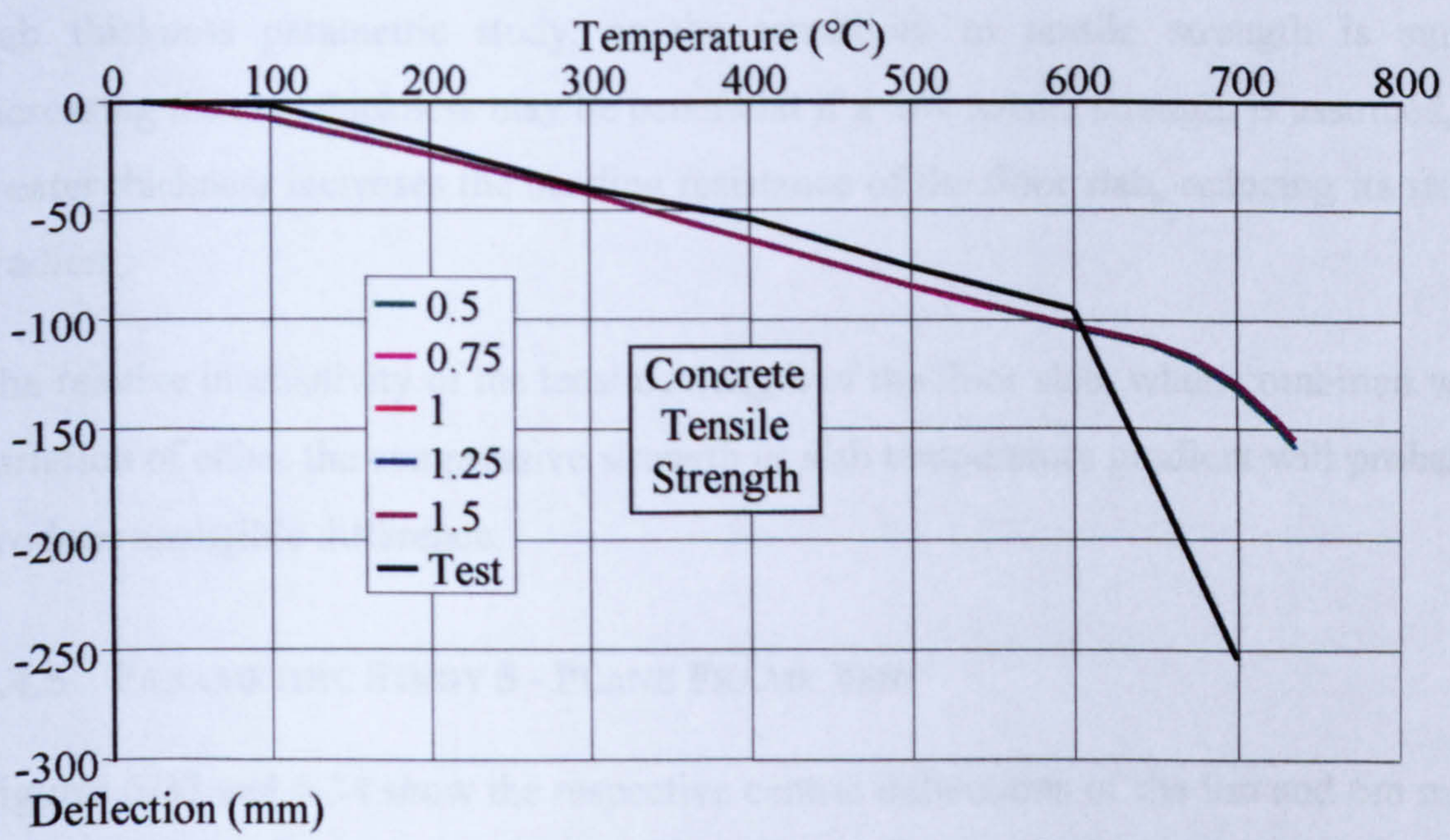

Figure 6-31. Parametric study 4 - Plane Frame Test, mid-span of 9m main beam

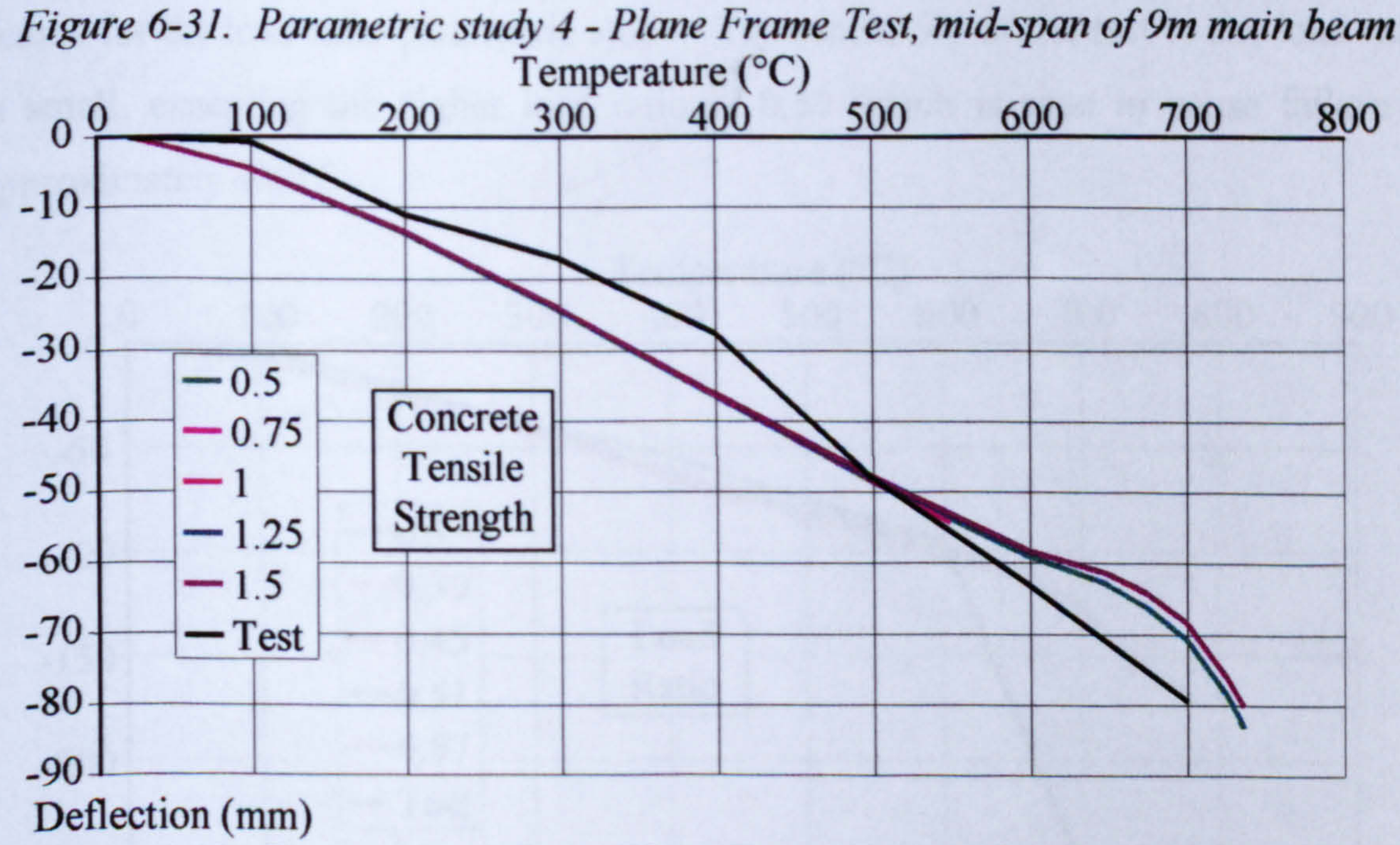

Figure 6-32. Parametric study 4 - Plane Frame Test, mid-span of 6m main beam

The slab tensile strength does not appear to affect the spread in deflections at all for the plane frame test, is therefore unimportant.

It should be noted that for lower tensile strengths of 0.5 and 0.75 of the original $2.5N/mm^2$ the structure failed early due to excessive cracking around the internal columns.

Should the thickness of the slab be increased or decreased during the maximum tensile strength parametric study, the deflections will probably follow those of the slab thickness parametric study, as the sensitivity to tensile strength is small. Increasing the slab thickness may be beneficial if a low tensile strength is assumed, as greater thickness increases the bending resistance of the floor slab, reducing its stress gradient.

The relative insensitivity of the tensile strength of the floor slab, when combined with variation of either the compressive strength or slab temperature gradient will probably produce negligible difference.

6.4.5 PARAMETRIC STUDY 5 - PLANE FRAME TEST

Figures 6-33 and 6-34 show the respective central deflections of the 9m and 6m main beams for the load ratio parametric study. The sensitivity of the test to the load ratio is small, excepting the higher load ratio of 0.57 which is seen to cause failure at approximately 450°C.

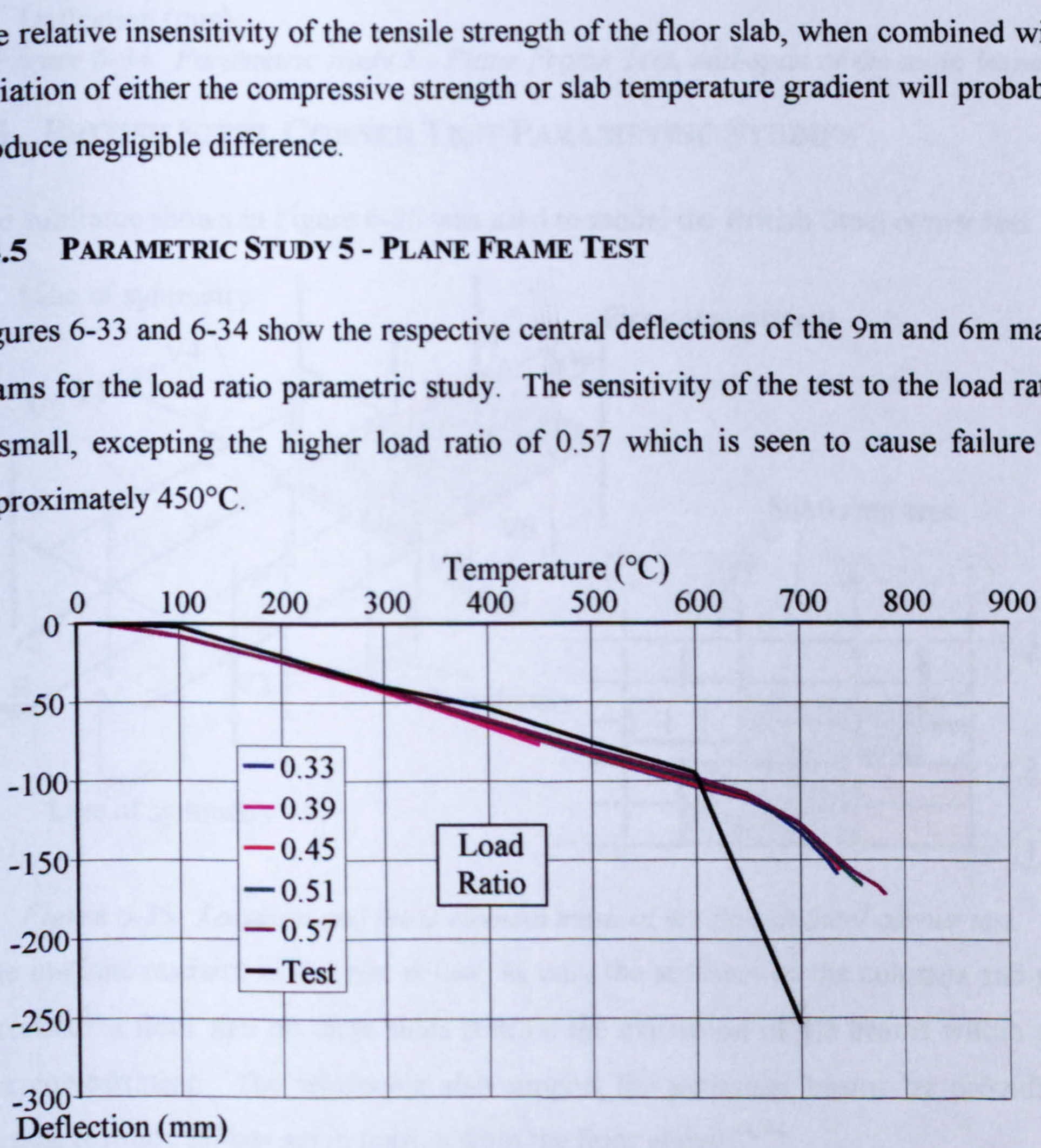

Figure 6-33. Parametric study 5 - Plane Frame Test, mid-span of 9m main beam

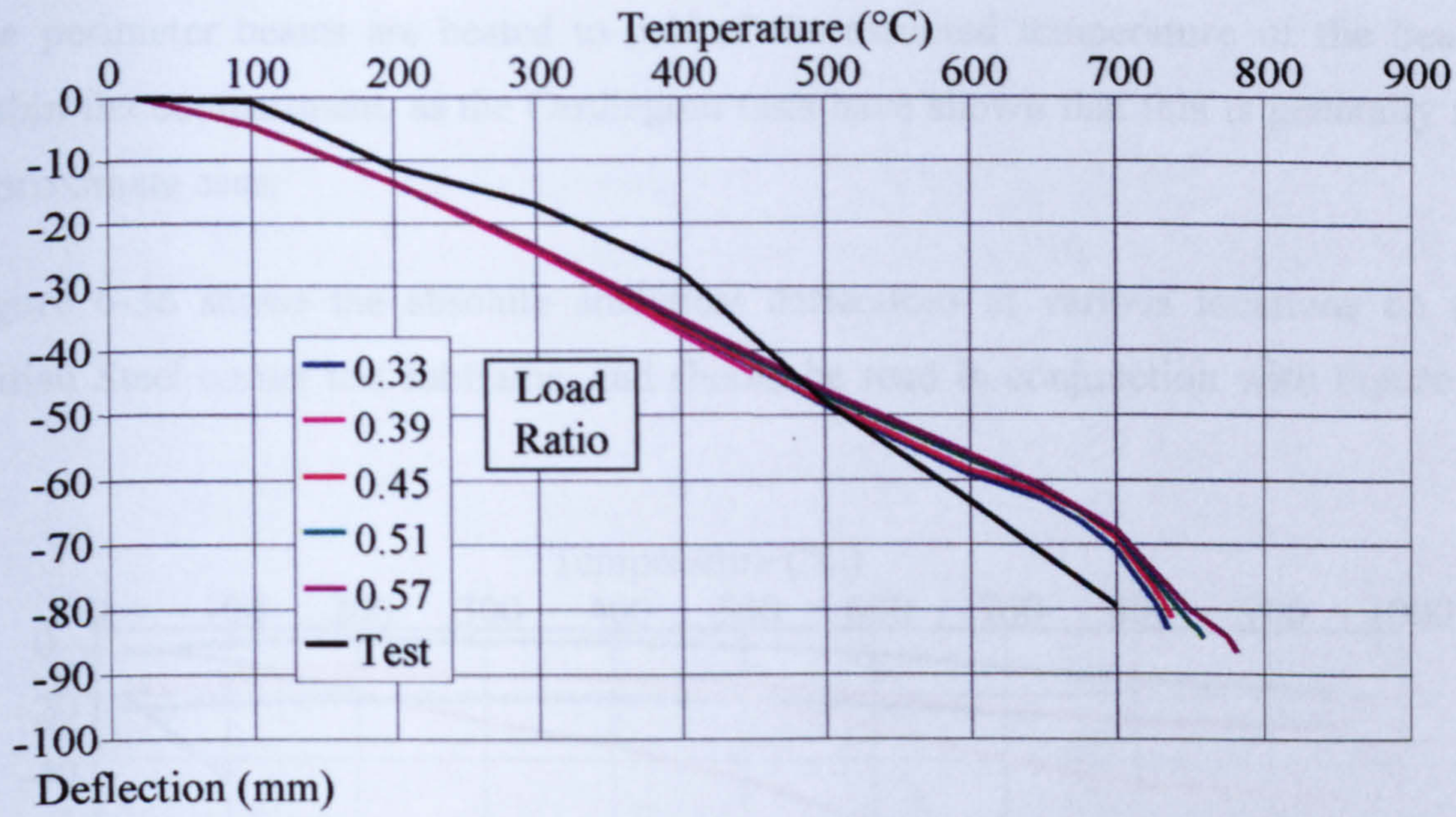

Figure 6-34. Parametric study 5 - Plane Frame Test, mid-span of 6m main beam

6.5 BRITISH STEEL CORNER TEST PARAMETRIC STUDIES

The subframe shown in Figure 6-35 was used to model the British Steel corner test.

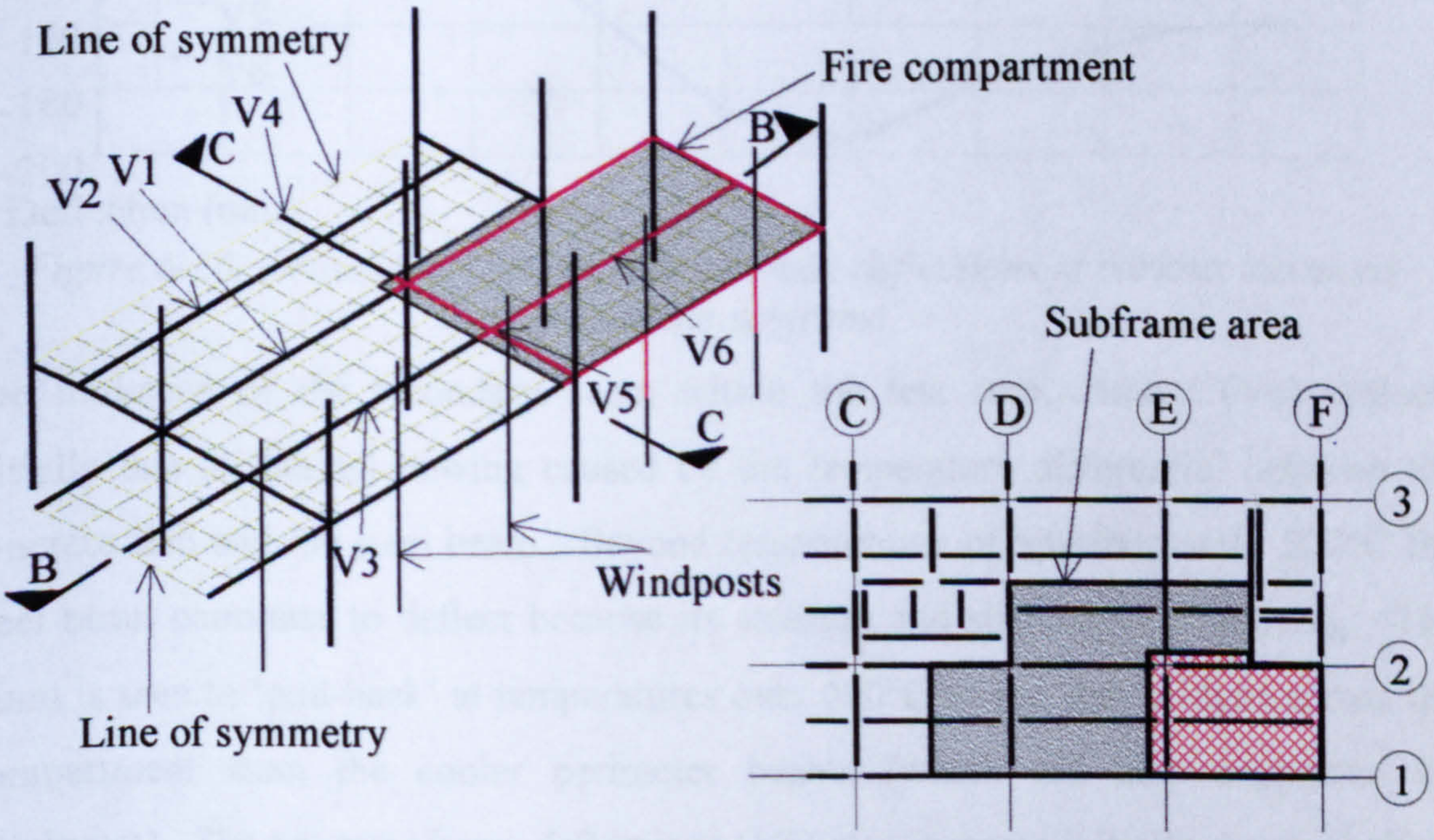

Figure 6-35. Location and finite element mesh of the British Steel corner test.

The in-plane restraint in this test is low, as only the stiffness of the columns and the surrounding floor slab on three sides restrain the expansion of the beams within the test compartment. The windposts also support the perimeter beams by providing vertical restraint as they act in tension from the floor above [23, 44].

The perimeter beams are heated to half of the assumed temperature of the beams within the compartment, as the Cardington tests have shown that this is generally the approximate case.

Figure 6-36 shows the absolute analytical deflections at various locations on the British Steel corner test subframe, and should be read in conjunction with Figure 6-35.

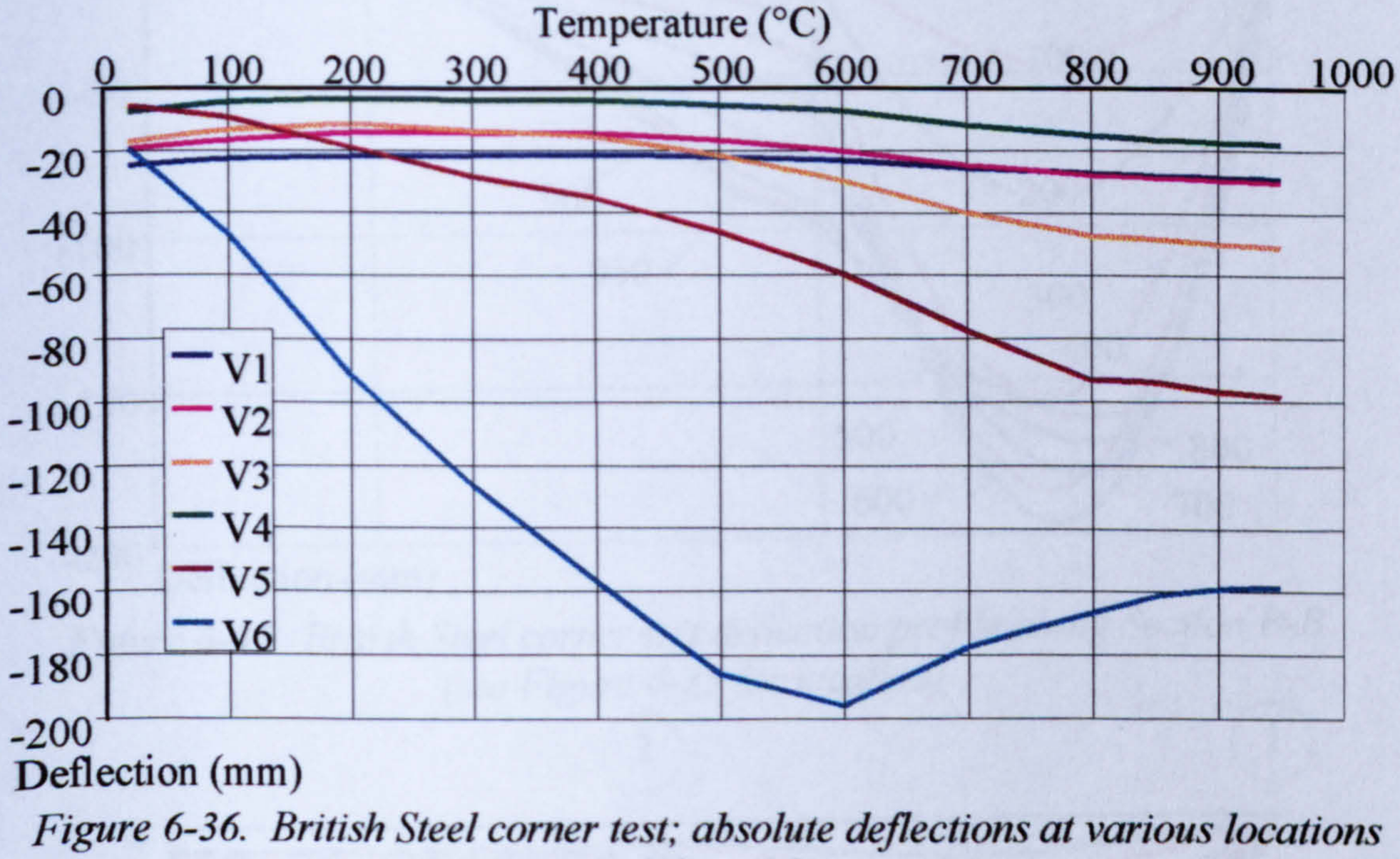

Figure 6-36. British Steel corner test; absolute deflections at various locations around the subframe

The mid-span of the secondary beam within the test compartment (V6) deflects initially due to thermal bowing caused by the temperature differential between the concrete slab and the steel beam. Beyond temperatures of approximately 500°C the steel beam continues to deflect because its strength and stiffness are reducing. The beam is seen to 'pull-back' at temperatures over 600°C as the slab bridges across the compartment from the cooler perimeter beams (which are also supported by windposts). The 6m main beam deflections (V5) also increase initially due to thermal bowing and then continue from approximately 500°C due to loss of the beam's strength and stiffness. Little 'pull-back' is demonstrated on this beam, as the concrete slab is less able to span easily from surrounding beams. This lack of restraint leads to lower thermally induced axial loads (related to P-Δ bending deflection) and thus there is less scope for 'pull-back'. Other deflections shown in this figure are taken at the mid-span of adjacent secondary beams (V1, V2 and V3) and the mid-span of the 9m main beam (V4). These all deflect in hogging during the early stages of the analysis

as the centre of the test compartment sags, causing the continuous floor to pivot about the beams on gridlines E and 2. As the strength and stiffness of the steel within the test compartment is lost, the surrounding structure attempts to return to its original shape. Figure 6-37 shows the progression of absolute deflections along Section B-B.

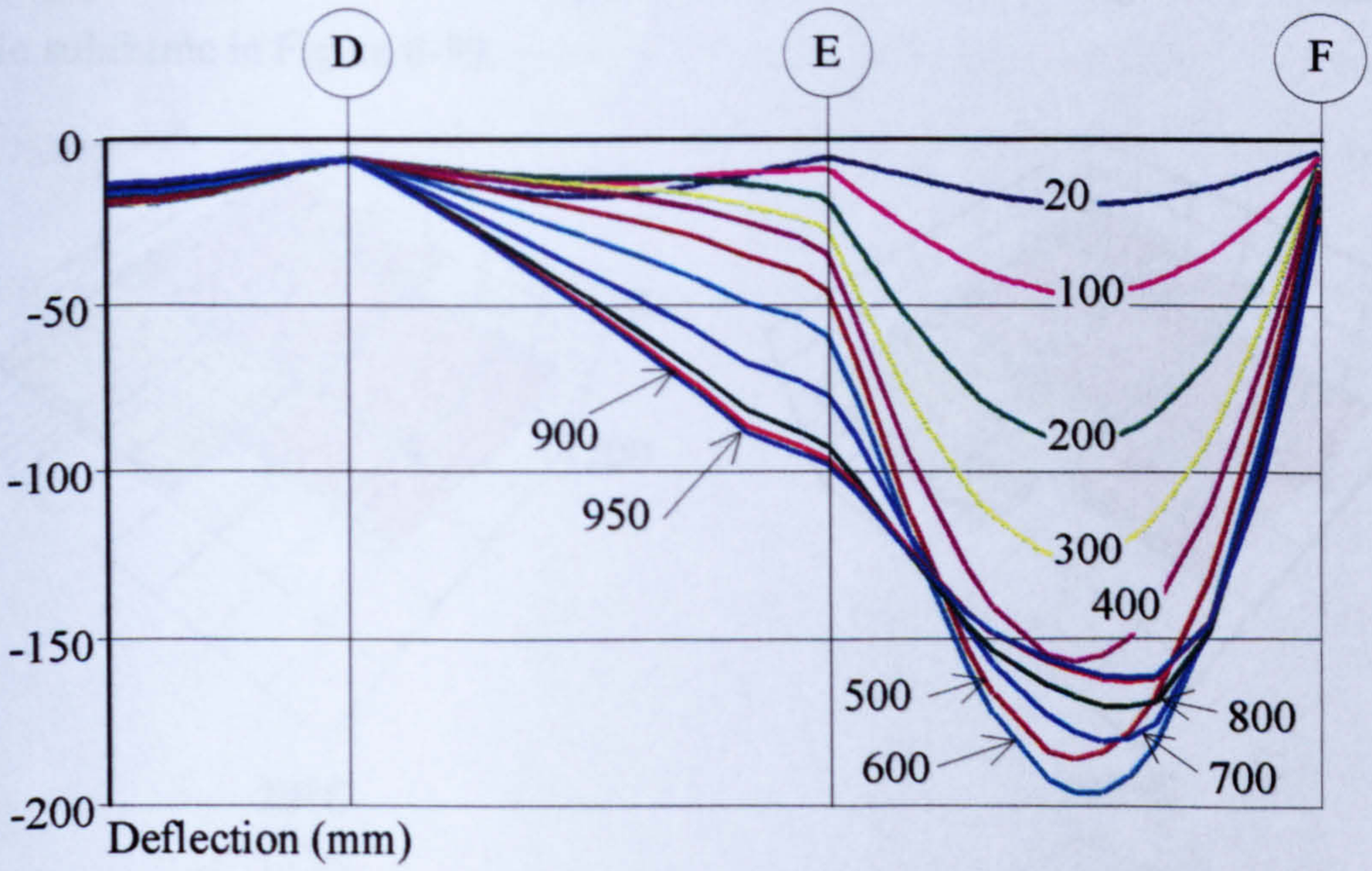

Figure 6-37. British Steel corner test deflection profile along Section B-B (see Figure 6-35 for location)

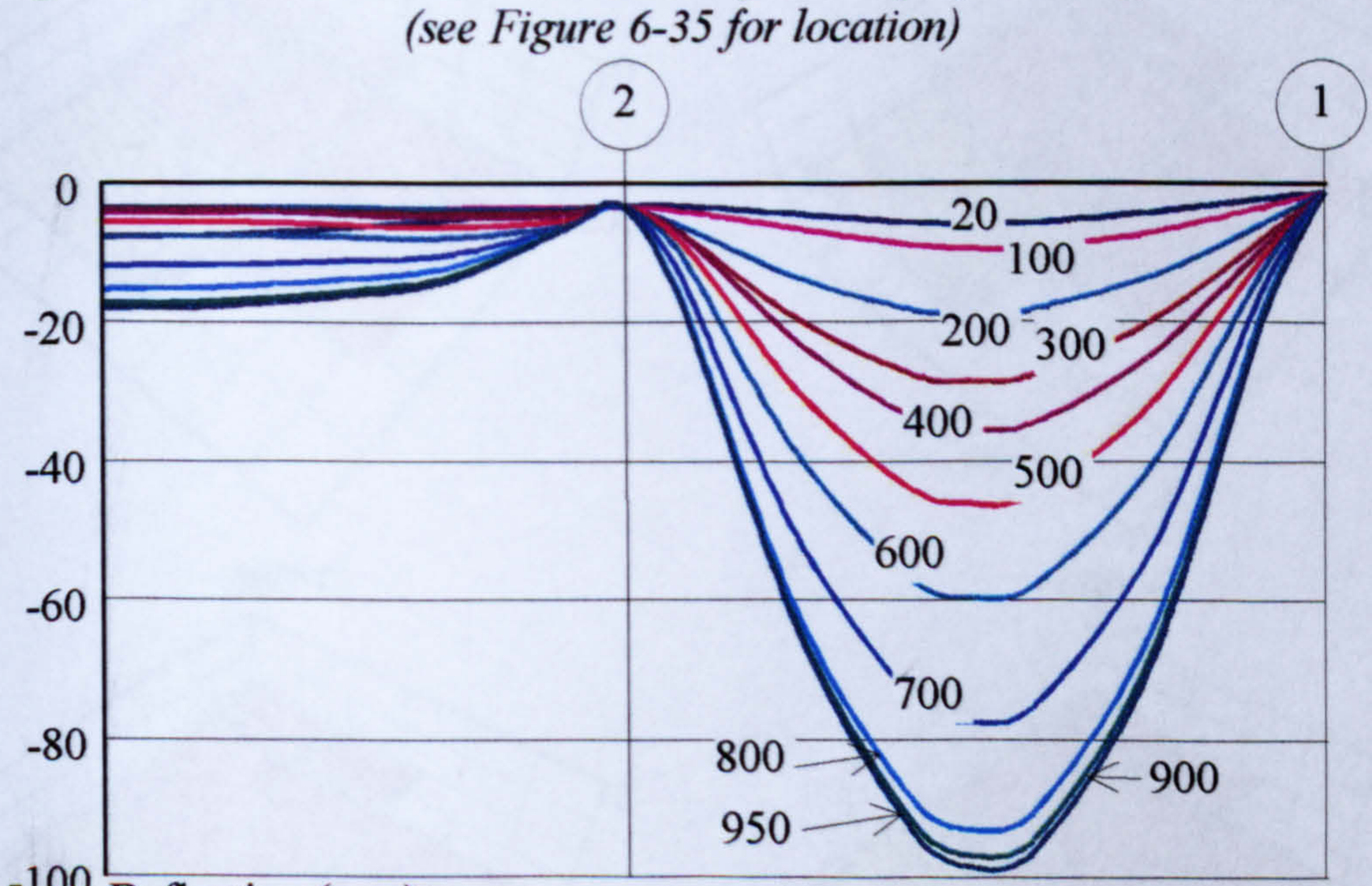

Figure 6-38. British Steel corner test progressive deflections along Section C-C (see Figure 6-35 for location)

The thermal bowing over the initial 500°C gives a fast rate of deflection, which then slows and begins to reverse for temperatures in the region 700°C to 950°C. The 6m main beam lying on gridline E clearly lends the fire compartment considerable support for temperatures up to 500°C. Beyond 500°C the strength and stiffness of the 6m main beam is significantly reduced so that it continues to deflect up to 950°C. It

may be supposed that at 950°C the maximum deflection of the 6m main beam has been achieved and the concrete floor slab spans across from the perimeter beam to the adjacent secondary beam.

The progression of deflections along Section C-C is shown in Figure 6-38 and for the whole subframe in Figure 6-39.

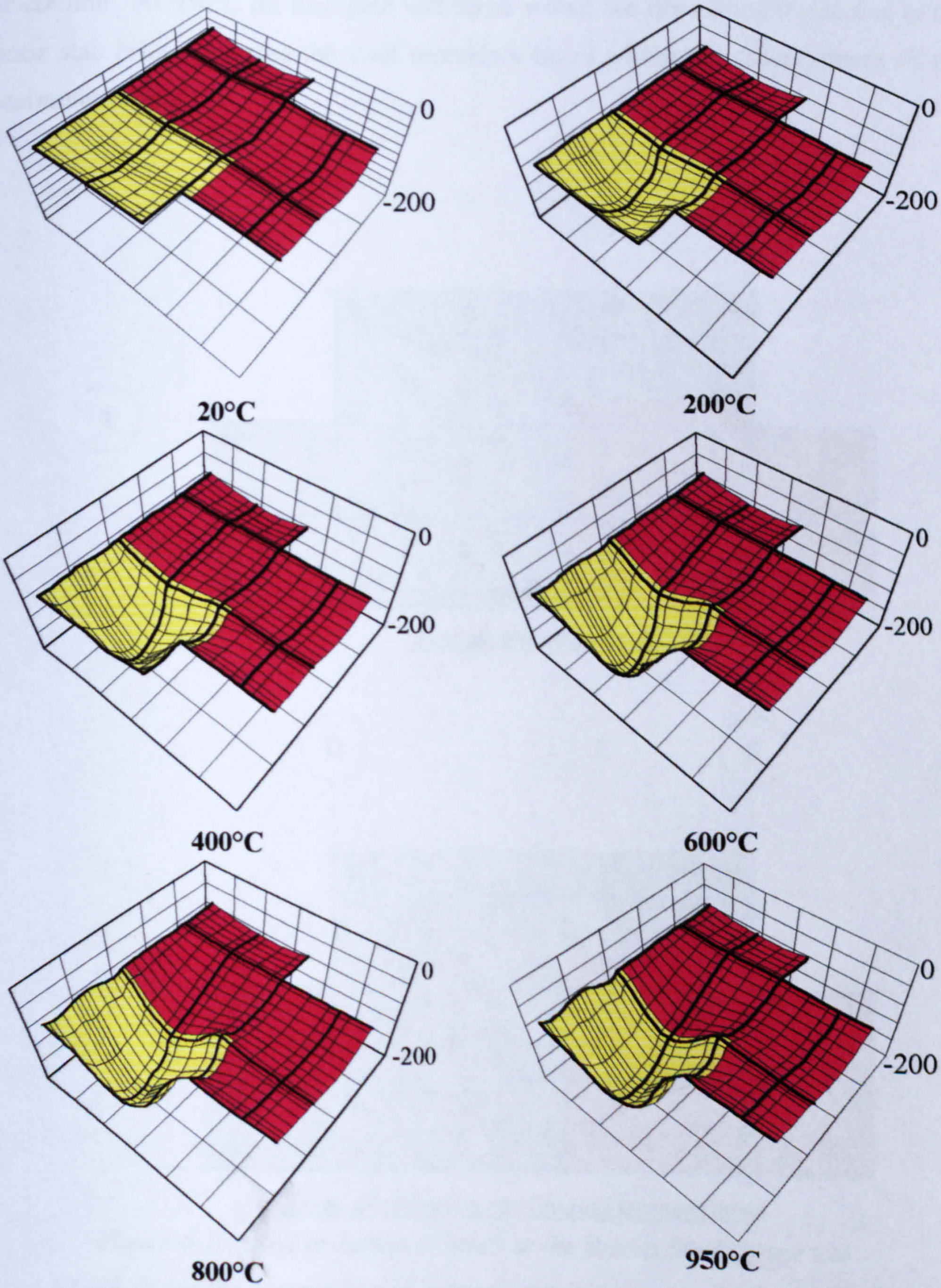

Figure 6-39. Progressive deflection of the British Steel corner test

Figure 6-40 represents the load paths at ambient temperature and at temperatures that are high enough for the strength and stiffness of the steel beams within the fire compartment to be significantly reduced (950°C).

The load path at ambient temperature is conventional in that the floor slab distributes the load to the secondary beams, which in turn transfer it to the relevant primary beam or column. At 950°C the load path will differ within the fire compartment due to the floor slab bridging across the steel secondary beam within the compartment to the perimeter beams.

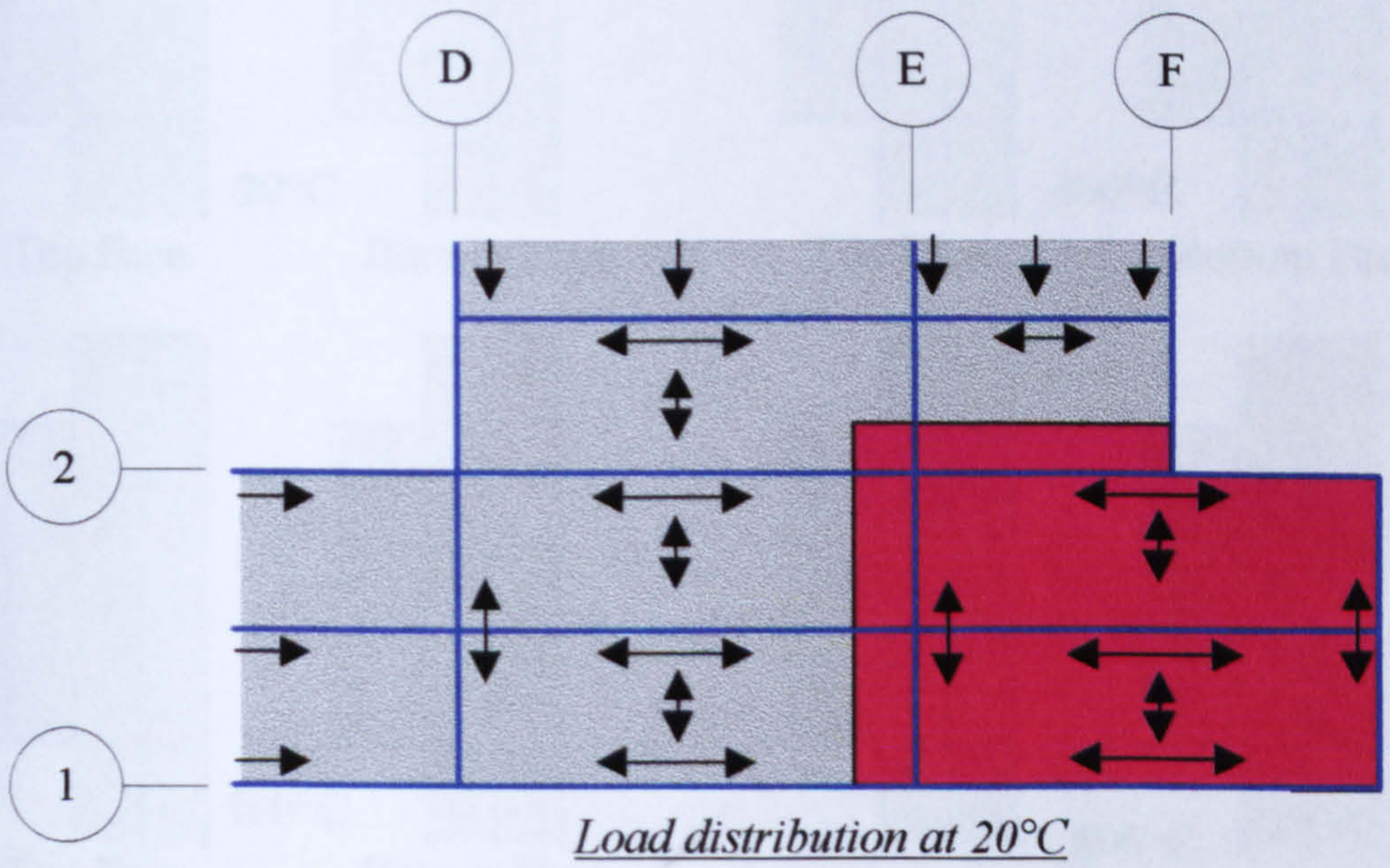

Load distribution at 20°C

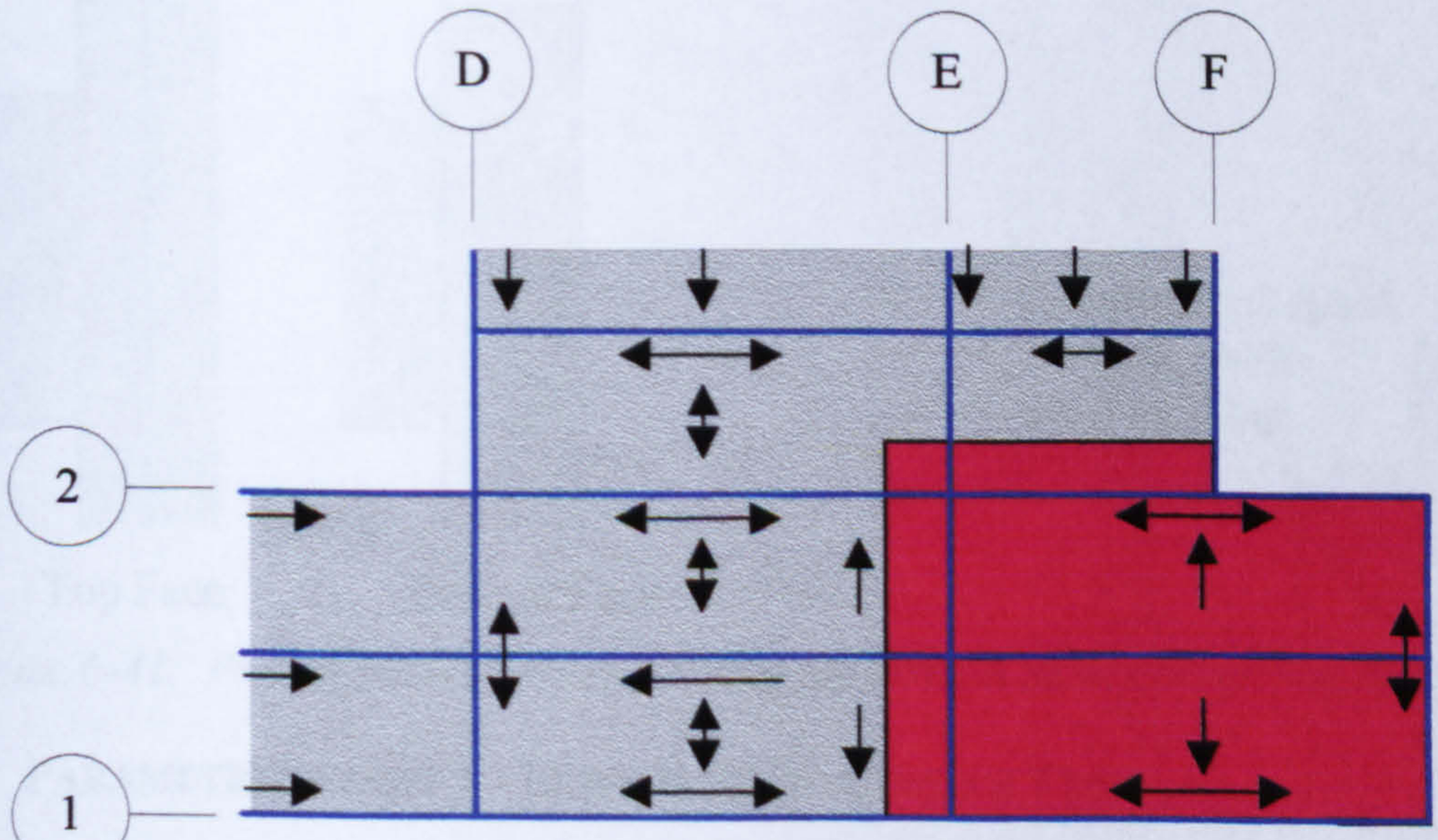

Load distribution at elevated temperatures

Figure 6-40. Redistribution of loads in the British Steel corner test

Figure 6-41 shows the propagation of concrete cracking across the fire compartment. At 20°C there is little tension cracking. As the temperature increases between 100°C

and 600°C, tension cracks develop mainly within the test compartment. Conversely, the hogging of the surrounding cool floor slabs causes tensile cracks to form over beams outside the fire compartment. At 400°C a small compression crack is seen to form at Gridline 2 due to extremely high stress gradients encountered around the column.

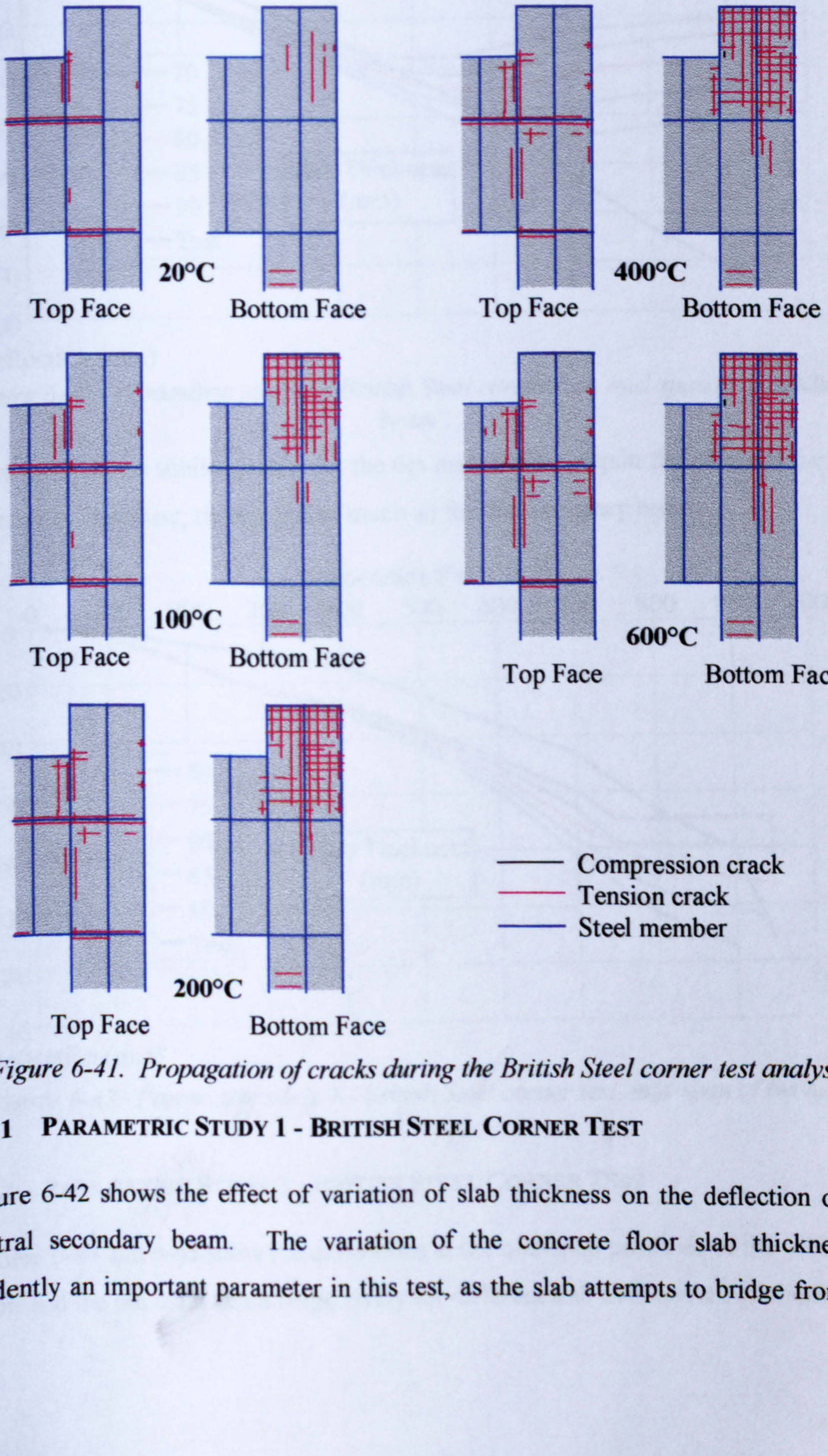

Figure 6-41. Propagation of cracks during the British Steel corner test analyses

6.5.1 PARAMETRIC STUDY 1 - BRITISH STEEL CORNER TEST

Figure 6-42 shows the effect of variation of slab thickness on the deflection of the central secondary beam. The variation of the concrete floor slab thickness is evidently an important parameter in this test, as the slab attempts to bridge from the

surrounding structure. As in the restrained beam test, there is an evident relief in the P-Δ bending deflection component due to the softening of the steel material.

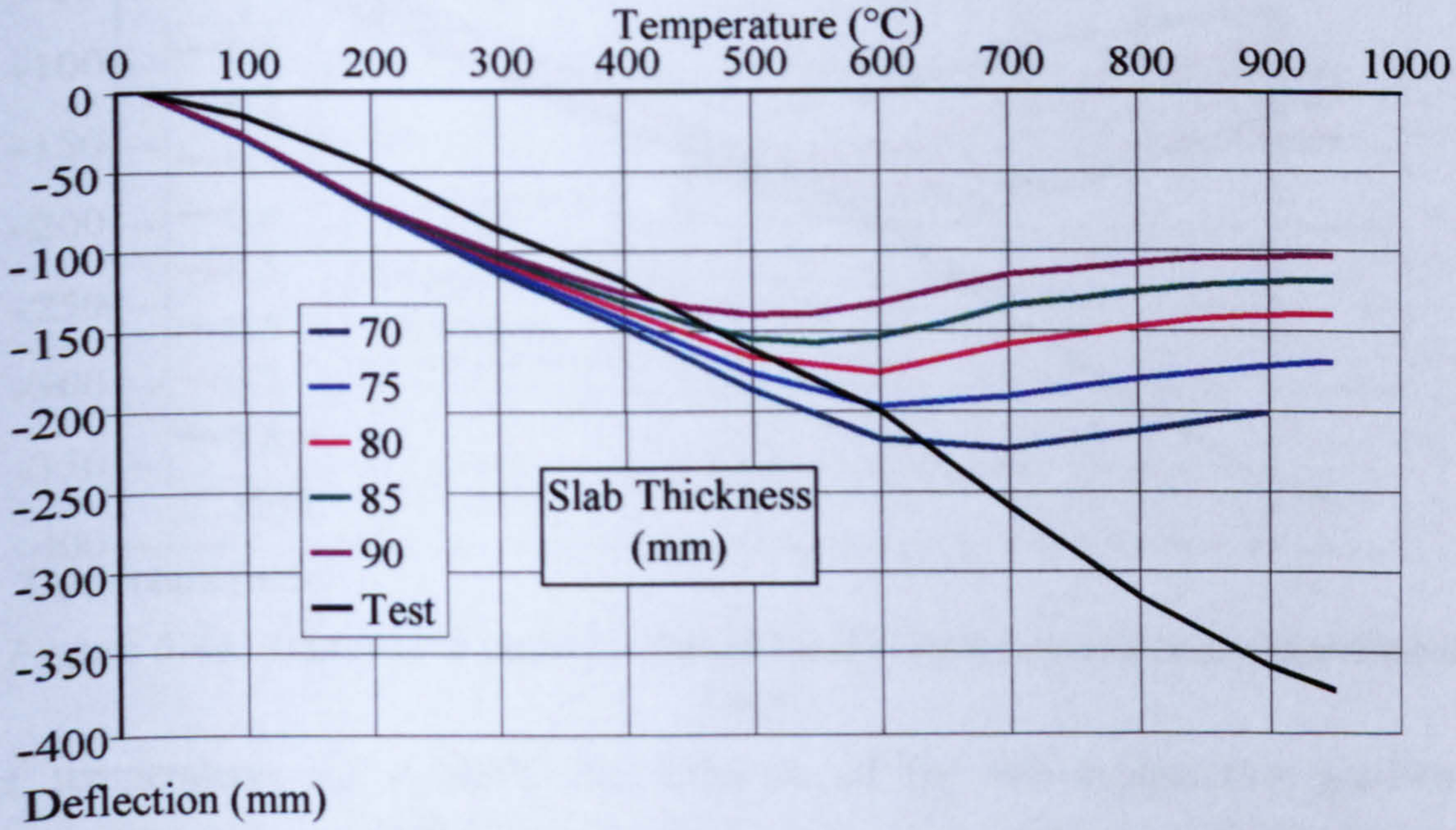

Figure 6-42. Parametric study 1 - British Steel corner test, mid-span of secondary beam

Figure 6-43 shows similar results for the 6m main beam. Again the effect of the slab thickness is important, though not so much so for the secondary beam.

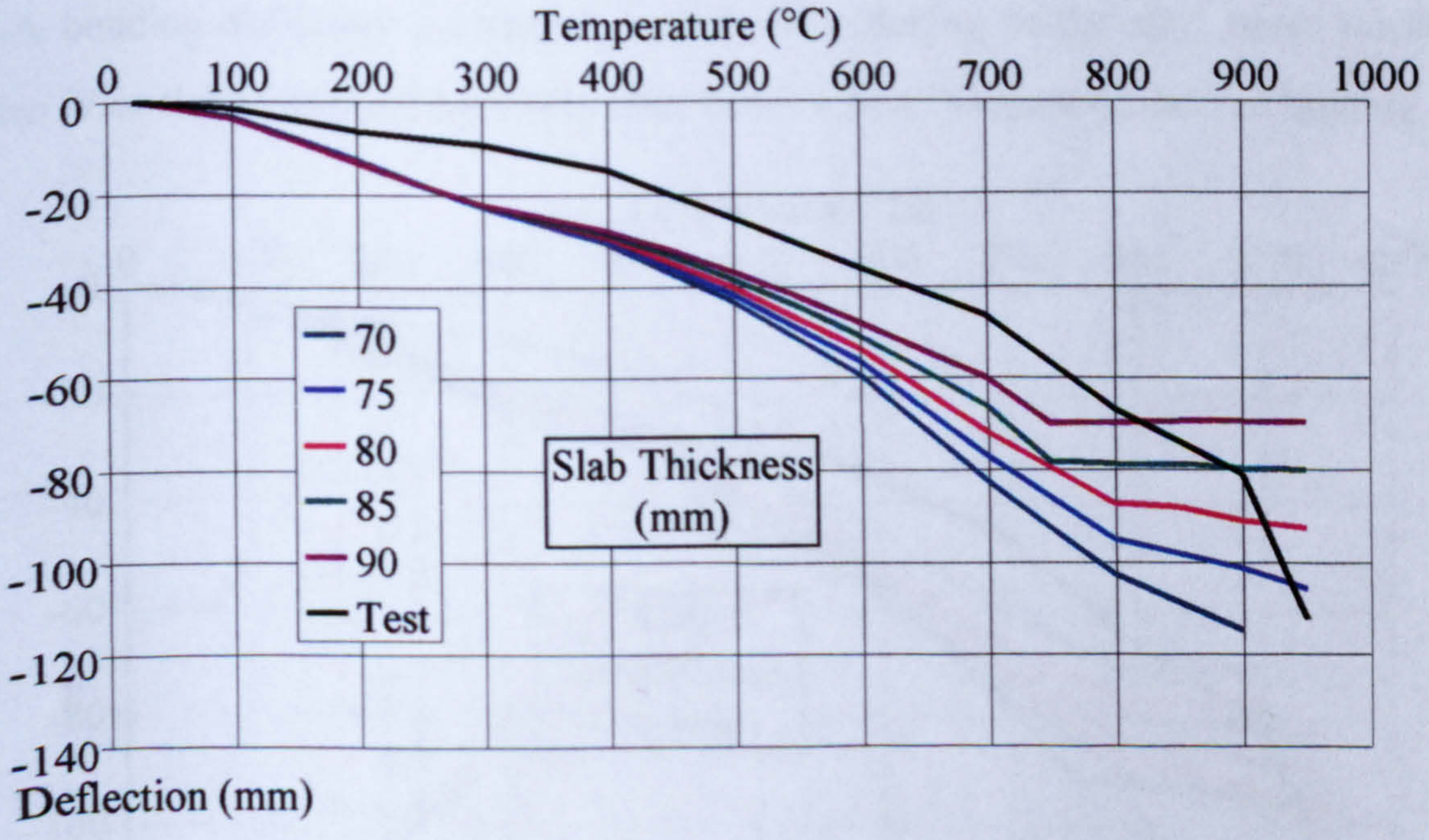

Figure 6-43. Parametric study 1 - British Steel corner test, mid-span of 6m main beam

6.5.2 PARAMETRIC STUDY 2 - BRITISH STEEL CORNER TEST

Figures 6-44 and 6-45 show the deflections at the mid-span positions of the secondary beam and the 6m main beam respectively for different slab temperature gradients.

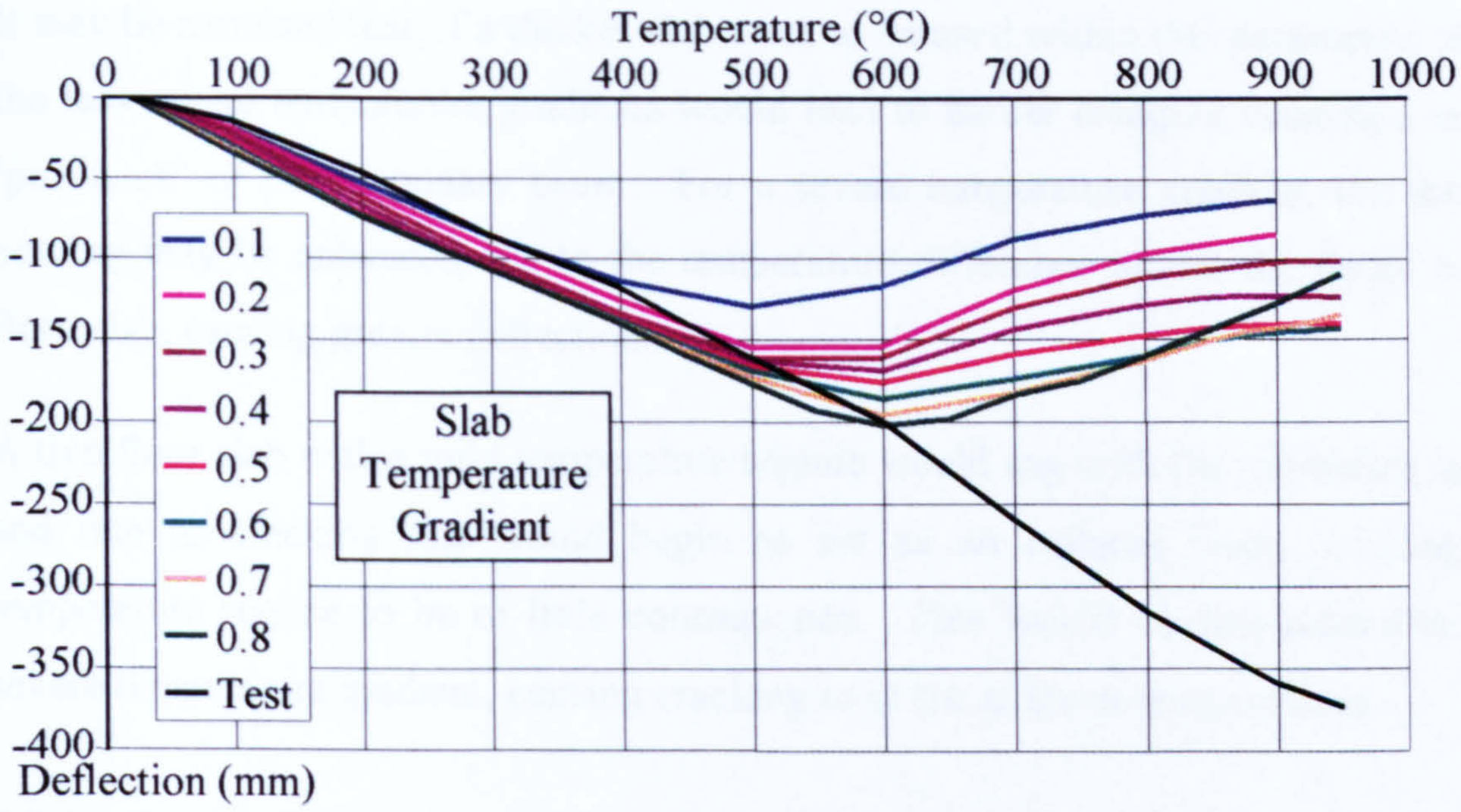

Figure 6-44. Parametric study 2 - British Steel corner test, mid-span of secondary beam

At temperatures up to 500°C the influence of the slab temperature gradient is negligible, with a small spread of results due to thermal bowing of the floor slab, therefore deflections must be produced by the temperature variation across the beam. However, when 500°C has been passed the floor slab temperature gradient is significant. At this stage 'pull-back' is evident, due to the decreased influence of the P-Δ bending deflection component because of softening of the steel beam material. The floor slab temperature gradient contributes a small amount of thermal bowing.

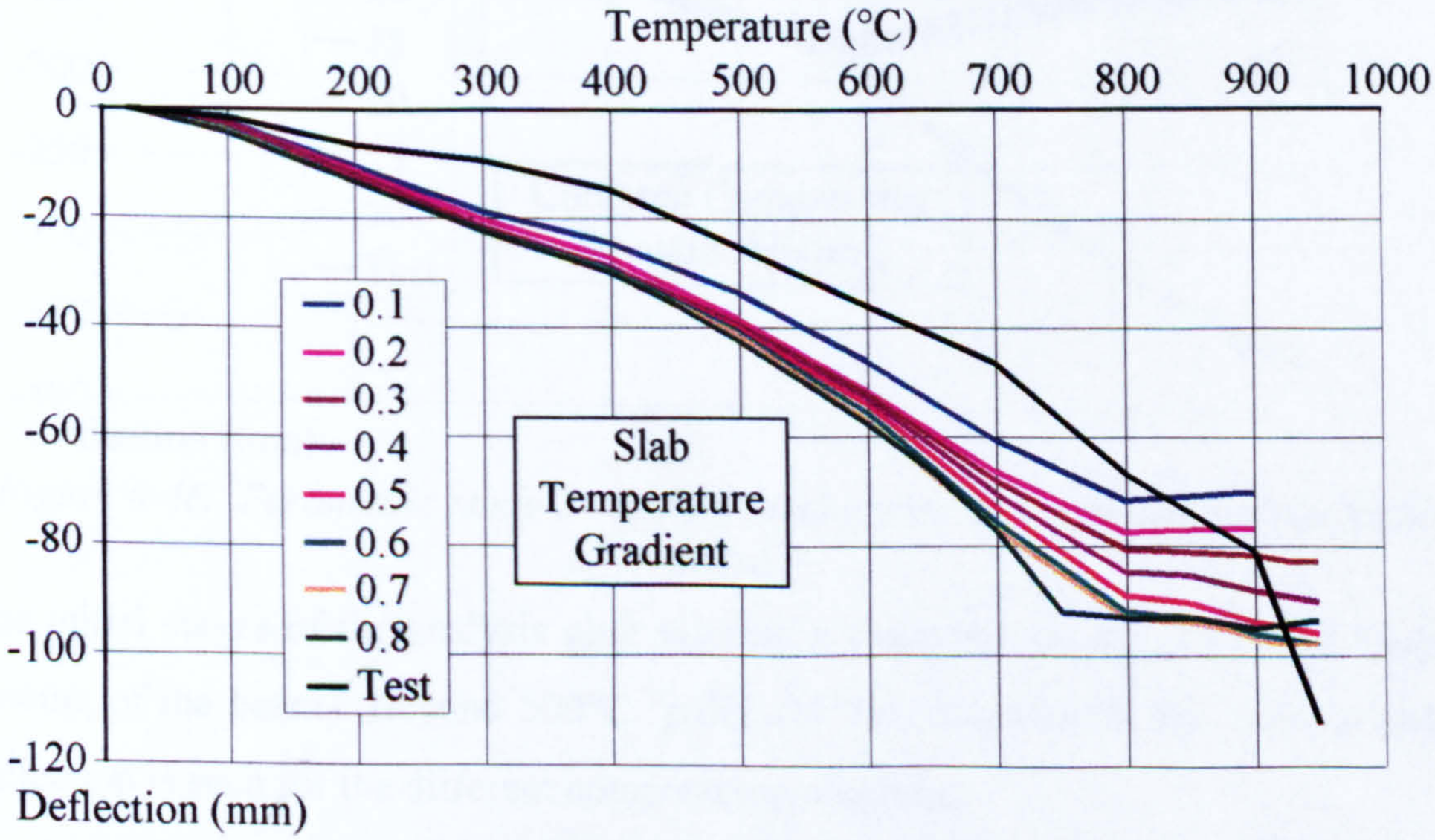

Figure 6-45. Parametric study 2 - British Steel corner test, mid-span of 6m main beam

It may be surmised that, if a thicker slab were to be used within this parametric study, the less severe temperature gradients would lead to earlier bridging causing a severe 'pull-back' of the secondary beam. For a severe temperature gradient, the thermal bowing may be enhanced due to the temperature difference across the depth of the floor slab, causing greater deflections.

A thin floor slab with a mild temperature regime would sag with the secondary beam, and due to cracking this would begin to act as an isolated beam, causing the temperature regime to be of little consequence. This would be emphasised with a severe temperature gradient, causing cracking to occur at lower temperatures.

6.5.3 PARAMETRIC STUDY 3 - BRITISH STEEL CORNER TEST

Figures 6-46 and 6-47 show the deflections of the mid-span positions of the central secondary beam and the 6m main beam for different compressive strengths of concrete.

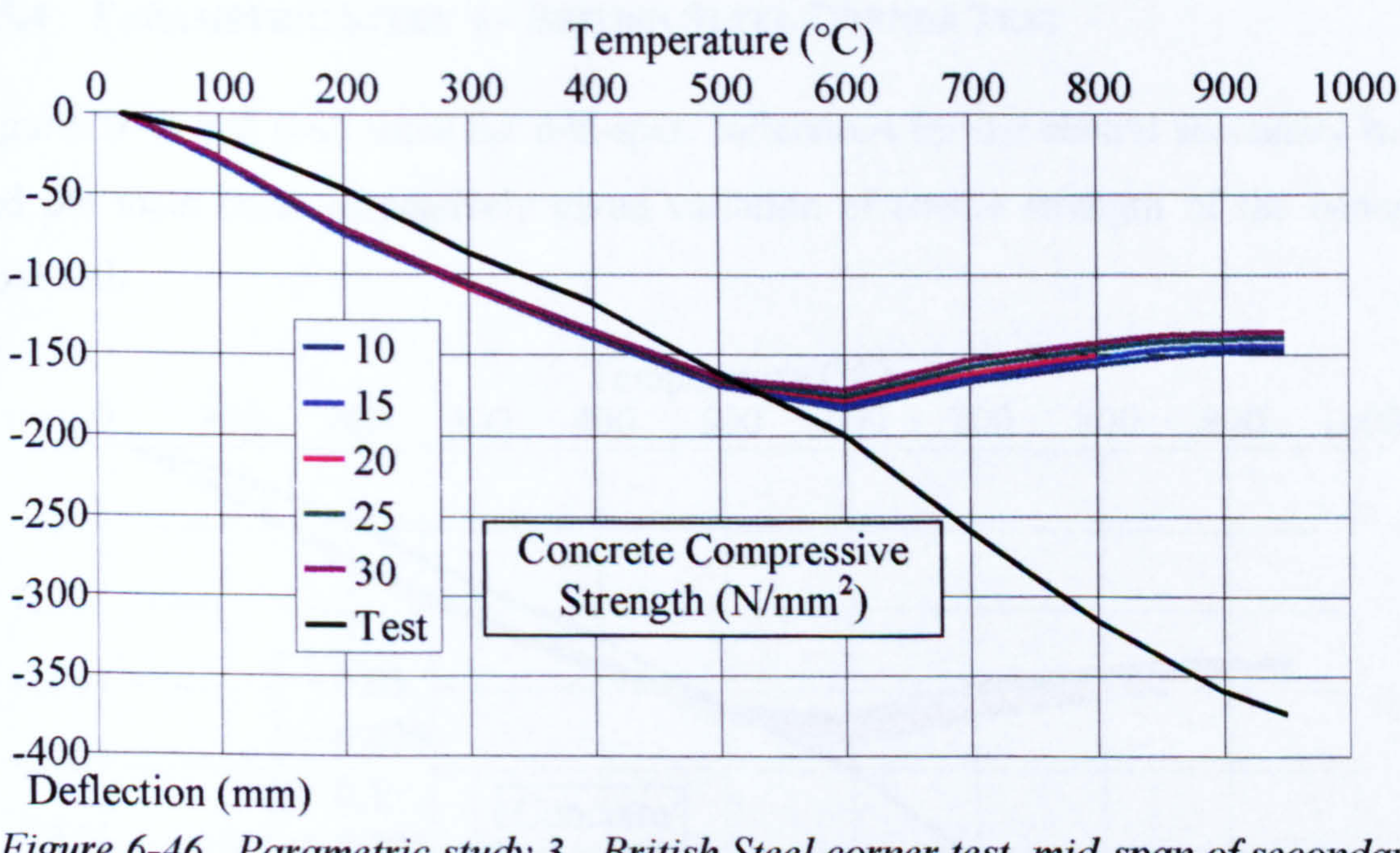

Figure 6-46. Parametric study 3 - British Steel corner test, mid-span of secondary beam

The initial stages of the analysis give sagging deflections caused mainly by thermal bowing of the beam. Beyond 500°C 'pull-back' is encountered, but little spread in deflection is seen for the different compressive strengths.

If the effect of the compressive strength is considered for a thinner or thicker slab, it may be assumed that the slab thickness will dominate the structural action. Likewise,

it may be assumed that the insensitivity to compressive strength will allow slab temperature gradients to dominate where these exist.

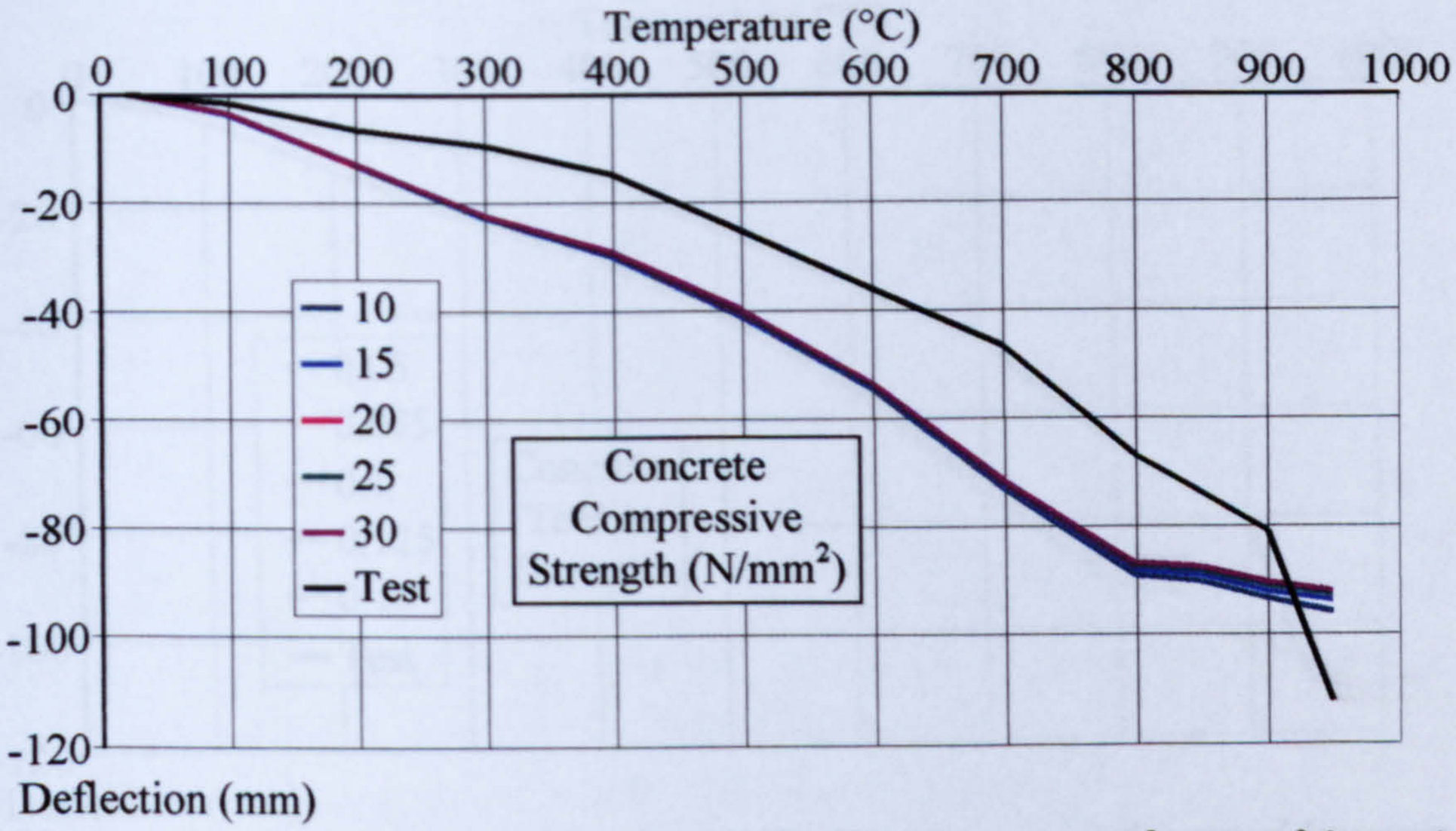

Figure 6-47. Parametric study 3 - British Steel corner test, mid-span of 6m main beam

6.5.4 PARAMETRIC STUDY 4 - BRITISH STEEL CORNER TEST

Figures 6-48 and 6-49 show the mid-span deflections for the central secondary beam and 6m main beam respectively given variation of tensile strength of the concrete floor slab.

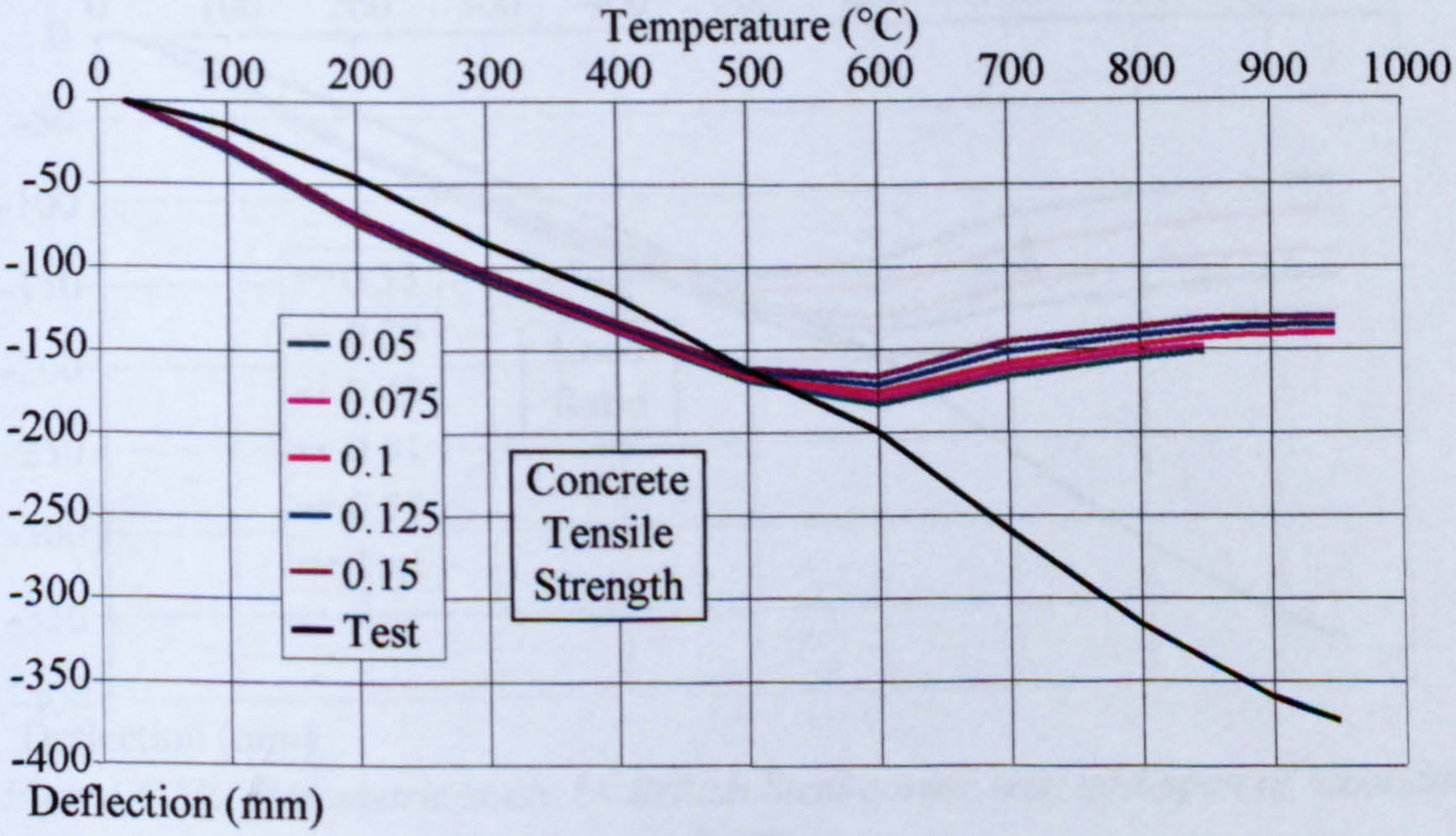

Figure 6-48. Parametric study 4 - British Steel corner test, mid-span of secondary beam

The tensile strength of the concrete floor slab appears to have negligible effect over the initial 500°C. Beyond this temperature, the tensile strength does have a small

effect, as this is the phase where the slab is dominant as the steel beam softens significantly.

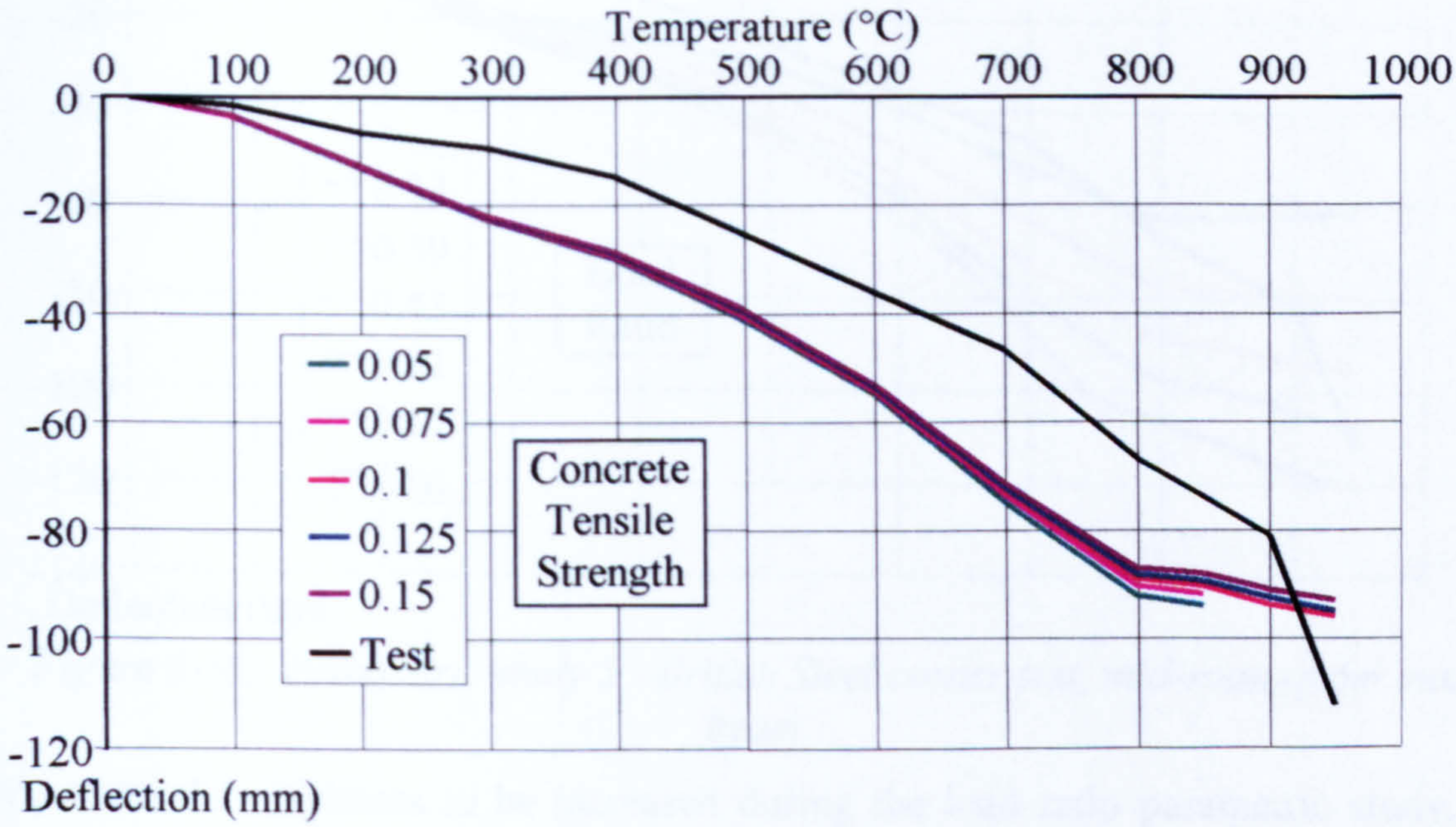

Figure 6-49. Parametric study 4 - British Steel corner test, mid-span of 6m main beam

6.5.5 PARAMETRIC STUDY 5 - BRITISH STEEL CORNER TEST

Figures 6-50 and 6-51 show the mid-span deflections of the central secondary beam and 6m main beam for different load ratios.

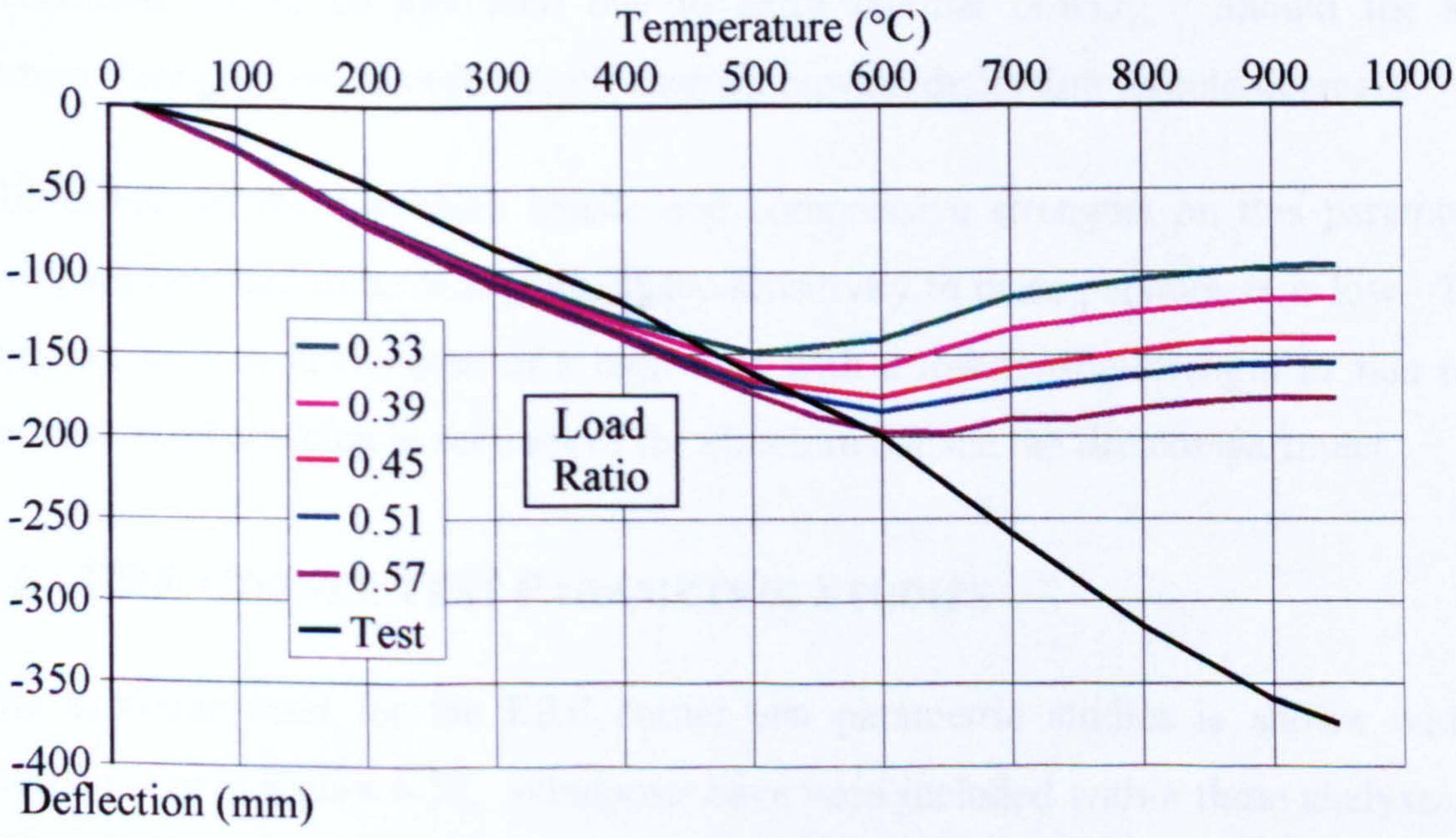

Figure 6-50. Parametric study 5 - British Steel corner test, mid-span of secondary beam

Over the initial 500°C the spread of results is very low, as the steel beam retains a large proportional of its material properties, thus dominating the structural action. Thereafter the load has greater effect as the beam material softens.

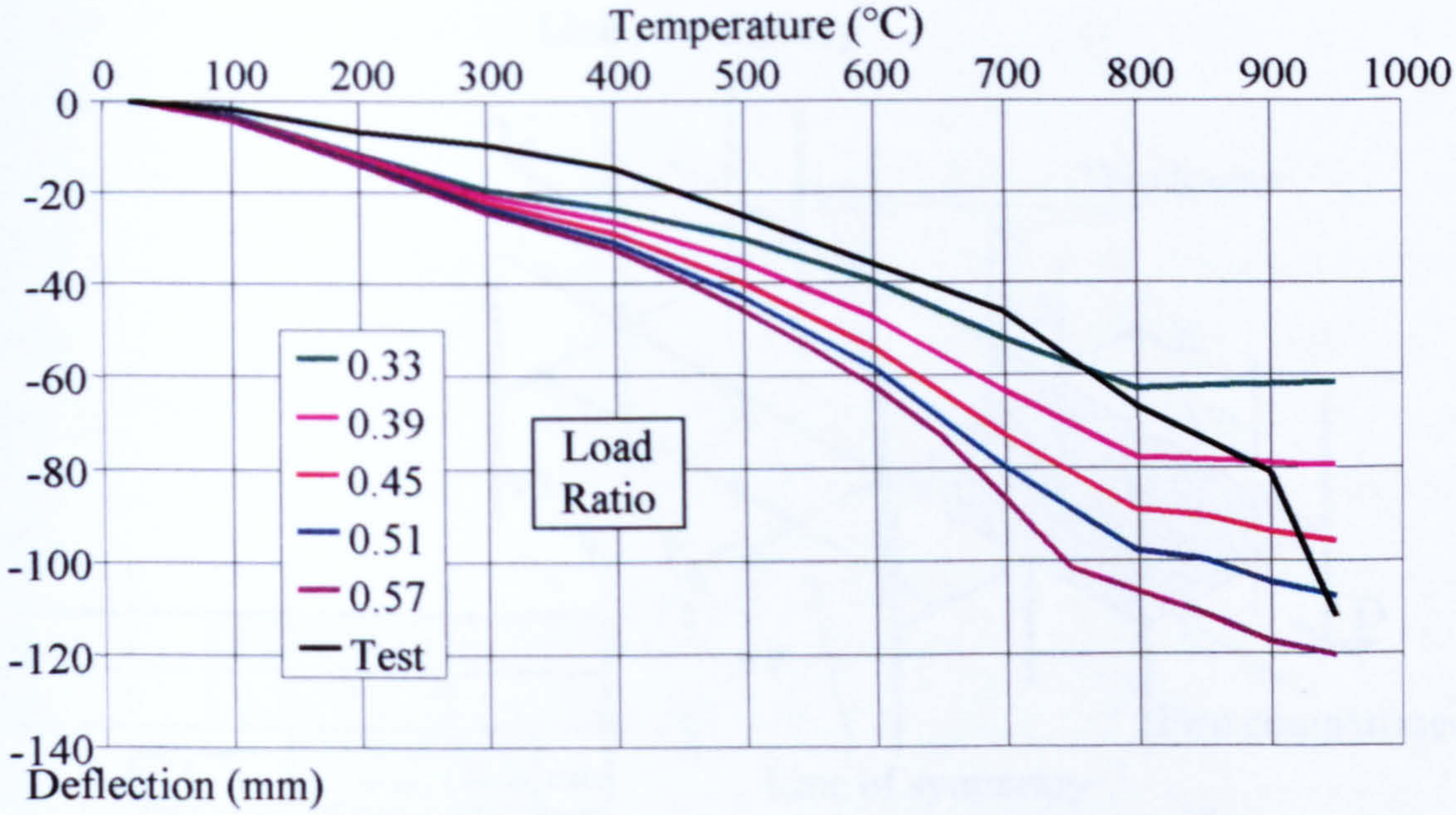

Figure 6-51. Parametric study 5 - British Steel corner test, mid-span of 6m main beam

Were the slab thickness to be increased during the load ratio parametric study, the deflections would logically be decreased, with an increased 'pull-back' on the secondary beam. Conversely a decrease of the thickness of the floor slab could lead to an increase in cracking for the higher loads, perhaps to the extent where the secondary beam would act as an isolated beam. It may be surmised that, should the slab temperature gradient be increased during the load ratio parametric study, the deflections would be increased due to extra thermal bowing. Should the slab temperature gradient be reduced, the thermal bowing deflections would decrease.

The effects of the maximum tensile and compressive strengths on this parametric study are assumed to be negligible, as the sensitivity to these parameters is low. This may not be true in the case of a high load with a low tensile strength as this may produce extra cracking in sections of the structure outside the fire compartment.

6.6 BRE Corner Test Parametric Studies

The subframe used for the BRE corner test parametric studies is shown with a location plan in Figure 6-52. Windposts have been included within these analyses, as Bailey [23, 44] has shown them to support the perimeter beam through tension from the floor above. Lateral restraint within the BRE corner test is supplied by continuity of the steel beams and floor slab. Vertical restraint is supplied to the perimeter beam as it is supported by the windposts.

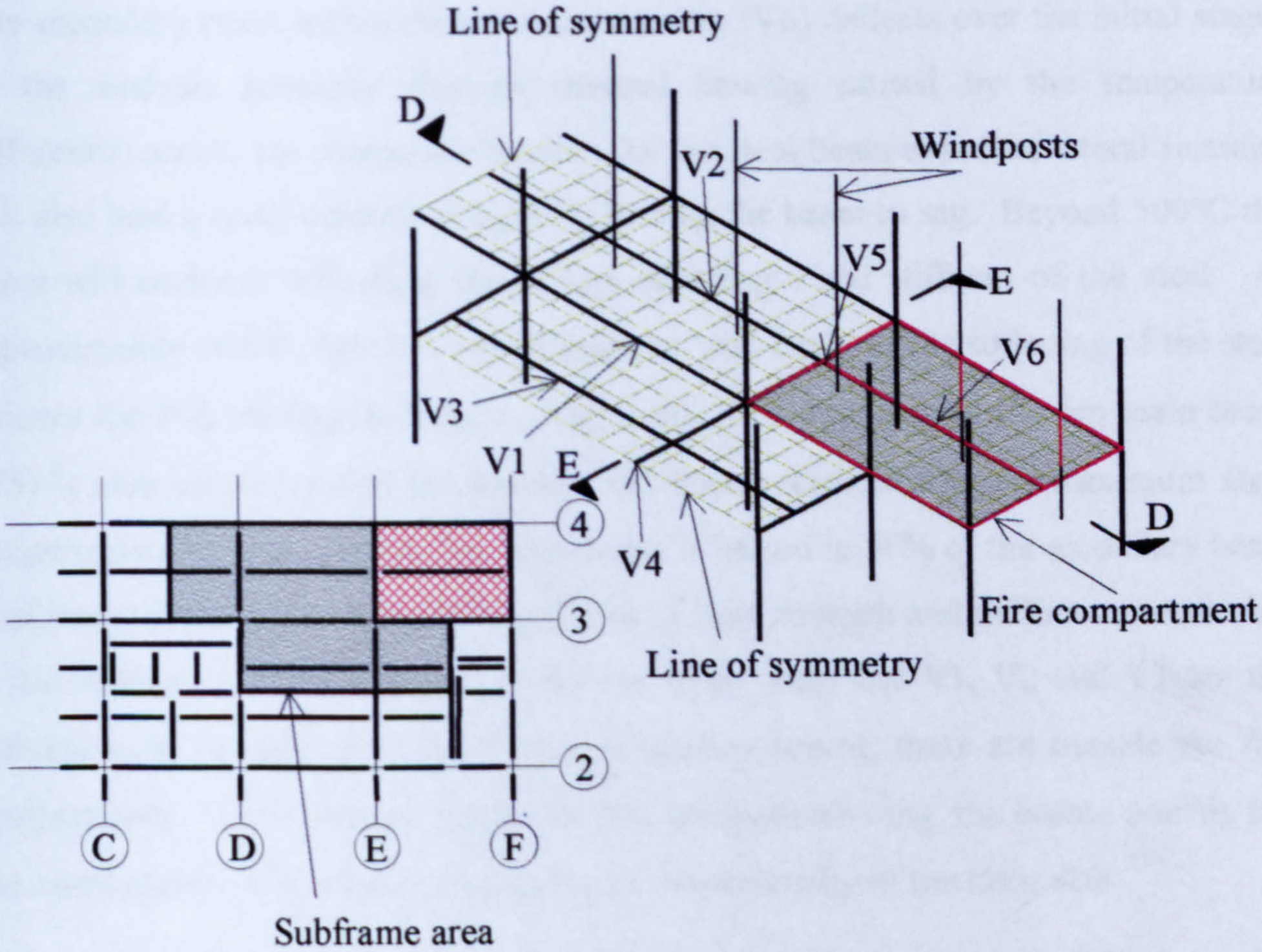

Figure 6-52. Location and finite element mesh of the BRE corner test.

Beams on the boundary of the compartment test and the perimeter beams have been heated to half the maximum temperatures of the internal secondary beam.

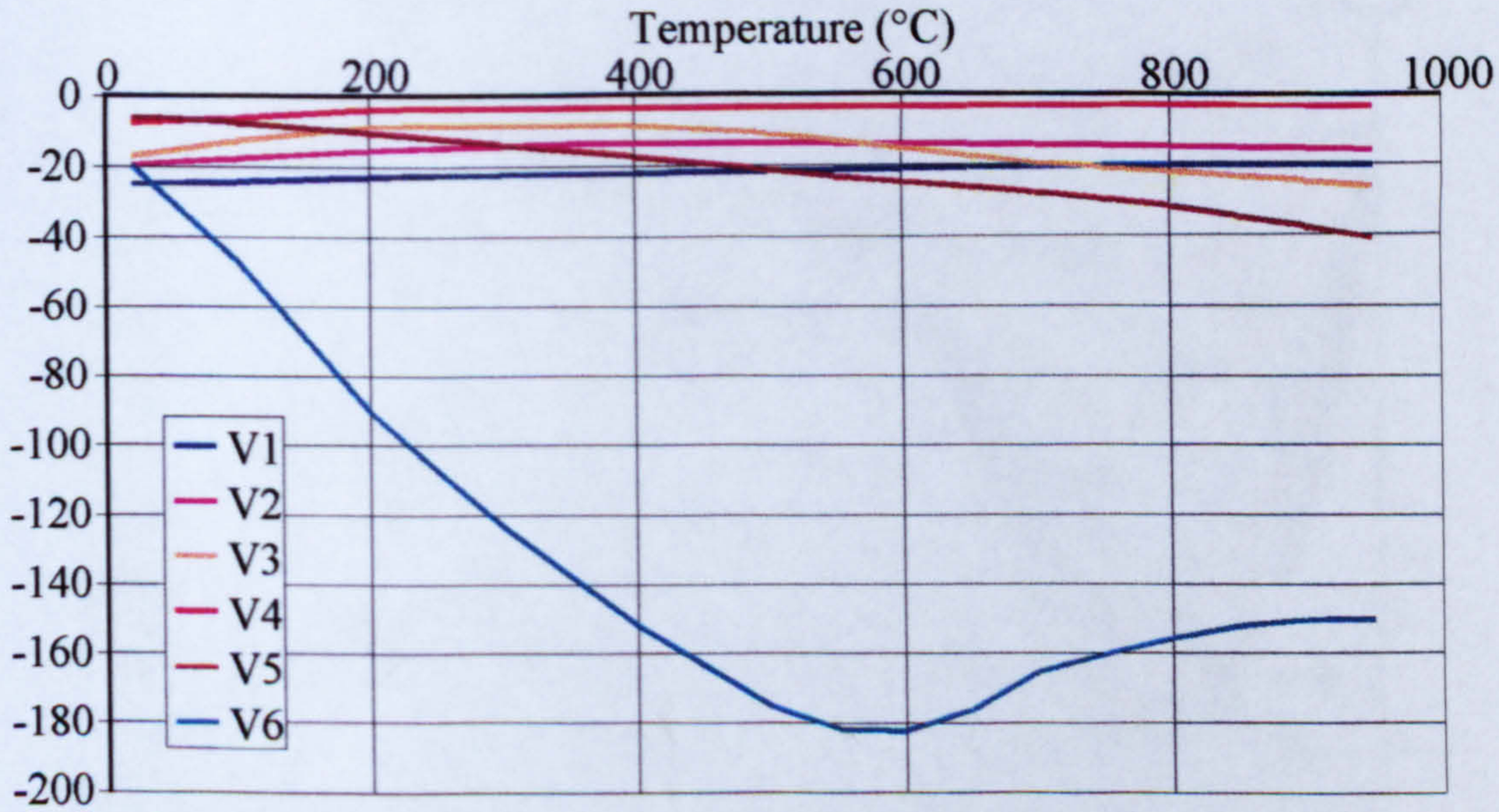

Figure 6-53. BRE corner test; absolute analytical deflections at various locations around subframe

The deflections at various locations around the BRE corner fire test are shown in Figure 6-53, which is to be read in conjunction with Figure 6-52.

The secondary beam within the test compartment (V6) deflects over the initial stages of the analysis primarily through thermal bowing caused by the temperature differential across the composite beams. As the steel beam expands, lateral restraint will also lend a small amount of rigidity, forcing the beam to sag. Beyond 500°C the beam will continue deflecting due to loss of strength and stiffness of the steel. At approximately 600°C, the steel beams begin to 'pull-back' as the softening of the steel reduces the P-Δ bending deflection component. The mid-span of the 6m main beam (V5) is also subject to thermal bowing and lateral restraint up to a maximum steel temperature of 950°C. As the 6m main beam is heated to 50% of the secondary beam maximum temperature, only a nominal loss of steel strength and stiffness occurs. V4 is the deflection at the mid-span of the 9m main beam and V1, V2 and V3 are the deflections at the mid-span of adjacent secondary beams; these are outside the fire compartment. As the beams within the fire compartment sag, the beams outside the fire compartment will attempt to hog due to the continuity of the floor slab.

Figures 6-54 and 6-55 show the absolute deflection profiles of Sections D-D and E-E respectively.

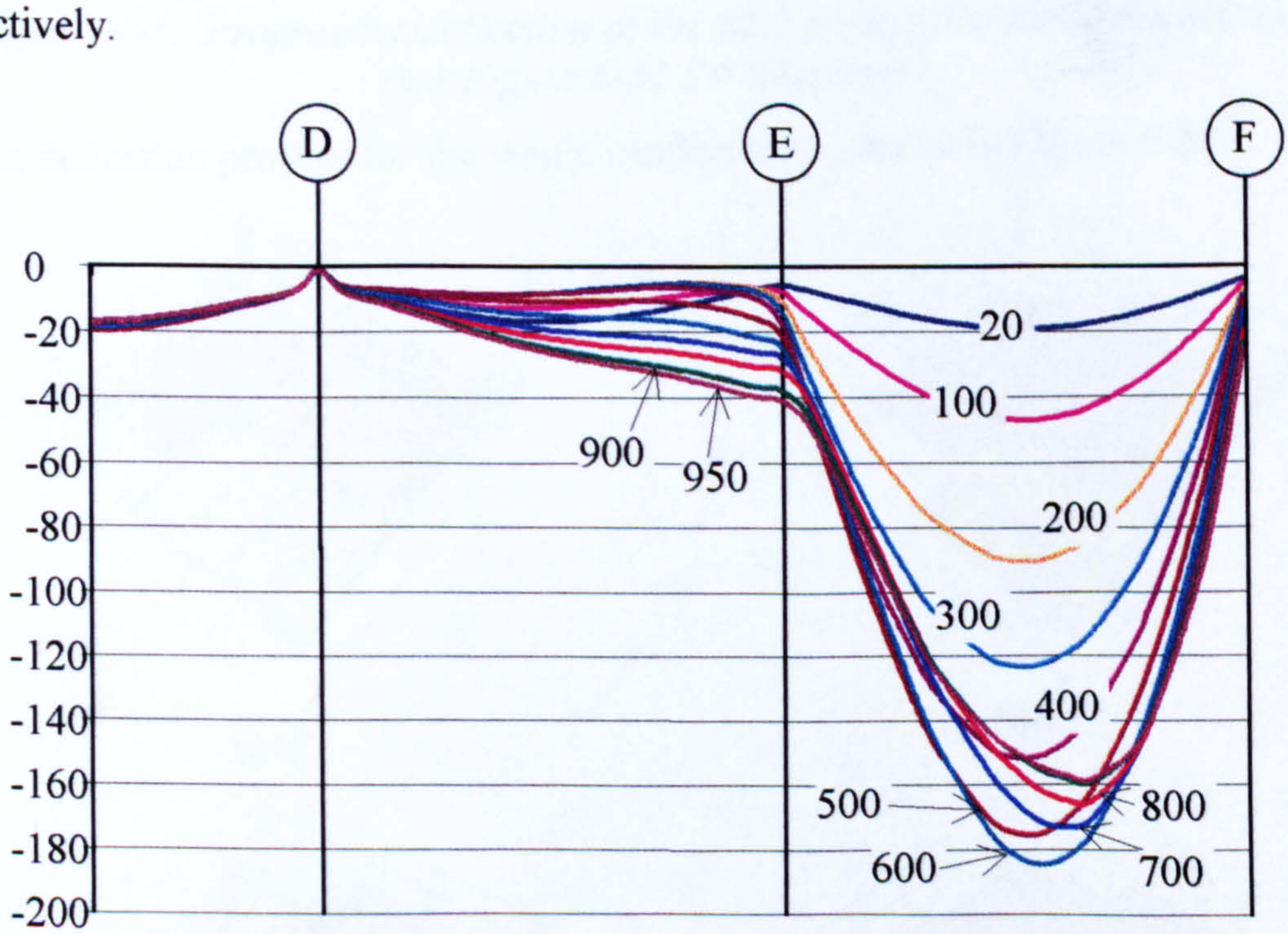

Figure 6-54. BRE corner test absolute deflection profile along Section D-D (see Figure 6-52 for location)

The rate of deflection over the initial 500°C (the period when thermal bowing is predominant) begins to reduce as the strength and stiffness of the steel beam decrease, and at approximately 600°C the secondary beam deflections reverse. The effect of

this on the secondary beam positioned between gridlines D and E is to cause it to hog up to 500°C, beyond which the rigidity of the beam within the compartment decreases rapidly, allowing this secondary beam to relax. The influence of the fire compartment beyond gridline D is considered to be small.

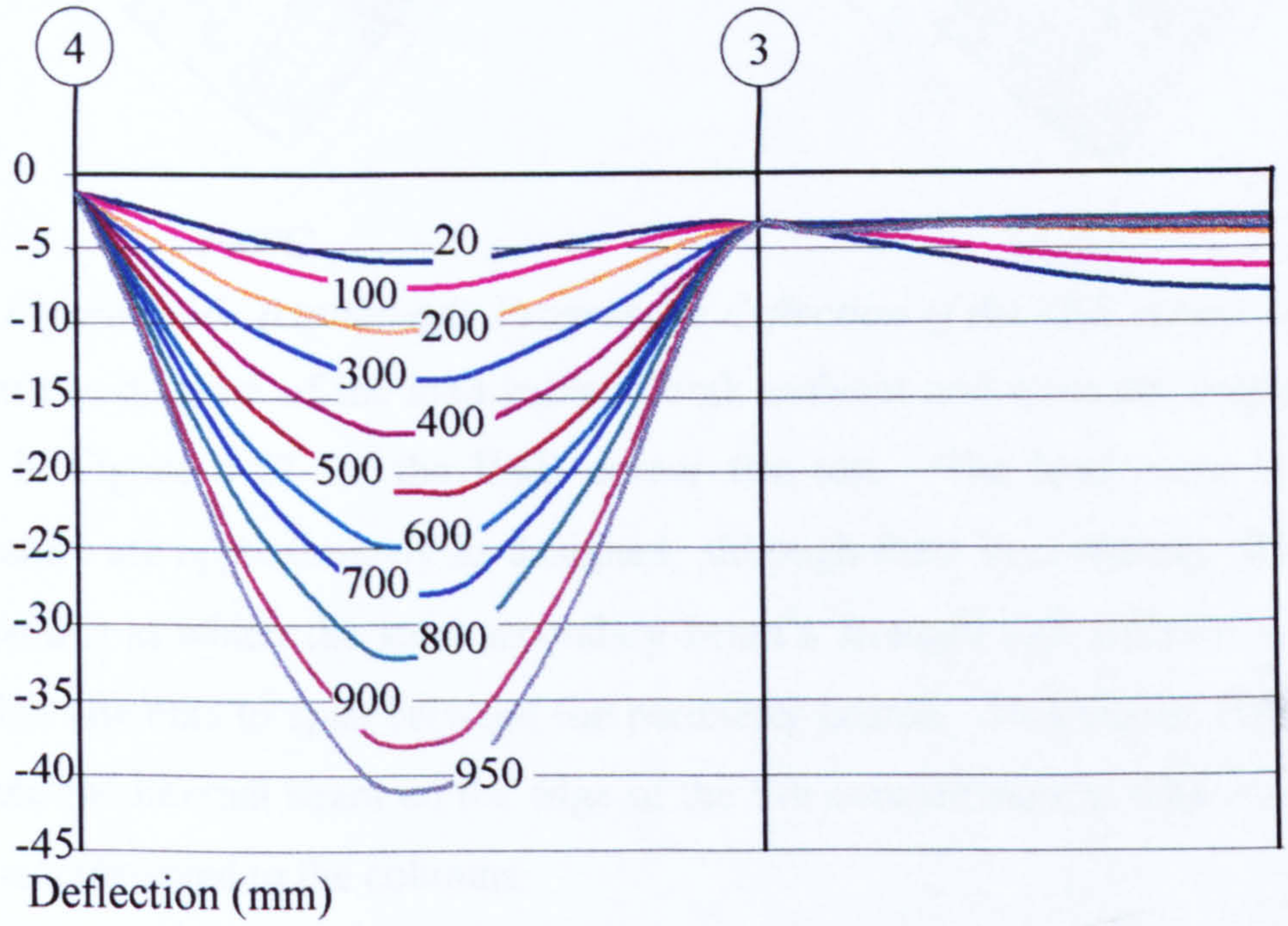

Figure 6-55. Progressive deflection of the BRE corner test along Section E-E (see Figure 6-52 for location)

Surface deflection profiles for the whole subframe are shown in Figure 6-56.

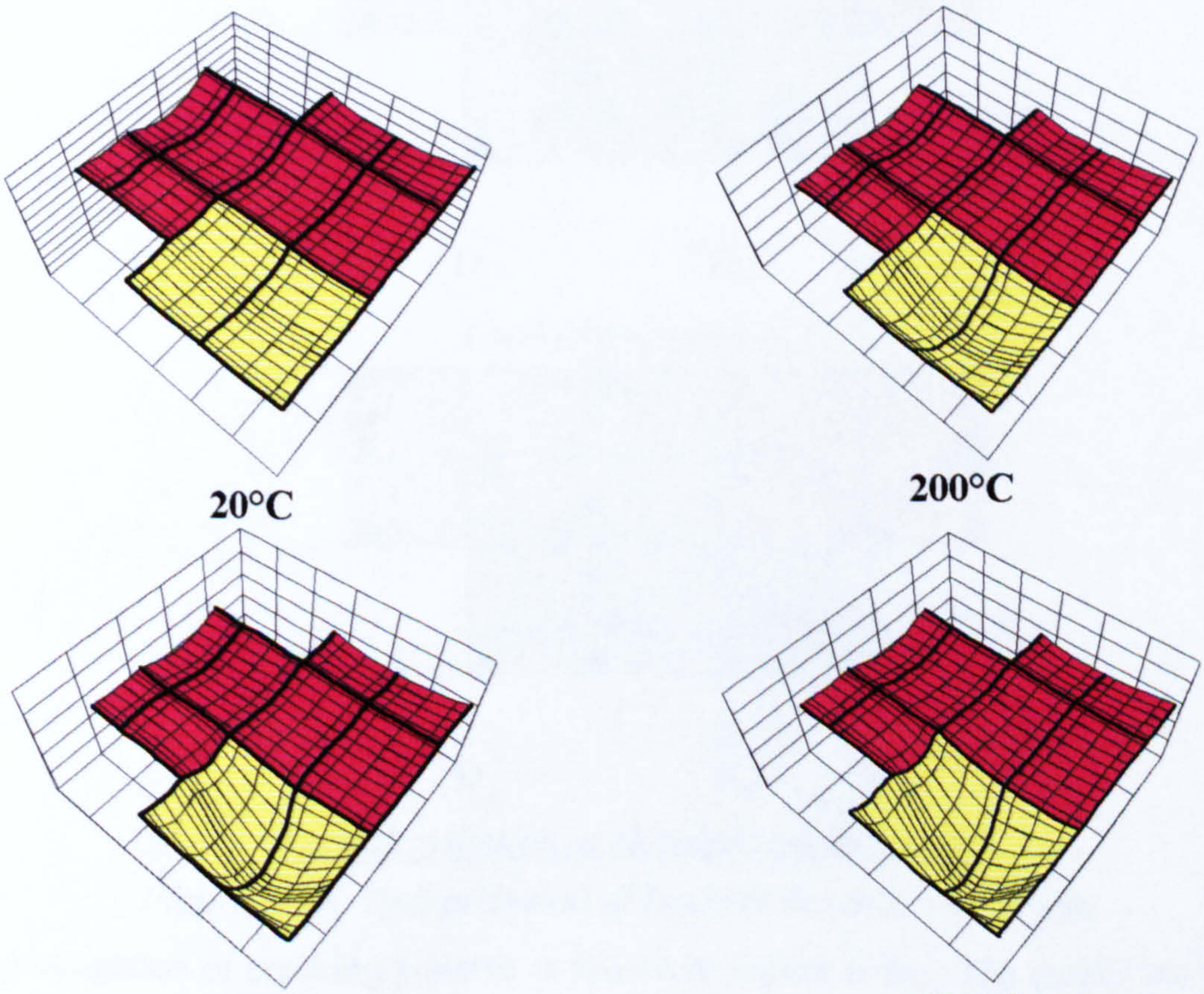

Figure 6-56. Progressive deflection of the BRE corner test

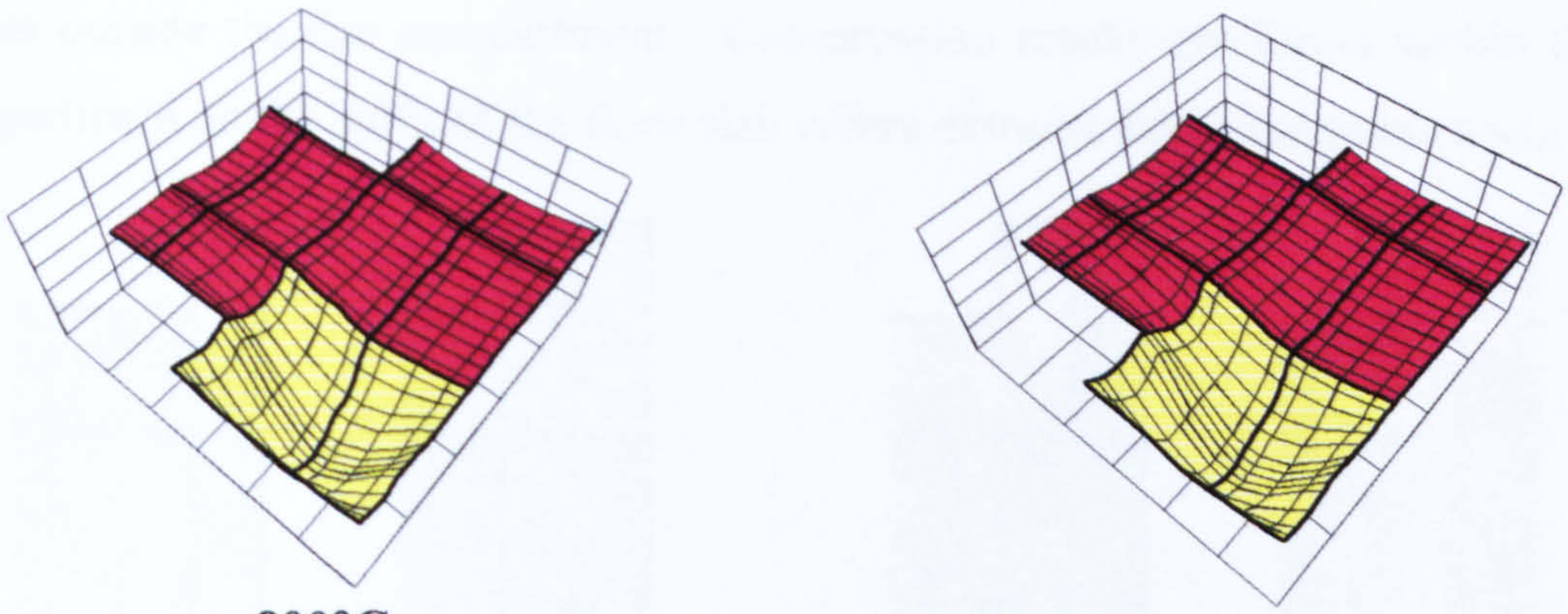

Figure 6-56. (continued) Progressive deflection of the BRE corner test

A schematic diagram of the load paths at both ambient and elevated temperatures is shown in Figure 6-57 for the BRE corner fire test. The load paths at ambient temperature are approximately as designed, although there is continuity of slabs. At temperatures at which the steel secondary beam's strength and stiffness is low, the floor slab attempts to span between the perimeter beams. This causes the perimeter beam and the internal beam on the edge of the fire compartment to take extra loading which is transferred to the columns.

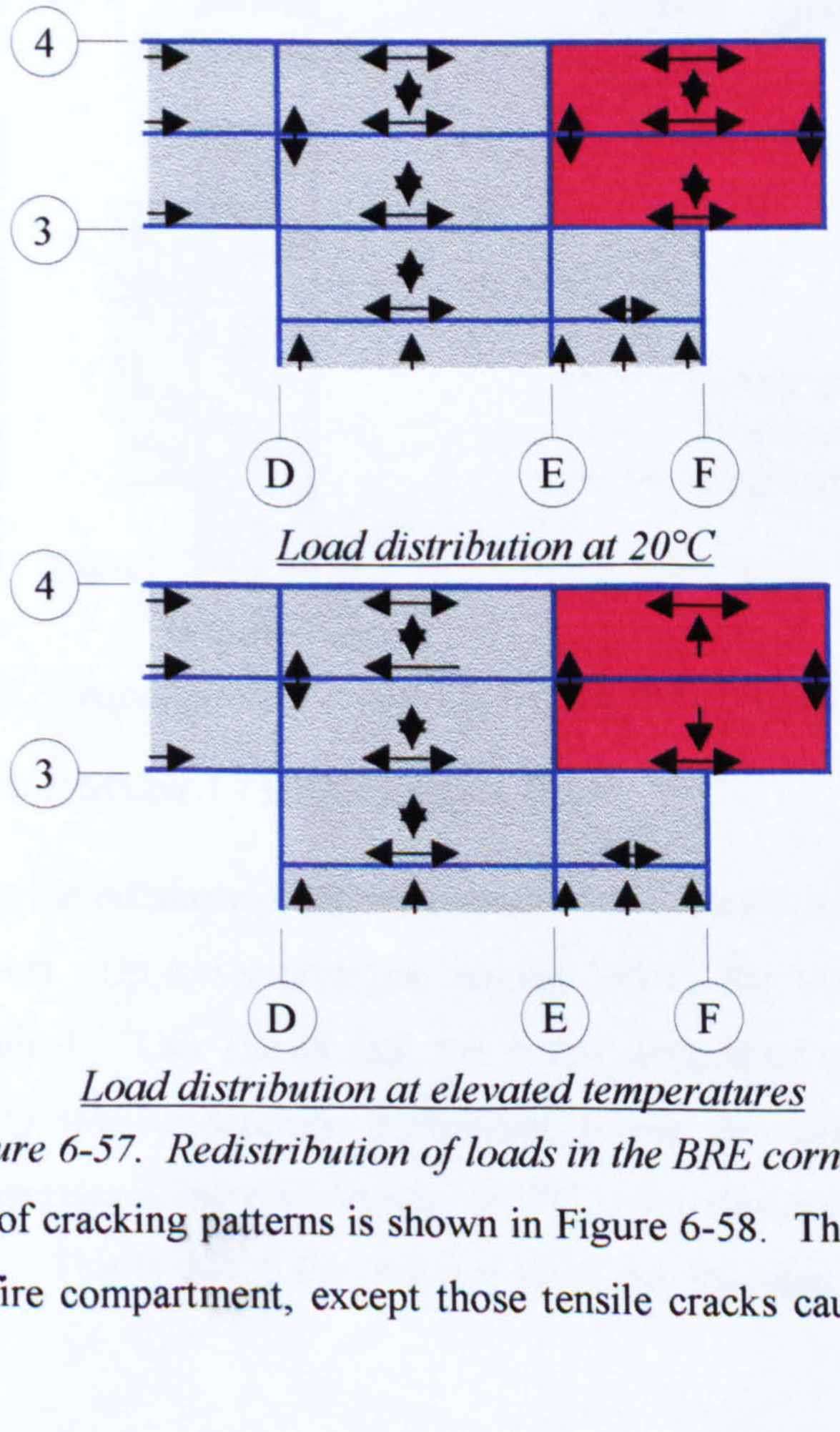

Load distribution at 20°C

Load distribution at elevated temperatures

Figure 6-57. Redistribution of loads in the BRE corner test

The propagation of cracking patterns is shown in Figure 6-58. The cracks are mainly confined to the fire compartment, except those tensile cracks caused by hogging of

beams outside the fire compartment. Compression cracks are found within the fire compartment on the soffit of the floor slab where extreme stress gradients occur.

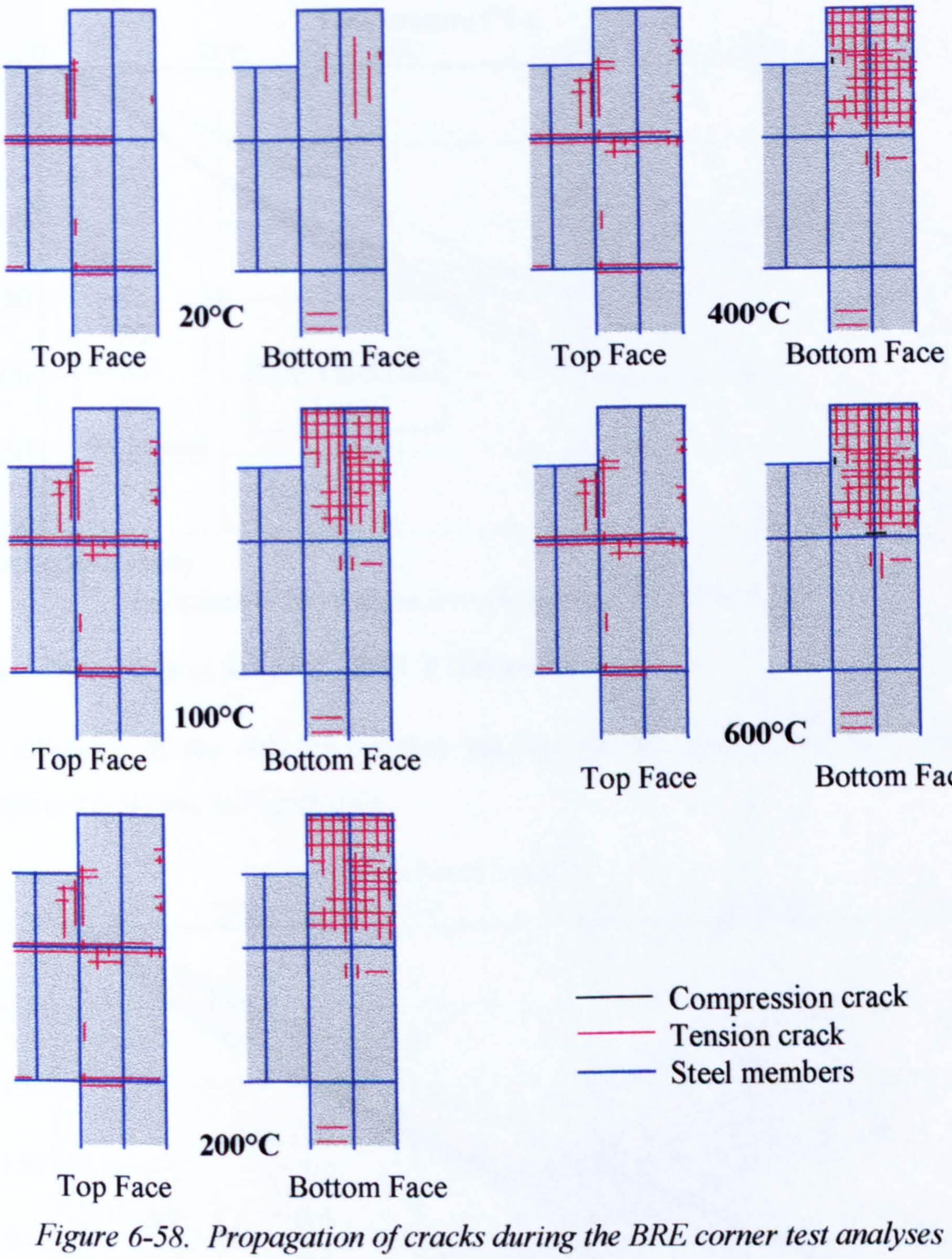

Figure 6-58. Propagation of cracks during the BRE corner test analyses

6.6.1 PARAMETRIC STUDY 1 - BRE CORNER TEST

Figure 6-59 shows the influence of slab thickness on the secondary beam deflection in the BRE corner test. Up to temperatures around 500°C, the variation in the beam deflection is nominal. This shows that the initial deflections are due to thermal bowing caused by the temperature differential across the steel beam. As the compartment temperatures increase beyond 500°C, the deflections begin to diverge and to "pull back". This is due to the concrete floor slab bridging from the perimeter

beam, reversing the deflections as the steel beam softens and allowing the P-Δ bending deflection component to reduce.

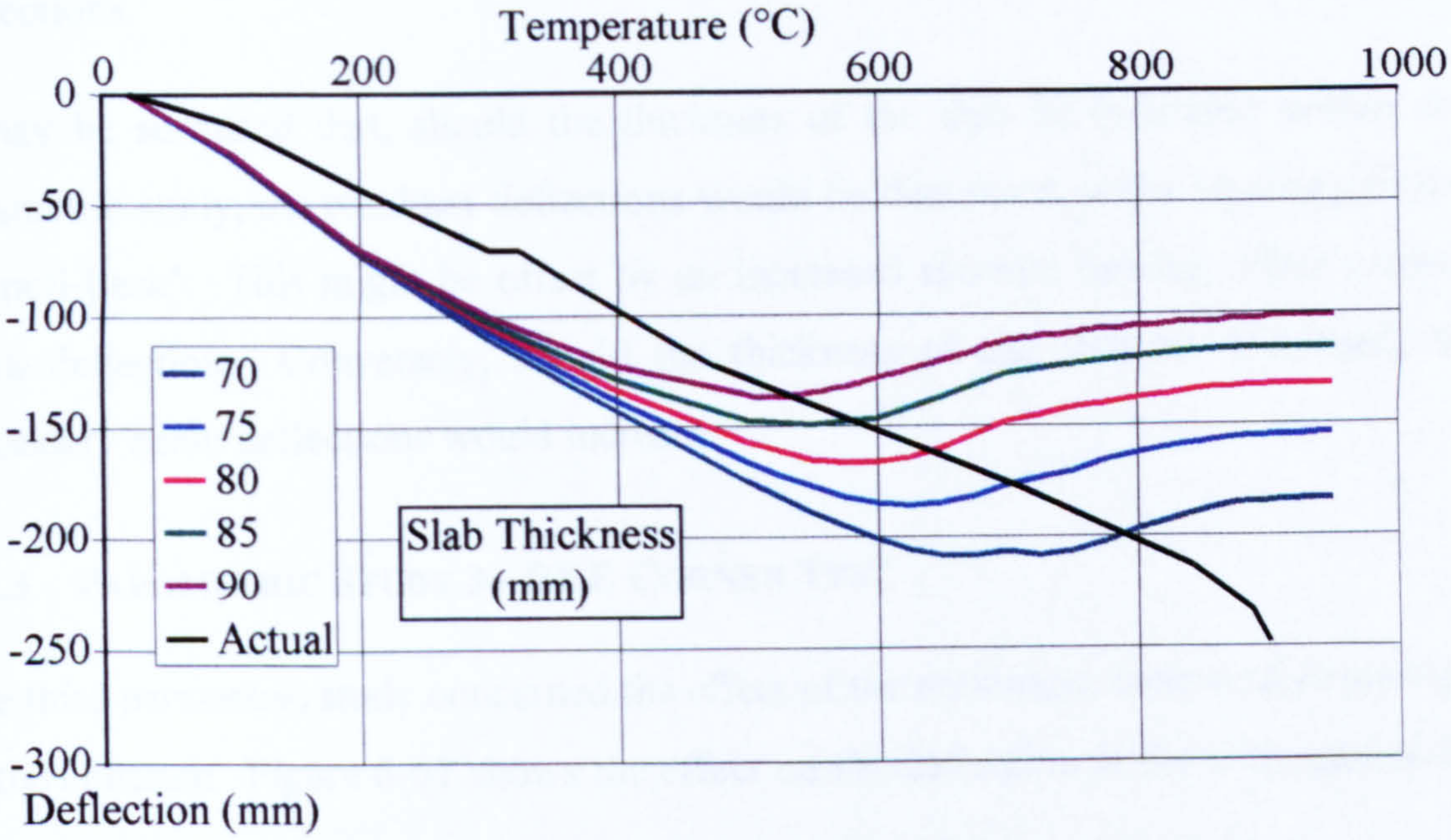

Figure 6-59. Parametric study 1 – BRE corner test

6.6.2 PARAMETRIC STUDY 2 - BRE CORNER TEST

The influence of the slab temperature gradient on the secondary beam mid-span deflections is shown in Figure 6-60.

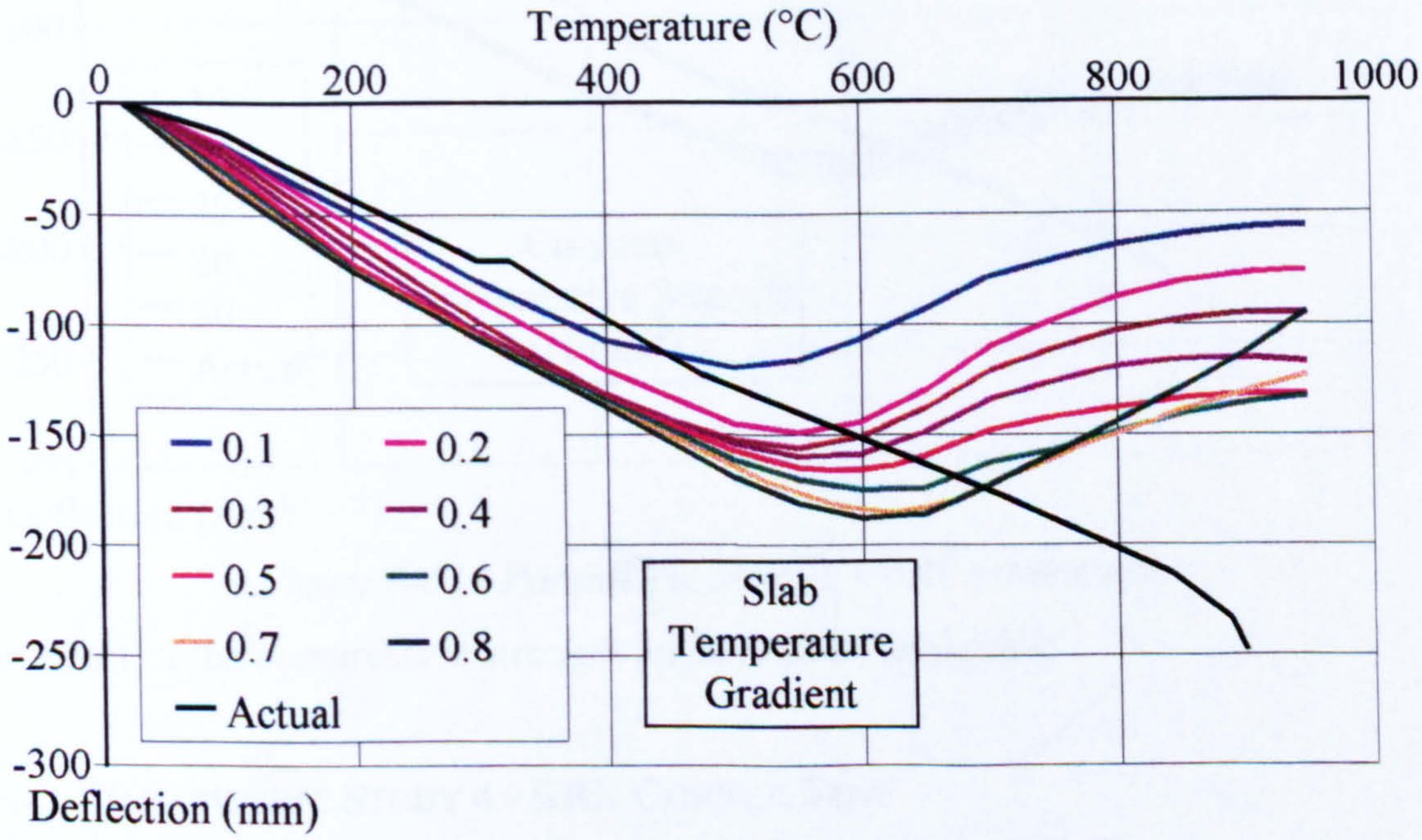

Figure 6-60. Parametric study 2 – BRE corner test

There is insignificant variation in deflections up to 500°C, and therefore these deflections may be attributed largely to thermal bowing of the beam. However, beyond 500°C there is a significant spread in results. At these temperatures the beam begins to lose strength and stiffness and therefore the P-Δ bending deflection

component reduces. This allows the concrete floor slab to span across the central beam, and thus the temperature regime within the slab dictates the subsequent deflections.

It may be surmised that, should the thickness of the slab be increased within this parametric study, the resultant deflections would be decreased as the structure begins to 'pull-back'. This might be offset by an increased thermal bowing effect causing extra deflection. Conversely, should the thickness of the slab be decreased, the secondary beam deflections would increase.

6.6.3 PARAMETRIC STUDY 3 - BRE CORNER TEST

The third parametric study concerned the effect of the maximum compressive strength of the concrete. Figure 6-61 shows the effect on the deflection at the mid-span of the secondary beam.

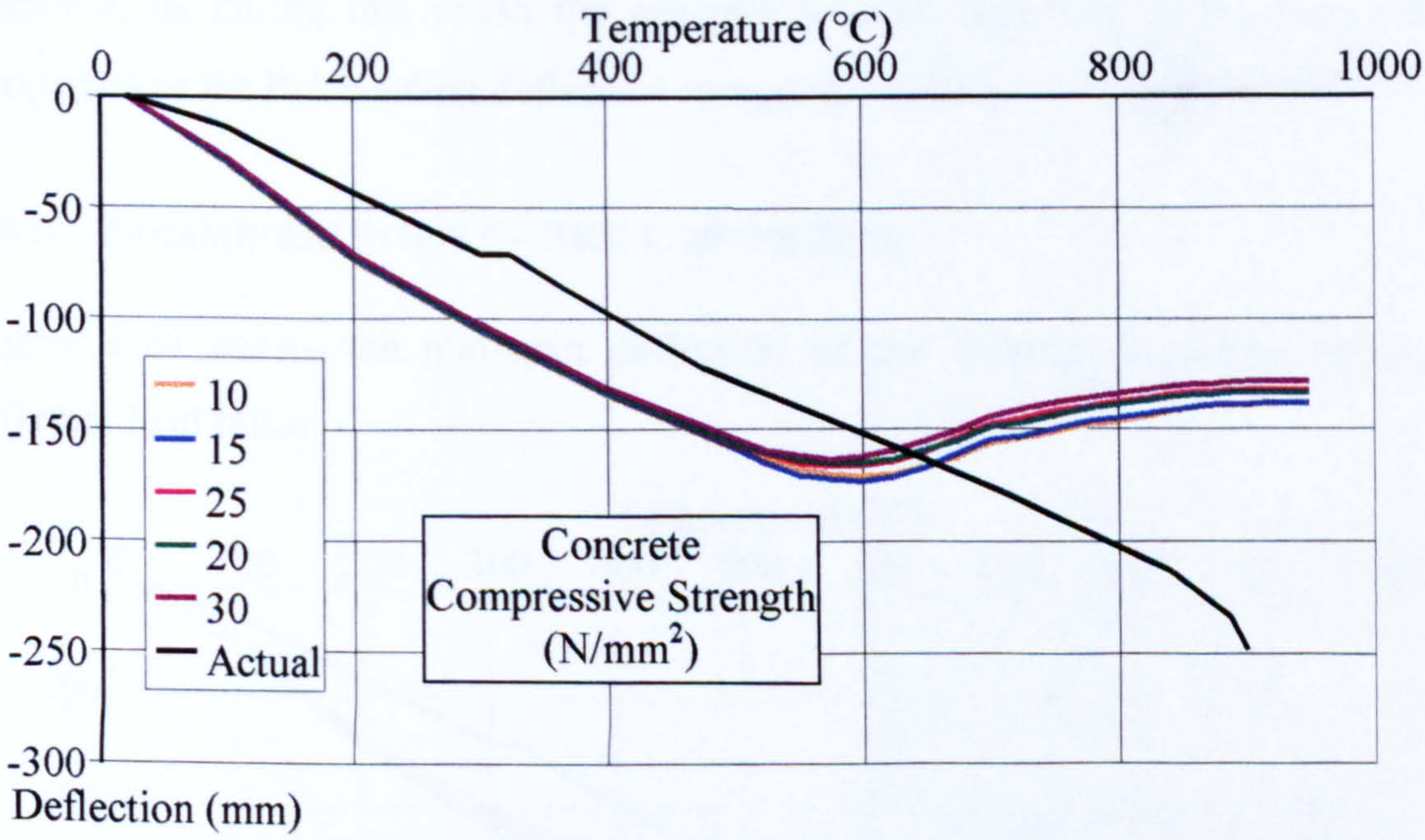

Figure 6-61. Parametric study 3 – BRE corner test

The effect of the compressive strength appears to be negligible.

6.6.4 PARAMETRIC STUDY 4 - BRE CORNER TEST

The effect of concrete tensile strength on the mid-span deflection of the secondary beam is shown in Figure 6-62.

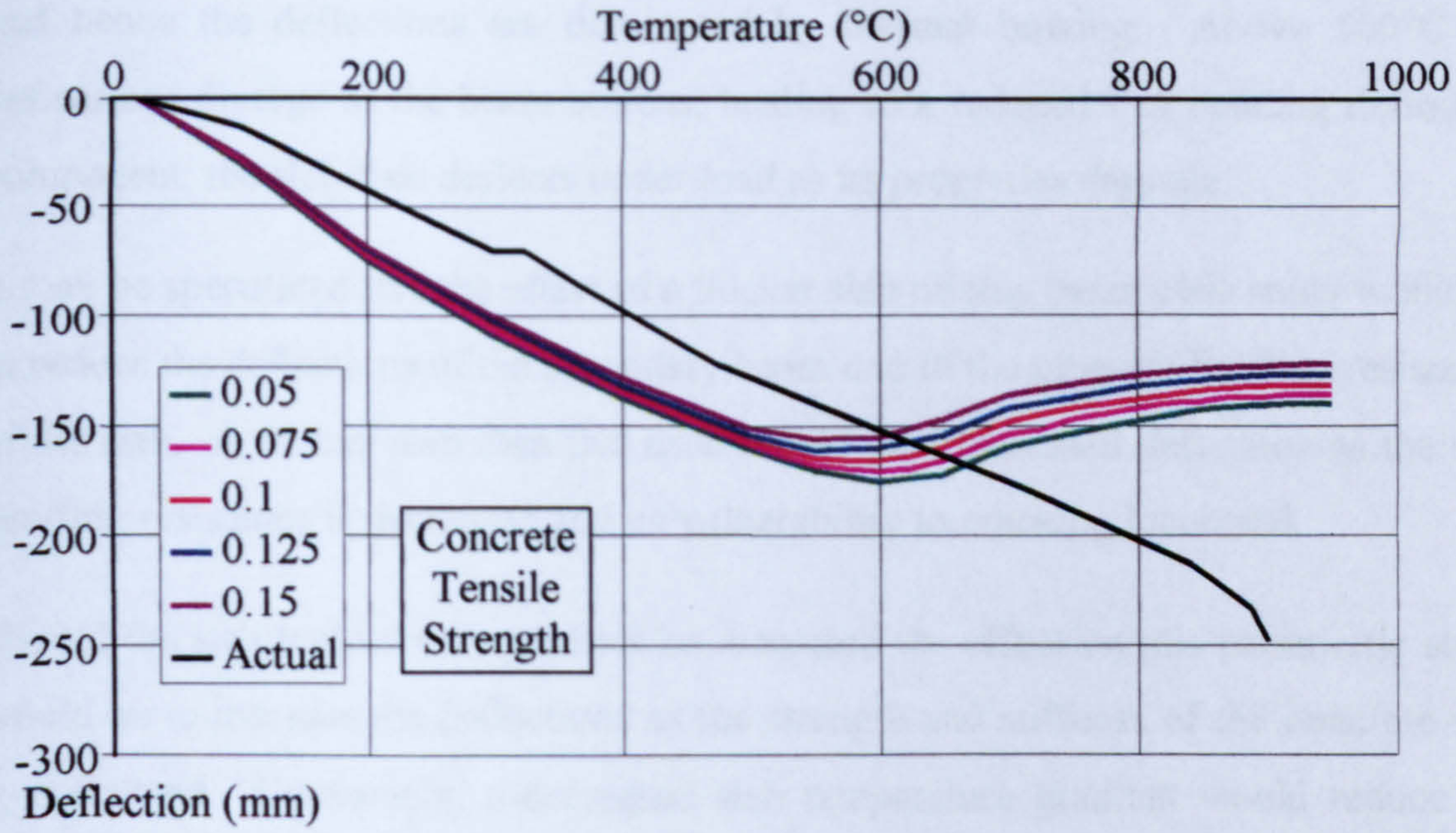

Figure 6-62. Parametric study 4 – BRE corner test

The deflection of the secondary beam is insensitive to the tensile strength over the initial 500°C. Beyond this temperature, there is some small variation in the deflection response, as during this phase the analysis is more sensitive to the floor slab's properties as the P-Δ bending deflection component reduces with temperature.

6.6.5 PARAMETRIC STUDY 5 - BRE CORNER TEST

Figure 6-63 shows the mid-span deflection of the cemtral secondary beam for different load ratios.

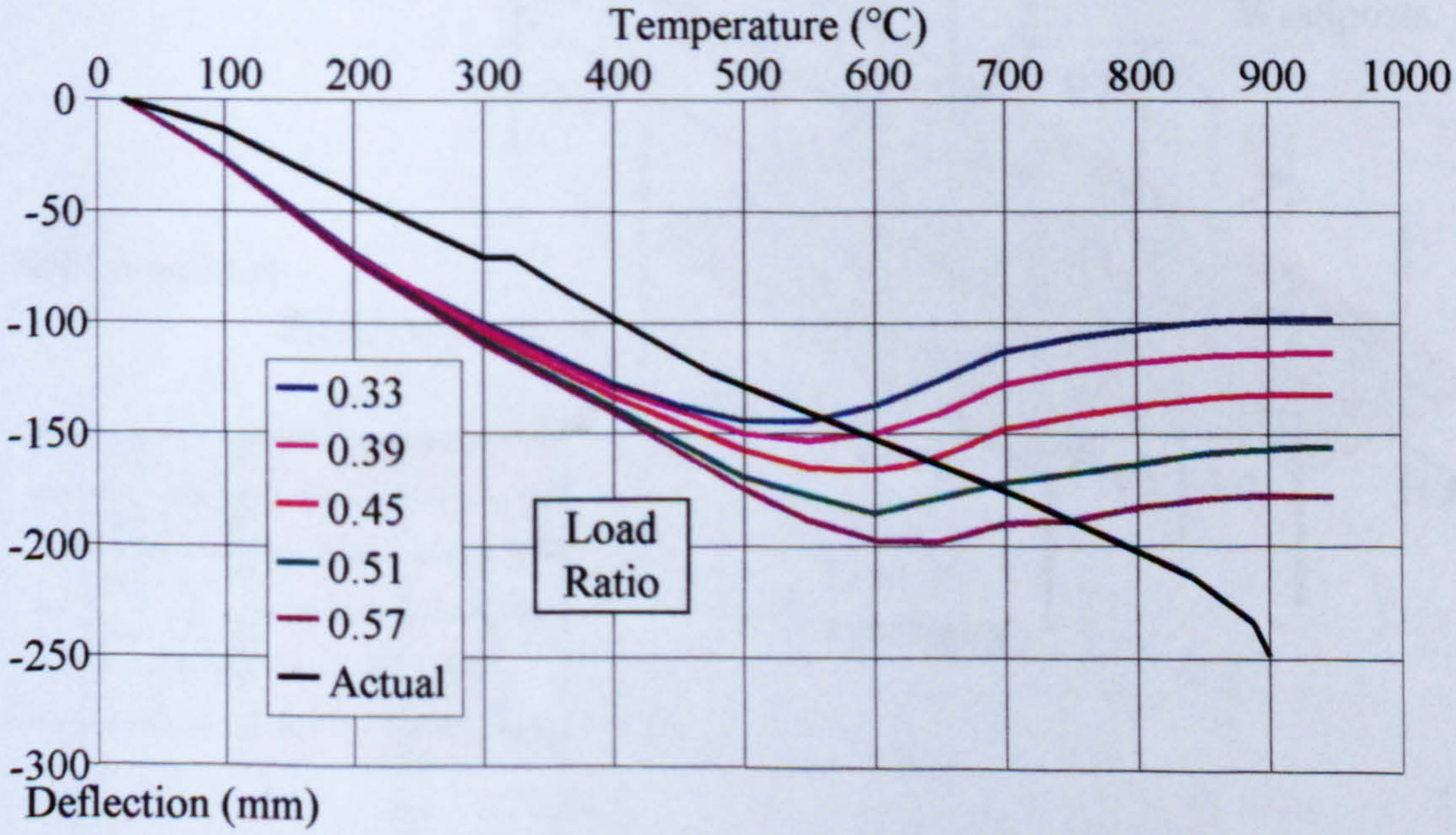

Figure 6-63. Parametric study 5 – BRE corner test

For the initial 500°C the deflection of the secondary beam has negligible variation, as the steel beam retains the majority of its strength and stiffness at these temperatures,

and hence the deflections are dominated by thermal bowing. Above 500°C the deflections diverge as the beam softens, leading to a reduced P-Δ bending deflection component; the slab then deflects under load as its properties degrade.

It may be speculated that the effect of a thicker slab on this parametric study would be to reduce the deflections of the secondary beam due to the inherent bending resistance of the slab. A thinner slab than that used would give increased deflection as the slab bending resistance is decreased and its vulnerability to cracking increased.

Should the slab temperature gradient be increased the effect on this parametric study would be to increase the deflections as the strength and stiffness of the concrete slab is decreased. Conversely, a decreased slab temperature gradient would reduce the secondary beam deflections.

The compressive and tensile concrete strengths would have a negligible effect on this parametric study, except perhaps for the case of thin slabs in conjunction with high loads.

6.7 Large Compartment Test Parametric Studies

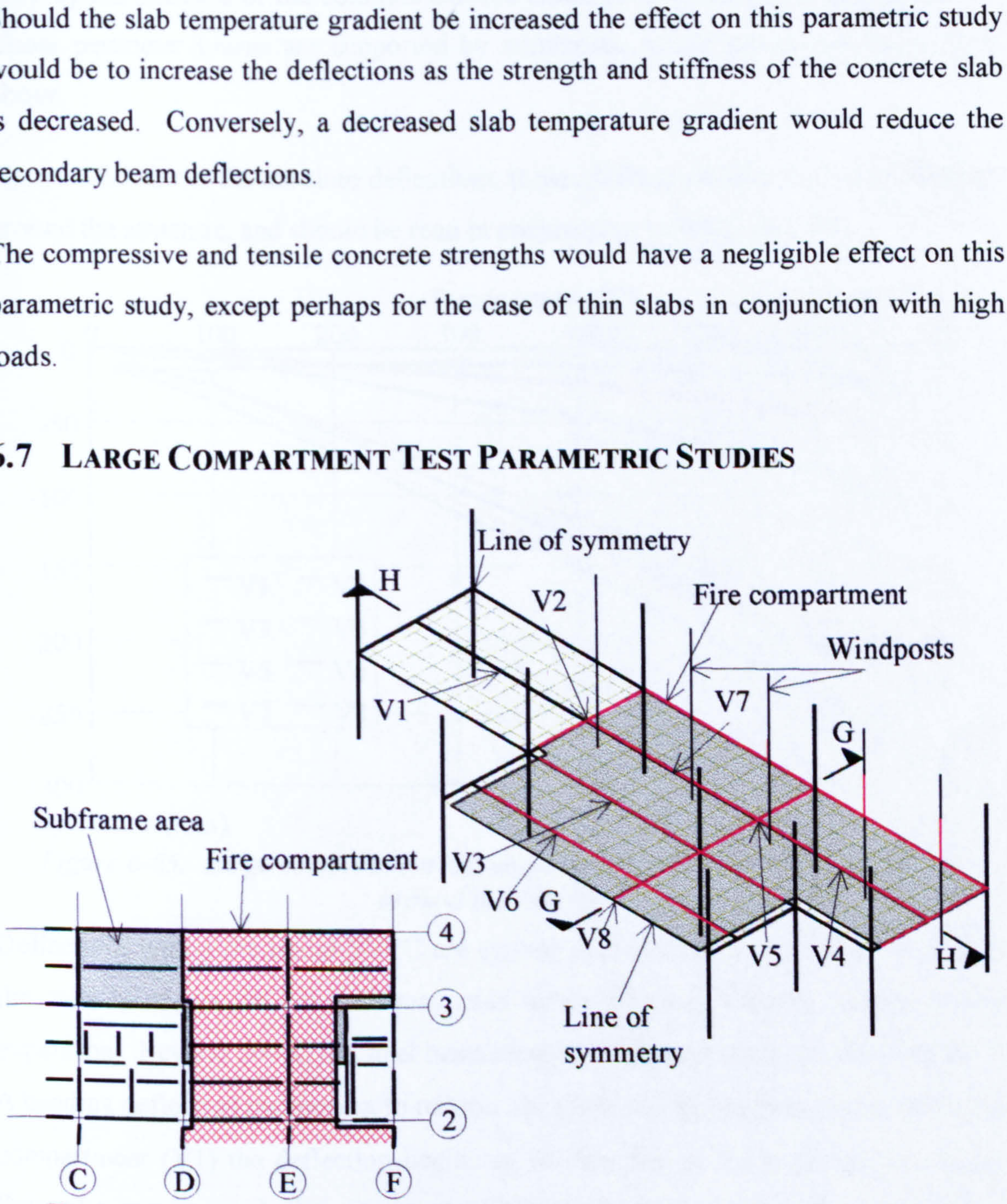

Figure 6-64. Location and finite element mesh of the large compartment test.

The subframe used for the previous fire test analyses has been extended to that shown in Figure 6-64. This is to allow better continuity across gridline D when modelling the large compartment test. Symmetry has been utilised for computational efficiency by assuming the structure is symmetrical about the centre-line of the 9m main beam.

The finite element subframe has been heated uniformly across the fire compartment except for the perimeter beams which have been heated to 50% of the steel maximum temperature within the compartment. The fire compartment is restrained in-plane only by the stiffness of the columns and the continuous structure beyond gridline D. These perimeter beams are supported by windposts, which act as ties to the floor above.

Figure 6-65 shows the absolute deflections at elevated temperatures at selected points around the structure, and should be read in conjunction with Figure 6-64.

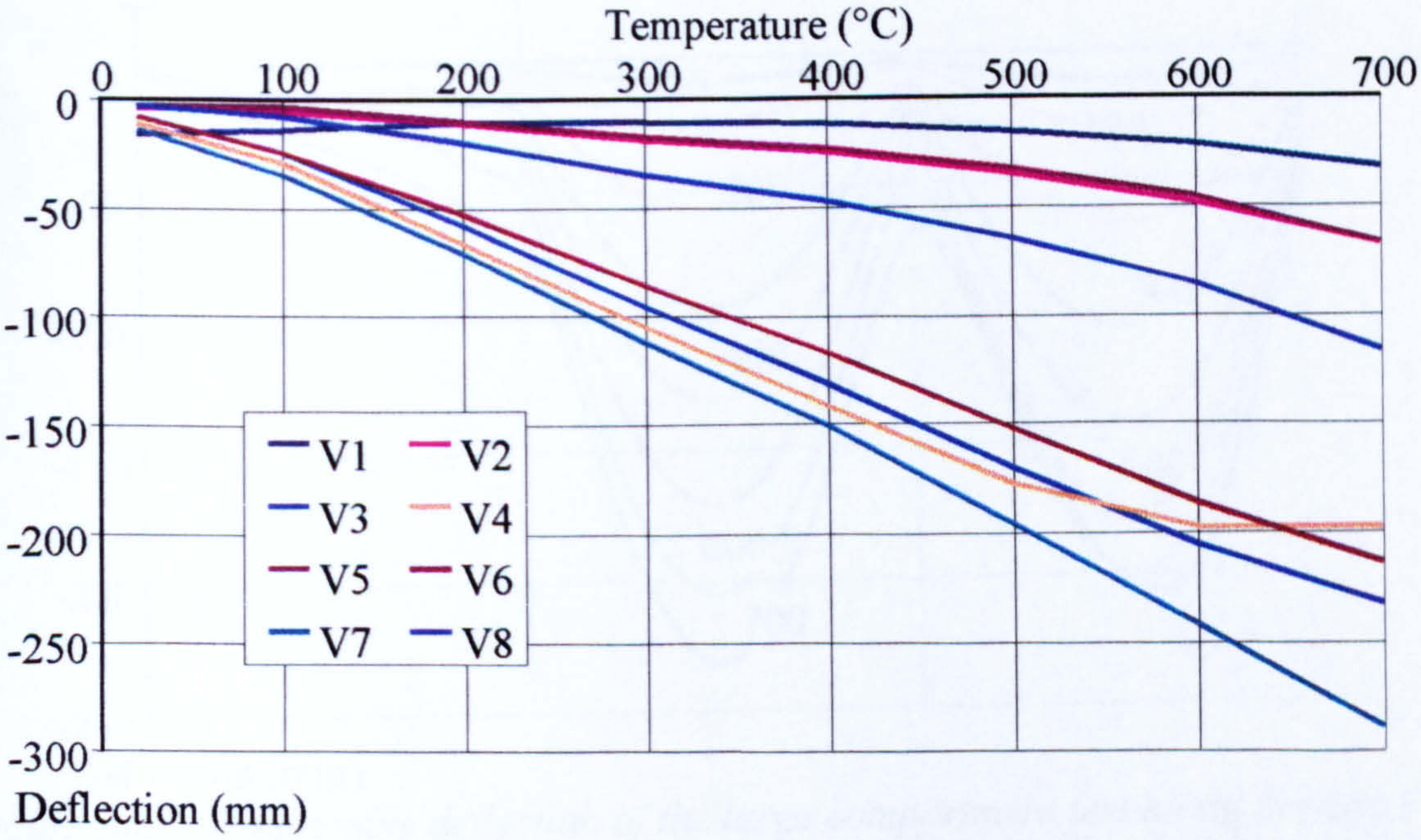

Figure 6-65. Large compartment test absolute deflections at various locations around the subframe

Deflections within the initial 500°C are caused predominantly by thermal bowing of the steel beam, as the columns may only apply nominal restraint against thermal expansion. Beyond 500°C the steel beams lose strength and stiffness, allowing the P-Δ bending deflection component to reduce. At a half-bay beyond the extent of the fire compartment (V1) the deflection begins to reverse due to the structural continuity. Beyond a maximum steel temperature of 500°C the beams within the compartment begin to 'relax' as they lose strength and stiffness allowing deflection V1 to attempt to

return to its original position. Deflection V2 is on the 6m main beam located on the edge of the fire compartment. This deflects at approximately the same rate as the 6m main beam found on gridline E (V5). The mid-span of the 9m main beam (V8) is seen to deflect to a maximum of approximately 120mm. The deflections at the centres of the 9m secondary beams (V3, V4, V6 and V7) all give similar results. It is interesting to note the deflections at V4 begin to reverse above 600°C, due to the bending properties of the floor slab as it spans between the cooler edge beams.

The finite element analysis of this structural subframe 'fails' at 700°C due to cracking of the concrete slab around the internal column situated at E3 and its opposite at E2.

Figures 6-66 and 6-67 show the deflection profiles along Sections F-F and G-G respectively.

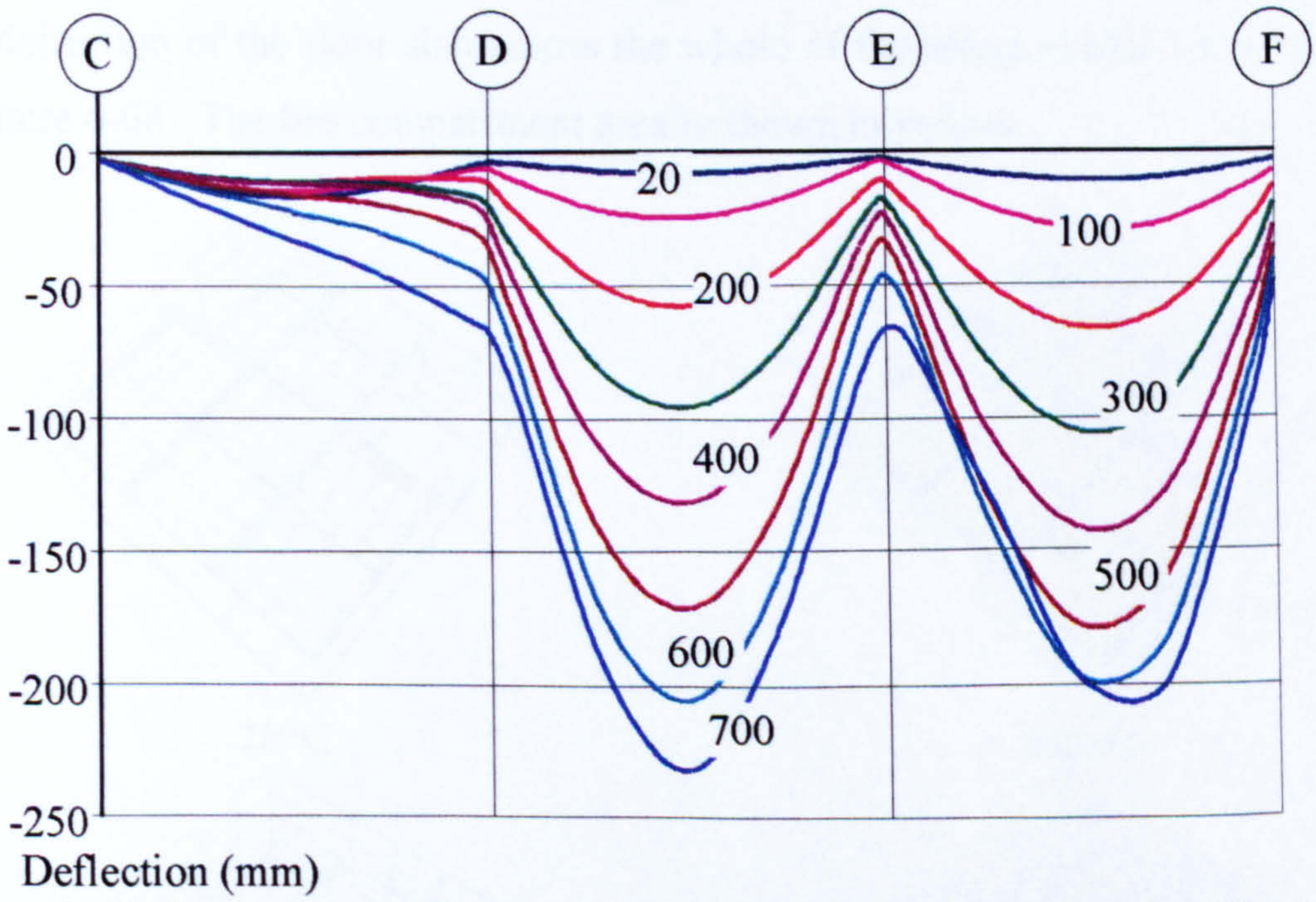

Figure 6-66. Progressive deflection of the large compartment test along Section F-F (see Figure 6-64 for location)

At 20°C, the maximum secondary beam deflection is 24mm between Gridlines E and F. As the temperature increases the deflection increases due to thermal bowing caused by the temperature differentials across the beams. At 500°C the strength and stiffness is reduced significantly, so that the P-Δ bending deflection component decreases. It may be noted that the secondary beam between Gridlines E and F begins to reverse its deflections at 600°C as the bending stiffness of the floor now exceeds that of the steel beams.

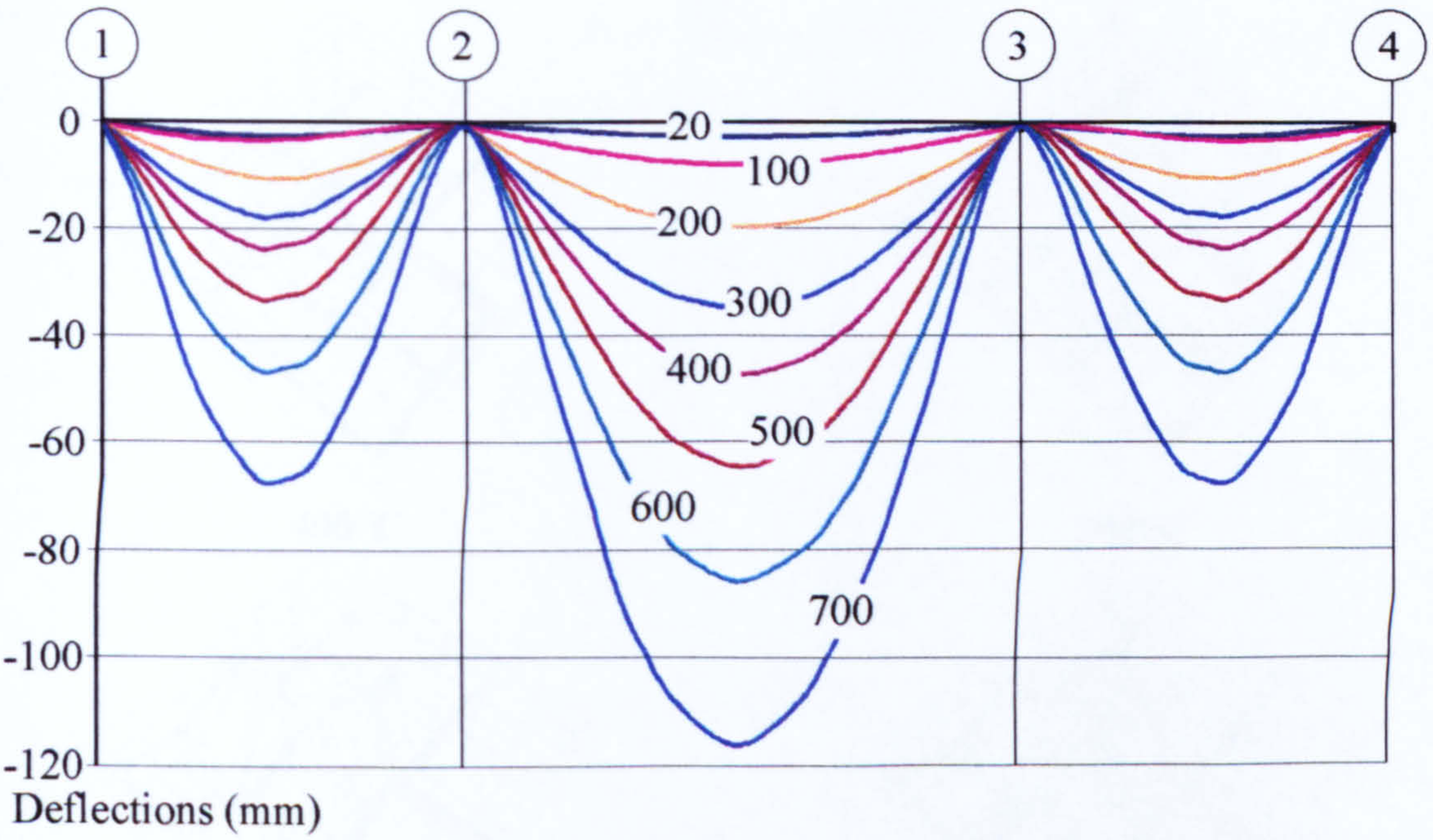

Figure 6-67. Progressive deflection of the large compartment test along Section G-G (see Figure 6-64 for location)

The deflection of the floor slab across the whole of the structural subframe is shown in Figure 6-68. The fire compartment area is shown in yellow.

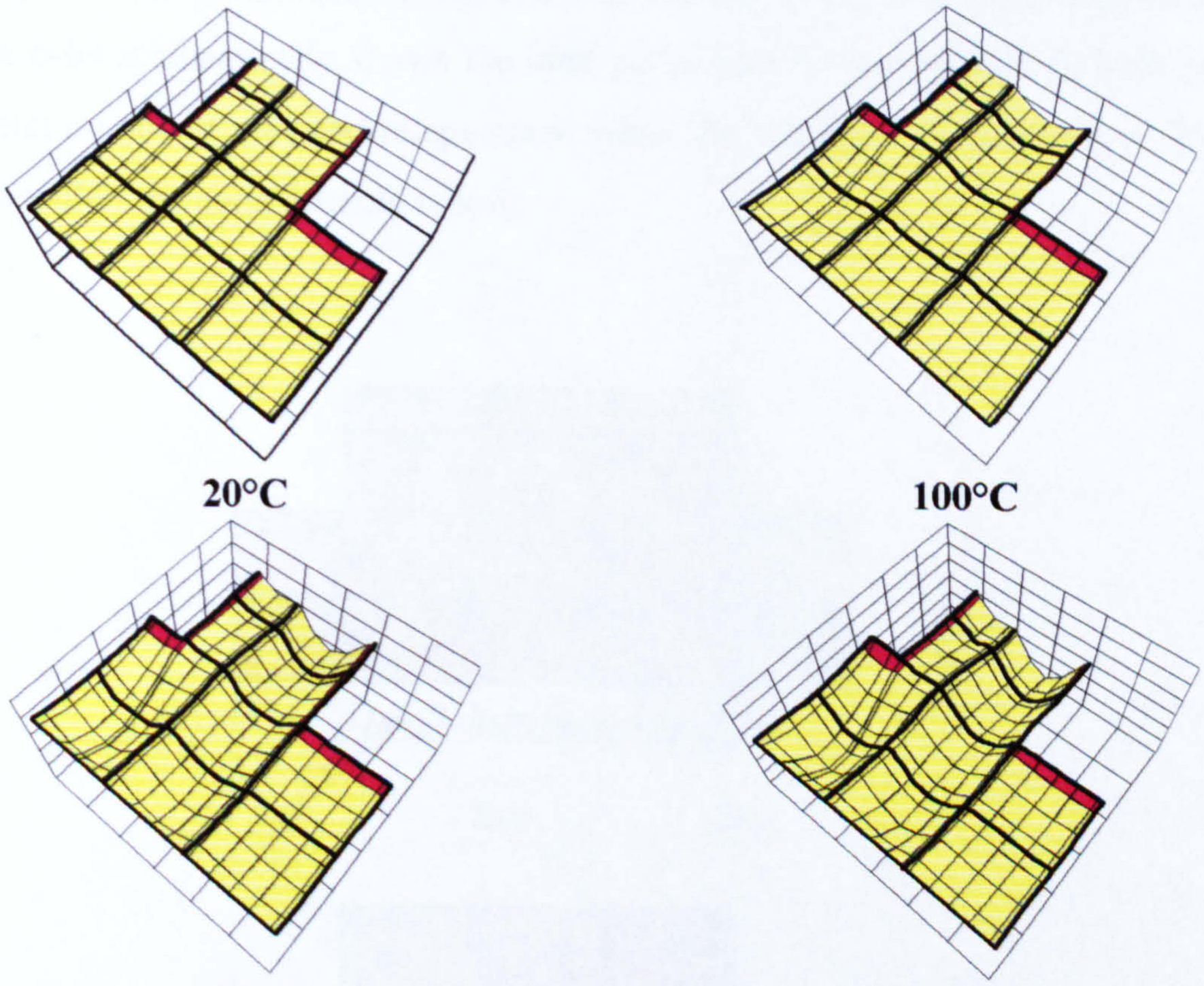

Figure 6-68. Progressive deflection of the large compartment test

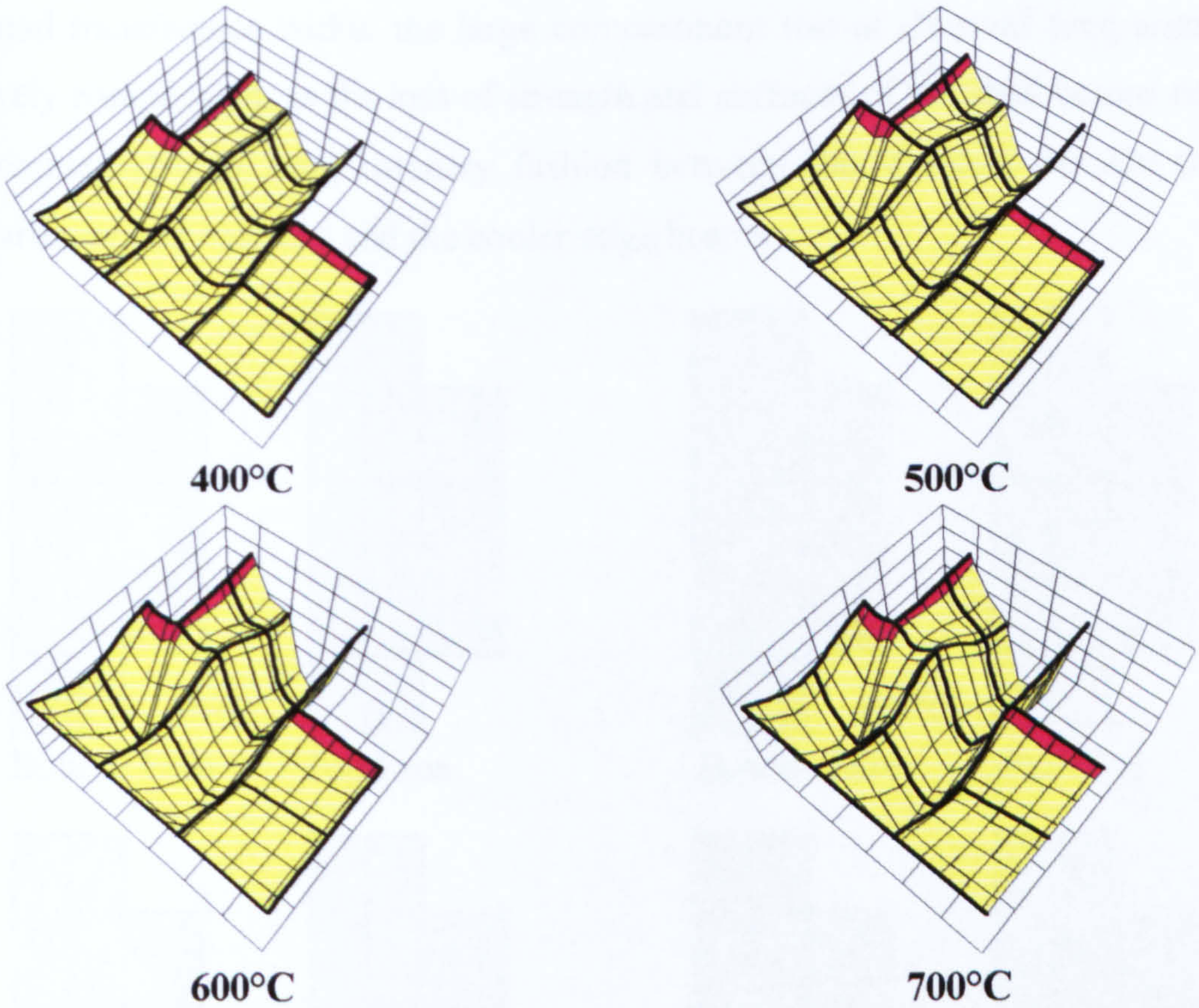

Figure 6-68. (continued) Progressive deflection of the large compartment test

Figure 6-69 schematically shows the load paths across the subframe at both ambient temperature and at elevated temperature when the strength and stiffness of the steel beams within the compartment is low.

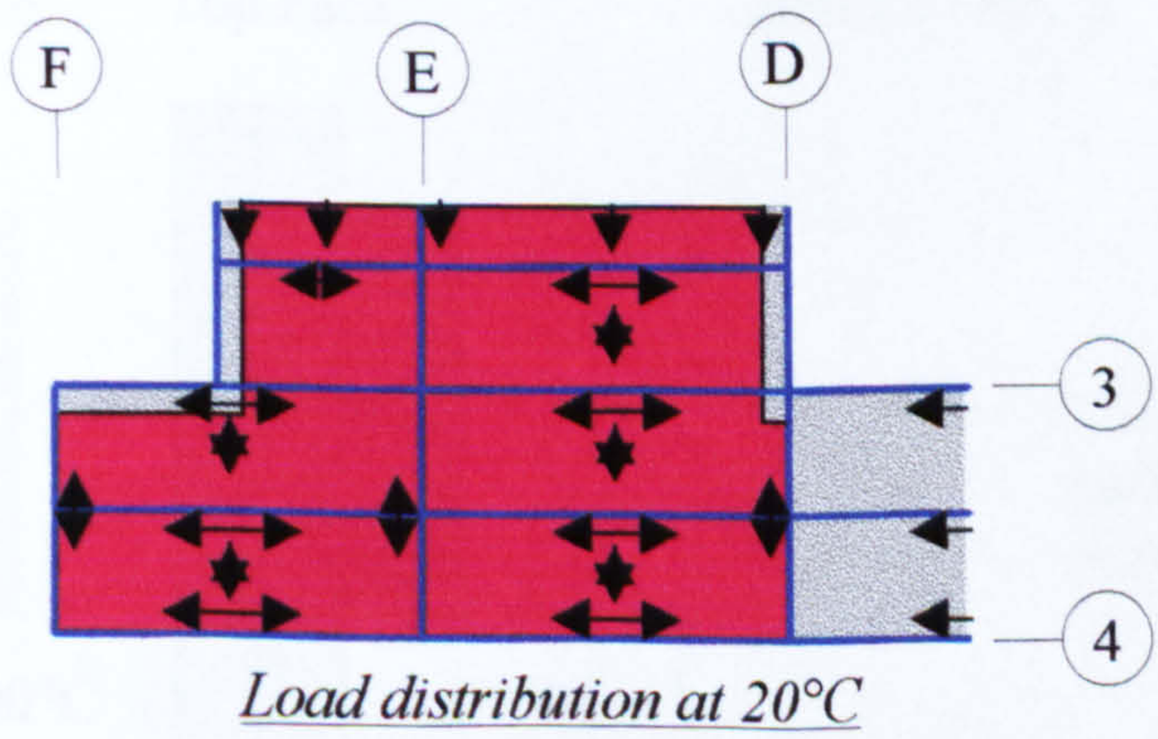

Load distribution at 20°C

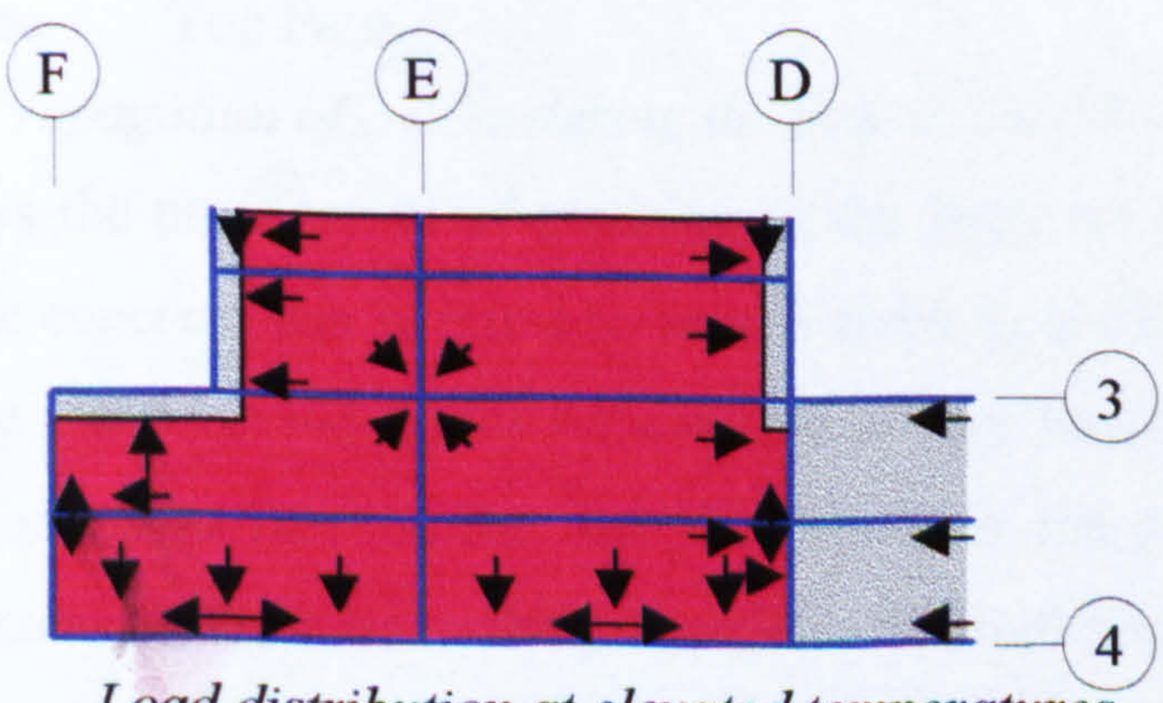

Load distribution at elevated temperatures

Figure 6-69. Redistribution of loads in the large compartment test

The load transference within the large compartment test at elevated temperatures is relatively complicated, as the loss of strength and stiffness of the steel beams requires the concrete slab to hang catenary fashion between the structure outside the fire compartment, the columns and the cooler edge beams.

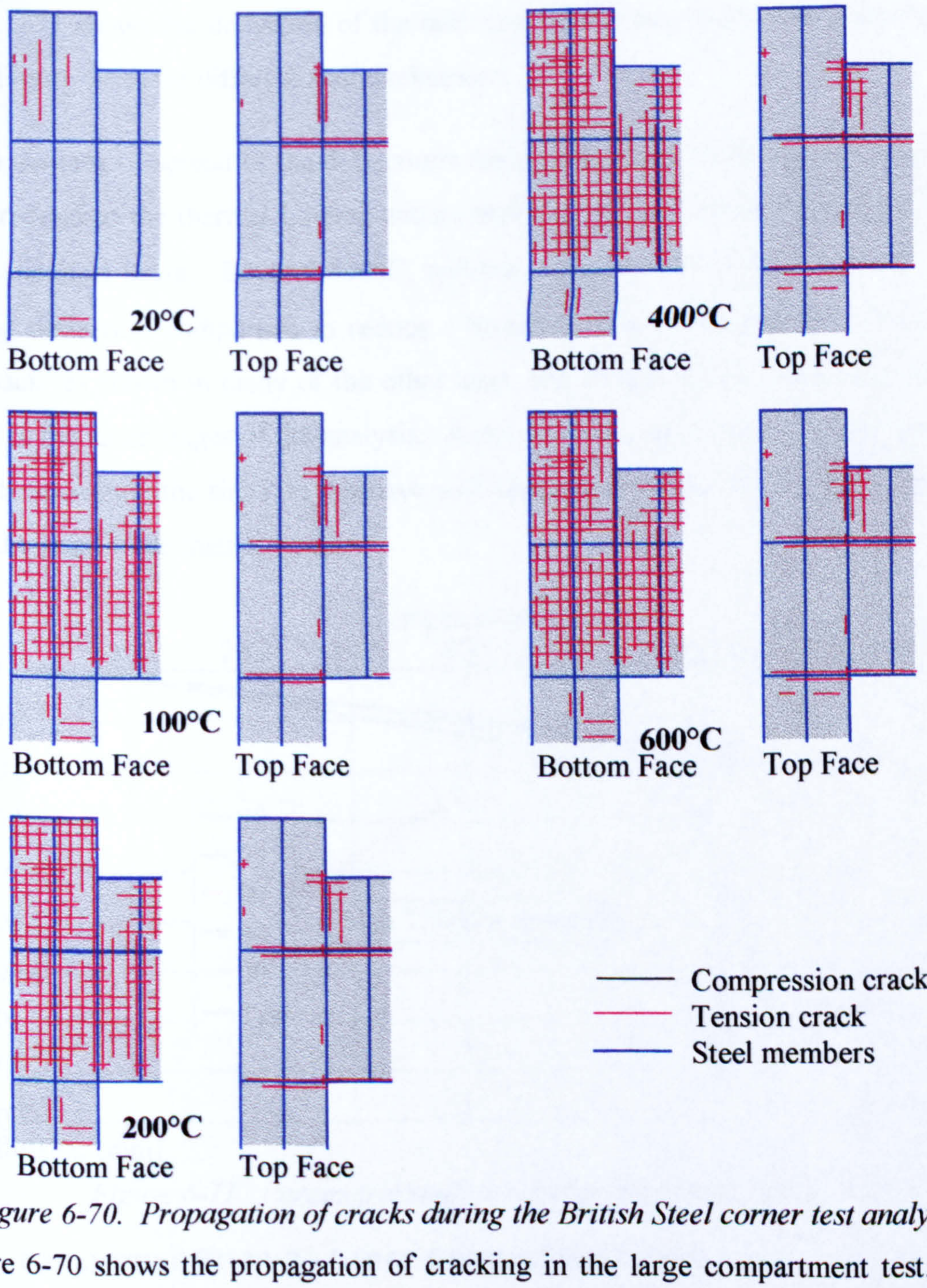

Figure 6-70. Propagation of cracks during the British Steel corner test analyses

Figure 6-70 shows the propagation of cracking in the large compartment test. The bottom face of the concrete slab is prone to tensile cracking during the initial 100°C, particularly where the floor slab spans between secondary beams. The majority of these cracks are small surface cracks that do not reach the reinforcement mesh. Irregularities in cracking occur along the perimeter of the building, due to the support

of the windposts from the floor above and around some of the columns where the concrete floor slab takes on a synclastic curvature.

6.7.1 PARAMETRIC STUDY 1 - LARGE COMPARTMENT TEST

Figure 6-71 shows the deflection of the mid-span of the secondary beam denoted as V7 in Figure 6-64, for different slab thicknesses.

Due to the lack of spread of the deflections during the initial 500°C, deflections may be accredited to the thermal bowing action produced by the temperature differential across the steel beam. Beyond 500°C, softening of the steel beam causes the P-Δ bending deflection component to reduce. However, this case does not exhibit the 'pull-back' as shown in many of the other tests, and neither does it have a spread of results in the latter stages of the analysis. Apart from the edge beams, which are at a lower temperature, the slabs do not have stiff supports between which they can span when the beams lose their strength.

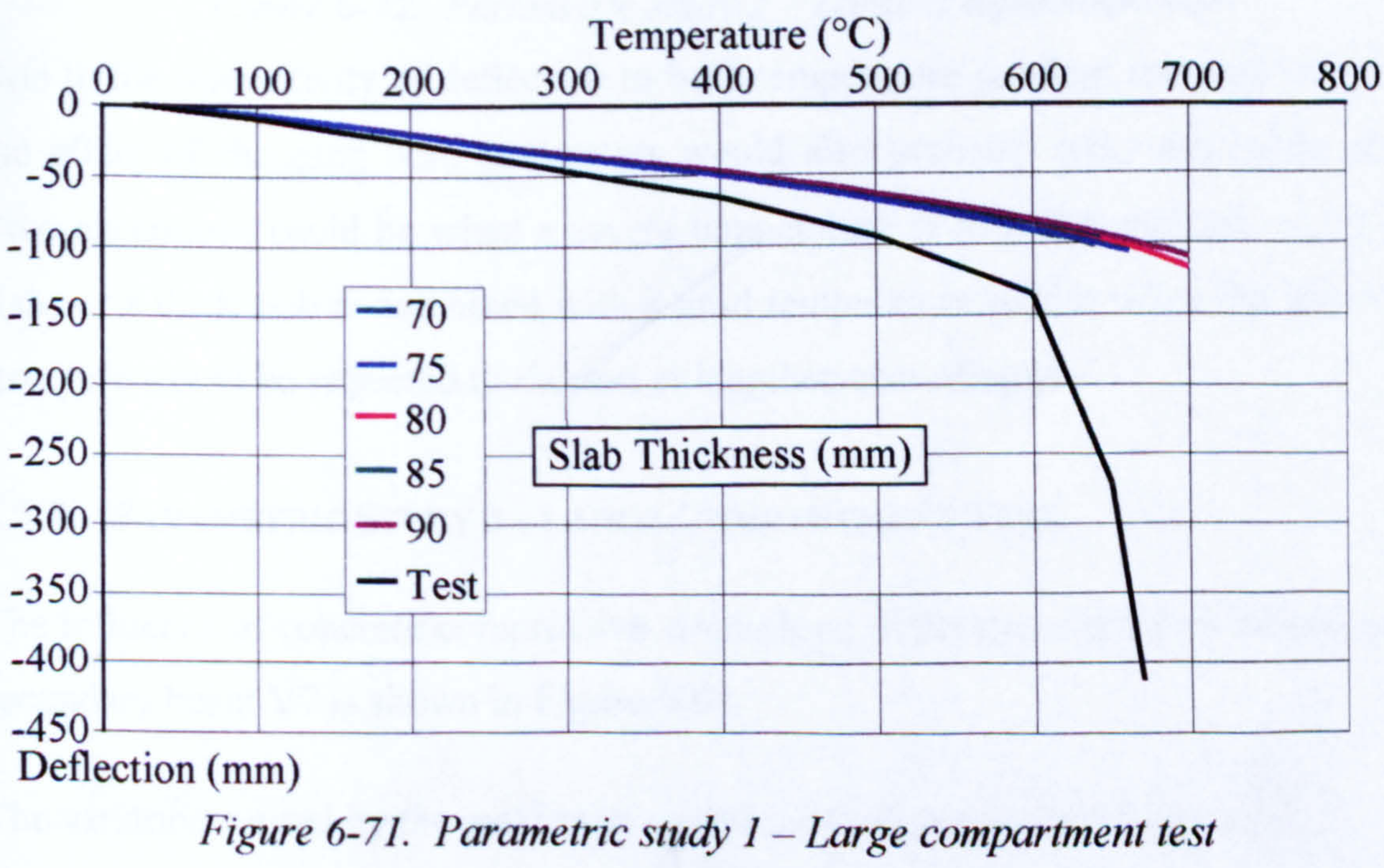

Figure 6-71. Parametric study 1 – Large compartment test

6.7.2 PARAMETRIC STUDY 2 - LARGE COMPARTMENT TEST

Figure 6-72 shows the influence of the slab temperature gradient on the mid-span deflection of the secondary beam.

Over the initial 500°C, the influence of the slab temperature gradient does appear to affect the deflection V7, although not greatly. This indicates that initial deflections

are caused by thermal bowing due to a temperature differential across the steel beam. Beyond this temperature the parameter does significantly affect the deflection, indicating that thermal bowing and/or weakening of the concrete is occurring at this stage.

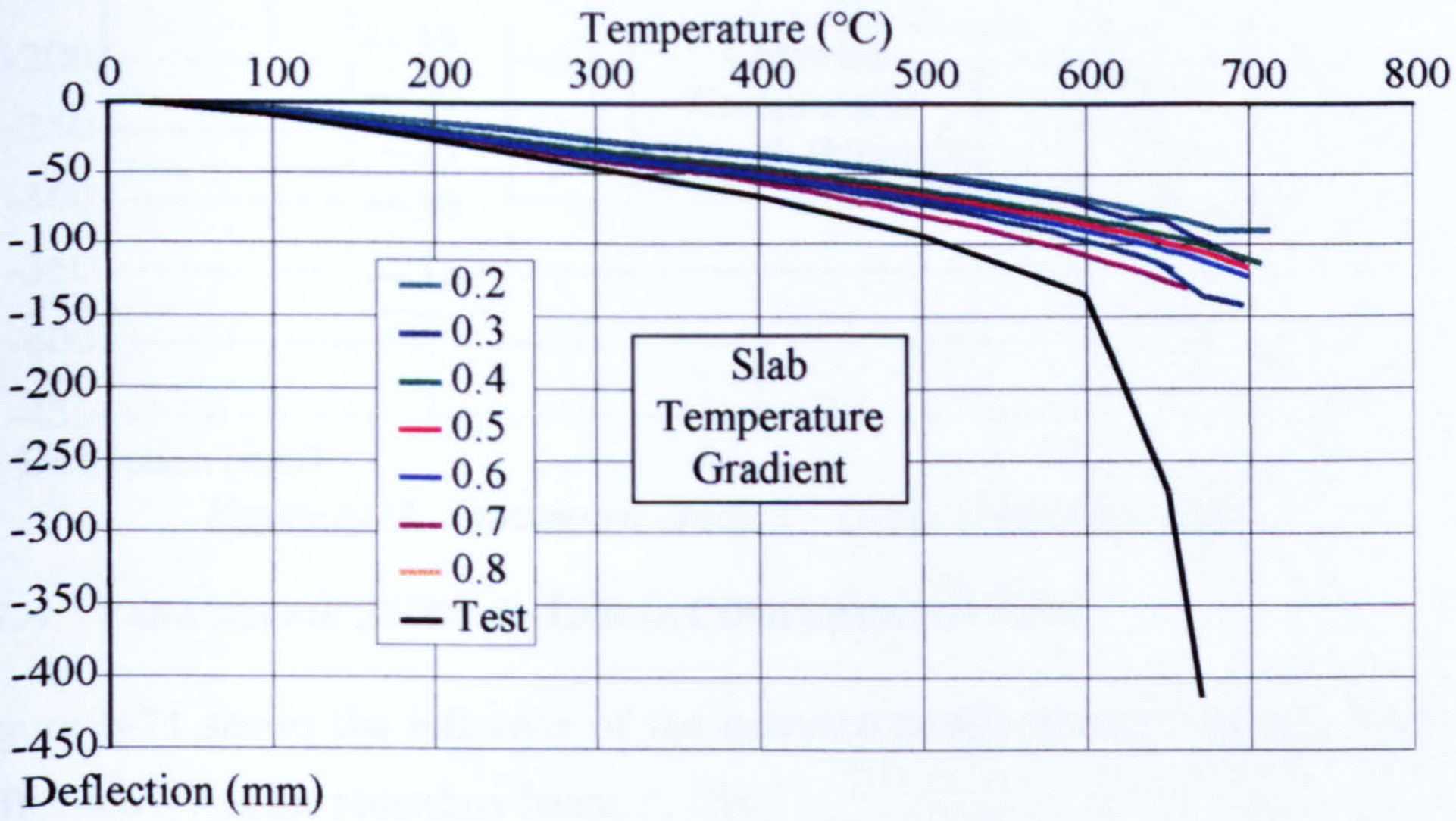

Figure 6-72. Parametric study 2 – Large compartment test

Due to the insensitivity of deflection to both temperature gradient and slab thickness, the effect of changing both parameters would also probably have negligible effect. Two exceptions could be when a severe temperature profile is combined with a thin slab, or a thick slab is combined with a mild temperature profile when the life of the structure would be expected to shorten or lengthen accordingly.

6.7.3 Parametric Study 3 - Large Compartment Test

The influence of concrete compressive strength on deflections of the mid-span of the secondary beam V7 is shown in Figure 6-64.

The variation caused by the maximum compressive stress appears to be small.

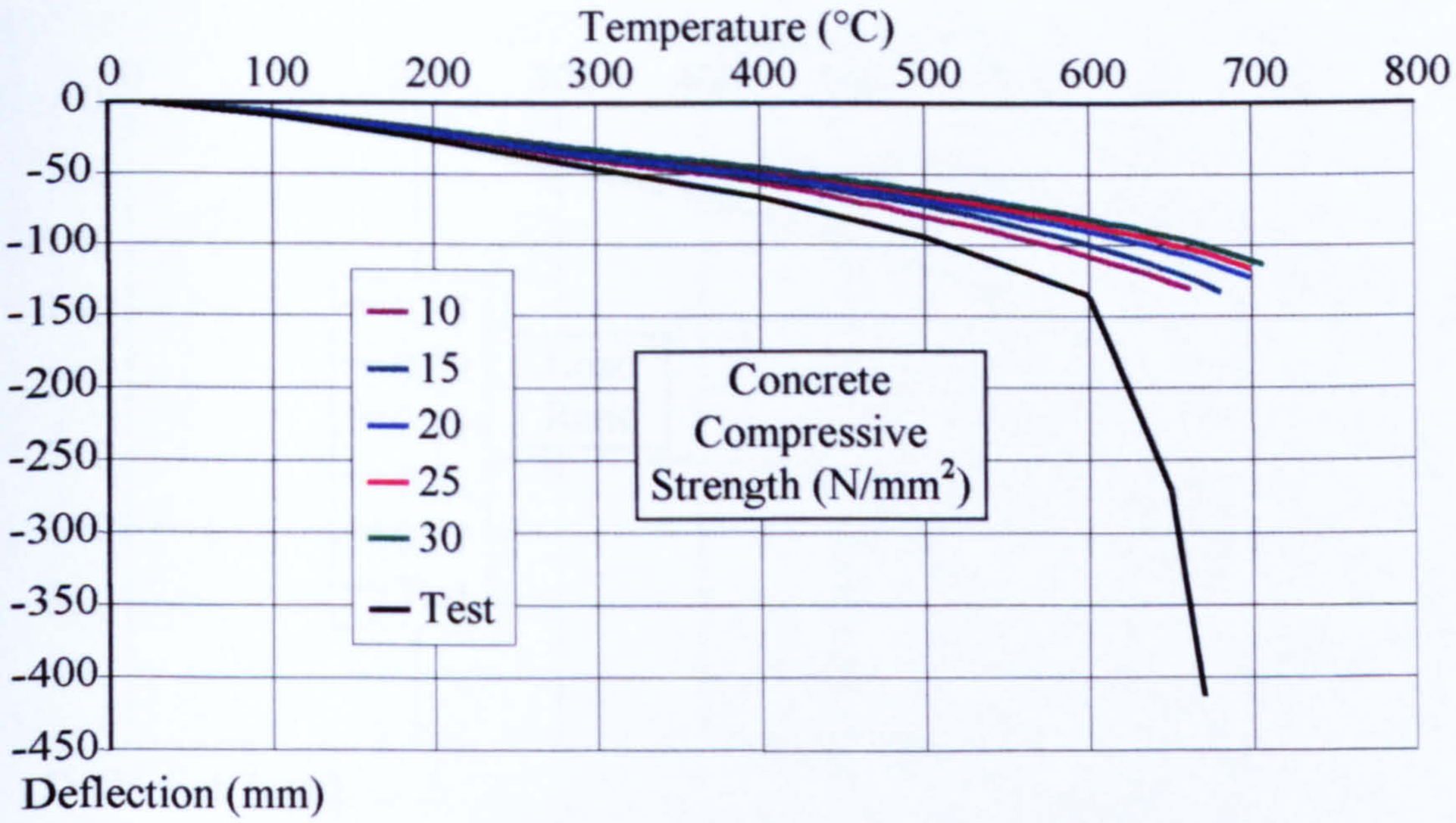

Figure 6-73. Parametric study 3 – Large compartment test

6.7.4 PARAMETRIC STUDY 4 - LARGE COMPARTMENT TEST

Figure 6-74 shows the influence of the concrete tensile strength on the mid-span deflection V7 of the secondary beam.

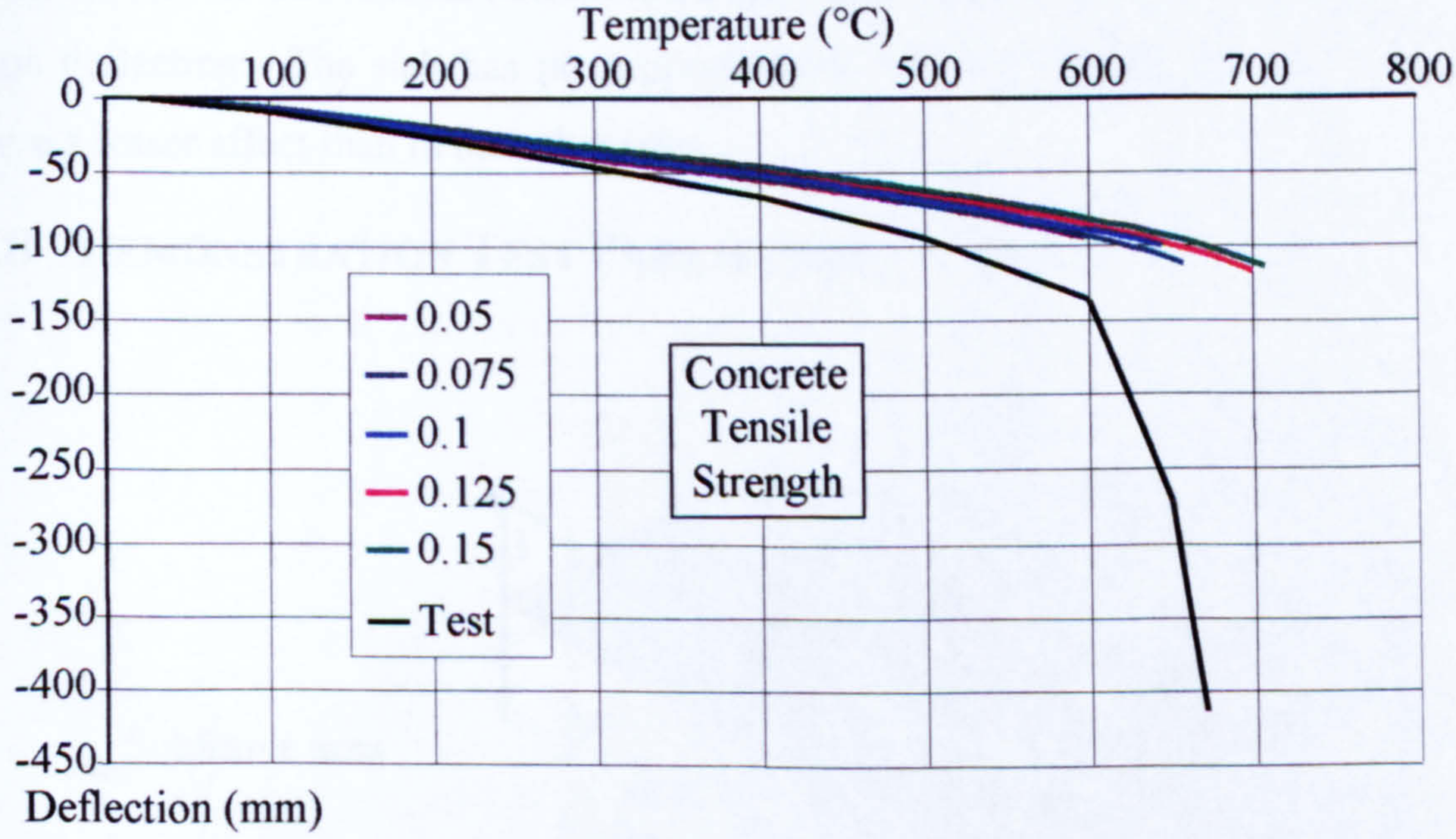

Figure 6-74. Parametric study 4 – Large compartment test

The variation of deflection due to the maximum tensile stress is deemed to be negligible.

6.7.5 PARAMETRIC STUDY 5 - LARGE COMPARTMENT TEST

The influence of load ratio has been investigated on deflection V7 at the mid-span of the secondary beam, and is shown in Figure 6-75.

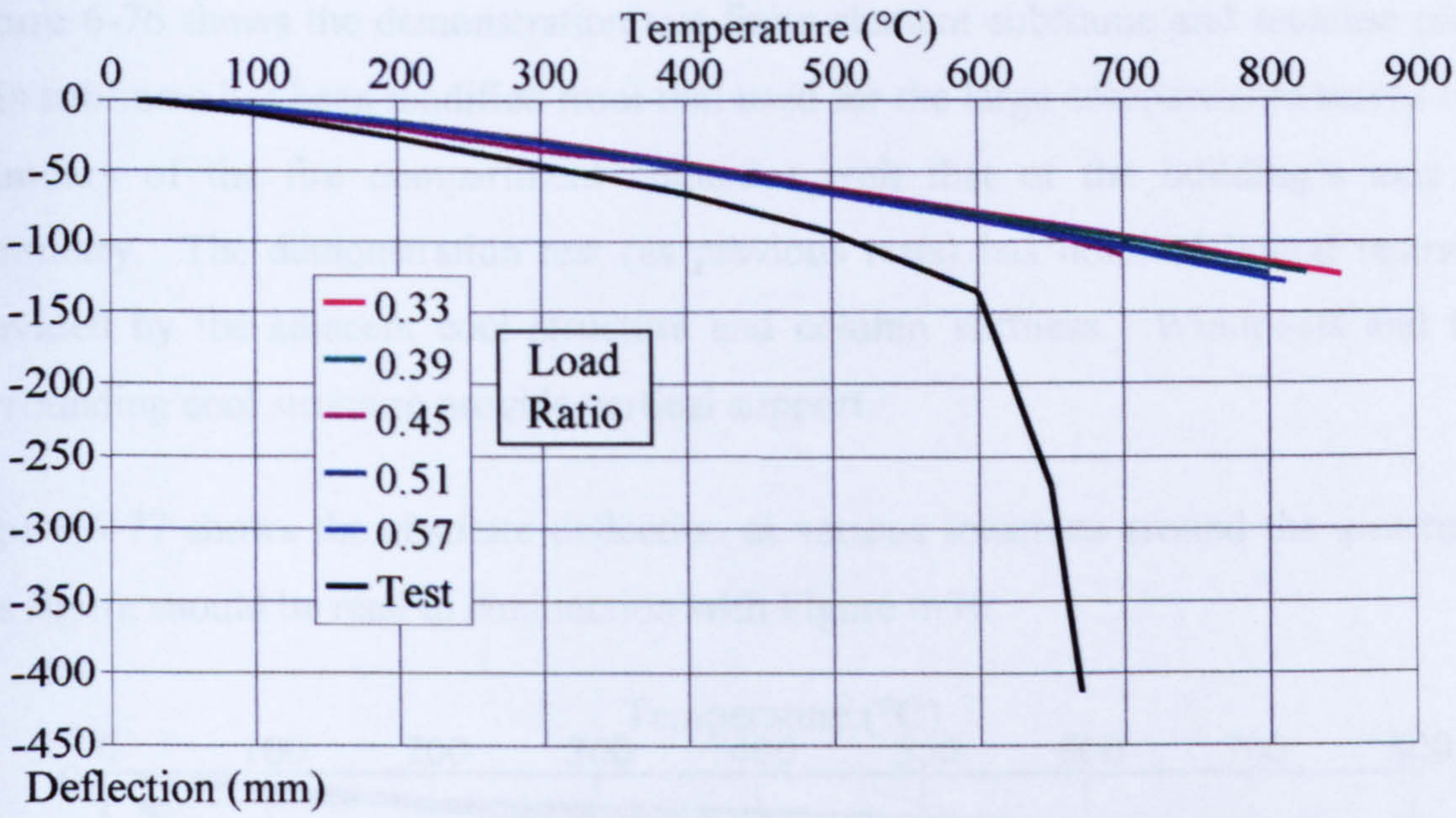

Figure 6-75. Parametric study 5 – Large compartment test

The resultant variation that is found in the load ratio parametric study is considered to be negligible.

The relative insensitivity of all five parametric studies within this test may be attributed to the steel beams (except the edge beams) losing strength and stiffness and thus deflecting. The slab has no supports from which to bridge and will therefore have a lesser effect than in the other tests.

6.8 Demonstration Test Parametric Studies

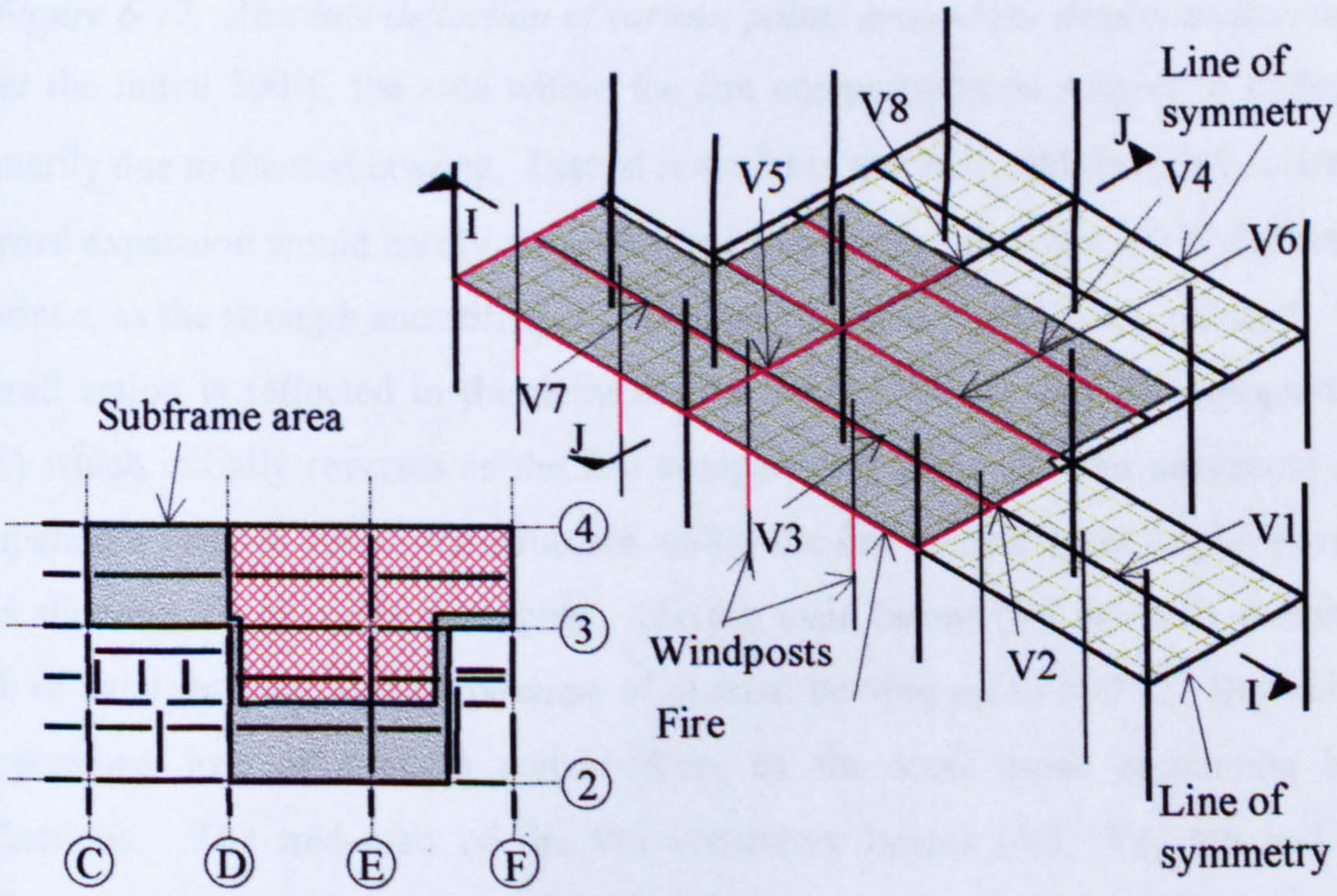

Figure 6-76. Location and finite element mesh of the demonstration test.

Figure 6-76 shows the demonstration test finite element subframe and location plan. This subframe has been modified from that used for the large compartment test as one boundary of the fire compartment coincides with that of the building's axis of symmetry. The demonstration test (as previous tests) has nominal lateral restraint provided by the adjacent cool structure and column stiffness. Windposts and the surrounding cool structure provide vertical support.

Figure 6-77 shows the absolute deflection at various locations around the structure; this figure should be read in conjunction with Figure 6-76.

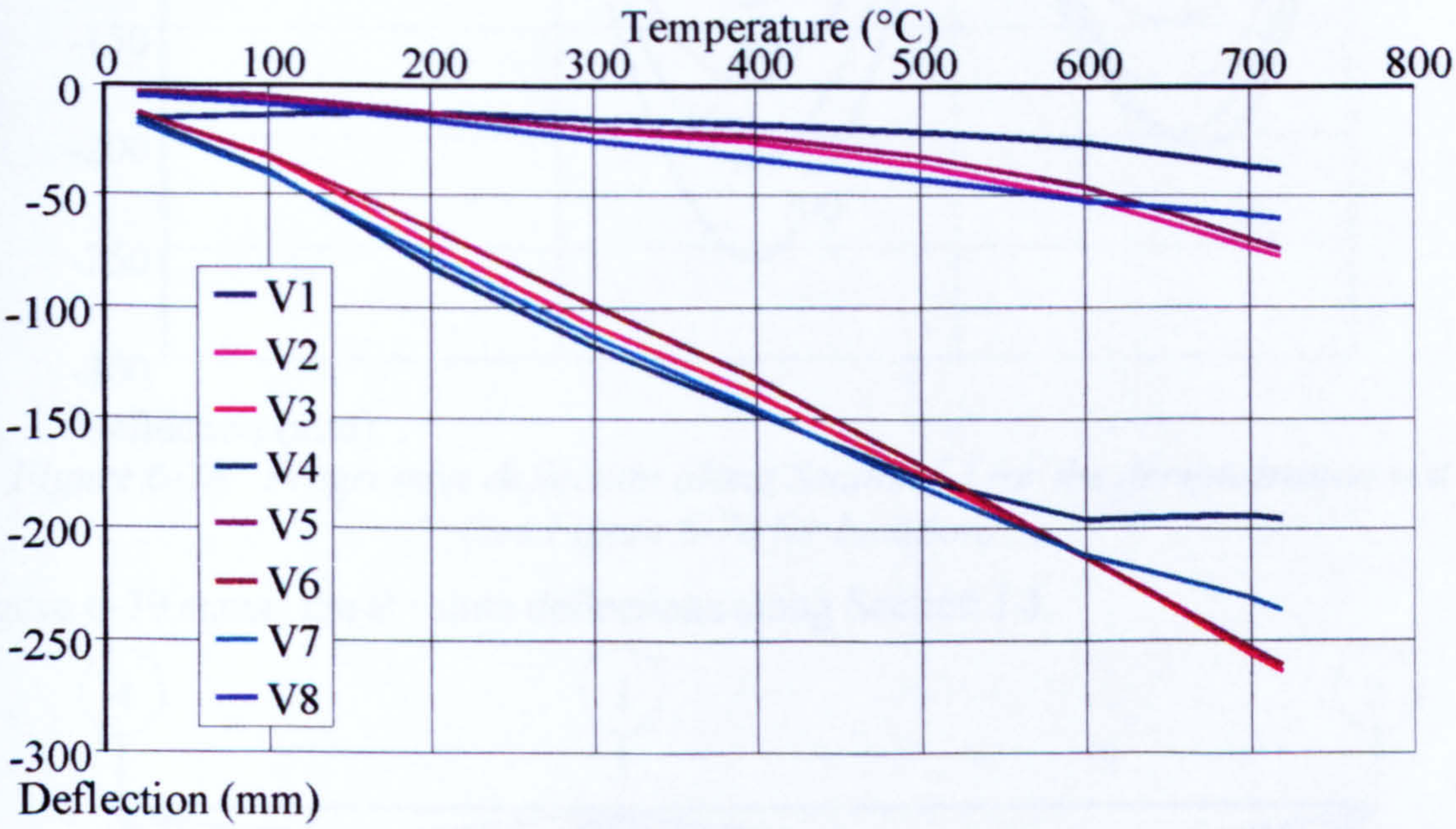

Figure 6-77. Absolute deflection of various points around the demonstration test

Over the initial 500°C the area within the fire compartment is subject to deflection primarily due to thermal bowing. Lateral restraint is nominal, and therefore restrained thermal expansion would hardly cause the structure to sag. Beyond 500°C deflections continue, as the strength and stiffness of the steel beam is significantly reduced. This overall action is reflected in the deflection measured outside the fire compartment (V1) which initially reverses as the fire compartment sags. As the maximum steel temperature reaches 500°C the structure within the fire compartment begins to relax, thus allowing V1 to revert to sagging. The 6m main beams (V2 and V5), due to the lack of axial restraint, deflect because of thermal bowing up to 500°C. Beyond this temperature, loss of strength and stiffness of the steel cause continuing beam deflections. The mid-span of the 9m secondary beams (V3, V4, V6 and V7) deflection according to a similar scheme. It is interesting to note the movement at V4 above 600°C, when the deflections attempt to reverse. This is possibly caused by the

restraint provided by the bending stiffness of the floor slab spanning across from the cooler sections of the structure. A series of absolute deflection profiles along Section I-I is shown in Figure 6-78.

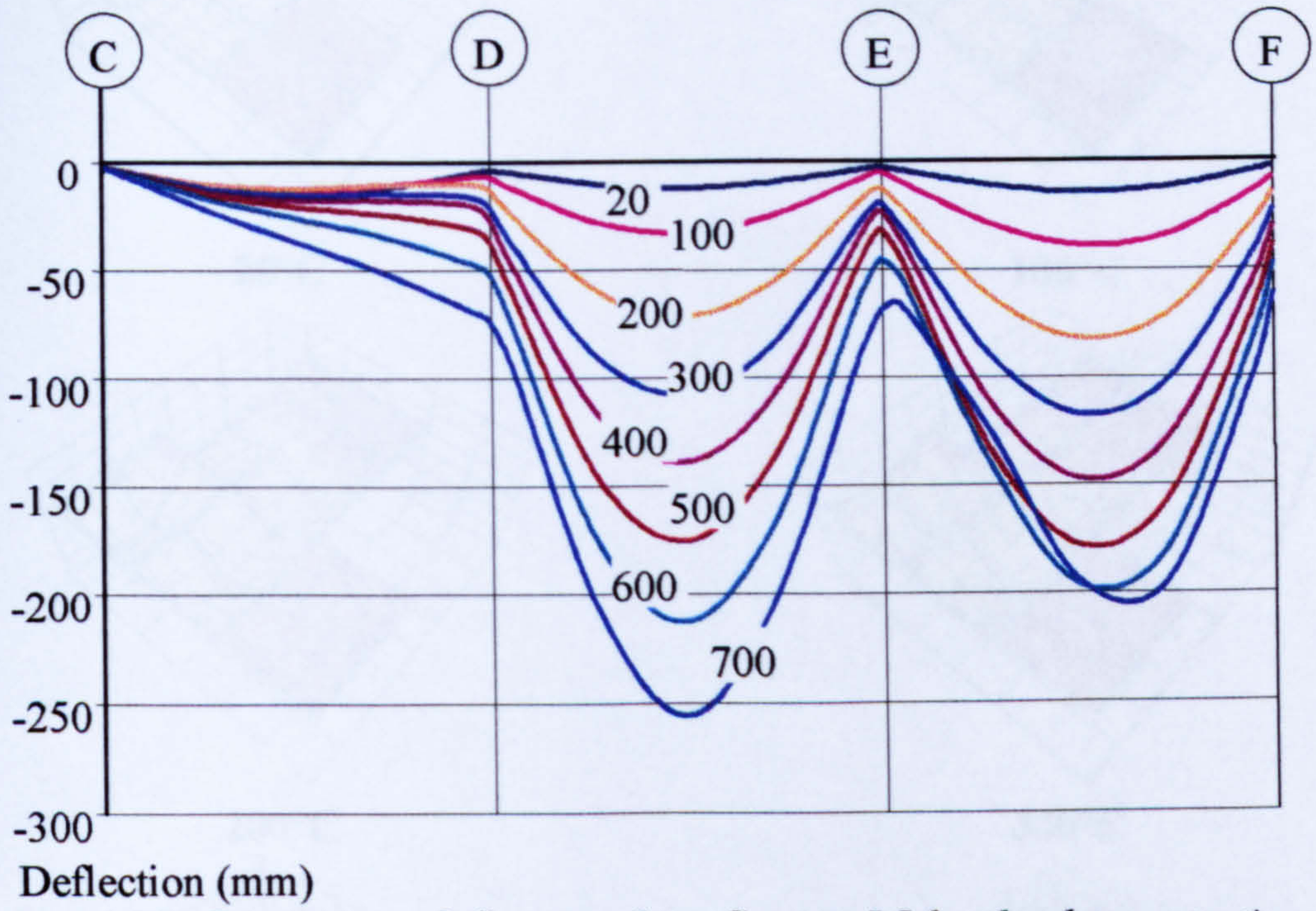

Figure 6-78. Progressive deflection along Section I-I for the demonstration test (see Figure 6-76 for location)

Figure 6-79 shows the absolute deflections along Section J-J.

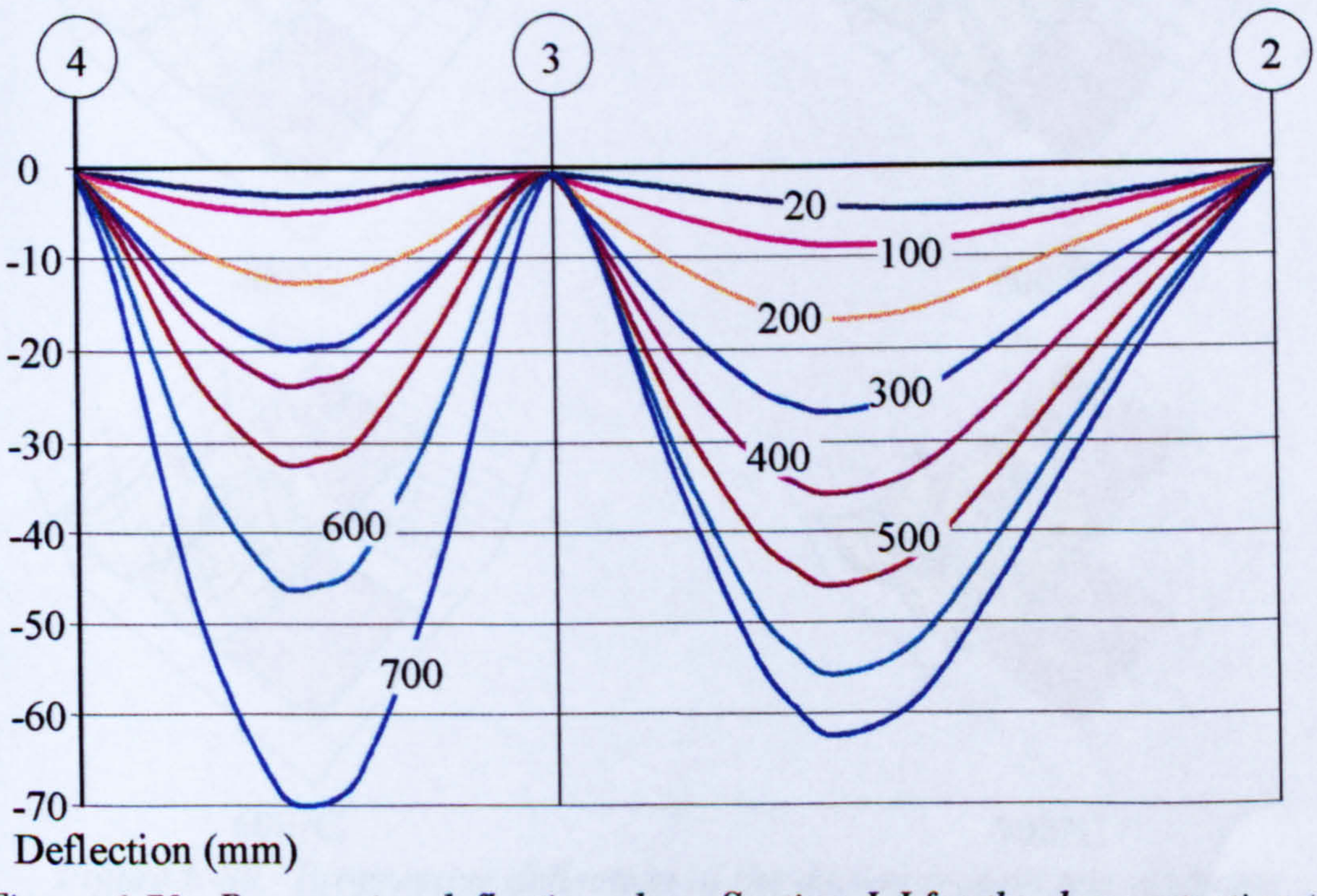

Figure 6-79. Progressive deflection along Section J-J for the demonstration test (see Figure 6-76 for location)

The absolute deflection profiles of the whole structure at increasing steel temperatures are shown in Figure 6-80.

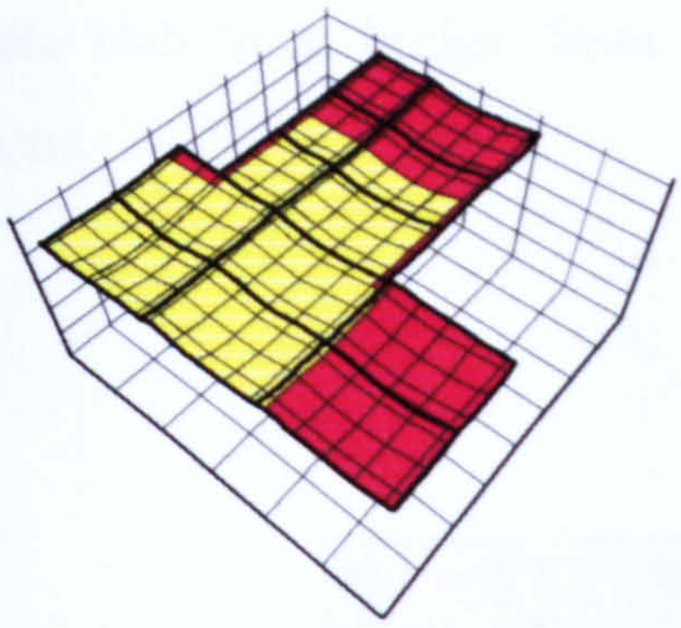

20°C

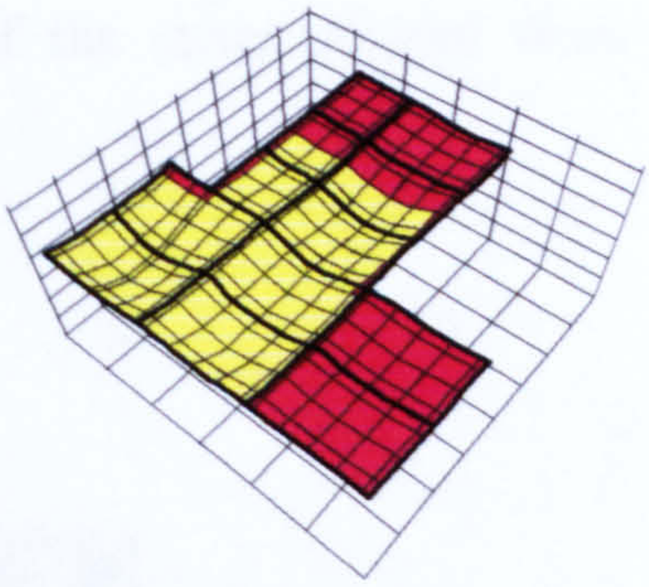

100°C

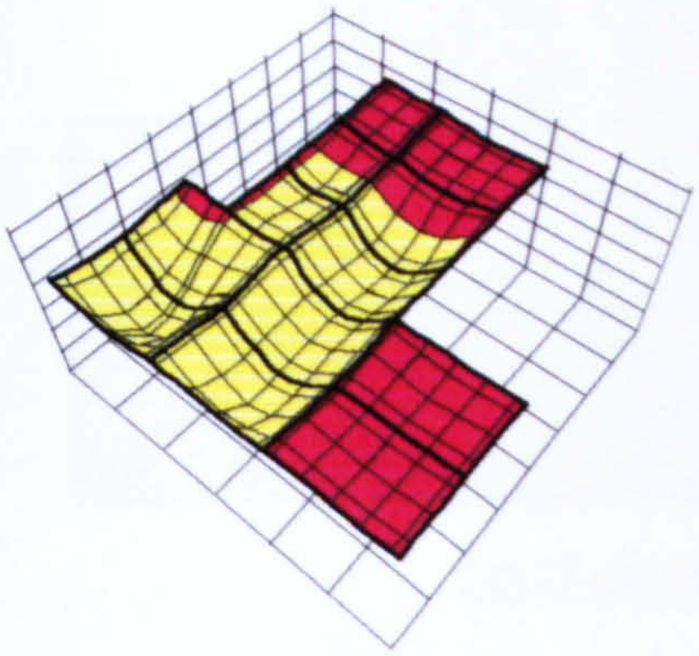

200°C

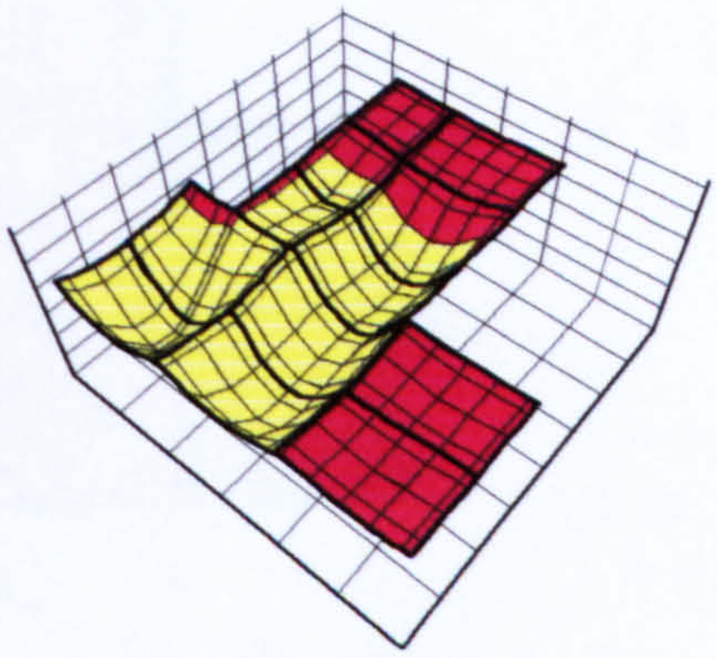

300°C

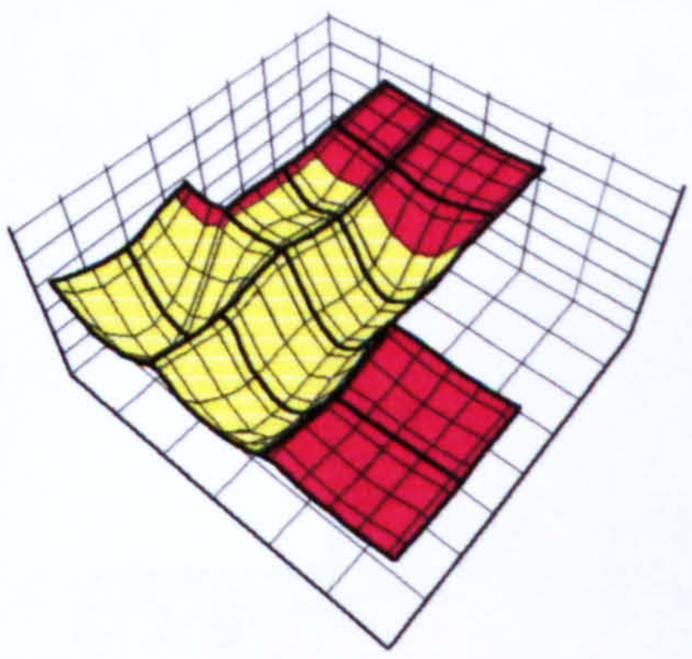

400°C

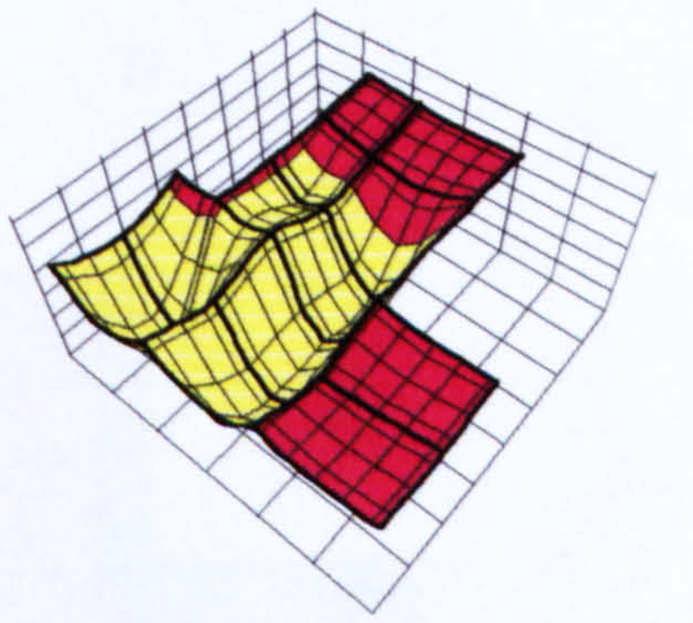

500°C

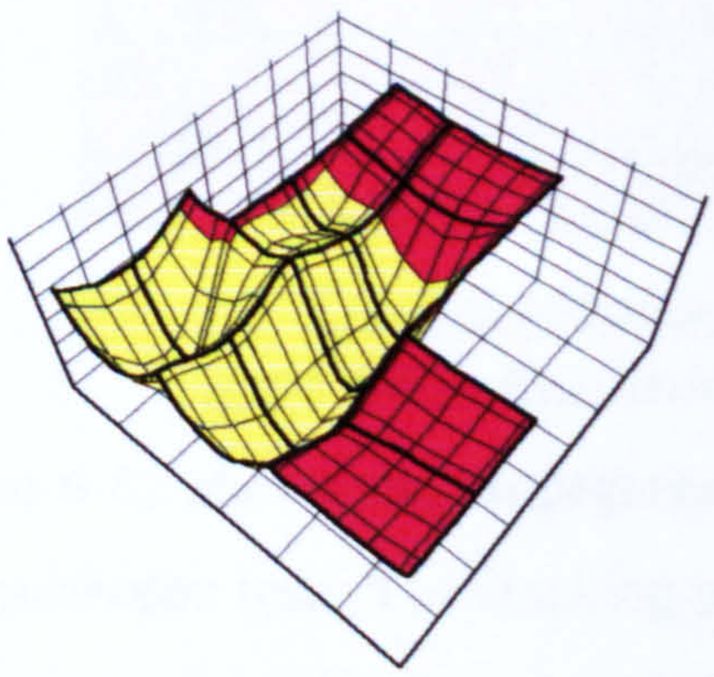

600°C

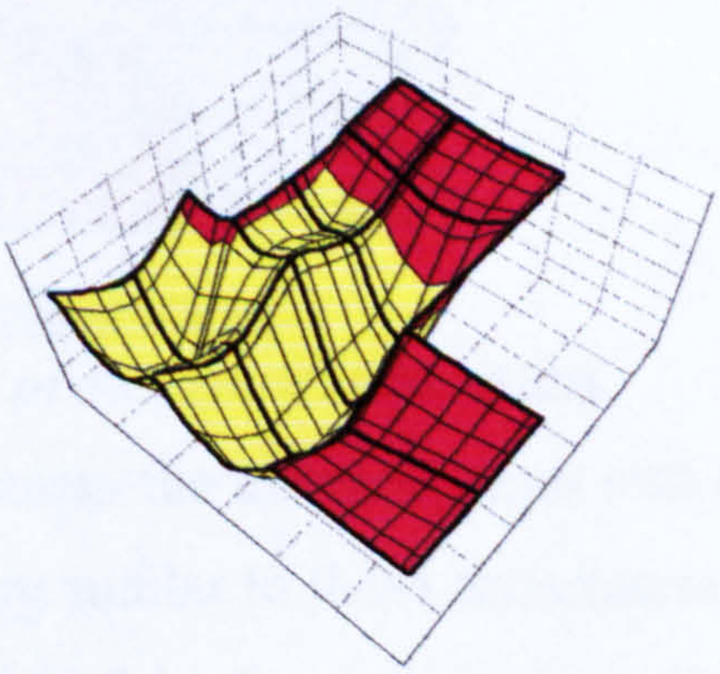

700°C

Figure 6-80. Progressive deflection of the demonstration test subframe

As the structure deflects, the load paths will change through the structure. Figure 6-81 shows the load paths at the extremes of temperature, the first at ambient temperatures and the second at a temperature (725°C) such that the strength and stiffness of the steel beams within the fire compartment are negligible. Hence the

concrete slab must bridge from cool sections of the structure and from column junctions.

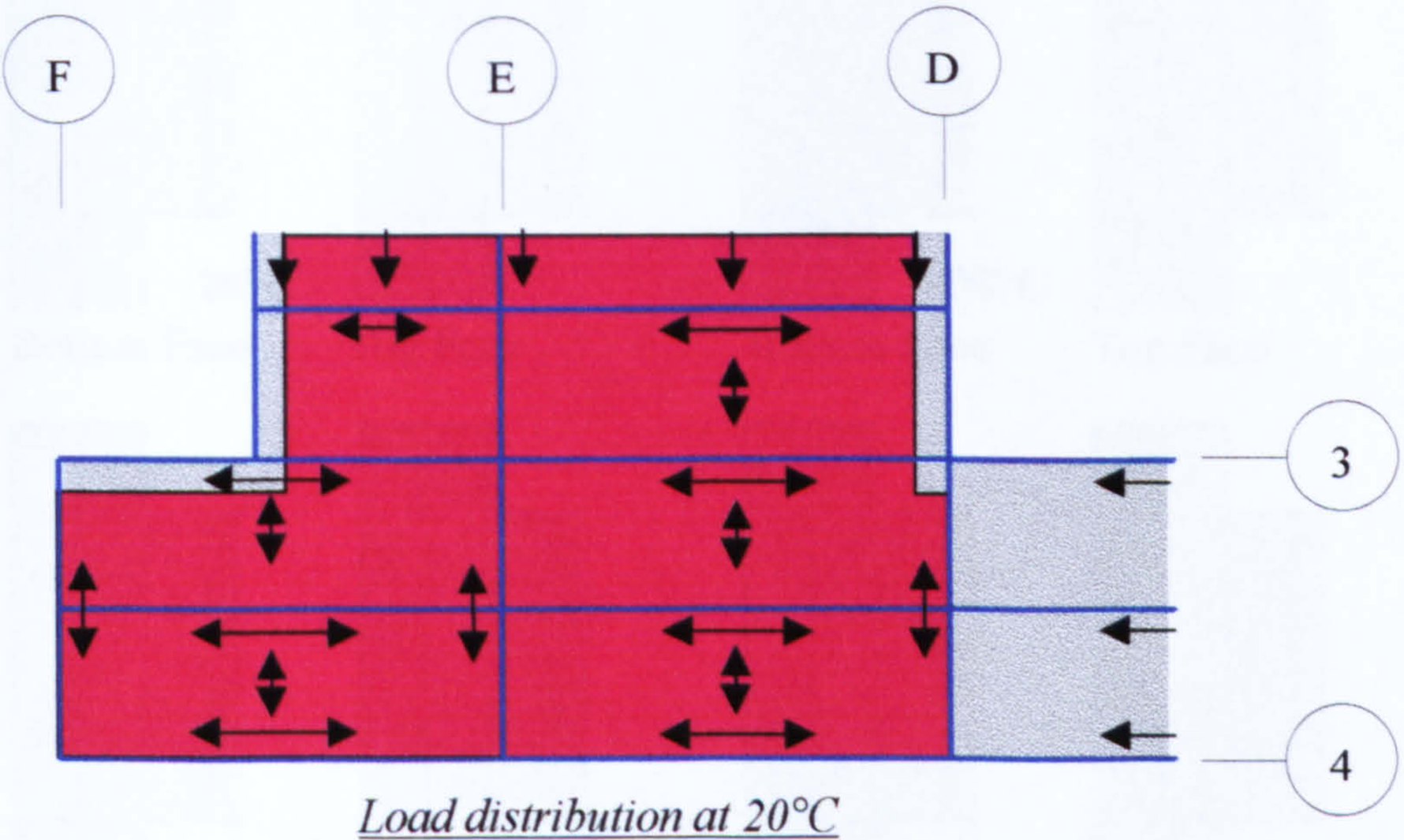

Load distribution at 20°C

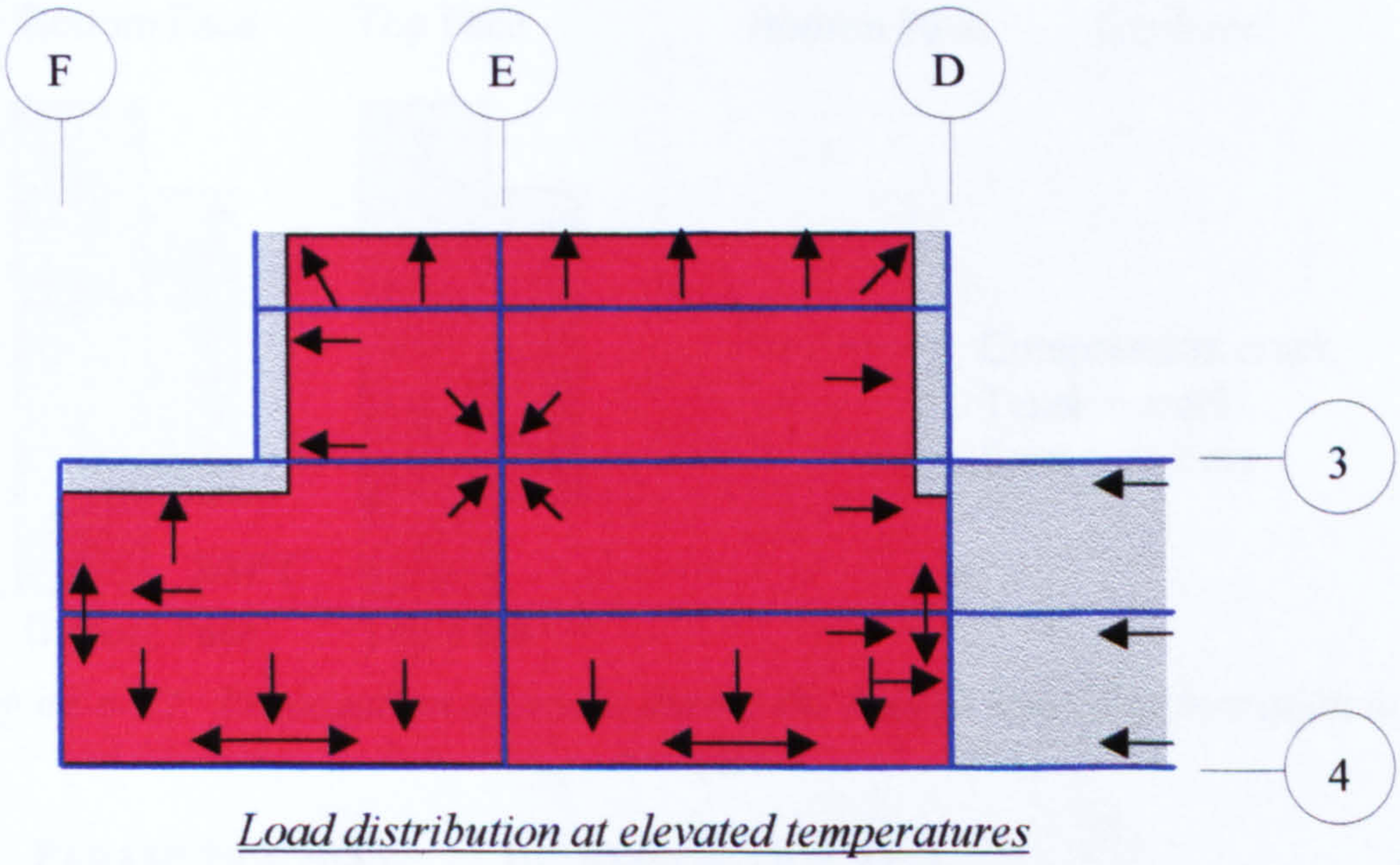

Load distribution at elevated temperatures

Figure 6-81. Redistribution of loads in the demonstration test

Figure 6-82 shows the propagation of cracks across the concrete floor slab for the demonstration test. The cracking patterns are very similar to those experienced in the large compartment test, except that along the edge of the fire compartment (half-way between gridlines 2 and 3) the upper face has tension cracks due to the slab hogging across the boundary line.

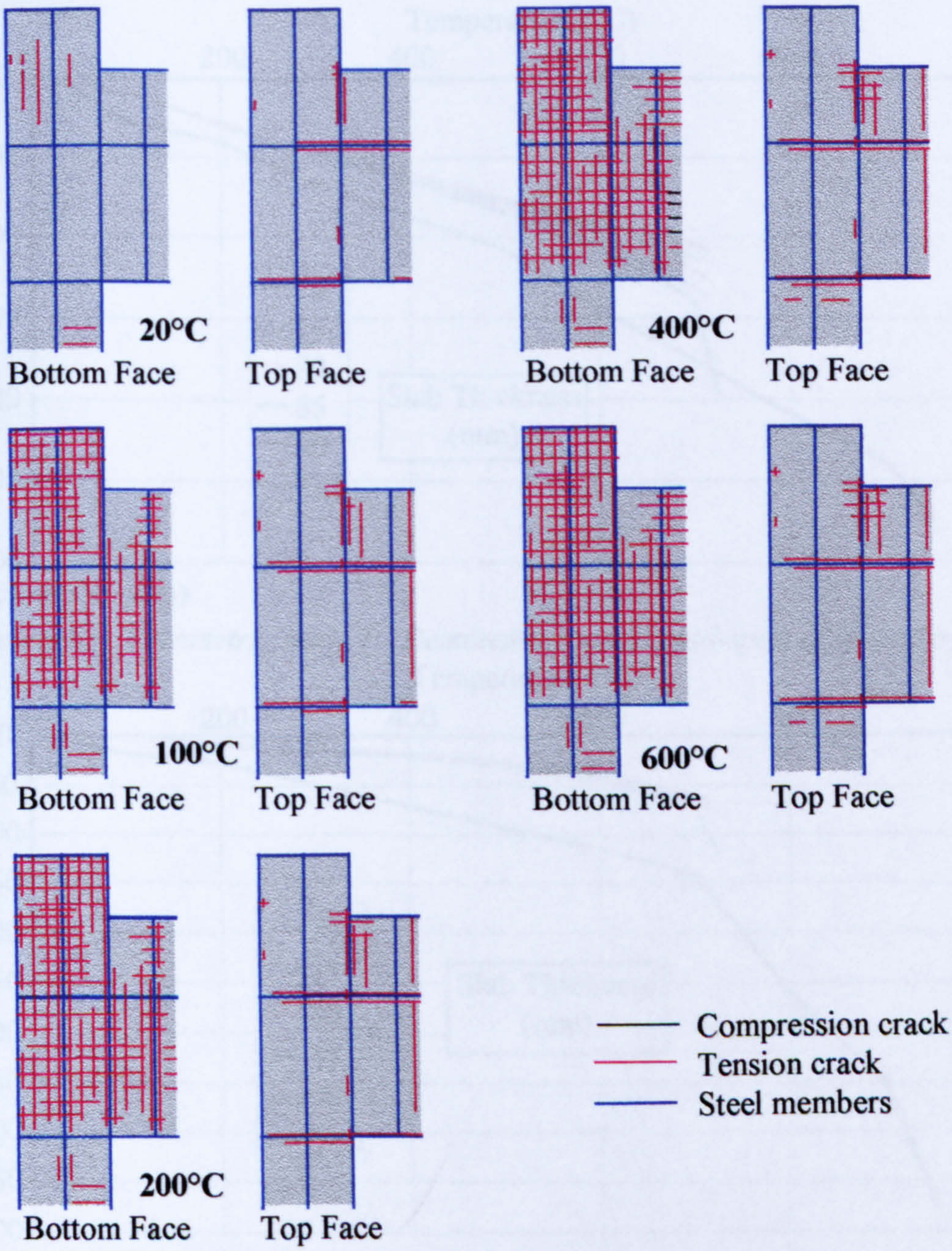

Figure 6-82. Propagation of cracks during the British Steel demonstration test analyses

6.8.1 PARAMETRIC STUDY 1 - DEMONSTRATION TEST

Figures 6-83 and 6-84 show deflections at the mid-span of the secondary beam (V6 on Figure 6-76) and the 6m main beam (V5 on Figure 6-76). The variation between deflections for changes in slab thickness for the 6m main beam is negligible, but for the 9m secondary beam a small variation is observed. This lack of variation in the parametric study is probably attributable to the supporting beams losing strength and stiffness and deflecting at an approximately equal rate, in similar fashion to the large compartment test.

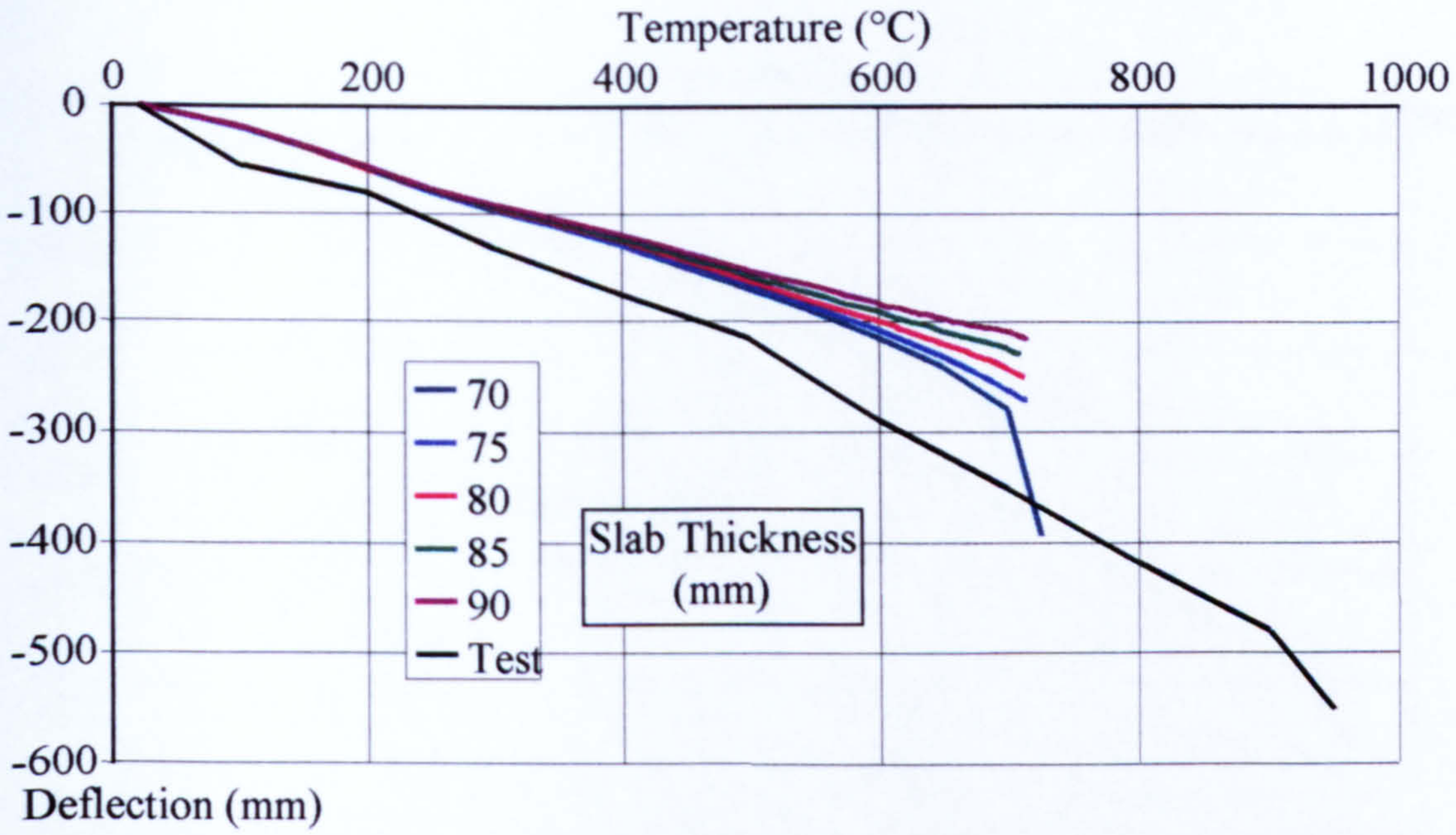

Figure 6-83. Parametric study 1 - Demonstration test, mid-span of secondary beam

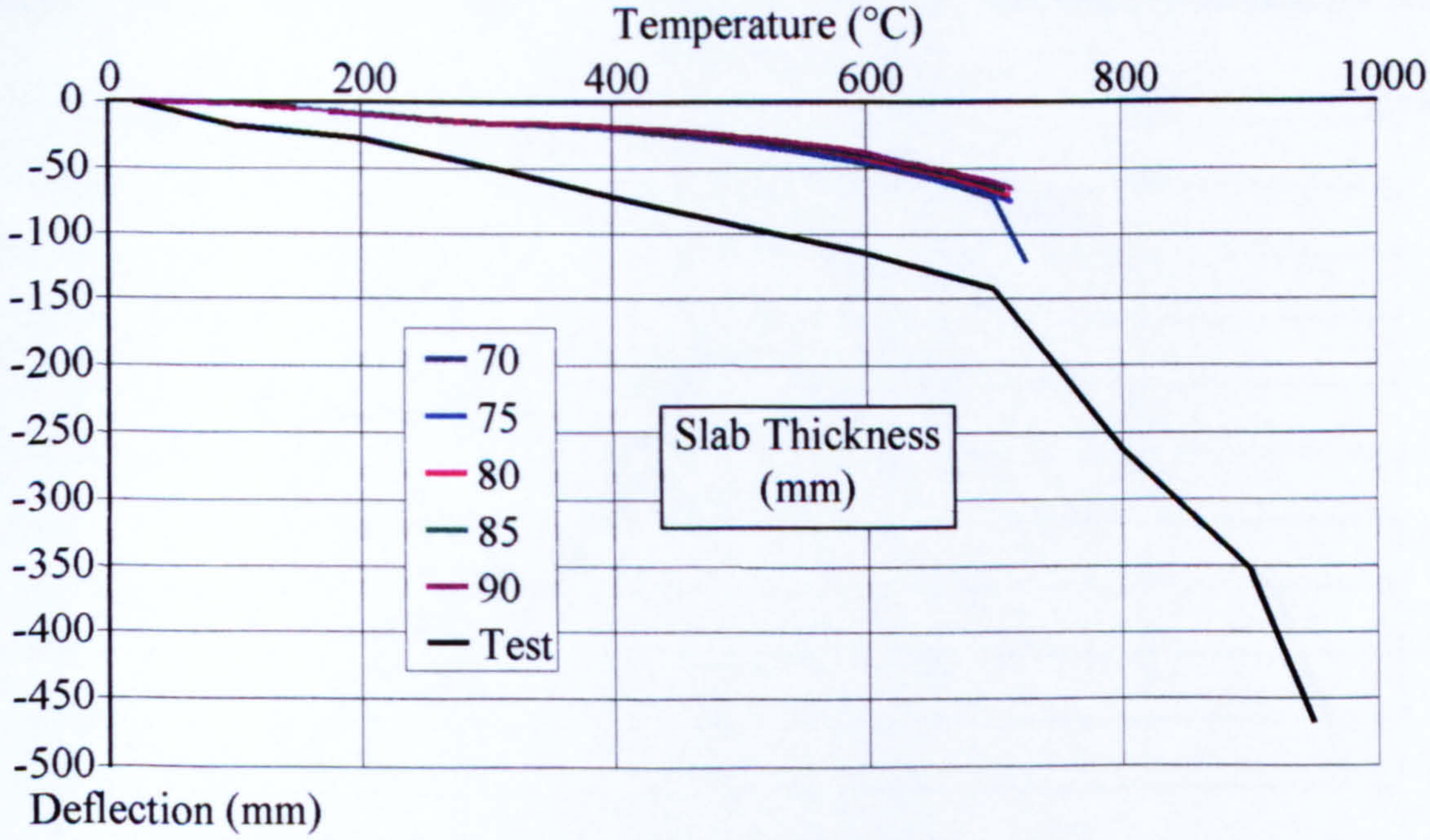

Figure 6-84. Parametric study 1 - Demonstration test, mid-span of 6m main beam

6.8.2 PARAMETRIC STUDY 2 - DEMONSTRATION TEST

The influence of the variation of the temperature gradient through the slab on the mid-span deflection of the secondary beam and the 6m main beam are shown in Figures 6-85 and 6-86. The variation in both cases is almost negligible up to a steel maximum temperature of 500°C. Therefore, any deflections in this period must be attributable to thermal bowing due to a temperature difference of slab and steel beam. Beyond 500°C the deflections begin to vary, although no obvious pattern is observed.

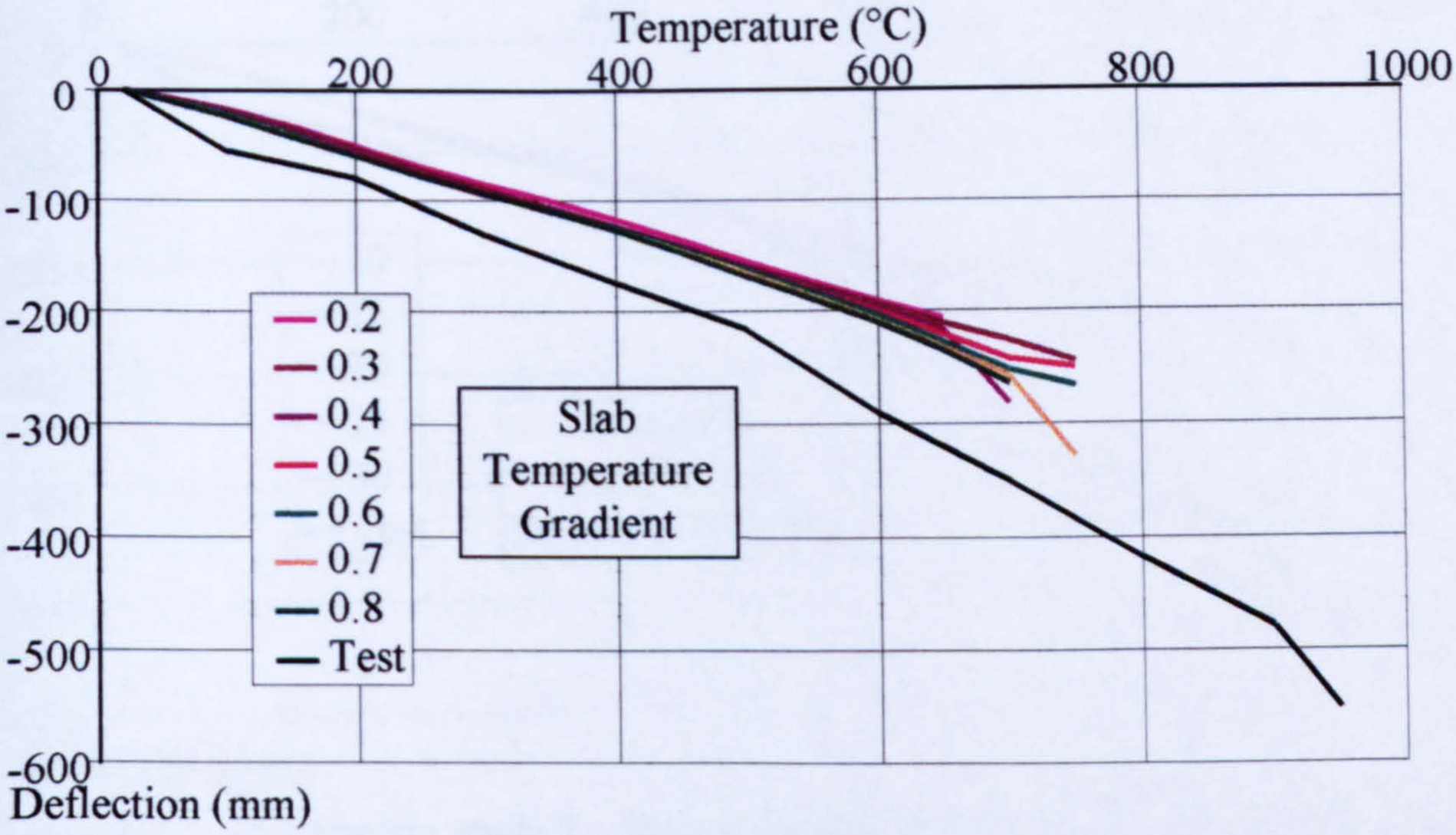

Figure 6-85. Parametric study 2 - Demonstration test, mid-span of secondary beam

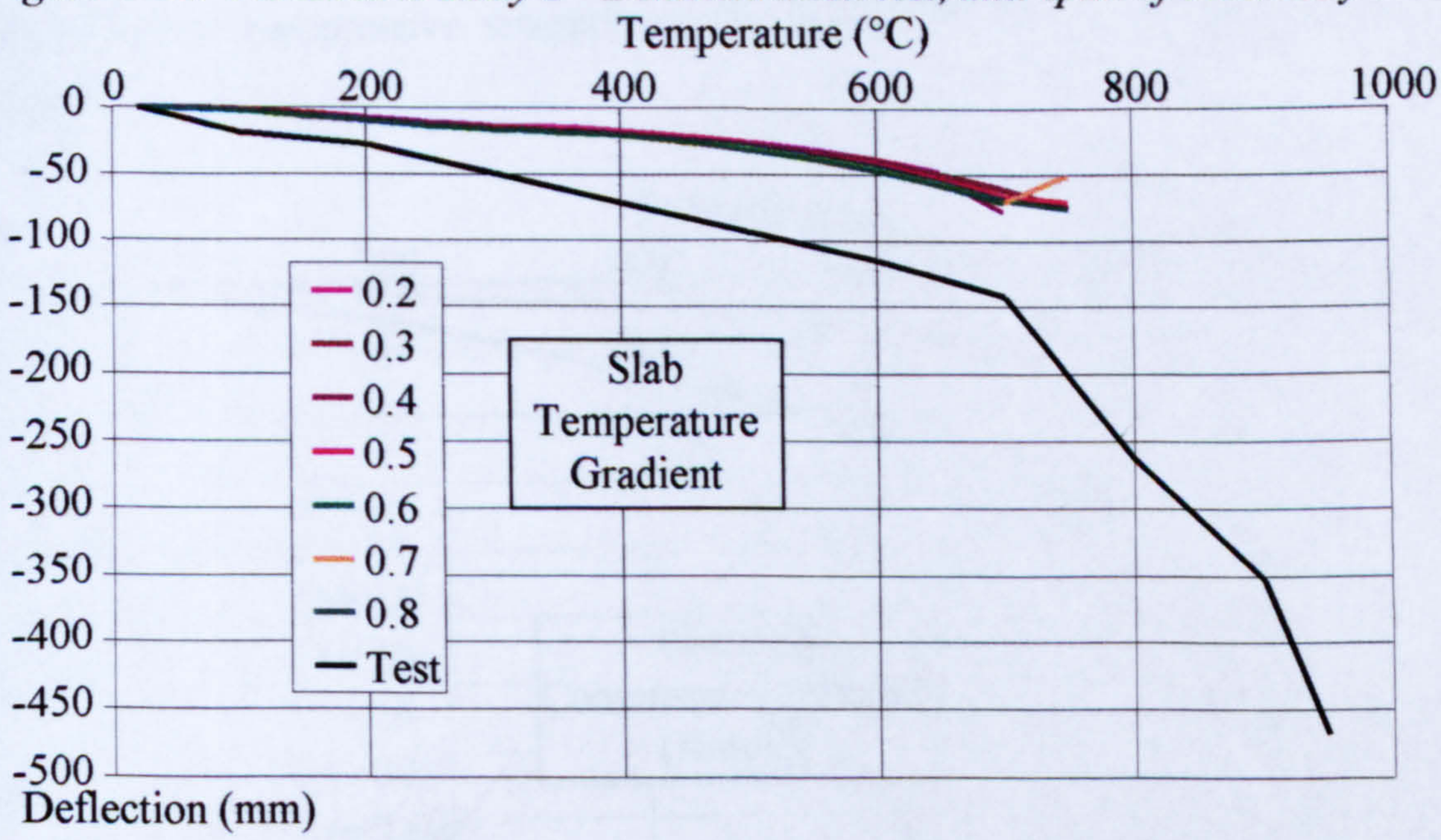

Figure 6-86. Parametric study 2 - Demonstration test, mid-span of 6m main beam

Should the slab thickness parametric study be combined with that of the slab temperature gradient, it might safely be assumed that the effect would be negligible due to the relative insensitivity to both parameters.

6.8.3 PARAMETRIC STUDY 3 - DEMONSTRATION TEST

The influence of the concrete compressive strength on the mid-span deflections of the secondary beam and the 6m main beam are shown in Figures 6-87 and 6-88 respectively.

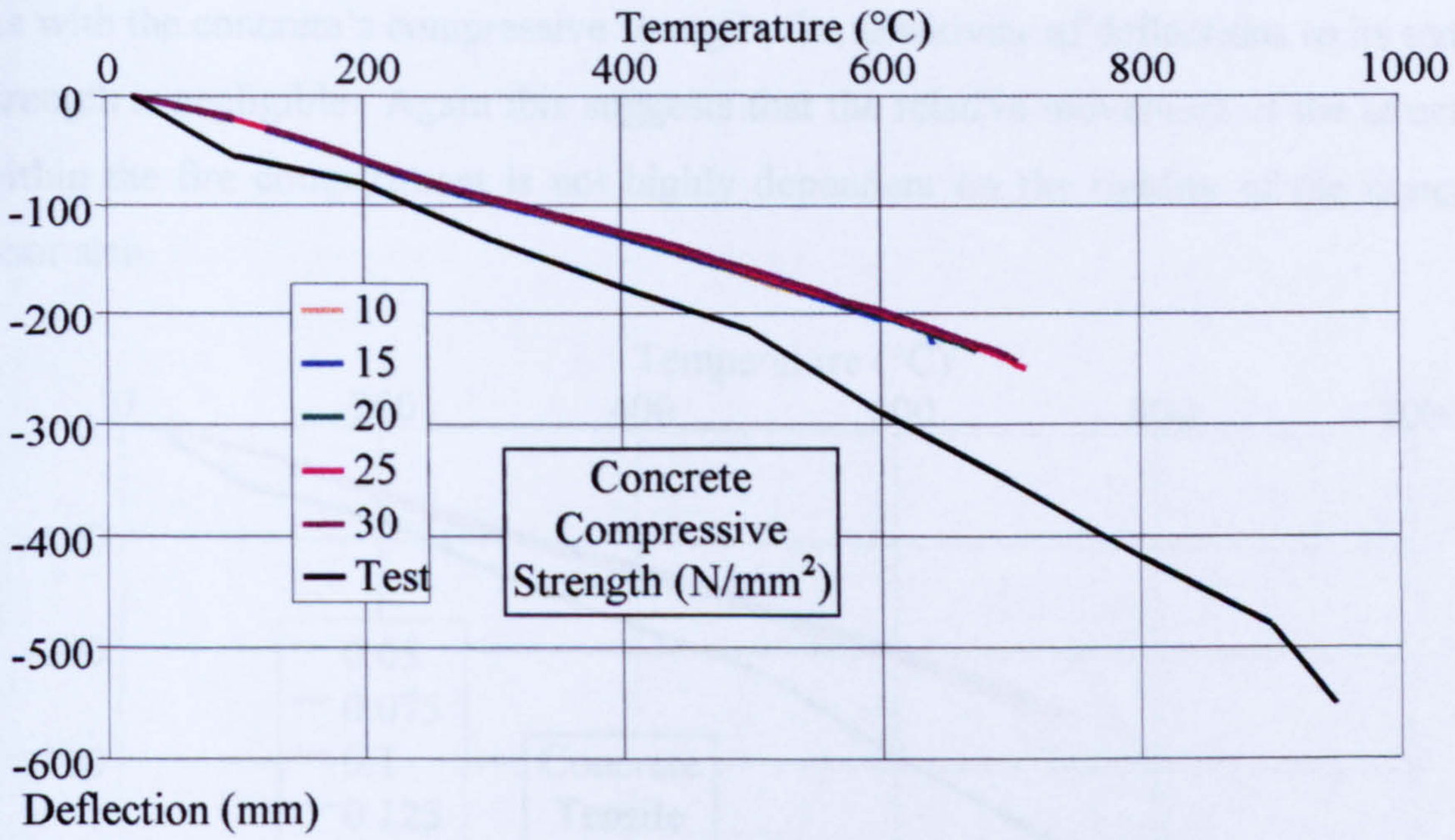

Figure 6-87. Parametric study 3 - Demonstration test, mid-span of secondary beam

The effect of compressive strength on the overall structural action appears to be negligible.

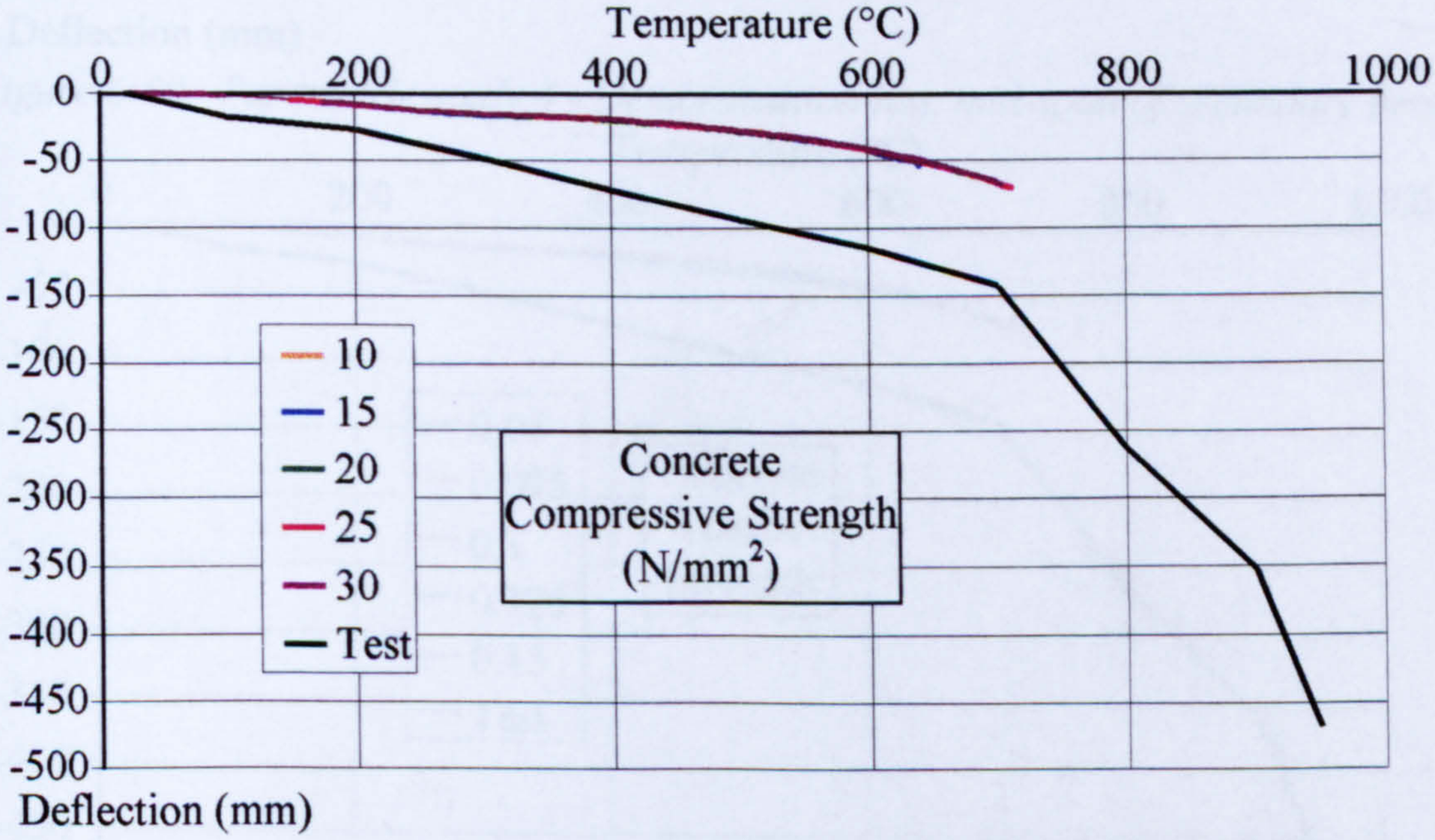

Figure 6-88. Parametric study 3 - Demonstration test, mid-span of 6m main beam

Should a vatiation of maximum compressive stress be combined with either a change of slab thickness or slab temperature gradient, the relative insensitivity to each of the parameters will result in negligible difference.

6.8.4 PARAMETRIC STUDY 4 - DEMONSTRATION TEST

Figures 6-89 and 6-90 show the deflections at the mid-span of the secondary beam and the 6m main beam for a range of concrete tensile strength.

As with the concrete's compressive strength, the sensitivity of deflections to its tensile strength is negligible. Again this suggests that the relative movement of the structure within the fire compartment is not highly dependent on the rigidity of the concrete floor slab.

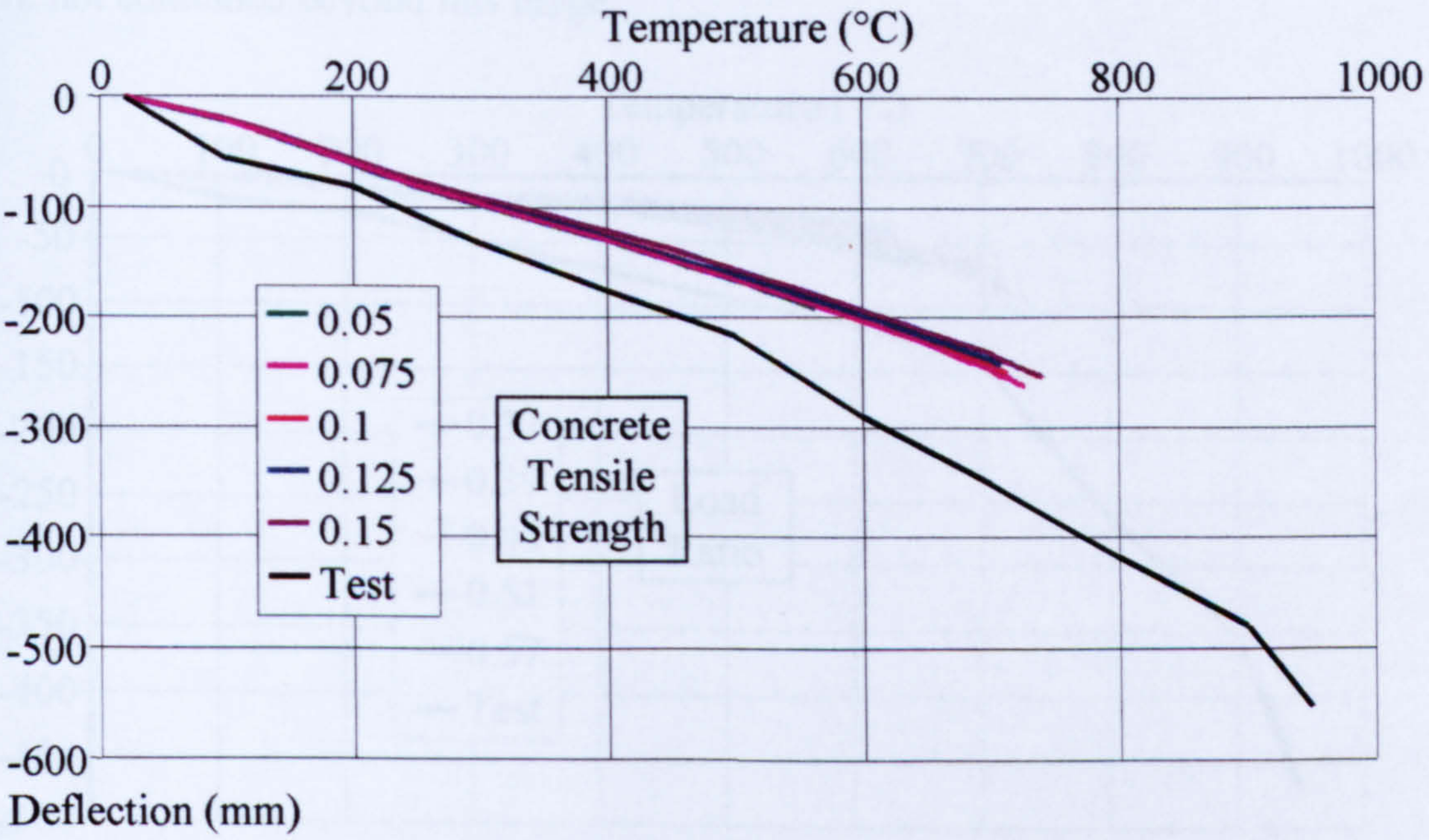

Figure 6-89. Parametric study 4 - Demonstration test, mid-span of secondary beam

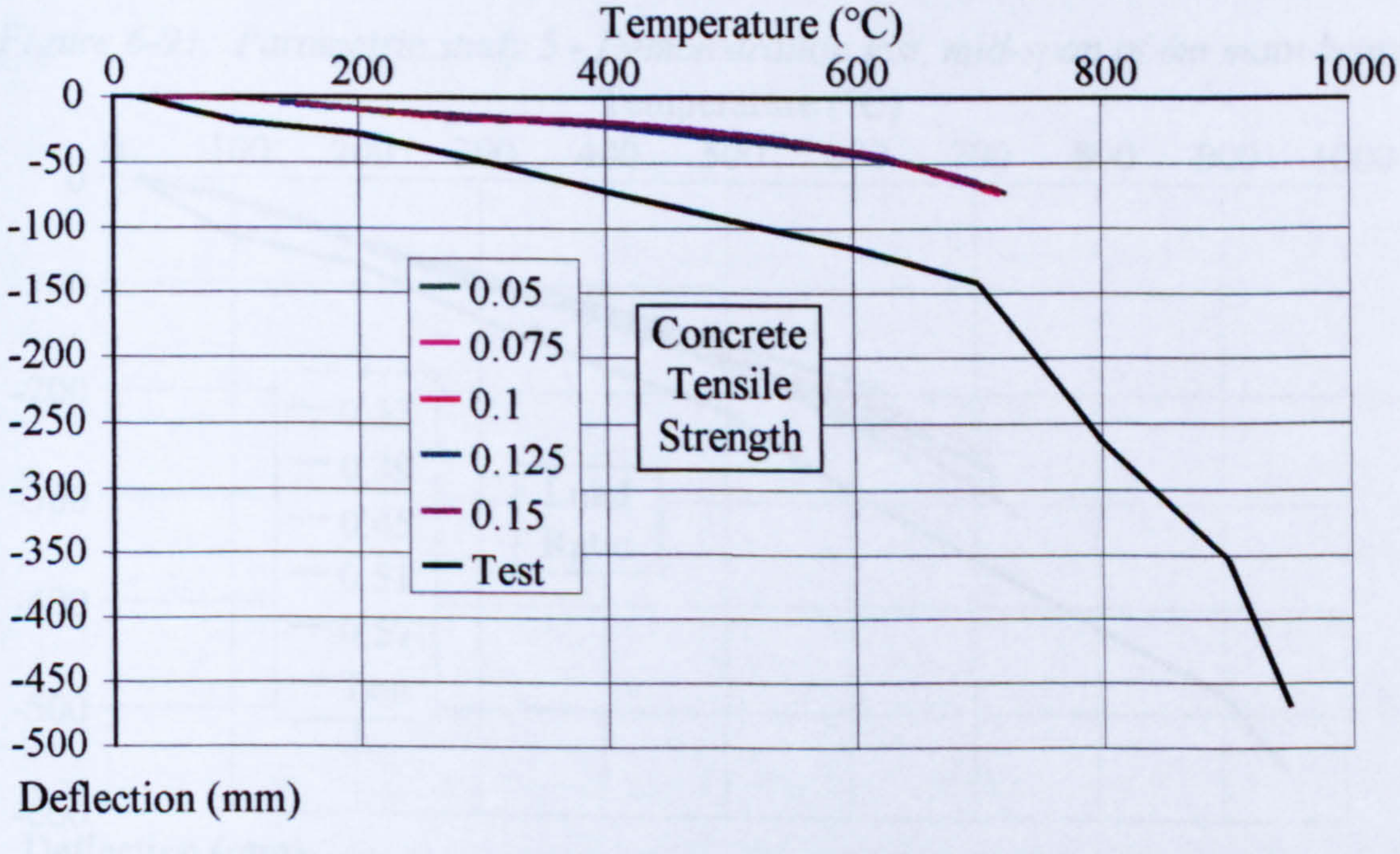

Figure 6-90. Parametric study 4 - Demonstration test, mid-span of 6m main beam

6.8.5 PARAMETRIC STUDY 5 - DEMONSTRATION TEST

Figures 6-91 and 6-92 show the mid-span deflections of the secondary beam and the 6m main beam respectively for a range of load ratios.

As in the previous studies the initial 500°C steel temperature rise results in deflection caused by thermal bowing, after which loss of strength and stiffness of the steel beams causes continuing deflection. The variation produced by the load ratio parameter is not great in the temperature range up to 650 - 700°C, although the curves have not continued beyond this range.

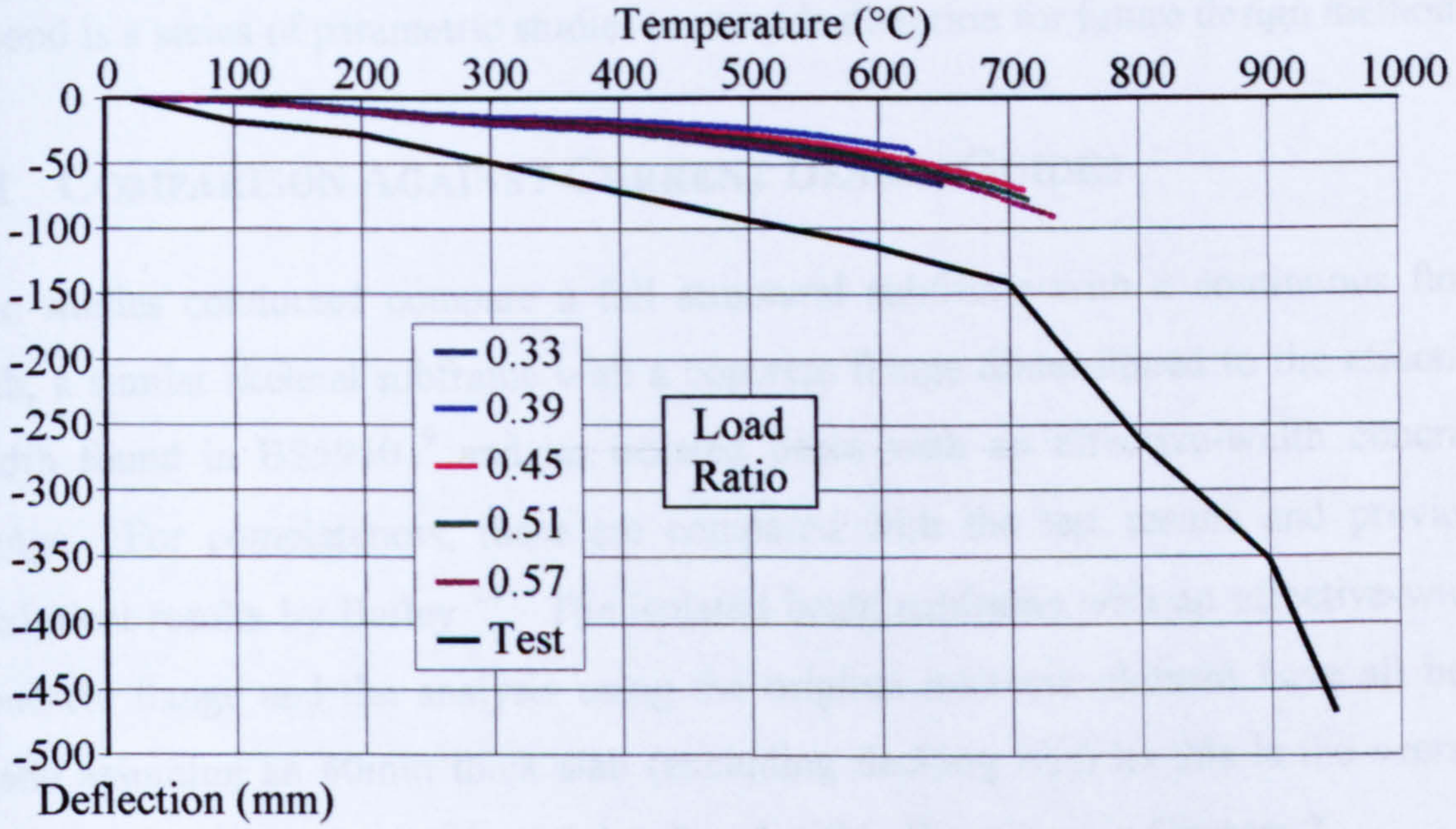

Figure 6-91. Parametric study 5 - Demonstration test, mid-span of 6m main beam

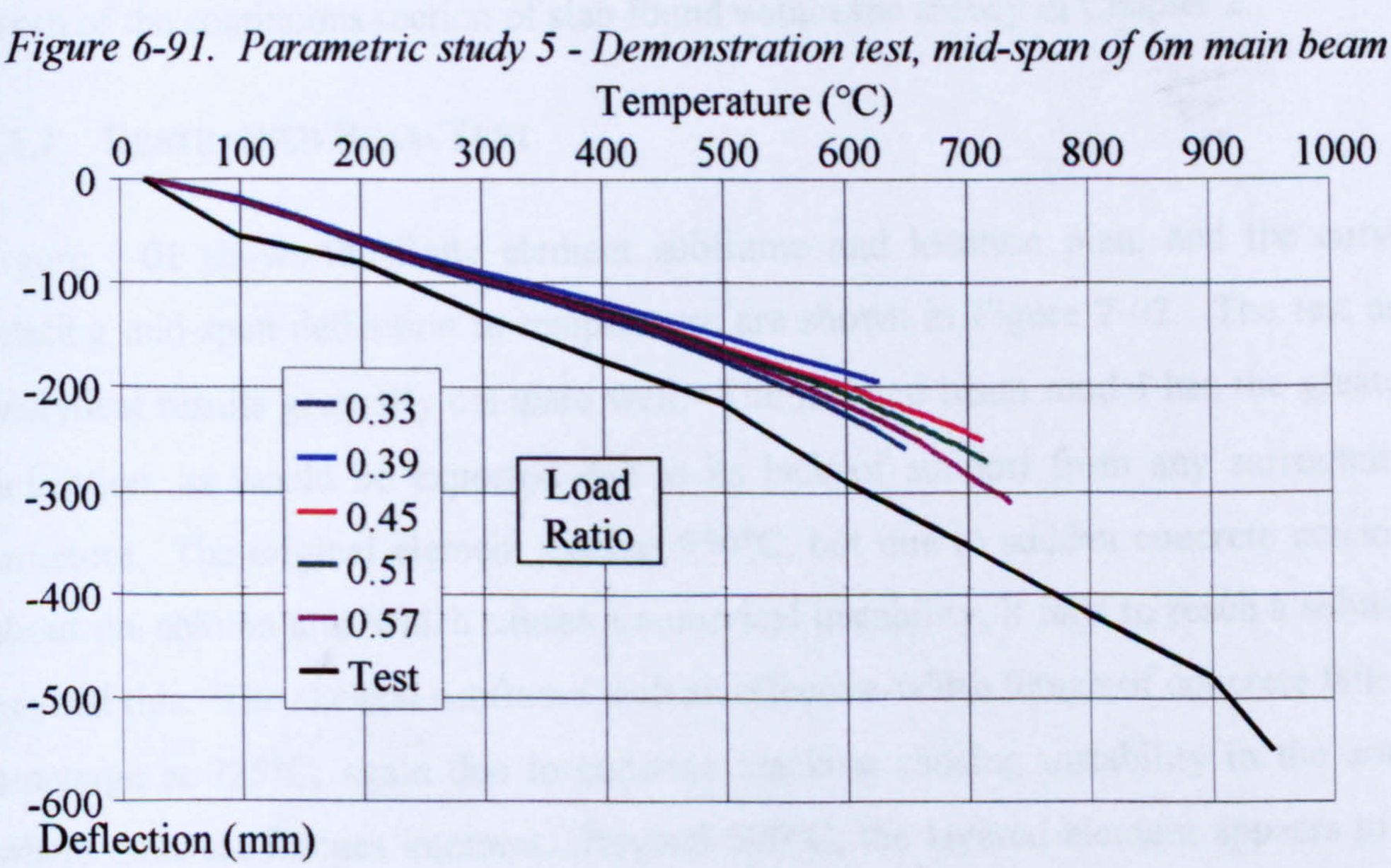

Figure 6-92. Parametric study 5 - Demonstration test, mid-span of secondary beam

7 GENERAL ANALYSIS OF THE CARDINGTON STUDIES

This chapter describes two sets of analyses based on the Cardington tests. The first is a comparison between current design methods, which treat the beam and an effective width of concrete flange in isolation, and a more complete building analysis. The second is a series of parametric studies to provide direction for future design methods.

7.1 COMPARISON AGAINST CURRENT DESIGN GUIDES

The studies conducted compare a full structural subframe with a continuous floor slab, a similar skeletal subframe with a concrete flange dimensioned to the effective width found in BS5950 [9] and an isolated beam with an effective-width concrete flange. For completeness, these are compared with the test results and previous analytical results by Bailey [44]. The isolated beam subframe with an effective-width concrete flange and the analysis using the original isotropic element have all been made assuming an 80mm thick slab (excluding decking ribs) as this is the average depth of the continuous section of slab found within the survey in Chapter 2.

7.1.1 RESTRAINED BEAM TEST

Figure 7-01 shows the finite element subframe and location plan, and the curves relating mid-span deflection to temperature are shown in Figure 7-02. The test and analytical results generally compare well. The isolated beam model has the greatest deflection, as would be expected due to its lack of support from any surrounding structure. The original element reaches 950°C, but due to sudden concrete cracking about the column area which causes a numerical instability, it fails to reach a solution beyond this. The skeletal subframe with an effective-width flange of concrete fails to converge at 725°C, again due to concrete cracking causing instability in the zones where concrete flanges intersect. Beyond 500°C, the layered element appears to be over-stiff and not to crack as expected. This leads to bridging action where the diminishing stiffness of the steel beam is increasingly outweighed in importance by the stiffness of the concrete slab, and as a result the calculated deflections based on this representation are generally less than for other models.

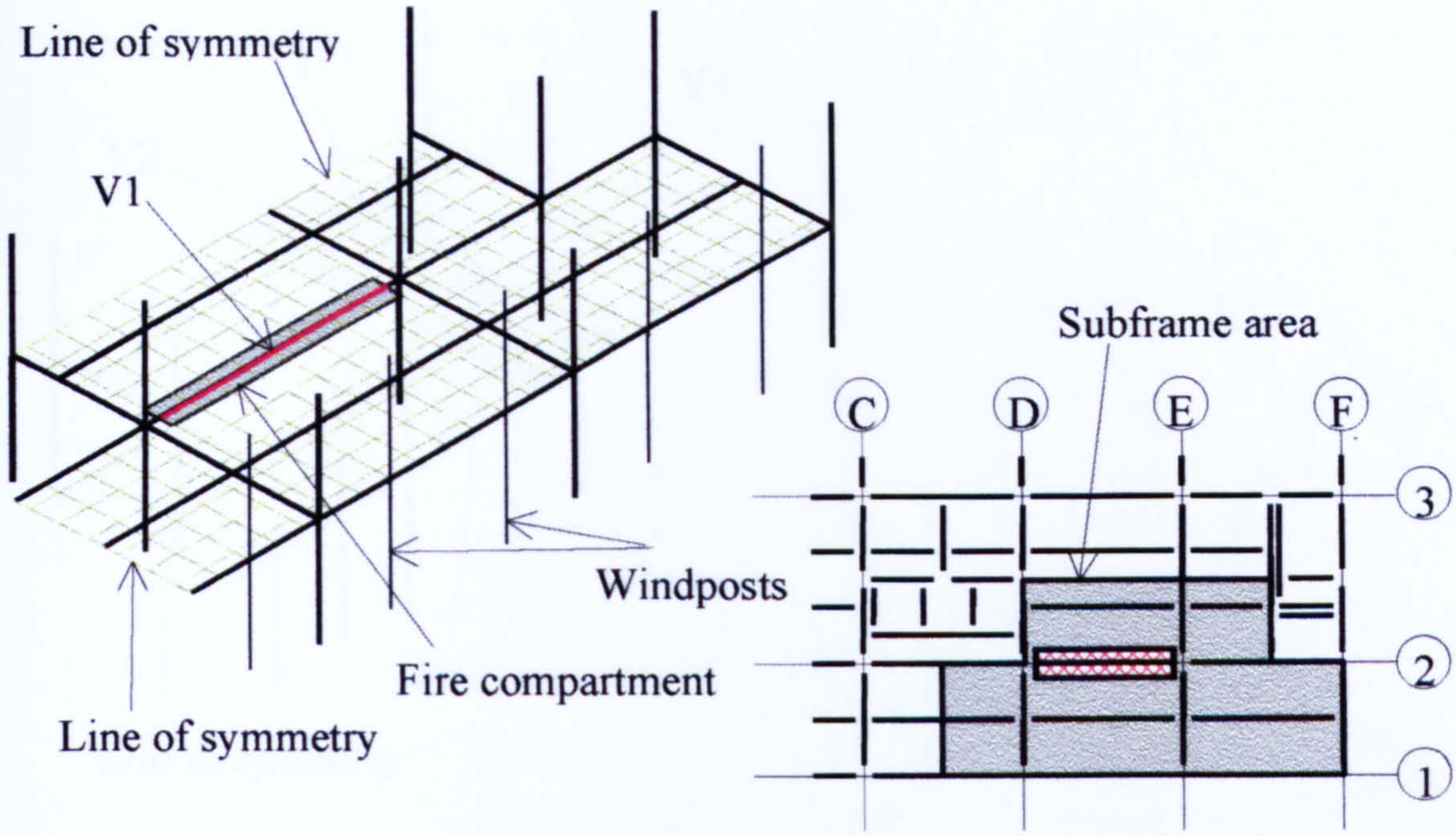

Figure 7-01. Location and finite element mesh of the restrained beam test.

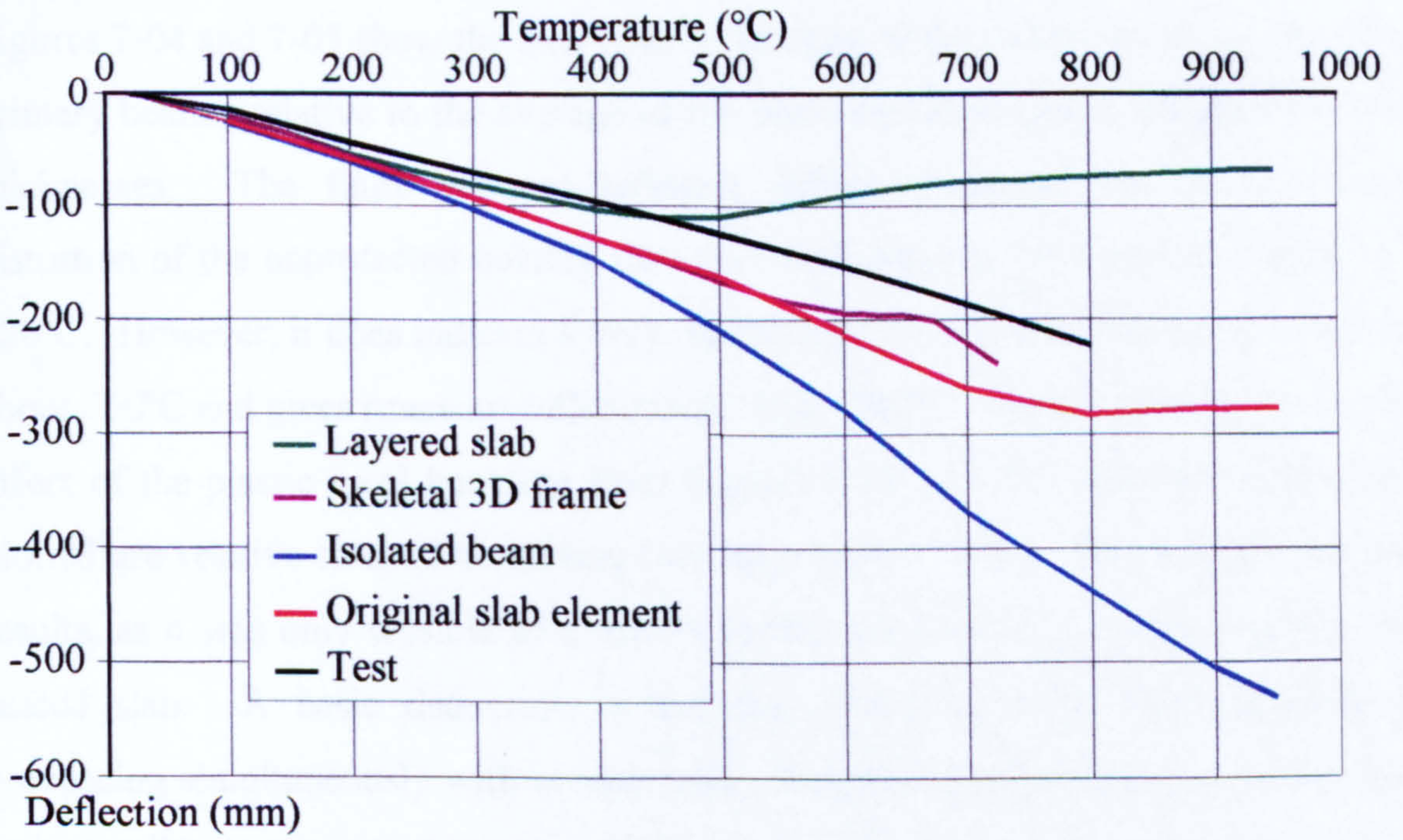

Figure 7-02. Central deflection of the restrained beam test – Position V1

7.1.2 PLANE FRAME TEST

The finite element mesh and boundary conditions for modelling the plane frame test are shown in Figure 7-03. In this case it is possible that the secondary composite beams may be the major factor in supporting the heated structure, so that the floor slab may make only a minor contribution to the mechanics of the load-redistribution to adjacent structure. The top 500mm of the column head has been left fully exposed to heating.

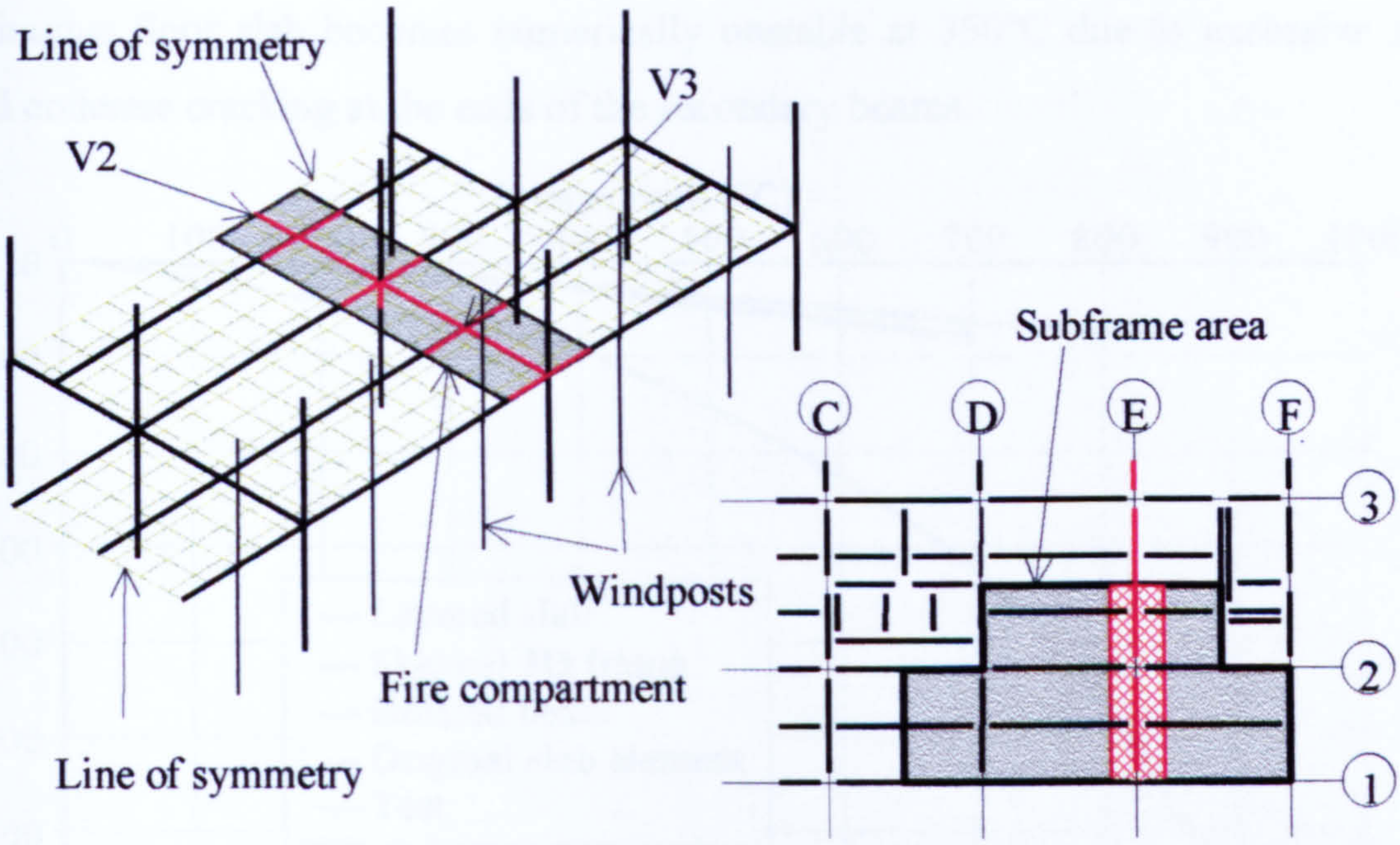

Figure 7-03. Location and finite element mesh of the plane frame test

Figures 7-04 and 7-05 show the mid-span deflections of the outer- and inner-spanning primary beams, relative to the average of the beam end deflections, for different slab thicknesses. The finite element software cannot represent the cross-sectional distortion of the unprotected column tops that took place in the test in the region of 620°C. However, it does indicate a very rapid increase of absolute deflection beyond about 650°C and gives runaway deflection at about 680°C. It is not possible to see the effect of the plastic local buckling from Figures 7-04 or 7-05, since the deflections plotted are relative to the line joining the beam-ends. This is also true for the test results, as it was only feasible to measure deflections relative to the floor above the heated slab. A basic deduction is that the observed plastic local buckling is proceeding simultaneously with considerable compressive axial straining, and it may be impossible to separate these two effects.

Figures 7-04 or 7-05 show comparisons between test and analyses for the plane frame test at deflection positions V2 and V3. In both cases the isolated beam was found to have the greatest deflection, as expected. All other analyses can be seen to follow closely the deflection path found during the test until the beam bottom flange temperature is approximately 600°C. At this temperature, some of the test deflections appear to begin to run away, and this is not predicted by VULCAN. The analysis of the skeletal subframe containing simple concrete-flanged beams rather than a fully

continuous floor slab becomes numerically unstable at 350°C due to excessive and rapid concrete cracking at the ends of the secondary beams.

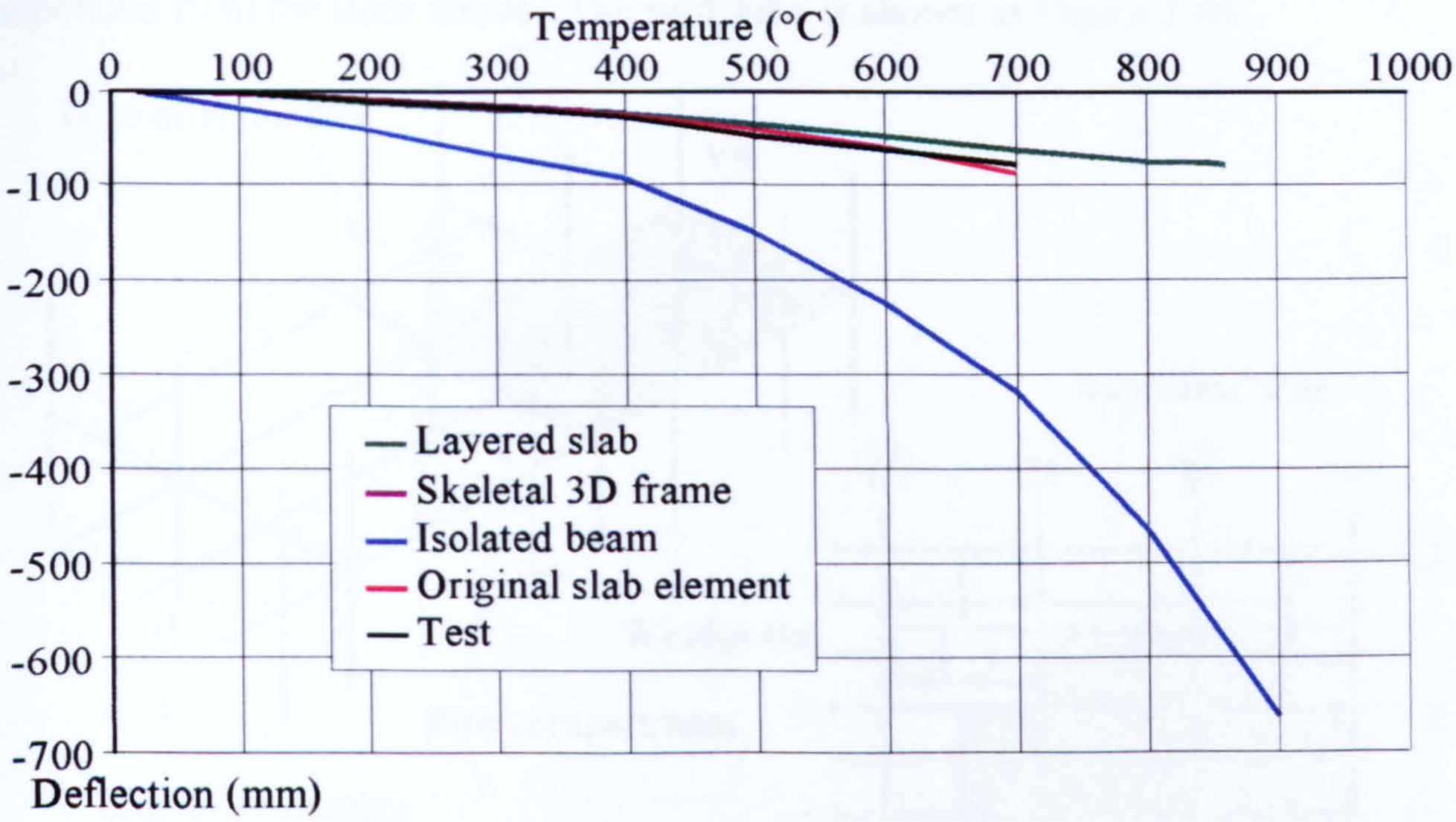

Figure 7-04. Central deflection of the 6m main beam in the plane frame test – Position V2

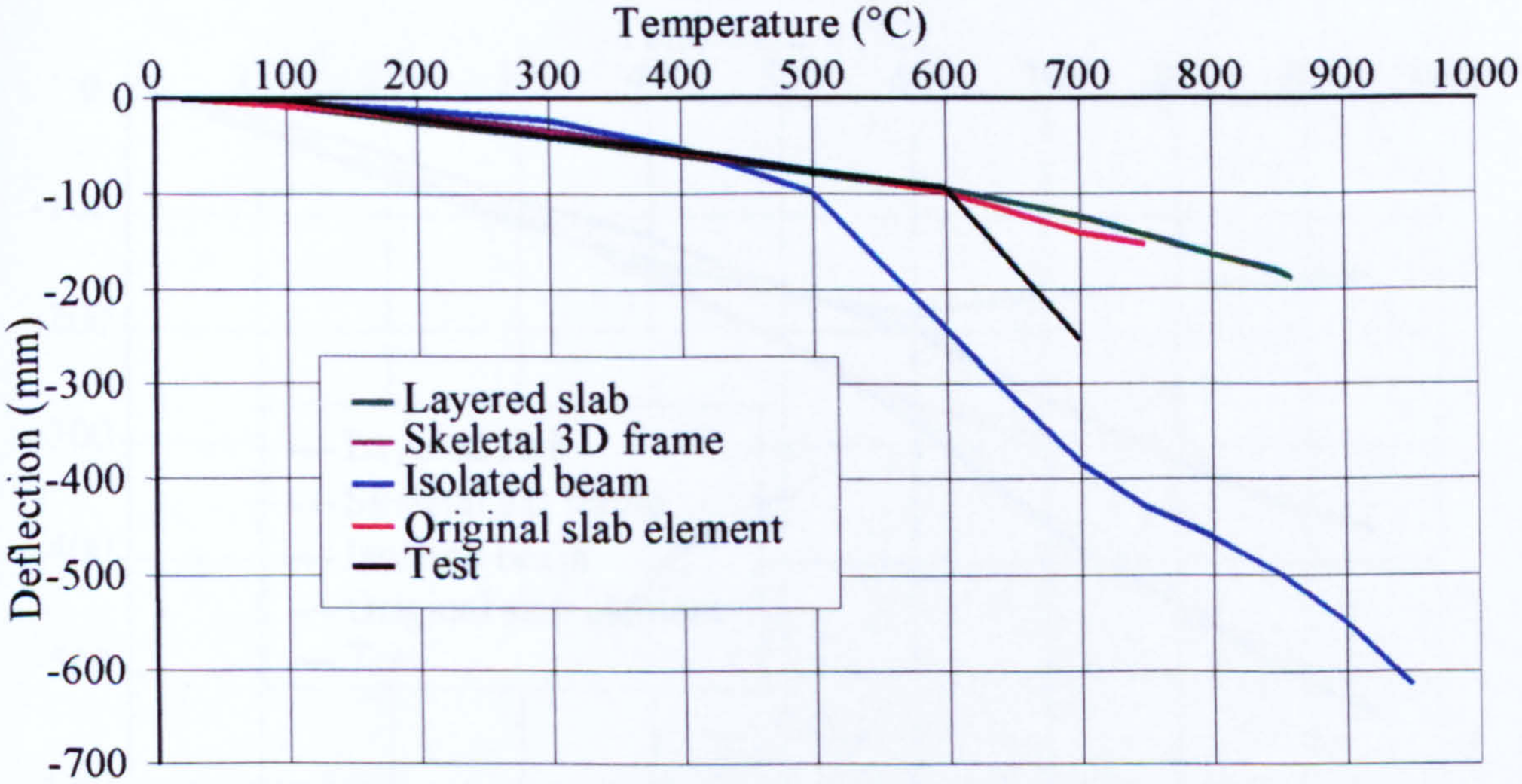

Figure 7-05. Central deflection of the 9m main beam in the plane frame test – Position V3

7.1.3 BRE CORNER TEST

The BRE corner test location, and the finite element mesh used, is shown in Figure 7-06. For the purpose of the analyses, the heated perimeter beams were assumed to have a lower flange temperature of 50% of that of the main beams. Temperatures recorded during the test suggest that this is a reasonable assumption. Studies by Bailey [44] have also shown that, when analysing the corner test, it is important to take

into account the windposts on the structure perimeter. The windposts have been found to provide support to the perimeter beam by acting as tension members suspended from the floor above. The subframe is shown in Figure 7-06.

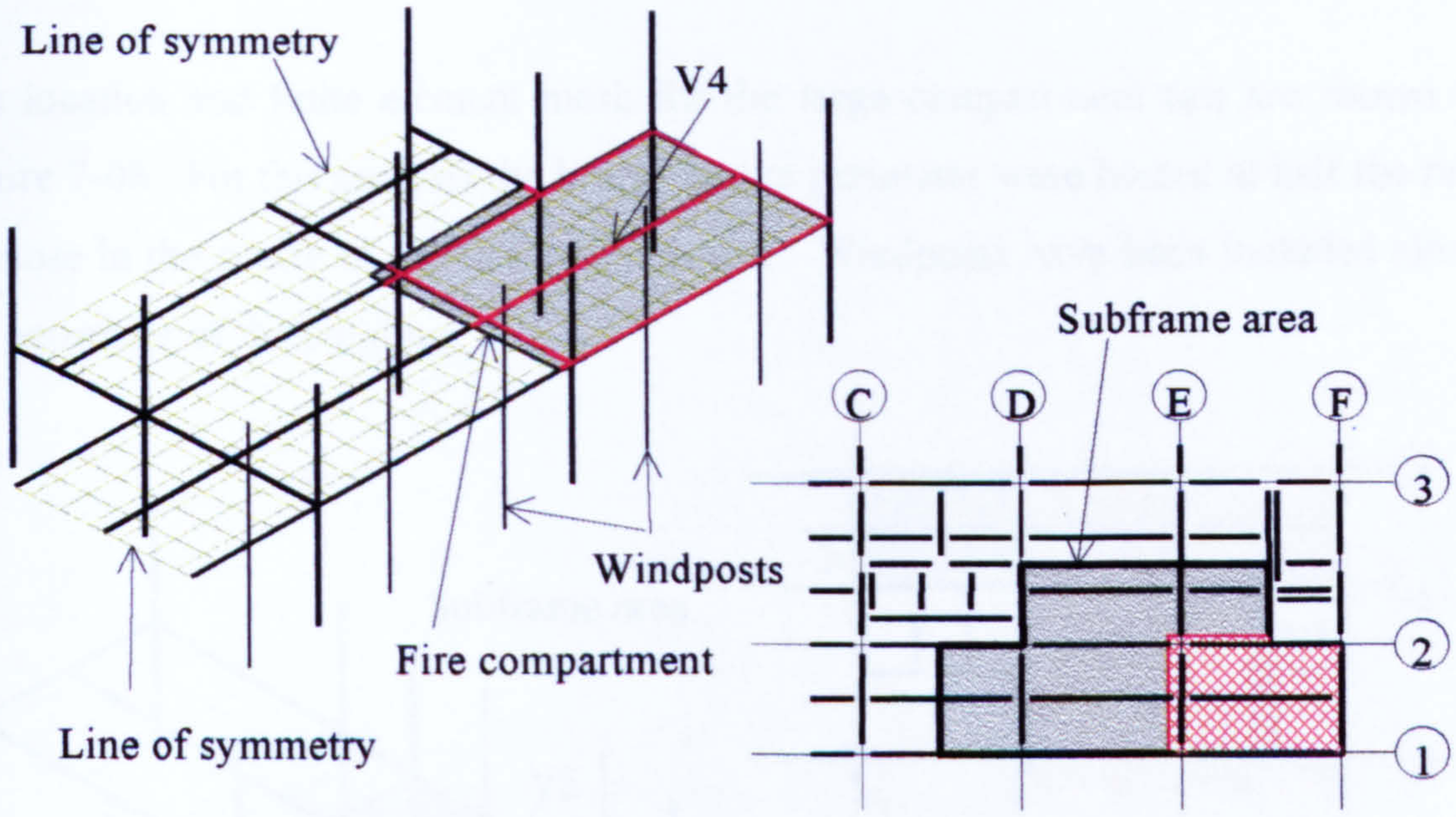

Figure 7-06. Location and finite element mesh of the BRE corner test

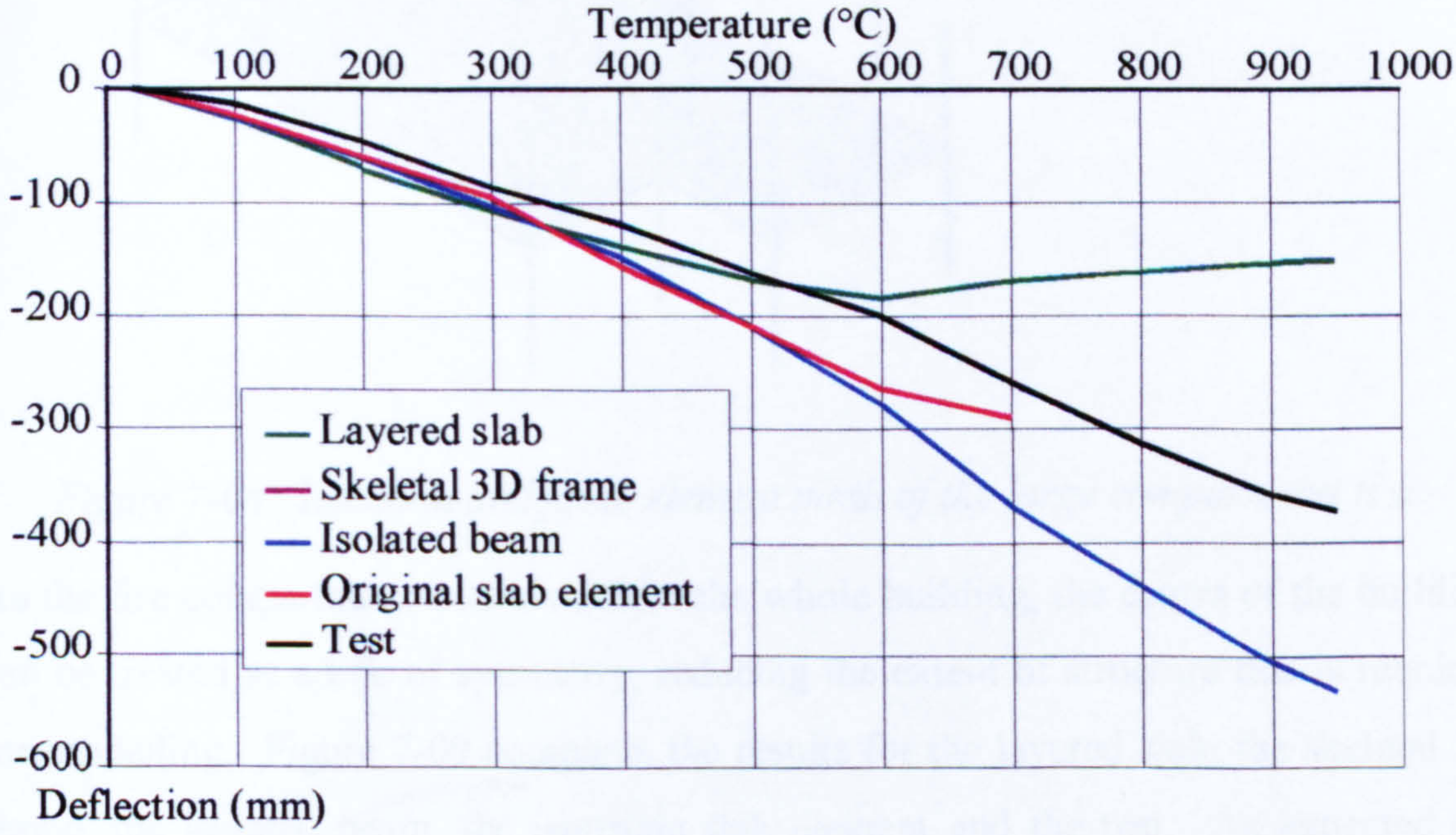

Figure 7-07. Central deflection of the internal secondary beam in the BRE corner test – Deflection V4

Figure 7-07 shows the deflections predicted by the different model arrangements compared to the actual test deflections at deflection position V4. This shows good comparison between the full subframe and the actual test data. The isolated beam, as expected, gives the greatest deflections. The analyses of the fully continuous subframe all give good comparisons and, as in the restrained beam test, bridging

action becomes increasingly important at higher temperatures, causing the beam to be pulled back towards its original position.

7.1.4 LARGE COMPARTMENT TEST

The location and finite element mesh for the large compartment test are shown in Figure 7-08. For this analysis the beams on the perimeter were heated at half the rate of those in the centre of the fire compartment. Windposts have been included along the perimeter of the building.

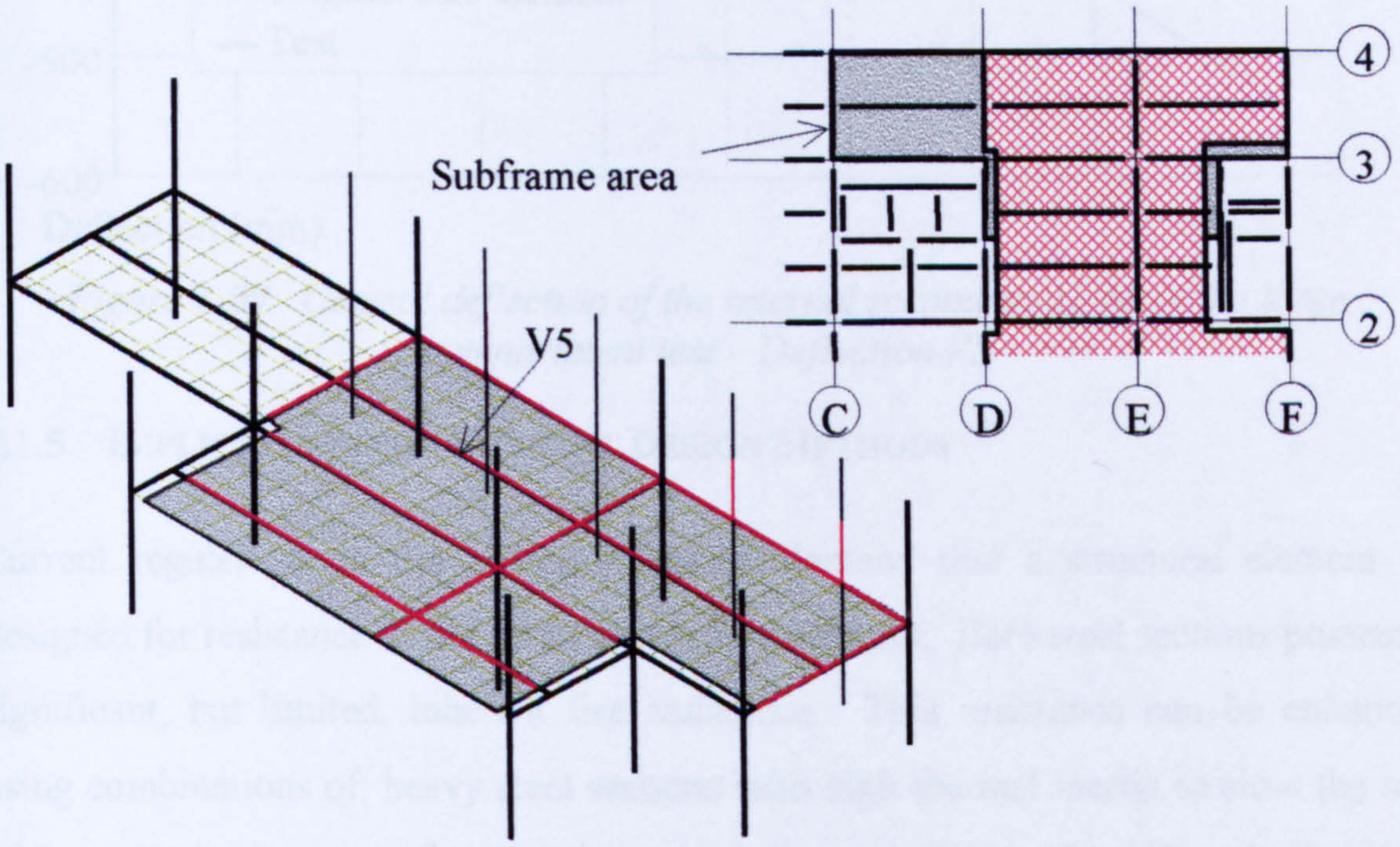

Figure 7-08. Location and finite element mesh of the large compartment test.

As the fire compartment extends across the whole building, the centre of the building can be treated as a line of symmetry, reducing the extent of structure that is required for modelling. Figure 7-09 compares the results for the layered slab, the skeletal 3D frame, the isolated beam, the isotropic slab element and the test. As expected the isolated beam deflects most quickly

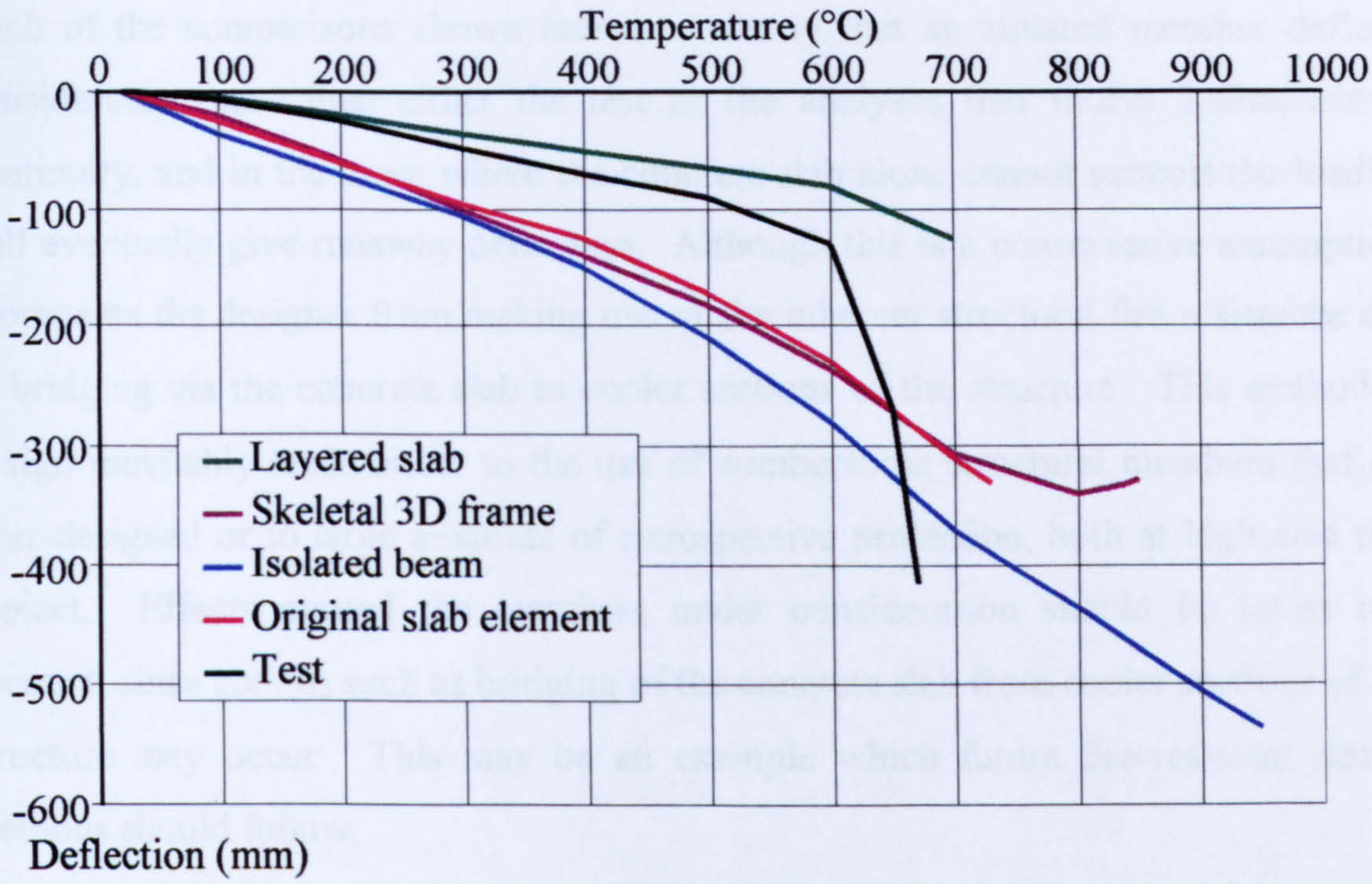

Figure 7-09. Central deflection of the internal secondary beam in the large compartment test – Deflection V5

7.1.5 Implications for Current Design Methods

Current regulations in the United Kingdom demand that a structural element be designed for resistance to fire as an isolated component. Bare steel sections possess a significant, but limited, inherent fire resistance. This resistance can be enhanced using combinations of: heavy steel sections with high thermal inertia to slow the rate of temperature increase; fire-resisting material properties; steel sections built into a wall or floor to increase the inherent shielding and insulation; active protection of the section and water sprinkler systems. These are largely defensive approaches in which the structural elements are not designed for the fire but are simply protected against fire effects using mainly passive measures. In contrast, design procedures for other actions such as wind or earthquakes become part of the normal design process. Typical solutions include moment connections, sway-frames and cross-bracing. Current building regulations in the United Kingdom also insist that structures should be designed to avoid disproportionate collapse as a result of localised structural damage. It is therefore, arguable that the modern structural designer should be designing for fire as a basic limit state, rather than simply using retrospective passive protection.

Each of the comparisons shown indicates clearly that an isolated member deflects considerably more than either the test or the analyses that model 3-dimensional continuity, and in the cases where the concrete slab alone cannot support the loading will eventually give runaway deflection. Although this is a conservative assumption, it prevents the designer from making use of the inherent structural fire resistance due to bridging via the concrete slab to cooler sections of the structure. This method of design inevitably leads either to the use of cumbersome structural members that are over-designed or to large amounts of retrospective protection, both at high cost to a project. Effects around the members under consideration should be taken into account, since actions such as bridging of the concrete slab from cooler sections of the structure may occur. This may be an example which future fire-resistant design methods should follow.

7.2 Qualitative Analysis of the Cardington Parametric Studies

The parametric studies described in Chapters 4 and 6 for the Cardington fire tests have been evaluated qualitatively, particularly with the future of structural fire design developments in mind.

7.2.1 Slab Bridging

As the temperatures within a fire compartment increase, the steel beams begin to decrease in strength and stiffness. This in certain cases will allow the slab – being less dominant at low temperatures – to dominate the structural action. This can significantly increase the fire resistance of the structure. Three specific cases for the Cardington studies follow:

A single heated beam with unheated or mildly heated adjacent beams. A single heated beam with adjacent beams that are capable of sustaining extra load will perform well. Examples of this case occurring at Cardington are the Restrained Beam Test and the British Steel and BRE Corner tests. The beam initially sags due to thermal bowing caused by the temperature differential between the steel beam and the floor slab. However, beyond approximately 500°C, the increase in deflection is more due to loss of strength and stiffness of the steel. At this stage, the concrete slab –

through its bending strength - will begin to support the steel beam by spanning from the supporting elements. Often the residual bending stiffness of the concrete floor slab will dominate the degradation of the steel beam and the thermal bowing effect and tend to attempt to return to its original position. The situations in which this occurs for the Cardington tests, at least in three- dimensional modelling studies, are shown in Figure 7-10.

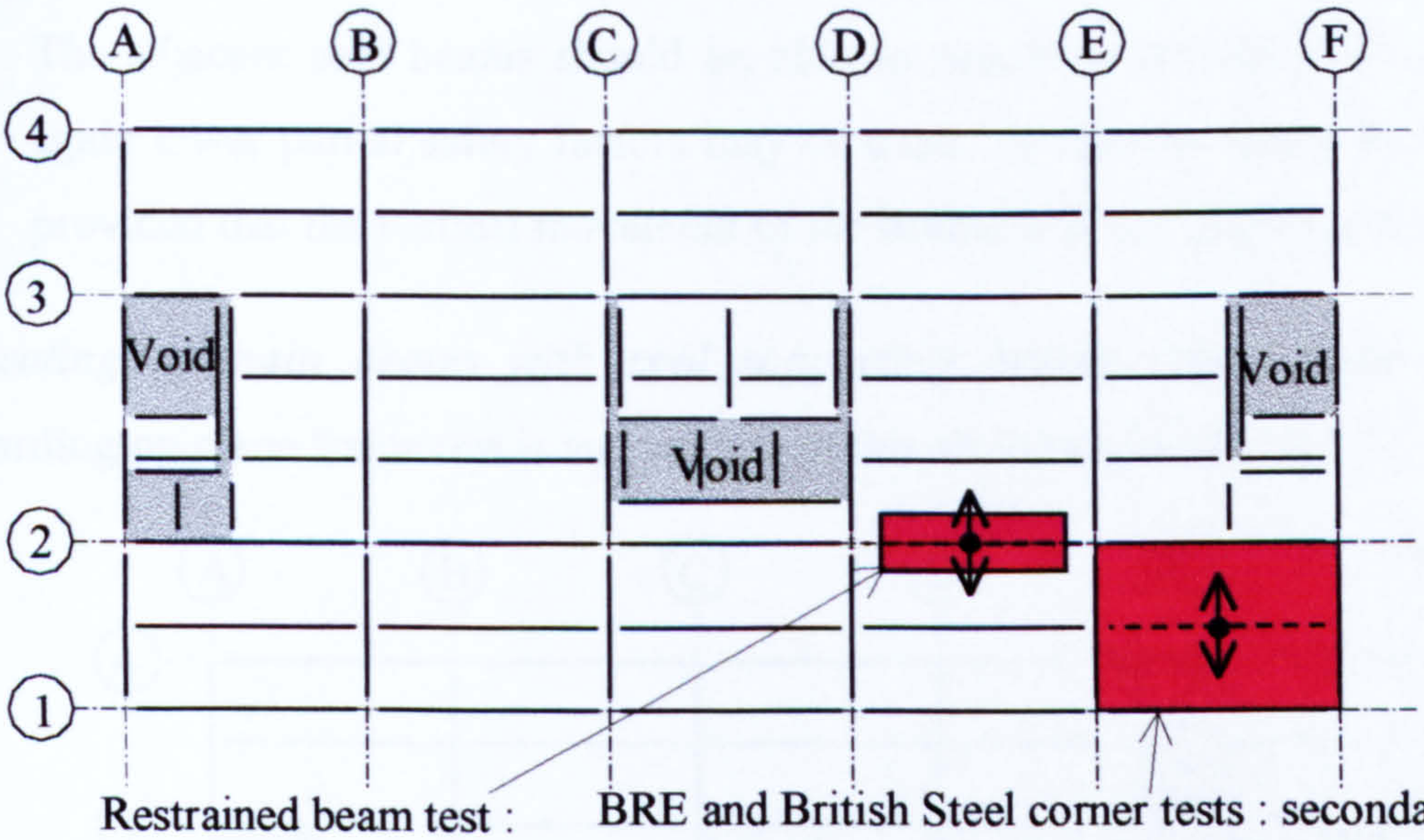

Restrained beam test : spanning between two cold secondary beams

BRE and British Steel corner tests : secondary beams span between two partially heated beams; one of which is supported by windposts in tension.

Figure 7-10. Schematic drawing of two examples of a floor slab spanning between adjacent beams

In order to take advantage of this behaviour when designing steel beams for fire, a number of issues need to be addressed as follows:

1. The fire compartment must be clearly defined and the maximum temperatures calculated.

2. The elements supporting the floor slab over the fire compartment should be identified. These may be beams in cool sections of the structure or beams otherwise protected. For example, a perimeter beam with windposts above may be considered to provide effective support, provided that the windposts themselves can carry in tension the load usually carried by the edge beam under fire conditions.

3. The ability of the concrete slab to span longer distances (on the assumption that the heated beam is capable of carrying no loading) should be considered. The

elastic modulus and maximum tensile and compressive stresses for the heated section of concrete slab should be reduced according to EC4 [11] but reduced partial safety factors may be applied. Deflection limits may be ignored, because it is the overall survival of the structure that is important. However, the vertical movement should not be sufficient to jeopardise the performance of any firewalls below the slab.

4. The adjacent cool beams should be able to accommodate the extra loading but again lower partial safety factors may be used. Deflection limits need not apply provided that the vertical movement of the beams will not destroy any firewalls.

Heating of main beams with cool supporting beams remote from fire. The Cardington plane frame test is an example of this as shown in Figure 7-11.

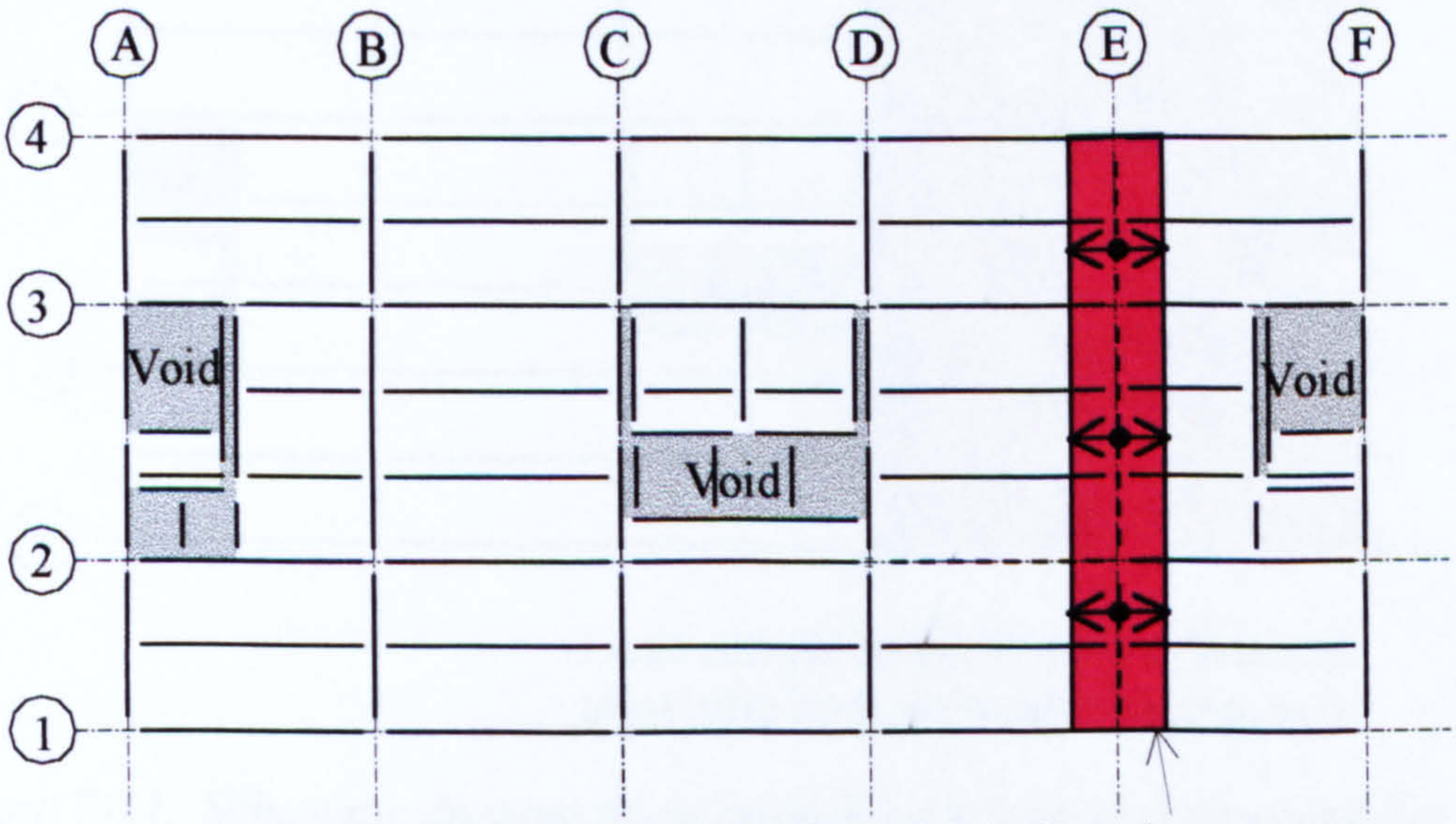

Plane frame test where floor slab is forced to span between main beams or longitudinally between columns.

Figure 7-11. Schematic drawing of an example of a floor slab spanning between adjacent beams.

In normal circumstances, a concrete floor slab (such as that found in the plane frame test) will span between secondary beams. In the event of a fire, the secondary beams begin to lose strength and stiffness. In the case of the plane frame test only the end portions of the beams were within the fire compartment and affected in this way. Consequently, there was a tendency for the concrete slab to span the heated area in place of the main beams.

Large compartments with all beams heated. The large compartment test and the demonstration test are both examples of this, as they cover a large area where all

steelwork is exposed to fire. This causes the whole floor area to deflect, and hence all steelwork deflects similarly so that the stiffness of the floor (or adjacent beams) cannot be utilised. Whether the floor slab may ultimately be used as a tensile membrane between the supporting columns is debatable, as the floor slab in the regions around a column will be acting in hogging. This forces the floor slab into tension leaving the reinforcement as the only reliable structural material in a small, highly-stressed region. This situation is shown in Figure 7-12. If the primary supporting beams are fire-protected, the floor slab (if continuous across them) should be capable of being designed to span between them as a membrane, as this longer line of support will produce much lower distributed stresses in the slab.

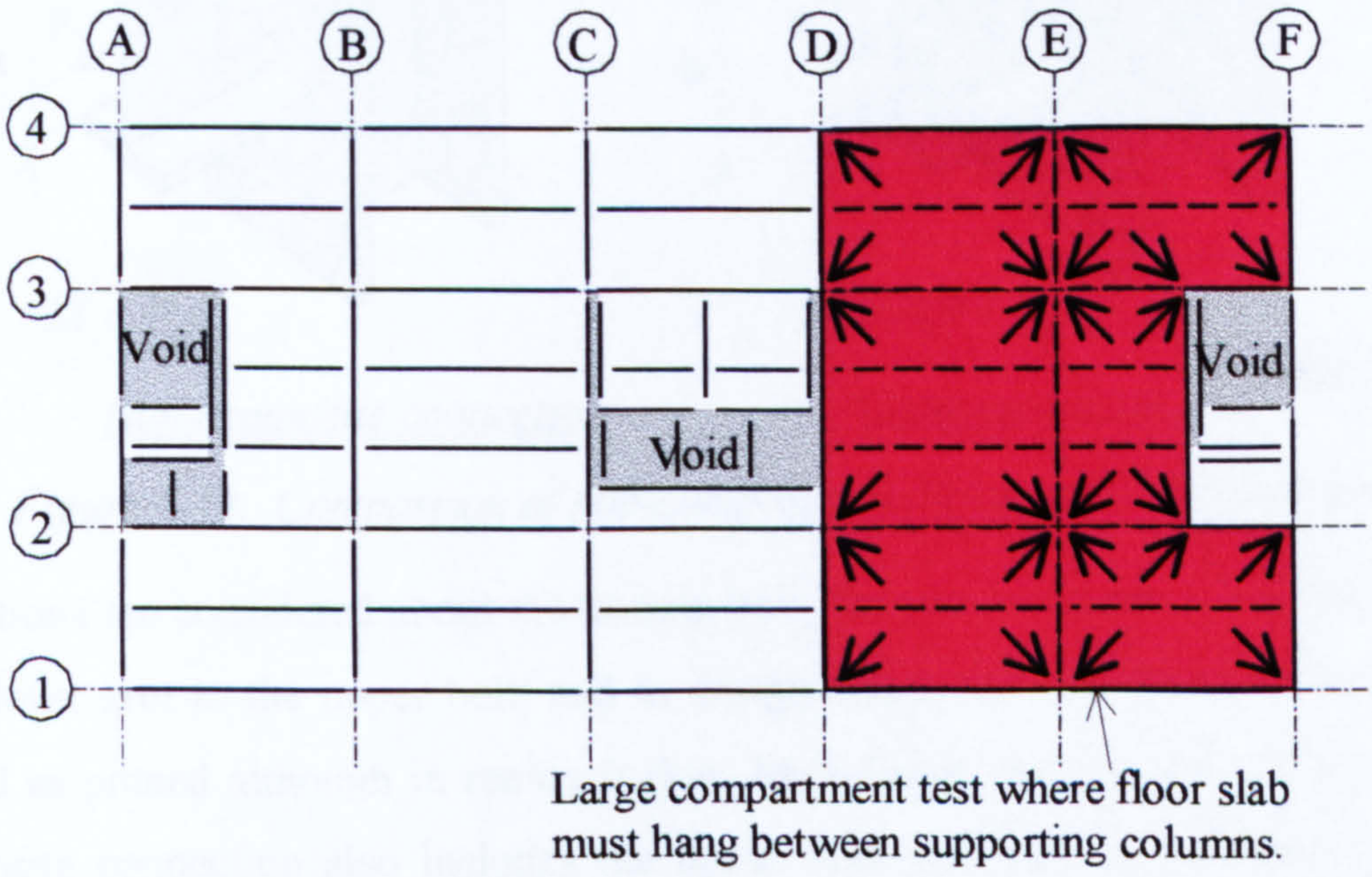

Figure 7-12. Schematic drawing of an example of a floor slab spanning between adjacent beams

When this parametric study is considered in the light of the slab thickness survey detailed in Chapter 2, it is important to recognise that between the beams the thickness of concrete is likely to be higher than that specified by the designer. This is due to ponding of the concrete caused by the deflection of decking when casting slabs. Whether this phenomenon could (or should) be taken into account at the design stage is questionable, as it cannot be guaranteed that slabs will be thicker than specified. This leads to the conclusion that it is best to be aware of the extra slab thickness, but to treat it as an 'undeclared' factor of safety.

7.2.2 CONNECTION STRENGTH AND STIFFNESS

The rotational strength and stiffness of a steel connection is dependent on the length of the lever arm available between its resultant tension and compression forces. This is illustrated in Figure 7-13 for a tab-plate (as used at Cardington).

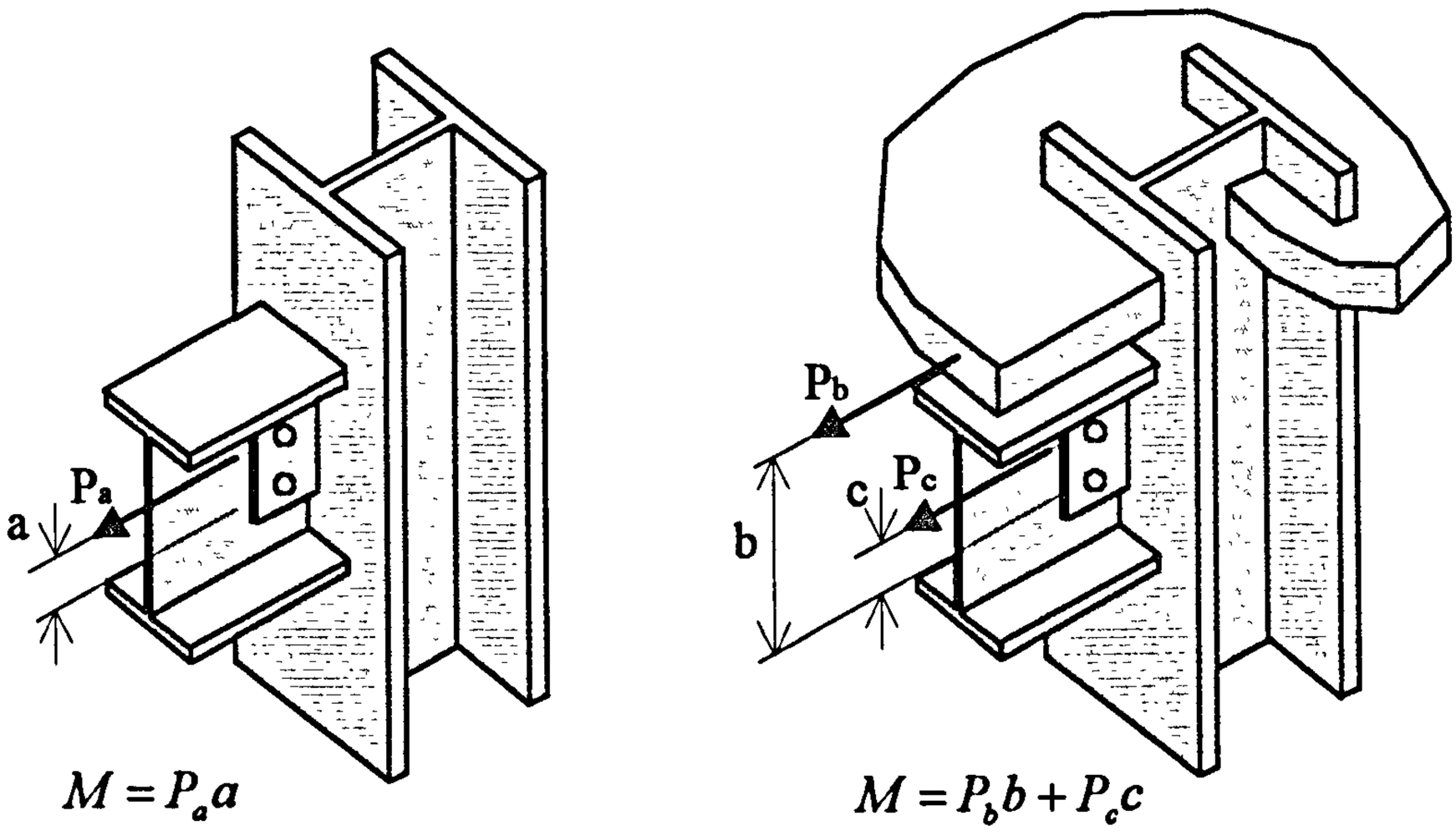

Non-composite connection *Composite connection*

Figure 7-13. Comparison of non-composite and composite connections

If rotations are considered about the bottom bolt, the non-composite connection has a short lever arm to the upper bolt, and in design this type of connection is normally treated as pinned although in reality it does have finite strength and stiffness. The composite connection also includes the upper bolt, but has the advantage that the concrete floor slab mesh is also capable of resisting tension. It was assumed that this resistance against rotation could be utilised in fire design, after a series of tests by Lawson [69]. The principle is shown in Figure 7-14.

Whether connection resistance should be included in design is questionable, as the lower flange of the restrained beam was seen to have buckled in the hogging zone at the edge of the furnace. This is believed to have happened at approximately 530°C, effectively creating a hinge (refer to Chapter 2). Beams also buckled locally in some of the other five Cardington tests, but due to their complexity, increased size and reduced level of instrumentation compared with the restrained beam test, it was harder to determine the temperature at which the buckles occurred. Similar local buckling behaviour was also noted in the Broadgate fire report [22].

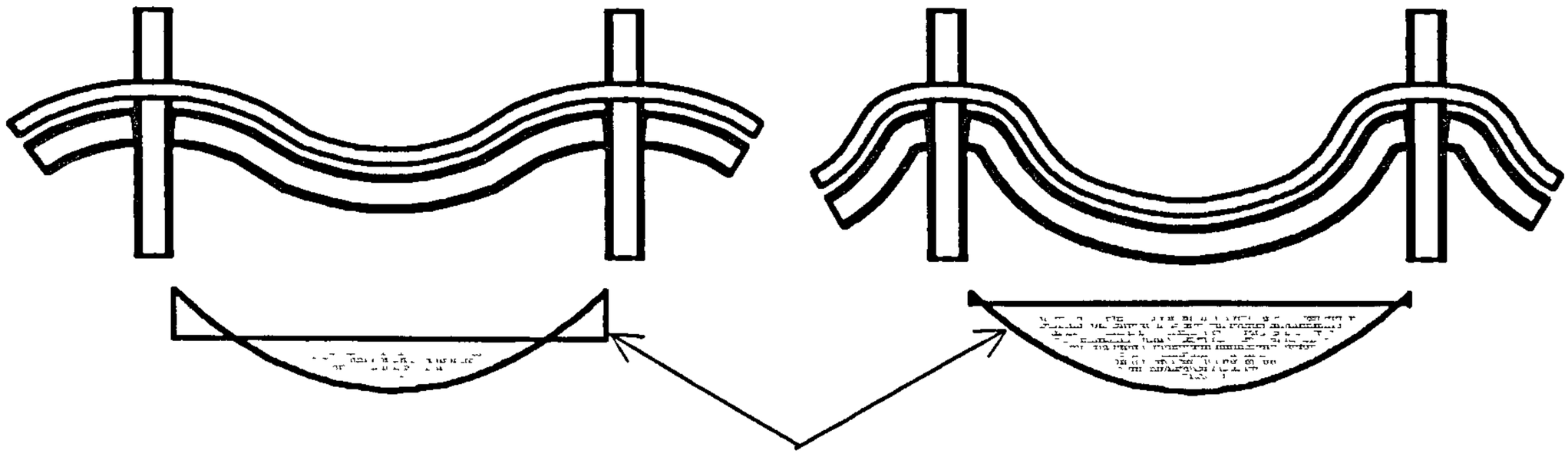

Figure 7-14. Effect of local beam buckling on connection influence in fire

Unfortunately, VULCAN is unable to accommodate cross-sectional distortion (such as local buckling) of the steel beams. It was found from the parametric studies that the effect of the strength and stiffness of the secondary beam connections was negligible in all the tests. However, in the restrained beam test a small difference was noted at temperatures beyond 700°C. This may be attributed to the cracking of the floor slab, allowing the beam to begin to act as an isolated member with an effective-width concrete flange.

Currently, design guidence exists which directs the fire engineer to utilise the strength and stiffness of the connections in determining the effectiveness of a building structure in fire. The evidence found in the Cardington parametric studies contradicts this possibly giving cause for designers to rethink their attitude towards the strength and stiffness of connections in fire [44, 54].

7.2.3 SUBFRAME EXTENTS

Currently design of composite building structures to resist fire uses BS5950 [9] or EC4 [11], both of which encourage designers to treat a beam as having an effective-width concrete upper flange. This is obviously a very conservative assumption as the continuity of the concrete slab is lost, and use of computer models with continuous floor slabs may be feasible in the future.

8 DISCUSSION AND CONCLUSIONS

Much experimental research has been conducted in the last two decades on the actual behaviour of steel and composite members at elevated temperatures, and more recently on full-scale test frames. The purpose of this has been to establish the extent to which fire protection of structural elements is necessary, as this increases both the cost and time of construction. However, these tests are very expensive, and so there is a need for accurate computer modelling. By establishing confidence in the ability of software to model the response of any frame in any fire scenario, these tests can be reduced in number by analytical studies which can be performed much more cheaply. Recent full-scale tests on the Cardington composite test frame have shown that previous computer simulations (considering plane frames or three-dimensional skeletal frames) do not model the true structural behaviour. However, the VULCAN finite element model is in principle capable of analysing complex three-dimensional composite structures with reinforced concrete floor slabs and has been tested against test results whenever possible. Comparisons with test results have shown that the model is generally accurate in its predictions of both member and overall building behaviour, although some aspects are still under development.

Extensive studies have been conducted in this work to establish the influence of various parameters. These include the thickness of the floor slab, the compressive and tensile strengths of the concrete of the floor slab, the secondary beam connection strength and stiffness, the floor slab temperature gradient, subframe size and the load ratio.

8.1 CARDINGTON PARAMETRIC STUDIES USING THE ISOTROPIC FLOOR SLAB ELEMENT

The six Cardington fire tests were modelled using the VULCAN finite element software and the sensitivity of behaviour to the values of various parameters was studied. The conclusions regarding these parametric studies are discussed in detail within Chapter 7. However, here they will be dealt with briefly here, and future extensions considered.

The thickness of the slab is clearly very important to the fire resistance of composite buildings, particularly when slabs are able to bridge from adjacent cool steel beams surrounding the fire compartment. During the initial stages of a fire, up to 500°C, the fire compartment deflects, largely due to thermal bowing of the steel beams. Beyond 500°C, the behaviour is controlled by the nature of the fire compartment and its adjacent cool structure. In the Restrained Beam and the British Steel and BRE Corner test analyses the softening of the steel causes its P-Δ bending deflection component to reduce, while the slab is capable of carrying the load by spanning across the heated beam, hence producing 'pull-back'. In the Plane Frame test, the concrete cannot span from the adjacent beams, and the effect of slab thickness is negligible. In contrast, the Large Compartment and Demonstration tests include large sections of heated floor. There is therefore very little opportunity for the slab to span across the fire-affected steel members to supports, and the effect of the floor slab thickness is negligible.

The secondary beam connections do occasionally have a small effect on the structural performance, although this only occurs when the concrete floor slab has extensively cracked so that a heated beam acts in the same way as an isolated beam. In large test compartments the effect of the secondary beam connection strength and stiffness is negligible. Questions have been raised about the validity of design procedures which rely on the stiffness of connections in a fire, because of the commonly observed formation of a local buckle of the lower flange close to the supports, greatly reducing the joint stiffness. This could perhaps be studied using VULCAN by simply placing a spring element at the position on the steel beam where a buckle will occur (assuming either a known or predicted position). The spring element would be required to maintain stiffness equivalent to that of the steel beam until the conditions at which the buckle is expected to form occur. Such conditions could be calculated in terms of the combination of the axial thrust and connection moment, given the known strength and stiffness reductions due to the elevated temperatures. This could at some stage be taken further so that a 'buckling spring element' is included at the ends of beams, and where steel beams cross the boundary of a fire compartment. The 'buckling spring element' would base its moment-rotation curve on a combination of material degradation and the local buckling strength at the relevant temperature. Once the buckling strength is exceeded, the buckle may be assumed to have formed and so the

rotational and axial stiffnesses would be sharply decreased. The buckling capacity could be estimated using methods similar to those used by British Steel [72].

A further program modification which might relieve the heavy computational work in modelling extensive subframes is to use a 'super-element'. This would involve defining an entire storey (or perhaps a whole building), apart from the actual fire compartment, as a single element. This 'super-element' would then provide the elastic stiffnesses around the perimeter nodes of the fire compartment, allowing a considerably smaller subframe to be used with rotational and axial stiffnesses positioned around the perimeter nodes to simulate the action of the surrounding building.

8.2 Modelling Floor Slabs Using Laminated Flat Shell Elements

Bailey [44] and the author have shown that the structural effects of the floor slab acting compositely with the supporting steel frame have a significant effect on the building behaviour during a fire. Analytical work previous to Bailey's included the floor slabs only as the flanges of composite beams, using the effective width concept, and thus ignoring the continuous nature of the floor slab. Including the continuous slab has two significant effects as follows:

- The floor slab gives rise to greater deflections at lower temperatures as it restrains the expansion of the steel beam and therefore increases the thermal curvature effect.

- The floor slab may bridge from adjacent cool members, diverting load paths away from weakening heated members. It is possible that structural collapse may be avoided when very high temperatures are reached due to this bridging action.

Bailey's floor slab model [44] used an isotropic flat shell element with nodal points coinciding with those of the one-dimensional beam-column elements to create full-interaction composite action. The concrete floor slab was assumed to be linear-elastic with cracking behaviour modelled by reducing its thickness so that a maximum stress gradient was not exceeded.

Extending the flat shell element to a layered formulation has enabled greater accuracy in the inclusion of material non-linearities, anisotropic properties, thermal expansion and bowing, material degradation and a more sophisticated concrete cracking model. These were incorporated into VULCAN successfully and were validated extensively for convergence errors at elevated temperatures and against closed-form solutions. The flat shell element was then validated against test data for a simple concrete slab loading test at ambient temperature, and against two composite beam tests at elevated temperature.

Following this development a brief study using the new laminated slab element was conducted on a subframe comprising a single beam and a concrete floor slab, simply supported on all four sides, exposed to increasing temperatures. Firstly, the subframe was studied using different cracking assumptions, of which the best option appeared to be uni-directional cracking as defined by normal stresses. This was also the method used in the test validations. The second study concerned the influence of boundary conditions, and confirmed that bridging clearly takes place in circumstances where the slab may span across supports. The third study looked at the effect of slab thickness, showing that a thin slab may induce 'run-away' due to cracking of the slab; this causes the beam to act as if it is isolated. The fourth and final study involved the effect of the slab temperature gradient. This concluded that the more severe temperature gradients produced larger deflections than uniform temperature patterns.

The current method of modelling the slab gives a reasonably good representation, although extra improvements could be made, as follows:

Partial Composite Action

Slip between steel beam and concrete slab may be incorporated into the formulation using a shear element to join the slab to the beam. These elements would be sited between the beam and slab nodes, and would model the shear characteristics of the stud connectors as temperatures rise.

Improved Material Model for Concrete

The current layered cracking model appears to result in structural behaviour which is considerably 'over-stiff', especially when considered in a case such as the restrained

beam test where in the latter stages bridging of the slab takes effect. Huang [66] has already implemented a more sophisticated model in VULCAN (as discussed in Section 5.11.1). Other possibilities for the continued development of VULCAN could be to use principal stresses at each of the gauss points, rather than the current system of orthogonal cracking across the whole element. Another improvement would be to replace the simple cracking envelope for the concrete with one such as that used by Rots and Blaauwendraad [70] or Feenstra and De Borst [71].

CONCRETE SPALLING

Spalling of concrete when subject to elevated temperatures is a subject that has only recently begun to be researched in detail. This has two important effects. Firstly, it progressively reduces the thickness of the slab and consequently reduces its moments of area which control stiffness. Secondly, it removes the protective effect of the lower layers of concrete from the reinforcement mesh, allowing it to heat very rapidly. In the latter case a real collapse of a slab is a distinct possibility, leading to breaches in compartmentation and possible fire spread. Both effects could clearly be implemented within the slab formulation, but are in need of input from detailed research on the spalling phenomenon itself.

However, when concrete spalling is considered for a slab arrangement that uses profiled steel decking as permanent formwork (as at Cardington), the concrete cannot fall away and will hence contribute with slightly reduced insulation properties.

GEOMETRIC NON-LINEARITIES

A basic improvement which could be made to the floor slab simulation is to take into account the effects of geometric non-linearity [47]. This is important at high deflections, where the lengths of the element's middle surface differs considerably from their horizontal projection, as shown in Figure 8-01. This results in a 'P-Δ' effect from lateral stress so that (depending on the boundary conditions) the deflection of the slabs may be greatly affected.

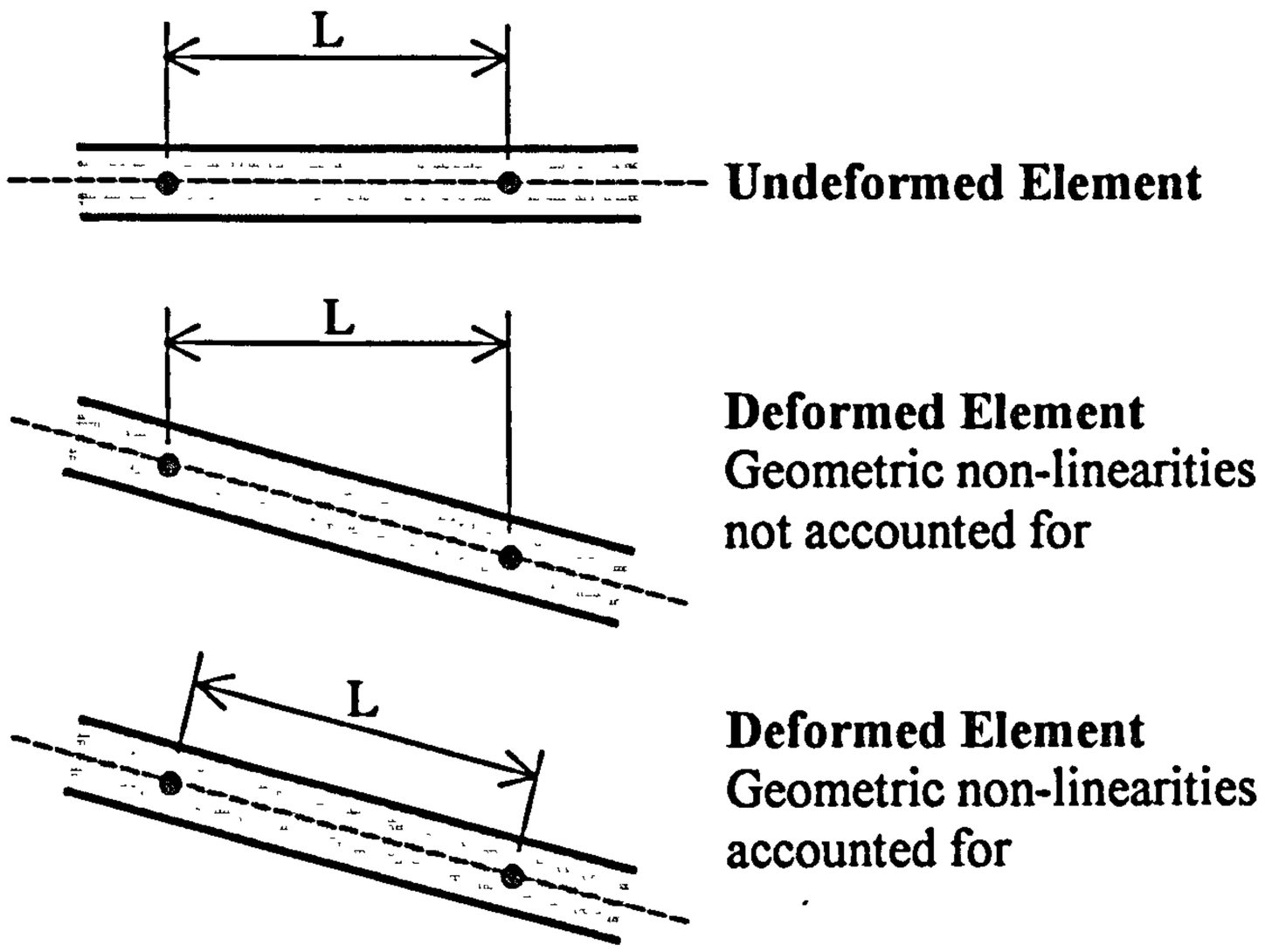

Figure 8-01. Slab element geometric non-linearities

TEMPERATURE PROFILES

In the current version of VULCAN the temperature profile through the floor slab has been simplified so that a uniformly increasing gradient is maintained at all times. This should be generalised to include more specific temperature profiles, including for instance the plateau at about 100°C which tends to happen for some time as the water content of the concrete is evaporated. This is detailed in Chapter 2.

Another possibility for future development could be to include a heat transfer model within the analysis.

MODELLING OF REINFORCEMENT

Reinforcement within the slab could be modelled using a different method from the smearing technique now used for elastic modulus and strength. A new method is currently being investigated at Delft University of Technology in which the Gauss points within the plate elements are 'weighted' to simulate the reinforcement. As no publications have yet been published, little is known of this method and its possible relevance to VULCAN. Alternatively, it is possible to use steel line elements between existing slab nodes to represent bars, either individually or collectively which may be a better way to implement reinforcement into VULCAN. One drawback this latter method has is that it obviously requires many more elements, potentially increasing the computing time and power required.

8.3 General Analysis of the Cardington Studies

A comparison against current design documents was made for the fully continuous analysis of the Restrained Beam test, the Plane Frame test, the BRE Corner test and the Large Compartment test. The current design guides are based on the assumption of isolated beams with composite concrete flanges of different effective widths. This has been compared against skeletal frame models including an effective-width concrete flange, fully continuous floor slab grillages for both the isotropic and layered slab elements and the test results. The results indicate that the assumptions made in the design guides give much higher deflections than those found when using a continuous structure, either in analysis or in reality, for all four tests analysed. This ultimately leads to unnecessarily conservative and expensive design, particularly where bridging of the floor slab can easily take place.

It is perhaps advisable that design documents should be extended to allow the modern fire engineer to use finite element software to model the continuous structure, as this will lead to more efficient protection strategies. It is of course essential that such modelling should be carried out with care and some insight into the behaviour. This is allowed in the new Eurocodes, but will probably remain the province of relatively specialised engineers for some years to come. For the benefit of general structural designers it is now possible to use finite element software such as VULCAN to examine a range of scenarios with typical fire compartments to postulate simplified guidelines for use in routine design.

8.4 Concluding Remark

The future of structural fire engineering must be based on a realistic appreciation of the behaviour of continuous structures in fire, relative to the basic requirements of integrity and stability. The existing 'standard furnace test' on isolated elements gives no real indication of the performance in the majority of cases, although it usually constitutes a very loose lower bound to the behaviour. This could be advanced using reliable finite element models. It may be argued that as fire is an accidental occurrence, these models should only consider the ultimate integrity of the structure. Considering a building as an entity could perhaps allow local failure in the form of buckling and member deformation, provided that disproportionate collapse is avoided;

this is perhaps the direction that future design guides should take. If this is adopted, fire protection of many secondary and main beams may be unnecessary, providing that slab continuity is maintained. This would lead to much less expensive structures with no loss of safety and to reduced construction times. However, fire resistance of loaded columns is required in most cases, and this may require some passive protection. This is a much more convenient process on site, which causes only minimal disruption to other activities.

9 REFERENCES

1. *Fire Safe Steel Structures – Benefits for Economy and Architecture*
   International Seminar, Luxembourg, 1994.
2. Read, R.E.H. and Morris, W.A.
   Aspects of Fire Precautions in Buildings,
   Building Research Establishment, 1983.
3. *The Building Regulations, Approved Document B: Fire Safety*
   Department of the Environment and the Welsh Office, HMSO, 1991.
4. Latter, R.,
   The European Market for Construction Steelwork
   New Steel Construction, **2** (5), October 1994.
5. *BS 476: Fire Tests on Building Material and Structure, Part 21: Methods of Determination of the Fire Resistance of Load-bearing Elements of Construction*
   BSI, London, 1987.
6. *ISO 834: Fire Resistance Tests – Elements of Building Construction*
   1985.
7. *BS 476: Fire Tests on Building Material and Structure, Part 20: Method of Determination of the Fire Resistance of Elements of Construction (General Principles)*
   BSI, London, 1987.
8. *BS 449: The Use of Structural Steelwork in Building*
   BSI, London, 1969.
9. *BS 5950: Structural Use of Steelwork in Building, Part 8: Code of Practice for Fire Resistant Design*
   BSI, London, 1990.
10. *Eurocode 3: Design of Steel Structures: Part 1.2:Structural Fire Design (Draft)*
    European Committee for Standardisation, 1993.
11. *Eurocode 4: Design of Composite Steel and Concrete Structures (Draft): Part 1.2: Structural Fire Design*
    European Committee for Standardisation, 1992.
12. Lawson, R.M. and Newman, G.M.
    Fire Resistant Design of Steel Structures – A Handbook to BS5950: Part 8
    The Steel Construction Institute, 1990.
13. Kirby, B.R. and Preston, R.R.
    High Temperature Properties of Hot-rolled Structural Steels for Use in Fire Engineering Studies
    Fire Safety Journal, **13**, 1988, pp90-102.
14. Wainman, D.E. and Kirby, B.R.
    Compendium of UK Standard Fire Test Data on Unprotected Structural Steel
    British Steel Report (Swinden Labs), 1987.
15. Bravery, P.N.R.
    Cardington Large Building Test Facility, Construction Details for the First Building
    BRE, 1993.

16. Owens, G.W. and Knowles, P.R.
Steel Designers Manual: 5th Edition
The Steel Construction Institute, 1994.

17. Kirby, B.R.
ECSC Project: Behaviour of a Multi-storey Steel Framed Building Subject to Natural Fires; Test 1: Restrained Beam; Data Files: Temperature Measurements (Draft)
British Steel plc, 1995.

18. Kirby, B.R.
ECSC Project: Behaviour of a Multi-storey Steel Framed Building Subject to Natural Fires; Test 1: Restrained Beam; Data Files: Deflection Measurements (Draft), Part D1
British Steel plc, November 1995.

19. Kirby, B.R.
ECSC Project: Behaviour of a Multi-storey Steel Framed Building Subject to Natural Fires; Test 1: Restrained Beam; Data Files: Deflection Measurements (Draft), Part D2
British Steel plc, December 1995.

20. Kirby, B.R.
ECSC Project: Behaviour of a Multi-storey Steel Framed Building Subject to Natural Fires; Test 1: Restrained Beam; Data Files: Rotation Measurements (Draft)
British Steel plc, 1995.

21. Kirby, B.R.
ECSC Project: Behaviour of a Multi-storey Steel Framed Building Subject to Natural Fires; Test 1: Restrained Beam; Data Files: Strain Gauge Measurements (Draft)
British Steel plc, 1995.

22. Newman, G.M.
Investigation of the Broadgate Phase 8 Fire. Structural Fire Engineering
The Steel Construction Institute, 1990.

23. Bailey C.G., Burgess I.W. and Plank R.J.
Computer simulation of a full-scale fire test
The Structural Engineer, 1996, **74**, No. 6, pp 93-100.

24. Najjar, S.R., Burgess, I.W. and Plank, R.J.
Non-linear studies of the Cardington Composite Frame in Fire Conditions Using 3DFIRE
DCSE/93/7, University of Sheffield, 1993.

25. Kirby, B.R.
ECSC Project: Behaviour of a Multi-storey Steel Framed Building Subject to Natural Fires; Test 2: Plane Frame; Data Files: Temperature Measurements (Draft), Part T1
British Steel plc, July 1996.

26. Kirby, B.R.
ECSC Project: Behaviour of a Multi-storey Steel Framed Building Subject to Natural Fires; Test 2: Plane Frame; Data Files: Temperature Measurements (Draft), Part T2
British Steel plc, December 1996.

27. Kirby, B.R.
ECSC Project: Behaviour of a Multi-storey Steel Framed Building Subject to Natural Fires; Test 2: Plane Frame; Data Files: Deflection / Displacement Measurements (Draft)
British Steel plc, 1996.

28. Kirby, B.R.
ECSC Project: Behaviour of a Multi-storey Steel Framed Building Subject to Natural Fires; Test 2: Plane Frame; Data Files: Rotation Measurements (Draft)
British Steel plc, 1996.

29. Kirby, B.R.
ECSC Project: Behaviour of a Multi-storey Steel Framed Building Subject to Natural Fires; Test 2: Plane Frame; Data Files: Strain Gauge Measurements (Draft)
British Steel plc, 1996.

30. Kirby, B.R.
ECSC Project: Behaviour of a Multi-storey Steel Framed Building Subject to Natural Fires; Test 3: Corner Compartment; Data Files: Temperature Measurements (Draft); Part T1
British Steel plc, September 1996.

31. Kirby, B.R.
ECSC Project: Behaviour of a Multi-storey Steel Framed Building Subject to Natural Fires; Test 3: Corner Compartment; Data Files: Temperature Measurements (Draft); Part T2
British Steel plc, December 1996.

32. Kirby, B.R.
ECSC Project: Behaviour of a Multi-storey Steel Framed Building Subject to Natural Fires; Test 3: Corner Compartment; Data Files: Temperature Measurements (Draft); Part T3
British Steel plc, December 1996.

33. Kirby, B.R.
ECSC Project: Behaviour of a Multi-storey Steel Framed Building Subject to Natural Fires; Test 3: Corner Compartment; Data Files: Deflection / Displacement Measurements (Draft)
British Steel plc, 1996.

34. Kirby, B.R.
ECSC Project: Behaviour of a Multi-storey Steel Framed Building Subject to Natural Fires; Test 3: Corner Compartment; Data Files: Rotation Measurements (Draft)
British Steel plc, 1996.

35. Kirby, B.R.
ECSC Project: Behaviour of a Multi-storey Steel Framed Building Subject to Natural Fires; Test 3: Corner Compartment; Data Files: Strain Gauge Measurements (Draft)
British Steel plc, 1996.

36. Lennon, T.
Cardington Fire Tests: Instrumentation Locations for Corner Fire Test
B.R.E., 1995.

37. Lennon, T.
Cardington Fire Tests: Instrumentation Locations for the Large Compartment Fire Test
B.R.E., 1996.

38. Kirby, B.R.
ECSC Project: Behaviour of a Multi-storey Steel Framed Building Subject to Natural Fires; Test 4: Office Fire (Demonstration); Data Files: Temperature Measurements (Draft); Part T1
British Steel plc, October 1996.

39. Kirby, B.R.
ECSC Project: Behaviour of a Multi-storey Steel Framed Building Subject to Natural Fires; Test 4: Office Fire (Demonstration); Data Files: Temperature Measurements (Draft); Part T2
British Steel plc, December 1996.

40. Kirby, B.R.
ECSC Project: Behaviour of a Multi-storey Steel Framed Building Subject to Natural Fires; Test 4: Office Fire (Demonstration); Data Files: Temperature Measurements (Draft); Part T3
British Steel plc, December 1996.

41. Kirby, B.R.
ECSC Project: Behaviour of a Multi-storey Steel Framed Building Subject to Natural Fires; Test 4: Office Fire (Demonstration); Data Files: Deflection Measurements (Draft)
British Steel plc, 1996.

42. Kirby, B.R.
ECSC Project: Behaviour of a Multi-storey Steel Framed Building Subject to Natural Fires; Test 4: Office Fire (Demonstration); Data Files: Strain Gauge Measurements (Draft); Part T3
British Steel plc, 1996.

43. *First Results from the Large Building Test Facility*
First Cardington Conference, B.R.E., 16 - 17 November 1994.

44. Bailey C.G.
Simulation of the Structural Behaviour of Steel-Framed Buildings in Fire
PhD Thesis, University of Sheffield, 1995.

45. El-Zanaty, M.H. and Murray, D.W.
Non-linear Finite Element Analysis of Steel Frames
ACSE J. Struct. Div., 1983, **109** (ST2) pp. 353-368

46. Zienkiewicz, O.C. and Taylor, R.L.
The Finite Element Method. Fourth Edition, Volume 1: Basic Formulation and Linear Problems
McGraw-Hill Book Company, 1991.

47. Zienkiewicz, O.C. and Taylor, R.L.
The Finite Element Method. Fourth Edition, Volume 2: Solid and Fluid Mechanics, Dynamics and Non-linearity
McGraw-Hill Book Company, 1991.

48. Bathe, K. and Wilson, E.L.
Numerical Methods in Finite Element Analysis.
Prentice-Hall, Inc., 1976.

49. Saab, H.A.
Non-linear Finite Element Analysis of Steel Frames
PhD Thesis, University of Sheffield, 1990.

50. Saab, H.A. and Nethercot, D.A.
Modelling Steel Frame Behaviour under Fire Conditions
Engineering Structures, **13** (4), 1991, pp. 371-382.

51. Najjar, S.R.
Three-dimensional Analysis of Steel Frames and Subframes in Fire
PhD Thesis, University of Sheffield, 1994.

52. Lawson, R.M.
Enhancement of Fire Resistance of Beams by Beam to Column Connections
Technical Report SCI, Publication 086, 1990.

53. El-Rimawi, J.A., Burgess, I.W. and Plank, R.J.
Modelling the behaviour of steel frames and subframes with semi-rigid connections in fire
University of Sheffield, Department of Civil and Structural Engineering, Research Report DCSE/93/S/02, 1993.

54. Leston-Jones, L.
The Influence of Semi-Rigid Connections on the Performance of Steel Framed Structures in Fire
PhD Thesis, University of Sheffield, 1997.

55. Al-Jabri, K.S., Lennon, T., Burgess, I.W. and Plank, R.J.
Behaviour of Steel and Composite Beam-Column Connections in Fire
2nd World Conference on Steel in Construction, Proceedings, 1998.

56. Bathe, K. and Dvorkin, E.N.
Short Communication: A four-node plate bending element based on Mindlin/Reissner plate theory and a mixed interpolation
International Journal for Numerical Methods in Engineering, 1985, **21**, pp. 367-383.

57. Crisfield, M.A.
A Fast Incremental / Iterative Solution Procedure that Handles 'Snap-Through'
Computers and Structures Journal, Vol. 13, pp 55-62.

58. Kirby, P.A. and Nethercot, D.A.
Design for structural stability
Collins, 1985.

59. Shepherd, P.G.
Performance of Restrained Columns in Steel-Framed Construction
E.P.S.R.C. Final Report, Project Number GR/K61593,December 1998.

60. Meek, J.L.
Computer Methods in Structural Analysis
Chapman and Hall, 1991.

61. Howlett, J.H., Jenkins, W.M. and Stainsby, R.
Joints in Structural Steelwork
Pentech Press, 1981.

62. Hinton, E. and Owen, D.R.J.
Finite Element Software for Plates and Shells
Pineridge Press, 1984.

63. Timoshenko, S., and Woinowsky-Krieger, S.
Theory of Plates and Shells
McGraw-Hill, 1959.

64. Timoshenko, S., and Goodier, J.N.
Theory of Elasticity
McGraw-Hill, 1970.

65. Duddeck, H., Griebenow, G. and Shaper, G.
Material and Time Dependant Non-linear Behaviour of Cracked Reinforced Concrete Slabs
Non-linear Behaviour of Reinforced Concrete Spatial Structures, Volume 1, Preliminary Report IASS Symposium held in Darmstadt, Editors Mehlhorn, G., Ruhle, H. and Zerna, W., Dusseldorf, pp101-113, 1978.

66. Huang, Burgess, I.W. and Plank, R.J.
Non-linear Analysis of Reinforced Concrete Slabs Subject to Fire
DCSE/97/F/3, University of Sheffield, 1997.

67. *CP 117: Composite Construction in Structural Steel and Concrete*
BSI, London, 1965.

68. *BS8110: Structural Use of Concrete, Part 2: Code of Practice for Special Conditions*
BSI, London, 1985.

69. Lawson, R.M.
Behaviour of Steel Beam to Column Connections in Fire
The Steel Construction Institute, 1989.

70. Rots, J.G. and Blaauwendraad, J.
Crack Models for Concrete: Discrete or Smeared? Fixed, Multidirectional or Rotating?
Heron, Delft University of Technology, The Netherlands, 1989.

71. Feenstra, P.H. and De Borst, R.
Aspects of Robust Computational Modelling for Plain and Reinforced Concrete
Heron, Delft University of Technology, The Netherlands, 1993.

72. O'Connor, M.A. and Martin, D.M.
Behaviour of a Multi-storey Steel Framed Building subjected to Fire Attack
2nd World Conference on Steel in Construction, Proceedings, 1998.

73. Witteveen, J.
Some aspects with regard to the behaviour of the calculation of steel structures in fire
Symposium N°. 2 – Behaviour of Structural Steel in Fire, Fire Research Station, Borehamwood, Herts, 24th January 1967.

74. Marchant, E.
A Complete Guide to Fire and Buildings
Medical and Technical Publishing Company, London, 1972.

75. Knight, D.
The Behaviour of Steel Structures in Fire
BHP Technical Bulletin, **16** (2), November 1972.

76. Culver, C.G.
Steel column buckling under thermal gradients
ASCE J. Struct Div., 1972, **98** (ST8), pp 1853 – 1865.

77. Ossenbrugen, P.J., Aggarwal, V., and Culver, C.G.
Steel column failure under thermal gradients
ASCE J. Struct Div., 1973, **99** (ST4), pp 727 – 739.

78. Ossenbrugen, P.J., Aggarwal, V., and Culver, C.G.
Buckling of steel columns at elevated temperatures
ASCE J. Struct Div., 1973, **99** (ST4), pp 1054 – 1071.

79. Brockenbrough, R.
Theoretical stresses and strains from heat curving
ASCE J. Struct Div., 1973, **99** (ST4) pp 1421 – 1444.

80. Cheng, W. and Mak, K.
Computer analysis of steel frames in fire
ASCE J. Struct Div., 1970, **96** (ST7), pp 855 – 867.

81. Furumura, F., and Shinohara, Y.
Inelastic behaviour of protected steel beams and frames in fire
Report of the Research Laboratory of Engineering Materials, N°. 3, 1978, pp 1 – 14.

82. Kruppa, J.
Collapse temperature of steel structures
ASCE J. Struct Div., 1979, **105** (ST7), pp 1769 – 1787.

83. Iding, R., and Bresler, B.
Effect of fire exposure on steel frame buildings
Final Report, WJE N°. 78124 Jannay Elstner and Associates Inc., September 1979.

84. Jain, P. and Rao, R.
Analysis of steel frames under fire environment
Int. Journal for Numerical Methods in Engineering, 1983, **19**, pp 1467 – 1478.

85. Baba, S., and Nagura, H.
Effect of material properties on the deformation of steel frames in fire,
Proceedings of JSCE Structural Eng./Earthquake Eng., 1985, **2** (1), pp 47 – 57.

86. Dotreppe, J., Franssen, J., and Schleich, J.
Numerical simulation of fire resistance tests on steel and composite structural elements and frames
Fire Safety Science – Proceedings of the First International Symposium, October 1985.

87. Sharples, J.R.
The Strength of Partially Exposed Steel Columns in Fire
MPhil Thesis, University of Sheffield, 1987.

88. Olawale, A.O.
Collapse Behaviour of Steel Columns in Fire
PhD Thesis, University of Sheffield, 1988.

89. Olawale, A.O. and Plank, R.J.
The collapse analysis of steel columns in fire using a finite strip method
Int. Journal for Numerical Methods in Engineering, 1988, **26**, pp 2755 – 2764.

90. El-Rimawi, J.
The Behaviour of Flexural Members under Fire Conditions
PhD Thesis, University of Sheffield, 1989.

91. Burgess, I.W., El-Rimawi, J. and Plank, R.J.
A secant stiffness approach to the fire analysis of steel beams
J. Constr. Steel Research, 1988, **11**, pp 105 – 120.

92. Jeyarupalingam, N. and Virdi, K.S.
Steel Beams and Columns Exposed to Fire Hazard. Structural Design for Hazardous Loads
Edited by J.L. Clarke, F.K. Garas and G.S.T. Armer, E & FN Spon, 1992.